Award Number:
W81XWH-10-1-0149

TITLE:
Cytoprotection: Immune and Matrix Modulation of Tissue Repair

PRINCIPAL INVESTIGATOR:
Gerald T. Nepom, MD, PhD

CONTRACTING ORGANIZATION:
Benaroya Research Institute at Virginia Mason, Seattle, WA 98101

REPORT DATE:
April 2013

TYPE OF
REPORT: Final

PREPARED FOR: U.S. Army Medical Research and Materiel Command
Fort Detrick, Maryland 21702-5012

REPORT DOCUMENTATION PAGE

Form Approved
OMB No. 0704-0188

1. REPORT DATE	2. REPORT TYPE	3. DATES COVERED
April 2013	Final	**15 March 2010 – 14 March 2013**

4. TITLE AND SUBTITLE
Cytoprotection: Immune and Matrix Modulation of Tissue Repair

5a. CONTRACT NUMBER

5b. GRANT NUMBER
W81XWH-10-1-0149

5c. PROGRAM ELEMENT NUMBER

6. AUTHOR(S)
Gerald T. Nepom, MD, PhD
Robert B. Vernon, PhD

E-Mail: nepom@benaroyaresearch.org

5d. PROJECT NUMBER

5e. TASK NUMBER

5f. WORK UNIT NUMBER

7. PERFORMING ORGANIZATION NAME(S) AND ADDRESS(ES)
Benaroya Research Institute at Virginia Mason
Seattle, WA 98101-2795

8. PERFORMING ORGANIZATION REPORT NUMBER

9. SPONSORING / MONITORING AGENCY NAME(S) AND ADDRESS(ES)
U.S. Army Medical Research and Materiel Command
Fort Detrick, Maryland 21702-5012

10. SPONSOR/MONITOR'S ACRONYM(S)

11. SPONSOR/MONITOR'S REPORT NUMBER(S)

12. DISTRIBUTION / AVAILABILITY STATEMENT
Approved for Public Release; Distribution Unlimited

13. SUPPLEMENTARY NOTES

14. ABSTRACT
Our overall goal was to create new therapies to regulate tissue reparative processes through the use of specific extracellular matrix (ECM) components, which play a significant role in regulating the inflammatory processes that follow injury, creating cytoprotective environments that promote healing. Focusing on aspects of tissue repair, we invented ECM scaffolds comprised of engineered proteoglycans and natural collagen, which emphasize enhancement of elasticity, strength, and cellular integration with the host. Subsequently, we refined our studies to address a key challenge to clinical application of this technology, the host inflammatory response. We have met the goals of our two multi-part aims to: (1) identify novel cytoprotective mediators associated with regulatory lymphocytes and innate immune activation and (2) use cytoprotective ECM hydrogels to promote the development of function and host-integration of a novel skeletal muscle implant (the "myobridge"), designed to replace native skeletal muscle lost to traumatic injury. We completed the project with the benefit of an approved no-cost extension.

15. SUBJECT TERMS
Inflammation, tissue repair, extracelluar matrix, collagen scaffolds, cytoprotection

16. SECURITY CLASSIFICATION OF:			17. LIMITATION OF ABSTRACT	18. NUMBER OF PAGES	19a. NAME OF RESPONSIBLE PERSON
a. REPORT	b. ABSTRACT	c. THIS PAGE			USAMRMC
U	U	U	UU	167	19b. TELEPHONE NUMBER *(include area code)*

Table of Contents

Final Report

..... Page

List of Personnel.....4

Introduction.....5

Body.....6

Aim 1 Task 1 7
Task 2.....7
Task 3.....8
Task 4.....12
Task 5.....21
Task 6.....23
Task 7.....24
Task 8.....29
Aim 2 Task 9 31
Task 10.....43
Task 11.....48
Task 12.....61
Task 13.....63
Task 14.....70
Task 15.....71

Key Research Accomplishments.....71

Reportable Outcomes 76

Conclusion 80

Appendices.....86

List of Personnel Receiving Pay from the Research Effort

1	Nepom, Gerald	MD, PhD
2	Allen, Margaret	MD
3	Buckner, Jane	MD
4	Cerosaletti, Karen	PhD
5	Hamerman, Jessica	PhD
6	Sanda, Srinath	MD
7	Vernon, Robert	PhD
8	Ziegler, Steven	PhD
9	Aye, Theingi	
10	Beauchamp, Mary	
11	Chen, Janice	
12	D'Amico, Leonard	PhD
13	Dennis, James	PhD
14	DeSouza, Anjali	
15	Gebe, John	PhD
16	Gessay, Griffin	
17	Gooden, Michel	
18	Han, Hongwei	PhD
19	Kitajima, Masayuki	PhD
20	Kinsella, Michael	PhD
21	Lo Kuan, Emma	PhD
22	Luo, Jun	PhD
23	Ma, Sheree	
24	McCulloch-Olson, Marli	
25	Nguyen, Tuan	
26	Ni, Minjian	PhD
27	Pang, Lisa	
28	Preisinger, Anton	
29	Petty, Loreen	
30	Pfleger, Christian	PhD
31	Pottle, Jessica	
32	Robbins, Aleksandr	
33	Thorpe, Jerill	
34	Weaver, Matthew	PhD
35	Welikson, Robert	PhD
36	Wilson, Heather-Marie	PhD
37	Xu, Whitney	
38	Yue, Betty	

USAMRMC Award No: **W81XWH-10-1-0149**

Project Title: **Cytoprotection: Immune and Matrix Modulation of Tissue Repair**

Report: **FINAL REPORT (3/15/10 – 3/14/13)**

1. INTRODUCTION

1.1 Subject, Purpose, and Scope of the Research

Recent advances in molecular and cellular biology offer an opportunity to create new therapies to regulate tissue reparative processes through the use of specific extracellular matrix (ECM) components, which play a significant role in regulating the inflammatory processes that follow injury, creating cytoprotective environments that promote healing. Prior to the current project, the Benaroya Research Institute's Center for Inflammation and Tissue Repair (CITR) developed a number of tissue repair strategies that utilized engineered ECM scaffolds comprised of proteoglycans and natural collagen, which emphasized enhancement of elasticity, strength, cellular survival and orientation, and optimal integration with host tissue. The current research program expands on this prior work to address a key challenge to clinical application of our engineered tissue repair technology – the host inflammatory response. This new program in *cytoprotection* addresses a major barrier to effective cell-based therapies, namely, that, after treatment with regenerating or reconstituted cells or stem cells, the viability of those therapeutic cells is often threatened by the noxious microenvironment of inflamed tissue.

The research program consists of a coordinated set of projects that address two Specific Aims (listed below). The goal of projects in Aim 1 is to develop and evaluate specific cytoprotective modulators of tissue-immune interactions. The goal of Aim 2 is to develop an engineered tissue model (a "myobridge" for replacement of skeletal muscle) and use it as a test-bed to evaluate promising cytoprotective strategies identified in Aim 1 for their capacity to control inflammation, improve cell survival, and promote healing.

1.2 Specific Aims

Aim 1 To develop ECM hydrogels with cytoprotective properties, including mechanical resistance to shear, binding sites for specific bioactive molecules, and sites for retention of regulatory lymphocytes. Novel cytoprotective mediators associated with regulatory lymphocytes and innate immune activation will be identified using siRNA (human and mouse) and knockout animal models, and potential biomarkers for monitoring efficacy in humans will be evaluated in a pilot clinical research study.

Aim 2 To use cytoprotective ECM hydrogels in customized skeletal muscle implants to evaluate a novel engineered tissue, referred to as a "myobridge," designed to enable rapid reconstruction of extensive skeletal muscle wounds. Cytoprotection from inflammation-mediated damage, vascularization, and myocyte differentiation within the graft will be evaluated.

This Final Report includes all work performed under Tasks 1–15.

1.3 Scope of this Report

Aim 1 was organized into **Tasks 1–8**. All work under Aim 1 was finished as of 3/14/12. Aim 2 was organized into **Tasks 9–15**. Aim 2 was continued as a no-cost extension through 3/14/13. This Final Report describes the results generated by work conducted under all 15 Task headings.

2. BODY

2.1. Statement of Work

The research program is 3 years in duration and is organized into 15 specific Tasks, which are indicated below.

Specific Aim 1: Cytoprotective Mechanisms of Immune Regulation

Task 1 *(Months 1–9)* Develop and test stable, shear-resistant HMW-HA/fibrillar collagen hydrogels on dye-cut 2.9 mm nylon mesh rings.

Task 2 *(Months 2–12)* Validate microwell plate assay for expression using murine T cells and hydrogel rings at collagen:HMW:HA ratios of 8:1, 4:1, 2:1, 1:1, 1:2, 1:4, and 1:8.

Task 3 *(Months 6–18)* Supplement hydrogel microwell GFP-FOXP3 assay with rapamycin, IL-10, and TGF-β, with and without gelatin sponge component.

Task 4 *(Months 1–12)* Perform flow cytometry assays for lineage deviation with 11 siRNA constructs (listed in the proposal) using human naïve CD4+ T cells.

Task 5 *(Months 12–24)* Evaluate *in vivo* candidate siRNA using DO11.10-Treg transfection.

Task 6 *(Months 1–8)* Evaluate siRNA for TREM-2 and DAP12 for inhibition of TNF production by THP-1 cells.

Task 7 *(Months 6–24)* Measure TLR activation by cytokine production and phospho-specific antibodies in CD18 and BCAP KO mice, and map BCAP domains as potential therapeutic targets.

Task 8 *(Months 6–24)* Measure serum biomarkers in 20 human subjects treated with IL1RA after inflammatory stimulus.

Specific Aim 2: The CITR Cytoprotective Implant (CI) and Myobridge

Task 9 *(Months 3–12)* Production of the three-layer CI "sandwich".

Task 10 *(Months 6 –16)* Evaluation of prototype CI in rat dermal pockets for histological monitoring of biodegradation and in mouse dermal pockets for evaluation of regulatory T cell responses.

Task 11 *(Months 1–12)* Development of myobridges using uniaxial supports and collagen gels populated with myoblast cells. Histological evaluation of cultured myobridges for cell survival, new muscle cell generation, proliferation and differentiation.

Task 12 *(Months 12–24)* Implantation of cell-seeded myobridge into female F344 rat anterior tibialis, with histological analysis after 3 weeks.

Task 13 *(Months 12–24)* Supplementation of myobridge with CoPP and regulatory modulators from Aim 1, prior to implantation.

Task 14 *(Months 16–24)* Co-transplantation of myobridge and CI to evaluate effects of CI-mediated immunomodulation on integration of the myobridge with host tissues.

Task 15 *(Months 18–24)* *In vitro* seeding of myobridge prototypes with human MDSC for evaluation of human cell compatibility with hydrogel components.

2.2. Final Report for Aim 1 (Tasks 1–8) and Aim 2 (Tasks 9–15)

Tasks 1, 2, and 3

Tasks 1, 2, and 3 were components of Aims 1A and 1B, which focused on development of high molecular weight hyaluronan (HMW-HA)-based hydrogels as a delivery system for sustained release of growth factors and cytokines. HMW-HA is a polysaccharide glycosaminoglycan (GAG) found in many tissues, which has natural cytoprotective and wound repair-promoting properties. HMW-HA is associated with tissue repair as a consequence of its unique mechano-chemical properties (e.g., a hygroscopic character, viscoelasticity, and high negative charge) and its ability to modulate cell behavior by interacting with other ECM molecules or with

specific cell surface receptors. Early response to tissue injury includes the formation of a provisional ECM rich in HMW-HA and fibrin, which supports fibroblastic invasion and penetration of new blood vessels into the wound site. In the past two years, our researchers have uncovered a novel anti-inflammatory mechanism for HA, in which HMW-HA acts as a co-stimulator of regulatory T cell (Treg) activation through binding of CD44v6, resulting in persistence of FOXP3 gene expression, a transcriptional regulator, which promotes maintenance of the regulatory phenotype. In Aim 1, we evaluated different approaches to retain HMW-HA in the wound or graft site for ultimate inclusion in our Cytoprotective Implant (Aim 2).

Task 1

Develop and test stable, shear-resistant HMW-HA/fibrillar collagen hydrogels on dye-cut 2.9 mm nylon mesh rings (Robert Vernon, PhD).

Task 1 evaluated the capacity of HMW-HA/fibrillar collagen hydrogels to adhere to nylon mesh rings as a basis for the microwell plate assay described in Task 2. The rings chosen were dye-cut from nylon (Nitex) mesh with a mesh weave of 100 micron square spacing providing an open space of 44% per unit area of mesh. This material is wettable by the hydrogel prior to crosslinking, meaning that the hydrogel will intercalate into the open spaces of the mesh to provide stable mechanical attachment. We observed that hydrogels with relatively high ratios of collagen adhered better than hydrogels with relatively high ratios of HMW-HA. In addition to Nitex nylon mesh, we also evaluated open-pore polyvinyl alcohol (PVA) sponge materials of various pore sizes. The 3-dimensional labyrinth of pores within these materials provided a significantly larger area for attachment of ECM hydrogels than standard nylon mesh, but without the associated problem of physical instability. We determined that PVA sponge with an average 90 micron pore diameter supported HMW-HA and other ECM (e.g., collagen) hydrogels adequately.

Conclusions, Task 1

It was determined in Task 2 (see below) that the microwell plate assay did not provide the sensitivity needed to evaluate GFP/FOXP3 expression in T cells and the analytical approach was shifted from the microwell assay to more conventional flow-cytometry methods. Notably, however, the use of PVA sponge as a support for ECM hydrogels was successfully translated into an *in vivo* model of immunomodulation, described in Tasks 3 and 10.

Task 2

Validate microwell plate assay for expression using murine T cells and hydrogel rings at collagen: HMW:HA ratios of 8:1, 4:1, 2:1, 1:1, 1:2, 1:4, and 1:8 (Gerald Nepom, MD, PhD).

Task 2 tested a microwell plate assay system for evaluating effects on GFP/FOXP3 induction in murine T cells. We first evaluated the Wallace Victor plate reader and the Packard Fusion fluorescence imager for their ability to discriminate levels of fluorescence seen with titrations of CD4+GFP/FOXP3+ sorted Treg or CFSE-labeled CD4+ T cells. The Packard fluorescence imager had by far greater sensitivity. Using this apparatus, we evaluated a variety of clear plastic cell culture systems. We found that only specifically-designed fluorescence analysis plates had low enough backgrounds to allow us to discriminate levels of fluorescence seen with titrations of CD4+GFP/FOXP3+ sorted Treg or fluorescently (CFSE)-labeled CD4+ T cells. Within this system, using fixed CFSE-labeled CD4+ T cells, we found no difference in the ability to detect fluorescence by cells (a) embedded within hydrogels, (b) plated on top of hydrogels, or c) plated on plastic alone without hydrogels present. Notably, however, the fluorescence analysis plates adversely affected the viability of CD4+GFP/FOXP3+ sorted Treg as well as CFSE-labeled CD4+ T cells such that all cells cultured with these plates were dead (as indicated by 7AAD/Annexin V positivity) within 48 hours. This effect on cell viability indicated that use of this system as a high-throughput assay for GFP/FOXP3 expression was not working adequately. Accordingly, we shifted our analytical approach towards conventional flow-cytometry methods, with which we have extensive experience.

In order to use conventional flow-cytometry to measure expression of GFP/FOXP3 by T cells cultured in 3-dimensional ECM hydrogels, the cells must be rapidly released from the gels for assay. To facilitate cell release, evaluated Extracel-SS™ — a HMW-HA hydrogel available from Glycosan Biosystems (Salt Lake City, UT) that incorporates a novel PEGSSDA crosslinker. PEGSSDA can be cleaved with low concentrations of disulfide bond reducing agent, thereby permitting liquefaction of the hydrogel for cell release while avoiding damage to the cells. In all other respects, this hydrogel biomaterial is identical to the HMW-HA formulation described in the original application. Using Extracel-SS as a support medium in combination with conventional flow cytometry, we established that a 2:2:1 ratio of HMW-HA:collagen (gelatin):PEGSSDA crosslinker induces the highest levels of GFP/FOXP3 expression by cultured Treg. This ratio is the same as that recommended for lymphocyte work by the manufacturer.

Conclusions, Task 2

We determined that the microplate assay was problematic with respect to signal sensitivity and T cell viability; therefore, we shifted our analytical approach to conventional flow-cytometry, adapting an existing HMW-HA hydrogel formulation to this form of readout. This hydrogel became the basic support medium for our studies performed in Task 3.

Task 3 Supplement hydrogel microwell GFP-FOXP3 assay with rapamycin, IL-10, and TGF-β, with and without gelatin sponge component (Gerald Nepom, MD, PhD).

As mentioned in the narrative for Task 2 above, we found it was not possible to use the microwell format to analyze GFP/FOXP3 induction results and, therefore, we switched to flow-cytometry-based analysis. Using this approach, we evaluated the effects of gelatin sponge inclusion on FOXP3 induction. We found that the gelatin sponge added structural integrity to the gel such that it can be manipulated for assay. However, upon the inclusion of T cells in the hydrogel, the gelatin sponge is degraded within 3-4 days, indicating that these cells produce collagenases. The gelatin sponge appears to have no discernable impact on FOXP3 induction, perhaps because there is already gelatin in the Extracel HA hydrogel preparation. In sum, these data suggest to us that the gelatin sponge adds structural integrity to hydrogels polymerized *in vitro* and that there is no functional disadvantage vis-à-vis FOXP3 induction to having the gelatin sponge present.

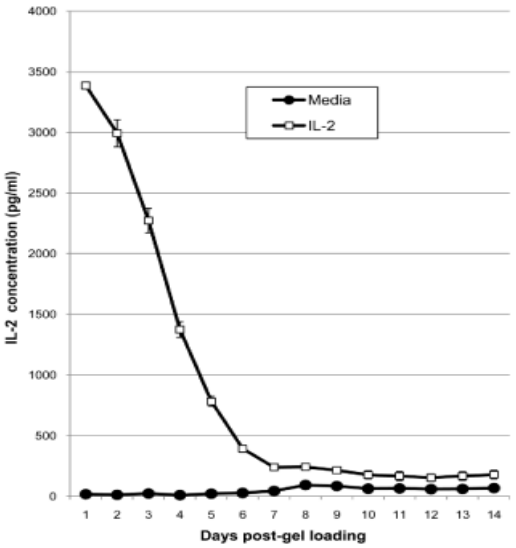

Figure 1. Extracel HP hydrogels release IL-2 over time. *Extracel HP gels of 200 µl volume were polymerized and then incubated overnight in 200µl of RPMI containing 1600 IU/ml (20,000 pg) of IL-2. The gel was then washed once in RPMI and incubated in 200 µl of fresh RPMI. The RPMI was removed after 24 hours and stored for subsequent analysis of IL-2 or TGF-β content by ELISA. This process was repeated every 24 hours for 14 days. The experiment was performed three times. One representative experiment is shown.*

Subsequently, we developed methods to evaluate the capacity of hydrogels to incorporate cytokines to stimulate FOXP3 expression by T cells. For these experiments, we used Extracel-HP™ HMW-HA hydrogel, which contains heparin that can bind to a variety of heparin-binding growth factors, including the ILs and transforming growth factor (TGF)-β. We began looking at IL-2 and evaluated the capacity of our hydrogel preparation to retain this cytokine over 14 days. We found that for gels of 200 µl volume incubated in media containing 20,000 pg of IL-2, the average total IL-2 stored by the gel at the end of 14 days for three experiments was 12,742 pg with a standard deviation of 8%. This was equivalent to a retention rate of at least 63% of the original IL-2 loaded into the gel. Importantly, at the end of 14 days the gels still released IL-2 over baseline, indicating that there is potential for long-term bioactivity. The kinetics of release of IL-2 are shown in **Figure 1**.

In follow-on experiments, we performed analogous work examining the kinetics of IL-10 release. We found that for gels of 200 µl volume incubated in media containing 20,000 pg of IL-10, the average total IL-10 stored by the gel at the end of 8 days was 13,341 pg with a standard deviation of ~6%. This was equivalent to a

retention rate of at least 67% of the original IL-10 loaded into the gel. As with IL-2, after 14 days the gels were still releasing IL-10 over baseline (**Figure 2**). These data indicate that the hydrogels can be used as a depot for IL-10 storage and release for biological applications.

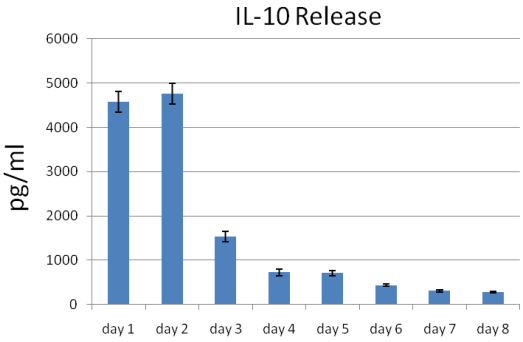

Figure 2. Extracel-HP hydrogels release IL-10 over time. *Extracel-HP gels of 200 µl volume were polymerized and then incubated overnight in 200 µl of RPMI containing 20,000 pg of IL-10. The gel was then washed once in RPMI and incubated in 200 µl of fresh RPMI. The RPMI was removed after 24 hours and stored for subsequent analysis of IL-10 content by ELISA. This process was repeated every 24 hours for 8 days. The experiment was performed two times. One representative experiment is shown.*

In addition to the work to incorporate cytokines like IL-2, and IL-10 into HMW-HA hydrogels, we also devised a method to deliver a TCR ligation using the same hydrogel platform. Streptavidin added to the gel mixture allows for incorporation of biotinylated anti-CD3 antibodies (Ab). The streptavidin/Ab complex provides a stimulatory signal through the TCR complex necessary for TR1 induction. These agents, along with IL-2 and TGF-β, are added to the HMW-HA hydrogel prior to crosslinking the hydrogel. The complete hydrogel platform can deliver all of the necessary signals to induce FOXP3+ regulatory T cells. A schematic of this design is shown in **Figure 3A**. This combination of bioactive agents appears to be an exceptionally efficient and innovative system for FOXP3 induction *in vitro*.

We adapted the hydrogel system described above to induce FOXP3+ Treg from CD4+ GFP/FOXP3- precursors *in vivo*. For these experiments, we injected an un-crosslinked gel mixture comprised of thiol-

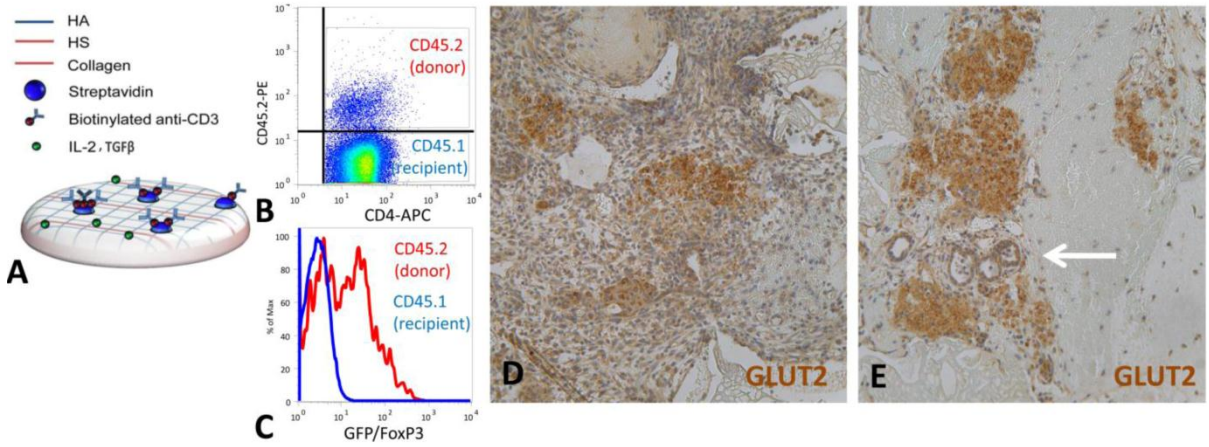

Figure 3. An injectable HA-based gel promotes GFP/FOXP3 induction in vivo and attenuates destruction of transplanted allogeneic islets. ***(A)*** *schematic of a hydrogel designed to induce FOXP3+ Treg. CD4+GFP/FOXP3- precursors taken from CD45.2 mice (donors) were embedded within this gel and injected IP into CD45.1 mice not carrying the GFP marker (recipients). This gel or a control gel lacking the HA/HS component was injected IP following surgical implantation of islets. After 4 days splenocytes were isolated from recipient animals and evaluated for expression of CD45.2* ***(B)*** *as well as GFP/FoxP3* ***(C).*** *The islet implant was also retrieved and sections were stained for GLUT2 to identify embedded islets****. (D and E)*** *Representative images are shown for implants retrieved from an animal which received the collagen-only control gel* ***(D)*** *or the tolerizing gel containing HA and HS* ***(E)****.The white arrow in marks neovascularization. Data are representative of two independent experiments.*

complexed HMW-HA / heparin (HS) / collagen (COL) with TGF-β (50 ng/ml) and IL-2 (200 IU/ml), along with a crosslinking agent, polyethylene glycol, into the peritoneal space of recipient mice carrying the marker CD45.1. CD4+GFP/FOXP3 T cells carrying the CD45.2 marker were also loaded within the gel substrate prior to gel crosslinking. After 4 days, we assessed FOXP3 expression in T cells taken from the spleens and lymph nodes of mice that received the implants. CD45.2 expression allowed us to identify cells of donor origin in CD45.1 recipient animals (**Figure 3B**). We observed that the donor CD45.2 T cells that were FOXP3- at the time of injection became FOXP3+, indicating that our gel was capable of inducing FOXP3 *in vivo* (**Figure 3C**).

To assess the functionality of this system in inducing tolerance, we used an allogeneic islet transplant model. Here, 300 BALB/c islets were transplanted into CD45.1 C57Bl/6 mice within a 6 mm polyvinyl alcohol (PVA)/collagen sponge (developed in Task 2) that was placed through an abdominal incision onto the omentum of recipient mice. Our hydrogels, along with CD45.2 CD4+GFP/FOXP3 depleted T cells, were injected IP 6 hours after surgery. Four days later animals were sacrificed, splenocytes were isolated and the islet implants were harvested. We found that animals that received a control gel where extra collagen was substituted for the HA/HS component had extensive infiltration of the transplanted sponge and destruction of the resident islets (**Figure 3D**). In contrast, animals that received our gels had attenuated remodeling and minimal islet destruction (**Figure 3E**). Notably, the gel still permitted neovascularization (marked with a white arrow in Figure 3E) of the PVA/collagen sponge implant that contained the allogeneic islets, indicating that our hydrogel promoted immune tolerance while not interfering with neovascularization of engrafted tissue.

Collectively, the data summarized in Figs 1–3 indicated that (1) we could induce FOXP3+ T cells *in vivo* from FOXP3- cells exposed to our extracellular matrix hydrogel formulation, and (2) this hydrogel appears to have some utility in mitigating destruction of allogeneic islets in a transplant model. Our desired application for this platform would be to use it to induce FOXP3+ Treg *in vivo* for therapeutic purposes, which, for human patients, would require induction of Treg *in situ*, without the T cell transfer that we used in our mouse models. In subsequent experiments, however, we observed that HA/HS hydrogels loaded with IL-2 and TGF-β were unable to induce FOXP3+ Treg *in situ*, apparently because they did not interact with T cells or other lymphocytes *in vivo*. This phenomenon was a likely consequence of the intrinsic biocompatibility of HA and HS, which appeared to preclude a local inflammatory response. In subsequent experiments, however, we tried a novel approach to tolerance induction, using the same hydrogel materials and cytokines that efficiently induced regulatory T cells *in vitro*, but administering them in an intra-nasal solution in conjunction with an antigen-specific mouse model of airway hypersensitivity.

In parallel studies, we found that high molecular weight hyaluronan (HMW-HA) promotes the induction of functional type 1 Tregs (TR1 cells) from memory T cell precursors. The TR1 progenitor cells in this system are CD4+CD62L-FOXP3- effector memory cells, suggesting that these cells have previously encountered their cognate antigens and assume a regulatory phenotype when they do so again in the context of intact HA. Exposure to HMW-HA engendered a regulatory phenotype in these cells, which persisted even after they were withdrawn from contact with HA. Consistent with this finding, we generated TR1 *in vitro* using HMW-HA and transferred these into an *in vivo* mouse model of colitis where they prevented disease. In addition, we demonstrated that CD44 crosslinking by HMW-HA in the setting of a low-dose T cell receptor (TCR) signal resulted in production of the immunomodulatory cytokine, interleukin-10 (IL-10). Collectively, our data suggest that HMW-HA promotes immune tolerance through effects on regulatory T cells and IL-10.

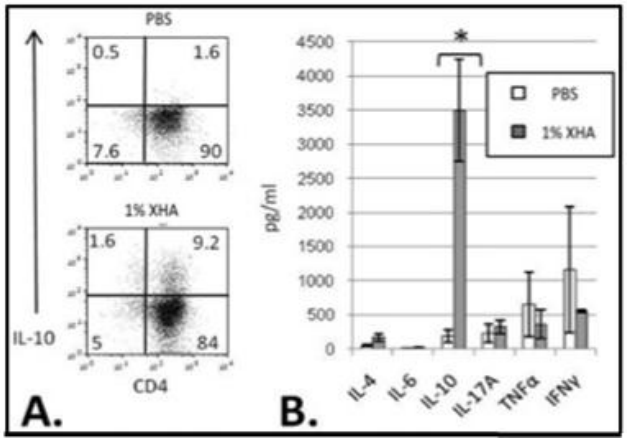

Figure 4. XHA promotes TR1 induction. *CD4+CD26L-/GFP/FoxP3- memory T cells were activated with anti-CD3/28 antibodies and IL-2 for 96 h in the presence or absence of 1% crosslinked HMW-HA (XHA). (**A**) Representative intracellular IL-10 staining, as shown by FACS. (**B**) Concentrations of cytokines in cell culture supernates using the same conditions as in panel A (n = 4 experiments). No such IL-10 production was seen in the setting of either collagen, basement membrane matrix (Matrigel) or fibrin gel controls (data not shown).*

Notably, our HMW-HA data suggested a potential therapeutic opportunity for using HMW-HA in the induction of IL-10-based immune tolerance. Consistent with this, HMW-HA treatment is anti-inflammatory in several settings. However, HMW-HA can also degrade into low molecular weight (LMW)-HA and induce inflammation. Consequently, the therapeutic use of HA requires strategies to maintain HA integrity *in vivo.* One way to maintain the integrity of HA is through chemical crosslinking. Accordingly, we used a commercial, clinical-grade, crosslinked HA preparation (Extracel®, from Glycosan Biosystems, Inc.) that is marketed for stem-cell culture. Extracel contains thiol-modified HA, as well as a thiol-reactive crosslinker, polyethylene

glycol diacrylate. Extracel also contains collagen and/or fibronectin, but we omitted these molecules and referred to this modified formulation of chemically-crosslinked HA alone as XHA. Crosslinking helps ensure that HA does not biodegrade into smaller fragments. Thiol-mediated chemical crosslinking mimics the crosslinking of HA *in vivo* by native crosslinkers such as IαI and TSG-6. In this context, XHA is a synthetic bio-mimetic of provisional wound matrix.

We recently found that XHA is an exceptionally efficient and innovative system for TR1 induction. Using a 1% XHA preparation, along with conventional T cell precursors, we observed substantial IL-10 production *in vitro* (**Figure 4**). Our data indicate that HMW-HA only induces TR1 expression in the setting of TCR ligation. To provide this activation for our *in vitro* work, we added biotinylated anti-CD3 and anti-CD28 antibodies and streptavidin to the HMW-HA prior to crosslinking. For our *in vivo* work, however, we rely on endogenous antigen-presenting cells to activate the T cells.

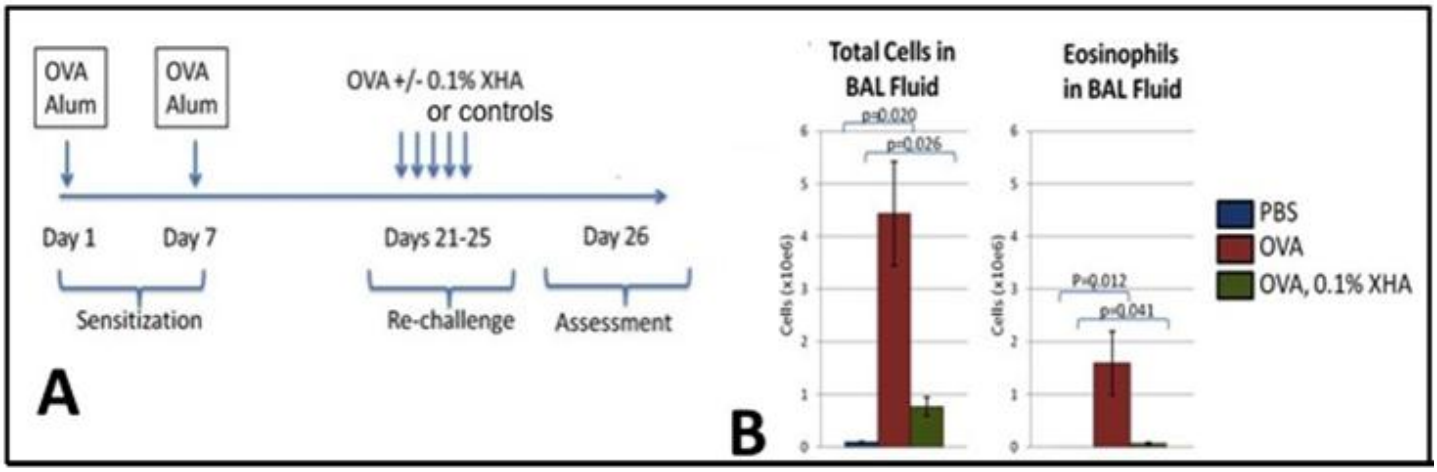

Figure 5. Airway treatment with 0.1% XHA ameliorates inflammation in a mouse model of airway hypersensitivity (AHS). A) *AHS protocol schematic. To evaluate the pro-tolerogenic attributes of HA, we have used an established mouse model of AHS where ovalubumin (OVA), a chicken egg protein, serves as an antigenic trigger. Mice are sensitized with OVA and the adjuvant alum on Days 1 and 7. They are then re-challenged with OVA administered intra-nasally on Days 21–25 with or without 0.1% XHA.* ***B)*** *Total leukocyte and eosinophil counts in bronchoalveolar lavage (BAL) fluid obtained at the end of the experiment. Total cell numbers and eosinophilia are the readouts for airway inflammation in this model. N = 6 mice per group. Data are representative of 2 experiments.*

For the work *in vivo*, we sought to evaluate whether XHA can prevent disease in a well-characterized mouse model of airway hypersensitivity (AHS) where ovalbumin (OVA), a chicken egg protein, serves as the antigenic trigger (**Figure 5A**). In this model, mice are sensitized to OVA in adjuvant and subsequently challenged with OVA aerosols. AHS is then assessed using cellular, physiological, and histological assays. These include analysis of bronchoalveolar lavage (BAL) fluid for cytokines, cell counts and eosinophilia, and histological analysis of airway hyper-responsiveness and remodeling. Inflammation in this model is highly sensitive to treatment with transferred natural Treg (nTreg) or exogenous IL-10. A 0.1% XHA solution was found to reduce total leukocytes and eosinophils in BAL fluid (**Figure 5B**). These data indicate that XHA is able to ameliorate inflammatory disease in an antigen-specific model of airway hypersensitivity.

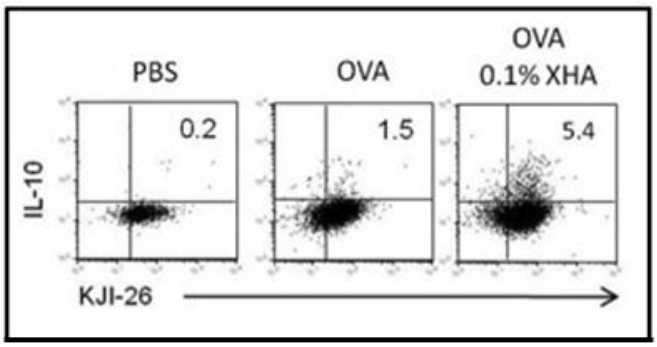

Figure 6. Intra-nasal treatment with 0.1% XHA promotes induction of antigen-specific, IL-10-producing T cells. *We repeated the experimental protocol in Figure 2 in DO11.10/RAG -/- mice carrying a TCR specific for OVA. Upon the completion of the protocol, lymphocytes were isolated from these mice and stained for intracellular IL-10 and for the DO11.10 OVA-specific TCR (using a monoclonal antibody, clone KJI-26). Fluorescence-activated cell sorting (FACS) gating is shown for the CD4+ T cell subset.*

To evaluate whether XHA could induce OVA-specific TR1 cells, we repeated the protocol of Figure 5 using DO11.10/RAG-/- mice, a strain that carries an OVA-specific TCR. We indeed found that a subset of

CD4+, OVA-specific cells was induced to express IL-10 (**Figure 6**). This indicates that T cells that come into contact with their cognate antigen in the setting of XHA *in vivo* produce IL-10. Notably, an antigenic signal was required for this IL-10 induction: XHA alone did not induce IL-10+ cells (data not shown). This antigenic stimulus is presumably delivered by antigen-presenting cells that present OVA to T cells in the setting of XHA. In this protocol, XHA functions as an adjuvant that induces antigen-specific, IL-10 producing T cells. This is a highly novel approach to immune modulation and may prove useful for the management of inflammation in a variety of settings, including body wounds and inhalation injuries to the airway.

Conclusions, Task 3

Our original objective for Task 3 was to develop injectable hydrogels for use in induction of Tregs *in vivo*. This approach appeared to be problematic after we found that immune cells do not easily traffic to the thiol-crosslinked HMW-HA-based hydrogels *in vivo* because this material is immunologically silent. A contributing factor to this silence may be the resistance of the hydrogel to penetration by immune cells—a consequence of its hydrogel character that requires high concentrations of HMW-HA and a high degree of thol-crosslinking. An alternative approach, under development in Aim 2 (Tasks 9 and 10), involves sustained delivery of soluble HA via an implantable, sustained (time) release device. In this system, the HA is not in the form an impenetrable hydrogel (it is not crosslinked), yet, because it is released slowly into the surrounding tissue, it may be available locally for a time sufficient enough to promote tolerance. In this context, but in a different application, experiments in Task 3 have had success with tolerance induction by delivering a dilute solution of HMW-HA together with antigen via the intra-nasal route. Using this approach, we have been able to ameliorate the development of inflammation in a mouse model of antigen-specific airway hypersensitivity. This is a promising tool for tolerance induction that could lead to better treatments for allergy and asthma. We have filed a pair of patents on this technology and have received a fundable score on an R01 grant proposal to pursue this research further.

Task 4

Perform flow cytometry assays for lineage deviation with 11 siRNA constructs (listed in the proposal) using human naïve CD4+ T cells (Jane Buckner, MD).

Task 4 is a component of Aim 1C which is derived from the finding that the lineage of a naïve CD4+ T cell is determined by the cytokine milieu in which it is activated. Recent studies have not only identified multiple CD4+ T cell lineages, but have also established that the phenotype of previously committed CD4+ T cells can be altered in response to factors in the local environment. Task 4 took advantage of this information to enhance Treg activation, development, and persistence in engineered ECM hydrogels.

Identification of specific environmental factors that regulate key genetic pathways which, in turn, control T cell behavior may prove to be an effective means to control inflammation and improve wound repair, in conjunction with the HA modulation explored in this project. Aim 1C focused on a set of 11 genes that we believe are likely to influence T cell function. These target genes code for the cytokines IL-6, IL-23R and IL-21, the signal transduction factors Stat-1, -3 and -5, PTPN-2 and -22, and the transcription factors FOXP3, RORγt and T-bet.

Task 4 focused on introducing small interfering (si)RNAs into naïve human CD4+ T cells to inhibit expression of the target

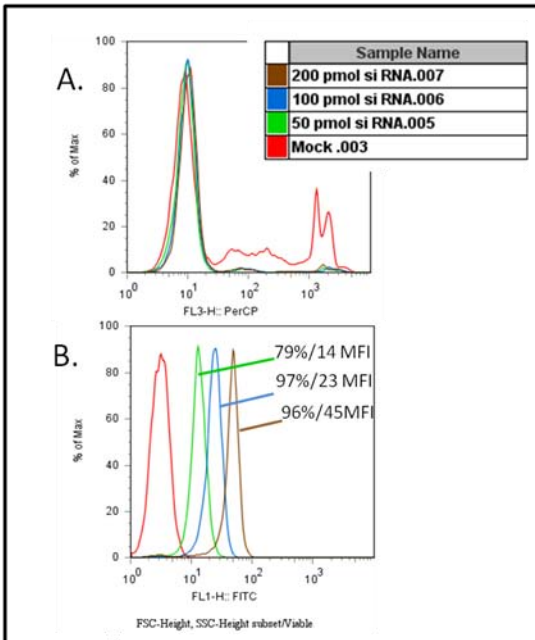

Figure 7. ***Efficient transfection of hematopoietic cells.*** *A pro-B cell line was mock transfected or transfected with increasing concentrations of an Alexa 488 labeled siRNA using Amaxa nucleofection. Cells were stained with Viaprobe and analyzed by flow cytometry 2h post transfection to assess cell viability (A) and transfection efficiency (B). The percent siRNA transfected cells and the mean fluorescence intensity (MFI) are indicated for each siRNA concentration.*

genes with the goal of identifying pathways for lineage deviation that skew T cell maturation toward regulatory (i.e., Treg) commitment, survival, and function. siRNA inhibition of the target genes is predicted either to affect the generation of T cells with regulatory properties or to stabilize a regulatory phenotype in existing Tregs. Key experiments to determine an efficient method for introducing siRNAs into lymphocytes revealed that Amaxa nucleofection was the most efficient and least damaging to cells (**Figure 7**). Using 100 pmol of an Alexa 488-conjugated siRNA, we found 97% of cells were transfected using the Amaxa system (**Figure 7B**) without significant cell death, as shown by exclusion of the Viaprobe dye (**Figure 7A**). Given the high efficiency of transfection achieved with Amaxa nucleofection, we predicted that sorting of siRNA transfected cells would not be required prior to functional analysis of siRNA knockdown.

Table I. Sigma MISSION siRNA targets.

Gene target	siRNA start (bp)	Exon	Target sequence	Comment
PTPN2	991	7	GATTCTCATACATGGCTATAA	will repress both isoforms
	645	5	AAGTCGTATTATACAGTACAT	
	651	5	TATTATACAGTACATCTACTA	
	428	3	GGCACAAAGGAGTTACATCTT	
	421	3	TAGAAGAGGCACAAAGGAGTT	
PTPN22	1068	12	CTGAGAAAAATCACACTCTCC	
	616	7	TGAAAAAAGGAAATCTGATTA	
	1640	13	GACTCTAAACACCAAATACGT	
	1406	13	TCTAATTCTAAACCTGTAAAT	
	927	10	GGACACAGAGGCCTTCATTCA	
STAT1	1950	18	TGTTGGGAGAGAAGCTTCTTG	
	1033	9	CAAAATAATAGAGTTGCTGAA	
	1373	11	CCTCAGAGGCCGCTGGTCTTG	
	605	4	TTGGAGAATAACTTCTTGCTA	
	802	6	ACAGAAAGAGCTTGACAGTAA	
STAT3	1029	8	AGAAAACTGGATAACGTCATT	validated siRNA
	1981	19-20	AACGAAGGGTACATCATGGGC	
	1810	17	CAGCTGACTACACTGGCAGAG	
	515	3-4	GCAGGTATCTTGAGAAGCCAA	
	2053	20	ACCTTCCTGCTAAGATTCAGTG	
STAT5A	1967	12	TCCTGTTTGAGTCTCAGTTCA	corepress STAT5A and STAT5B
	2866	20	CCTGACCATGTACTCGATCAG	
	1950	12	AGAGGAGAAGTTCACAGTCCT	
	2887	20	GATGGAGAATTCGACCTGGAT	
	2627	17	ACCTGAGCTATCTCATCTATG	
STAT5B	2196	16	ATGAAGTATACTCCAAATACT	
	1891	14	TGACGGTGTGATGGAAGTGTT	
	1490	11	ACAATCCTGTTTGAATCCCAG	
	494	4	ATCCGCCATATSTTGTACAAT	
IL-6	266	2	AGAACGAATTGACAAACAAAT	
	198	2	GCCCCAGTACCCCCAGGAGAAG	
	366	3	GCACTGGCAGAAAACAACCTG	
	246	2	AGACAGCCACTCACCTCTTCA	
	381	3	AACCTGAACCTTCCAAAGAT	

We selected siRNAs for targeting 6 of the 11 genes proposed in Task 4 (**Table I**). Since siRNAs are known to cause off-target effects related to their primary sequence, we performed all functional analyses using a minimum of two unique sequence siRNAs per target gene. A total of five MISSION siRNAs (Sigma) were to be tested for each target gene in order to identify at least two siRNAs that could successfully inhibit gene expression. These siRNAs were designed using the Rosetta siRNA design algorithm that maximizes specificity and minimizes off-target effects. Universal negative controls were included in each experiment, as well as two siRNA knockdown positive controls specific for GAPDH and cyclophilin B. Target gene expression was to be assessed by qPCR and Western blot.

We adapted and optimized the transfection protocol indicated above for primary lymphocytes and confirmed that it resulted in highly efficient transfection, and high viability, in both T cells and B cells isolated from human PBMCs (data not shown). Importantly, the entire population of T or B cells took up siRNA after transfection, precluding, as we predicted, the need for cell sorting of transfected lymphocytes prior to functional assays. We established that a siRNA concentration of 50-100 pmol was optimal to test individual siRNAs for knockdown efficiency in T cells. Higher siRNA concentrations did not result in further knockdown, but did increase off-target effects. We developed qPCR assays to assess gene expression using either SYBR green chemistry or Taqman probes. Expression of siRNA targeted genes was compared relative to expression of the same gene in cells transfected with a negative control siRNA (siRNA that does not recognize human transcripts). A validated siRNA for Lamin A/C was used as a positive control to confirm transfection efficiency and specificity for each experiment. Using this optimized protocol, we found that Lamin A/C expression was reduced by 60-70% in T cells transfected with 100 pmol Lamin siRNA (not shown).

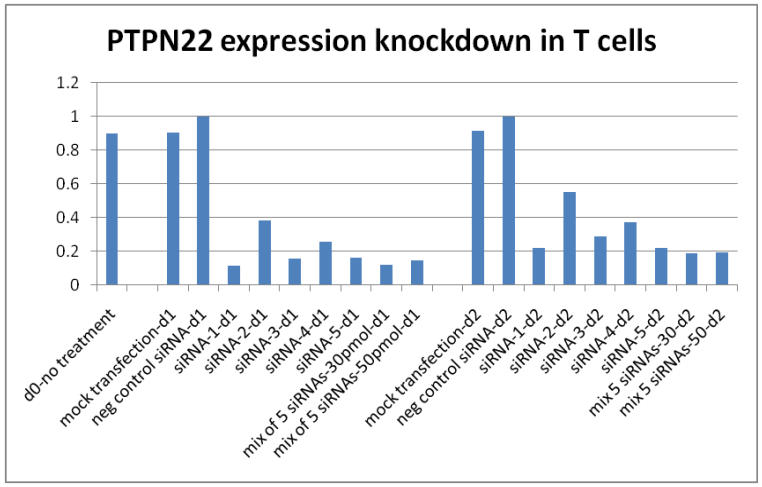

Figure 8. PTPN22 siRNA transfection results in 85-90% knockdown of PTPN22 expression in T cells by 24 hours. *Naïve CD4+ T cells transfected with siRNAs using Amaxa Human T Cell Nucleofector Kit and assayed by qPCR for PTPN22 expression after 24 (d1) and 48 (d2) hours. siRNA #1, #3, and #5 result in efficient knockdown of 85-90% by 24 hours, and continued knockdown of 72-78% at 48 hours.*

Subsequently, we tested the knockdown efficiency of a number of gene-specific siRNAs for use in functional experiments, with the goal of identifying two highly-effective siRNAs per knockdown target in order to be able to control for off-target effects. This was accomplished for the PTPN22 phosphatase in T cells. We found 3 siRNAs that target PTPN22 and result in knockdown greater than 80% by 24 hours post transfection, and greater than 70% knockdown after 48 hours (**Figure 8**). We identified at least 1 siRNA for the PTPN2 phosphatase that results in 62% knockdown of PTPN2 mRNA in T cells (**Figure 9**).

We performed additional experiments to validate the time course of siRNA target gene knockdown and quantitate protein reduction. **Figure 10** shows a time course for PTPN22 knockdown at the level of RNA. We found that knockdown of PTPN22 RNA persists through 3 days but by day 4 RNA levels were returning to untransfected cell levels. Similar results were observed for PTPN2 knockdown. We observed that protein knockdown of PTPN2 lags behind RNA knockdown by ~ 48 hours, with detectable knockdown at the protein level observed at 3 days after siRNA transfection (**Figure 11**).

We also evaluated the phenotypic effects of PTPN22 and PTPN2 knockdown in T cells. We examined T cell receptor (TCR) signaling in PTPN22 siRNA transfected T cells since PTPN22 is known to modulate TCR signal strength. Using calcium flux as a readout of TCR signaling, we observed that PTPN22 siRNA #1 increased the peak calcium flux in T cells compared to mock or universal negative control siRNA transfected T cells (**Figure 12**). An increase in calcium flux is the expected result since PTPN22 normally functions to dephosphorylate an activating tyrosine in the active site of the TCR-associated kinase Lck. When we analyzed whether this effect was present in the naïve or memory T cell subset, we found that the memory, but not naïve, T cells displayed increased calcium

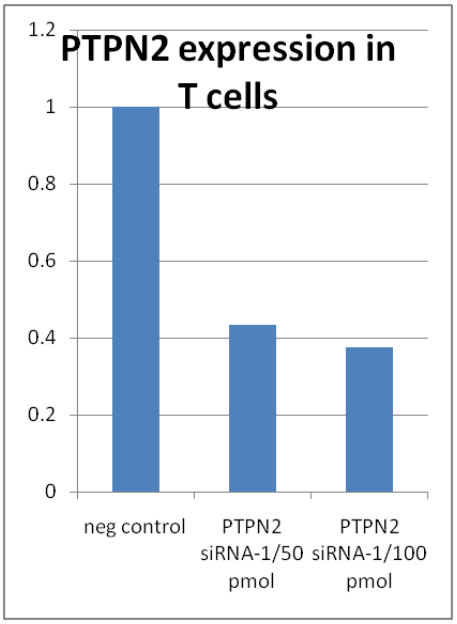

Figure 9. PTPN2 siRNA transfection results in 60% knockdown of PTPN2 expression in T cells. *Naïve CD4+ T cells transfected with siRNAs using Amaxa Human T Cell Nucleofector Kit and assayed by qPCR for PTPN2 expression after 48 hours. siRNA #1 transfection (at 50 and 100 pmol) results in approximately 60% knockdown (57% and 63%. respectively) of PTPN2 mRNA compared to a negative control siRNA.*

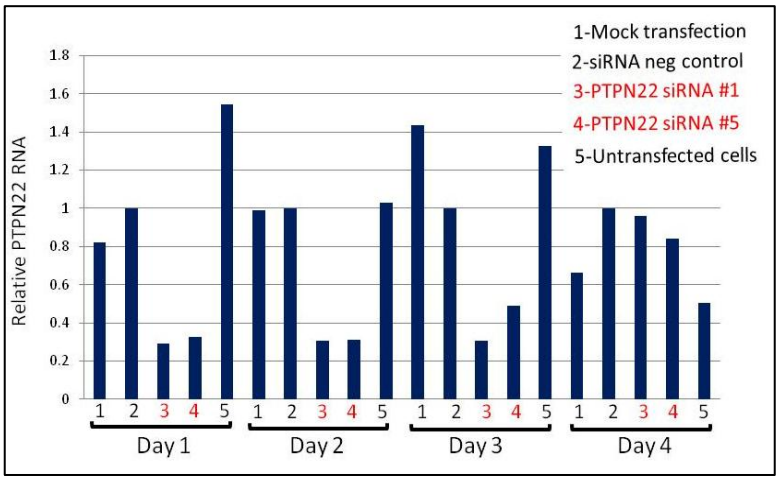

Figure 10. siRNA-specific knockdown of PTPN22 RNA in T cells. *Primary CD4+ T cells were isolated from peripheral blood by negative selection and were transfected with 100 pmol of the indicated PTPN22 siRNAs, or a universal negative control siRNA. Untransfected T cells or T cells that were mock transfected with no siRNA served as controls. IL-2 at 10 IU/ml was added after transfection and cells were harvested for RNA isolation each day for a total of 4 days. PTPN 22 RNA expression was assayed by Taqman qPCR and RNA levels were expressed relative to the universal negative control siRNA.*

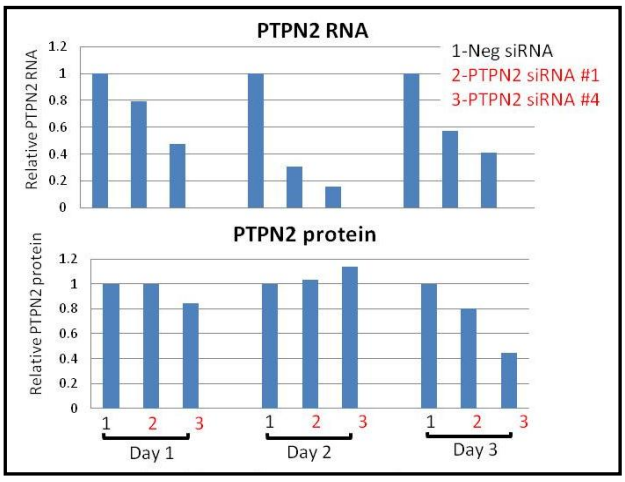

Figure 11. siRNA knockdown of PTPN2 RNA and protein expression in T cells. *Primary CD4+ T cells were transfected by Amaxa nucleofection with 100 pmol of the indicated PTPN2 siRNAs or the universal negative control siRNA. Cells were maintained in 10 IU/ml IL-2 and harvested each day for 3 days. RNA and protein were isolated and assayed by Taqman qPCR to assess PTPN2 RNA levels or assayed by western blot with a PTPN2-specific polyclonal antibody to evaluate protein levels. Protein was quantitated by densitometry. RNA and protein levels were expressed relative to the levels detected in the universal negative control siRNA-transfected cells.*

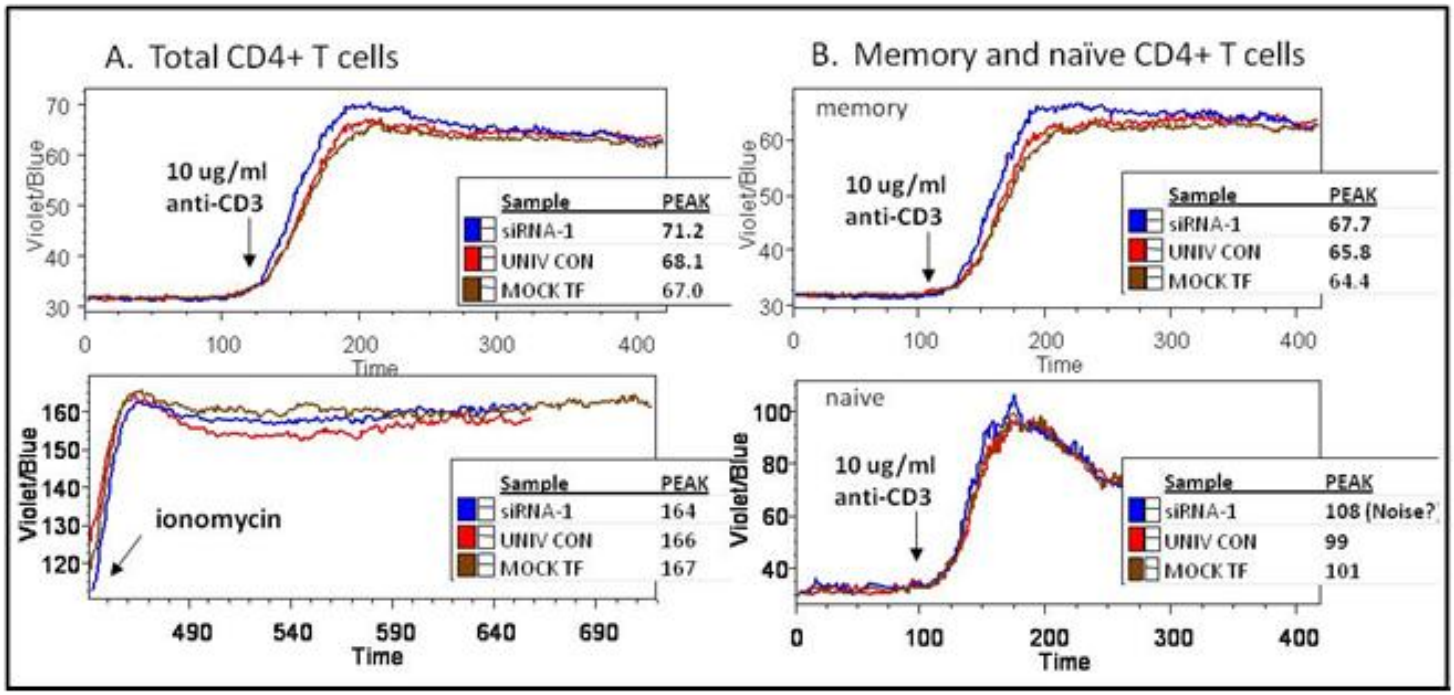

Figure 12. Increased calcium flux in PTPN22 siRNA-transfected T cells. *CD4+ T cells were isolated from peripheral blood and were transfected with 100 pmol of PTPN22 siRNA, universal negative control siRNA, or were mock-transfected. 48 h after transfection, the T cells were harvested, surface-stained, and loaded with the calcium indicator dye Indo-1 AM. After establishing baseline calcium levels by flow cytometry, TCR stimulation was achieved by the addition of 10 µg/ml of anti-CD3 and the kinetic profile was monitored for 7 min. PMA/Ionomycin was then added to measure peak calcium release from each sample. Panel A shows total CD4+ T cells. Panel B shows CD4+CD45RO+ memory T cells in the upper panel and CD4+CD45RO– naïve T cells in the lower panel.*

flux. These findings are consistent with our previous results showing that control T cells, carrying a gain of function mutation in PTPN22, have altered calcium flux in the memory T cell compartment.

PTPN2 functions to modulate cytokine signaling, including the response to IL-2. To assess the phenotypic effect of PTPN2 knockdown, we examined the phosphorylation of the STAT5 transcription factor (pSTAT5) in the IL-2 pathway after treatment of siRNA-transfected T cells with IL-2 (**Figure 13**). We observed a reduction in the percentage of pSTAT5 positive cells with both PTPN2 siRNAs, consistent with our previous findings in control subjects carrying a sequence variant that reduces PTPN2 expression. This effect was most evident in the CD25-high fraction of T cells, which are the most responsive to IL-2.

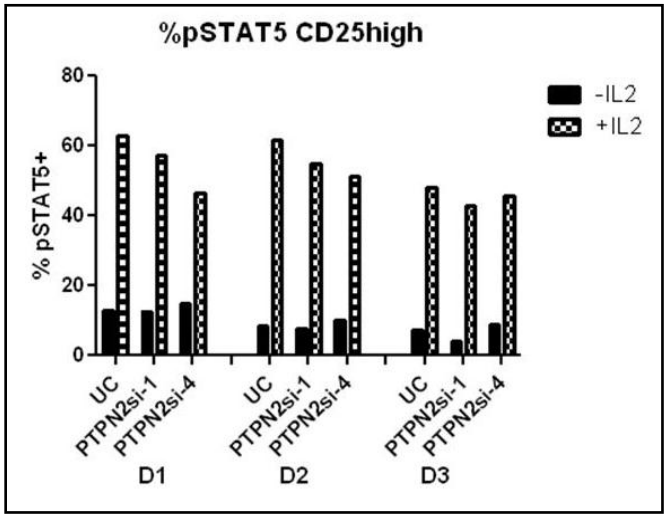

Figure 13. Reduced STAT5 phosphorylation after IL-2 treatment in PTPN2 siRNA-transfected T cells*. Primary CD4+ T cells were isolated from peripheral blood by negative selection and transfected by Amaxa nuceofection with PTPN2 siRNAs, or a universal negative control siRNA (UC). Cells were maintained in the presence of 50 ng/ml of IL-4 and harvested at day 1, 2, and 3. Cells were exposed to 100 IU/ml of IL-2 for 20 min, fixed, permeabilized, and then stained for phospho-STAT5 (pSTAT5) and other T cell surface markers. pSTAT5-positive cells in the CD25-high T cells are shown +/- IL-2 treatment.*

In parallel studies, we expanded our evaluation of siRNAs to new target genes, including STAT3 and the IL-6 receptor. **Figure 14** shows knockdown of RNA levels of the transcription factor STAT3 after transfection of three unique STAT3 siRNAs. One of the STAT3 siRNAs, siRNA #1, was validated as a functional STAT3 siRNA, and it displayed the greatest reduction in STAT3 RNA. STAT3 is a transcription factor that functions in several cytokine pathways including the IL-6 pathway, which is important in the generation of pro-inflammatory Th17 cells.

Collectively, our results for Year 1 (illustrated in Figures 7–14) showed that: (1) our protocol to introduce siRNAs into naïve human CD4+ T cells works and successful transfection of siRNA can result in efficient RNA knockdown, and (2) that specific consequences arise from RNA knockdown, which include reduced expression of the cognate protein and effects on cell function that correspond to inhibition of the target genes (e.g., PTPN22, PTPN2).

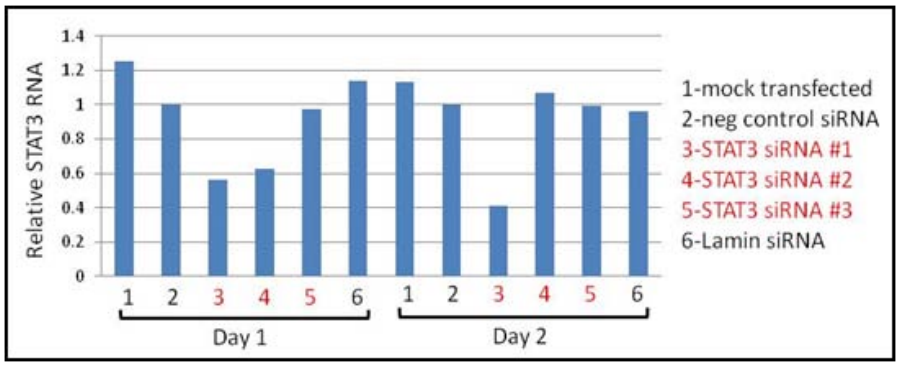

Figure 14. Reduced STAT3 RNA levels in siRNA-transfected T cells. *Primary CD4+ T cells were isolated from peripheral blood by negative selection and transfected by Amaxa nuceofection with 100 pmol of STAT3 siRNAs, a universal negative control siRNA, a Lamin siRNA, or were mock-transfected. Cells were maintained with 10 IU/ml of IL-2 and were harvested on days 1 and 2 after transfection. RNA was isolated and STAT3 RNA levels were assessed by Taqman qPCR. STAT 3 RNA levels are expressed relative to STAT3 levels in the universal negative control transfected cells.*

We found that siRNA knockdown of target gene (i.e., PTPN2 and PTPN2) RNA persisted through 3-4 days in human CD4+ T cells and protein knockdown lagged behind RNA knockdown by ~48 hr. The phenotypic consequences of knockdown of PTPN22 and PTPN2 were modest changes in TCR signaling and IL-2 signaling, respectively.

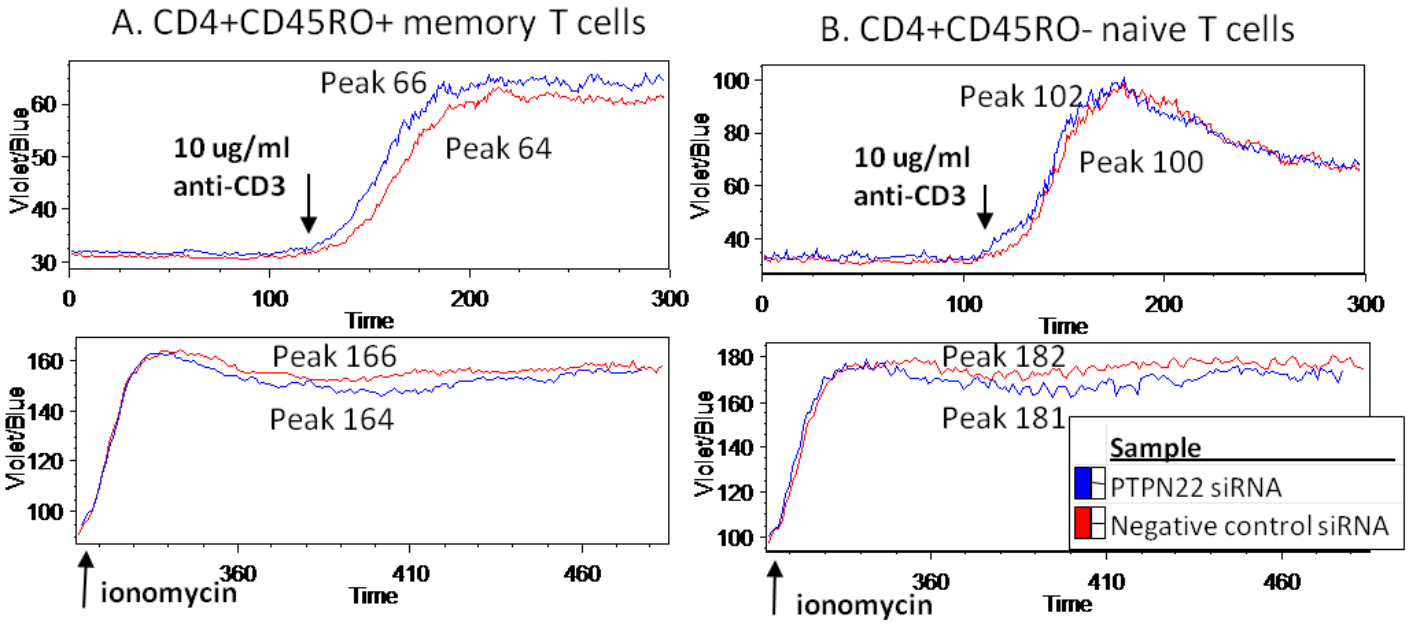

Figure 15. Increased calcium flux in PTPN22 siRNA transfected memory T cells*. CD4+ T cells were isolated from peripheral blood and were transfected with 200 pmol of PTPN22 siRNA or universal negative control siRNA. 48h after transfection, T cells were harvested, surface stained and loaded with the calcium indicator dye indo-1 AM. After establishing baseline calcium levels by flow cytometry, TCR stimulation was achieved by the addition of 10 μg/ml of anti-CD3 and the kinetic profile was monitored for 7 minutes. PMA/Ionomycin was added to measure peak calcium release from each sample.* ***(A)*** *CD4+CD45RO+ memory T cells with anti-CD3 in the upper panel and ionomycin in the lower panel.* ***(B)*** *The same plots for CD4+CD45RO- naïve T cells.*

In Year 2, we repeated and extended phenotypic analyses of knockdown of PTPN22. We replicated calcium flux following TCR stimulation in PTPN22 siRNA transfected T cells. Similar to our previous results, we observed that PTPN22 siRNA increased the peak calcium flux in memory T cells, but not naïve T cells, compared with a negative control siRNA (**Figure 15**). An increase in calcium flux is the expected result since PTPN22 normally functions to dephosphorylate an activating tyrosine in the active site of the TCR-associated kinase Lck, down-regulating TCR signaling, and this phenotype is more evident in memory T cells. However, the effect was modest. As a second measure of the effect of PTPN22 siRNA on TCR activation, we measured

phosphorylation of several key signaling molecules in the TCR signaling cascade, including PLC-γ1, Akt, and CD3-ζ. As shown in **Figure 16**, we were not able to detect reproducible differences in phosphorylation of PLC-γ1, Akt, or CD3-ζ between PTPN22 siRNA transfected CD4+ T cells vs. cells transfected with a negative control siRNA at 2 or 3 days post transfection, despite a 70-80% knockdown of PTPN22 RNA in these cells.

To target the generation of Th17 cells, we tested siRNAs specific for the IL-6 receptor (IL-6R) and STAT3, the transcription factor that functions in IL-6 signaling. Transfection of human CD4+ T cells with an IL-6R siRNA resulted in ~40% reduction of IL-6R RNA over 3 days (**Figure 17**). Flow cytometry detected a two-fold reduction in IL-6R protein on the surface of the transfected T cells and a reduction in phosphorylated STAT3 after IL-6 treatment (**Figure 18**). However, subsequent experiments have not replicated the reduction in IL-6 signaling in IL-6R siRNA transfected T cells.

Transfection of human CD4+ T cells with siRNAs for STAT3 resulted in 40-60% reduction of STAT3 RNA (**Figure 17**). Analysis of total STAT3 levels by intracellular staining and flow cytometry revealed a 30% reduction in STAT3 protein at day 5 after transfection (**Figure 19**). To determine if STAT3 knockdown interfered with cytokine signaling, we treated siRNA transfected cells with IL-21, which signals via STAT3, and analyzed phospho-STAT3 levels. As shown in **Figure 19**, the mean fluorescence intensity of phosphoSTAT3 was reduced in STAT3 siRNA transfected cells, as compared with cells transfected with the negative control siRNA. However, we did not observe a reproducible reduction in phospho-STAT3 after

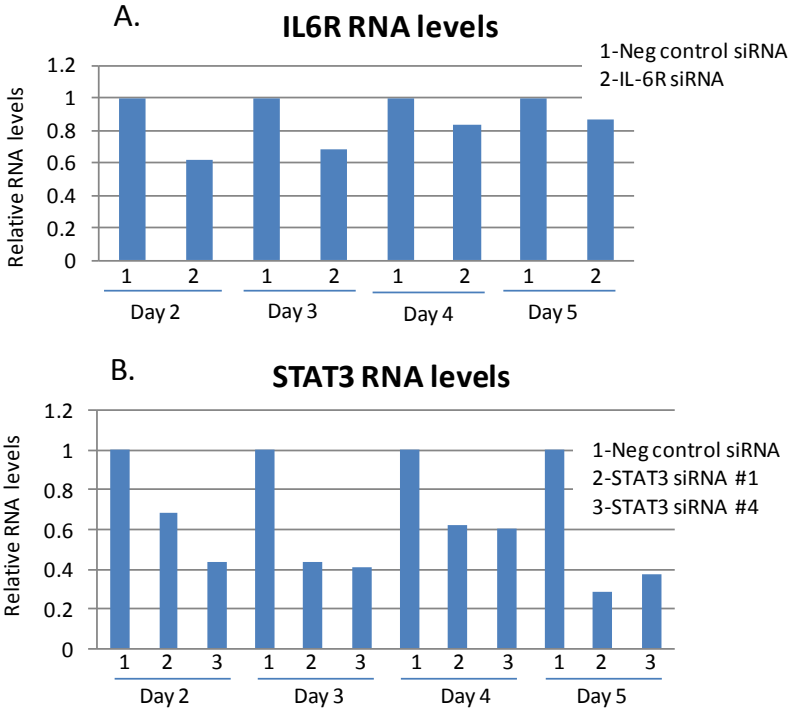

Figure 3. RNA knockdown following transfection of CD4+ T cells with IL-6 receptor or STAT3 siRNAS. Primary CD4+ T cells were isolated by negative selection and transfected with 200pmol of the indicated siRNAs. Cells were harvested at the indicated days after transfection,

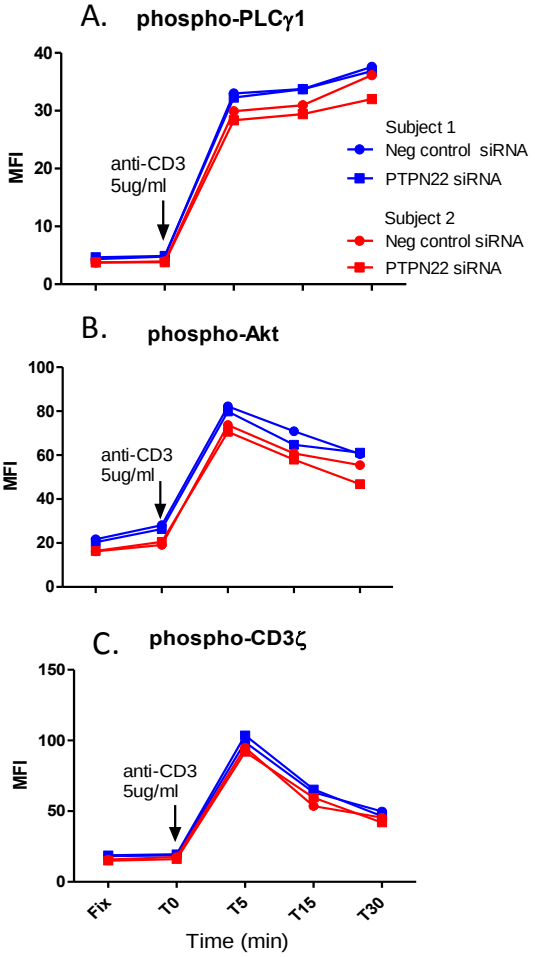

Figure 16. Phosphorylation of TCR signaling molecules in siRNA transfected CD4+ T cells following TCR stimulation. *CD4+ T cells were purified by negative selection and transfected with 200 pmol of the indicated siRNAs. 48h after transfection, cells were stimulated with anti-CD3 and cross linker and fixed and permeabilized at the indicated time points. Cells were stained with phospho-specific antibodies for PLC-γ1* ***(A)****, Akt* ***(B)****, or CD3ζ* ***(C)*** *and were analyzed by flow cytometry. Graphs show mean fluorescence intensity (MFI).*

Figure 17 (Left). RNA knockdown following transfection of CD4+ T cells with IL-6 receptor or STAT3 siRNAS. *Primary CD4+ T cells were isolated by negative selection and transfected with 200 pmol of the indicated siRNAs. Cells were harvested at the indicated days after transfection, RNA purified, and IL-6R* ***(A)*** *or STAT3* ***(B)*** *RNA levels were assessed by qPCR using Taqman probes. RNA levels are expressed relative to the levels detected in T cells transfected with a negative control siRNA.*

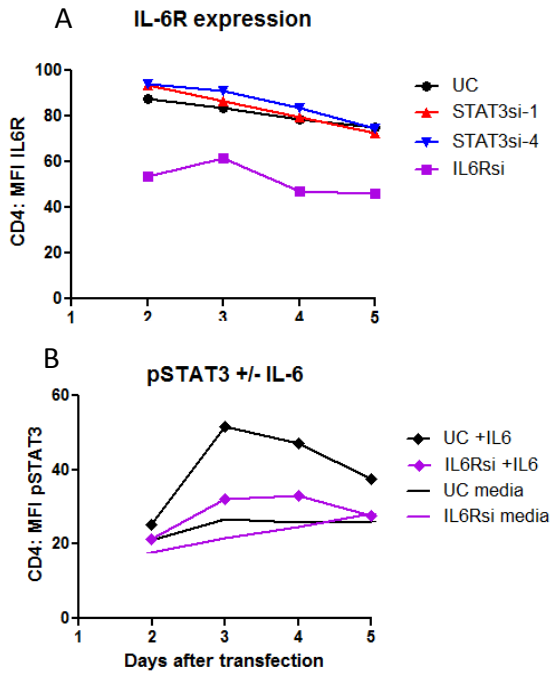

Figure 18. IL-6R siRNA reduces IL-6R expression and signaling. *CD4+ T cells purified by negative selection were transfected with 200 pmol of a negative control siRNA (UC), STAT3 siRNA #1, STAT3 siRNA #4, or an IL-6R siRNA and were placed into culture with 10 IU/ml IL-2. On days 2-5 after transfection, cells were stained for IL-6R surface expression* ***(A)*** *or were treated +/- IL-6, fixed, and permeabilized and stained with an antibody specific for phosphorylated STAT3 Y705* ***(B)****. Cells were analyzed by flow cytometry and mean fluorescence intensity was determined.*

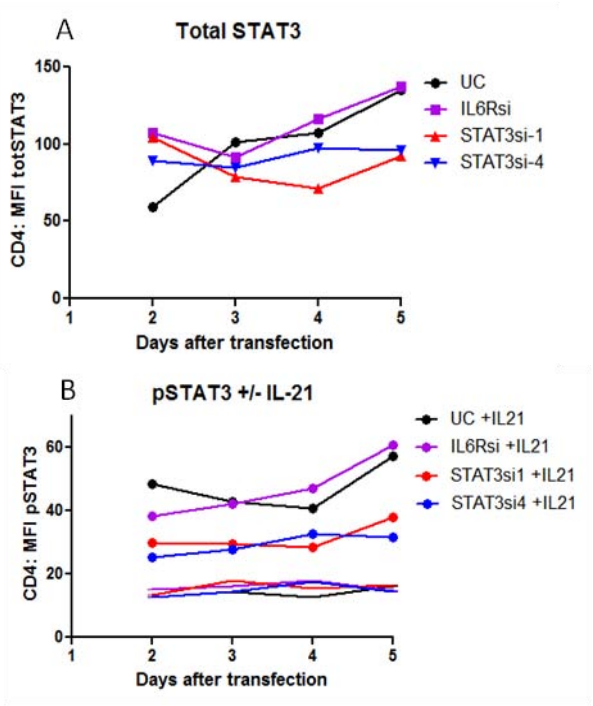

Figure 19. STAT3 siRNA reduces STAT3 expression and phosphorylation. *CD4+ T cells purified by negative selection were transfected with 200 pmol of a negative control siRNA (UC), STAT3 siRNA #1, STAT3 siRNA #4, or an IL-6R siRNA and were placed into culture with 10 IU/ml IL-2. On days 2-5 after transfection, cells were treated +/- IL-21, fixed, and permeabilized and stained with an antibody specific for total STAT3 protein* ***(A)*** *or an antibody specific for phosphorylated STAT3 Y705* ***(B)****. Cells were analyzed by flow cytometry and mean fluorescence intensity was determined.*

treatment of siRNA transfected T cells with IL-6, suggesting that the knockdown achieved was suboptimal. Taken together, the results of the functional experiments demonstrated modest or undetectable phenotypes, despite achieving reproducible knockdown of target RNA with siRNA transfection. Given these results, we investigated two alternative methods of RNA interference (RNAi): lentiviral transduction of short hairpin (sh)RNAs and siRNA introduction into T cells using a CD7 single chain antibody.

Lentiviral encoded shRNAs have recently been used successfully by others for RNAi knockdown in primary human T cells. To establish lentiviral shRNA knockdown in our hands, we purchased a pLKO.1 turboGFP lentiviral construct and a paired pLKO.1 shGFP construct. The plasmids were packaged by co-transfection of HEK293T cells along with envelope and packaging plasmids, and viral supernatants were collected for 48h and concentrated. Viral supernatants and shRNA knockdown were validated by infecting HEK293T cells. As shown in **Figure 20**, over 90% of 293T cells expressed GFP on day 5 after infection with

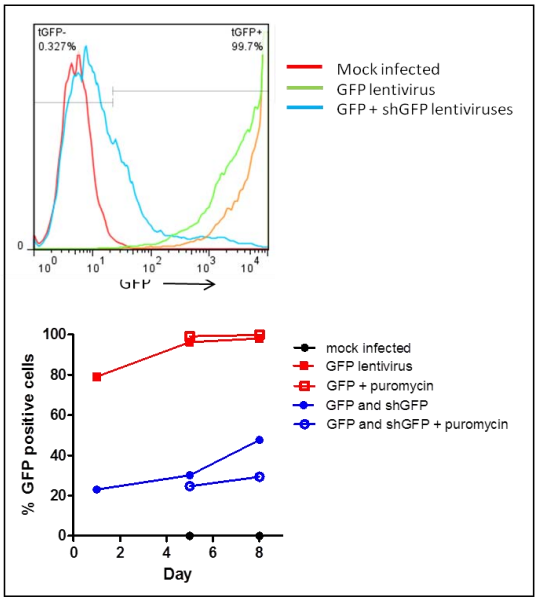

Figure 20. Validation of lentiviral shRNA knockdown in HEK293T cells. *Lentiviruses encoding GFP or an shRNA specific for GFP (shGFP) were used to infect HEK293T cells. On day 4 after infection, puromycin was added to cultures to select for infected cells. GFP expression was assessed at the indicated times by flow cytometry of live cells and is expressed in the graph as the percent GFP positive of total live cells.*

GFP viral particles, whereas only ~20% of 293T cells infected with both GFP and shGFP viral particles expressed GFP. Knockdown of GFP expression was maintained through day 8 by adding puromycin to the cultures, since a puromycin resistance gene is encoded on the lentiviral plasmid. GFP expression in shRNA transduced cells increased to 40% in 293T cells grown without puromycin. These results confirmed functional lentivirus production and infection, and demonstrated an 80% knockdown of GFP protein expression by day 5 after infection with shRNA.

We performed lentiviral infection of primary human CD4+ T cells using the GFP and shGFP plasmids. We did not detect significant infection of unstimulated CD4+ T cells. Lentiviral infection of stimulated T cells resulted in ~10% of cells expressing GFP on day 4, which increased with puromycin selection to >80% of T cells on day 8. Co-transduction of GFP and shGFP viral particles reduced GFP expression to <10% of cells (**Figure 21**).

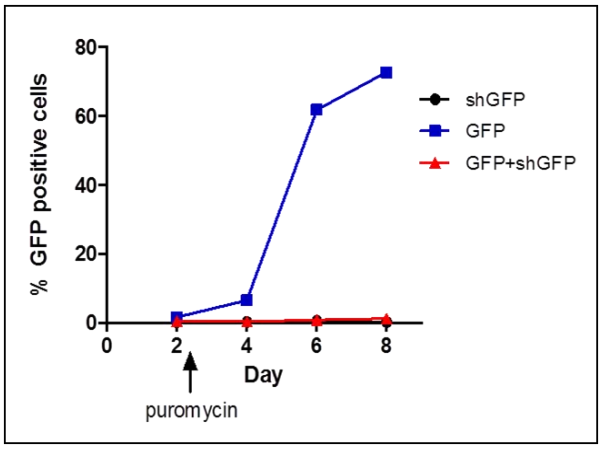

Figure 21. Lentiviral infection of primary human CD4+ T cells. *CD4+ T cells were stimulated overnight with plate-bound anti-CD3/CD28 and were then infected with concentrated lentiviruses encoding GFP or a shRNA specific for GFP (shGFP). At Day 2 after infection, puromycin was added at 2.5 μg/ml to select for infected cells. Expression of GFP was analyzed by flow cytometry on the indicated days, gating on live cells., and is expressed as the percent of live cells that were GFP- positive.*

As an alternative approach for achieving siRNA delivery and knockdown in primary T cells, we utilized an anti-CD7 single chain antibody-protamine fusion protein that has been shown to deliver siRNAs *in vitro* and *in vivo* to human and mouse T cells (Kumar et al., *Cell* 134: 577-586, 2008). CD7 is expressed on all mouse and human T cells and is rapidly internalized, making it a useful vehicle for introducing molecules into cells. A positively charged protamine peptide coupled to the C-terminus of the single chain anti-CD7 (scFvCD7) enables binding of siRNA molecules (~6 siRNAs/scFVCD7) via charge interactions. The siRNA-decorated scFvCD7 molecules are then mixed with T cells, where CD7 is bound by the scFvCD7/siRNA complex, and is internalized. To test this reagent, received in collaboration with Dr. Premlata Shankar, we bound an Alexa Fluor 488-coupled siRNA to the scFvCD7 reagent and tested for transduction of Jurkat T cells (human), which express CD7. As shown in **Figure 22**, we observed 100% of Jurkat cells took up the fluorescently labeled siRNA at 3 hr post-treatment, with a concomitant decrease in CD7 expression. At 24 hr post-treatment, Jurkat cells were still fluorescent, indicating the siRNA was internalized and CD7 was re-expressed on the cell surface. The scFvCD7/siRNA was not toxic to the cells, with only 9% dead cells at the highest concentration used. Using a siRNA that targets the PTPN2 phosphatase we observed 80% knockdown of PTPN2 RNA at 48h and 30% knockdown of PTPN2 protein at 72 hr in Jurkat T cells.

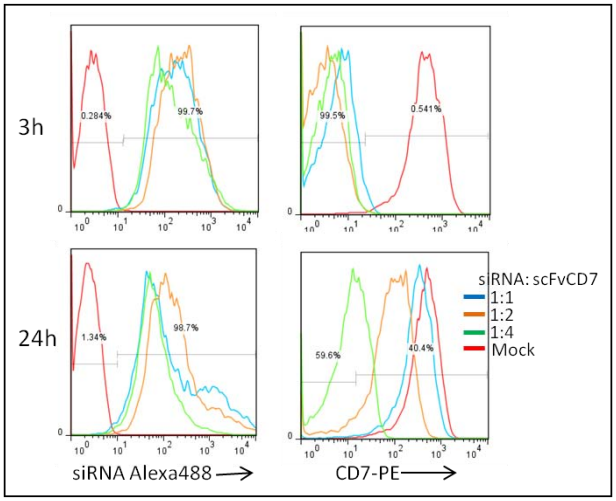

Figure 22. siRNA delivery to Jurkat T cells using a single chain anti-CD7-protamine fusion protein (scFvCD7). *100pmol of Alexa488 labeled siRNA was complexed with scFvCD7 at the indicated ratios at room temperature for 15 min and then added to Jurkat cells for 3h at 37°C. Media was replaced and Jurkat cells were continued in culture. siRNA uptake and CD7 surface expression were analyzed by flow cytometry at 3h and 24h after addition of the scFvCD7/siRNA complex.*

In subsequent studies, we tested the anti-CD7 single-chain antibody in primary human CD4+ T cells and in the alginate sphere delivery system (developed as part of Task 9) as a means of delivering siRNAs *in vivo* in wound repair settings. To adapt the scFvCD7 reagent for *in vivo* delivery, we performed experiments in collaboration with Dr. Vernon to determine if the scFVCD7/siRNA complexes could be delivered via alginate-poly-L-lysine (PLL) spheres.

For these experiments, alginate spheres were constructed containing 1.5 µg (approximately 50 pmol) of the scFvCD7 reagent alone, or pre-complexed with 50 pmol of the Alexa Fluor 488-coupled siRNA. This concentration of scFVCD7 and siRNA are suboptimal for knockdown purposes, but the goal of this experiment was to demonstrate delivery. The spheres were then placed in culture with Jurkat T cells in a 96-well plate, and CD7 expression and Alexa Fluor 488 fluorescence were measured on the Jurkat cells by flow cytometry over several days to monitor scFvCD7/siRNA delivery (**Figure 23**). Based on previous experiments in Task 9 with delivery of fluoresceinated immunoglobulin, we expected the CD7 reagent to be delivered slowly over 3–5 days. Our results showed a modest diminution of CD7 expression at 24 h in the Jurkat cells cultured with the scFvCD7 loaded spheres, with no accompanying fluorescence. By 72 h, CD7 expression had returned to pretreatment levels. We did not detect any fluorescence in the Jurkat cells cultured with the scFvCD7/siRNA-loaded spheres and no fluorescence was detected in the spheres when the experiment was terminated. We believe that the negative charges of the alginate may have disrupted the scFVCD7 interaction with the fluoresceinated siRNA, which then freely diffused out of the spheres. The scFVCD7 reagent may have also diffused out of the spheres rather quickly since it has a relatively low molecular weight (32 kDa), and the reduced expression we observed at 24 h may have been CD7 returning to pretreatment levels. Importantly, the spheres were not toxic to the T cells. Based on our results, we plan, in future projects, to reformulate our sustained delivery system to preserve the association between the scFvCD7 construct and the siRNA. Some of these experiments will be conducted under Task 9, which, as a part of Aim 2, is extended into 2013.

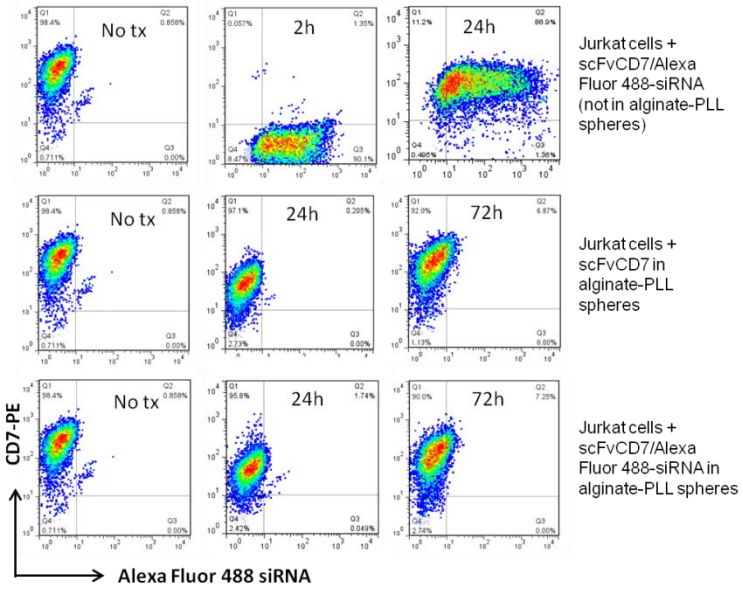

Figure 23. Delivery of scFvCD7/Alexa Fluor 488 siRNA complexes into Jurkat T cells via alginate-PLL spheres. Top: *Jurkat T cells were incubated in the presence of a 1:1 complex of scFvCD7+ Alexa Fluor 488-labeled siRNA (100 pmol each) for the indicated time and CD7 expression and uptake of Alexa Fluor 488-labeled siRNA were monitored by flow cytometry.* ***Middle, Bottom:*** *Jurkat cells were incubated in the presence of alginate-PLL spheres loaded with 50 pmol of scFvCD7 or a complex of scFvCD7/Alexa Fluor 488-siRNA (50 pmol each) for the indicated time and assayed as above to monitor diffusion of the scFvCD7/siRNA from the spheres.*

Final studies for Task 4 were focused on achieving more robust functional phenotypes following siRNA knockdown of stimulated CD4+ T cells than were observed in our previous experiments, which used unstimulated T cells. Primary CD4+ T cells were stimulated *in vitro* with plate bound anti-CD3 antibody and soluble anti-CD28 for 3 days and were then transfected with 100 pmol of Lamin or PTPN2 siRNA using Amaxa transfection optimized for stimulated human T cells. As shown in **Figure 24**, stimulated CD4+ T cells were efficiently transfected, with nearly 100% of cells taking up fluoresceinated siRNA. There was only 10% cell death 1 h after transfection, which did not increase after 48 hr. RNA was harvested from the cells at 48 hr, 72 hr, and 96 hr after transfection, and Lamin and

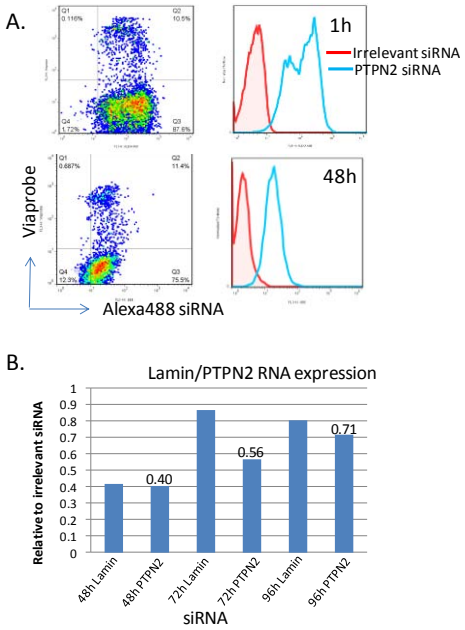

Figure 24. SiRNA gene specific knockdown in stimulated CD4+ T cells. *CD4+ T cells were isolated from frozen PBMC by negative selection and were stimulated in vitro with plate bound anti-CD3 and soluble anti-CD28. After 3d, cells were Amaxa transfected with 100 pmol of the indicated siRNA.* ***(A)*** *Transfection and viability was assessed by flow cytometry 1 and 48h after transfection.* ***(B)*** *RNA expression was analyzed by qPCR at the indicated times, and was expressed relative to an irrelevant siRNA.*

PTPN2 RNA levels were assessed by qPCR. We found RNA levels were reduced by 60% at 48 hr, 44% at 72 hr and 29% at 96 hr. This level of PTPN2 RNA knockdown is comparable to the reduction in PTPN2 RNA levels observed with the *PTPN2* rs1893217 autoimmune risk allele, which correlates with decreased cytokine signaling in T cells. Future experiments will evaluate the functional phenotypes associated with siRNA-mediated knockdown in stimulated CD4+ T cells.

Conclusions, Task 4

In Task 4, we developed protocols for efficient transfection of siRNAs into unstimulated primary T and B cells, which resulted in gene-specific knockdown. siRNAs for PTPN22, PTPN2, STAT3, and IL-6R were validated, and were shown to elicit a 40–80% reduction in gene-specific RNA for 3–4 days following transfection. We also showed that RNA knockdown was associated with a reduction in corresponding protein synthesis that lagged behind the RNA knockdown by 24–48 hr. Functionally, siRNA- mediated knockdown of the above gene targets in unstimulated CD4+ T cells was associated with modest phenotypes, which included: (1) increased TCR signaling in PTPN22 siRNA-transfected cells, as measured by calcium flux, which was consistent with the role of PTPN22 in dampening TCR signal strength; (2) decreased IL-2 signaling in PTPN2 siRNA-transfected cells, which copies the phenotype induced by a genetic variant in PTPN2 that reduces PTPN2 expression; and (3) decreased IL-6 signaling in cells transfected with either IL-6R or STAT3 siRNAs.

We have developed a variety of approaches improve the efficiency of siRNA-mediated gene knockdown in order to increase in the magnitude of functional phenotypes. These include shRNA delivery via lentiviral infection of stimulated CD4+ T cells, siRNA delivery into unstimulated or stimulated CD4+ T cells by single-chain anti-CD7 antibody, and transfection of siRNA into stimulated CD4+ T cells. All three of these methods successfully deliver shRNA/siRNA into T cells. Future projects will refine these methods with an objective of maximizing the duration and magnitude of functional T cell phenotypes that suppress inflammation and improve wound repair.

Collectively, the findings made under Task 4 have important implications for our future research. The PTPN22 siRNAs are an invaluable tool to reverse the immune phenotypes resulting from the 1858T genetic variant in PTPN22 that causes susceptibility to various autoimmune diseases. The PTPN2, STAT3, and IL-6R siRNAs can modulate IL-6 signaling which drives Th17 cell differentiation, which we are currently testing. In summary, we have made good progress in towards the goal of modulating CD4+ T cell development using shRNA/siRNAs.

Task 5

Evaluate *in vivo* candidate siRNA using DO11.10-Treg transfection (Steven Ziegler, PhD).

Task 5 is the *in vivo* arm of Aim 1 C (begun in Year 2), which extended the studies described in Task 4 to *in vivo* models of Treg function, using the DO11.10 mouse model. We and others have shown that transfer of activated DO11.10 effector cells into lymphopenic (Rag-deficient) mice that express ovalbumin in the pancreas (RIP-mOVA mice) results in the rapid onset of diabetes. However, co-transfer of DO11.10-derived Tregs can block disease onset **(Figure 25)**. To test the genes identified in the siRNA knockdown screen described in Task 4, we transfected DO11.10-Tregs with the specific siRNAs and tested the ability of those cells to protect in the co-transfer disease model. Essentially, the immune system attack against ovalbumin in the pancreas in this model is a surrogate for immunologically-mediated tissue injury, and therefore is a model for the types of tissue injury and repair under study in the CITR, which can occur in many different tissue contexts. The advantage of using this particular mouse is that, when the RIP-mOVA pancreas is injured, there is a very direct and simple biomarker for tissue damage, namely loss of insulin and resultant hyperglycemia, which makes this an ideal model system for our studies.

After transfer into the RIP-mOVA/Rag-/- host mice (referred to as RO mice), the naïve DO11.10+ T cells begin to express FOXP3 and take on a Treg-type phenotype (these cells are referred to as *induced Tregs*, or iTregs), resulting in durable tolerance in the mice. To understand the pathways involved in this process, we

eliminated, through genetic ablation, specific genes suggested to be involved in this process. These include cytokine genes IL-6 (tested in Task 4), IL-17, IL-21, IFNγ, and transcription factors STAT1, STAT4, and T-bet.

To begin to understand the pathways involved in these processes, we generated DO mice that lacked specific cytokine or transcription factor genes already shown to be involved in CD4+ T cell function. We tested the role of signature cytokines for the Th1 (IFN-γ) and Th17 (IL-17A) lineages in our model system. As shown in **Figure 26**, IL-17A-deficient DO/RAG T cells were similar to wild-type DO/RAG T cells following transfer. The mice receiving these cells developed tolerance when left untreated, and developed disease when either immunized or injected with poly I:C. In contrast, RO/RAG mice that received DO/RAG T cells lacking IFN-γ developed tolerance normally in the absence of inflammatory stimulation, but also maintained tolerance in the presence of inflammation. These data suggest that expression of IFN-γ by the transferred T cells following inflammatory stimulation inhibits the ability of the cells to induce FOXP3 and become iTregs.

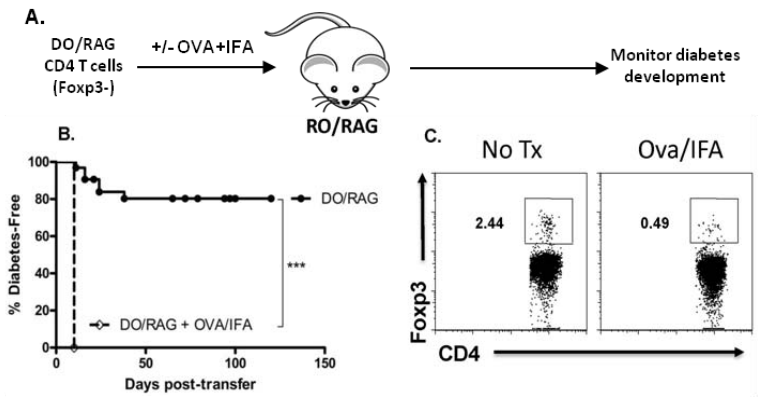

Figure 25. Immunization can undermine tolerance and de novo Foxp3 induction in tissue-specific CD4+ T cells. (A) *Schematic of model used.* ***(B)*** *DO/Rag T cells were transferred into RO/RAG recipients (2 x 10^5). Controls were left untreated (solid line) and one group of mice was injected with OVA/IFA (200 µg) 1 day after transfer (dashed line). Blood glucose was monitored and mice were considered diabetic at > 250 mg/dL blood glucose. Data are presented as % disease free.* ***(C)*** *Mice were sacrificed on day 13 and spleens from control (No Tx) and immunized (Ova/IFA) mice and cells were stained with CD4, KJ1-26 (specific for DO11.10 TCR), and FOXP3. KJ1-26+ cells were gated, and CD4 and FOXP3 expression determined. Numbers indicate % cells in the gate. Representative plots are shown, n = 3–4 mice per group.*

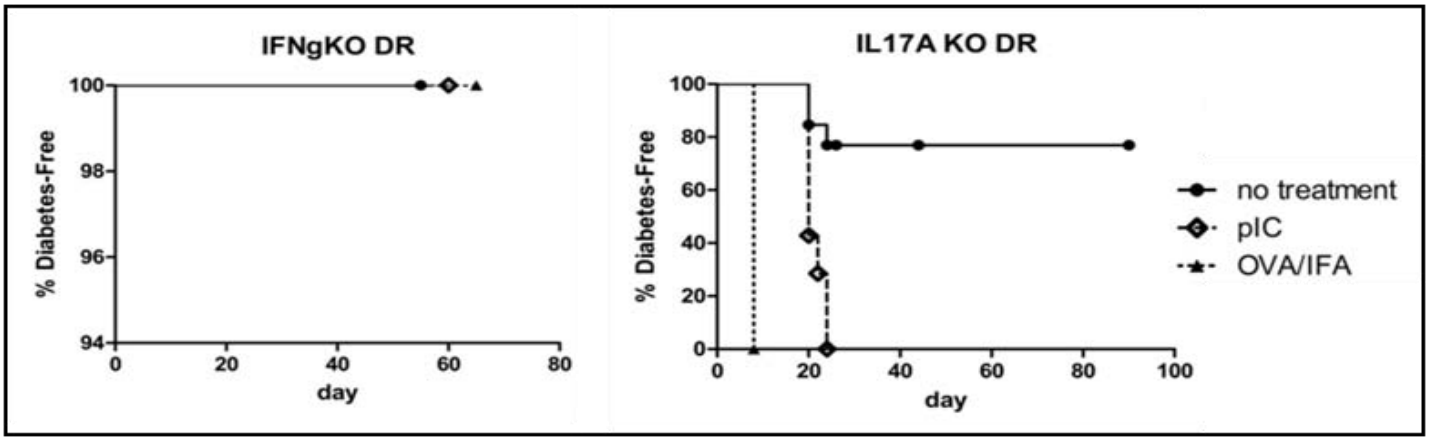

Figure 26. IFN-γ, but not IL-17A, is involved in the inhibition of iTreg generation following transfer of naïve CD4+ T cells. *CD4+ T cells were isolated from DO/RAG mice that also lacked IFN-γ (left panel) or IL-17A (right panel) and transferred into RO/RAG hosts. One day after transfer the mice were treated with PBS (no treatment), poly I:C (pIC) or ovalbumin in IFA (OVA/IFA). Disease development was then monitored by measuring blood glucose levels (BGL). Data are presented as % mice with normal blood glucose. Disease is defined as 2 consecutive BGL measurements of >250 mg/dL.*

In subsequent studies, we focused on the events that take place prior to transfer, asking whether the effect of polyI:C-mediated inflammation was directly on the naïve T cells, or on another cell population. DO/RAG mice were given polyI:C on days -2 and -1, and then CD4+ T cells were isolated on day 0 and transferred into RO/RAG mice. As controls, T cells from untreated DO/RAG mice were transferred into RO/RAG and either left untreated, or given polyI:C one day after transfer. As shown in **Figure 27**, T cells from the mice pre-treated with polyI:C protected as well as those from untreated mice, suggesting that inflammation alone is not enough to drive disease development.

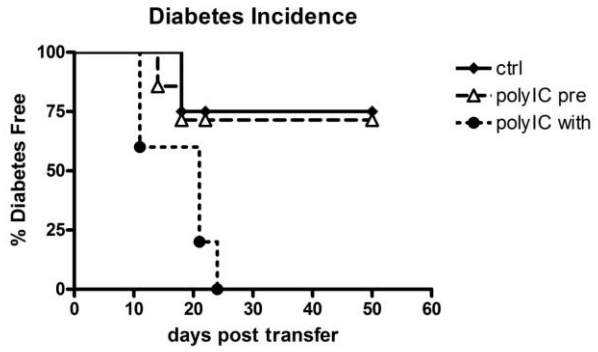

Figure 27. Prior exposure to non-specific inflammation does not affect iTreg generation in vivo. *CD4 T cells were isolated from either control mice or mice treated with polyI:C on days -2 and -1 before isolation (poly IC pre). T cells were transferred into RO/RAG hosts and disease progression measured by blood glucose levels. ctrl: no-pretreatment and no post-treatment; poly IC with: no pretreatment and poly I:C given on day 1 and 2 post-transfer.*

We next performed a similar experiment, isolating spleen and lymph nodes from from polyI:C-treated or untreated DO/RAG mice. However, instead of isolating CD4+ T cells for transfer into RO/RAG hosts, we cultured them *in vitro* with antigen (OVA peptide) in the presence or absence of TGF-β to assess their ability to develop into iTregs. To our surprise, the T cells from the polyI:C-treated mice displayed a marked increase in FOXP3+ cells **(Figure 28)**. These data suggests that the exposure of the naïve T cells to non-specific inflammatory stimuli "primes" them to differentiate into iTregs when they encounter their cognate antigen. We are now using both genetic and antibody blockade techniques to identify the factors involved in this phenomenon.

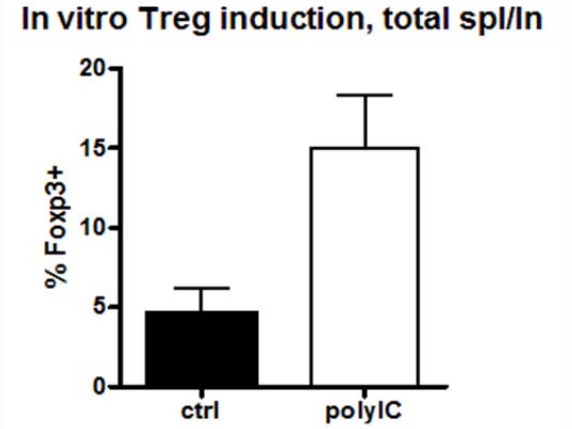

Figure 28. Increased iTreg differentiation after exposure to non-specific inflammation. *DO/RAG mice were given polyI:C or PBS on days -2 and -1, and the following day spleens and lymph nodes were isolated and cultured with OVA +/- TGF-β for 5 days. At that time the cells were analyzed for expression of CD4 and FOXP3 by flow cytometry. Data are shown as % CD4+FOXP3+ cells, and averaged 4 mice/group.*

Conclusions, Task 5

Using a genetic approach we have characterized the pathways involved in the *in vivo* conversion of naïve CD4+ T cells to induced regulatory T cells (iTregs). We have also uncovered a novel mechanism for generating iTregs involving the pre-exposure of naïve CD4+ T cells to non-specific inflammatory stimuli. In future studies, we will test whether a similar phenomenon exists for human T cells.

Task 6

Evaluate siRNA for TREM-2 and DAP12 for inhibition of TNF production by THP-1 cells (Jessica Hamerman, PhD).

Task 6 was a component of Aim 1D (Part 1). While Aims 1B and 1C targeted the adaptive immune response through control of Treg maturation and function, Aim 1D evaluated innate immune regulators as potential targets for anti-inflammatory intervention during wound repair. Specifically, Aim 1D assessed several endogenous inhibitors of the macrophage inflammatory response, TREM-2, BCAP, and β2 integrins, with the goal of developing strategies to downmodulate the macrophage inflammatory response as one of the multi-faceted approaches for cytoprotection examined in this project.

The macrophage inflammatory response is potently activated by pattern recognition receptors which include the TLR family, which, when ligated, results in the secretion of pro-inflammatory cytokines, such as tumor necrosis factor, IL-12, and IL-6, as well as chemokines that attract other immune cells. One mechanism by which the inflammatory response is controlled is through endogenous inhibitors or negative regulators of TLR signaling. In Aim 1D, we proposed to investigate several inhibitors of TLR signaling, with the long-term goal to develop strategies for turning on these inhibitory pathways with either small molecules or soluble

proteins that can be incorporated into the Cytoprotective Implant hydrogels to modulate the macrophage inflammatory response during wound repair.

We have spent several years investigating the anti-inflammatory receptor complex made up of the Triggering Receptor Expressed on Myeloid cells (TREM)-2 receptor and its dialkyl phosphate (DAP)12 signaling chain. Using mouse models, we have shown that TREM-2/DAP12 inhibits macrophage TLR responses both *in vitro* and *in vivo*. Accordingly, for the initial part of this project (Task 6), we investigated whether TREM-2 and DAP12 might serve as innate immune regulators by dampening inflammatory responses in human macrophages. To accomplish this, we performed experiments to knock down TREM-2 and DAP12 in human monocytes and monocyte-derived macrophages, using a set of corresponding siRNAs that targeted human TREM-2 and DAP12. We began our experiments by testing the effectiveness of the siRNAs in THP-1 cells, a monocyte-like cell line; however, we encountered difficulty in measuring the efficacy of knockdown when we used a flow cytometry-based method to detect of TREM-2 and DAP12 protein. As an alternative approach, we established a qPCR assay for measuring TREM-2 and DAP12 mRNA. **Figure 29** shows that we can measure TREM-2 mRNA in THP-1 cells and in cultured monocytes. Using the qPCR assay, we demonstrated that TREM-2 expression is induced on human monocytes after differentiation into macrophages in the presence of macrophage colony stimulating factor.

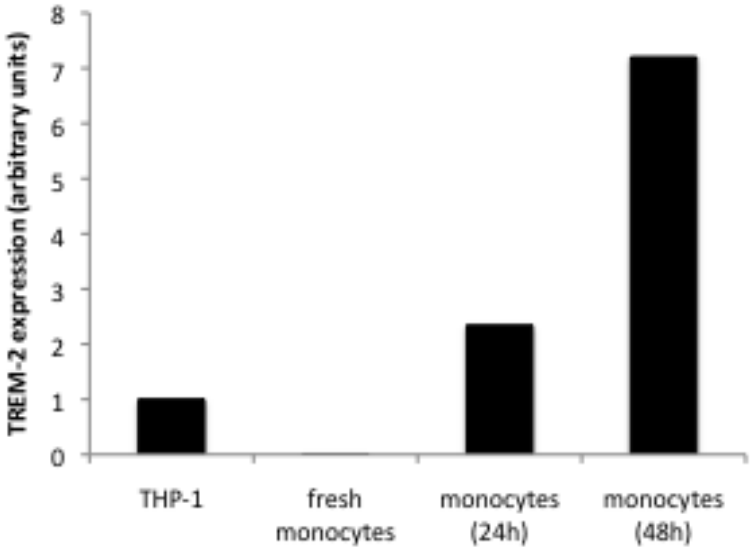

Figure 29. Expression of TREM-2 mRNA in THP-1 cells and CD14+ monocytes. *CD14+ monocytes were isolated from PBMCs and either lysed for RNA or plated for 24 or 48 hours to induce expression of TREM-2 and then lysed for RNA. cDNA from these monocytes, or from THP-1 cells, were subjected to qPCR analysis for TREM-2.*

Conclusions, Task 6

We conclude from our studies on Task 6 that the TREM-2 inhibitory receptor is not expressed on circulating monocytes, but that its expression is induced upon differentiation into macrophages *in vitro*. This finding suggests that the function of TREM-2 is to inhibit macrophage function in tissues, not to inhibit monocyte function in the blood. We were not able to achieve efficient knockdown of TREM-2 and DAP12 in human monocyte-derived macrophages during these studies. Future studies will focus on human macrophage cell lines, which may be more amenable to transduction with siRNAs.

Task 7

Measure TLR activation by cytokine production and phospho-specific antibodies in CD18 and BCAP KO mice, and map BCAP domains as potential therapeutic targets (Jessica Hamerman, PhD).

For Aim 1D, Parts 2 and 3 (addressed under Task 7), we investigated two novel inhibitors of TLR signaling, β2 integrins and BCAP, using knockout mice. We began experiments to analyze TLR responses in CD18 (β2 integrin)-deficient mice. Wild-type or CD18-deficient mice were injected with 100 μg of LPS and serum collected at 1, 2, 4 and 6 hr after injection. The amount of TNF, IL-6 and IL-12 p40 in the serum was then measured by using ELISA. As shown in **Figure 30**, CD18-deficient mice produced more TNF and IL-12 p40 than wild-type mice, though the kinetics of induction was identical between wild-type and CD18-deficient mice. These data showed that CD18 inhibits TLR responses *in vivo* as well as *in vitro* in macrophages.

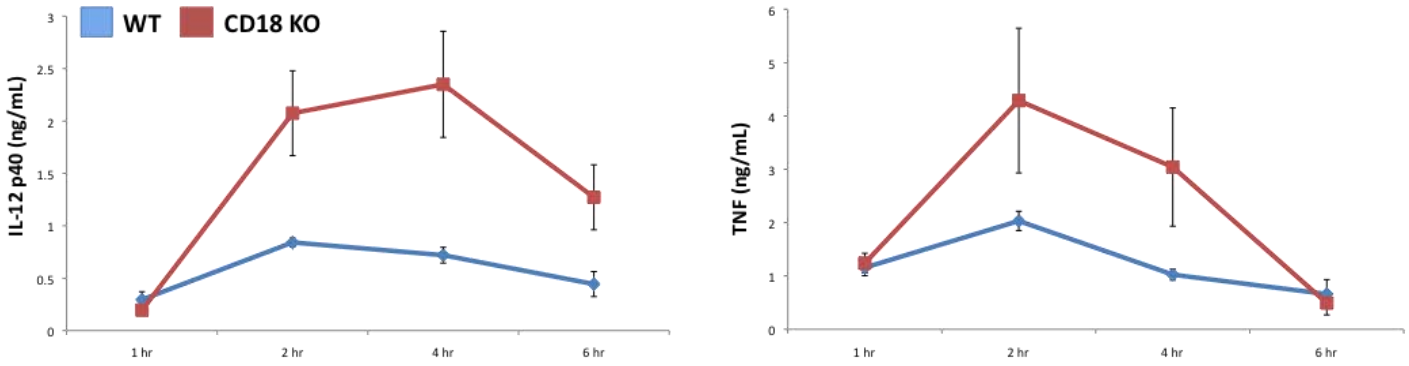

Figure 30. CD18 inhibits TLR responses in vivo. *Wild-type and CD18-deficient mice were injected with 100 μg of LPS. Serum was collected at 1, 2, 4 and 6 hours after injection. Serum cytokine amounts were measured by using ELISA. Wild-type mice (WT) are shown in blue and CD18-deficient mice (CD18 KO) in red. Data are shown as mean +/- SEM. N = 5 mice per group.*

We then compared cytokine production on a per cell basis from peritoneal macrophages from wild-type (WT) and CD18-deficient mice. We found that peritoneal macrophages from CD18-deficient mice produced more IL-6 and IL-12 p40 than those from WT mice, whereas the production of TNF was similar between the two genotypes (**Figure 31**). These data are similar to our findings with bone marrow-derived macrophages and further strengthen our conclusion that β2 integrins inhibit TLR signaling in a variety of macrophage populations.

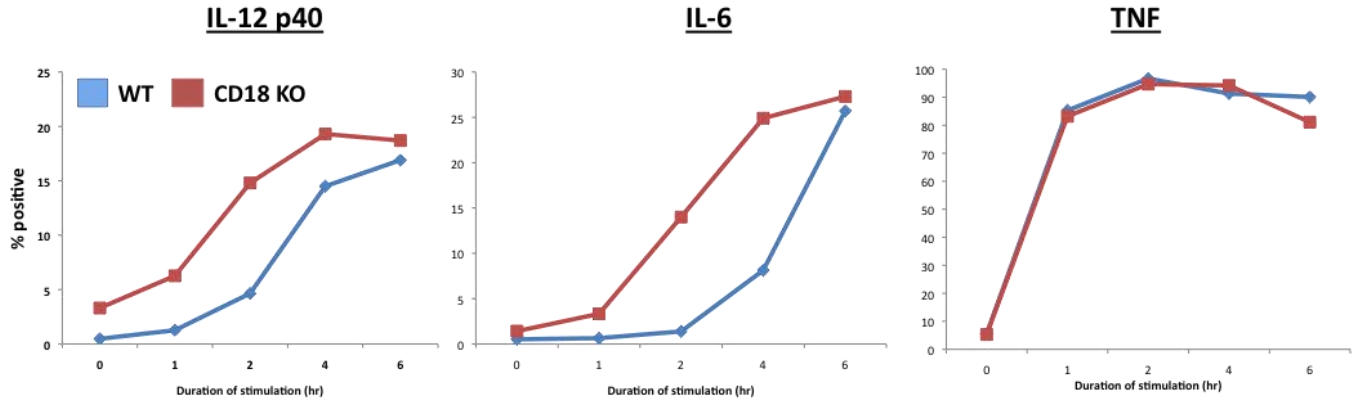

Figure 31. CD18-deficient peritoneal macrophages hyper-respond to TLR agonists. *Macrophages were isolated from the peritoneal cavity of WT and CD18-deficient mice 3 days after injection of thioglycollate broth. The cells were cultured overnight and then treated with LPS for the indicated times, with Brefeldin A added for the last 4 hours. After harvest, cells were surface stained for F4/80 to identify macrophages, stained intracellularly for IL-12 p40, IL-6 and TNF, and analyzed by flow cytometry. The data are represented as the percent of F4/80 macrophages producing each cytokine.*

We next expanded our studies beyond the inhibition of TLR responses by β2 integrins to investigate how BCAP inhibits TLR responses. This was done by comparing TLR-induced signal transduction in WT and BCAP-deficient macrophages. We treated WT and BCAP-deficient macrophages with LPS and prepared cytoplasmic extracts at different times after treatment. We then used SDS-PAGE and Western blot to examine the activation of the 3 MAPK signaling pathways and the activation of the NF-κB pathway. As shown in **Figure 32**, there was a slight enhancement of p38 MAPK and ERK phosphorylation after LPS treatment in BCAP-deficient macrophages in comparison with wild-type macrophages. In contrast, there was no change in the degradation of IκBα protein, the cytoplasmic inhibitor of NF-κB translocation to the nucleus (**Figure 33**). This led us to conclude that BCAP-deficiency subtly affects the activation of MAPK pathways, but does not affect NF-κB activation

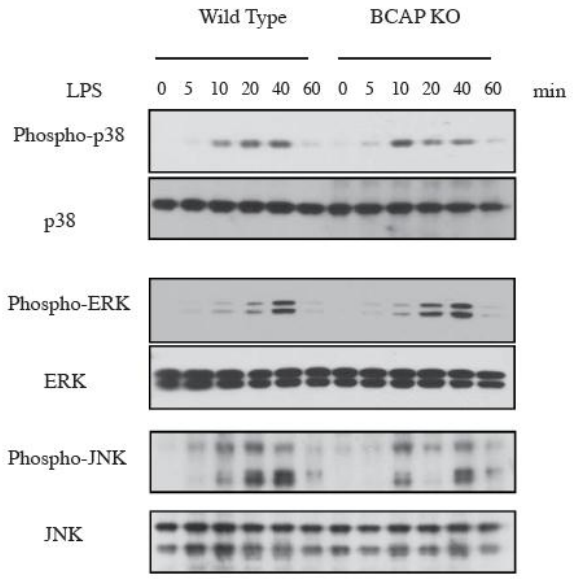

Figure 32. BCAP-deficient macrophages have slightly increased MAPK activation. *WT or BCAP-deficient bone marrow-derived macrophages were treated for the indicated amount of time with 1 ng/ml LPS after which the cells were lysed and cytoplasmic extracts were generated. Cytoplasmic extracts were separated by SDS-PAGE and Western blotted with antibodies specific for different MAPK proteins or their phosphorylated forms.*

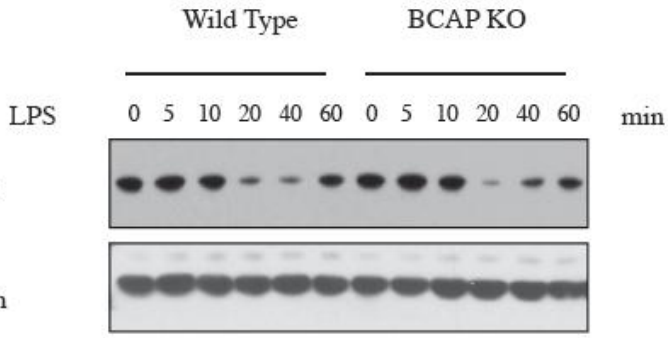

Figure 33. BCAP-deficient macrophages have no change in IkBα degradation. *WT or BCAP-deficient bone marrow-derived macrophages were treated for the indicated amount of time with 1 ng/ml LPS after which the cells were lysed and cytoplasmic extracts were generated. Cytoplasmic extracts were separated by SDS-PAGE and Western blotted with antibodies specific for IkBα or β-actin as a loading control.*

Our subsequent experiments examined how BCAP-deficiency affects activation of the PI3-kinase pathway downstream of LPS. To measure PI3K activity, we measured the phosphorylation of Akt after LPS treatment of WT and BCAP-deficient macrophages. As shown in **Figure 34A**, BCAP-deficient macrophages had significantly reduced Akt phosphorylation after LPS treatment compared to WT macrophages. To confirm that the BCAP-deficient macrophages had less PI3K activity than WT macrophages, we treated both types of macrophages with the PI3K inhibitor wortmannin. PI3K inhibition is known to increase TLR responses in WT macrophages, and we reasoned that if there was less PI3K activation in BCAP-deficient macrophages, then wortmannin would have a reduced effect on these cells compared to its effect on WT macrophages. As shown in **Figure 34B**, WT macrophages increased TLR-induced IL-6 and IL-12 p40 after treatment with wortmannin, but there was little increase in BCAP-deficient macrophages. Therefore, we concluded that PI3K activation after TLR ligation is reduced in the absence of BCAP.

We have shown by retroviral reconstitution that re-introduction of BCAP into BCAP-deficient macrophages can reduce TLR responses to a level similar to that seen in WT macrophages. To determine if the ability of BCAP to inhibit TLR responses depends upon its ability to bind to PI3K, we transduced BCAP-deficient macrophages with a

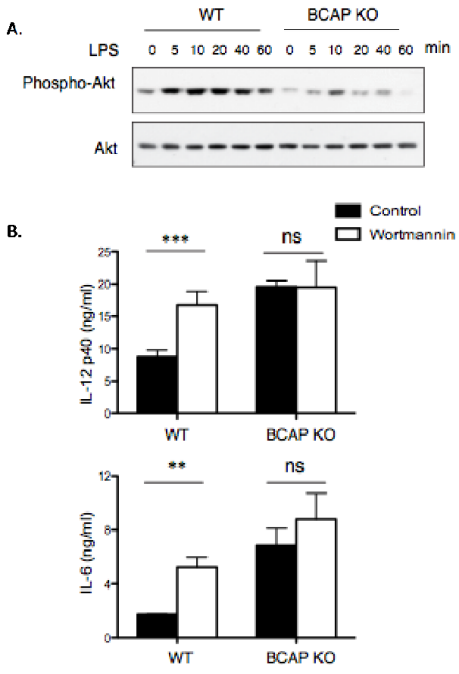

Figure 34. BCAP-deficient macrophages have reduced PI3K activity. (A) *WT or BCAP-deficient bone marrow-derived macrophages were treated for the indicated amount of time with 1 ng/ml LPS after which the cells were lysed and cytoplasmic extracts were generated. Extracts were separated by SDS-PAGE and Western blotted with antibodies specific for Akt or its phosphorylated form.* ***(B)*** *Macrophages were treated for 1 hour with 200 μM wortmannin and then with 25 nM CpG DNA for 16 hours. TNF and IL-6 secretion was measured by ELISA.*

retrovirus either encoding a mutant of BCAP that cannot associate with PI3K due to mutation of the tyrosines within the 4 YxxM motifs to phenylalanine (Y4F), or with the un-mutated (control) protein. We then compared the ability of the transduced macrophages to inhibit TLR responses. As shown in **Figure 35**, the ability of BCAP to inhibit TLR responses depended upon these 4 tyrosine residues and therefore upon PI3K binding. Collectively, our data showed that the ability of BCAP to inhibit TLR responses is through its binding and activation of the PI3K pathway.

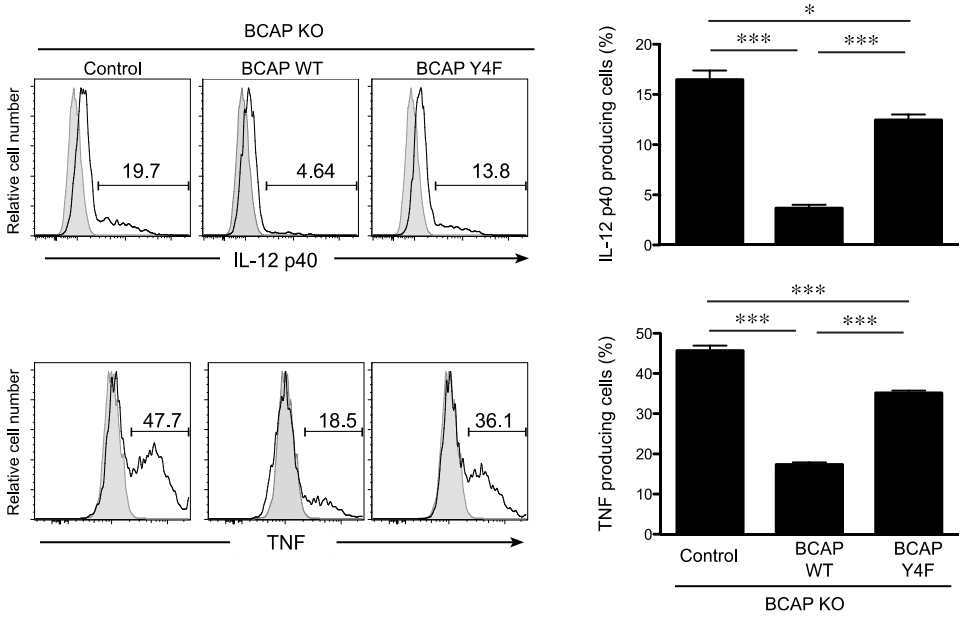

Figure 35. BCAP requires PI3K binding to inhibit TLR responses. *BCAP-deficient bone marrow-derived macrophages were transduced with empty retrovirus (control) or retroviruses encoding the wild-type BCAP protein (BCAP WT) or a mutated version of BCAP that cannot bind to PI3K (BCAP Y4F). Transduced macrophages were treated with CpG DNA (25 nM) and Brefeldin A for 6 hours and then TNF and IL-12 p40 production was measured by flow cytometry.*

The next series of studies was focused on β2 integrin-mediated inhibition of TLR responses. We have previously shown that macrophages lacking β2 integrins (CD18 KO) have increased IL-12 p40 and IL-6 secretion when compared to wild-type macrophages. As a follow up to these observations, we asked whether direct ligation of β2 integrins could inhibit TLR-induced cytokine production in wild-type macrophages. We performed these experiments in two ways. First, we took advantage of the fact that the adherence of macrophages to non-tissue-culture-treated plastic plates depends upon β2 integrin ligation. Therefore, we maintained macrophages in suspension in tubes with gentle rotation or plated them on dishes for 2 hr before activating with CpG DNA. TNF production was measured by intracellular cytokine staining. As shown in **Figure 36A**, macrophages that adhered to dishes through β2 integrins produced less TNF than macrophages maintained in suspension. We also adhered wild-type macrophages to plates coated with the β2 integrin ligand ICAM-1 or control protein and compared cytokine secretion after treatment with LPS by using ELISA. As shown in **Figure 36B**, cells plated on ICAM-1 Fc produced less TNF than those plated on uncoated wells (PBS) or control coated wells (IgG1 Fc). These data were consistent with our data generated with CD18-deficient macrophages showing that β2 integrins

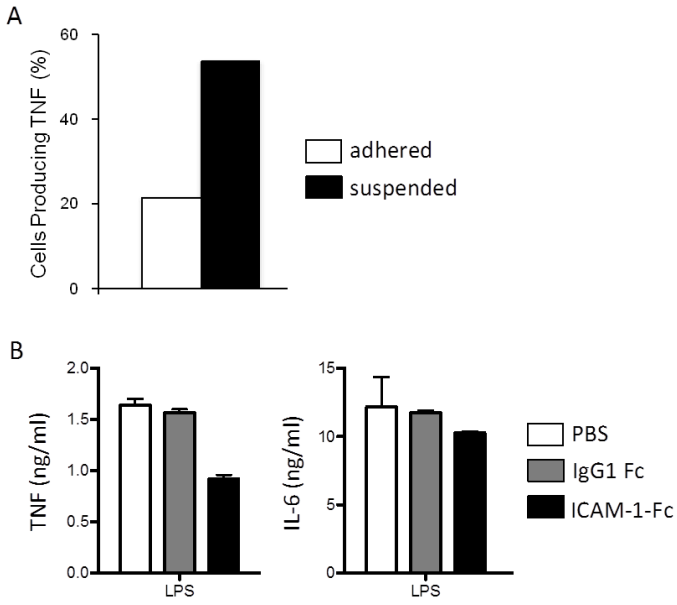

Figure 36. Direct ligation of β2 integrins inhibits TLR-induced pro-inflammatory cytokine production. (A) *Wild-type macrophages were maintained in suspension with gentle rotation or plated on non-tissue culture treated plates for 2 h and then treated with 10 nM CpG DNA for 2 h in the presence of Brefeldin A. Cells were then stained intracellularly for TNF and analyzed by flow cytometry.* ***(B)*** *Wild-type macrophages were plated on uncoated wells (PBS) or wells coated with control Fc fusion protein (IgG1 Fc) or ICAM-1 Fc fusion protein for 1 h and then treated with 0.5 ng/ml LPS overnight. Supernatants were then collected and TNF and IL-6 secretion measured by ELISA.*

serve to inhibit TLR responses.

Having finished our experiments investigating β2 integrins, we performed our last set of experiments investigating BCAP. We had previously showed that lipopolysaccharide (LPS)-induced MAPK activation and IκBα degradation were similar between wild-type and BCAP-deficient macrophages (IκBα is one member of a family of cellular proteins that function to inhibit the NF-κB transcription factor). Moving forward from this finding, we examined an additional readout of the NF-κB pathway: nuclear translocation of the NF-κB subunits c-rel and p65 in response to LPS. As shown in **Figure 37**, the nuclear translocation of c-rel and p65 was greatly reduced in BCAP-deficient macrophages in comparison to wild-type macrophages. This was a surprising finding given that the upstream degradation of IκBα was identical in the presence and absence of BCAP. This result was also surprising given that the BCAP-deficient macrophages produce more cytokines after TLR stimulation, even in the presence of the low levels of nuclear NF-κB subunits that we find. These data showed that BCAP is a pleiotropic signaling adapter downstream of TLR signaling and we plan future grant applications to further investigate this interesting molecule.

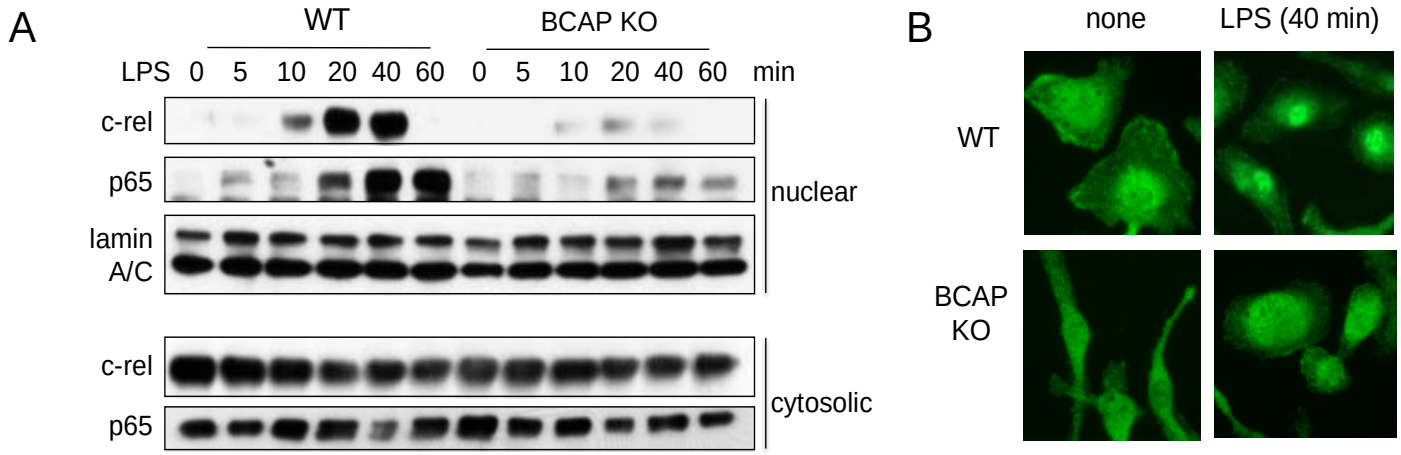

Figure 37. Reduced c-rel and p65 accumulation in the nucleus in the absence of BCAP. ***A)*** *Bone marrow-derived macrophages from wild-type (WT) or BCAP-deficient (BCAP KO) mice were incubated with LPS for the indicated times, separated into cytosolic and membrane fractions, and blotted as indicated.* ***B)*** *Macrophages were incubated with LPS, then fixed, permeabilized and stained for c-rel.*

Conclusions, Task 7

In Task 7, we have confirmed that β2 integrins inhibit TLR responses not only in bone marrow-derived macrophages, but also in inflammatory macrophage populations directly *ex vivo* and *in vivo* in mice. This finding supports the hypothesis that targeting β2 integrins may be a viable strategy for reducing inflammation during wound healing. We have also identified the mechanism by which BCAP inhibits macrophage inflammatory responses, which gives us valuable information for designing strategies to promote BCAP-mediated inhibition. Future studies will identify small molecule or protein agonists of the β2 integrin and BCAP pathways that could be incorporated into hydrogel constructs for treatment of injury to reduce inflammation during wound healing.

Task 8

Measure serum biomarkers in 20 human subjects treated with IL1RA after inflammatory stimulus (Srinath Sanda, MD).

This Task was a component of Aim 1E. Cytokines mediate tissue injury and cellular dysfunction across a broad range of diseases. Specific cytokines, such as IL-6 and IL-8, are emerging as important mediators in sepsis and as prognostic indicators of systemic inflammation in patients with traumatic injury. Our conceptual understanding of wound healing has evolved to include a complex interaction of inflammatory cytokines. Over the past decade, numerous agents have been developed to block the action of specific cytokines. These therapies have revolutionized the treatment of autoimmune conditions, such rheumatoid arthritis and inflammatory bowel disease. However, given the broad range of inflammatory mediated diseases, cytokine modulating agents may have utility in other areas of medicine, as has recently been observed with the beneficial effect of the administration of TGF-β3 in wound healing.

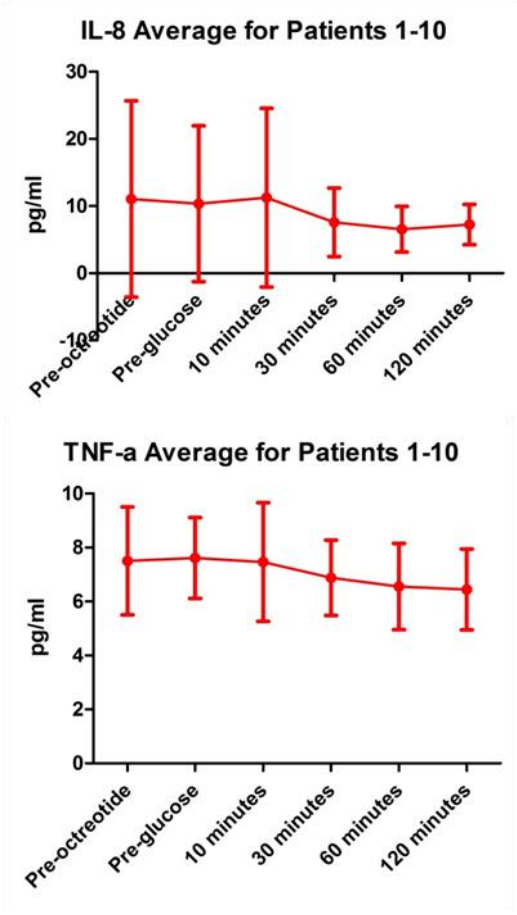

Figure 38. IL-8 and TNF-α in serum of patients during visit 1 (before anakinra).

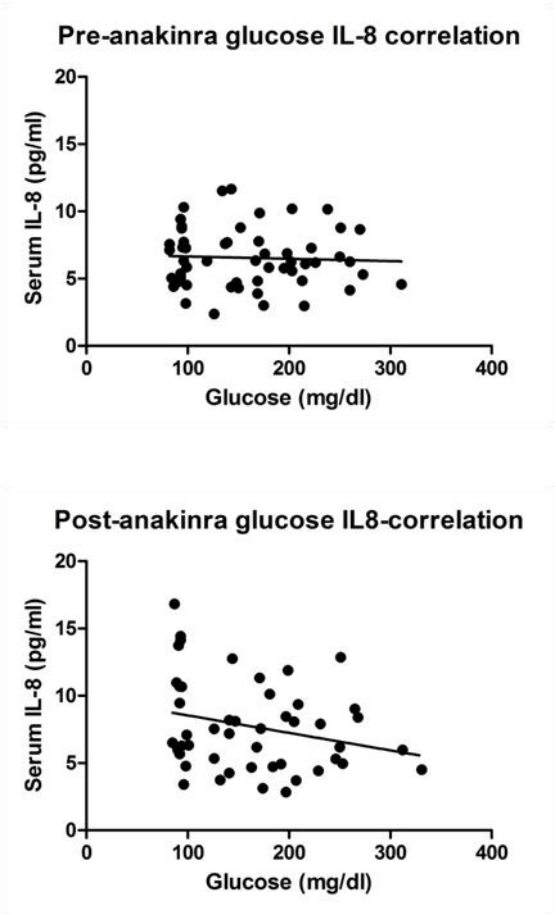

Figure 39. Correlations between glucose and serum IL-8 in patients before and after exposure to anakinra.

Aim 1E tested the protective role of inflammatory cytokine blockade in humans prior to an inflammatory stimulus. After receipt of Human Subjects approval, we began to test the protective role of inflammatory cytokine blockade in humans prior to an inflammatory stimulus (induced hyperglycemia). The study design involved a total of 10 patients and use of a 3-day course of anti-cytokine blockade after the first study visit and prior to repeating the induced hyperglycemia. Each patient presented to the clinical research center (CRC) and received an octreotide infusion to temporarily halt endogenous insulin secretion. They then received an IV bolus of glucose and had serum and peripheral blood mononuclear cells (PBMCs) collected for the next two hours. The subjects then received a daily dose of an IL-1 receptor antagonist, *anakinra*, for 3 days and returned to the CRC for a repeat of the

octreotide/glucose combination. No significant adverse events occurred during the course of the study. Our major focus was the measurement of serum IL-8, a major inflammatory cytokine that is easily and reliably measured in serum following induced hyperglycemia.

In our analysis of all 10 patients, we did not see a significant difference in serum cytokines with hyperglycemia, which suggests that this model may be inadequate to induce significant levels of inflammation. We have tested serum for IL-1β, IL-6, TNF-α, and IL-8. The IL-1β and IL-6 levels were too low to accurately quantify. Graphs of the IL-8 and TNF-α data during the first visit (before exposure to the IL-1 receptor antagonist anakinra) are shown in **Figure 38**. There was no difference in correlations between glucose and either IL-8 or TNF-α before or after anakinra. Correlations for IL-8 with glucose are shown in **Figure 39**.

We next performed assays on the frozen PBMCs and analyzed changes in intracellular signaling molecules and surface markers on the monocytes and T cell populations. Given our prior experience with anti-IL-1 therapy, we assessed whether hyperglycemia in the presence or absence of IL-1 blockade would result in changes in monocyte surface markers and IL-17 expression in CD4+ T cells. After analyses of the 10 subjects, we did not observe statistically significant differences in any of these phenotypic markers before and after glucose, regardless of the presence or absence of the IL-1 receptor antagonist anakinra.

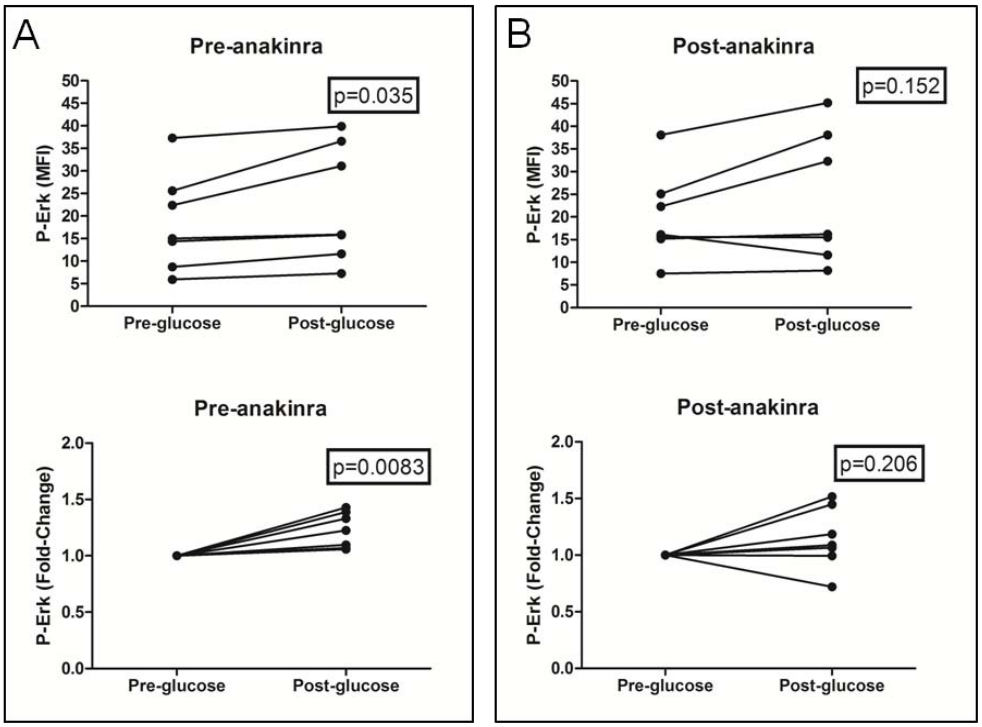

Figure 40. Analysis of ERK phosphorylation in PBMCs isolated from patients pre- and post-hyperglycemia in the presence or absence of anakinra.

We hypothesized that acute hyperglycemia may have an early effect on T cell activation, since several signaling molecules are common to both the T cell receptor and the insulin receptor. We analyzed changes in phosphorylation of AKT and ERK, two signaling molecules downstream of the T cell receptor and the insulin receptor in subjects 4–10, given the lack of additional PBMCs for these analyses in subjects 1–3. No changes in AKT phosphorylation by flow cytometry were detected. Interestingly, we detected consistent and significant changes in phosphorylation of ERK by both MFI and fold-differences with hyperglycemia during visit 1 (pre-anakinra) (**Figure 40A**). However, when the patients were made hyperglycemic in the presence of anakinra, the differences in phosphorylation of ERK were gone (**Figure 40B**). These findings suggesedt that hyperglycemia may serve as a stimulus for early T cell activation and that such a stimulus may be mediated by IL-1β.

Subsequently, we preformed RNA-sequence analysis on whole blood RNA collected at the baseline visit, +60 minutes, and +120 minutes, pre- and post-glucose glucose/anakinra. Expression data on the 81 differentially expressed genes and genes related to immune function from all 10 subjects were averaged and presented as a heat map **(Figure 41)** (fold changes ranged from +2 to -2). It was clear that even a modest degree of hyperglycemia (see average glucose excursion for both pre-and post-anakinra visits below the heat map) significantly altered the expression of multiple genes. The most intriguing findings were related to induction of genes in the IL-1 pathway, such as caspase 4. IL-1 blockade with anakinra reversed these changes in inflammation-associated genes. The degree and rapidity of IL-1 gene expression with a modest stimulus is

novel. These data supported our initial hypothesis that hyperglycemia is an inflammatory stimulus and that cytokine blockade can prevent hyperglycemia induced inflammation.

Conclusions, Task 8

We conducted a novel clinical research study investigating the effects of IL-1 blockade on a generic inflammatory stimulus, hyperglycemia. Our study suggests that the inflammatory changes induced by hyperglycemia are mild, as neither our cellular analysis nor serum analysis demonstrated any significant difference in markers before or after hyperglycemia or any impact of IL-1 blockade. However, we were able to detect clear changes in certain inflammatory genes induced by hyperglycemia, such as caspase 4. More importantly, we showed that expression of these genes was inhibited by the use of drug that blocks the activity of IL-1 (the IL-1 receptor antagonist anakinra). Collectively, our data have established the proof-of-principle that inflammatory stimuli rapidly induce gene expression and that pre-emptive treatment with anti-inflammatory drugs prevents this gene expression. Future studies will focus on directly addressing the functions of hyperglycemia-induced genes, which may have implications for treatment of a variety of diseases, including diabetes.

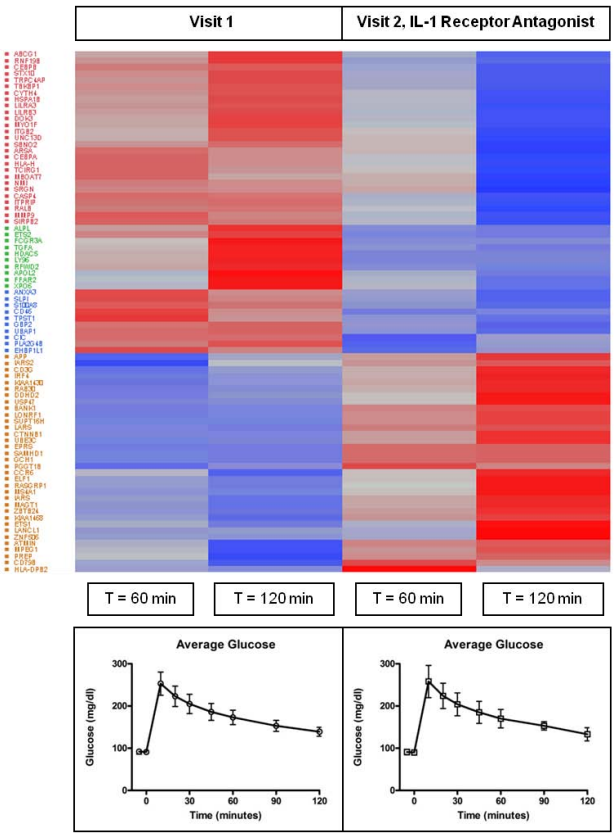

Figure 41. Gene expression analysis rendered as a heat map. *Upregulation of gene expression is indicated by warm (red) tones. Gene downregulation is indicated by cool (blue) tones.*

Task 9

Production of the three-layer CI "sandwich" (Robert Vernon, PhD).

Task 9 was a component of Aim 2A which involved the design and fabrication of the Cyotprotective Implant (CI). The design of the CI incorporated a number of novel features to optimize its functional properties: (1) a thin, flat, flexible shape to conform to the varied dimensions of wound beds and graft sites; (2) a composition of ECM components that are nontoxic and biodegradable; and (3) inclusion of bioactive molecules selected for immune modulation, stimulation of angiogenesis, cell differentiation, and tissue regeneration. These bioactive molecules would be bound to the CI's ECM to be released over time as the ECM biodegrades *in vivo*. An initial form for the CI was three-layered sandwich consisting of a crosslinked HMW-HA hydrogel compressed between two gelatin sponges (**Figure 42**). Initial experiments focused on material selection for the CI. For the gelatin scaffold component, we produced prototype 0.75–1 mm thick gelatin sponges made by casting 10% bovine gelatin in a mold, followed by crosslinking with glutaraldehyde (GA) and freeze-drying. We also produced gelatin sponges crosslinked with 1-ethyl-3-(3-dimethylaminopropyl)-carbodiimide/N-hydroxysuccinimide (EDC/NHS), which is significantly less cytotoxic than GA and yields sponges with similar strength. The EDC/NHS crosslinked gelatin sponges were easily cut into a variety of shapes and could be perforated with 0.4 mm diameter holes (**Figure 43**). The sponges rehydrated readily, absorbing 85+% of their total weight of water. In addition to our

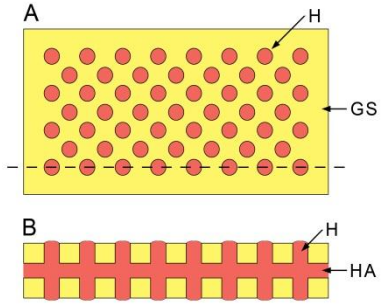

Figure 42. Concept for the CI. (A) *Surface of the CI shows one of the gelatin sponges (GS – tan), which is perforated with an array of holes (H), each 0.4 – 0.5 mm in diameter and filled with HMW-HA gel (pink).* ***(B)*** *A cross-section through the CI (dotted line in A) shows the top and bottom gelatin sponges (tan) and the central HMW-HA layer (HA-pink).*

own gelatin sponge constructs, we evaluated a commercially-available crosslinked gelatin sponge product (Gelita-Spon™, Invotec International, Jacksonville, FL) (**Figure 44**). This product is approved for clinical use, with a degradation rate of up to 4 weeks.

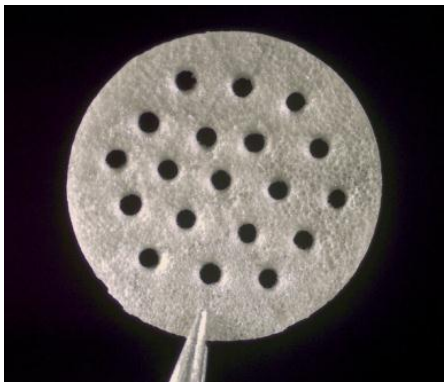

Figure 43. Example of a 0.75 mm thick, 8 mm diameter, disk-shaped gelatin sponge prototype. *The prototype is perforated with an array of 0.4 mm diameter holes. The gelatin in this prototype was crosslinked with EDC/NHS.*

Figure 44. Sample block of Gelita-Spon™ gelatin sponge (unhydrated).

In subsequent studies, we began to develop approaches for sustained release of cytokines within the CI. We determined that the HMW-HA hydrogel incorporating crosslinked heparin (Extracel-HP) could bind and release heparin-binding immunomodulatory growth factors, such as IL-2 and IL-10 (Task 3). In addition to this depot for storage and release of growth factors, we evaluated sustained release from calcium-crosslinked alginate hydrogel (in the form of 2 mm diameter spheres) as a way to deliver bioactive agents over extended time periods. We evaluated alginate alone and also alginate that incorporated heparin-Sepharose microbeads (**Figure 45**), which substantially increased the growth factor binding capacity of the alginate.

Significantly, we were able to show that alginate spheres loaded with the angiogenic cytokine vascular endothelial growth factor (VEGF) could release this molecule in a sustained fashion over a period of at least 2 weeks (**Figure 46**). VEGF is an important component of the CI for its capacity to induce vascular growth within wound sites and at the sites of regenerative tissue grafts.

A particularly exciting development was our finding that the alginate can be used as a sustained release agent to deliver soluble HMW-HA. Our results indicated that the rate of release of HMW-HA could be controlled by the length of time the alginate was crosslinked with Ca^{++} (**Figure 47**).

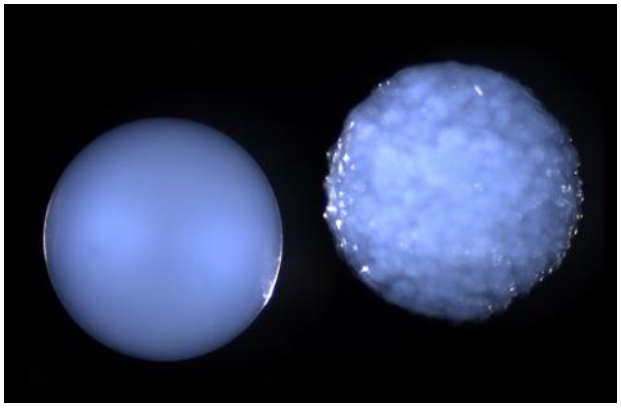

Figure 45. Alginate spheres of 2 mm diameter. *The sphere on the left is comprised of Ca^{++}-crosslinked alginate only. On the right, a similar alginate sphere is filled with heparin-Sepharose microbeads with an average diameter of 90 microns.*

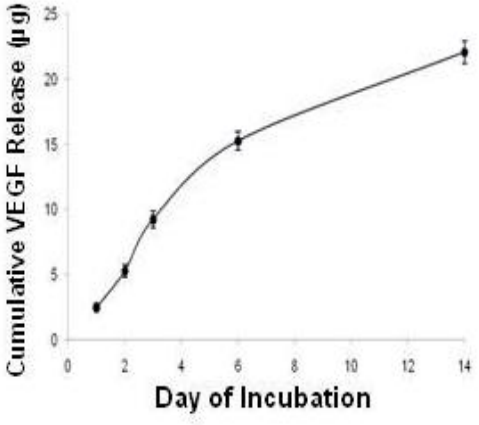

Figure 46. Sustained release of VEGF from alginate spheres. *Alginate spheres of 2 mm diameter (without heparin-Sepharose microbeads – similar to the one shown on the left side of Figure 4) were loaded with 50 ng of VEGF and incubated in culture medium in vitro under physiological conditions for two weeks. During this time, the release of VEGF into the culture medium was assessed at specific time points. Over the two-week period, approximately half of the VEGF was released. Release kinetics were bilinear, with a steeper release in the first week followed by a shallower release in the second week.*

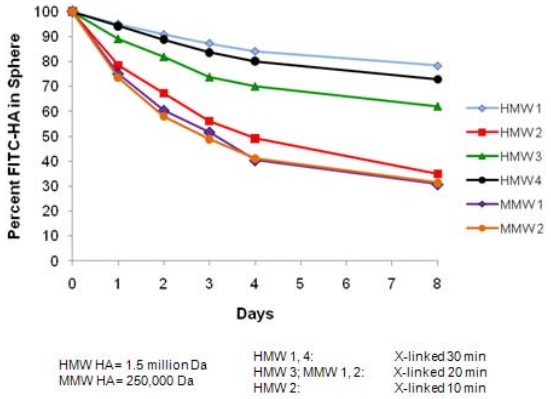

Figure 47. Sustained release of HA from alginate is influenced by molecular weight and the degree of crosslinking. *Alginate spheres containing fluorescent (FITC)-labeled HMW-HA were monitored for HA release over 8 days. Alginate crosslinked with Ca^{++} for increasing lengths of time released the HA at a slower rate. HA of lower MW (middle molecular weight [MMW]-HA) was released more rapidly than HMW-HA.*

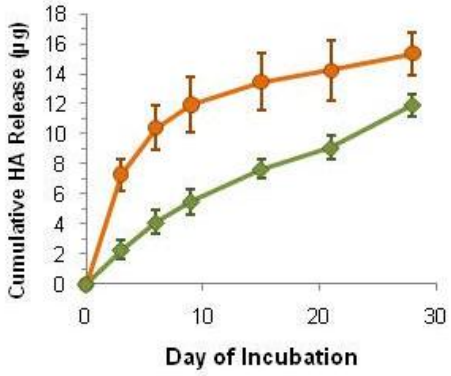

Figure 48. Sustained release of HMW-HA from alginate is prolonged and influenced by the degree of crosslinking. *Alginate spheres (2 mm in diameter) each containing 32 µg of HMW-HA and 0.8 µg of fluorescent (FITC-conjugated) HMW-HA as a tracer were monitored for HA release under physiological conditions in vitro over 28 days. Alginate was crosslinked with Ca^{++} for 15 min (orange plot) and 30 min (green plot). The 30 min crosslink time resulted in release of HA in a linear manner over the course of the study. Notably, only a third of the HA was released from this sphere set (n = 5) in 28 days, suggesting a potential for sustained release of up to 3 months.*

Importantly, release of the HMW-HA occurred over a prolonged period of time (**Figure 48**). In light of our finding that HMW-HA stimulates regulatory T cells (Task 3), the capacity to deliver this molecule locally over a prolonged period via sustained release (using biocompatible alginate) may prove to be an effective means to control inflammation within wound and graft sites.

In addition to development of alginate-mediated, sustained release of HMW-HA, we explored methods to use alginate hydrogels to deliver immuno-modulatory compounds of lower molecular weights. For these studies, we used alginate spheres coated with poly-L-lysine (PLL) (**Figure 49**). Addition of a PLL coating to alginate spheres creates an outer "shell" of high density positive charge on the sphere, which has the potential to slow the diffusion of bioactive compounds from the interior of the sphere and serve as a depot of positive

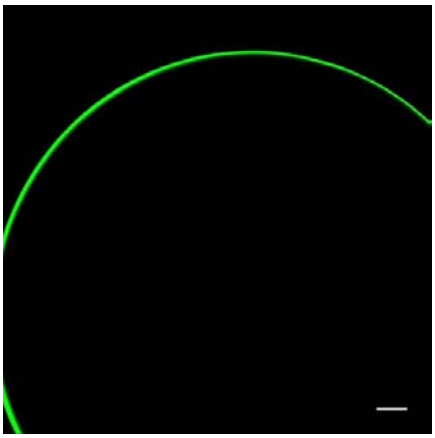

Figure 49. A PLL-coated alginate sphere. *An alginate sphere of 2 mm diameter was incubated for 1.5 h in 1 mg/ml of PLL and then stained with genepin to reveal the PLL bound to the alginate. In this confocal microscopic image, the PLL layer is seen as a thin, fluorescent green shell on the surface of the alginate. Scale bar = 100 microns.*

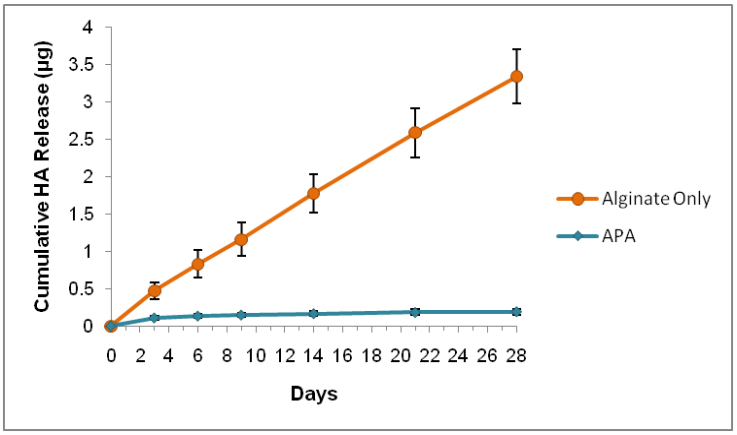

Figure 50. Effect of PLL exposure on release of HMW-HA from alginate. *Ca^{++} - crosslinked, 2 mm alginate spheres containing HMW-HA and fluorescent HMW-HA tracer were incubated for 1.5 h in 1 mg/ml of PLL or saline only and then were monitored for HA release under physiological conditions in vitro. The spheres lacking the PLL coat released HA in a linear fashion over 28 days (orange plot), whereas the spheres coated with PLL did not release HA (blue plot). n = 5 for both sphere sets.*

charges to retain negatively charged immunomodulatory compounds, such as IL-10 and TGF-β. We first evaluated the effect of alginate on release of HMW-HA. We found that incubation of alginate spheres in a solution of 1 mg/ml of PLL for 1.5 hours completely blocked the release of HMW-HA over 28 days (**Figure 50**). In subsequent studies, we showed that coating the spheres using lower concentrations of PLL did not block HMW-HA release, but, instead, permitted release at rates lower than for uncoated spheres (**Figure 51**).

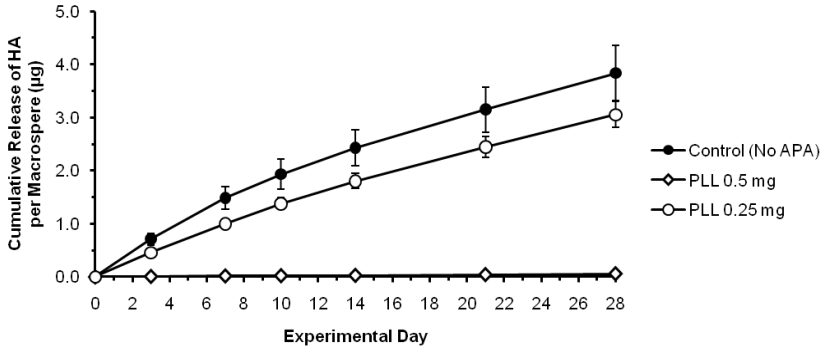

Figure 51. Sustained release of HMW-HA from alginate is modulated by coating with PLL. *Alginate spheres (2 mm in diameter) containing 16 µg of HMW-HA and 0.8 µg of fluorescent HMW-HA as a tracer were monitored for HA release for 28 days under physiological conditions in vitro. Exposure of the alginate spheres to PLL at 0.5 mg/ml for 30 min effectively blocked release of HMW-HA. In contrast, exposure of a similar set of spheres to PLL at 0.25 mg/ml allowed a linear release of HMW-HA at a rate lower than that measured for control spheres that were not exposed to PLL. Standard deviations for each sphere set (n = 5 for each set) are shown. In the graph key, "APA" refers to "alginate/PLL/alginate", as the spheres that were coated with PLL received a thin surface coat of alginate over the PLL layer.*

In parallel studies, we explored methods to use PLL-coated alginate matrices to deliver immunomodulatory compounds with substantially lower molecular weights than HMW-HA. We focused on modulating the release of antibodies, with the objective of delivering antibodies with immunomodulatory properties within the CI. Initial results were encouraging. Alginate spheres coated with PLL at 0.25 mg/ml showed a linear release of polyclonal antibodies directed against immuno-globulin isotype G (IgG) over a 14 day period (**Figure 52**). Exposure to PLL at 0.125 mg/ml resulted in a higher release rate, whereas PLL coated at 0.0625 mg/ml yielded release rates like that of uncoated controls. These experiments showed that release of antibodies from alginate

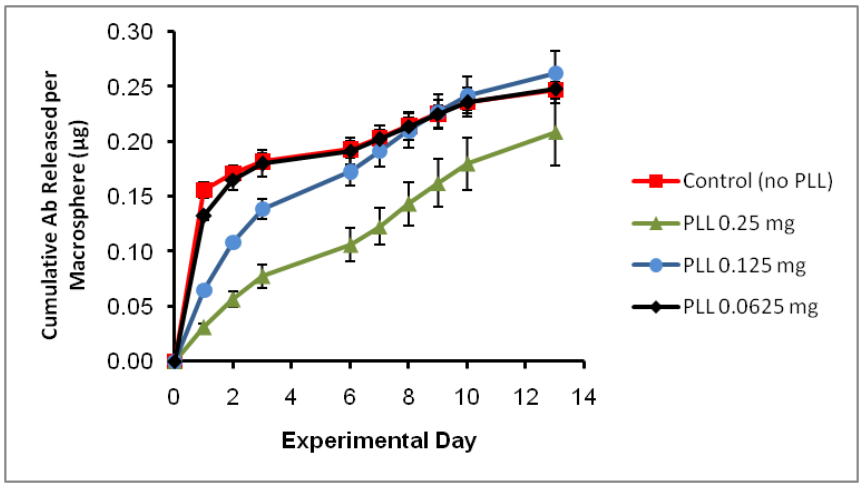

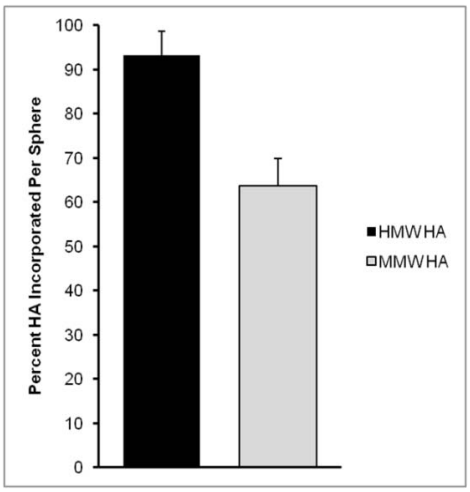

Figure 52. Sustained release of antibodies from PLL-coated alginate spheres. *Alginate spheres (2 mm in diameter), containing 0.8 µg of an IgG fraction of polyclonal goat antibodies to mouse IgG, were monitored for antibody release for 14 days under physiological conditions in vitro. Exposure of the alginate spheres to PLL at 0.25 mg/ml for 30 min resulted in a linear release of antibody. Release rates were higher for spheres exposed to PLL at 0.125 mg/ml. PLL coated at 0.0625 mg/ml yielded antibody release rates that were similar to uncoated control spheres. Standard deviations for each sphere set (n = 5 for each set) are shown.*

Figure 53. HMW-HA and MMW-HA are retained by alginate with high efficiencies. *Spheres (8 µL in volume) made of 2% alginate containing 2 µg of fluoresceinated-HMW-HA or MMW-HA were crosslinked (gelled) for 30 min with 0.1M $CaCl_2$, washed briefly with HEPES-buffered saline / 2 mM $CaCl_2$, then immediately dissolved with EDTA to release the bound HA, which was quantitated by fluorimetry. Over 90% and 60% of the HMW-HA and MMW-HA added to the alginate (respectively) was retained during the process of alginate gelation.*

could be modulated by PLL and that specific levels of exposure to PLL could result in release with linear kinetics.

In subsequent studies, we continued our work with HA, which the Nepom group (under Task 3) had shown works as an activator for Treg function. We evaluated sustained release under physiological conditions *in vitro* of both HMW-HA (MW of 1.5 million Da) and "middle" molecular weight (MMW)-HA (MW of 120,000 Da). Both forms of HA were retained by alginate with high efficiencies, over 90% for HMW-HA and over 60% for MMW-HA (**Figure 53**). Not surprisingly, HMW-HA and MMW-HA had markedly different profiles of release over time. MMW-HA was released relatively rapidly (98% within two weeks). In contrast, only 4.6% of HMW-HA was released within two weeks (**Figure 54**). These experiments suggested that use of HA of different MW classes could be an effective means to control HA release rate for specific applications.

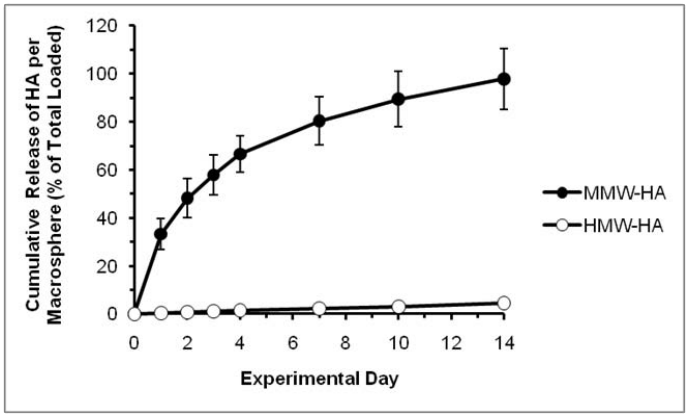

Figure 54. HMW-HA and MMW-HA are released at markedly different rates from alginate hydrogels. *Spheres (8 µL in volume) made of 2% alginate containing 2 µg of fluoresceinated HMW-HA or MMW-HA were crosslinked (gelled) for 30 min with 0.1M $CaCl_2$, washed briefly with HEPES-buffered saline / 2 mM $CaCl_2$, then incubated at 37°C in phosphate-buffered saline / 2 mM $CaCl_2$ medium for two weeks. During this time, the medium was repeatedly assayed for release of HA. Essentially all (98%) of the MMW-HA was released over the two weeks, whereas less than 5% of the HMW-HA was released during this time period.*

With respect to our work with PLL-coated alginate, we extended our initial experiments that evaluated the release of a "generic" polyclonal antibody against IgG to include tests of the release of an antibody to CD3e, a component of the CD3 T cell receptor (TCR). Binding of "functional" forms of the CD3e antibody to the TCR initiates T cell activation and proliferation. In these experiments, we showed that anti-CD3e antibody could be released from PLL-coated alginate spheres in a controlled,linear manner (**Figure 55**).

In parallel with our studies of sustained release of immunomodulators *in vitro*, we conducted sustained release studies *in vivo* in which alginate spheres loaded with either HA or anti-CD3e antibody were incorporated into CI test-beds and implanted into mice in a mesenteric pocket. These studies showed that the alginate spheres were highly biocompatible and released the compounds in bioactive forms that elicited appropriate (i.e., angiogenic/immunomodulatory) responses from their target cell types within the host.

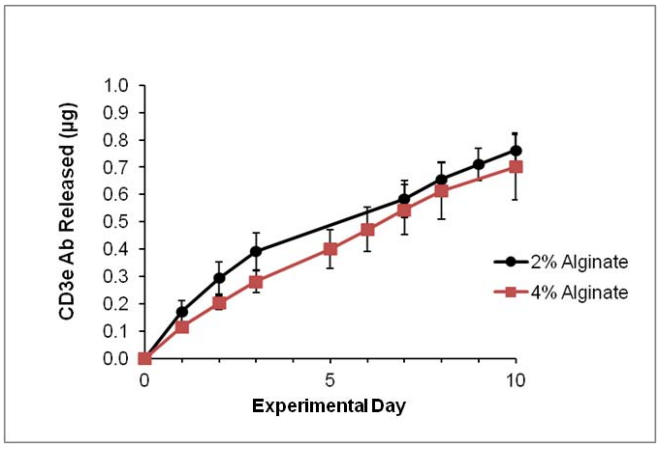

Figure 55. Release in vitro of anti-CD3e antibody from PLL-coated alginate hydrogels *Spheres (10 µL in volume) made of 2% or 4% alginate containing 2.5 µg of fluoresceinated-anti CD3e antibody were crosslinked (gelled) for 30 min with $CaCl_2$, coated with PLL, and given a final surface coating of alginate to produce alginate-poly-L-lysine-alginate (APA) spheres. The spheres were incubated at 37°C in HEPES-buffered saline / 2 mM $CaCl_2$ medium for 10 days. During this time, release of the antibody from both the 2% and 4% alginate spheres was similar and essentially linear.*

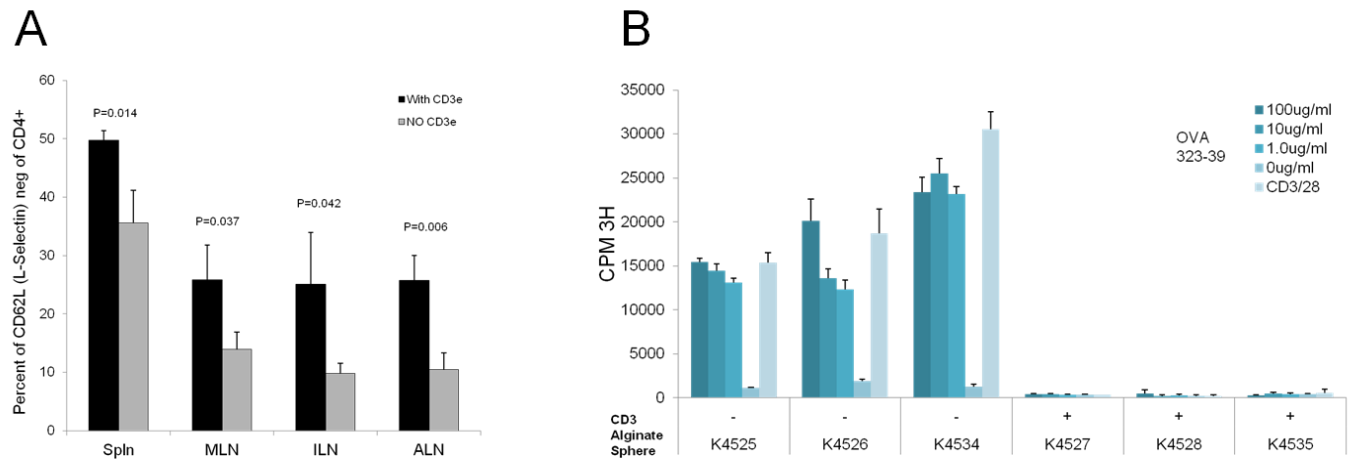

Figure 56. Sustained (time)-release of immunomodulatory anti-CD3e monoclonal antibody from CI test-beds influences T cell behavior in mice. (A) *Results of an experiment in which B6 mice received CIs, each containing a single alginate sustained release sphere either loaded with 5 µg of anti-CD3e antibody (black bars) or lacking the antibody (negative controls – gray bars). After 7 days, CD4+ T cells were isolated from four locations within the animals: the spleen (Spln) and the mesenteric, iliac, and axillary lymph nodes (MLN, ILN, and ALN, respectively). These T cells were assessed for their degree of immune "activation", as indicated by their loss of the molecule L-selectin.* ***Implants that contained the anti-CD3e antibody were significantly more effective at activating T cells than were control implants that lacked the antibody. (B)*** *An experiment performed using the RO/RAG mouse model of autoimmune (type 1) diabetes. As in the experiment described in Panel A, mice received implants either containing anti-CD3e antibody or lacking the antibody. Subsequently, the mice received an injection of DO11.10 CD4+ T cells and a priming injection of ovalbumin (OVA) peptide. After 11 days, CD4+ T cells were removed from the mice and exposed in culture to various concentrations of the OVA peptide, to reactivate the cells. CD4+ T cells from the three mice that received implants lacking antibody (animals K4525, K4526, and K4534, shown on the left-hand side of the graph) were stimulated by the OVA peptide to proliferate (as measured by incorporation of ^{3}H-thymidine). In contrast, immune cells from the three mice that had received the anti-CD3e antibody-loaded implants (animals K4527, K4528, and K4535, shown on the right-hand side of the graph) had very low proliferative responses after OVA peptide exposure, which indicated that the antibody had strongly influenced T cell behavior.*

In initial experiments *in vivo* in B6 mice, we observed that sustained release of a functional anti-CD3e monoclonal antibody (clone 145-2C11) from CI test-beds containing alginate/PLL spheres could activate CD4+ T cells from their resting state into an immunomodulatory state (**Figure 56A**). CD4+ T cells include both T helper cells and T regulatory (Treg) cell populations. In subsequent experiments, we showed that sustained release of the functional anti-CD3e monoclonal antibody *in vivo* in RIP-OVA/Rag-/- (RO/RAG) mice, which model autoimmune (type 1) diabetes (described under Aim 1, Task 5) resulted in a lack of proliferation of autoreactive CD4+ T cells (**Figure 56B**). The cause of the suppression of proliferation has not yet been determined, but it is likely the result of elimination of the autoreactive T cells by anti-CD3e antibody-induced apoptosis, a known effect of this particular antibody clone. Whatever the cause, the suppression of T cell activity by the anti-CD3e antibody was reflected by the absence of immune attack *in vivo* of both native and transplanted pancreatic islets in RO/RAG mice treated with the antibody (discussed in Task 10).

In addition to the *in vivo* studies using the anti-CD3e antibody, we studied the influence of sustained release of MMW-HA on T cell behaviors *in vivo*. For the studies with MMW-HA, we designed a new CI test-bed consisting of a polyvinyl alcohol sponge with peripheral holes to hold six alginate spheres, each of 10 µL volume (2 mm diameter) (**Figure 57**).

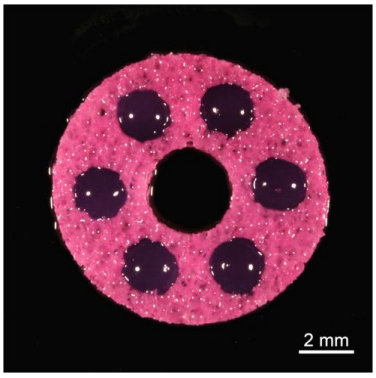

***Figure 57. A CI test-bed** includes a central hole (empty here) for addition of transplanted cells or tissues and six peripheral holes, each containing an alginate sphere loaded with MMW-HA.*

From our prior experiments, we showed that the release of MMW-HA from uncoated alginate spheres *in vitro* was compatible with the time required to induce an autoimmune response in our RO/RAG mouse model—essentially 100% of the MMW-HA was released from the spheres within 2 weeks (**Figure 58A**). Consequently, our initial experiment evaluated the immunomodulatory effects of MMW-HA *in vivo*, rather than testing the effects of HMW-HA, which has a much slower, more prolonged release from

alginate (the relatively slow release of HMW-HA may prove useful for long-term immunomodulatory treatments). CIs incorporating six alginate spheres, each loaded with 32 µg of MMW-HA (for a total of 192 µg of HA in each test-bed) were implanted into the mesenteric pockets of two RO/RAG mice (one of these mice died from a post-operative injury). Two additional control mice received CIs with alginate spheres lacking HA. After 11 days, CD4+ T cells were removed from the mice and exposed in culture to various concentrations of ovalbumin peptide to induce cell activation and proliferation.

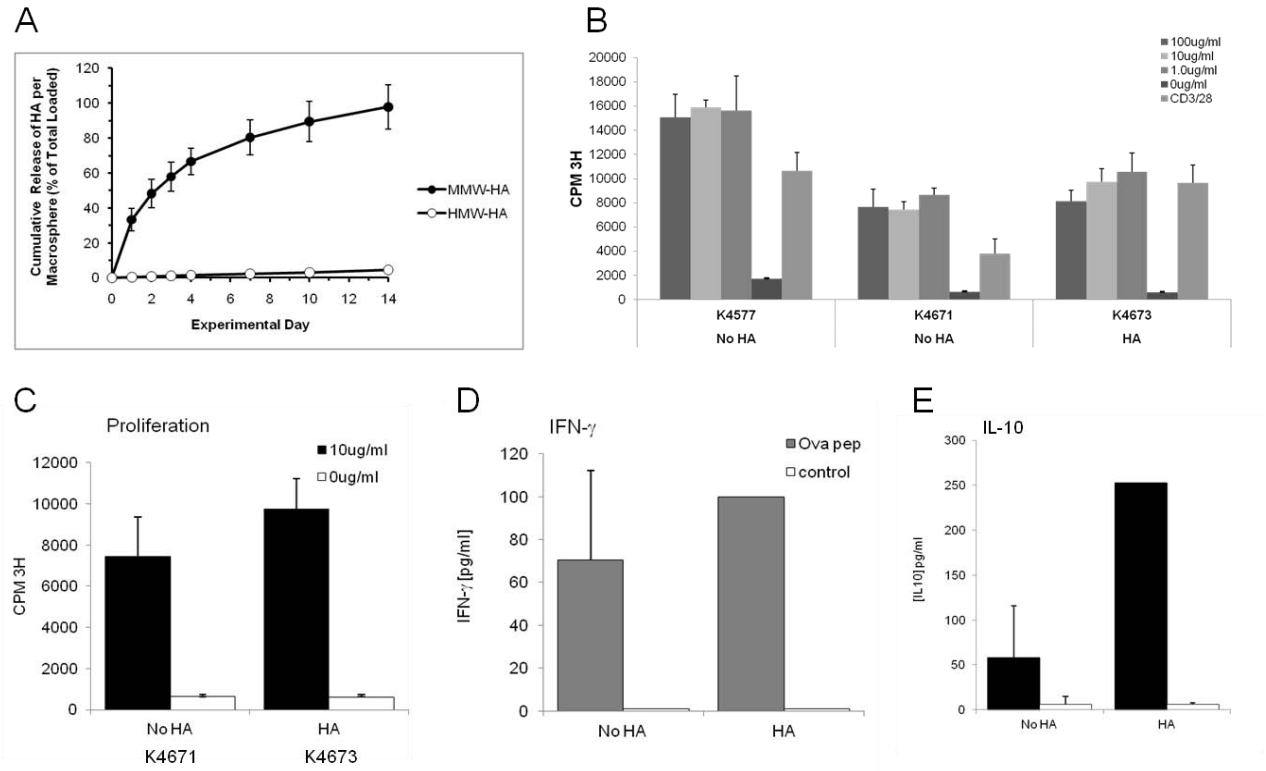

Figure 58. Sustained (time)-release of MMW-HA from CI test-beds influences T cell behavior in mice. (A) *Kinetics of release of MMW-HA (solid circles) and HMW-HA (open circles) from uncoated alginate spheres in vitro over a period of 14 days. Essentially 100% of the MMW-HA is released within this time period. (**B**) An experiment performed using the RO/RAG mouse model of autoimmune (type 1) diabetes, as described in Figure 9B, but substituting MMW-HA for the anti-CD3e antibody. CD4+ T cells from both control (NO HA) and experimental (HA) mice could be stimulated to proliferate by exposure to ovalbumin (OVA) peptide. (**C, D**) Graphs indicating similarity in proliferation **(C)** and gamma interferon (IFN-γ) production **(D)** between CD4+ T cells from control (NO HA) and experimental (HA) mice. **(E)** Graph indicating a significant increase in IL-10 production by CD4+ T cells from experimental (HA) vs. control (NO HA) mice.*

As shown in **Figure 58B**, the one surviving mouse that received MMW-HA and the two control mice all had proliferating CD4+ T cells. Therefore, the MMW-HA was not causing T cell apoptosis, which we suspected the anti-CD3e antibody was causing (**Figure 56B**). A comparison between the proliferation of CD4+ T cells from the MMW-HA-treated mouse and a control mouse showed no significant difference (**Figure 58C**). Moreover, the CD4+ T cells from both control mice and the MMW-HA-treated mouse produced similar levels of gamma interferon (IFN-γ), a cytokine produced by activated T cells (**Figure 58D**). Therefore, exposure to MMW-HA *in vivo* did not negatively affect the survival or the immunocompetence of the CD4+ T cell population. Importantly, however, the CD4+ T cells from the MMW-HA-treated mouse produced significantly more IL-10 than did corresponding cells from the control mice (**Figure 58E**). IL-10, which is secreted by activated CD4+ T helper and Treg populations, has potent immunosuppressive effects, acting to inhibit T cell proliferation and downregulate antigen presentation by antigen-presenting cells. *Our results, therefore, suggested that sustained release of a soluble form of HA in vivo can induce CD4+ T cell-mediated immunosuppression.*

In follow-on experiments, however, we substituted an F(ab)2 fragment of the 145-2C11 anti-CD3e antibody for the intact antibody we used in our initial studies. The F(ab)2 fragment has been shown to exert immunosuppressive effects without inducing cell death. We implanted standard PVA sponge discs, each containing 5 µg of the anti-CD3e F(ab)2 fragment in a single alginate/PLL sphere, into B6 mice to determine if delivery of this agent could influence T cell activity after 7 days *in vivo*. CD4+ T cells isolated from the spleens, and lymph nodes (mesenteric, inguinal, and axillary) from untreated (control) and F(ab)2-treated mice showed no significant differences in total numbers (**Figure 59**). Moreover, there were no significant differences in the level of activation of the CD4+ T cells in the controls and F(ab)2-treated mice, as indicated by low level expression of CD62L (L-selectin), low expression of CD62L combined with high expression of CD44 (the hyaluronan receptor), or upregulation of FoxP3—a transcription factor associated with Treg activation and persistence (**Figure 60**). These negative results suggest that the amount of F(ab)2 antibody administered to the mice may have been too low to obtain a biological effect.

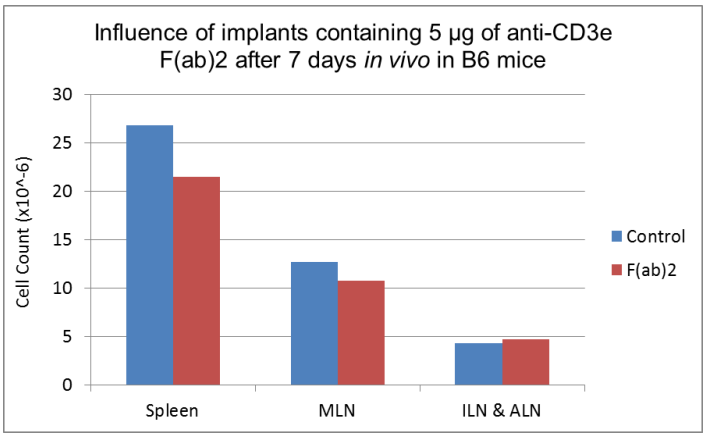

Figure 59. Influence of implants each containing 5 µg of anti-CD3e F(ab)2 antibody on CD4+ T cell numbers in B6 mice after 7 days in vivo (red bars)*. Control mice received implants lacking the antibody (blue bars). MLN, ILN, and ALN refer to mesenteric, inguinal, and axillary lymph nodes, respectively.*

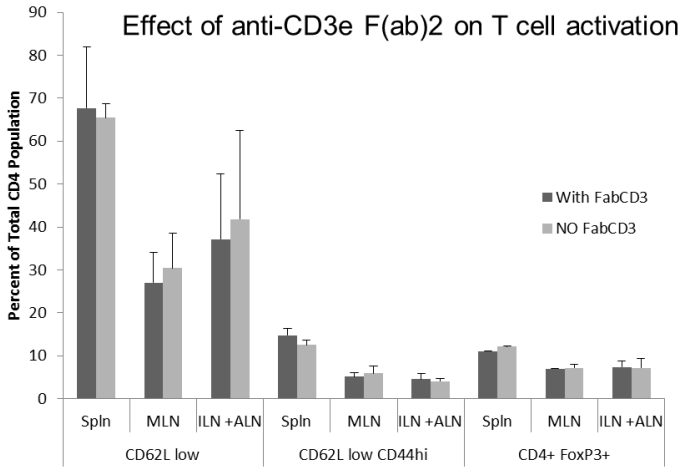

Figure 60. Influence of implants each containing 5 µg of anti-CD3e F(ab)2 antibody on expression of activation markers by CD4+ T cells in B6 mice after 7 days in vivo (dark gray bars). *Control mice received implants lacking the antibody (light gray bars). MLN, ILN, and ALN refer to mesenteric, inguinal, and axillary lymph nodes, respectively. Markers analyzed include CD62L (L-selectin), CD44 (hyaluronan receptor), and FoxP3 (a transcription factor upregulated in Tregs).*

In subsequent studies, we evaluated alginate-based delivery of TGF-β in our CI. As in our previous studies with other immunomodulatory cytokines, we evaluated the performance of the CI in RO/RAG mice. We implanted CIs (in the mesenteric location) containing alginate spheres loaded with 5 µg of TGF-β or normal saline (controls). On the day following implantation, we immunized the recipient mice with 50 µg of OVA peptide and transplanted DO.11 CD4+ T cells into the mice. On day 10, the spleens and mesenteric lymph nodes were harvested to collect the transplanted T cells. We found that the

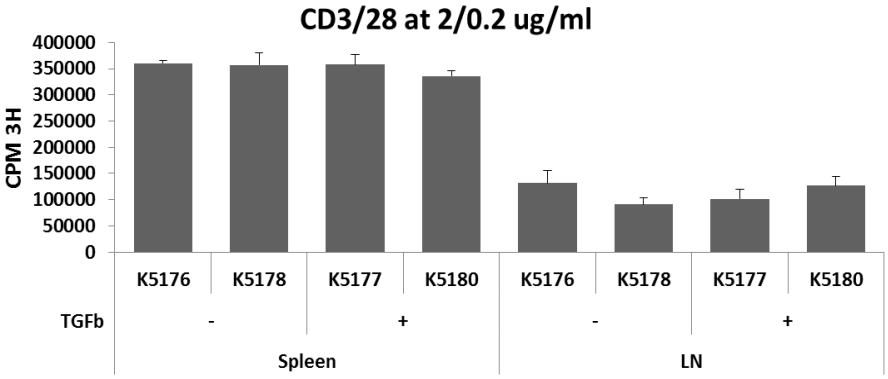

Figure 61. Response of isolated CD4+ T cells to anti-CD3/CD28 antibody stimulation in vitro. *DO.11 T-cells were introduced into RO/RAG mice that had been implanted with CIs containing either 5 µg of TGF-β or saline (controls) and stimulated with OVA peptide. Ten days later, the CD4+ T-cells were isolated from the spleens and mesenteric lymph nodes (LN) and stimulated in vitro with antibodies to CD3 and CD28. Cell proliferation in response to antibody exposure was similar between the TGF-β-treated group and the control group. "K" numbers identify specific mice.*

T cells isolated from the TGF-β-treated and control mice had similar responses to anti-CD3/CD28 antibody stimulation *in vitro* (**Figure 61**). This was expected, as exposure to anti-CD3/CD28 antibodies is a potent general stimulator for T cells. The data indicated that, compared to controls, the TGF-β in the CI did not cause a measurable loss (or increase) of T cells in the host mouse. These results were underscored by similar levels of anti-CD3/CD28-elicited production of interferon-gamma (IFNγ) by T cells from the TGF-β-treated and control mice (**Figure 62**). IFNγ production is a general indicator of T cell stimulation.

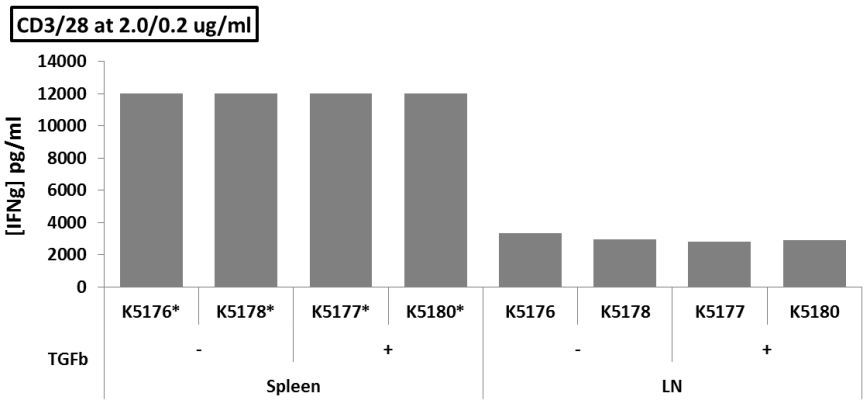

Figure 62. IFNγ response of isolated CD4+ T-cells to anti-CD3/CD28 antibody stimulation in vitro. *DO.11 T-cells were introduced into RO/RAG mice that had been implanted with CIs containing either 5 µg of TGF-β or saline (controls) and stimulated with OVA peptide. Ten days later, the CD4+ T-cells were isolated from the spleens and mesenteric lymph nodes (LN) and stimulated in vitro with antibodies to CD3 and CD28. IFNγ production in response to antibody exposure was similar between the TGF-β-treated group and the control group. "K" numbers identify specific mice.*

Although the responses of CD4+ T cells to generalized stimulation by anti-CD3/CD28 antibodies was similar between the TGF-β-treated and control mice, differences were seen in the recall response to OVA peptide, which, in this model, represents the specific autoimmune antigen. Spleen- and lymph node-derived CD4+ T cells from TGF-β-treated mice had an elevated level of proliferation in response to OVA peptide in comparison to the saline-treated controls (**Figure 63**).

Collectively, these studies showed that TGF-β released from the CI via the alginate spheres was bioactive and could modulate the responses of CD4+ T cells to a specific autoantigen.

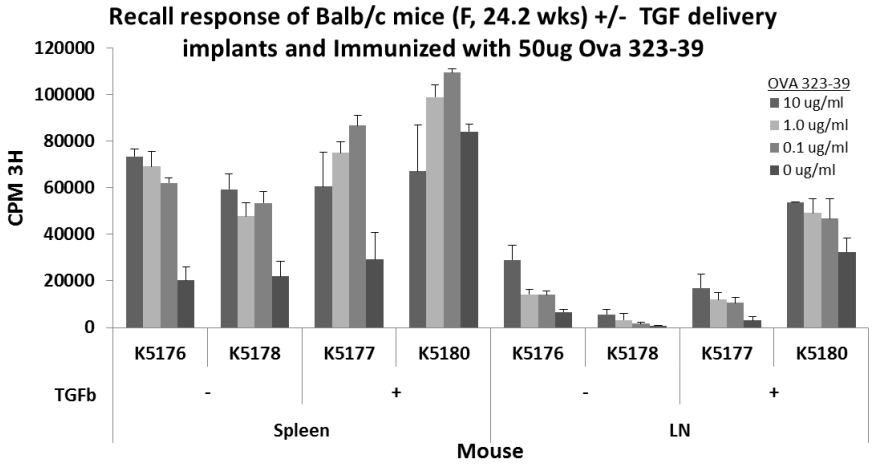

Figure 63. Proliferative response of isolated CD4+ T-cells to OVA peptide stimulation in vitro. *DO.11 T-cells were introduced into RO/RAG mice that had been implanted with CIs containing either 5 µg of TGF-β or saline (controls) and stimulated with OVA peptide. Ten days later, the CD4+ T-cells were isolated from the spleens and mesenteric lymph nodes (LN) and stimulated in vitro with graded quantities of OVA peptide. Cell proliferation in response to OVA exposure was greater in the TGF-β-treated group compared to the control group. "K" numbers identify specific mice.*

In a final set of studies, we examined the potential of induced pluripotent stem cells (IPSCs) as candidate cells for replacement of diseased, injured, or lost tissues. When exposed to a specific set of culture conditions, IPSCs have the potential to differentiate into many cell lineages, including muscle, nerve and vascular endothelial cells—cell types that are of particular relevance to the engineered muscle replacement (myobridge) project described in Aim 2B. Importantly, as IPSCs are derived from the patient, they would not be expected to elicit a significant immune rejection response.

Although the properties of the IPSCs themselves (e.g., their origin, state of differentiation, and homogeneity as a population) are critical to their therapeutic performance, of equal importance is the nature of the extracellular environment that surrounds the IPSCs, both during their maturation *in vitro* and following their engraftment in the patient. In native tissues, ECM components are critical mediators of cell survival, function, and maintenance of differentiation. In this context, we have examined the types of ECM produced by IPSCs

from mice with a focus on determining whether ECM synthesis is modulated as the cells differentiate. For these studies, we used qRT-PCR to assay the expression of mRNAs representing a spectrum of ECM molecules, as well as molecules associated with ECM synthesis and processing. We evaluated *undifferentiated IPSCs* (UIPSCs) derived from two mouse sources: dermal fibroblasts (fibro-UIPSCs) and pancreatic islets (islet-UIPSCs) and their *Stage 4-differentiated IPSC* (DIPSC) counterparts (fibro-DIPSCs and islet-DIPCs). qRT-PCR assays of these cells revealed striking differences in ECM mRNA expression, not only between UIPSCs and DIPSCs, but also between the fibroblast-derived and islet-derived populations.

Fibro- and islet-UIPSCs showed little or no expression of collagen mRNAs (**Figure 64A–D**), but expression of all collagen mRNAs was increased in both fibro- and islet-DIPSCs. Notably, collagen-3 (involved in early deposition of interstitial ECM in the embryo and in wounds), collagen-4 (a major component of basement membranes), and collagen-5 (involved in the organization and stabilization of collagen 1 fibrils) were very highly expressed by fibro-DIPSCs, but substantially less so by islet-DIPSCs. mRNA for collagen 1, the major structural collagen of interstitial ECM, was significantly and equally up-regulated in fibro- and islet-DIPSCs, but at levels 60- and 40-fold less than collagen -3 and -5, respectively. Expression of laminin-1 mRNA (**Figure 64E**) by fibro-DIPSCs was much higher than in islet-DIPSCs. In this respect, the expression of mRNA for laminin-1 was similar to that of collagen-4, which associates structurally with laminin in basement membranes. Notably, however, expression of laminin-1 mRNA by fibro- and islet-UIPSCs was similar to that of their differentiated counterparts, which likely reflects the requirement for laminin very early in embryogenesis.

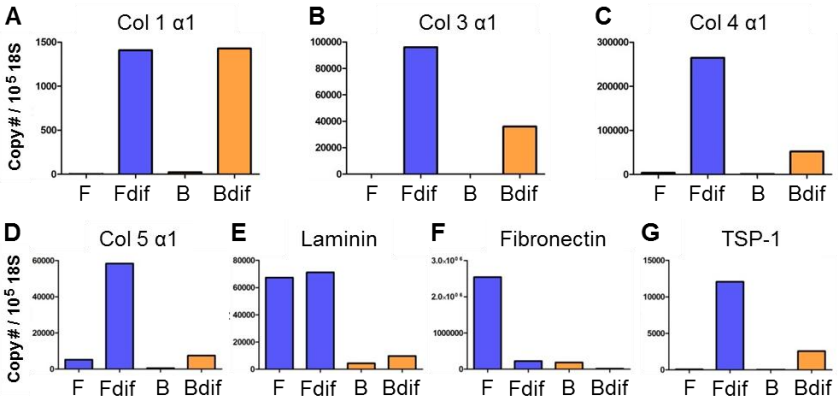

***Figure 64. mRNAs for a variety of ECM components are differentially expressed by UIPSCs of different origin and during UIPSC differentiation. Blue bars** = fibroblast-derived UIPCs (F) and DIPSCs (Fdif). **Orange bars** = Islet-derived UIPCs (B) and DIPSCs (Bdif). **(A–D)** Alpha chains for collagen types -1, -3, -4, and -5. **(E)** B1 subunit of laminin-1. **(F)** Cellular fibronectin. **(G)** Thrombospondin (TSP)-1. All mRNAs are expressed as relative copy number / 10^5 18S rRNA.*

In contrast to the collagen and laminin mRNAs, levels of cellular fibronectin mRNA (**Figure 64F**) were extremely high in fibro-UIPSCs and strongly down-regulated in fibro-DIPSCs. Islet-UIPSCs and DIPSCs expressed relatively low levels of this mRNA. Thrombospondin (TSP)-1 mRNA was barely detectable in UIPSCs, but was strongly up-regulated in fibro-DIPSCs (**Figure 64G**). This upregulation is interesting given the dynamic role that TSP-1 is thought to play in cell-ECM interactions. TSP-1 is a "matricellular" glycoprotein that can bind to a variety of other ECM components such as fibrinogen, laminin, fibronectin, and collagen-5. TSP-1 also interacts with a variety of cell adhesion receptors and ECM proteolytic enzymes.

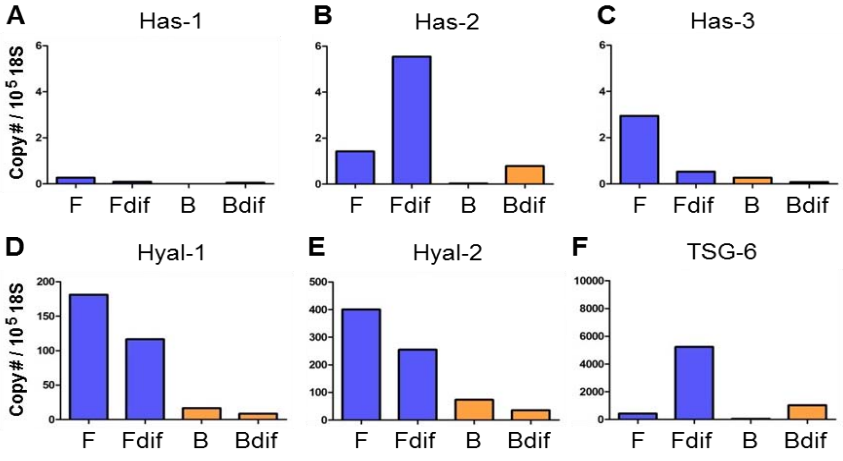

***Figure 65. Differential expression of mRNAs for HA synthesis, cleavage, and stabilization. Blue bars** = fibroblast-derived UIPCs (F) and DIPSCs (Fdif). **Orange bars** = Islet-derived UIPCs (B) and DIPSCs (Bdif). **(A–C)** HA synthase (Has) isoforms. **(D, E)** Hyaluronidase (Hyal) isoforms. **(F)** TSG-6. All mRNAs are expressed as relative copy number / 10^5 18S rRNA.*

The glycosaminoglycan (GAG) *hyaluronan* (HA) is the major non-proteinaceous component of native

ECM. HA is critical to the organization, assembly, and homeostasis of ECM and plays a central role in inflammation. HA has differential effects that relate to its chain length. It is synthesized by *HA synthases* (Hases) in high MW forms (HMW-HA) (1 x 10^6 Da or greater) that are generally anti-inflammatory. Following secretion, HA is cleaved by *hyaluronidases* (Hyals) into a continuum lower MW forms, the lowest of which (<3 kDa) are pro-inflammatory and stimulate angiogenesis. ECM components referred to as *HA-binding molecules*, such as versican and TSG-6, attach to and crosslink HMW-HA into macromolecular structures that are resistant to degradation.

Given the importance of HA in the biology of native ECM, we examined the expression of mRNAs for the major isoforms of Has (1–3) and Hyal (1, 2) by UIPSCs and DIPSCs. Among the four IPSC lines, Has-1 mRNA levels were negligible (**Figure 65A**). In contrast, Has-2 mRNA was expressed at significantly higher levels than Has-1 mRNA and was up-regulated in both fibro- and islet-DIPSCs relative to their UIPSC counterparts (**Figure 65B**) (the up-regulation was higher in fibro-DIPSCs than in islet-DIPSCs). Has-3 was down-regulated by DIPSCs (**Figure 65C**), which is particularly of interest, given that Has-3 mediates the synthesis of lower MW HA.

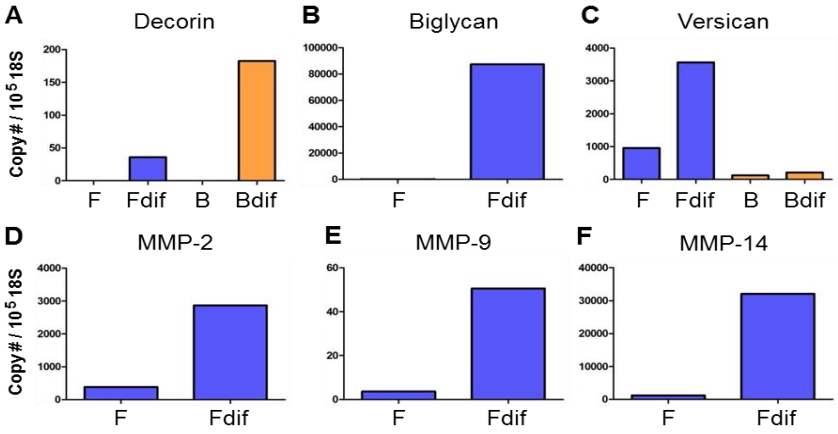

***Figure 66. Differential expression of mRNAs for PGs and MMPs. Blue bars** = fibroblast-derived UIPCs (F) and DIPSCs (Fdif). **Orange bars** = Islet-derived UIPCs (B) and DIPSCs (Bdif). **(A–C)** PGs decorin, biglycan, and versican. **(D–F)** MMPs -2, -9, and -14. All mRNAs are expressed as relative copy number / 10^5 18S rRNA.*

Our finding that Has-2 is the primary Has isoform expressed by DIPSCs is not surprising, given the predominance of Has-2 in most tissues. As in native tissues, the abundance of Has-2 mRNA in DIPSCs was quite low, which does not necessarily reflect a low abundance of HA in pericellular ECM, as the synthetic rates of the HASes are very high.

In contrast to Has-2, mRNAs for Hyal-1 and -2 were expressed at relatively high levels in fibro-UIPSCs (and much less in islet-UIPSCs) and moderately diminished in DIPSCs (**Figure 65D, E**). Such contrary regulation of Hyals vs. Hases is characteristic of HA modulation in native tissue. Of greater significance was the finding that TSG-6 mRNA was substantially up-regulated by DIPSCs relative to UIPSCs (**Figure 65F**). TSG-6 is a major HA-binding molecule that, with other ECM components, promotes HA structural stability and resistance to degradation. Collectively, the mRNA data related to HA synthesis and turnover suggest that IPSC differentiation is associated with increases in HA synthesis, stability, and persistence.

A final set of analyses examined the expression of mRNAs for proteoglycans (PGs) and matrix metalloproteinases (MMPs). Among a variety of effects, the small PGs decorin and biglycan promote collagen-1 fibril formation and are important for controlling collagen fibril diameter and spacing. The large PG versican is an important HA-binding molecule that, like TSG-6, promotes HA crosslinking and resistance to degradation.

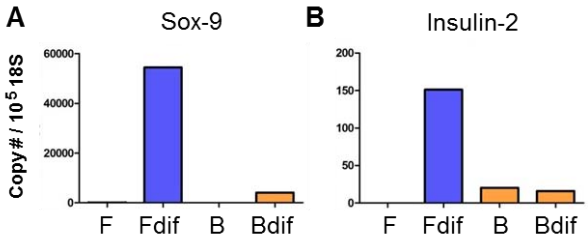

***Figure 67. Differential expression of mRNAs for Sox-9 and insulin.** Blue bars = fibroblast-derived UIPCs (F) and DIPSCs (Fdif). **Orange bars** = Islet-derived UIPCs (B) and DIPSCs (Bdif). **(A)** Sox-9, **(B)** Insulin-2. All mRNAs are expressed as relative copy number / 10^5 18S rRNA.*

Decorin mRNA was not expressed by the UIPSCs, but was up-regulated modestly by fibro-DIPSCs. In contrast, islet-DIPSCs substantially up-regulated decorin mRNA (**Figure 66A**). Biglycan mRNA was profoundly up-regulated by fibro-DIPSCs and was present in very high abundance (**Figure 66B**) (islet-IPSCs have not yet been evaluated). Versican mRNA was also significantly up-regulated by fibro-DIPSCs; however, little was expressed by islet-IPSCs (**Figure 66C**). mRNAs for MMP-2

and -9, which degrade a variety of ECM proteins, and membrane-bound MMP-14 (MT1-MMP), which is involved in MMP-2 activation and ECM proteolysis at the cell surface, were all strongly up-regulated in fibro-DIPSCs (**Figure 66D–F**) (islet-IPSCs remain to be evaluated).

Fibro-DIPSCs expressed much higher levels of the differentiation markers Sox-9 and insulin than did the islet-DIPSCs (**Figure 67**). Given that higher levels of these molecules represent a higher state of differentiation of the fibro-DIPSC population vs. the islet-DIPSC population, our evaluation of ECM mRNA expression by the fibro- and islet-derived IPSC populations suggests that greater levels of IPSC differentiation are associated with stronger modulation (either by up- or down-regulation) of the ECM environment surrounding the cells. *In general, we find that IPSC differentiation favors a profoundly increased synthesis of a variety of ECM macromolecules, which might be accompanied by increases in stability and persistence of some components (e.g., HA) and by increases in turnover of others (e.g., collagens). In any event, the dramatic increase in ECM production that accompanies IPSC differentiation might have significant consequences on the capacity for these cells to survive, grow differentiate and organize into replacement tissues.*

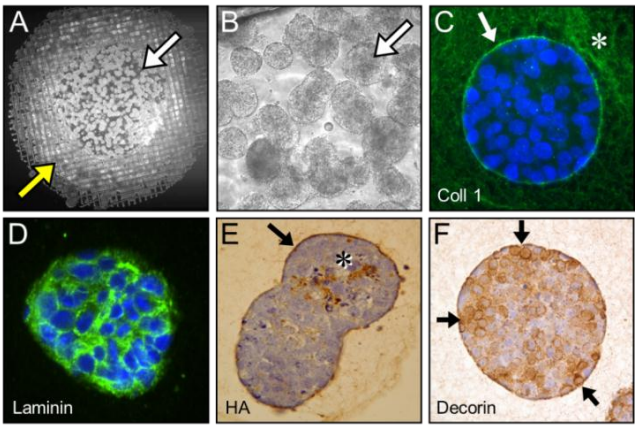

Figure 68. Cytochemical evaluation of ECM production by IPSCs in vitro. (A–F) *Mouse UIPSC aggregates were cultured 4 days in type I collagen hydrogels.* ***(A)*** *Darkfield image of the collagen gel with UIPSC aggregates (white arrow) and the 6 mm diameter nylon mesh ring (yellow arrow).* ***(B)*** *Detail of the UIPSC aggregates (e.g., arrow) of panel A.* ***(C)*** *Aggregate stained for type 1 collagen (green). The collagen gel (asterisk) is positive. A thin zone of intense staining on the aggregate's surface (arrow) may represent newly-synthesized collagen and/or remodeling of the collagen gel by the surface cells.* ***(D)*** *Intense intercellular staining for laminin (green).* ***(E)*** *Staining for HA reveals a dense layer (brown) on the aggregate's surface (arrow) and deposits of HA within the aggregate (asterisk).* ***(F)*** *Stain for the PG decorin reveals a thin layer of reactivity on the aggregate's surface (arrows) and strong reactivity by individual cells within the aggregate. In C and D, cell nuclei are stained with DAPI (blue).*

In a parallel study, we placed UIPSCs from mice in our type I collagen hydrogel culture system as a way to directly examine the types of ECM that the cells produce. The UIPSCs were dispersed in the collagen as aggregates (**Figure 68A, B**) which continued to grow in size over the 4-day culture period. After culture, the cell-populated gels were fixed, embedded in paraffin, sectioned and immunostained for specific ECM molecules. Notably, each of the four different ECM components we stained for had a unique pattern of labeling: collagen 1 stained strongly on the aggregate surface (**Figure 68C**), which may represent newly-synthesized collagen and/or remodeling of the collagen gel. Laminin showed intense staining between cells (**Figure 68D**). Labeling for HA was intense on the aggregate surface and also was concentrated in dense deposits within the aggregate **(Figure 68E**), whereas decorin was positive at the aggregate surface and in the cytoplasm of individual cells within the aggregate (**Figure 68F**). The differences in localization of these ECM molecules, which represent four distinct types of ECM, suggest a complex role for ECM within these aggregates and point to non-uniform behaviors by these undifferentiated cells. Such non-uniformity might be generated by variations in microenvironment (perhaps due to cell position within the aggregate) or by other factors that induce divergence of cell programming.

Conclusions, Task 9

Task 9 has had considerable success in developing alginate (with and without PLL coating) as a platform for sustained release of bioactive compounds *in vivo*. We have demonstrated linear, sustained release *in vitro* of 3 distinctly different compounds from alginate spheres: (1) the protein cytokines VEGF and TGF-β, (2) the GAG HA of two distinct MW classes (HMW of 1.5 million Da and MMW of 120,000 Da), and (3) antibodies, including the immunomodulatory antibody to CD3e of the T cell receptor. To our knowledge, we are the first group to develop alginate as a medium for sustained release of HA and antibodies. Importantly, we found that all of the macromolecules we evaluated *in vivo* retained biological activity after release from alginate in host mice, which included immunomodulatory effects by MMW-HA, TGF-β, and anti-CD3e antibody. Collectively,

our results indicate a high level of utility of alginate for animal-based studies of sustained release. Moreover, the biocompatible characteristics of alginate and the use of this material in human therapeutic trials (e.g., as an encapsulation medium for islet transplant), suggest that alginate might an application as a sustained release medium in human patients.

Task 9 also included an analysis of the ECM produced by IPSCs as they differentiate. This work is particularly important for regenerative therapies that utilize IPSCs, as the quantity and composition of ECM produced by engrafted IPSCs will likely have a significant influence on the character of the graft, particularly with respect to the efficiency of revascularization, maintenance of IPSC differentiation, structural reorganization of the IPSCs into functional tissue, and inflammatory/fibrotic responses by the host.

Task 10

Evaluation of prototype CI in rat dermal pockets for histological monitoring of biodegradation and in mouse dermal pockets for evaluation of regulatory T cell responses (Robert Vernon, PhD).

Our initial studies, evaluated the response of host mice to prototype CI scaffold materials comprised either of gelatin sponge or of crosslinked HMW-HA hydrogel. We observed that commercially-available medical grade gelatin sponge (Gelita-Spon™) was degraded *in vivo* within 3–4 days, a rate too rapid to be useful for our application. In subsequent studies, we evaluated the degradation properties of implanted HMW-HA (Extracel-HP) hydrogels after 7 days of residence in the peritoneal cavity of mice (in contact with gut mesentery). By histology (**Figure 69**), we found evidence of a measured degradation of the HMW-HA hydrogel by macrophage-like "giant cells", associated with a fibrovascular cellular infiltrate (**Figure 69A**). This degradation was accompanied by vascularization of the site **Figure 69B**). The process of degradation was accelerated by reducing the degree of thiol-crosslinking of the hydrogel (**Figure 69C**).

At the same time, we evaluated the immune response of mice to our alginate spheres (Task 9). We found that, after implantation *in vivo*, the alginate was not immunogenic, did not support infiltration by cells, and did not biodegrade appreciably (**Figure 70**). The absence of degradation of the alginate underscored our confidence that the bioactive compounds loaded into our alginate spheres would be released in a sustained manner after the spheres were implanted *in vivo*, as they were *in vitro* (Task 9).

Our histological data **(Figure 69)** indicated that Extracel-HP is not easily infiltrated by cells. This difficulty in cellularization may underlie the observation in Task 3 that immune cells did not easily traffic to the thiol-crosslinked HMW-HA-based hydrogels *in vivo*. It is for this reason that we pursued an alternative

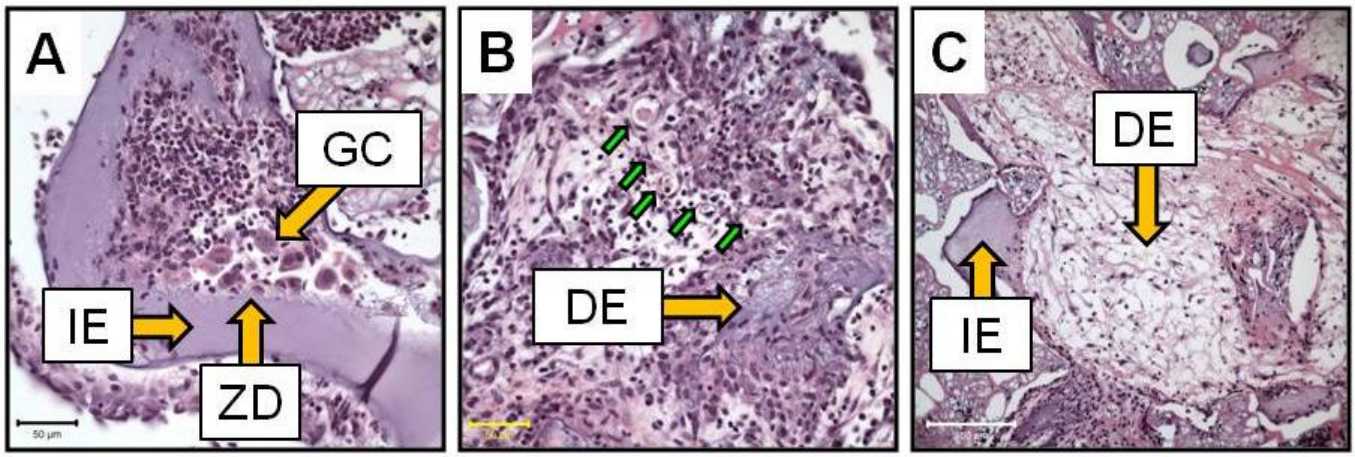

Figure 69. Cellular response to Extracel-HP 7 days after implantation in the mouse peritoneal cavity. *Micrographs are of paraffin sections cut at 8 microns and stained with hematoxylin and eosin.* ***(A)*** *Areas of intact Extracel (IE) show uniform basophilia and do not contain cells. Cellular infiltrate contains giant cells (GC) that make contact with the Extracel matrix in a "zone of degradation" (ZD) where the Extracel is broken down.* ***(B)*** *Where the implant has become colonized by cellular infiltrate, degraded Extracel (DE) is observed in association with neovasculature (green arrows).* ***(C)*** *An implant containing Extracel with half the amount of thiol crosslinking than was done for the implant shown in Panels A and B is cellularized more rapidly. Areas of intact Extracel (IE) and cellularized, degraded Extracel (DE) are shown.*

approach, which involved sustained delivery of soluble HA via our alginate spheres (Task 9). In this system, the HA is not in the form an impenetrable hydrogel (it is not crosslinked), yet, because it is released slowly into the surrounding tissue, it may be available locally for a time sufficient enough to promote immune tolerance (as suggested in **Figure 58**).

For evaluation of cellular responses to local delivery of immunomodulatory agents, we developed a standardized cytoprotective implant (CI) that is implanted into the peritoneal cavity of mice (**Figure 71**). To provide vascularization, the CI was wrapped in a fold (pocket) of gut mesentery. This form of CI utilizes a polyvinyl alcohol (PVA) sponge scaffold that supports a type I collagen hydrogel. The PVA scaffold was not cytotoxic and appeared to elicit a minimal foreign-body response. The type I collagen hydrogel allowed for efficient exchange of nutrients and waste products and readily supported ingrowth of mesenteric vasculature from the host mouse. At the center of the CI was placed an alginate sphere for sustained release of bioactive agents. As indicated in Task 9, some versions of the CI could hold up to six alginate spheres (**Figure 57**).

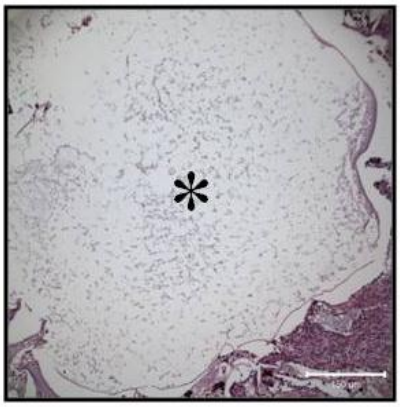

Figure 70. A 2 mm diameter alginate sphere 7 days after implantation in the mouse peritoneal cavity. *Micrograph is of a paraffin section cut at 8 microns and stained with hematoxylin and eosin. The sphere (asterisk) is largely intact. The alginate appears as a precipitate – a consequence of removal of water from this highly-hydrated hydrogel during histological processing.*

As a readout for immunomodulation, we used the DO11.10 mouse model described under Aim 1, Task 5. We and others have shown that transfer of activated DO11.10 CD4+ T effector cells, which recognize a peptide of the chicken protein ovalbumin, into lymphopenic (Rag-deficient) mice that express ovalbumin in the pancreas (RIP-OVA/Rag-/-, referred to as RO/RAG mice), results in the rapid onset of diabetes. This model is a rapid, sensitive means to evaluate approaches to suppress the T cell cytotoxic response directed against pancreatic islet cells, which models autoimmune dysregulation as well as elements of the inflammatory response.

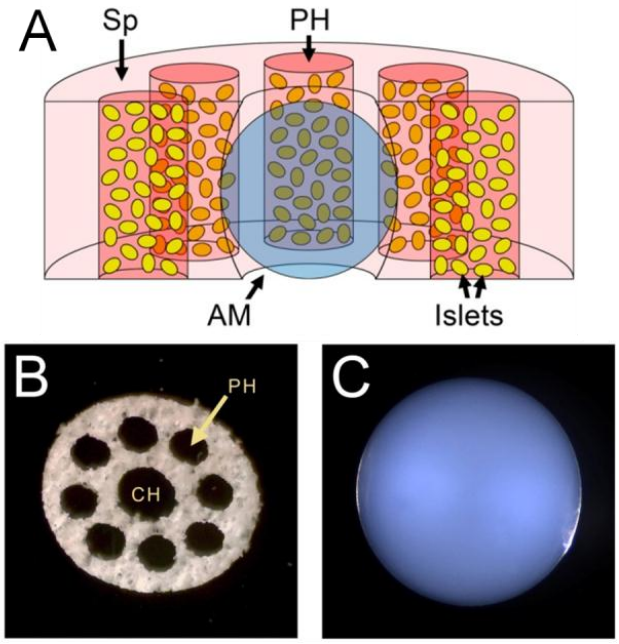

Figure 71. Design of a bioengineered cytoprotective implant (CI) for use in mice. (A) *Cut-away diagram of the CI with the components shown to scale. A disk-shaped PVA sponge (Sp) scaffold provides mechanical support. An alginate "macrosphere" (AM) time-release capsule (blue) occupies the central hole of the sponge. Eight peripheral holes (PH) in the sponge (5 appear in this cut-away) contain islets (yellow) suspended in a type 1 collagen hydrogel (reddish-pink). The collagen hydrogel also infuses the sponge (light pink). For clarity, the pores of the sponge are not depicted.* ***(B)*** *A PVA sponge scaffold oriented to show the central hole (CH) and peripheral holes (PH). The scaffold is 6 mm in diameter.* ***(C)*** *An alginate time-release capsule of 2 mm diameter.*

In conjunction with the DO11.10 mouse model, we used the sustained release technology developed in Task 9 to deliver immunomodulatory anti-CD3e antibody and MMW-HA locally within CIs grafted into RO/RAG mice. Histological results of the experiments utilizing the anti-CD3e antibody are shown in **Figures 72 and 73**. These results indicate that sustained release of the anti-CD3e antibody within the CI protected both the transplanted islets within the CI (**Figure 72**), and the native pancreatic islets (**Figure 73**) from autoimmune

attack. As suggested by the cell proliferation data shown in **Figure 56B**, this immunoprotective effect was likely the result of elimination of the autoreactive T cells by anti-CD3e antibody-induced apoptosis.

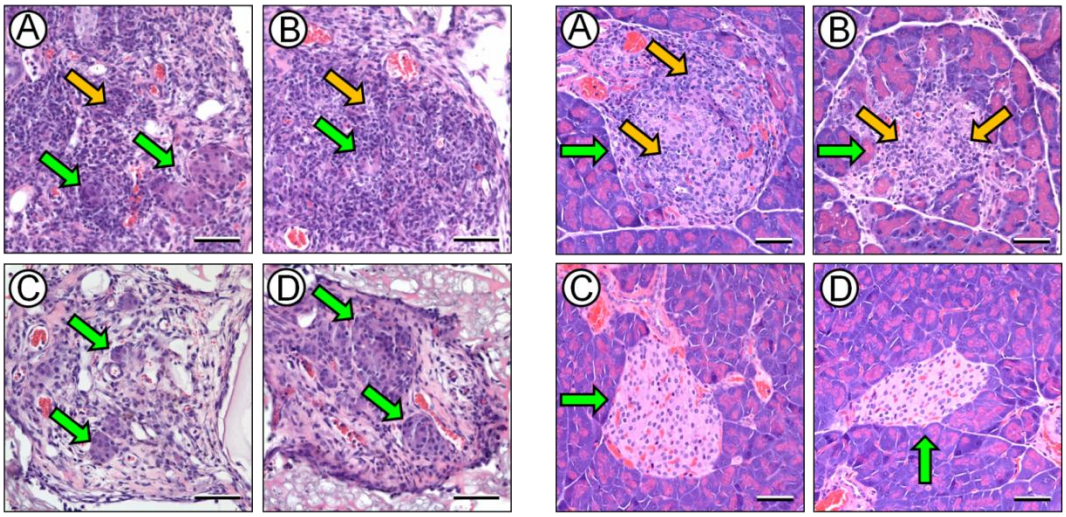

Figure 72 (left panel) and 73 (right panel). Effect of sustained (time) release of immunomodulatory anti-CD3e antibodies on the host response to engrafted CIs (Figure 72) and on autoimmune attack of native, pancreatic islets (Figure 73). *CIs incorporating 200 donor islets were implanted into RO/RAG mice in mesenteric pockets. Each CI contained a single alginate sustained release sphere loaded with antibody carrier buffer only (negative controls – **A, B**) or loaded with 5 µg of anti-CD3e antibody (**C, D**). After injection of DO11.10 CD4+ T cells and OVA priming, as described in **Figure 56B**, the CIs and pancreata were removed at Day 11 of the experiment and processed histologically. **Figure 72. (A, B)** Host cellular infiltrates within negative control CIs include high numbers of lymphocytes, as indicated by the presence of abundant basophilic nuclei (orange arrows) in the section. These lymphocytes have begun to surround and penetrate the donor islets (green arrows). **(C, D)** In contrast to the negative controls, the CIs incorporating the anti-CD3e antibody have a much lower level of lymphocytic infiltrate and the implanted islets (green arrows) are clearly visible. **Figure 73. (A, B)** Native islets (green arrows) in the pancreata of mice that received the negative control CIs have an abundant lymphocytic infiltrate (orange arrows) representing an autoimmune response mounted against the islets. **(C, D)** In contrast to the negative controls, native pancreatic islets (green arrows) of mice that received the CIs incorporating anti-CD3e antibody have no evidence of lymphocytic infiltrate. In both Figures, specimens are stained with H & E. All scale bars are 100 µm.*

In follow-on studies, we used our sustained release technology to deliver immunomodulatory MMW-HA locally within CIs grafted into RO/RAG mice. Two earlier experiments indicated that MMW-HA delivered from our CI prototype might have been modulating the Treg response, as shown by upregulation of the immunosuppressive cytokine interleukin (IL)-10. In a third repeat experiment, we engrafted CIs each containing donor RO/RAG islets and 5 alginate spheres, each loaded with 50 µg of MMW-HA (250 µg of MMW-HA total per CI) and one alginate sphere containing 50 ng of VEGF to stimulate vascular growth in the implant. The CIs were removed after 18 days and prepared for histology. As with the previous experiments with MMW-HA, there was no statistical difference between interferon (IFN)γ production by CD4+ T cells isolated from the spleens or mesenteric lymph nodes of the MMW-HA-treated mice vs. control mice (IFNγ is a cytokine produced by activated T cells) (**Figure 74**). Unlike the previous experiments, which showed an increase in IL-10 production by CD4+ T cells in the mice exposed to MMW-HA, as compared with controls, in the present experiment we did not see a

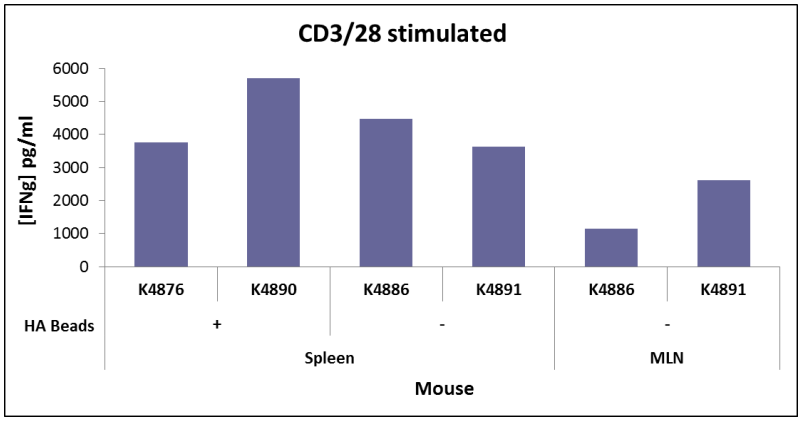

Figure 74. Production of IFNγ by CD4+ T cells isolated from the spleens and mesenteric lymph nodes (MLN) of mice. *Mice (ID numbers K4876, K4890) received implants containing MMW-HA ("HA beads+") or implants lacking MMW-HA (control mice K4886, K4891 "HA beads–"). IFNγ production was elicited in vitro by exposure to antibodies against CD3 and CD28.*

statistically significant difference in IL-10 production between the MMW-HA-treated and control mice (**Figure 75**). Histological analyses showed the presence of leukocytic infiltrate into the CIs that did not receive MMW-HA, as expected in the RO/RAG autoimmune model.

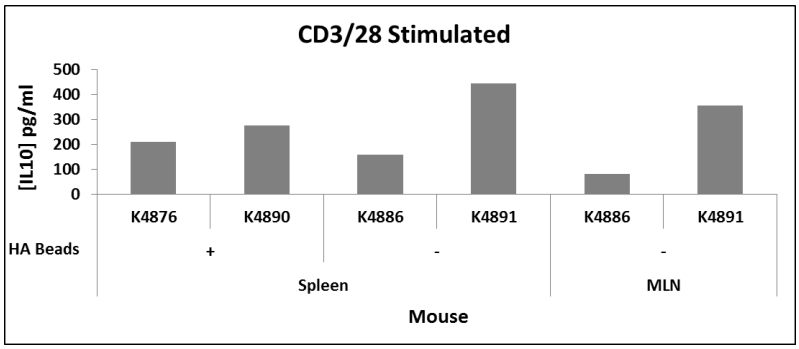

Figure 75. Production of IL-10 by CD4+ T cells isolated from the spleens and mesenteric lymph nodes (MLN) of mice. *Mice (ID numbers K4876, K4890) received implants containing MMW-HA (HA beads+) or implants lacking MMW-HA (control mice K4886, K4891 (HA beads–). IL-10 production was elicited in vitro by exposure to antibodies against CD3 and CD28.*

In experiments done in parallel with the MMW-HA sustained release studies *in vivo* reported above, we used alginate to deliver TGF-β locally within CIs grafted into RO/RAG mice, with IL-10 production as the readout. Alginate spheres were loaded with 5 µg of TGF-β or normal saline (controls). On the day following implantation, we immunized the mice with 50 µg of OVA peptide and transplanted DO.11 CD4+ T cells into the mice. On day 10, the spleens and mesenteric lymph nodes were harvested to collect the transplanted T cells. We found that the T-cells isolated from the TGF-β-treated and control mice produced similar levels of IL-10 in response to anti-CD3/CD28 antibody stimulation *in vitro* (**Figure 76**). This was expected, as exposure to anti-CD3/CD28 antibodies is a potent general stimulator for T-cells. Like the IFNγ data shown in **Figure 62**, the IL-10 data indicated that, compared to controls, the TGF-β in the CI did not cause a measurable loss (or increase) of T-cells in the host mouse.

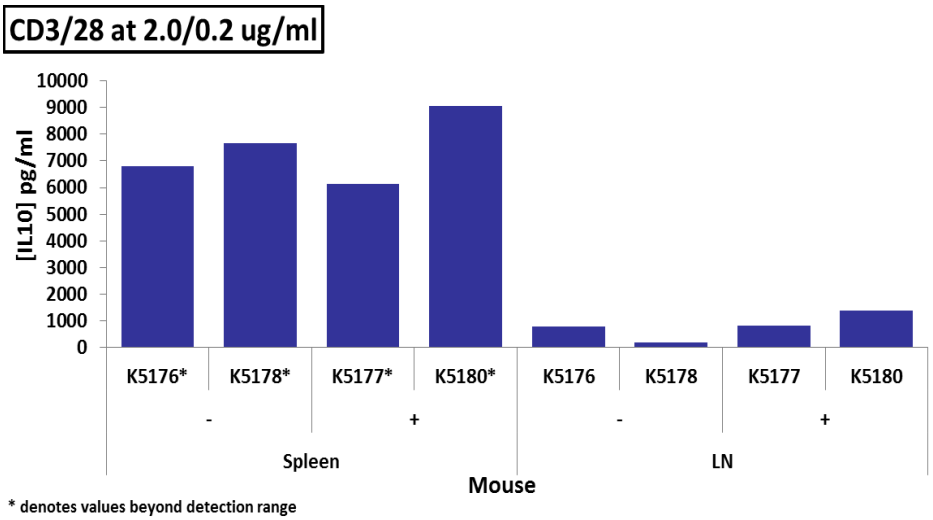

* denotes values beyond detection range

Figure 76. IL-10 production of isolated CD4+ T-cells in response to anti-CD3/CD28 antibody stimulation in vitro. *DO.11 T-cells were introduced into RO/RAG mice that had been implanted with CIs containing either 5 µg of TGF-β or saline (controls) and stimulated with OVA peptide. Ten days later, the CD4+ T-cells were isolated from the spleens and mesenteric lymph nodes (LN) and stimulated in vitro with antibodies to CD3 and CD28. IL-10 production in response to antibody exposure was similar between the TGF-β-treated (+) group and the control (–) group. "K" numbers identify specific mice.*

Although IL-10 production by CD4+ T-cells to generalized stimulation by anti-CD3/CD28 antibodies was similar between the TGF-β-treated and control mice (as was IFNγ production) differences were seen in IL-10 produced as a result of the recall response to OVA peptide, which, as stated previously, represents the specific autoimmune antigen in this model. Splenic CD4+ T-cells from TGF-β-treated mice produced elevated levels of IL-10 in response to OVA peptide in comparison to the saline-treated controls (**Figure 77**). As mentioned earlier, IL-10 is secreted by activated CD4+ T helper and Treg populations, and has potent immunosuppressive effects, acting to inhibit T-cell proliferation and down-regulate display of antigen by antigen-presenting cells. Our results, therefore, suggest that sustained release of TGF-β *in vivo* may be able to induce CD4+ T-cell-mediated immunosuppression in response to a specific autoantigen.

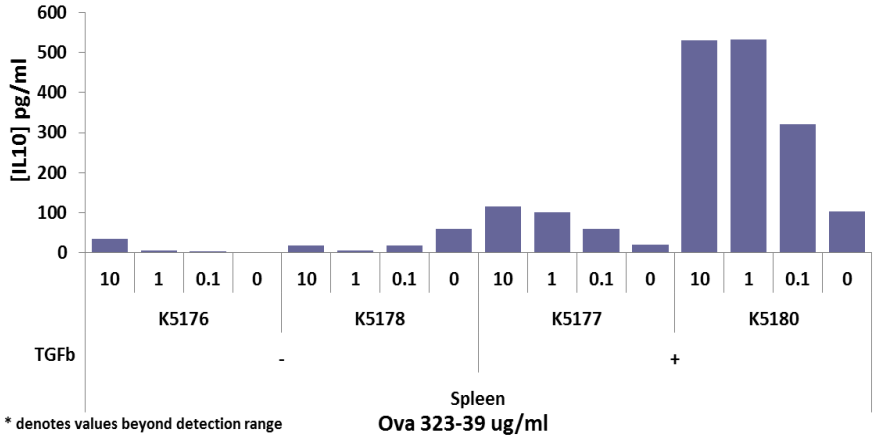

Figure 77. IL-10 production by isolated CD4+ T-cells in response to OVA peptide stimulation in vitro. *DO.11 T-cells were introduced into RO/RAG mice that had been implanted with CIs containing either 5 µg of TGF-β or saline (controls) and stimulated with OVA peptide. Ten days later, the CD4+ T-cells were isolated from the spleens and stimulated in vitro with graded quantities of OVA peptide. IL-10 production in response to OVA exposure was greater in the TGF-β-treated group compared to the control group. "K" numbers identify specific mice.*

Task 10 focused on evaluating the effects of local delivery of immunomodulatory and other cytokines after engraftment of the CIs into mice. Accordingly, for our final set of studies, we used our sustained release technology to examine the effects of VEGF delivery on the early-stage survival of implanted tissue, using the islet model that we have described previously. We found that delivery of 20 ng of VEGF into the CIs via alginate microspheres significantly improved islet survival in the CIs within 24 h after implantation. (**Figure 78**). This effect was not due to stimulation of host vascularization of the islets by the VEGF, because 24 h is too short a time for blood vessels to grow into the CI. Rather, the improved islet survival was likely due to direct effects of VEGF on the engrafted islets. This result is very important in that it indicates: (1) that our sustained release technology can deliver physiologically-meaningful levels of bioactive compounds within a very short time after engraftment, and (2) the released bioactive compounds can exert a direct effect on the engrafted tissue. This capability will likely prove critical to improving the survival of engrafted cells and tissue constructs, particularly during the early phases of engraftment prior to the establishment of a vascular supply to the graft.

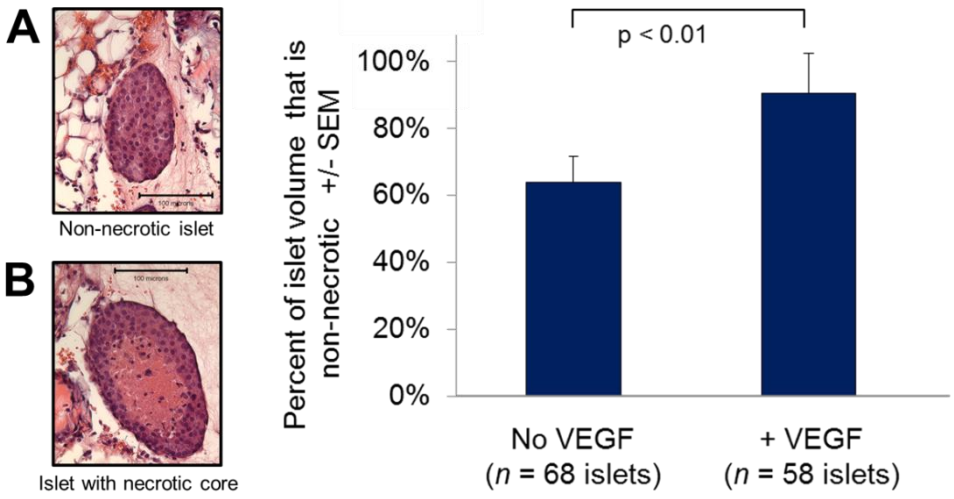

Figure 78. Sustained release of VEGF in the CI has a rapid influence on graft survival in vivo. *Each CI contained islets and an alginate sphere loaded with 20 ng of VEGF. Twenty-four h after implantation, the CIs were removed, embedded in paraffin, sectioned, stained with hematoxylin/eosin, and the islets in the CIs scored for level of necrosis, which indicated post-implantation damage.* ***(A)*** *Example of a healthy, non-necrotic islet with a fully-cellularized interior. Note the even distribution of cell nuclei (blue) throughout the islet.* ***(B)*** *Example of an islet with necrosis at the core, as indicated by an eosinophilic (pink) zone generally lacking cell nuclei (blue). The graph at right shows that treatment with VEGF increases the percent of islet mass that is healthy (i.e., non-necrotic).*

Additional studies examined the effects of sustained release of VEGF on IPSC growth in the CI. As mentioned under Task 9, IPSCs may prove to be of critical importance to the replacement of diseased, injured, or lost tissues. We prepared CIs, loaded with mouse IPSCs, which also included alginate spheres containing either 20 ng of VEGF or buffer only (controls). These CIs were grafted into mice of the same strain. After 24 days, the CIs were removed from the host mice and photographed to record the growth of the IPSCs in the implant. We found that the CIs that had received the VEGF had very significant growth of IPSCs in the implant, whereas the CIs that had not received VEGF had minimal growth (**Figure 79**). Of note, the CIs that had received VEGF appeared well-vascularized which indicated that the VEGF was being released from the alginate in a bioactive form. It is likely that the enhanced vascular response by the host mice, induced by the VEGF, was responsible for stimulating the growth of the IPSCs. These results continued to validate the effectiveness of our alginate-based method of cytokine delivery within the CI.

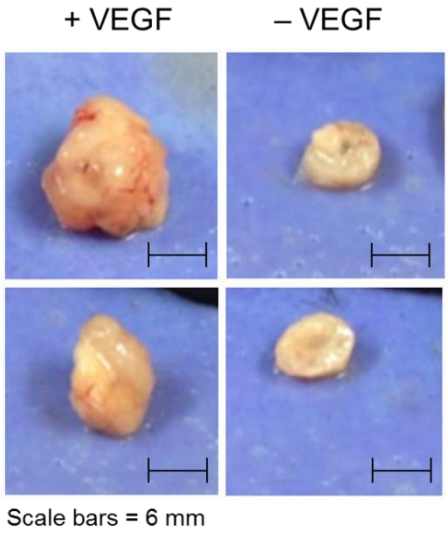

Figure 79. Sustained release of VEGF in CIs stimulates the growth of IPSCs in vivo. *CIs loaded with mouse IPSCs and with alginate spheres containing either 20 ng of VEGF (+ VEGF) or buffer only (– VEGF) were grafted into mice of the same strain. After 24 days, the CIs were removed and photographed to record the growth of the IPSCs in the implant. The CIs that had received VEGF had very significant growth of IPSCs (left panels) whereas the CIs that had not received VEGF had minimal growth (right panels). The CIs that had received VEGF were well-vascularized, as indicated by the presence of surface blood vessels.*

Conclusions, Task 10

Task 10 served as the translational arm of Aim 2A, in which methods for sustained release of bioactive compounds developed in Task 9 were tested for biological activity in mouse models *in vivo*. Work performed under Task 10 has resulted in the development of a novel CI that incorporates a PVA sponge scaffold, collagen hydrogel, and one or more alginate constructs for sustained release of bioactive compounds. This form of CI promises to have a wide range of applicability as an *in vivo* experimental test-bed and, potentially, as a therapeutic device (with some modifications to the design and selection of materials). Importantly, experiments performed with this CI have shown that sustained release of compounds with pro-angiogenic (e.g., VEGF) and immunomodulatory (e.g., antibodies, HA, TGF-β) properties locally within the implant can promote vascularization of the graft and exert modulatory effects on the host immune system.

Task 11

Development of myobridges using uniaxial supports and collagen gels populated with myoblast cells. Histological evaluation of cultured myobridges for cell survival, new muscle cell generation, proliferation and differentiation (Margaret Allen, MD).

Developing fabrication techniques for myobridge constructs

A major goal of Task 11, a component of Aim 2B, was to develop myobridges that would be suitable for later *in vivo* implantation, with an eye to providing a milieu for implanted myoblast cells that will foster cell survival and proliferation while reducing ambient host inflammation. In preliminary studies, we had shown that upregulation of heme oxygenase-1 (HO-1) by a specific transcriptional activator, cobalt protoporphyrin (CoPP), increased the percentage of muscle-derived stem cells (MDSCs) that survived an *in vitro* regimen of hypoxia /

reoxygenation, designed to mimic the stresses of *in vivo* cell implantation. So, our initial experiments explored whether CoPP might be an appropriate additive to construct scaffolds.

Type I collagen gels with CoPP

In our initial studies, rat MDSCs were seeded into 100% collagen gels that were then suspended on Nitex nylon mesh frames and cultured for 5 days. Groups of construct scaffolds (n = 2 scaffolds per group) differed in CoPP treatment and delivery route: (1) control type I collagen gels without additives, (2) 25µM CoPP added to the culture differentiation medium (DM) 24 h after cell seeding, (3) 25µM CoPP added to the scaffold upon seeding, and (4) 25µM CoPP added to the scaffold upon seeding plus CoPP added to the medium at 24 h after seeding. After 5 days of culture, constructs were collected and formalin fixed.

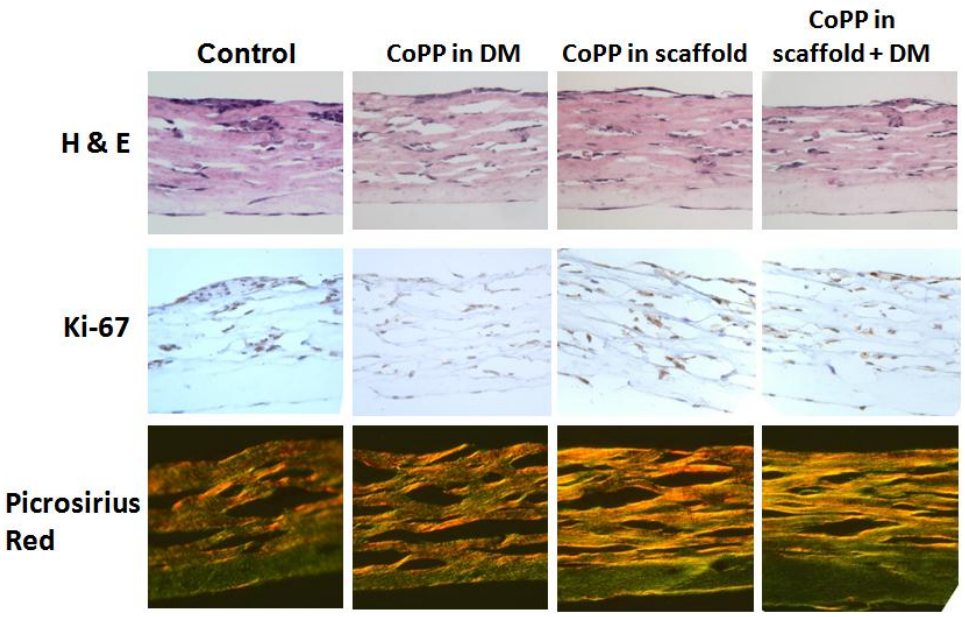

Figure 80. Histology of rat MDSCs seeded into collagen gels treated with CoPP.

The results (**Figure 80**) suggested that adding CoPP increased the numbers of surviving cells, especially those deep within the constructs. CoPP treatment also appeared to increase MDSC proliferation within the scaffolds, visualized as more cells exhibiting Ki-67 staining (indicative of dividing cells) in all CoPP-treated specimens. Finally, more picrosirius red staining was seen in the groups in which CoPP had been incorporated into scaffolds, suggesting that the capacity for MDSCs to reorganize collagen was enhanced in CoPP-treated scaffolds.

Combined collagen/hyaluronan gels with CoPP

In subsequent experiments (**Table 2**), CoPP was added to two candidate scaffold materials for myobridge fabrication: 100% collagen and a mixture of 95% Type 1 collagen with 5% HyStem-HP™. HyStem-HP (Glycosan Biosystems) is an ECM hydrogel that contains cross-linked HMW-HA which has been used to advantage in the growth of other stem cell types, but has not been previously used with skeletal myocytes. HMW-HA is expected to have anti-inflammatory properties and the cross-linking is designed to prevent breakdown into pro-inflammatory low molecular weight fragments. Heparin immobilized within the HyStem-HP would allow for slow release of growth factors (GFs). In addition, HyStem-HP might alter the stiffness of the construct which may make it easier to handle and implant surgically.

MDSCs were seeded into 100% collagen or 95% collagen/5% HyStem-HP constructs with and without the addition of 25µM CoPP to the scaffold. Constructs were seeded at cell densities of 2.2×10^6 cells/ml, or 10^6 cells in 450µl matrix per construct. We used rat serum to better simulate the milieu surrounding the construct after *in vivo* implantation in rats. After 24 h, the collagen constructs were incised laterally to instill tension and transferred to differentiation medium for *in vitro* for 2 or 3 weeks.

Table 2. Experimental design: constructs seeded with rat MDSCs cultured in vitro.

		Fixed in 10% buffered formalin	
	Initial Number	14 days	21 days
TREATMENT GROUPS			
100% collagen	4 constructs	2 constructs	2 constructs
100% collagen + CoPP	4 constructs	2 constructs	2 constructs
95% collagen/5% HystemHP	4 constructs	2 constructs	2 constructs
95% collagen/5% HystemHP + CoPP	4 constructs	2 constructs	2 constructs
** MDSCs suspended at 2.22x10^6 ml of matrix material (100,000 cells in 450 µl of matrix per construct).*			

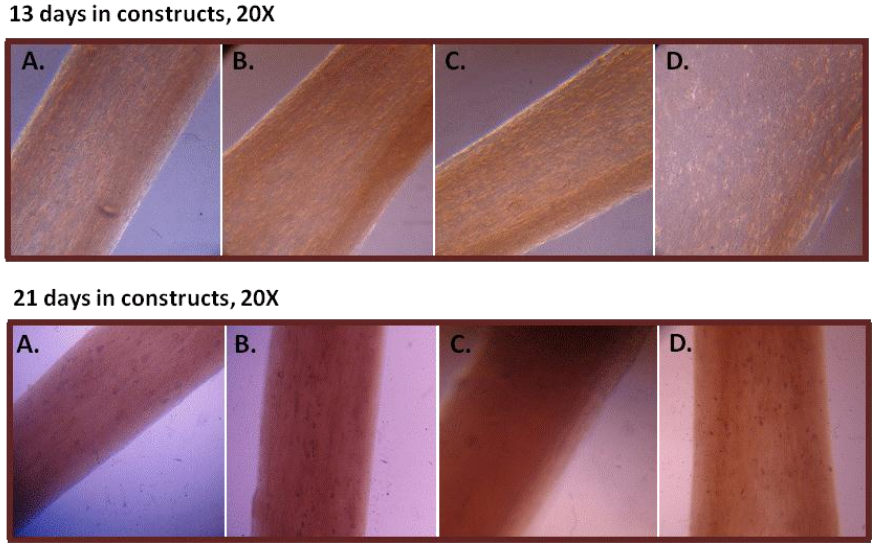

Figure 81. Rat anterior tibialis MDSCs grown in vitro on nylon frames in extracellular matrix scaffolds with or without CoPP:

A. *100% collagen*

B. *100% collagen + 25µM CoPP*

C. *95% collagen/5% Hystem-HP*

D. *95% collagen/5% Hystem-HP + 25µM CoPP.*

Figure 82. Rat MDSCs grown 13 days in vitro on nylon frames in extracellular matrix scaffolds with or without CoPP:

In the presence of CoPP, MDSCs appear to retain their immature state, at least by morphology. Cells in CoPP-treated matrix also appear to engage the matrix less, to elongate less, and to align less than cells grown in scaffolds without CoPP.

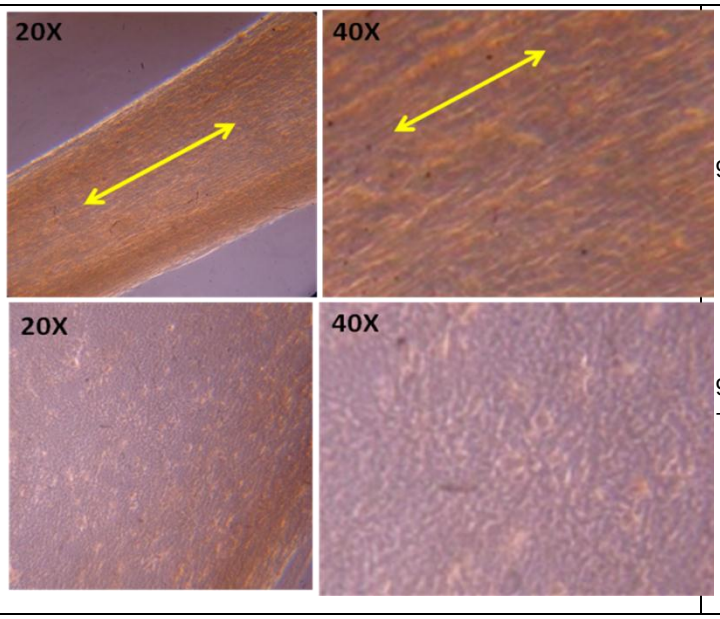

Histological results from these *in vitro* studies suggested that the addition of CoPP to either the 100% collagen matrix or to the combined collagen/HMW-HA matrix changed the appearance of the cells in the constructs, at least at the early 2-week time point (**Figures 81–83**). In the presence of CoPP, cells appeared rounder and less elongated, and exhibited less alignment during culture under uniaxial tension.

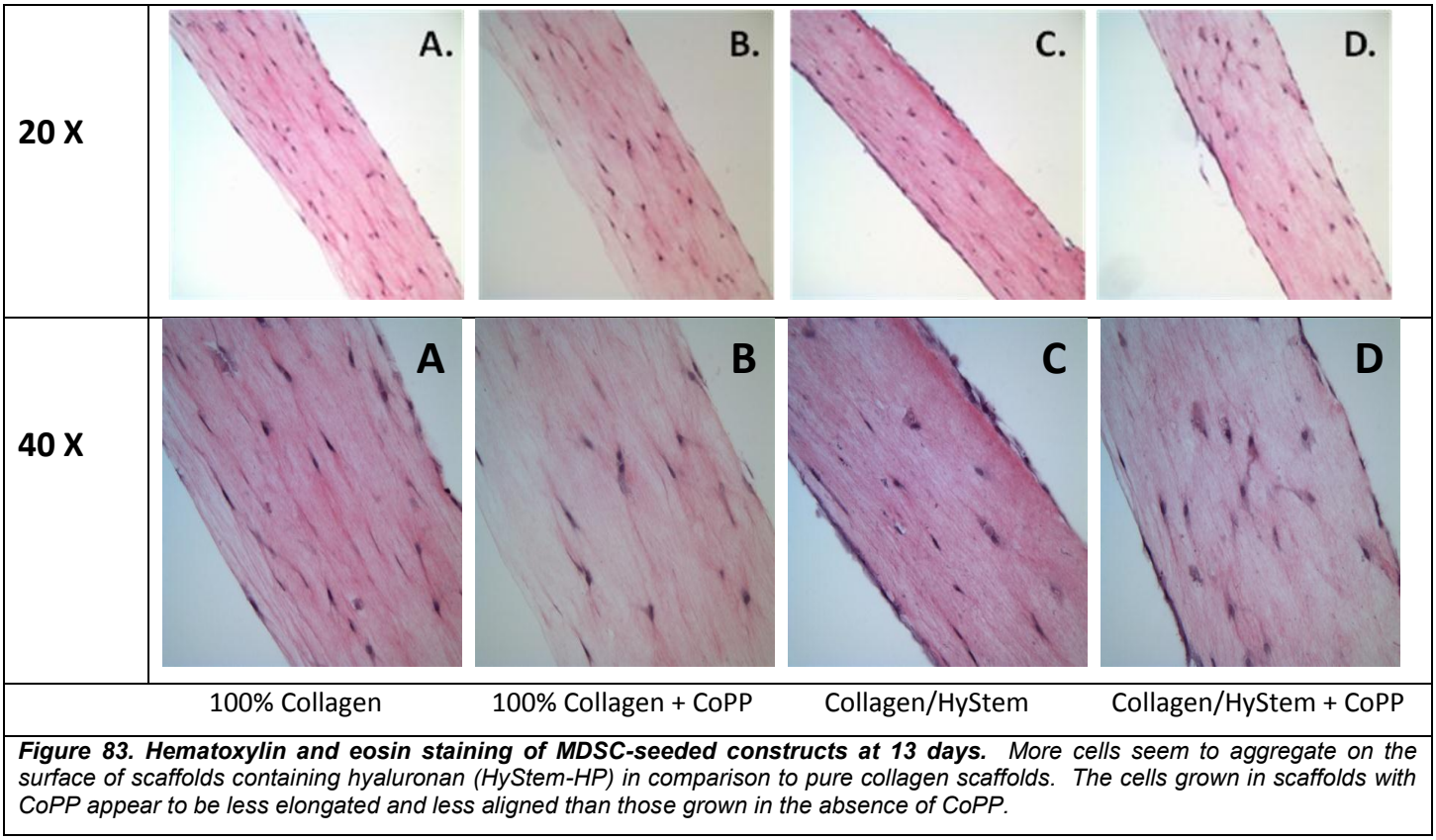

Figure 83. Hematoxylin and eosin staining of MDSC-seeded constructs at 13 days. *More cells seem to aggregate on the surface of scaffolds containing hyaluronan (HyStem-HP) in comparison to pure collagen scaffolds. The cells grown in scaffolds with CoPP appear to be less elongated and less aligned than those grown in the absence of CoPP.*

The histological results also suggested differences in cell behavior in the HMW-HA matrices (**Figure 83**). Cells in the combined collagen/HMW-HA matrices appeared to be more densely situated on the surface of the construct than the cells grown in 100% collagen. The stiffness of the HMW-HA matrix may have affected the penetration of seeded cells.

Picrosirius Red staining (**Figure 84**) showed that the presence of CoPP in the scaffold appeared to be associated with smaller sized collagen fibers in the construct. This again suggested that CoPP might have slowed the rate of differentiation, so that less collagen remodeling is occurring with the addition of CoPP. Alternatively, CoPP could be altering cell adhesion to matrix or the strength of cell traction on the matrix. If, indeed, CoPP slows MDSC differentiation, this might be advantageous for myobridge implants, since MDSCs that stay in a more immature state may have greater proliferative potential after *in vivo* implantation. This might facilitate more complete replacement of lost muscle.

Development of fabrication methods for myobridge constructs

In our intial *in vitro* studies, MDSC-seeded gels were suspended in small rectangular Nitex nylon mesh frames. However, more sophisticated constructs were necessary for the *in vivo* implants. The goal here was to develop a myobridge that supports MDSC growth and differentiation, but that is also "implant ready" for use in repairing rat hindlimb muscle defects in our rat model. "Implant ready" means that the construct would contain appropriate scaffold material infused with viable cells, and that the construct ends would be ready to be attached directly to both ends of the native muscle defect. In concept, the seeded cells would be pre-cultured under tension, so that they would already be aligned at the time of implantation.

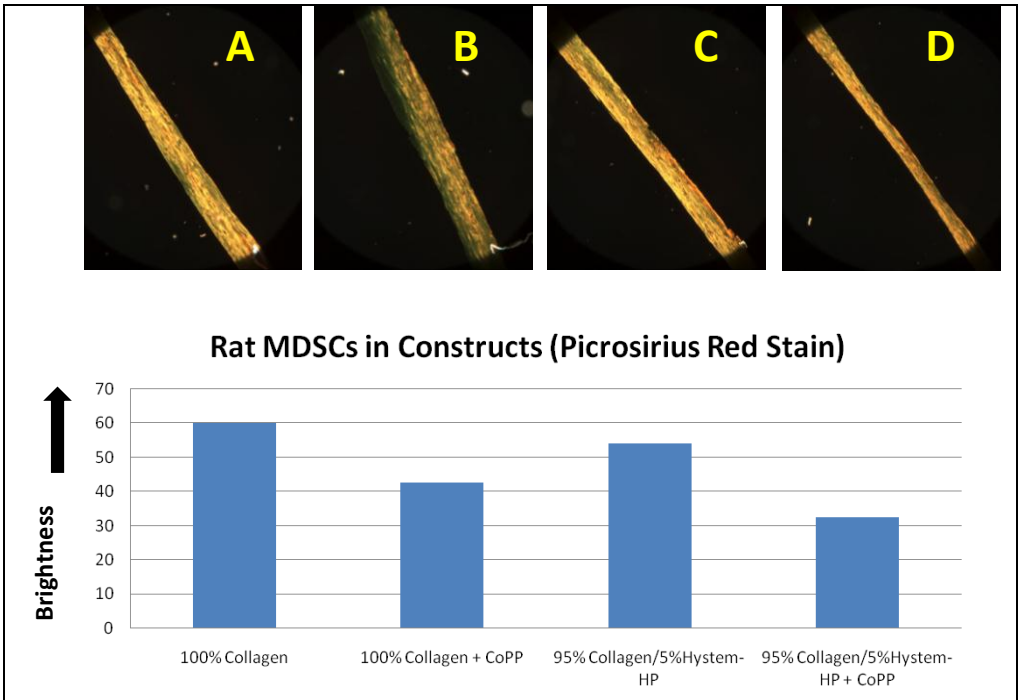

Figure 84. Collagen fiber size in MDSC-seeded constructs with/without CoPP.

*Picrosirius Red staining is a means to delineate the size of collagen fibers—thinner, more reticular fibers are greenish, while larger fibers are yellow to red. In both 100% collagen constructs **(A,B)** and in combined 95% collagen/5% Hystem-HP constructs **(C,D)**, the addition of CoPP **(B,D)** seemed to reduce the size of collagen fibers. This might indicate that the seeded cells have done less remodeling of collagen fibers in the presence of CoPP.*

Several design problems needed to be solved for this concept to be realized. First, the seeded cells aggressively and rapidly remodeled the collagen scaffold, shrinking its diameter, so the initial mold had to account for this and other geometric changes. Second, the collagen matrix had to be firmly tethered at either end of the construct in order to maintain tension during the shrinkage process; this tension also needed to be maintained during implantation. Third, the ends of the construct had to be suturable for easy surgical implantation. Ideally, the suture would also be biodegradable so that the implant eventually consists solely of cells and natural scaffold without synthetic material.

To address each of these requirements, the scaffold-suture construct was designed as shown in **Figure 85A**. Each of the ends were composed of resorbable 6.0 vicryl sutures that were tied to discs of Nitex mesh that were then immersed in a collagen matrix solution and allowed to polymerize, thus encasing the Nitex mesh within the collagen hydrogel polymer (**Figure 85B**).

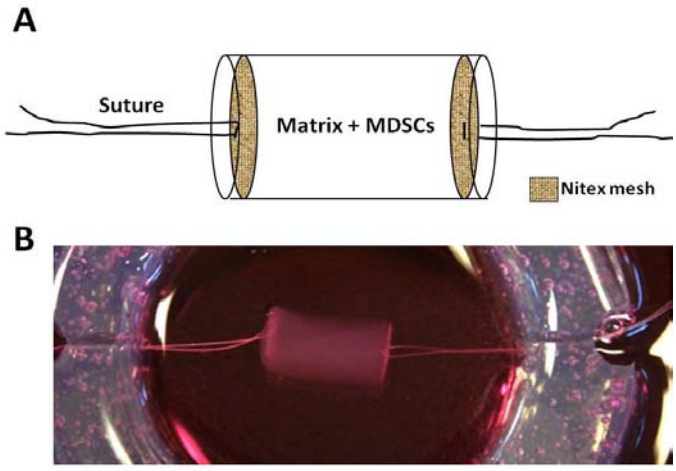

Figure 85. Scaffold-suture construct design. *The design of the construct **(A)** includes sutures attached to Nitex meshes which are gelled within the matrix material containing muscle-derived stem cells (MDSCs). An example of a fully-polymerized collagen-based test construct is shown in **(B)**.*

The entire fabrication process is illustrated in **Figure 86**. First, silicone "coffin molds" were fabricated by pouring a base layer of silicone and then pouring a second layer that contained Teflon mold blocks. The Teflon blocks were then removed after the silicone had cured (**Figure 86A**), leaving a rectangular space (coffin) in the silicone. Subsequently, thin slits were cut into the silicone to connect with the two narrow walls of the coffin. These slits secured both of the sutures, with their attached Nitex discs.

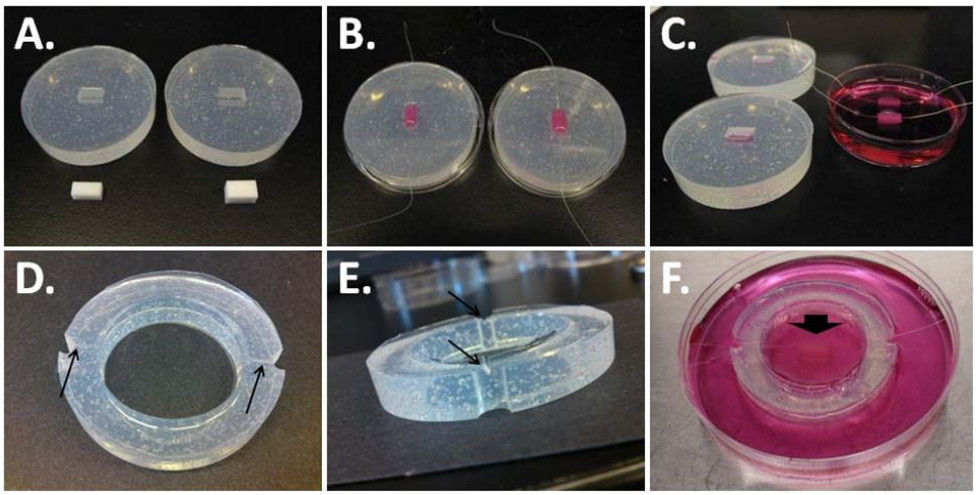

Figure 86. Fabrication of scaffold-suture constructs using silicone molds. *"Coffin molds" are formed around Teflon blocks* ***(A)*** *and the suture/Nitex assemblies placed into the mold and the collagen/MDSC composite is allowed to polymerize around the Nitex material, tethering both ends* ***(B)****.Once polymerized, the entire construct can be removed and placed into culture medium* ***(C)****. To culture the constructs, a ring of silicone is formed* ***(D*** *and* ***E)*** *with two slits (arrows) to hold the suture ends in place. A complete culture setup within a 100 mm culture dish is shown in* ***(F)****, where the suture ends of the construct are tethered to the silicone ring with the construct (arrow) held in the center of the ring. The 100 mm culture dish is filled with enough culture medium (pink) to immerse the construct and then is placed in a tissue culture incubator.*

To prepare the scaffold-suture constructs, the suture/Nitex assemblies were placed within the sterilized mold into which was poured the ECM scaffold material with suspended cells. Collagen with MDSCs was the initial ECM/cell combination of choice. Subsequently, the filled mold was placed in a humid chamber at 37° C to polymerize the collagen **(Figure 86B**). After the collagen had polymerized, the entire construct was gently transferred into medium-filled culture plates (**Figure 86C**). To culture the constructs *in vitro*, a silicone ring was produced by pouring silicone into a 60 mm dish that has a 35 mm dish in the center. After the silicone had cured, two cuts were made, bisecting the ring with thin slots to hold the construct sutures in place (**Figure 86D, E**). The sutures of the polymerized construct were inserted into the slots of the silicone ring, which was then placed into a 100 mm culture dish (**Figure 86F**). The dish was filled with enough culture medium to immerse the construct, and then placed in a tissue culture incubator. During culture, the MDSC-collagen composite underwent cell-mediated contraction, which put the entire construct under tension and oriented both the collagen fibrils and the seeded cells in parallel to the long axis of the construct.

Pilot in vivo implants

To investigate the responses of rats to materials that were to be incorporated into myobridge prototypes, a set of pilot experiments were performed, which are summarized in **Table 3**.

Table 3. Experimental design: treatment groups for in vivo implants conducted to date.

AT = Anterior tibialis muscle

Pilot Study - Myobridge Implantation		**Implant Procurement**			
	Initial Number	**Week 1**	**Week 2**	**Week 3**	**Week 4**
Removal of AT Muscle	2 rats		1 rat		1 rat
Removal of AT Muscle replaced with Vicryl Suture	2 rats		1 rat		1 rat
Removal of AT Muscle replaced with 100% Hystem HP	4 rats	1 rat	1 rat	1 rat	1 rat
Removal of AT Muscle replaced with 100% rat type 1 collagen	4 rats	1 rat	1 rat	1 rat	1 rat
Removal of AT Muscle replaced with 100% Hystem HP with MDSCs	4 rats	1 rat	1 rat	1 rat	1 rat
Removal of AT Muscle replaced with 50% Hystem/50% collagen with MDSCs	4 rats	1 rat	1 rat	1 rat	1 rat
Removal of AT Muscle replaced with 100% rat type 1 collagen with MDSCs	4 rats	1 rat	1 rat	1 rat	1 rat
** MDSCs cells suspended at 2.22x10^6 /ml of matrix material*					
*** 300 µl of matrix implanted into cavity where AT muscle had occupied (66,700 MDSCs implanted)*					

In the first group, the anterior tibialis (AT) muscle was simply excised, fixed, and measured to determine mold dimensions. Next, various suturing techniques were tested for securing Vicryl sutures to the AT tendon and muscle remnants to hone the implant techniques for these scaffold-on-a-suture constructs. Then, the first set of *in vivo* implants was performed, implanting acellular scaffold materials alone without cells. These experiments served as baseline studies to examine the extent and time course of native muscle regeneration and muscle cell repopulation of the scaffolds without cell implantation. The rats tolerated the implants well. They were able to walk on their operated legs and did not show signs of local inflammation. We determined that the Hystem HP scaffolds absorbed water and increased in size after implantation (the 100% collagen scaffolds did not absorb water). The size change by the Hystem biomaterial was taken into consideration in calculating construct sizes. We also found that it was not practical to close the fascia over the implanted construct—it was better to close the skin only.

At the appropriate end point (**Table 3**) the left hindlimbs were procured and fixed in 10% buffered formalin for a minimum of 5 days. Each implant was then sectioned off the bone, leaving a margin of surrounding muscle, and processed for histology. Upon sectioning, some of the construct tissues began to delaminate, likely due to the differences in composition and density between the soft gels and surrounding denser fascia and skin. This problem has been seen in other tissues (e.g., mouse ears) and was corrected by lengthening processing times. From these pilots, we determined that the constructs and cells were well tolerated and did not elicit an inflammatory reaction. We also learned that cell differentiation needed to be induced prior to implantation for the construct to develop enough stiffness to facilitate surgical manipulation.

The finalized version of the myobridge construct was developed in Year 2 (**Figure 87**). For the transplant studies *in vivo*, the construct was lengthened to fill the AT muscle defect and the nylon (Nitex) mesh used in the prototype was replaced with surgical-grade Vicryl (polyglactin 910) mesh which biodegrades within six weeks after implantation.

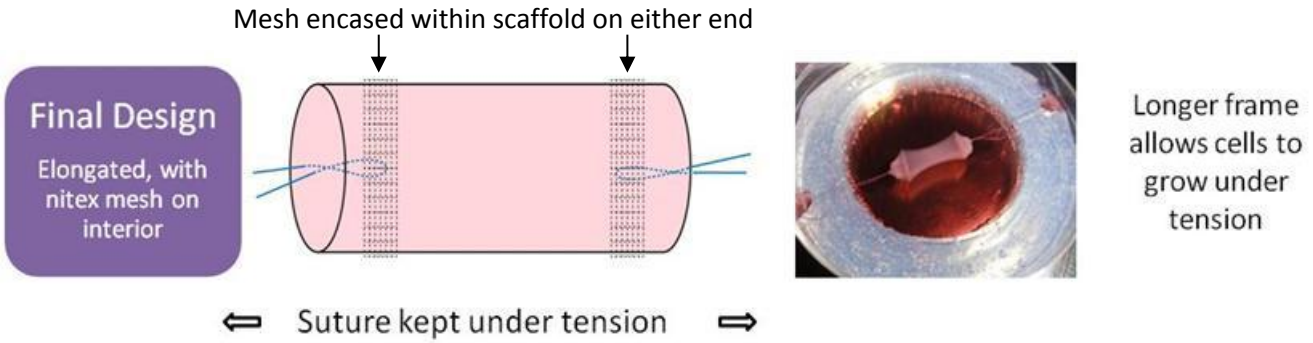

Figure 87. Final version of the myobridge construct.

Biomechanical testing

The relationship between ECM stiffness and myoblast differentiation was tested using C2C12 mouse myoblasts and primary mouse skeletal myoblasts. Constructs were subjected to passive strain testing to quantify construct stiffness/elasticity. Young's modulus was calculated from the following equation where the numerator is equivalent to tensile stress and denominator represents an applied strain:

$$E = \frac{F/A_0}{\Delta L/L_0}$$

Stress/strain curves were generated for each construct. After each stretch, the tensile force was allowed to reach a steady-state value before the next strain interval was introduced. The constructs were not strained to failure, but instead were visually monitored so testing could be halted before tearing occurred. A calibration curve was performed using known masses, allowing the amplitude of the traces to be converted to force readings in Pascals.

Mechanical testing data were collected from constructs composed of different ratios of type I collagen to (Hystem-HP. Constructs made of different matrices were seeded with 3.33×10^6 C2C12 cells/ml and incubated for 21 days in differentiation media. **Figure 88A** shows the calculated Young's moduli of the cell-seeded constructs. Even slight alterations in the ratio of collagen to HMW-HA affected the stiffness of the construct. Whereas the 50% collagen/50% HMW-HA constructs had the highest stiffness of the three mixtures, increasing the amount of collagen relative to HMW-HA caused the stiffness to decrease from about 9 Pa to 4 Pa (**Table 4**). Such a result indicated that the HMW-HA polymerized into a stiffer hydrogel than did collagen.

The HMW-HA component, Hystem-HP, has been used to advantage in the growth of other stem cell types, but was not previously used with myogenic stem cells or skeletal muscle. HMW-HA is expected to have anti-inflammatory properties and the thiol cross-linked HyStem-HP is designed to prevent HMW-HA breakdown by host enzymes into pro-inflammatory low molecular weight fragments.

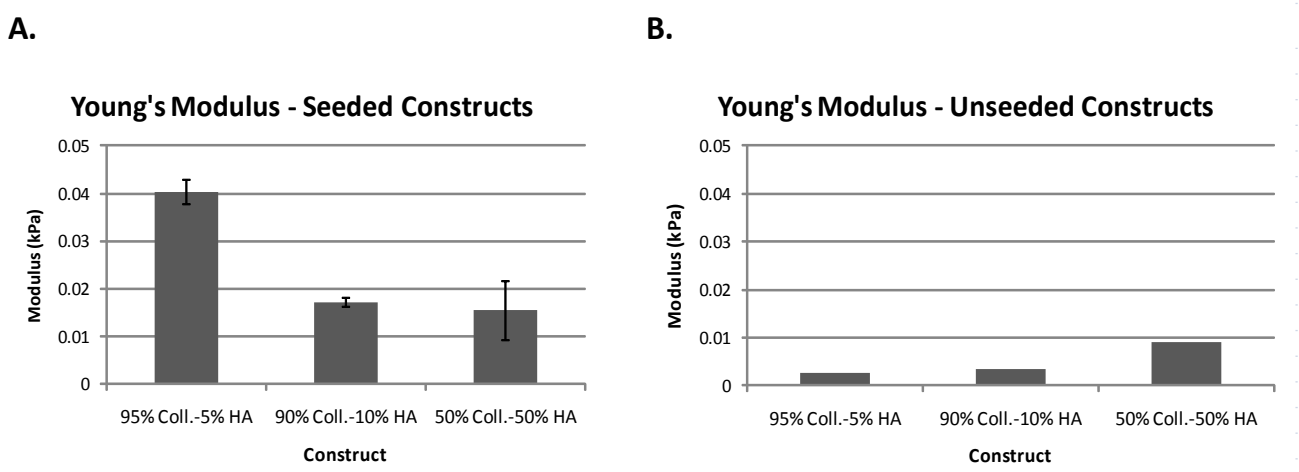

***Figure 88. Young's modulus for three ECM compositions using C2C12 cells**. Young's modulus in cell-seeded **(A)** and unseeded **(B)** constructs cultured for 21 days. Shaded areas show Young's modulus for normal adult skeletal muscle. The cells here are immature, so exact duplication of adult skeletal muscle stiffness is not expected. Error bars show standard deviations.*

Table 1. Collected stiffness data for unseeded and seeded constructs (corrected).

Table 4. Stiffness of constructs seeded with cells or lacking cells

	ACELLULAR		
Composition	95% Coll.-5% HA	90% Coll.-10% HA	50% Coll.-50% HA
Stiffness	0.0026 kPa	0.0035 kPa	0.0090 kPa
Std. Dev.	0.0018	N/A	N/A

	CELLULAR		
Composition	95% Coll.-5% HA	90% Coll.-10% HA	50% Coll.-50% HA
Stiffness	0.0404	0.0173	0.0156
Std. Dev.	0.0027	0.0009	0.0062

Addition of cells profoundly increased construct stiffness (compare **Figures 88A**, **B**). Furthermore, the effect of adding HMW-HA was the opposite in cellularized constructs vs. acellular constructs (**Table 4**) At the cell-seeding density used, greater relative amounts of HMW-HA caused the stiffness of the seeded constructs to decrease significantly (95% collagen/5% HMW-HA vs. 50% collagen/50% HMW-HA, $p < 0.05$). In future studies, we would like to match the stiffness of adult skeletal muscle, which is reported in the literature as varying from 6–12 kPa). The stiffnesses of our cellularized constructs were lower than this range. However, we recognized that the cells we used were relatively immature and were unlikely to engage the ECM scaffold to the

same extent as adult myocytes would—an increase in the stiffness of our constructs would be expected after the cells fully differentiated and remodeled the surrounding ECM.

Source of myoblasts (primary satellite cells) isolated from mouse hindlimb muscle tissue

We tested the relationship between ECM stiffness and myoblast differentiation using the C2C12 mouse myoblast cell line and primary mouse myoblasts, but in follow-on experiments, we changed our cell source to skeletal muscle satellite cells, which more reliably produce a higher yield of myogenic precursors. We were able to isolate and characterize satellite cells from mouse hind limb and we found that these cells could generate myofibrils within our constructs (**Figure 89**).

Confocal microscopy of constructs seeded with primary mouse myoblasts

Evaluation of primary mouse myoblasts (satellite cells) embedded in 1 mg/ml collagen constructs were performed using confocal microscopy in conjunction with LIVE/DEAD assays (Invitrogen), phalloidin staining to visualize actin organization, and propidium iodide to label cell nuclei. Confocal scans were performed at various depths to characterize cell development and interaction within the constructs (**Figure 89**).

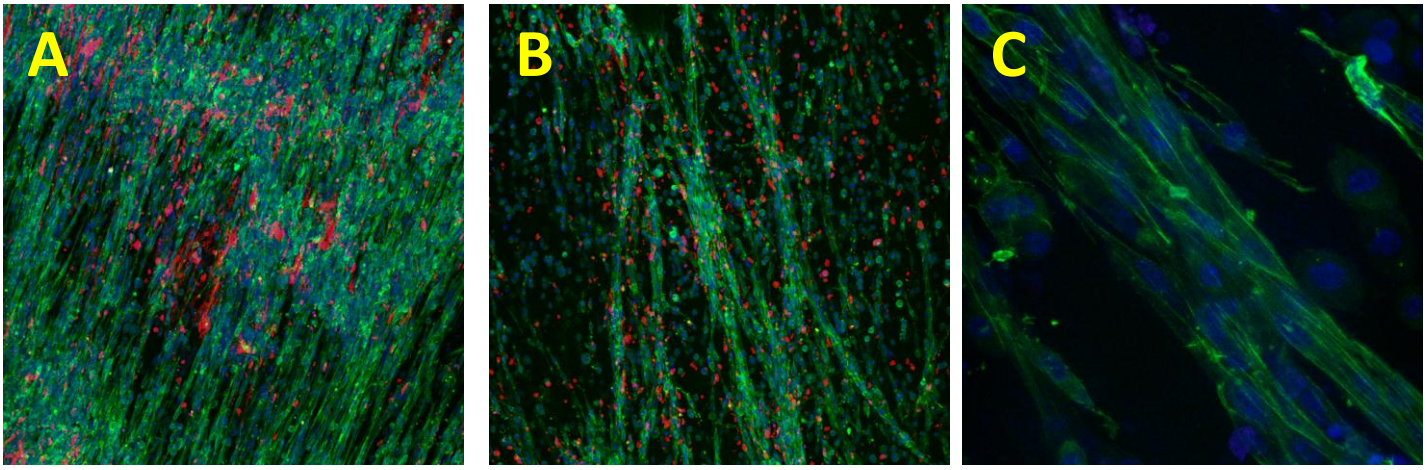

Figure 89. Representative confocal z-stacked images of constructs fabricated from 1 mg/ml collagen hydrogels seeded with primary mouse myoblasts (satellite cells). ***(A & B)*** *Myoblasts embedded within a collagen construct at high* ***(A)*** *and low* ***(B)*** *cell seeding densities.* ***(C)*** *Higher magnification of the construct in panel B showing myofibrils (green) stained for actin using phalloidin. Nuclei of dead cells are shown in red. All cell nuclei are shown in blue.*

In these studies, we observed higher levels of cell death in constructs composed solely of collagen (at 1 mg/ml). Cell death was lower in collagen gels supplemented with Hystem-HP.

Isolation and culture of muscle stem (satellite) cells from rat EDL and AT muscle tissue

For our constructs, we developed technologies to isolate satellite cells (myoblasts) from rat AT and extensor digitorum longus (EDL) muscles. Rat satellite cells from freshly excised AT and EDL muscles were isolated using pronase digestion, then cultured on gelatin-coated tissue culture dishes. Early passages of the proliferative, undifferentiated muscle cells from the EDL and AT showed that ~30% from the EDL and ~25% from the AT expressed MyoD (**Figures 90A and 91A**)—a key transcriptional regulator of skeletal muscle commitment and differentiation. When induced to terminally differentiate, these cells formed fused myotubes and began to express contractile proteins such as myosin (**Figures 90B and 91B**). To expand the cultured myoblasts we tested two previously published mitogen-rich growth media conditions; one based on DMEM (Kastner et al., 2000) and one based on Hams F-12K (Rando and Blau, 1994). To test whether the rat satellite cells could be expanded, we compared the myogenic potential of rat satellite cells following passage (**Figure 92**). Satellite cells from successive passages were grown in either DMEM or F12-K based growth media and then switched to low-mitogen differentiation media. Four days after the switch, the cells were fixed and probed with anti-myosin antibody and DAPI nuclear stain. Myogenic index was measured as percent of total nuclei associated with a myosin-positive cytoplasm. The myogenic index for satellite cells grown in DMEM or F12-K

decreased after successive cell passaging. A possible explanation for this is that even in the most favorable culture conditions for the satellite cells, the 70–80% of non-muscle cells in the culture still out-compete them.

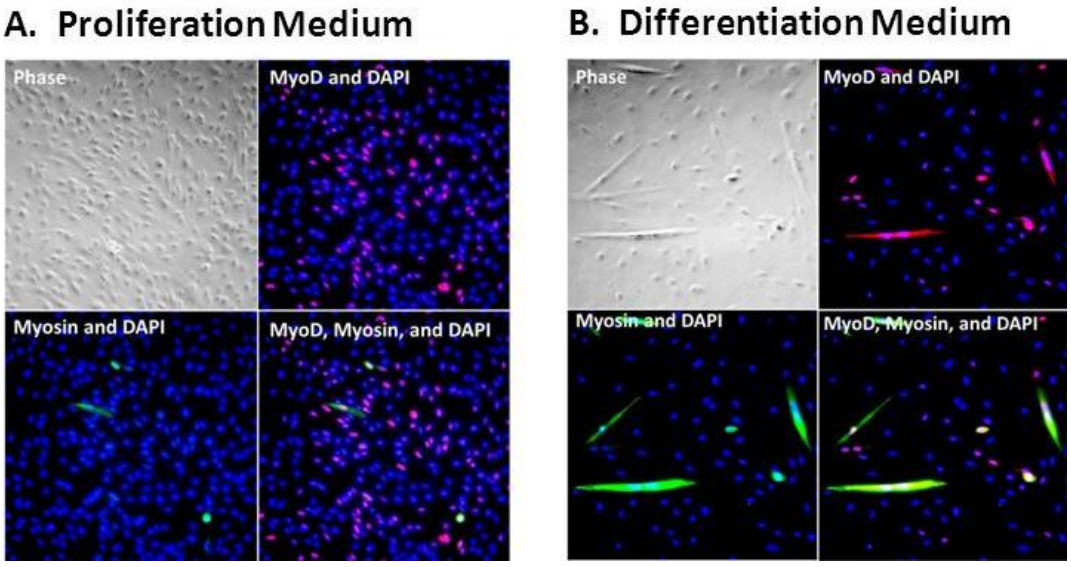

Figure 90. Satellite cells isolated from 16-week-old rat EDL muscle express MyoD and can differentiate into myosin-positive myotubes*. Cells isolated from the EDL muscle were cultured in mitogen-rich media for several days* ***(A)****, fixed and then probed with anti-MyoD (red nuclei) and anti-myosin (green cells) antibodies. Nuclei were counterstained with DAPI (blue).* ***(B)*** *Four days after mitogen withdrawal, MyoD-positive cells form elongated fused myotubes and express myosin, a marker of late-stage muscle differentiation.*

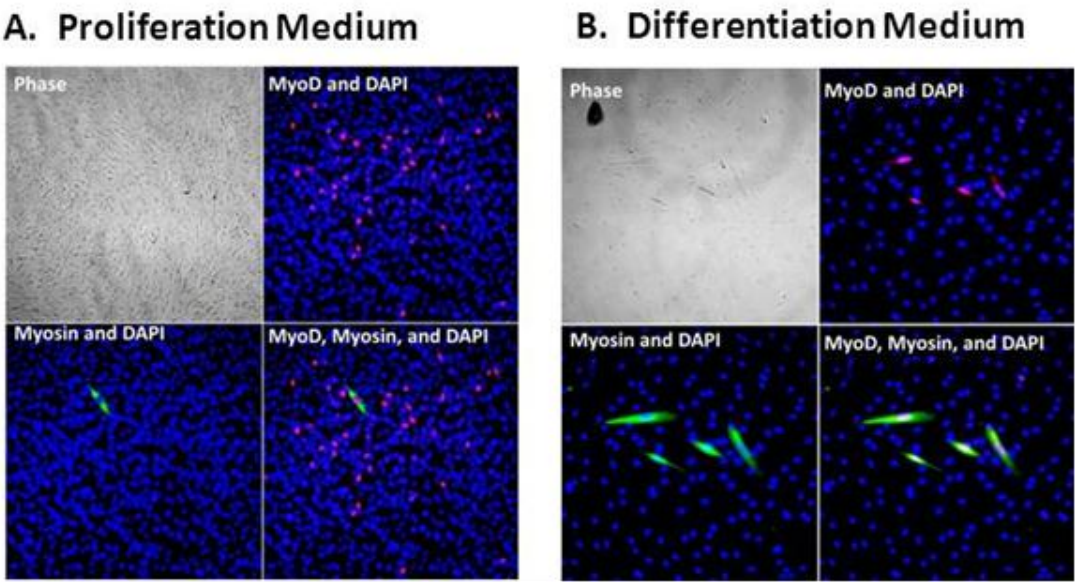

Figure 91. Satellite cells isolated from 16-week old rat AT muscle express early and late markers of skeletal muscle differentiation. A) *Cells isolated from the AT muscle were cultured under proliferation conditions and probed with an antibody specific for the early muscle regulatory marker, MyoD (red nuclei). When placed under differentiation conditions* ***(B)****, the AT satellite cells formed myosin-positive (green) myotubes. All cell nuclei were counterstained with DAPI (blue).*

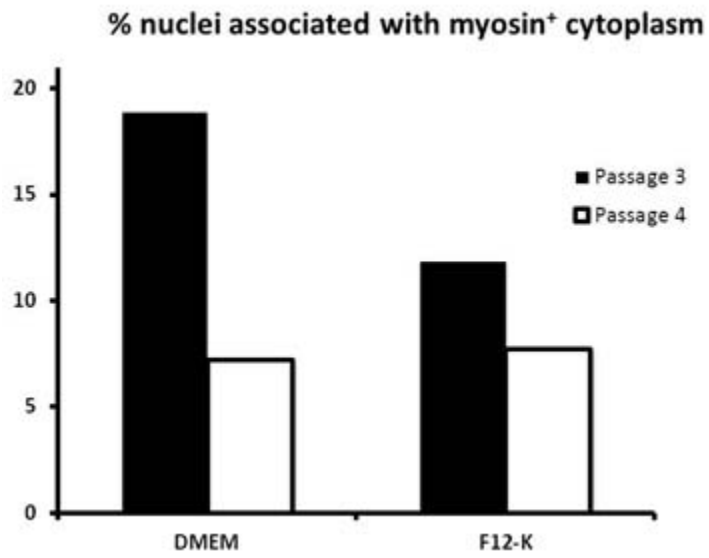

Figure 92. Passaging primary rat muscle cell cultures has a negative effect on the myogenic capacity of the cells. *Rat muscle cells from the AT were expanded in DMEM or F12-K based growth media and tested for myogenic potential after being switched to low-mitogen differentiation media. Four days after the switch, the cells were fixed, probed with anti-myosin antibody and then counterstained with DAPI nuclear stain. Myogenic potential of the muscle cultures was quantified as the percent of nuclei associated with myosin-positive cells expanded in either DMEM or F12-K mitogen-rich media. In both media conditions, a decrease in the percentage of cells capable of muscle differentiation was observed with successive passages.*

References

Kastner, S., M. C. Elias, et al. (2000). *"Gene expression patterns of the fibroblast growth factors and their receptors during myogenesis of rat satellite cells."* J. Histochem. Cytochem. 48(8): 1079-1096.

Rando, T. A. and H. M. Blau (1994). *"Primary mouse myoblast purification, characterization, and transplantation for cell-mediated gene therapy."* J. Cell Biol. 125(6): 1275-1287.

Development of methods to maximize myoblast purity

The presence of highly proliferative fibroblasts imposes a major limitation for primary muscle cell cultures. Differential adhesion techniques have nominally improved myoblast purity, but higher levels of purity have been achieved recently based on selection of cells for expression of α7 integrin (α7 ITGR), a muscle-specific cell surface antigen. To determine if the cells in our rat primary cultures expressed α7 ITGR, we immunostained the cultures with O26, a mouse antibody specific for rat and human α7 ITGR (**Figure 93**). The results showed that many of MyoD+ cells in the culture (**Figure 93B**) also expressed α7 ITGR (**Figure 93C, D**). Based on this result, we did a FACS analysis using the O26 antibody on freshly isolated rat primary cells and found that ~80% of cells expressed α7 ITGR (**Figure 94**). A pilot experiment which enriched for α7 ITGR+ cells using a magnetic microbead method resulted in a population of cells that were twice as myogenic as those that were not enriched

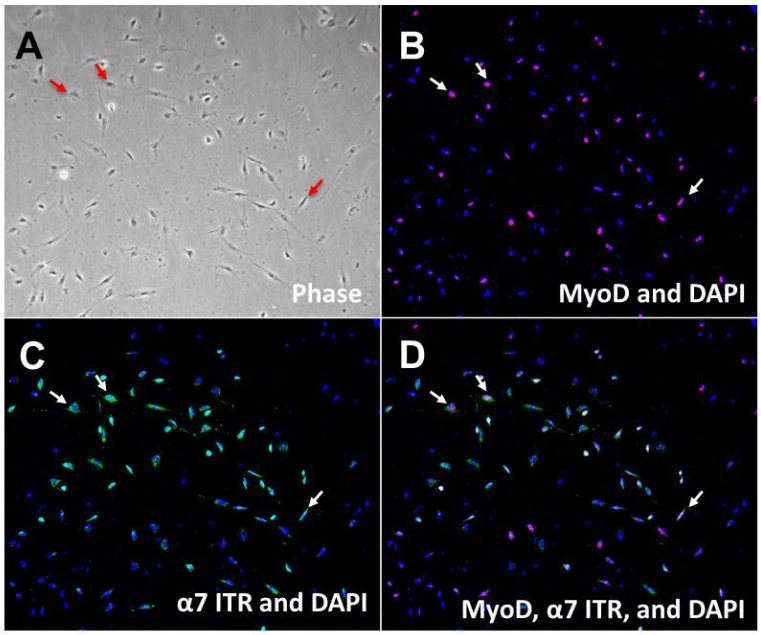

Figure 93. MyoD+ rat myoblasts express and α7 integrin (α7 ITGR). *Proliferating rat muscle cells were immunostained with monoclonal antibodies specific for MyoD (5.8A) (red in **B** and **D**) and α7 ITGR (O26) (green in **C** and **D**). Cells that expressed both markers were detected in the merged image **(D)**. Arrows in **B–D** indicate representative MyoD+, and α7 ITGR+ myogenic cells.*

(**Figure 95**). These studies demonstrated that enrichment using α7 ITGR selection had the potential to increase the myogenic potential of our primary cultures.

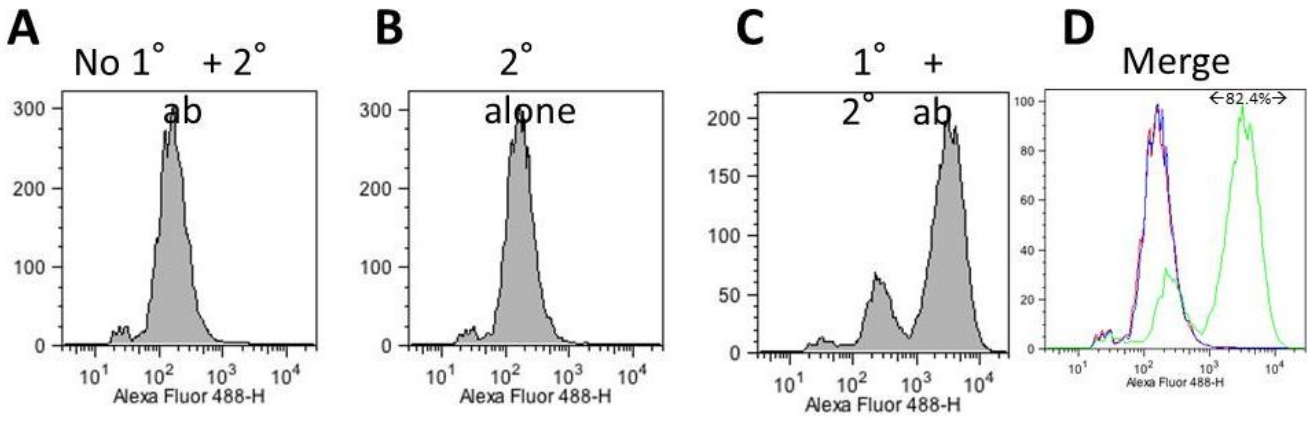

Figure 94. FACS detection of α7 ITGR on rat myoblasts. *Four-day old rat skeletal muscle myoblasts were incubated with:* ***(A)*** *no antibodies,* ***(B)*** *Alexa-Fluor 488-conjugated goat anti-mouse 2° antibody only, or* ***(C)*** *O26 anti-α7 ITGR 1° antibody followed by incubation with 2° antibody. FACS analysis shows ~80% of muscle cells isolated from rat adult tibialis anterior and gastrocnemius when incubated with both 1° and 2° antibodies* ***(C*** *and* ***D)*** *exhibit α7 ITGR reactivity.* ***D*** *is a merged image of* ***A–C****.*

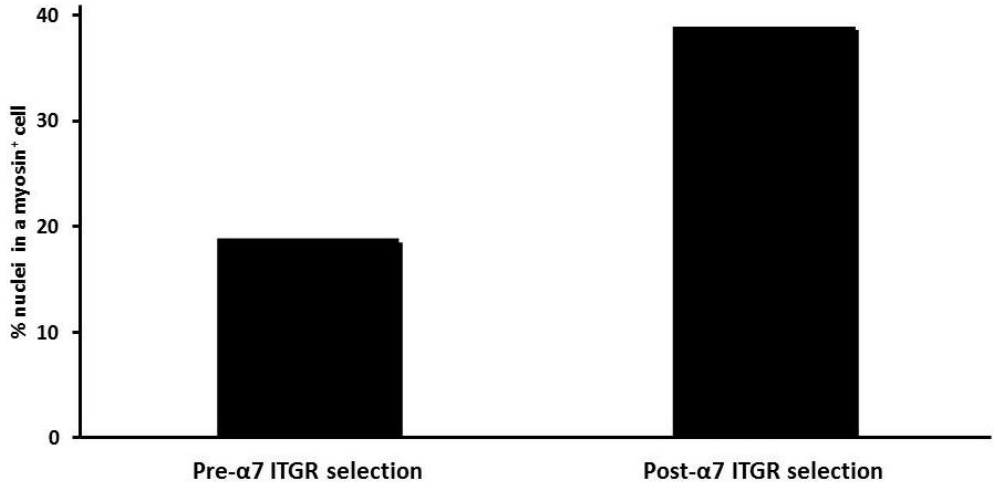

Figure 95. Differentiation indices of myoblasts purified by magnetic bead separation. *Myoblast cells were first incubated with anti-α7 ITGR IgG antibody (O26) and then incubated with magnetic beads conjugated to goat anti-mouse IgG (Miltenyi). Cells that bound the magnetic beads were isolated using a magnetic separator and LS column per the manufacturer's instructions (Miltenyi). Aliquots of cells pre- and post-α7 ITGR-selection were then cultured in proliferation medium for 2 days and subsequently switched to differentiation medium for 3 days. The cells were then fixed and immunostained with anti-myosin heavy chain (MHC) antibody and the nuclei counterstained with DAPI. Myogenic differentiation was scored by counting the total number of nuclei in MHC+ cells and dividing that number by the total number of nuclei in all cells (i.e., MHC+ plus MHC– cells). The results are expressed as a percentage (the differentiation index).*

Subsequent studies refined the methodology of magnetic bead-mediated purification of rat myoblasts. Primary rat muscle cells were incubated with anti-α7 ITGR and then magnetic beads conjugated to a 2° antibody (Ab), goat anti-mouse IgG (Miltenyi). Cells were passed over a magnetic separator, washed, and bound cells eluted with buffer. To assess the degree of purification, cells in the Applied-Sample, Flow-Through, and Eluent fractions were labeled with Alexa-Fluor 488-conjugated goat anti-mouse Ab and examined by fluorescence-activated cell sorting (FACS) analysis (**Figure 96A**). The results showed that magnetic bead purification with anti-α7 ITGR produced a cell population that was ~94% α7 ITGR+ from a starting population that was ~75% α7-ITGR+. We next examined the total number of α7-ITGR+ cells in each of the column fractions (**Figure 96B**). Cell counting combined with FACS analysis of multiple experiments revealed that ~44% of the α7-ITGR+ cells could be recovered from rat muscle preparations, while approximately 21% of the α7-ITGR+ cells were found in the Flow-Through population and 35% of the cells were lost.

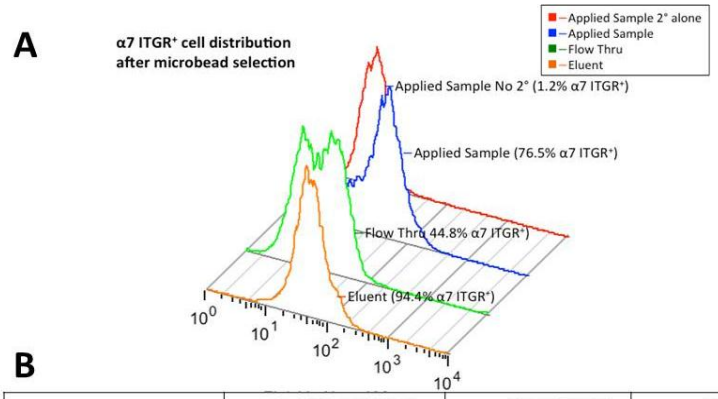

B

	Applied Sample	Flow Through	Eluent
Cell Number	3.61E+06	1.29E+06	1.28E+06
% Recovery	100.0	35.7	35.5
% α7 ITGR+	76.5	44.8	94.39
α7 ITGR+ cells	2.76E+06	5.78E+05	1.21E+06
% α7 ITGR+ recovery	100.0	20.9	43.7

Figure 96. α7 ITGR-based selection of rat myogenic cells. ***(A)*** *Elution profile of rat muscle cells incubated with anti-α7 ITGR mAb followed by goat anti-mouse IgG 2°Ab conjugated with MACS magnetic MicroBeads (Miltenyi Biotec) and separated on a MACS column. Applied, Flow-through and Eluent were incubated with goat anti-mouse IgG 2° Ab conjugated with Alexa-Fluor 488 and analyzed by FACS.* ***(B)*** *Representative quantification of total cell number and percent recovery of column fractions after a typical magnetic bead separation. Applied sample cell number was taken as 100% recovered.*

Cell tracking for studies in vivo

Two methods were considered to track donor vs. host cells: fluorescent Qtracker-labeling of donor cells, and sex mismatched chimeras where the donor cells are male and are tracked by Y-chromosome *in situ* hybridization. While the commercial Y-chromosome tracking method is accurate, it is also very expensive and the signal can only be detected in high magnification images, which makes the analysis very labor intensive. For this reason, we focused on the Qtracker labeling method using a Qtracker 605 kit (Invitrogen). Other investigators have reported that rat bone marrow-derived mesenchymal stem cells labeled with fluorescent Qdot 605 nanocrystals have been successfully engrafted into the liver or renal capsule of rats, and the Qdot 605^{+} cells were still detectable by fluorescence microscopy three weeks later.

To test the Qtracker system, primary muscle cells were labeled with Qdot 605 nanocrystals for one hour and then visualized live by fluorescence microscopy (**Figure 97**). Most cells took up the labeled particles, as indicated by bright red particles distributed in vesicles throughout the cytoplasm (**Figure 97, center panel**). To test if the Qdot 605-labeled muscle cells could be selected for α7 ITGR expression and then maintain a detectable level of fluorescence over time, we isolated the α7 ITGR+ cell fraction (Eluent) using the magnetic bead method and compared it with the non-binding fraction (Flow-Through) **(Figure 98**).

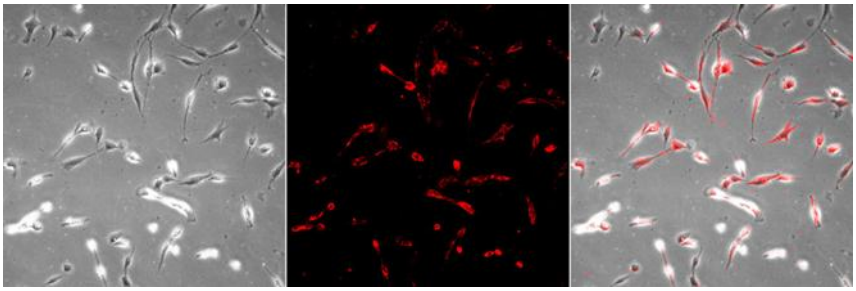

Figure 97. Qdot nanocrystal staining of α7 ITGR-selected rat muscle cells. *Phase-contrast (left panel), fluorescence (center panel) and merged (right panel) images are shown. Adherent rat muscle cells were labeled for one hour with 2 nM Qtracker 605.*

The majority of cells before **(Figure 98, Day 0, Applied Sample**) and after **(Figure 98, Day 0, Flow-Through**) the separation were fluorescently labeled. After two days in culture in proliferation media, many cells from the Flow-Through and Eluent fractions were still fluorescent; however, the fluorescence intensity was lower than at Day 0. After 6 days in culture, very few cells in the Flow-Through fraction were still positive for Qdot 605. In contrast, in cultures derived from the Eluent fraction, a significant number of cells (~30%) still retained their fluorescence after 6 days. Further FACS analysis revealed that the great majority of cells also expressed α7 ITGR. Although this demonstrates that the α7ITGR+, myogenic population in the muscle cultures can still remain fluorescently labeled after several days, we would not be able to track cells that have divided too many times and have lost their signal. To overcome this problem, we could test labeling at higher Qdot concentrations and incubate the cells in differentiation conditions where the cells will not divide as much.

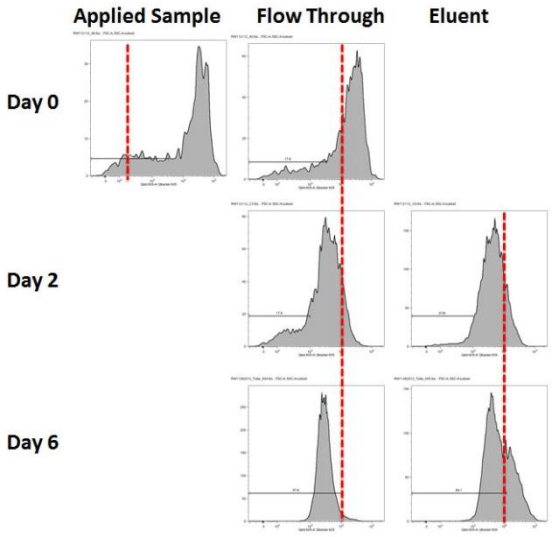

Figure 98. Qdot 605 fluorescent signals persist in a subset α7 ITGR-selected cells. *FACS analysis of Qdot fluorescence at Days 0, 2 and 6 in Applied, Flow-Through and Eluent samples. The Flow-Through and Eluent cells were plated on 6-well dishes and cultured for an additional 2 (Day 2) and 6 (Day 6) days. X-axis = fluorescence intensity, Y-axis = number of cells. The dashed red line indicates the same relative fluorescence intensity (1 x 10^4) on each histogram plot.*

Conclusions, Task 11

The major objective of Task 11 was the development of myobridge constructs suitable for *in vivo* implantation studies. To this end, the Task evaluated a number of relevant muscle cell precursors (MDSCs, satellite cells) and supportive scaffold hydrogels (native type I collagen, thiol-crosslinked HMW-HA hydrogel, and mixed hydrogels of collagen and HMW-HA). In addition, Task 11 evaluated the use of CoPP as a supplement to enhance muscle cell survival in implants prior to host vascularization. Results from these studies indicated that satellite cells were a more reliable source of muscle cell precursors than MDSCs. Importantly, CoPP treatment increased myogenic cell proliferation and the capacity to reorganize collagenous scaffolds. At the same time, CoPP appeared to slow myogenic cell differentiation, which is considered to be advantageous in a transplant setting, as prolonged post-transplant proliferation of myogenic cells will likely be necessary for a full replacement of lost muscle. The studies of scaffold composition revealed that increasing the proportions of HMW-HA in the composite collagen/HMW-HA hydrogel led to increased stiffness in acellular constructs, but actually reduced stiffness in constructs populated with cells. As adhesion of cells to HMW-HA is typically less than adhesion of cells to type I collagen, the reduced stiffness of the cellularized HMW-HA constructs may indicate that adhesive interactions between cells and the ECM scaffold are critical to enhancing the overall strength of the construct.

Finally, work under Task 11 generated new approaches for fabricating muscle replacements (e.g., incorporating the suture directly into the cellularized hydrogel construct) and improved techniques for purifying muscle satellite cells away from contaminating fibroblasts. We will continue to use and refine these methodologies in future studies of engineered muscle replacements.

Task 12

Implantation of cell-seeded myobridges into female F344 rat anterior tibialis (AT) muscle (Margaret Allen, MD).

Task 12 evaluated the graft and host responses following implantation of the engineered myobridges developed in Task 11 into recipient rats. Initial studies examined host responses to the scaffold biomaterials in the absence of cells. We observed that none of the hydrogels made from either type I collagen, Hystem-HP, or collagen/Hystem-HP mixtures elicited an inflammatory reaction in rats.

Myobridge prototypes incorporating type I collagen scaffolds and α7 ITGR-selected muscle satellite cells were engrafted into rats into the space left after excision of the AT muscle **(Figure 99**). Tension was applied to the myobridge by attaching the sutures at each end the construct (see **Figures 85, 87**) to the proximal and distal remnants of the host's AT muscle. After closure of the fascia and skin over the construct (a space was left at the end of the incision to reduce the risk of post-surgical "compartment syndrome") the grafts were left in place for one week, after which time they were removed for histological analyses. Masson's trichrome staining (**Figure 100**) revealed that at one week post-implantation, the myobridges were well cellularized and included areas of relatively sparse, disorganized collagen fibrils (similar to the organization of the constructs *in vitro*) interspersed with zones containing more densely-packed, aligned collagen fibers and cells. Sections stained with phalloidin revealed the presence of actin-rich, elongated cells (indicative of a more differentiated state of myogenesis) within the constructs (**Figure 101**).

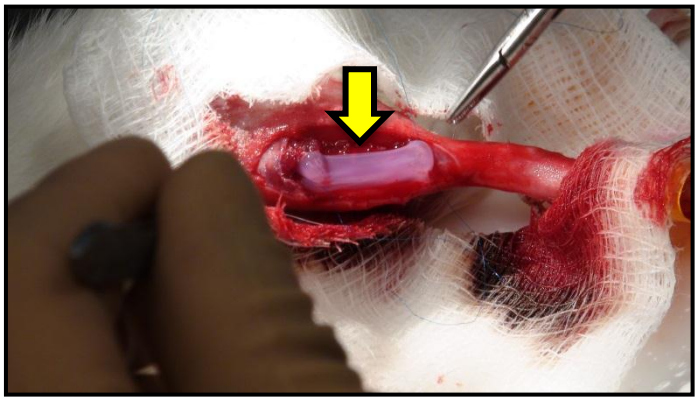

Figure 99. Engraftment of a myobridge construct (arrow) into an AT defect made in a host rat.

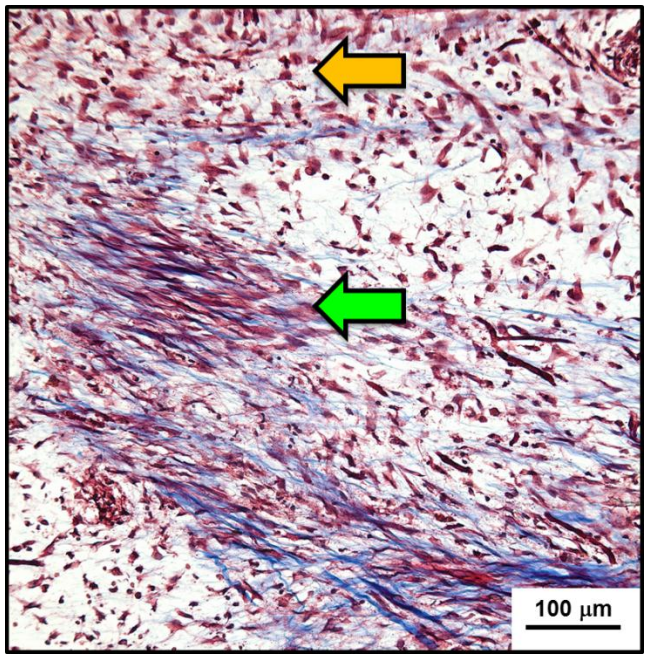

Figure 100. Myobridge prototype comprised of α7 ITGR-selected muscle satellite cells seeded into a type I collagen hydrogel scaffold 1 week after implantation into a host rat. *Areas of the myobridge contain satellite cells with disorganized collagen fibers (orange arrow) interspersed with more organized areas (green arrow) comprised of aligned collagen fibrils (blue stain) and cells (pink stain). Specimen is stained with Masson's trichrome.*

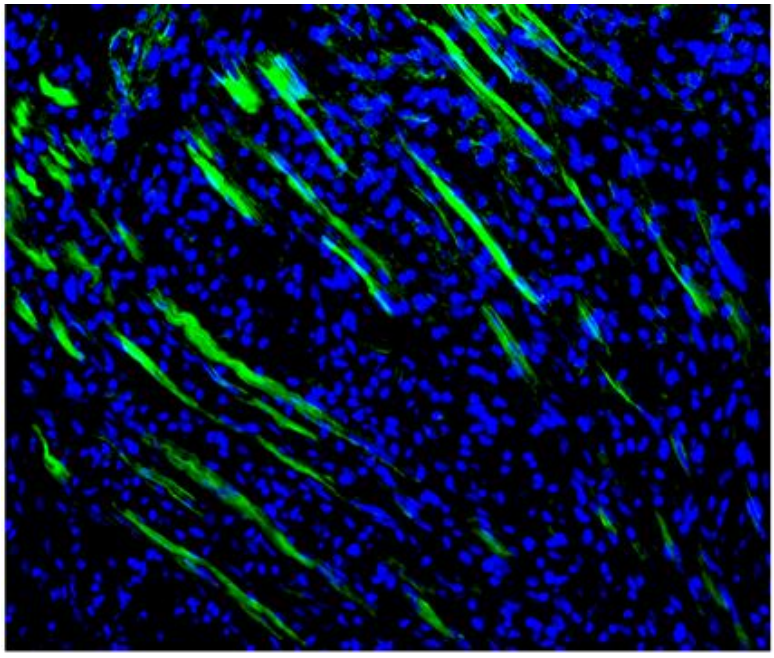

Figure 101. Myobridge prototype comprised of α7 ITGR-selected muscle satellite cells seeded into a type I collagen hydrogel scaffold 1 week after implantation into a host rat—evaluation of differentiated muscle cell phenotypes. *The section was stained with Alexa-Fluor 488 phalloidin (green) to identify actin-rich cells representing a myogenic phenotype. Note that the phalloidin-positive cells are highly elongated, which is typical of a differentiated state. Cell nuclei are counterstained with DAPI (blue).*

Evaluation of the myobridges 4 weeks after implantation revealed that the constructs had lost much of their volume, shrinking into flat bands that lay on the surface of the tibia (**Figure 102**). This phenomenon was attributed to loss of water from the hydrogel, which is typical when hydrogels are implanted *in vivo*. It was determined that subsequent myobridge prototypes will need to be populated with cells at much higher concentrations in order to limit the shrinkage of the supportive scaffold.

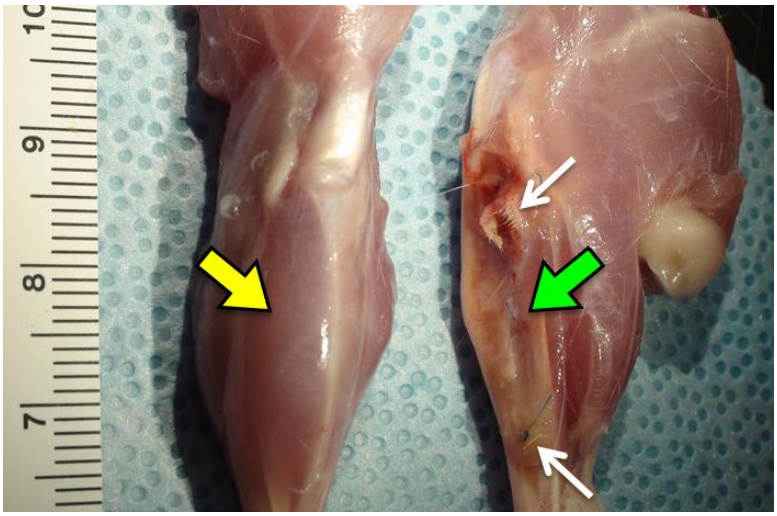

Figure 102. Myobridge prototype comprised of α7 ITGR-selected muscle satellite cells seeded into a type I collagen hydrogel scaffold 4 weeks after implantation. *Control leg (left) shows intact, native AT muscle (yellow arrow). Grafted leg (right) shows area of the myobridge (green arrow). The two supportive Vicryl meshes at both ends of the construct (white arrows) are also shown.*

Conclusions, Task 12

Work under Task 12 showed that myobridge prototypes could be implanted into a muscle defect of considerable size in recipient rats. Importantly, the design of the myobridge suture interface was validated *in vivo*—after implantation, the cellularized collagen hydrogel scaffold did not pull free from the Vicryl meshes that held the anchoring sutures. Moreover, it was apparent that after 1 week *in vivo*, the collagen hydrogel was intact and there were myogenic cells expressing a differentiated phenotype. However, maintenance of scaffold integrity was problematic after 4 weeks *in vivo*, which was a consequence of substantial shrinkage. This shrinkage was likely due to removal of water. In follow-on studies that are now ongoing, we are attempting to mitigate the shrinkage problem by increasing the cellularity of the construct and by adding HMW-HA, which resists dehydration.

Task 13

Supplementation of myobridges with CoPP and regulatory modulators from Aim 1, prior to implantation (Margaret Allen, MD).

In studies preliminary to this project, we showed that upregulation of the cytoprotective factor HO-1 by its transcriptional activator, CoPP, increases the survival of MDSCs *in vitro* under hypoxia/reoxygenation protocols designed to mimic the ischemic stress of *in vivo* cell implantation. For these *in vitro* studies, CoPP is simply added to the cell culture medium. In Task 13, we explored whether CoPP would be an appropriate additive to be released from within construct scaffolds and thus be available to modify the myobridge environment post-implantation.

In vitro studies of CoPP effects on satellite cells

We first evaluated the effects of CoPP on primary mouse myoblast differentiation and proliferation/dedifferentiation (**Figure 103**). Mouse myoblasts were seeded onto collagen-coated plates in proliferation medium (Ham's F-12K supplemented with 20% FBS, 2% horse serum, 10 ng/ml of basic fibroblast growth factor, and antibiotics). Twenty-four h after plating, cells were switched to differentiation medium (DMEM supplemented with 20% horse serum and antibiotics) with and without 25 μM CoPP. Plates were collected for analyses at 0 h, 12 h, 24 h, 36 h, and 48 h after the change of medium. Cultures were pulsed with BrdU 1 h prior to collection at each time point. Proliferating cells (identified by BrdU incorporation) and terminally-differentiated muscle cells (identified by expression of myosin) were scored as a percentage of the total cell number (determined by counting all cell nuclei). This assay provided a means to analyze the effects of CoPP on muscle cell proliferation and differentiation.

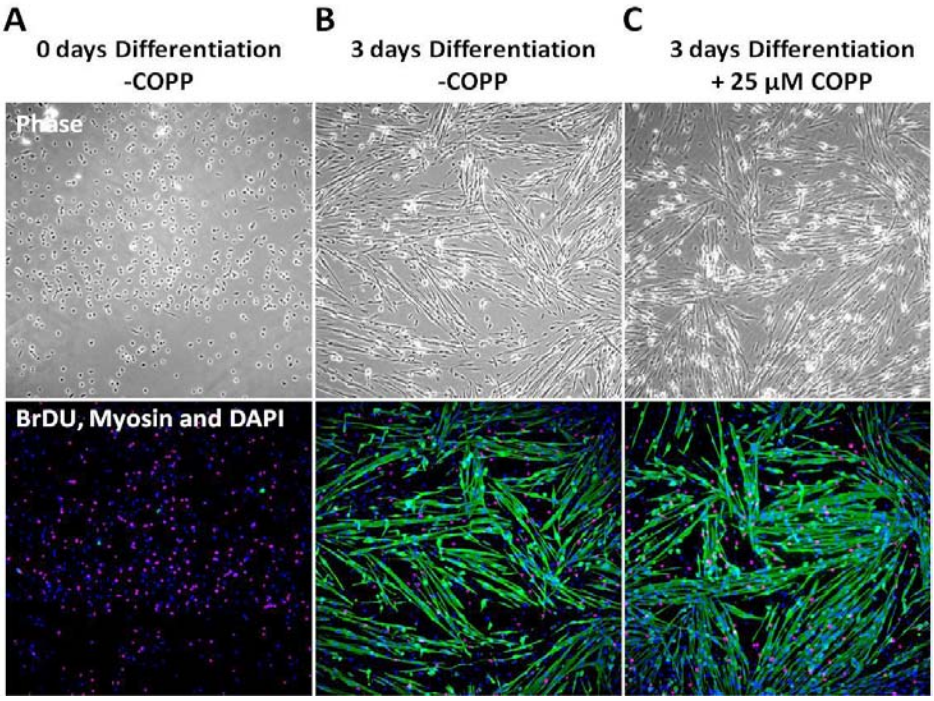

Figure 103. Effects of CoPP on satellite cell proliferation and differentiation at 48 h. (A) *Undifferentiated.* ***(B)*** *Differentiation in absence of CoPP.* ***(C)*** *Differentiation in presence of CoPP.*

Blue = DAPI-stained cell nuclei;
Green = MF20 antibody staining for myosin;
Red = BrdU-staining of nuclei in proliferating cells.

Experiments were also performed to examine how CoPP affected the growth and differentiation of satellite cells seeded into collagen, Hystem-HP, and collagen/ Hystem-HP hydrogel constructs. For these *in vitro* studies, a hypoxia chamber was used to mimic the ischemic conditions that cells experience in the critical period immediately after *in vivo* implantation, but prior to host vascularization. Experiments explored the effects of adding CoPP to cellularized, three-dimensional constructs exposed to hypoxia. Also, HMW-HA was added to the construct in the form of the thiol-crosslinked HA hydrogel, Hystem-HP.

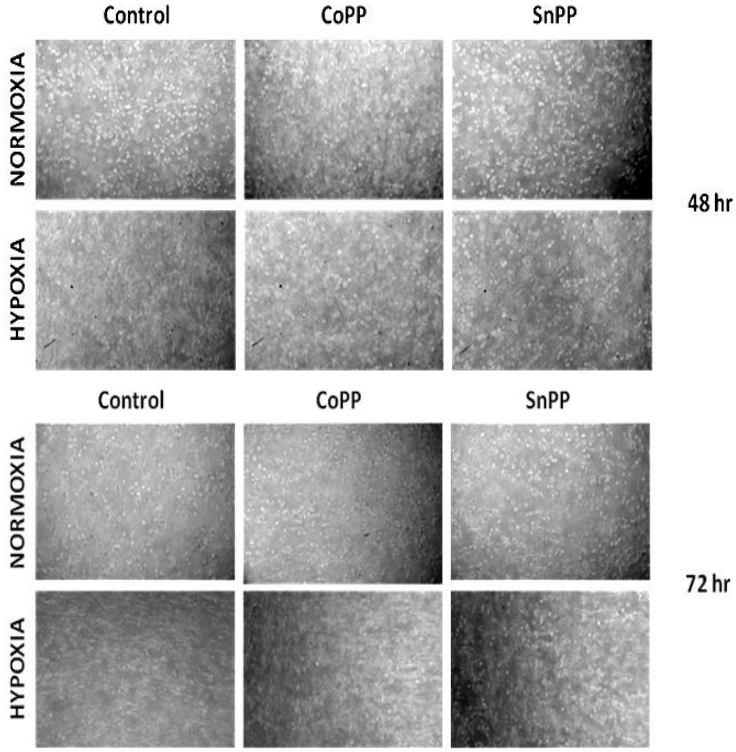

Figure 104. Three-dimensional constructs comprised of collagen/HMW-HA matrices seeded with primary mouse myoblasts. *Photographs taken under phase contrast microscopy at 48 and 72 h. Constructs are comprised of 0.95 mg/ml type I collagen and 0.05 mg/ml Hystem-HP HMW-HA hydrogel.*

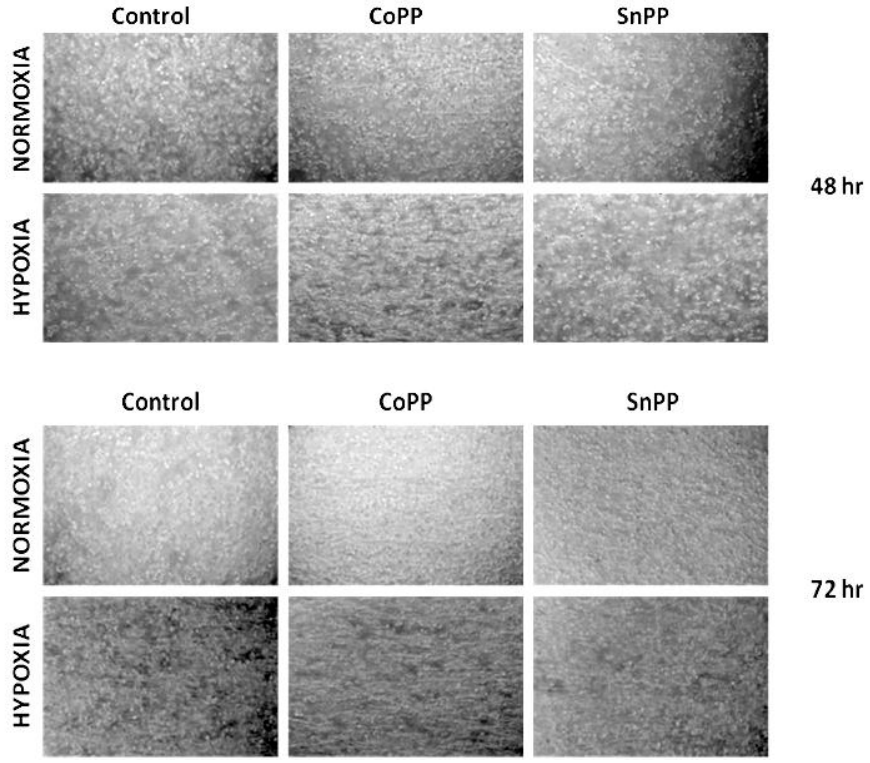

Figure 105. Three-dimensional constructs comprised of collagen/HMW-HA matrices seeded with primary mouse myoblasts. *Photographs taken under phase contrast microscopy at 48 and 72 h. Constructs are comprised of 0.5 mg/ml type I collagen and 0.5 mg/ml of Hystem-HP.*

Murine satellite cells were isolated, expanded, and seeded at 1 x 10^6 cells/ml into matrices prepared of collagen: Hystem-HP ratios of either 0.95: 0.05 mg/mg per ml or 0.50:0.50 mg/mg per ml. 25 μM CoPP, the HO-1 inducer, or 25 μM SnPP, an HO-1 activity inhibitor, was added to the matrix at the time of cell seeding. Constructs were incubated for 24 h in proliferation medium and then switched to differentiation medium. Half the constructs were placed in a hypoxia chamber (0.5% O_2, 5% CO_2, 37^{o}C) and half were incubated under normoxic conditions (atmospheric O_2, 5% CO_2, 37^{o}C) for 72 h. Constructs were imaged by phase contrast microscopy at 24, 48 and 72 h.

Under phase contrast microscopy, hypoxia appeared to enhance cell alignment within the constructs (**Figures 104, 105**) and this phenomenon was more evident in constructs with higher HA content (**Figure 105**). The addition of CoPP to the matrices appeared to further enhance cell alignment, again most notable at 72 h in the constructs with higher levels of HA (**Figure 105**, bottom middle panel of the 72 h series). After 72 h, constructs were stained with the LIVE/DEAD staining kit (Invitrogen), fixed overnight in 4% paraformaldehyde, and then stained with phalloidin to visualize F-actin filaments and with propidium iodide to visualize cell nuclei (**Figures 106, 107**). Cells were then analyzed by confocal microscopy as z-stacks comprised of 76 scans, each 2 μm deep across a depth of 150 μm. The z-stacked images showed enhanced axial alignment of F-actin positive cells and greater cell density with the combination of CoPP and higher HA content under conditions of hypoxia **(Figure 107**). This effect of CoPP on hypoxic cultures were lost with the addition of the HO-1 inhibitor, SnPP. Collectively, these results suggested that, even for constructs cultured under tension, exposure to hypoxia and the addition of CoPP to the scaffold may improve the degree of cell alignment. These findings suggested that cell alignment could be maintained even after the constructs are implanted *in vivo*.

In subsequent studies, we seeded the constructs with rat satellite cells. Rat satellite cells were isolated, expanded, and seeded at 1.67 x 10^5 cells per ml into matrices prepared from combinations of type I collagen and Hystem-HP using collagen: Hystem-HP in ratios of either 0.5:0.5 mg per ml or 2:0.5 mg per ml. 25 µM of CoPP was added (or not) to the cultures at the time of cell seeding. Constructs were incubated for 24 h in proliferation medium, then switched to differentiation medium. Half of the constructs were placed in a hypoxia chamber (0.5% O_2, 5% CO_2, 37°C) for 72 h and half were incubated under normoxic conditions (atmospheric O_2, 5% CO_2, 37°C). Constructs were imaged by phase contrast microscopy at 24, 48, 72, 120, and 192 h. After 13 days in culture, constructs were incubated with BrdU for 3 h, followed by LIVE/DEAD staining, fixation overnight in 4% paraformaldehyde, and then staining with phalloidin and propidium iodide. Cells were then analyzed under phase contrast illumination or under epifluorescence illumination using a laser scanning confocal microscope. By phase contrast microscopy, hypoxia appeared to enhance rat satellite cell alignment within the collagen constructs containing lower amounts of collagen, similar to what was previously seen with murine satellite cells (**Figures 108, 109**). In the constructs with higher collagen concentrations, cell alignment under hypoxia was not observed (**Figure 109**). Addition of CoPP to the cultures appeared to further enhance cell alignment, most notable at 72 h in the constructs with lower collagen concentrations (**Figure 109**). Addition of CoPP to the constructs with higher collagen concentrations did not affect cell alignment at normoxia, but may have had a minor effect on enhancing alignment in a hypoxic environment. At the higher collagen concentrations, CoPP appeared to enhance cell numbers (**Figure 110**). Under normoxia, 77 cells/unit area with CoPP vs. 53 without CoPP. Under hypoxia, 37 cells/unit area with CoPP vs. 16 without CoPP). CoPP did not appear to alter cell numbers at the lower collagen concentration. Enhanced axial alignment of F-actin-positive cells was observed in constructs containing lower collagen and cultured under conditions of hypoxia (**Figure 111**). Our observations indicated that addition of CoPP to cellularized matrices also reduced the numbers of dead cells (**Figure 112**).

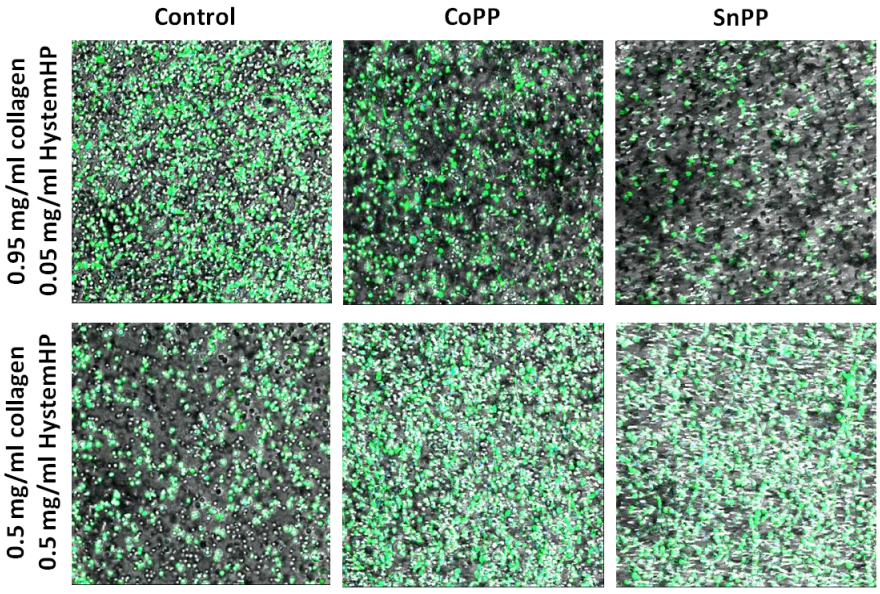

Figure 106. Confocal analysis of constructs after 72 h of <u>normoxia</u> (atmospheric O_2). LIVE/DEAD staining*

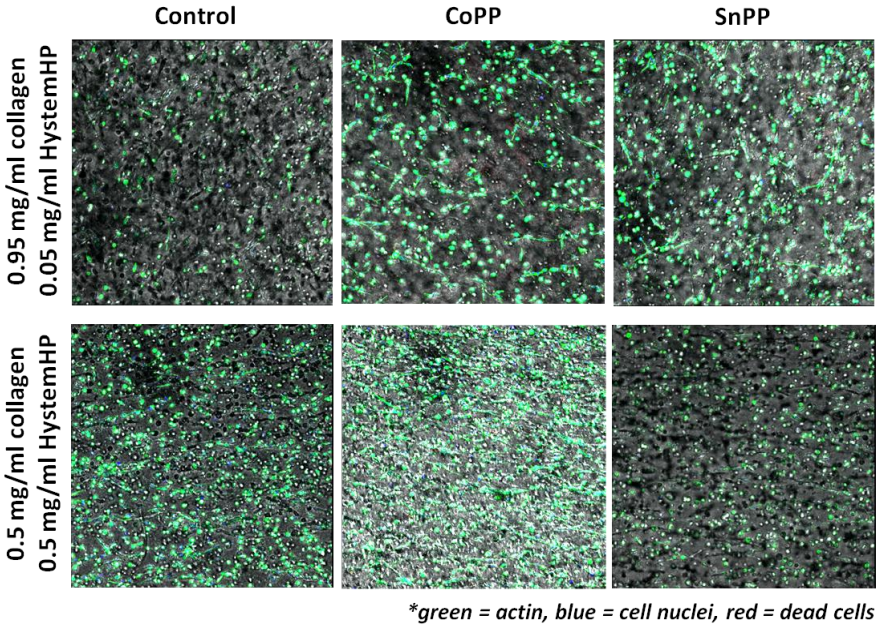

Figure 107. Confocal analysis of constructs after 72 h of <u>hypoxia</u> (0.5% O_2). LIVE/DEAD staining*

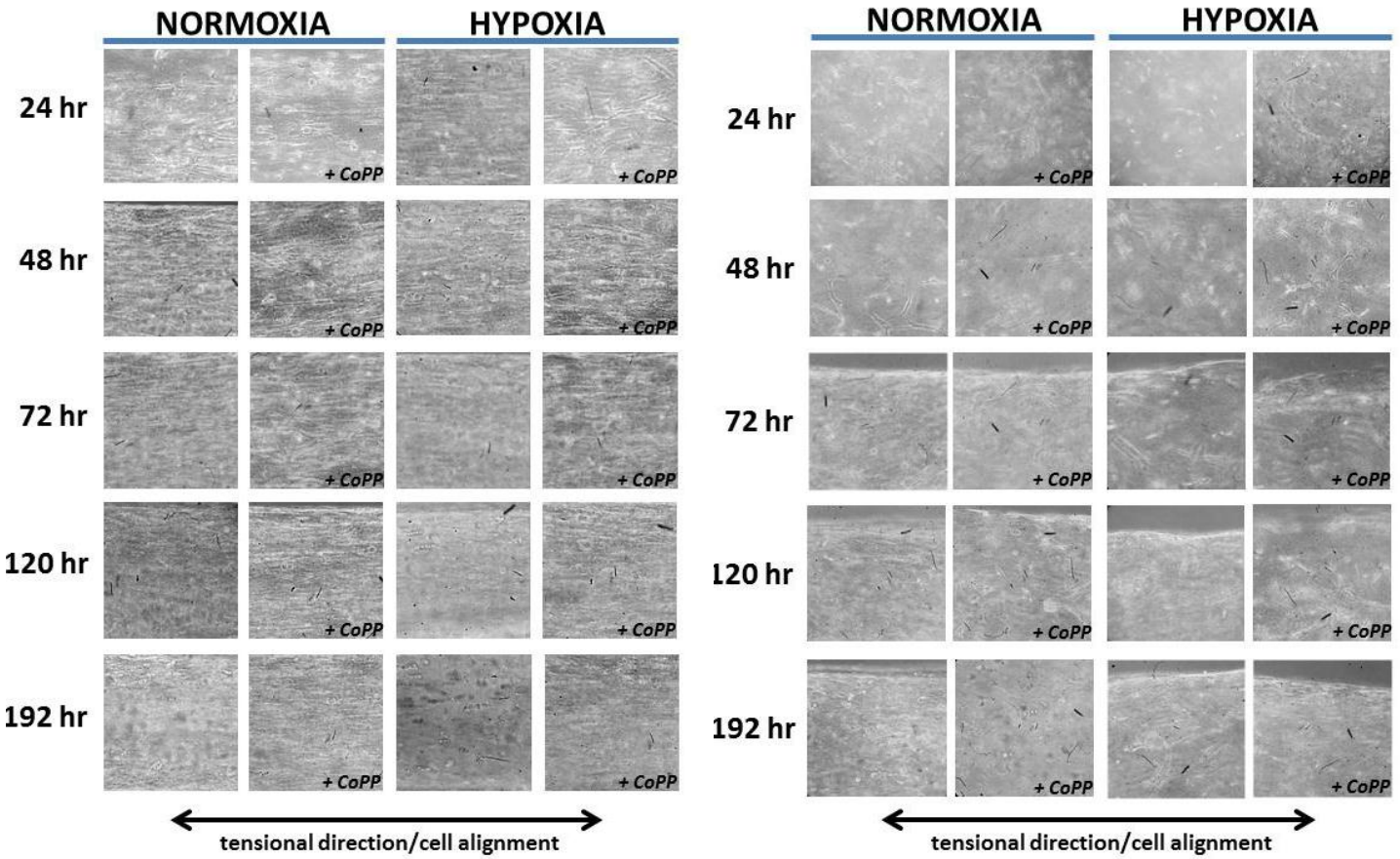

Figure 108. (Left Group of Panels) *Constructs comprised of 0.5 mg/ml type I collagen and 0.5 mg/ml Hystem-HP.*

Figure 109. (Right Group of Panels) *Constructs comprised of 2 mg/ml type I collagen and 0.5 mg/ml Hystem-HP.*

Of note, there was a striking difference in the degree of cell-traction-mediated remodeling of scaffolds comprised of low vs. high concentrations of collagen, irrespective of hypoxia or addition of CoPP. Remodeling of scaffolds by rat satellite cells was much more extensive at lower collagen concentrations, whereas higher collagen concentrations limited remodeling (**Figure 113**).

Thus far, we had compared rat satellite cell growth and differentiation in scaffolds prepared from collagen:Hystem-HP in ratios of either 0.5:0.5 mg/ml or 2:0.5 mg/ml. A limited number of myotubes were observed in the constructs that contained 0.5 mg/ml

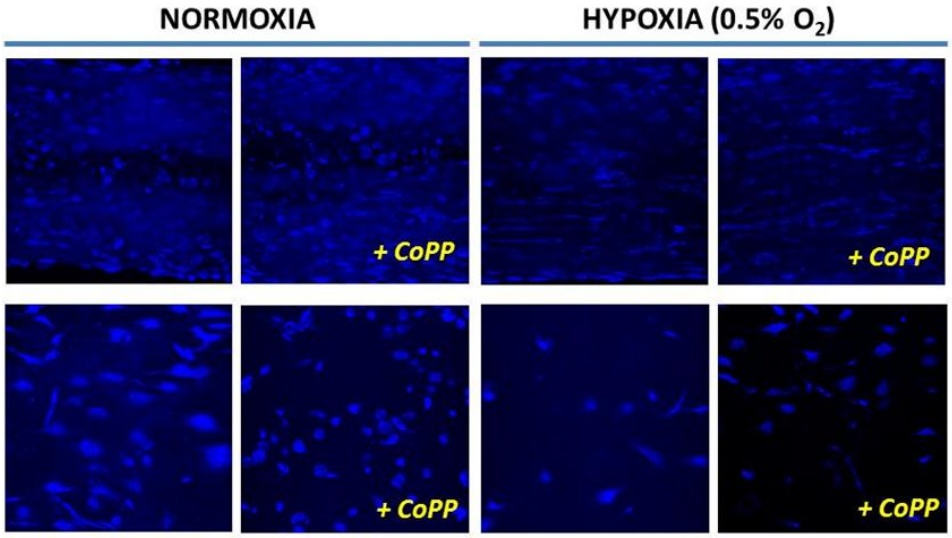

Figure 110. Confocal images of constructs after 13 days in differentiation medium. *Cell nuclei are stained with DAPI (blue). In the* ***top series of 4 panels****, the scaffolds are comprised of 0.5 mg/ml collagen: 0.5 mg/ml Hystem-HP. In the* ***bottom series of 4 panels****, the scaffolds are comprised of 2 mg/ml collagen: 0.5 mg/ml Hystem-HP.*

collagen and none in the constructs that contained 2 mg/ml collagen. In subsequent studies, we compared 0.5 mg/ml collagen vs. 1 mg/ml collagen with Hystem-HP concentration remaining at 0.5 mg/ml. Myotubes were observed in constructs containing 1 mg/ml collagen (**Figure 114**), but no myotubes were seen in constructs containing 0.5 mg/ml collagen. These results suggested that an intermediate collagen content of 1.0 mg/ml favored myotube formation, although the number of myotubes was still low. The need to maximize myotube formation led us to pursue a method for obtaining purer myoblast populations from satellite cells as described in Task 11 of this report.

The next series of studies evaluated the effect of CoPP supplementation on cell survival and differentiation in myobridges seeded with α7 ITGR-purified satellite cells under normoxic and hypoxic conditions *in vitro*. Rat muscle cells were isolated and then passed through an α7 ITGR Miltenyi magnetic bead column and split into Pre-Sorted, Flow-Through and Eluent fractions, as described in Task 11. These fractions were then incorporated into myobridges composed of 2% collagen/1 mg/ml Hystem that were polymerized in coffin molds (**Figure 86**). The myobridges were then cultured at normoxic and hypoxic conditions, with or without supplementation with CoPP. Confocal images of myobridges populated with the Flow-Through cell fraction **(Figure 115)** showed that the cells formed much denser populations under normoxic conditions than when cultured under hypoxic conditions and that hypoxic cells treated with CoPP had more myotubes than cells

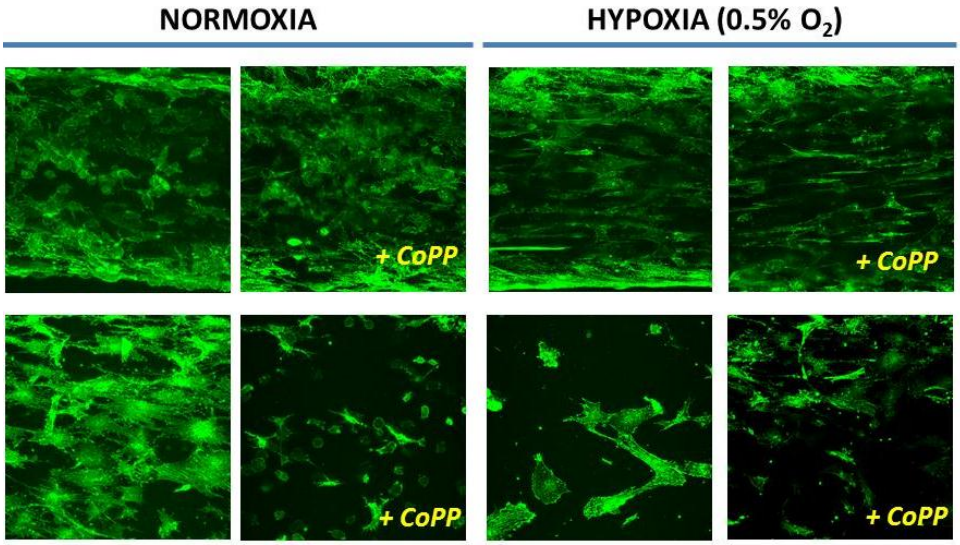

Figure 111. Confocal images of constructs after 13 days in differentiation medium. *Cells are stained with phalloidin to show cytoplasmic actin (green). In the* ***top series of 4 panels****, the scaffolds are comprised of 0.5 mg/ml collagen: 0.5 mg/ml Hystem-HP. In the* ***bottom series of 4 panels****, the scaffolds are comprised of 2 mg/ml collagen: 0.5 mg/ml Hystem-HP.*

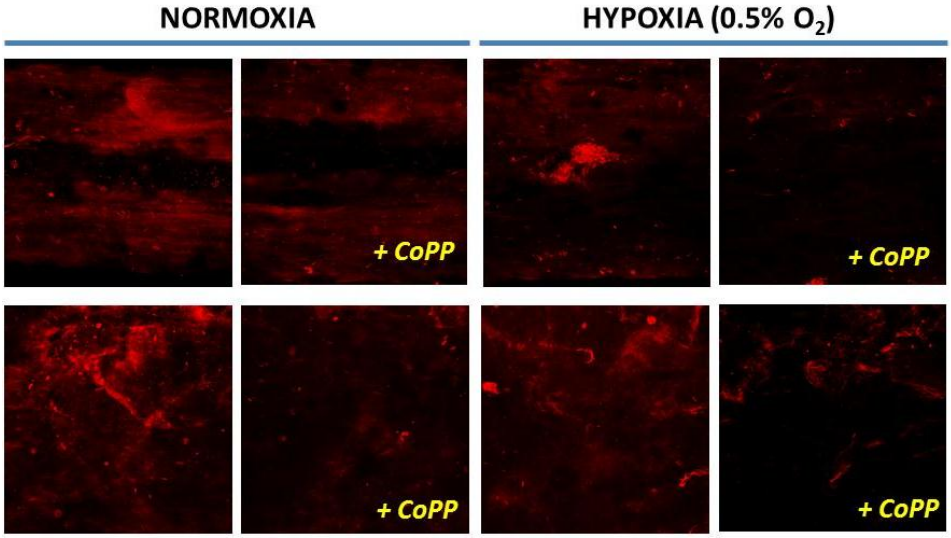

Figure 112. Confocal images of constructs after 13 days in differentiation medium. *Cells are stained with LIVE/DEAD stain to show dead cells (red). In the* ***top series of 4 panels****, the scaffolds are comprised of 0.5 mg/ml collagen: 0.5 mg/ml Hystem-HP. In the* ***bottom series of 4 panels****, the scaffolds are comprised of 2 mg/ml collagen: 0.5 mg/ml Hystem-HP.*

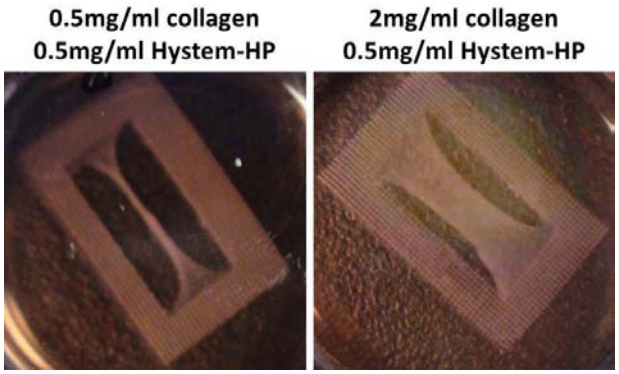

Figure 113. Constructs after 13 days in differentiation medium. *Extensive remodeling of the scaffold is seen in the construct incorporating 0.5 mg/ml of collagen (left panel) vs. 2 mg/ml of collagen (right panel).*

not treated with CoPP. Myobridges containing the Eluted cell fraction **(Figure 116)** formed more myosin-positive myotubes than myobridges fabricated using the Flow-Through cells. There was a greater abundance of both phalloidin-positive and myosin-positive cells under hypoxic conditions than under normoxia. In addition, it appeared that the addition of CoPP promoted the survival of the fibroblastic cells, as there appeared to be more phalloidin-positive cells in the hypoxia + CoPP group than in the hypoxia group that was not exposed to CoPP.

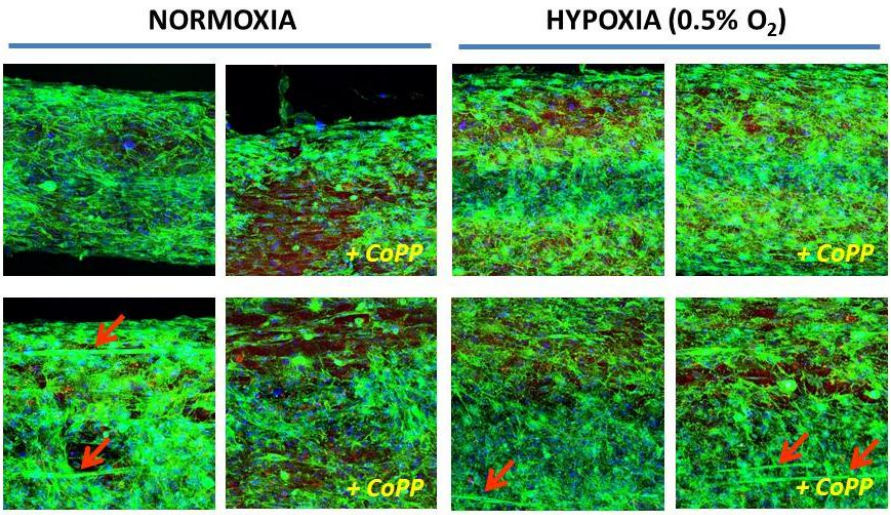

Figure 114. Three-dimensional constructs comprised of collagen/HMW-HA matrices seeded with primary rat myoblasts at 1 x 10^6 cells/ml. *Confocal analysis of constructs after 72 h in differentiation medium. Merged images of LIVE/DEAD and phalloidin staining show a significant number of fibroblasts in the construct. Some myotubes were present in 1 mg/ml collagen:0.5 mg/ml Hystem-HP (denoted by red arrows). Blue stain = all cell nuclei, red stain = dead cells, green stain = actin. In the **top series of 4 panels**, the scaffolds are comprised of 0.5 mg/ml collagen: 0.5 mg/ml Hystem-HP. In the **bottom series of 4 panels**, the scaffolds are comprised of 1 mg/ml collagen: 0.5 mg/ml Hystem-HP.*

Conclusions, Task 13

To avoid rejection of engineered muscle replacements, it would be desirable to utilize the patient's own cells for fabrication of the construct. One of the major challenges in muscle regeneration is the protection of the relevant cell populations from hypoxia, which may occur at three stages of construct preparation: (1) prior to and immediately after isolation from the patient (particularly if the cells are isolated from an area of injury), (2) during culture *in vitro*, especially when the cells are incorporated into a 3-dimensional scaffold of sufficient thickness to reduce the efficiency of diffusional exchange with the culture medium, and (3) just after implantation into the patient, where vascularization of the construct may not be fully developed. Task 13 extended our investigations into whether upregulation of the cytoprotective factor HO-1 by its transcriptional activator, CoPP, could increase the survival of muscle cell precursors. The results of our studies indicated that, in general, hypoxia inhibited cell survival. However, this negative effect was mitigated by the presence of CoPP. Under hypoxic conditions, the presence of CoPP in cultures of mouse or rat muscle cell precursors seeded into myobridge constructs resulted in: (1) reduced levels of cell death, (2) increased cell density in the construct, (3) a higher degree of cell alignment, and 4) increased levels of myotube formation. Our studies indicate that CoPP will be a useful

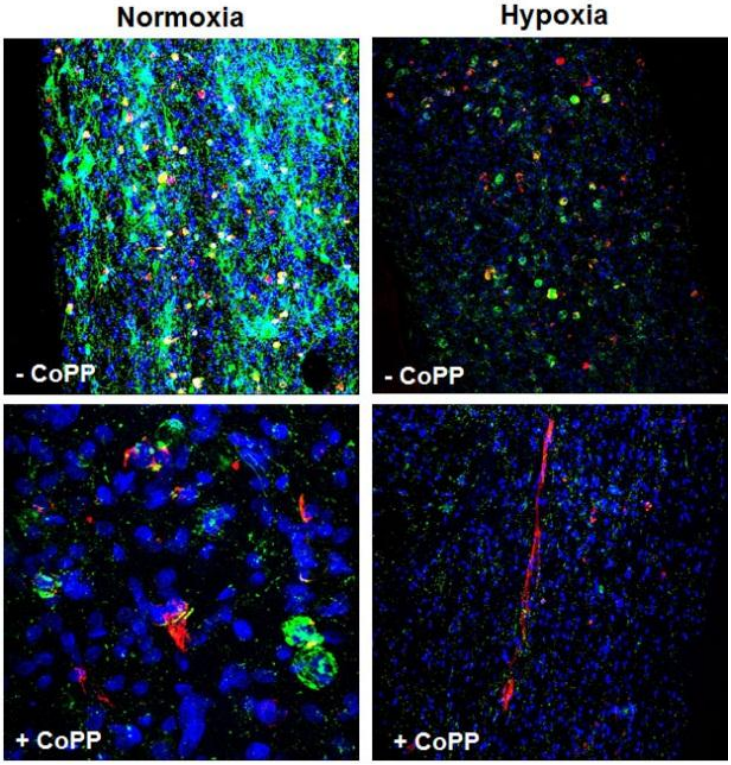

Figure 115. "Flow-Through" cell populations labeled to reveal myosin (anti-myosin antibody–red) and actin (phalloidin–green). *Myobridges cultured under conditions of normoxia and hypoxia without CoPP (- CoPP) are shown on the top. Myobridges cultured under conditions of normoxia and hypoxia in the presence of CoPP (+ CoPP) are shown on the bottom. The myobridges treated with CoPP showed more myosin-positive myotubes than those cultured in the absence of CoPP. Nuclei in all the myobridges are stained with DAPI (blue).*

supplement to the *in vitro* culture environment of myogenic cells and scaffolded muscle constructs.

Task 14

Co-transplantation of myobridges and CIs to evaluate effects of CI-mediated immunomodulation on integration of the myobridge with host tissues (Margaret Allen, MD).

Task 14 studied ways to integrate the sustained release (alginate sphere) technology developed in Task 9 into myobridge constructs. For this work, acellular collagen constructs were produced which incorporated five alginate beads per construct for implantation into rat AT defects. One cm of AT muscle was removed, leaving muscle tissue adjacent to the implanted construct to allow cell migration and angiogenesis into the construct. Three rats received implants with alginate spheres without growth factors (controls). An additional three rats received implants containing alginate spheres with 50 ng VEGF per sphere for a total of 250 ng VEGF per construct. After implantation, the skin was sutured closed over the construct. The suture was used to orient the construct when the implant, adjacent muscle, and skin were excised at 10 days post-implant. By 10 days, host vessel infiltration was seen in all of the acellular scaffolds (**Figures 117–119**). Leukocytes appeared to be more prevalent in the implants containing VEGF.

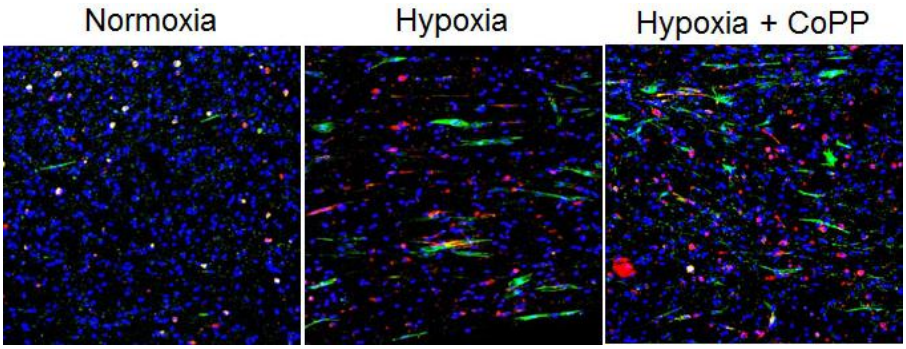

Figure 116. "Eluted" cell populations labeled to reveal myosin (anti-myosin antibody–red) and actin (phalloidin–green). *Myobridges are shown under normoxic conditions and hypoxic conditions without CoPP and under hypoxia with CoPP. Nuclei in all of the myobridges are stained blue.*

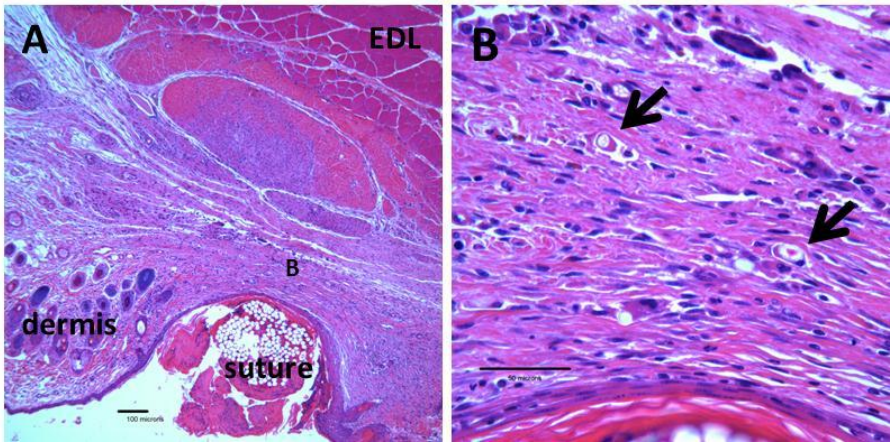

Figure 117. Cross-section of collagen construct with alginate beads 10 days after implantation into a rat AT defect. ***(A)*** *10X. Collagen construct is located between the suture and muscle tissue (EDL, seen in the upper right corner).* ***(B)*** *63X. Collagen is infiltrated by host cells. Capillaries are seen infiltrating the collagen construct at 10 days (denoted by black arrows).*

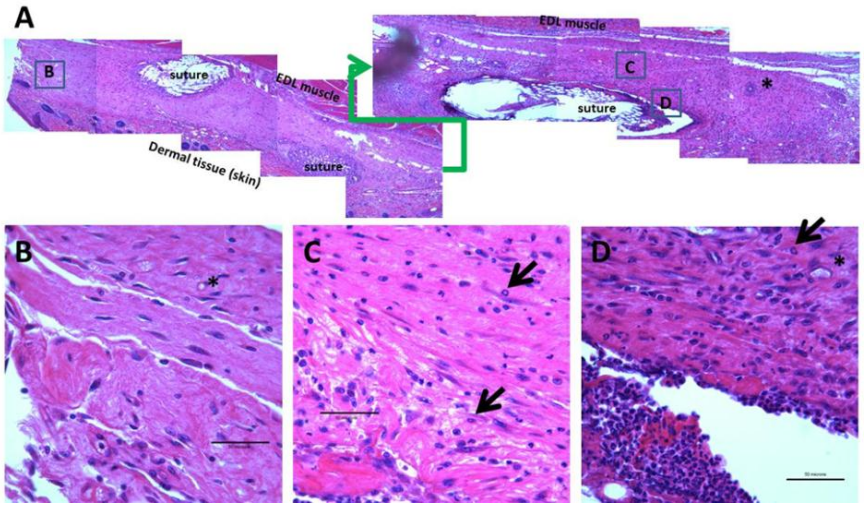

Figure 118. Longitudinal section of collagen construct with VEGF-containing alginate beads 10 days after implantation into a rat AT defect. ***(A)*** *10X.* ***(B–D)*** *63X. Collagen construct is present between the dermal layer and EDL muscle tissue (string-like tissue) and is infiltrated by host cells. A few neutrophils are denoted by arrows. Blood vessels are denoted by asterisks.*

Conclusions, Task 14

Task 14 showed that alginate spheres could be incorporated into myobridge scaffold materials and introduced into muscle defects without resulting in a major inflammatory response. We found that biologically-active VEGF is released from our alginate spheres in our CI test-beds (Tasks 9, 10) and there is evidence in Task 14 that sustained release of VEGF increases leukocyte infiltration, which may indicate an overall increase in vascularity of the myobridge scaffolds. Task 14 has provided a foundation for our studies of sustained release of bioactive agents in myobridge implantation sites. Additional studies are ongoing and plans are to continue the work beyond this current project.

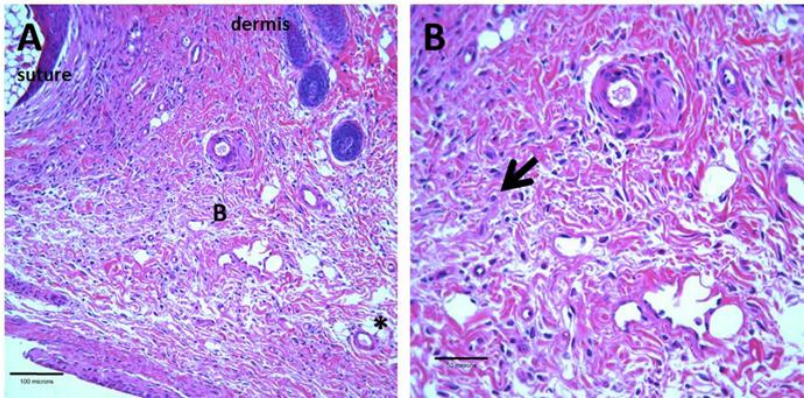

Figure 119. Cross-section of collagen construct with VEGF-containing alginate beads 10 days after implantation into a rat AT defect. ***A.*** *40X.* ***B.*** *63X. Collagen construct is present between the dermal layer and EDL muscle tissue and is infiltrated by host cells. Blood vessels (e.g., asterisk) are scattered throughout the construct, as are neutrophils (e.g., arrow).*

Task 15

***In vitro* seeding of myobridge prototypes with human myogenic stem cells for evaluation of human cell compatibility with hydrogel components (Margaret Allen, MD).**

We obtained IRB approval for our human subjects protocol and have been working toward setting up the detailed procedures with the physicians, nurses, and operating room staff in the Virginia Mason Medical Center Orthopedics Department for procuring donated skeletal muscle tissue from surgeries. Our protocol is being finalized and we plan to conduct the relevant assays in studies beyond this project.

3. KEY RESEARCH ACCOMPLISHMENTS (TASKS 1–15)

Task 1

- Established the use of nylon (Nitex) meshes to provide a stable mechanical attachment for extracellular matrix hydrogels in microwell plate assays. Determined that 100 micron mesh/44% open space nylon (Nitex) mesh works adequately for the microwell plate assay application.
- Identified new polyvinyl alcohol (PVA) sponge materials (90 micron pore diameter) that will support HMW-HA hydrogels. These materials may offer improved gel adhesion over nylon mesh.
- Determined that the nylon (Nitex) mesh material can be used for a new application in this project—as suture anchors for the myobridge constructs (Task 11). Also, the use of PVA sponge as a support for ECM hydrogels was successfully translated into *in vivo* model of immunomodulation, which was applied to work in Tasks 3 and 10.

Task 2

- Performed and finished evaluations of a microwell plate assay system for evaluating expression of GFP/FOXP3 in murine T cells. Established that the Packard fluorescence imager had the necessary sensitivity, but found that fluorescence signal from the cells was difficult to separate from backgrounds and that fluorescence analysis plates had cytotoxic properties. Our results indicated that an alternative, flow-cytometry-based assay would more effective at measuring the influence of HMW-HA hydrogels on GFP/FOXP3 expression by this cell type.
- The HMW-HA hydrogel formulation evaluated in Task 2 became the basic support medium for studies performed in Task 3.

Task 3

- Evaluated the effects of gelatin sponge inclusion on FOXP3 induction and found that the gelatin sponge adds structural integrity to hydrogels polymerized *in vitro* and that there is no functional disadvantage vis-à-vis FOXP3 induction to having the gelatin sponge present.
- Established methods to evaluate the capacity of HMW-HA to incorporate cytokines that stimulate FOXP3 expression by T cells. Showed that HMW-HA thiol-crosslinked hydrogels can bind IL-2 and IL-10 and can release these important immunomodulatory cytokines in a sustained manner, thereby indicating that HMW-HA hydrogels might be used as a means for local control of immune responses within wound and graft sites.
- Developed a new approach to incorporation of anti-CD3 and anti-CD28 antibodies in crosslinked HMW-HA hydrogels using biotinylated antibodies in conjunction with streptavidin. This new capability may provide a strong stimulus (via attachment of the antibodies to cell surface CD3 and CD28) that promotes the expansion and persistence of immunomodulatory regulatory T cells within wound and graft sites. The presence of CD3 and CD28 signaling within the HMW-HA hydrogel could substantially enhance the immunomodulatory effects of IL-2 and IL-10 that are co-delivered within the same HMW-HA hydrogel.
- Demonstrated a significant effect of heparan sulfate (HS) on amplifying the influence of TGF-β and IL-2 on induction of FOXP3 by T cell precursors. From these results, new HMW-HA hydrogel formulations were created that incorporated HS, anti-CD3 and anti-CD28 antibodies, IL-2, and TGF-β. These formulations stimulated a significant production of IL-10 from T cell precursors and induced the formation of FOXP3+ regulatory T cells from the precursor population.
- Evaluated the capacity of our immunomodulator-supplemented HMW-HA hydrogel system to induce FoxP3+ Treg from CD4+ GFP/Foxp3- precursors *in vivo*. Demonstrated that the implanted hydrogel was able to mitigate the destruction of allogeneic islets in a model of islet transplantation.
- Demonstrated that thiol-crosslinked HMW-HA lacking collagen/fibronectin (XHA) is an effective inducer of IL-10-producing regulatory T cells *in vitro*.
- Progressed to an *in vivo* mouse model of inflammation (airway hypersensitivity) induced by OVA protein to show that XHA instillation is able to promote the induction of antigen-specific, IL-10-producing regulatory T cells and reduce airway inflammation.

Task 4

- Established an optimized siRNA transfection method for unstimulated primary human T and B cells.
- Determined RNA and protein siRNA knockdown time course.
- Validated gene-specific knockdown of RNA expression (40-80%) for PTPN22, PTPN2, STAT3, and IL-6 receptor siRNAs.
- Determined that gene-specific siRNA knockdown was associated with modest functional phenotypes in unstimulated T cells, including:
    1. PTPN22- increased calcium flux in CD4+ T cells upon TCR cross-linking.
    2. PTPN2- decreased IL-2 signaling in CD4+CD25hi T cells.
    3. IL-6R- decreased IL-6 signaling in CD4+ T cells.
    4. STAT3- decreased IL-6 signaling in CD4+ T cells.
- Established gene-specific siRNA knockdown in stimulated CD4+ T cells.
- Established two alternative methods to obtain specific knockdown of gene expression in primary T cells, including:

1. Lentiviral infection of stimulated CD4+ T cells with plasmid encoded shRNAs.
2. Delivery of siRNAs into unstimulated CD4+ T cells with a single chain anti-CD7 antibody.

- Combined the single chain anti-CD7 siRNA delivery with alginate bead delivery to deliver siRNAs *in-vivo.*

Task 5

- Shown, using the RO/DO11.10 mouse model of autoimmunity *in vivo*, that ablation of the IL-17 cytokine gene does not affect generation of induced Tregs, whereas ablation of the IFNγ cytokine gene results in a reduction of induced Tregs.
- Discovered that exposure of naïve CD4+ T cells to non-specific inflammatory stimuli "primes" them to differentiate into induced Tregs when they encounter their cognate antigen.

Task 6

- Identified relevant siRNA sequences, received a set of siRNAs that target human TREM-2 and DAP12, and tested them in THP-1 cells, a monocyte-like cell line
- Initiated tests of additional antibodies for detection of TREM-2 and DAP12 so that we can measure knockdown at the protein level.
- Developed a qPCR assay for measuring TREM-2 and DAP12 mRNA that we can use to evaluate the efficacy of knockdown in THP-1cells and cultured monocytes.
- Demonstrated that TREM-2 expression is induced on human monocytes after differentiation into macrophages in the presence of macrophage colony stimulating factor.

Task 7

- Showed that β2 integrins inhibit TLR responses *in vivo* after LPS injection of mice, evidenced by the higher inflammatory cytokine levels in the serum of CD18-deficient mice than wild-type mice.
- Demonstrated that β2 integrins inhibit TLR responses directly *ex vivo* in thioglycollate-elicited peritoneal macrophages, an inflammatory macrophage population in mice.
- Found that direct ligation of β2 integrins by plating cells on tissue culture plastic or on plates coated with the β2 integrins ligand ICAM-1 causes inhibition of TLR responses.
- Demonstrated that BCAP-deficiency has a mild effect on MAPK activation and no effect on IkBa-degradation after LPS treatment of mouse macrophages. Surprisingly, BCAP delays the entry into the nucleus of the NF-kB subunits c-rel and p65.
- Showed that the in the absence of BCAP, macrophages have dramatically reduced activation of the PI3K pathway after LPS treatment.
- Discovered that the ability of BCAP to bind to PI3K is required for BCAP to inhibit TLR responses.

Task 8

- Collected whole blood RNA from 10 patients at the baseline visit and at 60 and 120 min after induction of hyperglycemia via administered glucose. Performed gene expression analysis on the RNA and showed that even a modest degree of hyperglycemia significantly increased expression of multiple genes in the IL-1 pathway. These genes were not induced by hyperglycemia after treatment with the IL-1 receptor antagonist, anakinra. These data support our initial hypothesis that hyperglycemia is an inflammatory stimulus and that cytokine blockade can prevent hyperglycemia-induced inflammation.

Task 9

- Developed a new approach, based on calcium-crosslinked alginate hydrogels, for sustained release of cytokines and HMW-HA from CIs. We developed a method to create crosslinked alginate spheres of reproducible diameter (2 mm) and we established that the spheres could be used as a medium for prolonged, sustained release of soluble HMW-HA, which has been shown to have anti-inflammatory properties. We demonstrated that the rate of release of HMW-HA from alginate could be varied by altering the molecular weight of the HA and/or the degree of crosslinking of the alginate with calcium. Significantly, we showed that HMW-HA could be released from alginate spheres in a linear fashion for extended periods of time (up to 3 months). In light of our finding that HMW-HA stimulates regulatory T-cells (Task 3), the capacity to deliver this molecule locally over a prolonged period via sustained release (using biocompatible alginate) may prove to be an effective means to control inflammation within wound sites and at the sites of regenerative tissue grafts.
- Showed that alginate spheres loaded with the angiogenic cytokine vascular endothelial growth factor (VEGF) could release this molecule in a sustained fashion over a period of at least 2 weeks *in vitro*. VEGF will likely prove to be an important component of the CI for its capacity to induce vascular growth within wound and graft sites.
- Developed poly-L-lysine (PLL)-coated alginate spheres for sustained release of immunomodulatory cytokines of low molecular weight. Studies showed that PLL coatings can effectively modulate the release of HMW-HA from alginate *in vitro*. Consequently, PLL coatings may be an effective method to modulate the kinetics of HMW-HA release from alginate *in vivo* and, potentially, control the release of other immunomodulatory compounds. Extended, local delivery of these cytokines may be an effective way prolong the presence of FOXP3+ Tregs within wound and graft sites.
- Demonstrated that an immunomodulatory antibody to CD3e (a component of the T cell immune response receptor) could be released from PLL-coated alginate spheres in a linear fashion for at least 10 days.
- Showed that alginate spheres loaded with either MMW-HA (uncoated spheres) or anti-CD3e antibody (PLL-coated spheres) could be incorporated into CI test-beds and implanted into mice in a mesenteric pocket. Significantly, these studies demonstrated that the alginate spheres were highly biocompatible and could release the compounds in bioactive forms that elicted appropriate (i.e., angiogenic/immunomodulatory) responses from their target cell types within the host, which included stimulation of the immunomodulatory cytokine IL-10 by lymphocytes of the host mice.
- Performed experiments examining the influence of the sustained release of TGF-β from alginate spheres within CIs on T cell responses *in vivo* in a model of autoimmunity (RO/RAG model). Showed that the delivered TGF-β was bioactive and could modulate the proliferative responses of CD4+ T-cells to a specific autoantigen.
- Evaluated expression of a spectrum of major ECM components by both undifferentiated and differentiated mouse IPSCs. Found that, in general, IPSC differentiation favors a profoundly increased synthesis of a variety of ECM macromolecules, which might be accompanied by increases in stability and persistence of some components (e.g., HA) and by increases in turnover of others (e.g., collagens). The dramatic increase in ECM production that accompanies IPSC differentiation might have a significant consequence on the capacity for these cells to survive, grow differentiate and organize into replacement tissues.

Task 10

- Established that unmodified Gelita-Spon gelatin sponge scaffold degrades after 3–4 days *in vivo* and evaluated the *in vivo* degradation rate of our HMW-HA hydrogels. By histology, we found evidence of a measured degradation of the HMW-HA hydrogel by macrophage-like "giant cells", associated with a

fibrovascular cellular infiltrate. This degradation was accompanied by vascularization of the site. Notably, the process of degradation was accelerated by reducing the degree of thiol-crosslinking of the hydrogel.

- Conducted studies to evaluate tissue responses to alginate spheres implanted *in vivo*. We determined by histology that alginate hydrogel is not immunogenic, does not support infiltration by cells, and does not biodegrade, at least over the short term. Therefore, the prolonged release kinetics of HMW-HA from alginate that we observe *in vitro* (Task 9) may be maintained after the spheres are implanted *in vivo*. We also determined that incorporation of VEGF into alginate spheres induced an angiogenic response following implantation *in vivo*.
- Developed a standardized cytoprotective implant (CI) for implantation into mice, thereby enabling the use of well-defined models of autoimmunity established for this species. The CI utilizes a polyvinyl alcohol sponge scaffold that supports a type I collagen hydrogel and encloses one or more alginate spheres for sustained release of bioactive agents.
- Used the PVA sponge/collagen CI to evaluate the delivery of an immunomodulatory agent (CD3e antibody) into RO/RAG mice (a model of autoimmune dysregulation). As a readout, we performed histological analyses of CIs implanted for 11 days into RO/RAG mice primed for induction of autoimmune responses against transplanted islets that were incorporated into the CIs. Autoimmune responses directed against native islets (i.e., in the animals' pancreata) were also evaluated. Results indicated that sustained release of anti-CD3e antibody within the CI (via the alginate spheres) protected both the transplanted islets and the native pancreatic islets from autoimmune attack.
- Showed that sustained release of TGF-β from CIs implanted into RO/RAG mice could modulate the IL-10-synthetic responses of CD4+ T-cells to a specific autoantigen (OVA peptide).
- Demonstrated that sustained release of VEGF (via alginate spheres) within CIs implanted into mice had profound effects, over the short term, on survival of implanted tissue (islets). This result is very important in that it indicates that our sustained release technology can deliver physiologically-meaningful levels of bioactive compounds within a very short time after engraftment. This capability will likely prove critical to improving the survival of engrafted cells and tissue constructs, particularly during the early phases of engraftment prior to the establishment of a vascular supply to the graft.
- Demonstrated that sustained release of VEGF (via alginate spheres) within CIs strongly promoted the growth of IPSCs in mice, as compared to control CIs that lacked VEGF. The growth of the IPSCs within the CIs that contained VEGF was likely due to direct effects of the released VEGF on host vascularization of the CI graft. These results underscored the effectiveness of our alginate-based method of cytokine delivery within the CI.

Tasks 11–15

- Developed design and fabrication methods for the "myobridge" construct test-bed, including a means to deliver tension to the construct during culture to encourage cell pre-alignment and to provide an integrated set of sutures to enable the construct to be attached to the proximal and distal remnants of the rat AT muscle.
- Demonstrated in rats that collagen and HMW-HA myobridge scaffolds do not elicit inflammatory responses.
- Showed that addition of thiol-crosslinked HMW-HA (Hystem-HP) to collagen gel constructs seeded with cells appears to reduce cell death within the scaffolds, but may delay cell alignment.
- Showed by biomechanical testing that adding cells to scaffold matrices induced marked changes in the stiffness and elasticity of the myobridge constructs, which was further influenced by the ratio of

collagen to HMW-HA (Hystem-HP) in the scaffold. Notably, higher cell density in the constructs promoted cell-cell interactions that allowed cell fusion during differentiation.

- Developed and optimized techniques to identify and purify highly myogenic rat muscle stem cell populations (satellite cells) by using flow cytometry and magnetic bead separation based on α7 ITGR expression.
- Demonstrated that extent of satellite cell alignment within myobridge constructs is markedly affected by ECM composition.
- Showed that under hypoxic conditions, the presence of CoPP in cultures of mouse or rat muscle cell precursors seeded into myobridge constructs resulted in: 1) improved levels of cell survival, 2) an increased cell density in the construct, 3) a higher degree of cell alignment and ECM reorganization, and 4) increased levels of myotube formation.
- Found that exposure of myoblast-seeded three-dimensional constructs to hypoxic conditions, as would occur after construct implantation *in vivo*, also fosters myoblast alignment.
- Showed that myobridge prototypes populated with α7 ITGR-selected satellite cells could be implanted into a muscle defect of considerable size in recipient rats. Importantly, the design of the myobridge suture interface was validated *in vivo*—after implantation, the cellularized collagen hydrogel scaffold did not pull free from the Vicryl meshes that held the anchoring sutures. Moreover, it was apparent that after 1 week *in vivo*, the collagen hydrogel was intact and there were myogenic cells expressing a differentiated phenotype.
- Determined that alginate spheres for sustained release of bioactive compounds could be incorporated into myobridge prototypes and would not elicit a major inflammatory response *in vivo*. Found that sustained release of VEGF within the myobridges via alginate spheres increased leukocytic infiltration.

4. REPORTABLE OUTCOMES

Awarded Grants

1. 1R01HL113294-01A (Bollyky, P.) 07/01/2012 – 06/30/2017
   NIH/NHLBI $250,000 direct costs, per annum
   ECM costimulation of immunoregulatory pathways in airway inflammation
   The goals of this project are to define how high molecular weight hyaluronan promotes the induction of IL-10 producing regulatory T-cells and to develop HA-based tools to induce TR1 *in vivo* using a mouse model of airway hypersensitivity.
   Concepts from Tasks 2 and 3 contributed to this grant.

2. 1 R01 DK096087-01 (Bollyky, P.) 07/01/2012 – 06/30/2017
   NIH/NHLBI $250,000 direct costs, per annum
   Extracellular matrix and the function and stability of FoxP3+ regulatory T-cells
   The goals of this project are to define how the extracellular matrix and the inflammatory milieu govern the stability and function of FoxP3+ regulatory T-cells in mouse models of autoimmune diabetes.
   Concepts from Tasks 2 and 3 contributed to this grant.

3. W81XWH-10-1-0789 (Allen, M.) 09/30/2010 – 09/29/2013
   DOD $130,500 direct costs, per annum
   Harnessing autologous stem cells to reconstruct skeletal muscle with innervation potential
   The goals of this project are to investigate the neurogenic differentiation of myogenic stem cells as a means to engender innervation in implanted myobridge constructs. Concepts from Tasks 9, 10, and 11 contributed to this grant.

4. Pioneer Research Award (Lee, U., PI, Allen, M./Dennis, J., mentors) 11/1/2012 – 10/31/2013
   Wilske Center for Translational Research, VM Medical Center $40,000 direct costs per annum
   Measuring hyaluronan and versican levels in connective tissues of women with pelvic floor disorders and exploring whether they are targets for improving surgical outcomes
   The goals of this project are to adapt the myobridge developed for the present project into a support for the bladder sphincter to treat urinary incontinence as a result of injury or childbirth. Concepts from Tasks 3 and 11 contributed to this grant.

5. AUS Foundation Award (Lee, U., PI, Allen, M., mentor) 03/01/2013 – 02/28/2015
   American Urogynecological Society $25,000 direct costs per annum
   Cytoprotection of urethral tissues from ischemia/reperfusion injury during simulated vaginal delivery
   The goals of this project are similar to the Pioneer Research Award above, emphasizing the role of immunomodulatory properties of extracellular matrix incorporated into the engineered construct. Concepts from Tasks 3 and 11 contributed to this grant.

Pending Grants

1. NIH R21 Application, "*Mitigating ischemia/reperfusion injury to prevent stress urinary incontinence"*. (U. Lee, Benaroya Research Institute, PI; J. Dennis, Co-investigator; Mentor: M. Allen). This proposal incorporated data generated from Task 11.
2. NIH P01 Application, "Immunogenicity of IPSCs" (V. Cirulli, U. of Washington, PI; T. Wight, R. Vernon, J. Gebe, G. Nepom, Benaroya Research Institute, Co-investigators). Funding Amount (total costs) $7,884,685. This proposal incorporated induced pluripotent stem cell (IPSC) data generated from Tasks 9 and 10 and data on the influence of HA on the immune system from Task 3.

Abstracts (Presented as Posters)

1. M Ni, AW MacFarlane IV, KS Campbell, and JA Hamerman. *BCAP mediated negative regulation of TLR signaling.* Regulatory Networks in Immunology and Inflammation Conference. June, 2010. Napa, CA, USA.
2. N Yee and JA Hamerman. *Inhibition of TLR Responses by β2 Integrins.* 14th International Congress of Immunology. August, 2010, Kobe, Japan.
3. J Kim, H-M Wilson, K. Kobashi, MD Allen. *Optimizing muscle stem cell constructs for pelvic floor reconstruction.* Society for Urodynamics and Female Urology Annual Meeting, Basic Science Poster Session. March, 2011, Phoenix, AZ, USA.
4. J McMichael. (M Allen & M Regnier, mentors). *Designing a skeletal muscle implant to improve trauma healing outcomes.* Oral Senior Thesis Presentation, University of Washington Undergraduate Research Symposium, Molecular and Cellular Bioengineering Session, May, 2011, Seattle, WA, USA.
5. M Ni, AW MacFarlane, M Toft, CA Lowell, KS Campbell, and JA Hamerman. *BCAP negatively regulates Toll-like receptor signaling in macrophages.* Immunology 2011. May, 2011, San Francisco, CA.
6. RE Welikson, H-M Wilson, GL Smith, JE Dennis, MD Allen. *Development of bioengineered myobridges with innervation potential to reconstruct extensive skeletal muscle damage.* Institute for Stem Cell and Regenerative Medicine's Annual Stem Cell Symposium. January, 2012, Seattle, WA, USA.
7. GL Smith, J McMichael, H-M Wilson, RB Vernon, TJ Kean, RE Welikson, KC Kobashi, JE Dennis, MD Allen. *Fabrication of a 3-D scaffold for skeletal muscle tissue engineering.* Society for Urodynamics and Female Urology Annual Meeting. February, 2012, New Orleans, LA, USA.

8. GL Smith, J McMichael, H-M Wilson, RB Vernon, TJ Kean, RE Welikson, KC Kobashi, JE Dennis, MD Allen. *Fabrication of a 3-D scaffold for skeletal muscle tissue engineering.* American Urological Association Annual Meeting. May, 2012, Atlanta, GA, USA.
9. JA Gebe, A Preisinger, MD Gooden, LA D'Amico, BB Yue, PL Bollyky, CS Kuhr, TR Hefty, GT Nepom, RB Vernon. *Non-encapsulated islet transplants in non-hepatic sites: Local delivery of reagents aids in islet engraftment and reversal of diabetes.* Immunology of Diabetes Society (IDS) meeting, June, 2012, Victoria, British Columbia, Canada.
10. JA Gebe, A Preisinger, MD Gooden, LA D'Amico, BB Yue, PL Bollyky, CS Kuhr, TR Hefty, GT Nepom, RB Vernon. *Non-encapsulated islet transplants in non-hepatic sites: Local delivery of reagents aids in islet engraftment and reversal of diabetes.* Federation of Clinical Immunological Societies (FOCIS) meeting, June, 2012, Victoria, British Columbia, Canada.
11. H-M Wilson, JE Dennis, MD Allen. *Cobalt protoporphyrin reduces skeletal muscle ischemia/reperfusion injury.* Advanced Technology Applications for Combat Casualty Care (ATACCC) Conference. August, 2012, Fort Lauderdale, FL, USA.
12. RE Welikson, J Luo, H-M Wilson, JE Dennis, MD Allen. *Development of bioengineered muscle with innervation potential to reconstruct extensive skeletal muscle damage.* Institute for Stem Cell and Regenerative Medicine's Annual Stem Cell Symposium. March, 2013, Seattle, WA, USA.

Papers and Manuscripts

1. PL Bollyky, SP Evanko, RP Wu, S Perigo, SA Long, B Kinsella, H Reijonen, K Guebtner, B Teng, CK Chan, KR Braun, J Gebe, GT Nepom, and TN Wight. Th1 cytokines promote T-cell binding to antigen-presenting cells via enhanced hyaluronan production and accumulation at the immune synapse. *Cell. Mol. Immunol.*, 2010, May 7(3):211-20. **PMC3027489**
2. PL Bollyky, RP Wu, BA Falk, JD Lord, SA Long, A Preisinger, B Teng, GE Holt, NE Standifer, KR Braun, C Xie, PL Samuels, RB Vernon, JA Gebe, TN Wight, and GT Nepom. ECM components guide IL-10 producing regulatory T-cell (TR1) induction from effector memory T-cell precursors. *Proc. Natl. Acad. Sci. USA*, 2011, May 10;108(19):7938-43. **PMC3093524**
3. SA Long, M Rieck, M Tatum, PL Bollyky, RP Wu, I Muller, JC Ho, HG Shilling, and JH Buckner. Low dose antigen promotes induction of FOXP3 in human CD4+ T cells. *J. Immunol*., 2011, Oct 1;187(7):3511-20. **PMC3178710**
4. M Ni, AW MacFarlane, M Toft, CA Lowell, KS Campbell, and JA Hamerman. B-cell adaptor for PI3K (BCAP) negatively regulates Toll-like receptor signaling through activation of PI3K. *Proc. Natl. Acad. Sci. USA,* 2012, Jan 3;109(1):267-72. **PMC3252908**
5. SP Evanko, S Potter-Perigo, PL Bollyky, GT Nepom, and TN Wight. Hyaluronan and versican in the control of human T-lymphocyte adhesion and migration. *Matrix Biol*., 2012, Mar;31(2):90-100. **PMC3288568**
6. RB Vernon, A Preisinger, MD Gooden, LA D'Amico, BB Yue, PL Bollyky, CS Kuhr, TR Hefty, GT Nepom, and JA Gebe. Reversal of diabetes in mice with a bioengineered islet implant incorporating a type I collagen hydrogel and sustained release of vascular endothelial growth factor. *Cell Transplantation,* 2012, Mar;21(10):2099-2110. **PMCID in process.**
7. NK Yee and JA Hamerman. β_2 integrins inhibit TLR responses by regulating NF-κB pathway and p38 MAPK activation. *Eur. J. Immunol*., 2013, Mar;43(3):779-92. **PMCID in process.**
8. PL Bollyky, RB Vernon, BA Falk, A Preisinger, MD Gooden, GT Nepom, JA Gebe. IL-10 activation *in vivo* from implants delivering activating signals *via* hyaluronan. *Clin. Dev. Immunol*, 2013 (submitted).

Oral Presentations

1. PL Bollyky. *High molecular weight hyaluronan actively promotes immune tolerance: mechanisms and potential applications.* Gordon Conference on Proteoglycans, July 2010, Proctor, NH, USA.
2. PL Bollyky. *High molecular weight hyaluronan actively promotes immune tolerance: mechanisms and potential applications.* ISHAS (International Society for Hyaluronan Sciences), June 2010, Kyoto, Japan.
3. PL Bollyky. *Hyaluronan and the regulation of adaptive immunity.* Tissue Engineering and Regenerative Medicine International Society Meeting, 2010, Orlando, FL.
4. JA Hamerman. *Regulation of inflammatory responses by ITAM signaling in macrophages.* "Bridging the Gap 2011" Symposium, 4th International Workshop on Cell Communication in Health and Disease, February 2011, Medical University of Vienna, Vienna, Austria.
5. SF Ziegler. *Foxp3, RORγt, and the regulation of Treg/Th17 differentiation and function.* FASEB Summer Conference on Autoimmunity, 2011, Saxtons River, VT.
6. PL Bollyky. *Hyaluronan and immune modulation.* Department of Pathobiology, 2011, Cleveland Clinic, Cleveland, OH.
7. SF Ziegler. *Foxp3, RORγt, and the regulation of Treg/Th17 differentiation and function.* Aegean Conference on Autoimmunity: Mechanisms and Novel Treatments, October 2011, Crete, Greece.
8. SF Ziegler. *Foxp3, RORγt, and the regulation of Treg/Th17 differentiation and function.* 2nd CMI Symposium on Immunology, November 2011.
9. PL Bollyky. *Extracellular matrix and immune regulation in autoimmune diabetes.* Helmholtz München, Diabetes Research Institute, Munich, Germany, 2011.
10. M Ni, AW MacFarlane, M Toft, CA Lowell, KS Campbell, JA Hamerman. *BCAP negatively regulates Toll-like receptor signaling in macrophages.* Immunology 2011, May 2011, San Francisco, CA.
11. SF Ziegler. *Regulation of type-2 inflammatory responses.* 51st Midwinter Conference of Immunologists, January 2012, Monterey, CA.
12. PL Bollyky, M Pickett, BA Falk, T Habib, A Long, D J Campbell, TN Wight, and G T Nepom. *High-molecular weight hyaluronan can substitute for IL-2 in IL-2R signaling.* 51st Midwinter Conference of Immunologists, January 2012, Monterey, CA.
13. JA Hamerman, MB Buechler, X Sun, T Teal, KB Elkon. *Type I IFN dependent alterations in myelopoiesis in mice overexpressing TLR7*. 51st Midwinter Conference of Immunologists, January 2012, Monterey, CA.

Patent and License Applications

1. COMPOSITIONS AND METHODS FOR MODULATING IMMUNE CELLS. PL Bollyky, GT Nepom, and MG Kinsella. International Patent Application No. PCT/US2010/060323. Filed: 12/14/10.
2. COMPOSITIONS AND METHODS FOR TREATING AIRWAY INFLAMMATORY DISEASES. PL Bollyky, GT Nepom, and MG Kinsella. U.S. Patent Application No. 61/496,956 Filed: 06/14/11.
3. IMPLANTABLE DEVICE FOR CELL TRANSPLANTATION AND METHODS OF USE. JA Gebe and RB Vernon. U.S. Patent Application No. 61/593,040 Filed: 01/03/12.

Degrees Obtained

Jon McMichael, University of Washington undergraduate student
Bachelor's degree in Bioengineering awarded June, 2011

Senior Thesis: *Designing a skeletal muscle implant to improve trauma healing outcomes*
Currently, Mr. McMichael is attending the School of Law, Arizona State University.
Mentors: Margaret Allen, BRI and Michael Regnier, Dept. of Bioengineering, University of Washington

Research Fellowships Completed

Jason Kim, MD, Gjanje Smith, MD, Bhavin Patel, MD
Virginia Mason Section of Urology, Department of Surgery
Mentors: Margaret Allen, MD, James Dennis, PhD, Una Lee, MD, and Kathleen Kobashi, MD

5. CONCLUSION

5.1. Task Summaries

Tasks 1 – 3

Tasks 1, 2, and 3 focused on the development of high molecular weight hyaluronan (HMW-HA)-based hydrogels engineered for sustained release of growth factors and cytokines. Tasks 1 and 2 were concerned with the creation of a microwell-based plate fluorescence assay to assess the effects of HMW-HA/collagen gel formulations on the induction of regulatory T cell (Treg) function, as measured by expression of fluorescent GFP/FOXP3 gene product. Task 1 was successful, in that a miniaturized nylon mesh ring-supported hydrogel format to support dispersed T cells for the microwell-based assay was developed. Task 2 evaluated the overall effectiveness of the microwell assay approach. From the Task 2 studies, it was determined that the assay was not effective in that it could not easily discriminate the GFP signal from the background. Also the plastic plates used in the assay were found to be cytotoxic to the T-cells. Follow-on studies under Task 2 resulted in the development of an alternative, flow-cytometry-based assay for GFP/FOXP3 expression in T cells. This cytometric assay was critical to the generation of the Task 3 results. In a broader perspective, the assay will be a very useful tool for future studies of T cell responses to specific extracellular matrix environments.

Using the cytometric assay for GFP/FOXP3 expression reported above, Task 3 results showed that HMW-HA hydrogels could act as depots for release of IL-2 and IL-10—cytokines that are capable of stimulating the expansion and activity of Tregs, thereby supporting the hypothesis that HMW-HA hydrogels might be used as a means for local control of immune responses within wound and graft sites. Moreover, additional work under Task 3 resulted in the development of a method to couple anti-CD3 and anti-CD28 antibodies into the HMW-HA hydrogels (using biotinylated forms of the antibodies in conjunction with streptavidin). This capability allows the HMW-HA hydrogel to provide interacting T cells with specific TCR signals that could act as potent stimulators of Treg expansion and persistence. These TCR signals would act in synergy with the signals provided by IL-2 and IL-10. The concept of providing multiple signals for Treg stimulation was further expanded by adding the extracellular matrix component heparan sulfate and the cytokine TGF-β to HMW-HA hydrogels. These bioactive molecules also promoted expansion of the Treg population. Collectively, these results indicate that extracellular matrix hydrogels can be produced that incorporate a number of molecular species which may act in concert to provide potent signals for induction of Treg persistence and function.

We did find, however, that crosslinked HMW-HA hydrogels are problematic in that they are not easily penetrated by migratory T cells. This problem has led us to explore the use of soluble (non-crosslinked) HMW-HA delivered via a sustained (time)-release device. In this approach, the HMW-HA would persist locally at wounds or sites of inflammation for an extended time, due to the presence of a depot of HMW-HA that is released into the tissue gradually. Importantly, the non-crosslinked HMW-HA is unlikely to form a hydrogel that would impede Treg migration, which is required for Tregs to encounter the HMW-HA and respond to its signals. The use of soluble HMW-HA in settings of sustained release is being evaluated in Tasks 9 and 10. In addition, we have used soluble HMW-HA in Task 3 to induce tolerance in a mouse model of antigen-specific airway hypersensitivity (for this application, the HMW-HA was delivered intra-nasally as a dilute solution). The use of soluble forms of HMW-HA, in association with other Treg-activating factors (e.g. anti-CD3/CD28

antibodies), may prove to be a highly-effective means of inducing local tissue- and organ-specific immunomodulation.

Task 4

Task 4 used small, interfering (si)RNAs introduced into naïve human CD4+ T-cells to inhibit expression of target genes predicted to affect the generation or stability of Tregs, or alternatively, prevent the generation of inflammatory T-cells of the Th17 lineage. Under this Task, we established methods to achieve an efficient transfection of siRNAs into primary T and B cells, resulting in gene-specific knockdown. Functionally, siRNA-mediated knockdown of the genes PTPN22, PTPN2, STAT3, and IL-6R in unstimulated CD4+ T cells was associated with changes in cell phenotype. Functionally, siRNA mediated knockdown of PTPN22 expression was associated with increased TCR signaling in CD4+ T cells, which is consistent with the role of PTPN22 in dampening TCR signal strength. Knockdown of PTPN2 expression correlated with decreased IL-2 signaling, which phenocopies the effect of a genetic variant in PTPN2 that reduces PTPN2 expression. These findings have important implications: the PTPN22 siRNAs are an invaluable tool to reverse the immune phenotypes resulting from the 1858T genetic variant in PTPN22 that causes susceptibility to various autoimmune diseases. The PTPN2, STAT3, and IL-6R siRNAs that we evaluated can modulate IL-6 signaling which drives Th17 cell differentiation.

Importantly, we have developed a variety of approaches to improve the efficiency of siRNA-mediated gene knockdown in order to increase in the magnitude of functional phenotypes. These include short hairpin (sh)RNA delivery via lentiviral infection of stimulated CD4+ T cells, siRNA delivery into unstimulated or stimulated CD4+ T cells by single-chain anti-CD7 antibody, and transfection of siRNA into stimulated CD4+ T cells. All three of these methods successfully deliver siRNAs and shRNAs into T cells. In summary, good progress has been made towards the goal of modulating CD4+ T cell development using si/shRNAs. Future projects will refine these methods with an objective of maximizing the duration and magnitude of functional T cell phenotypes that suppress inflammation and improve wound repair.

Task 5

Task 5 utilized a model of induced regulatory T cell (iTreg) generation mediated by transfer of naïve DO11.10+ T cells into RIP-mOVA/Rag-deficient mice. Alteration of tolerogenic pathways was achieved by ablation of specific genes, which included IL-6, IL-7, IL-21, and IFNγ. Notably, DO11.10 T cells (DO T cells) lacking IFNγ developed tolerance not only in the absence inflammation (as wild-type DO T cells do), but also in the presence of inflammation, suggesting that expression of IFNγ by T cells in an inflammatory environment inhibits the ability of the T cells to adopt a regulatory (iTreg) phenotype. This result underscores the effectiveness of combining the RIP-mOVA host (a readout for autoimmune dysregulation) with DO11.10 T cell transfer (the source of T cell-mediated regulation that can be modulated by genetic manipulation) as a means to dissect the mechanisms that mediate induction of tolerance. Task 5 has validated this approach, which, in future studies, will be applied to an expanded repertoire of gene sets.

Task 6

Task 6 assessed two endogenous inhibitors of the macrophage inflammatory response, the TREM-2 receptor and its dialkyl phosphate (DAP) 12 signaling chain, with the goal of developing strategies to downmodulate the macrophage inflammatory response as one of the multi-faceted approaches for cytoprotection examined in this project. Initially, these studies encountered difficulties with flow cytometry-based detection of TREM-2 and DAP12 to evaluate the efficacy of the knockdown. Therefore, efforts were shifted to set up a qPCR assay for measuring TREM-2 and DAP12 mRNA to evaluate the knockdown efficacy. This approach was successful; however, we were not able to achieve efficient knockdown of TREM-2 and DAP12 in human monocyte-derived macrophages using a set of corresponding siRNAs that targeted human TREM-2 and DAP12. Future studies will focus on human macrophage cell lines, which may be more amenable to transduction with siRNAs.

Task 7

The macrophage inflammatory response is potently activated by pattern recognition receptors which include the TLR family, which, when ligated, results in the secretion of pro-inflammatory cytokines, such as tumor necrosis factor, IL-12, and IL-6, as well as chemokines that attract other immune cells. One mechanism by which the inflammatory response is controlled is through endogenous inhibitors or negative regulators of TLR signaling, which include TREM-2 and DAP12, studied in Task 6. Additional inhibitors of TLR signaling include CD18 (β2 integrin) and BCAP, which were the subject of Task 7. In Task 7, we confirmed that β2 integrins inhibit TLR responses not only in bone marrow-derived macrophages, but also in inflammatory macrophage populations directly *ex vivo* and *in vivo* in mice. This finding supports the hypothesis that targeting β2 integrins may be a viable strategy for reducing inflammation during wound healing. We have also identified the mechanism by which BCAP inhibits macrophage inflammatory responses, which gives us valuable information for designing strategies to promote BCAP-mediated inhibition. Future studies will identify small molecule or protein agonists of the β2 integrin and BCAP pathways that could be incorporated into hydrogel constructs for treatment of injury to reduce inflammation during wound healing.

Task 8

Cytokines mediate tissue injury and cellular dysfunction across a broad range of diseases. Specific cytokines, such as IL-6 and IL-8, are emerging as important mediators in sepsis and as prognostic indicators of systemic inflammation in patients with traumatic injury. Task 8 evaluated the protective role of inflammatory cytokine blockade in humans (induced by administration of an IL-1 receptor antagonist, anakinra) prior to an inflammatory stimulus (induced hyperglycemia). Notably, this study found neither significant differences in levels of the serum cytokines IL-1β, IL-6, TNF-α, or IL-8 before or after hyperglycemia, nor any impact of IL-1 blockade with anakinra. However, we were able to detect significant changes in certain inflammatory genes induced by hyperglycemia, such as caspase 4. More importantly, we showed that expression of these genes was inhibited by IL-1 blockade with anakinra. Collectively, our data have established the proof-of-principle that inflammatory stimuli rapidly induce gene expression and that pre-emptive treatment with anti-inflammatory drugs prevents this gene expression. Future studies will focus on directly addressing the functions of hyperglycemia-induced genes, which may have implications for treatment of a variety of diseases, including diabetes.

Tasks 9 and 10

Critical elements required for successful engraftment of engineered tissue replacements are the rapid vascularization of the implant by the host and control of inflammation and tissue rejection. Task 9 (the CI development arm) and Task 10 (the *in vivo* test-bed arm) of Aim 2A sought to develop new approaches for sustained release of bioactive agents within a prototype engineered tissue replacement—the Cytoprotective Implant (CI). To this end, Tasks 9 and 10 explored the use of alginate hydrogels as vehicles for delivery of angiogenic and immunomodulatory compounds. Overall, the results of these studies were successful—we developed alginate and alginate/PLL spheres that could mediate the sustained release of the angiogenic cytokine VEGF and the immunomodulatory compounds HMW-HA, TGF-β, and anti-CD3e antibody. In addition, we identified parameters that could be altered to change the rate of release of these compounds from alginate. (e.g., alginate concentration, HA molecular weight, and thickness of the PLL-coating). Of greatest importance was our finding that all of the bioactive agents we selected could be released from alginate *in vivo* and retain angiogenic or immunomodulatory activity. Of particular significance to this project was the finding that HMW-HA, TGF-β, and anti-CD3e antibody could elicit immunoprotective responses from T cells, either in the form of T cell apoptosis (anti-CD3e antibody) or IL-10 production (HMW-HA, TGF-β).

In addition to our studies of alginate as a medium for sustained release, we developed novel CI test-beds that incorporated: 1) a PVA sponge scaffold that is durable, non-immunogenic, and sectionable; 2) a collagen hydrogel that supports the ingrowth of vasculature from the host; and 3) one or more alginate spheres for sustained release of bioactive compounds. This form of CI promises to have a wide range of applicability, not only as an *in vivo* experimental test-bed, but also (in a modified form) as a therapeutic device.

Finally, as we mentioned earlier, our preliminary studies that evaluated the ECM produced by IPSCs as they differentiated may prove to be particularly important for regenerative therapies that utilize patient-derived IPSCs as sources of cells. ECM produced by IPSC-derived cells within engineered implants will likely have a significant influence on the survival and differentiation of these cells, as well as important effects on host-derived vascularization, inflammation, and fibrosis. Future studies will build on the results generated under Tasks 9 and 10 to further develop alginate as a medium for sustained release, evaluate the immunomodulatory properties of specific ECM macromolecules, and evaluate the behaviors of IPSCs in the setting of engineered tissue replacements and immune responses.

Tasks 11–15

Tasks 11–15 constituted Aim 2B, the objective of which was to develop an engineered myobridge for replacement of skeletal muscle lost to disease or trauma. The principal design elements of the myobridge were: 1) a supportive scaffold of biocompatible ECM hydrogel, 2) a population of myoblast cells that could differentiate and organize into muscle fibers, and 3) bioactive agents that would promote the survival and differentiation of myoblasts and control undesirable inflammatory and fibrotic responses by the host. The myobridge served as the focal point for development of novel approaches to the fabrication of skeletal muscle replacements and also served as an *in vivo* test-bed for immunoprotective ECM formulations and sustained release technologies developed by other subprojects within this program.

Work under this Task set generated a number of important findings. Of note, we devised a novel method to connect the supportive hydrogel scaffold to proximal and distal sutures that enabled the myobridge to be axially tensioned *in vitro* in a manner that promoted the alignment of the resident cells. Also, these sutures provided a means to anchor the myobridge to the muscle remnants of the host. We were able to show that the scaffold/suture interface remained intact 4 weeks after implantation of myobridges into surgically-produced muscle defects in the rat leg.

We also investigated the influence of scaffold composition on the behavior of myoblasts. We found that addition of thiol-crosslinked HMW-HA to our standard fibrillar collagen hydrogels reduced cell death within the scaffolds, but appeared to delay cell alignment. Of particular significance was our finding that addition of CoPP to the myobridge constructs had an overall beneficial effect in the setting of hypoxia—CoPP improved cell survival and increased cell density, cell alignment, ECM reorganization, and myotube formation.

Finally, we developed and optimized techniques to identify and purify highly myogenic rat muscle stem cell populations (satellite cells) by using flow cytometry and antibody-based magnetic bead separation techniques. This work is particularly important for ensuring that the cells incorporated into muscle constructs represent a homogenous myoblast population that is minimally contaminated with unwanted cell types (e.g., fibroblasts).

5.2. "So What Section" – Evaluation of the Knowledge as a Scientific or Medical Product

This research program has a strongly translational focus—the primary objective being to develop a means to control the process of wound repair to achieve an optimal outcome where inflammation is controlled in a fashion that promotes healing and minimizes scarring. To achieve this objective, the problem has been addressed using a number of novel approaches (represented by Tasks 1–15) that are constituted to yield results that can be combined into a single device (medical product) that we refer to as the *Cytoprotective Implant* (CI). The overarching "theme" of each of these approaches—and of the CI as a whole—is that they make use of *natural* cellular processes and materials to achieve the desired result. These approaches include: 1) stimulation of the expansion, persistence, and activity of Tregs to make use of their native capacity to control the inflammatory process (*cytoprotection*), 2) the use of natural extracellular matrix (ECM) hydrogels, of specific formulations, as key stimulators of Treg-mediated cytoprotection, 3) the incorporation of strategies for local, sustained release of natural cytokines and ECM components from within the CI that will accelerate vascularization, provide long-lasting stimulation of Treg activity, and inhibit scar formation, and 4) the use of mechanically-strong natural, biodegradable ECMs as a supportive scaffold for the ECM hydrogel components.

We believe that use of natural cellular processes and materials to promote cytoprotection, combined with strategies of local delivery of bioactive agents, will optimize healing and minimize undesirable systemic side-effects.

Tasks 1–8 (Aim 1) included *basic science* studies to identify specific genes that control both the generation and functional phenotype of Tregs (Tasks 4 and 5), to characterize cell surface molecules that influence macrophage inflammatory responses (Tasks 6 and 7), and to evaluate the protective effects of inflammatory cytokine blockade (Task 8). The basic science studies were contributory to the development of the CI in that their results identified specific molecules that control immune cell behavior that could be targeted by bioactive agents incorporated within the CI. In addition to the basic science studies, there are elements of *applied science and engineering* which include the development of assays (Tasks 1, 2, and 6) and the design of ECM-based materials that provide mechanical support, bioactivity, and sustained release functions for the CI (Task 3). Some of the results generated by Aim 1 (notably, from Task 3) were incorporated directly into the designs for the CI. Other results produced by Aim 1, such as validation of the use of siRNAs to inhibit target genes in Tregs (Task 4), study of TLR inhibitors to control macrophage responses (Tasks 6 and 7), and use of *in vivo* autoimmune models to characterize the genes that control Treg generation and activation (Task 5) have the potential to identify molecular factors (which could be specific si/shRNAs, gene products, and/or drugs) that could be incorporated into later versions of the CI to improve its capacity to control inflammation and promote healing.

Tasks 9–15 (Aim 2) were the principal applied science and engineering arms of the research program. Tasks 9 and 10 (Aim 2A) focused on development of sustained release technologies for delivery of a variety of bioactive compounds into both the body of the engineered graft and the host tissue in the immediate vicinity of the graft. These two Tasks were founded on the idea that *local* delivery of bioactive compounds is the most effective means to influence the behaviors of the cell populations engineered into the graft, as well as to promote desirable responses form the host (e.g., vascularization of the graft) and suppress undesirable ones (e.g., inflammation, immune-mediated rejection, fibrosis). Local delivery of bioactive compounds is considered to be the best approach to limit undesirable side-effects that can arise after systemic delivery. Typically, side-effects from systemic delivery are the result of the need for high dosages and actions on non-target tissues and organs. The most important results generated by Tasks 9 and 10 were the development and validation of novel alginate hydrogel constructs capable of delivering compounds representing three distinct macromolecular classes: (1) proteinaceous cytokines (e.g., VEGF, TGF-β), (2) non-proteinaceous glycosaminoglycans (e.g., HMW-HA, MMW-HA), and (3) antibodies. Although alginate has been evaluated by others as a means for delivery of cytokines with basic isoelectric points, we showed that alginate is a more versatile medium for sustained release than was previously thought. To our knowledge, we are the first group to utilize alginate for sustained release of HA and antibodies. Our work in this area will continue, utilizing the PVA sponge/collagen implant developed under Task 10 as a test-bed for the effects of sustained release of bioactive compounds on cell survival and differentiation, vascularization, and immunoprotection.

Fabrication of engineered replacements for skeletal muscle is particularly challenging, as native skeletal muscle has a high cell density (in comparison to cartilage or bone, for example) and a high degree of cell alignment. In addition to these structural considerations, skeletal muscle replacements must incorporate a means by which they can be securely fastened to the appropriate sites of origin and action in the patient. Tasks 11–15 (Aim 2B) addressed these issues via a novel concept—the myobridge—in which the muscle construct is composed of individual engineered fascicles, each with its own set of proximal and distal biodegradable sutures. Each fascicle has a smaller diameter than the complete engineered muscle, which facilitates nutrient exchange as the fascicle matures *in vitro*. Each fascicle incorporates a scaffold made of ECM hydrogel (for our studies we used collagen and HMW-HA) of sufficient malleability and permeability to facilitate the proliferation and alignment of the resident myoblasts. Work under Aim 2B advanced this approach to skeletal muscle engineering with respect to fabrication techniques, scaffold material selection, and suture/scaffold interface.

One of the major challenges in the tissue engineering of muscle is the protection of the myoblast cell populations from hypoxia, which may occur after collection, during culture within supportive scaffolds *in vitro*,

and immediately after implantation into the patient, where vascularization of the construct may not be fully developed. Of relevance to this problem is the finding, under Aim 2B, that upregulation of HO-1 by CoPP had a variety of beneficial effects on myoblasts within myobridge constructs in the setting of hypoxia. Work in this area is ongoing, including evaluation of the potential for CoPP to promote the survival of native muscle after ischemic injury.

Another critical problem encountered in the development of engineered muscle constructs is the generation of pure myoblast cell populations. To avoid rejection of the engineered muscle, it would be desirable to utilize the patient's own cells for fabrication of the construct. Aim 2B evaluated new approaches to isolate and purify populations of myoblasts (satellite cells) from native muscle using specific antibodies to myoblast cell surface markers (e.g., α7 ITGR) in conjunction with magnetic bead isolation technology. We will continue to refine this approach in order to increase the efficiency of myoblast isolation and to screen out contaminating cell types. Antibody/magnetic bead isolation technology may prove to be the most economical and scalable method for isolation of viable myoblast cell populations from individual patients for use in muscle regeneration therapies.

6. APPENDICES

Abstracts (Presented as Posters)

1. M Ni, AW MacFarlane IV, KS Campbell, and JA Hamerman. *BCAP mediated negative regulation of TLR signaling.* Regulatory Networks in Immunology and Inflammation Conference. June, 2010. Napa, CA, USA.
2. N Yee and JA Hamerman. *Inhibition of TLR Responses by β2 Integrins.* 14th International Congress of Immunology. August, 2010, Kobe, Japan.
3. J Kim, H-M Wilson, K. Kobashi, MD Allen. *Optimizing muscle stem cell constructs for pelvic floor reconstruction.* Society for Urodynamics and Female Urology Annual Meeting, Basic Science Poster Session. March, 2011, Phoenix, AZ, USA.
4. J McMichael. (M Allen & M Regnier, mentors). *Designing a skeletal muscle implant to improve trauma healing outcomes.* Oral Senior Thesis Presentation, University of Washington Undergraduate Research Symposium, Molecular and Cellular Bioengineering Session, May, 2011, Seattle, WA, USA.
5. M Ni, AW MacFarlane, M Toft, CA Lowell, KS Campbell, and JA Hamerman. *BCAP negatively regulates Toll-like receptor signaling in macrophages.* Immunology 2011. May, 2011, San Francisco, CA.
6. RE Welikson, H-M Wilson, GL Smith, JE Dennis, MD Allen. *Development of bioengineered myobridges with innervation potential to reconstruct extensive skeletal muscle damage.* Institute for Stem Cell and Regenerative Medicine's Annual Stem Cell Symposium. January, 2012, Seattle, WA, USA.
7. GL Smith, J McMichael, H-M Wilson, RB Vernon, TJ Kean, RE Welikson, KC Kobashi, JE Dennis, MD Allen. *Fabrication of a 3-D scaffold for skeletal muscle tissue engineering.* Society for Urodynamics and Female Urology Annual Meeting. February, 2012, New Orleans, LA, USA.
8. GL Smith, J McMichael, H-M Wilson, RB Vernon, TJ Kean, RE Welikson, KC Kobashi, JE Dennis, MD Allen. *Fabrication of a 3-D scaffold for skeletal muscle tissue engineering.* American Urological Association Annual Meeting. May, 2012, Atlanta, GA, USA.
9. JA Gebe, A Preisinger, MD Gooden, LA D'Amico, BB Yue, PL Bollyky, CS Kuhr, TR Hefty, GT Nepom, RB Vernon. *Non-encapsulated islet transplants in non-hepatic sites: Local delivery of reagents aids in islet engraftment and reversal of diabetes.* Immunology of Diabetes Society (IDS) meeting, June, 2012, Victoria, British Columbia, Canada.
10. JA Gebe, A Preisinger, MD Gooden, LA D'Amico, BB Yue, PL Bollyky, CS Kuhr, TR Hefty, GT Nepom, RB Vernon. *Non-encapsulated islet transplants in non-hepatic sites: Local delivery of reagents aids in islet engraftment and reversal of diabetes.* Federation of Clinical Immunological Societies (FOCIS) meeting, June, 2012, Vancouver, British Columbia, Canada.
11. H-M Wilson, JE Dennis, MD Allen. *Cobalt protoporphyrin reduces skeletal muscle ischemia/reperfusion injury.* Advanced Technology Applications for Combat Casualty Care (ATACCC) Conference. August, 2012, Fort Lauderdale, FL, USA.
12. RE Welikson, J Luo, H-M Wilson, JE Dennis, MD Allen. *Development of bioengineered muscle with innervation potential to reconstruct extensive skeletal muscle damage.* Institute for Stem Cell and Regenerative Medicine's Annual Stem Cell Symposium. March, 2013, Seattle, WA, USA.

1. **M Ni**[1], AW MacFarlane IV[2], KS Campbell[2], and **JA Hamerman**[1]. *BCAP mediated negative regulation of TLR signaling.* Presented at the Regulatory Networks in Immunology and Inflammation Conference, June, 2010, Napa, CA.

   [1]Benaroya Research Institute, Seattle, WA

   [2]Fox Chase Cancer Center, Division of Basic Science, Institute for Cancer Research, Philadelphia, PA

B cell adaptor for phosphoinositide 3-kinase (BCAP) was originally identified as an adaptor molecule that binds to the p85 subunit of phosphatidylinositol 3-kinase (PI3K). BCAP-deficient mice have decreased numbers of mature B cells and attenuated B cell function. Here we investigated the responses of BCAP deficient mice to stimulation through Toll-like receptors (TLRs). BCAP-deficient macrophages produced higher concentrations of inflammatory cytokines in response to a variety of pathogenic stimuli in vitro. BCAP-deficient mice produced more IL-12 in response to LPS in vivo. The PI3K inhibitor wortmannin enhanced TLR mediated proinflammatory cytokine production in wild type macrophages but not in BCAP-deficient macrophages. Our findings suggest that BCAP negatively regulates TLR mediated signaling in macrophages.

2. **N Yee** and **JA Hamerman**. *Inhibition of TLR Responses by β2 Integrins.* Presented at the 14th International Congress of Immunology. August, 2010. Kobe, Japan.

Early responses to microbes are mediated by the activation of Toll-like receptors (TLR) on macrophages and dendritic cells (DCs). Upon engagement of TLRs, macrophages and DCs produce proinflammatory cytokines, leading to activation of the immune system and microbial clearance. We have identified a novel role for β_2 integrins in inhibiting TLR responses in macrophages and DCs. β_2 integrins, which are best characterized as adhesion molecules mediating the firm adhesion of traveling leukocytes, are heterodimeric receptors consisting of the β_2 subunit (CD18) bound to a member of the CD11 family of molecules. β_2 integrin-deficient ($CD18^{-/-}$) DCs display increased IL-12 p70, IL-6 and TNF production and cellular maturation in comparison with wild-type (WT) DCs following treatment with TLR agonists. $CD18^{-/-}$ macrophages produce increased IL-12 p40 upon TLR stimulation in comparison with WT macrophages. Direct ligation of β_2 integrins via ICAM-1 reduces the stimulatory effects of LPS and CpG in WT macrophages and DCs. In addition, serum levels of pro-inflammatory cytokines are increased in $CD18^{-/-}$ mice following LPS injection in comparison with WT mice, demonstrating that β_2 integrins are capable of inhibiting TLR activation *in vivo*. Macrophages and DCs share in common the expression of LFA-1 (CD11a/CD18) and Mac-1 (CD11b/CD18), however, $CD11a^{-/-}$ and $CD11b^{-/-}$ macrophages and DCs produce similar amounts of of pro-inflammatory cytokines following TLR stimulation as those from WT mice, arguing that LFA-1 and Mac-1 may share redundant functions in inhibiting TLR responses. These results demonstrate that signaling downstream of β_2 integrins negatively regulate TLR activation in macrophages and DCs.

3. Kim J, **Wilson H-M,** Kobashi K, **Allen MD.** *Optimizing muscle stem cell constructs for pelvic floor reconstruction*. Presented at the Moderated Basic Science Poster Session, Society for Urodynamics and Female Urology Annual Meeting, Phoenix, AZ, March 1, 2011.

Introduction: Stem cells derived from autologous skeletal muscle biopsies are currently in clinical trials for stress urinary incontinence via transurethral injection. However, for use in pelvic floor repair procedures, it may be advantageous to organize implanted muscle-derived stem cells (MDSC) on biodegradable scaffolds. We sought to optimize the conditions for MDSC growth within candidate scaffolds by varying the seeding densities and scaffold composition. ***Methods:*** MDSC were isolated from rat anterior tibialis using the pre-plating technique and were seeded at densities of between $2.2x10^6$ cells/ml and $4.4x10^6$ cells/ml onto Nitex frames using biodegradable scaffolds, which included 100% collagen and 95% collagen/5% high molecular weight hyaluronic acid (Hystem-HP™, Glycosan Biosystems). Hystem-HP is a hydrogel designed to promote expansion of stem cells. A mixture of collagen and Hystem-HP was selected to achieve a balance, allowing a proportion of MDSC to proliferate, while still allowing differentiation of MDSC to muscle fibers. The fully polymerized constructs were incised on the long edges to induce uniaxial tension for cell and scaffold fiber alignment. These constructs were observed for up to 21 days. Constructs were fixed and stained at 13 and 21 days with H&E. ***Results:*** Seeding densities of 3.3×10^6 and 4.4×10^6 cells/ml caused excessive scaffold traction that resulted in construct dehiscence within 48 hours. However, a seeding density of 2.2×10^6 cells/ml provided stable constructs that did contract, but were able to remain intact for 21 days. At that density, H&E staining showed a higher cell density with a definite subpopulation of cells that retained proliferative ability in the constructs seeded on 95%collagen/5%HystemHP when compared to 100% collagen. ***Conclusions:*** The preliminary findings here demonstrate that seeding density and scaffold composition are critical parameters to control in the generation of usable MDSC-seeded constructs suitable for *in vivo* implantation. Further studies are currently underway to quantify these differences for future creation of organized MDSC constructs for *in vivo* implantation.

4. *Oral Senior Thesis Presentation* & *Senior Thesis* by the University of Washington Bioengineering Student **Jon McMichael** (Margaret Allen, Michael Regnier, mentors). *Designing a skeletal muscle implant to improve trauma healing outcomes.*

- Presented at the University of Washington Undergraduate Research Symposium, Molecular and Cellular Bioengineering Session, May 20, 2011.
- Thesis accepted June 8, 2011 by the University of Washington Bioengineering Undergraduate Program. Bachelor's degree in Bioengineering, awarded June, 2011.

Skeletal muscle healing following severe trauma is often limited by the fact that electro-mechanical conduction between myocytes is damaged. This compromised interface means that stimulatory signals generated in the brain and peripheral nerves might not reach the muscle tissue distal to the traumatic site, leading to denervation atrophy, which can increase the risk of limb amputation. Currently, muscle flaps can be transferred to the wound to replace major muscle loss; however, success in increasing the level of neuromuscular signal transduction across the trauma site is rare because these additions generally do not become innervated. We present a seeded skeletal muscle implant to act as a unifying bridge between proximal and distal sides of the wound. The work was approached in a series of three phases. In the first, cell lines from rat muscle-derived stem cells were generated from three muscles in the leg. These cell lines maintain the potential to differentiate into the desired skeletal muscle cells, and thus were valuable for the seeding of the implant. Following this work, a series of collagen implant designs were created and evaluated for their mechanical properties. This design step ensured the highest possible level of uniformity between the implant and the surrounding tissue, and also encouraged proper stem cell differentiation. The final project phase was a biomechanical study of the seeded implant, focusing on the ability of muscle-derived stem cells and C2C12 cells to align and fuse, forming functional muscle fibers.

5. **Minjian Ni**[1], Alexander W MacFarlane[2], Kerry S Campbell[2], Clifford A Lowell[3], **Jessica A Hamerman**[1]. *BCAP negatively regulates Toll-like receptor signaling in macrophages.* Presented at Immunology 2011, San Francisco, CA, May 2011.

[1]Immunology, Benaroya Research Institute, Seattle, WA, United States.

[2]Institute for Cancer Research, Philadelphia, PA, United States.

[3]Department of Laboratory Medicine, San Francisco, CA, United States.

B cell adaptor for phosphoinositide 3-kinase (BCAP) was originally identified as an adaptor molecule that binds to the p85 subunit of phosphatidylinositol 3-kinase (PI3K). BCAP-deficient mice have decreased numbers of mature B cells and attenuated B cell function due to defects in B cell receptor signaling. BCAP is also expressed in macrophages, which activate PI3K downstream of Toll-like receptor (TLR) ligation. Here we investigated the responses of BCAP-deficient mice to stimulation through TLRs. BCAP-deficient macrophages produced higher concentrations of inflammatory cytokines in response to a variety of pathogenic stimuli in vitro. Additionally, BCAP-deficient mice produced more IL-12 in response to LPS in vivo. The TLR mediated Akt activation is impaired in BCAP-deficient macrophages. Furthermore, the PI3K inhibitor wortmannin enhanced TLR mediated proinflammatory cytokine production in wild type macrophages but not in BCAP-deficient macrophages. In B cells, YXXM motifs of BCAP are required for BCR induced PI3K activation. Surprisingly, we found that YXXM motifs of BCAP are only partially responsible for the BCAP mediated negative regulation of TLR signaling in macrophages. BCAP is constitutively phosphorylated and associated with PI3K in resting macrophages, and, unlike in B cells, does not require Syk for its phosphorylation. Taken together, our findings show that BCAP negatively regulates TLR signaling in macrophages partly through regulation of TLR-mediated PI3K activation.

6. **Welikson RE, Wilson H-M, Smith GL, Dennis JE, Allen MD.** *Development of bioengineered myobridges with innervation potential to reconstruct extensive skeletal muscle damage.* Presented at the Institute for Stem Cell and Regenerative Medicine's Annual Stem Cell Symposium, Seattle, WA, January 12, 2012.

Background: Massive muscle loss due to traumatic injury has little chance of repair by endogenous or standard therapeutic pathways. Bioengineered skeletal muscle using muscle stem cells and natural scaffold matrices is being developed to address such injuries. The goal of this research is to develop therapeutic skeletal muscle constructs using autologous muscle stem cells with natural matrix scaffolds. ***Methods:*** Primary stem and satellite cells with myogenic potential have been isolated to purity and rapidly expanded in the presence of bFGF. Theses myoblasts were used to generate "myobridges," which are elongated, implantable, skeletal muscle constructs formed using collagen and hyaluronan. To facilitate myobridge innervation, two diffusible neurotrophic growth factors, brain-derived neurotrophic factor (BDNF) and nerve growth factor (NGF), are being tested for their potential to induce interconnection with neurons. ***Results:*** Upon withdrawal of bFGF, the muscle stem cells differentiate into multinucleated, twitching myotubes that express muscle-specific structural proteins and form well-organized myofibrils. In these myotubes, acetylcholine receptors (AChRs), the transmembrane receptors required to form motor end plates, are frequently observed in clusters when stained with fluorescently-labeled bungarotoxin. When used to fabricate myobridges and kept at low growth factor conditions, the muscle stem cells form nodes along the myobridges that showed coalesced twitching. Immuno-analysis of myobridge sections revealed myosin^{+}/α-actinin^{+} myotubes throughout the construct, with the majority of staining localizing to the periphery. In addition, clusters of AChRs were found associated with myosin^{+} regions in the myobridge. ***Conclusions:*** Isolation and purification of highly proliferative muscle stem cells can be used to generate cellularized and functional myobridge constructs *in vitro* that express well-organized sarcomeres and clustered AChRs. ***Future plans:*** Future experiments are focused on identifying methods to produce more cellular, innervation-competent muscle constructs. These methods include increasing myobridge cell density, as well as the addition of BDNF and/or NGF.

Smith GL, McMichael J, Wilson H-M, PhD, Vernon RB, Kean TJ, **Welikson RE,** Kobashi KC, **Dennis JE, Allen MD.** *Fabrication of a 3-D scaffold for skeletal muscle tissue engineering.*

7. Accepted for presentation as a moderated poster at the Society for Urodynamics and Female Urology Annual Meeting, New Orleans, LA, February 28, 2012.

8. Accepted for presentation as a moderated poster at the American Urological Association Annual Meeting, Atlanta, GA, May 19, *2012*.

Introduction: A 3−D construct seeded with autologous cells on a biodegradable scaffold could serve as tissue replacement in pelvic floor reconstruction. Our goals are to design a scaffold that incorporates suture suitable for implantation and optimizes the conditions for a seeded implant in a 3−D construct by testing various formulations of collagen and hyaluronan. ***Methods:*** The C2C12 mouse myoblast cell line was used. Scaffold matrix components included collagen and hyaluronan (Hystem-HP™, Glycosan Biosystems). Constructs were seeded at 3, 4.5, and 6 $x10^5$ cells/ml and polymerized in a silicone mold. 1:1, 10:1 and 20:1 ratios of collagen:hyaluronan (C:H) were tested. Three scaffold designs were tested: constructs with a suture running through the middle, with Nitex mesh at the ends only, and with suture and mesh just inside the edges of the matrix. After 21 days, constructs were tested for passive stiffness. The constructs were then stained for dead cells, cell nuclei and filamentous actin, and confocal imaging was performed. ***Results:*** All construct conditions resulted in elongated, differentiated muscle cells with filamentous actin that appeared fused and multinucleated. C:H at 1:1 produced a more cellular construct with a greater proportion of elongated cells and fewer dead cells at 3 weeks than the 20:1 and 10:1 (C:H) samples (Figure1). Constructs seeded with 6 $x10^5$ cells/ml and C:H of 1:1 were 2x stiffer than those seeded at lower densities. The suture−only design (tension−free) resulted in random cell aggregation. Mesh alone also resulted in cell aggregation due to lack of integration of cells into the mesh. Combining suture and mesh allowed cells to integrate into the mesh and promoted rearrangement of the cells and matrix with development of uniaxial tension between suture ends which promoted cell elongation and alignment. ***Conclusions:*** Greater cell viability was observed in constructs with an equal ratio of C:H. Combining suture with mesh located inside the matrix promoted the development of uniaxial tension that allowed the cells to align in the direction of tension. A higher seeding density resulted in a stiffer construct. Further testing is needed to determine the viability and functionality of constructs *in vivo*.

Non-Encapsulated Islet Transplants in Non-hepatic Sites: Local Delivery of Reagents Aids in Islet Engraftment and Reversal of Diabetes

John A. Gebe[1], Anton Preisinger[1], Michel D. Gooden[2], Leonard A. D'Amico[1], Betty B. Yue[1], Paul L. Bollyky[1], Christian S. Kuhr[3], Thomas R. Hefty[3], **Gerald T. Nepom[1], and Robert B. Vernon[2]**

[1] Diabetes Program, Benaroya Research Institute, Seattle, WA 98101

[2] Hope Heart Matrix Biology Program at Benaroya Research Institute, Seattle, WA 98101

[3]Virgina Mason Medical Center, Seattle, WA 98101

9. *Presented at Immunology of Diabetes Society (IDS) meeting, June, 2012, Victoria, British Columbia, Canada.*

10. *Presented at Federation of Clinical Immunological Societies (FOCIS) meeting, June, 2012, Vancouver, British Columbia, Canada.*

Islet transplantation offers a potential cell replacement treatment for type 1 diabetes, but faces a number of significant challenges, including poor short-term islet survival and long term islet loss by alloimmunity and recurring autoimmunity.

Method:

To address these limitations we have developed a Bioengineered Islet Implant (BII) device that incorporates local biological reagent delivery. The BII consists of two integrated components: a poly-vinyl-alcohol scaffold to support islets within a collagen hydrogel, and a drug delivery mechanism located within the implant device through incorporating drug-alginate beads, that are designed to release their products over a two week period.

Results:

The implant device containing 450 islets is capable of reversing STZ-induced diabetes in B6 mice when implanted in mesentery or subcutaneous sites, and results in a near-normal glucose tolerance test after 45 days. Short-term islet survival measured at 24 hours is increased in recipient transplants utilizing BII incorporating local delivery of VEGF.

As proof-of-concept for delivery of local immunomodulators together with transplanted islets, we incorporated anti-CD3e MAb (2C11) within the BII, and found dramatically reduced

lymphocyte infltration into islets in the DO11/RIP-Ova murine model of T1D. In addition, local delivery within the BII of hyaluronic acid led to the generation of enhanced antigen-specific IL-10 responses.

Conclusion:

These data demonstrate the potential for a novel strategy of islet cytoprotection during transplantation, providing a suitable matrix and local immunomodulation capable of supporting islet cell implantation, survival, and function in non-hepatic sites without traditional encapsulation.

11. Wilson H-M, **Dennis JE**, **Allen MD**. ***Cobalt protoporphyrin reduces skeletal muscle ischemia/reperfusion injury*.** Presented at the ATACCC Conference, Fort Lauderdale, FL, August 13, 2012.

Background: Ischemic muscle injury can occur under a variety of circumstances, including long bone fractures, crush injuries, surgery, and compartment syndrome. Loss of muscle mass accounts for much of the resulting functional disabilities. Damage by ischemia is compounded by reperfusion injury, exposing the damaged tissue to additional oxidative and inflammatory stress. Heme oxygenase-1 (HO-1) has been shown to exhibit protective effects against ischemia/reperfusion (I/R) injury in many tissues. Cobalt protoporphyrin IX (CoPP) is a metalloporphyrin that upregulates HO-1 expression. CoPP is neither a pro-oxidant nor a substrate for the HO-1 molecule, which makes it a suitable therapeutic agent for the upregulation of HO-1. We hypothesized that administering CoPP to upregulate HO-1 would reduce skeletal muscle damage in a mouse model of hindlimb I/R injury. Further, we examined both standard preconditioning (pre-injury) and post-conditioning (post-injury) treatment protocols to determine whether the timing of HO-1 induction would influence the potential cytoprotective effects.

Methods: I/R injury in C57BL6 mice was produced by application of an orthodontic rubber band to one hindlimb for 2 hr followed by 24 hr of reperfusion. In the four treatment groups, cobalt protoporphyrin (CoPP), an inducer of *in vivo* HO-1 expression, was administered as a single 5 mg/kg intraperitoneal dose to mice either 24 hr prior to the onset of ischemia, 30 min after the onset of ischemia, immediately after the start of reperfusion, or 1 hr after the start of reperfusion (n=7 per group). In the control group, PBS was administered 24 hr prior to I/R injury (n=7). At the start of reperfusion, all mice were injected with Evans blue dye (EBD), an *in vivo* indicator of myocyte membrane permeability which was used to quantify compromised skeletal myofibers. Following 24 hr of reperfusion, mice were euthanized and the *gastrocnemius* and *tibialis anterior* muscles in both hind limbs collected for histology. Cross-sectional and longitudinal sections were examined to survey each muscle in its entirety. Uptake of EBD was assessed by ImageJ software to quantify the extent of muscle damage. Myeloperoxidase (MPO) was detected using anti-MPO (Abcam, Cambridge, MA) and assessed by ImageJ software to quantify the extent of muscle damage. To detect apoptosis, sections were stained for caspase-3 (Cell Signaling Technologies) and TUNEL (Boehringer Mannheim).

Results: Mice treated with CoPP 24 hr prior to or 30 min into ischemia, or at the start of reperfusion displayed 22, 32, and 29% reductions in Evans blue dye uptake, respectively, in *gastrocnemius* muscle compared to the same muscle in untreated mice and mice treated with 25 mg/kg SnPP (HO-1 inhibitor) 24 hr prior to ischemia. CoPP delivered 1 hr after the onset of reperfusion was ineffective. In the *tibialis anterior* muscle, CoPP treatment at the onset of reperfusion resulted in 27% less damage compared to controls, while the other treatment groups showed no protective effect.

Conclusions: The post-conditioning protocol, in which CoPP was delivered after ischemia (i.e. at the onset of reperfusion) reduced the extent of ischemic damage from I/R injury in both *gastrocnemius* and *tibialis anterior* skeletal muscles. In contrast, the preconditioning protocol, in which CoPP was delivered prior to and during ischemia, reduced muscle damage only in the *gastrocnemius* muscle. These results suggest that the post-conditioning protocol where CoPP is administered immediately following tourniquet removal would be suitable for adaptation to the clinical setting, allowing post-injury treatment to be initiated on patient arrival at the hospital.

12. **Welikson, RE, Luo J, Wilson H-M, Dennis JE, Allen MD.** *Development of bioengineered muscle with innervation potential to reconstruct extensive skeletal muscle damage.* Presented at the Institute for Stem Cell and Regenerative Medicine's Annual Stem Cell Symposium, Seattle, WA, March 15, 2013.

Background: Massive muscle loss due to traumatic injury has little chance of repair by endogenous or standard therapeutic pathways. Bioengineered skeletal muscle using muscle stem cells and natural scaffold matrices is being developed to address such injuries. The goal of this research is to develop therapeutic skeletal muscle constructs using autologous muscle stem cells with natural matrix scaffolds.

Methods: Primary muscle stem cells have been isolated from male adult mouse and rat muscle that express early- and late-stage skeletal muscle differentiation markers. Based on α7-intergrin (ITG) expression, a transmembrane receptor that binds to laminin and is expressed throughout muscle development, a purification method using magnetic bead separation has been developed that results in a highly myogenic stem cell sub-population. α7-ITG-positive muscle stem cells are then used along with collagen and high molecular weight hyaluronan (HA) to generate longitudinal implantable skeletal muscle constructs. The therapeutic potential of these constructs is being evaluated *in vivo* in our rat model of skeletal muscle injury. To determine whether the more purely myogenic α7-ITG-selected vs. a non-selected mixed muscle cell population is the optimal cell source, single constructs seeded with the two different cell populations are being implanted into leg wounds in rats in which the tibialis anterior muscle, vessels, and nerve connections have been surgically excised. Sutures on each end of the construct are used to anchor it to native muscle remnants, in order to correctly orient the construct while maintaining light tension.

Results: We have developed reproducible methods to isolate muscle stem cells based on α7-ITG expression. These myogenic cells can be differentiated into multinucleated, twitching myotubes that express muscle-specific structural proteins, form myofibrils, and express neuromuscular junction receptors. Analysis of the mixed population of cells obtained from adult rat muscle after three days of plating reveals that, at baseline, approximately 40-65% of the cell population expresses α7-ITG. In order to obtain a more pure population of myogenic cells, crude muscle cell isolates were then purified using magnetic bead separation that selected for α7-ITG-positive cells. This selection resulted in a cell population that was ~95% α7-ITG-positive. After three days under differentiation conditions, 60% of the selected cells formed myosin-positive, fused myotubes. In comparison, only 10% of unselected cells expressed myosin. The implanted cell-seeded constructs are now being evaluated one and four weeks post-implantation for cell density, and myogenic marker and neuromuscular junction expression.

Conclusions: The α7-ITG-selection method produced a cell population that was 95% α7-ITG positive, and showed a myogenic index nearly six times greater than unselected cells, a notable step forward in the fabrication of muscular constructs. It is envisioned that these constructs seeded with myogenic stem cells could be a modular, as well as a scalable bioengineered device for *in vivo* skeletal muscle reconstruction.

Papers and Manuscripts

1. PL Bollyky, SP Evanko, RP Wu, S Perigo, SA Long, B Kinsella, H Reijonen, K Guebtner, B Teng, CK Chan, KR Braun, J Gebe, GT Nepom, and TN Wight. Th1 cytokines promote T-cell binding to antigen-presenting cells via enhanced hyaluronan production and accumulation at the immune synapse. *Cell. Mol. Immunol.*, 2010, May 7(3):211-220. **PMC3027489**
2. PL Bollyky, RP Wu, BA Falk, JD Lord, SA Long, A Preisinger, B Teng, GE Holt, NE Standifer, KR Braun, C Xie, PL Samuels, RB Vernon, JA Gebe, TN Wight, and GT Nepom. ECM components guide IL-10 producing regulatory T-cell (TR1) induction from effector memory T-cell precursors. *Proc. Natl. Acad. Sci. USA*, 2011, May 10;108(19):7938-7943. **PMC3093524**
3. SA Long, M Rieck, M Tatum, PL Bollyky, RP Wu, I Muller, J-C Ho, HG Shilling, and JH Buckner. Low dose antigen promotes induction of FOXP3 in human CD4+ T cells. *J. Immunol*., 2011, Oct 1;187(7):3511-3520. **PMC3178710**
4. M Ni, AW MacFarlane, M Toft, CA Lowell, KS Campbell, and JA Hamerman. B-cell adaptor for PI3K (BCAP) negatively regulates Toll-like receptor signaling through activation of PI3K. *Proc. Natl. Acad. Sci. USA,* 2012, Jan 3;109(1):267-72. **PMC3252908**
5. SP Evanko, S Potter-Perigo, PL Bollyky, GT Nepom, and TN Wight. Hyaluronan and versican in the control of human T-lymphocyte adhesion and migration. *Matrix Biol*., 2012, Mar;31(2):90-100. **PMC3288568**
6. RB Vernon, A Preisinger, MD Gooden, LA D'Amico, BB Yue, PL Bollyky, CS Kuhr, TR Hefty, GT Nepom, and JA Gebe. Reversal of diabetes in mice with a bioengineered islet implant incorporating a type I collagen hydrogel and sustained release of vascular endothelial growth factor. *Cell Transplantation,* 2012, Mar;21(10):2099-2110. **PMCID in process.**
7. NK Yee and JA Hamerman. β_2 integrins inhibit TLR responses by regulating NF-κB pathway and p38 MAPK activation. *Eur. J. Immunol*., 2013, Mar;43(3):779-792. **PMCID in process.**

Cellular & Molecular Immunology (2010) 7, 211–220

www.nature.com/cmi

RESEARCH ARTICLE

Th1 cytokines promote T-cell binding to antigen-presenting cells *via* enhanced hyaluronan production and accumulation at the immune synapse

Paul L Bollyky, Stephen P Evanko, Rebecca P Wu, Susan Potter-Perigo, S Alice Long, Brian Kinsella, Helena Reijonen, Kelly Guebtner, Brandon Teng, Christina K Chan, Kathy R Braun, John A Gebe, Gerald T Nepom and Thomas N Wight

Hyaluronan (HA) production by dendritic cells (DCs) is known to promote antigen presentation and to augment T-cell activation and proliferation. We hypothesized that pericellular HA can function as intercellular 'glue' directly mediating T cell–DC binding. Using primary human cells, we observed HA-dependent binding between T cells and DCs, which was abrogated upon pre-treatment of the DCs with 4-methylumbelliferone (4-MU), an agent which blocks HA synthesis. Furthermore, T cells regulate HA production by DCs *via* T cell-derived cytokines in a T helper (Th) subset-specific manner, as demonstrated by the observation that cell-culture supernatants from Th1 but not Th2 clones promote HA production. Similar effects were seen upon the addition of exogenous Th1 cytokines, IL-2, interferon γ (IFN-γ) and tumor necrosis factor α (TNF-α). The critical factors which determined the extent of DC–T cell binding in this system were the nature of the pre-treatment the DCs received and their capacity to synthesize HA, as T-cell clones which were pre-treated with monensin, added to block cytokine secretion, bound equivalently irrespective of their Th subset. These data support the existence of a feedforward loop wherein T-cell cytokines influence DC production of HA, which in turn affects the extent of DC–T cell binding. We also document the presence of focal deposits of HA at the immune synapse between T-cells and APC and on dendritic processes thought to be important in antigen presentation. These data point to a pivotal role for HA in DC–T cell interactions at the IS.
Cellular & Molecular Immunology (2010) **7,** 211–220; doi:10.1038/cmi.2010.9; published online 15 March 2010

Keywords: dendritic cell; hyaluronan; immune synapse; pericellular matrix; Th1

INTRODUCTION

The pericellular matrix or glycocalyx is a 'coat' of hyaluronan (HA), proteoglycans and protein-associated glycans which extends outwards from the cell membrane of many cell types including all immune cells.[1–4] The precise composition and volume of the pericellular matrix varies substantially between cell types according to the state of activation.[2]

The primary structural component of the pericellular matrix is HA,[1,5] a repeating disaccharide of *N*-acetylglucosamine and *D*-glucuronic acid. The diameter of the pericellular matrix has been found to correlate with the level of HA secretion.[6] Conversely, the pericellular matrix can be made to disappear from most cells by treating cells with 4-methylumbelliferone (4-MU), an inhibitor for HA synthesis.[7,8] Three HA synthases, termed HAS1, HAS2 and HAS3, extrude HA directly through the plasma membrane. Pericellular matrix-associated HA is anchored to the cell surface by an HAS or cell-surface receptors such as CD44.[9] Additionally, a number of proteins and proteoglycans crosslink HA on the cell surface[9–11] and create higher order levels of structure that may be significant to the formation of this coat.[1] HA is a highly dynamic molecule and is constantly turned over *via* the activity of several hyaluronidases.[12]

While pericellular HA has well-established roles in osmotic balance, cell adhesion, control of proliferation and migration, and diffusion of nutrients and growth factors,[1] little is known about the importance of HA at the immune synapse (IS) between T cells and antigen-presenting cells (APCs). Mummert *et al.*[13] reported that HA produced and displayed on the surface of dendritic cells (DCs) contributed to both polyclonal and antigen-specific T-cell activation. They found that inhibition of HA production by DCs *via* 4-MU treatment or blockade with the HA-specific binding peptide, Pep-1, led to impaired T-cell proliferation, and diminished IL-2 and interferon γ (IFN-γ) production. These data suggest that pericellular HA facilitates T-cell activation in a paracrine manner. In addition to a well-documented role in adhesion in the context of migration and extravasation,[1] HA is known to promote DC maturation and upregulation of costimulatory molecules[14,15] and can stimulate both T cells and DCs individually *via* the receptors CD44[16,17] and TLR4.[18,19]

Benaroya Research Institute, Seattle, WA, USA
Correspondence: Dr PL Bollyky, Benaroya Research Institute, 1201 Ninth Avenue, Seattle, WA98101, USA.
E-mail: pbollyky@benaroyaresearch.org
Received 22 December 2009; revised 18 January 2010; accepted 21 January 2010

HA production is known to be positively regulated by proinflammatory cues and negatively regulated by anti-inflammatory agents, a paradigm which is consistent with a putative role for HA in promoting antigen presentation. Interestingly, the majority of cytokines, such as IFN-γ, tumor-necrosis factor (TNF)-α and IL-1β, which promote HA production in a variety of cell types tend to be associated with the T helper 1 (Th1) subset of T cells;[20–23] cytokines associated with the Th2 subset of T cells, such as IL-4, on the contrary, generally do not,[24–26] though there are exceptions.[27] This observation led us to investigate whether T cells might not directly influence cell-surface HA production by virtue of their cytokine production profiles.

We have evaluated the hypothesis that pericellular HA directly moderates DC–T-cell interactions. We have evaluated whether HA production by DC promotes the formation and stability of T-cell-DC binding. We have then asked whether individual Th1 cytokines or cultured media from Th1 clones have the capacity to positively influence T-cell binding to DC in an HA-dependant manner. Our results represent a novel, pivotal role for HA and the pericellular matrix in regulating DC–T-cell interactions.

MATERIALS AND METHODS

Reagents

HA with a molecular weight of 1.5×10^6 kDa was provided by Genzyme (Cambridge, MA, USA). 4-MU and *Streptomyces* hyaluronidase were obtained from Sigma-Aldrich (St Louis, MO, USA).

Human blood samples

Human peripheral blood mononuclear cell (PBMC) samples were obtained from healthy volunteers with informed consent, participating in a research protocol approved by the institutional review board of the Benaroya Research Institute at Virginia Mason (BRI, Seattle, WA, USA).

Isolation of leukocyte populations

Human PBMCs were prepared by centrifugation of peripheral blood over Ficoll–Hypaque gradients. $CD4^+$ T cells were isolated using the Dynal CD4 Positive Isolation Kit (Invitrogen, Carlsbad, CA, USA) as per the manufacturer's instructions. Purity of the resulting cell fractions was reliably >98% $CD4^+$ by flow cytometry; anti-CD4 Ab (RPA-T4), from BD-Biosciences (San Jose, CA) was used for this purpose. Cells were cultured in RPMI 1640 (Invitrogen) supplemented with 10% pooled human serum, 100 μg/ml penicillin, 100 U/ml streptomycin and 1 mM Na pyruvate (Invitrogen). Monocytes were isolated from the $CD4^-$ population as per the manufacturer's instructions.

Generation of monocyte-derived DCs

$CD4^-CD14^+$ cells (monocytes) were cultured in 24 well plates, 3×10^6 cells/well. Cells were cultured 4–6 days in the presence of IL-4 (50 ng/ml; R&D, Minneapolis, MN, USA) and granulocyte/macrophage colony-stimulating factor (5 ng/ml; BD Pharmingen, BD Biosciences). Cells were stained before and after this protocol for CD14, CD80 and CD86 to document their development into DCs. A representative staining example is shown in Supplementary Figure 1.

Generation and characterization of Th1 and Th2 clones

PBMCs from human leukocyte antigen (HLA) $DRB0404^+$ patients were stimulated as described earlier.[28] Briefly, cells were cultured with RPMI 1640 containing 10% (v/v) pooled human serum at the density of 5×10^6/ml, in the presence of a GAD65 555-567 (557I; NFIRMVISNPAAT) peptide at a concentration of 10 μg/ml. On day 10, the cells were transferred at a density of 4×10^6/ml onto 48-well plate that had been adsorbed with 8 μg/ml DRB0404 monomer containing GAD65 557I peptide major histocompatibility complex (MHC) in 1X phosphate-buffered saline (PBS) for 3 h at 37 °C. One microgram per milliliter of anti-CD28 antibody (BD Pharmingen, BD Biosciences) was added to the media and the cells incubated additional 5–6 days and stained using 10 μg/ml phycoerythrin-labeled 0404 tetramer for 2 h at 37 °C, and subsequently with fluorochrome-labeled anti-CD25 and anti-CD4 (BD Pharmingen, BD Biosciences) for 30 min on ice. Cells were then washed with PBS containing 1% fetal bovine serum and analyzed using a BD FACSCalibur flow cytometer (BD Biosciences). Data analysis was performed using CellQuest (BD Biosciences) software. $CD4^{high}CD25^+$ tetramer-binding cells were single-cell sorted into 96-well plates using a FACSVantage cell sorter (BD Biosciences). Sorted clones were expanded for 10–12 days by stimulation with irradiated unmatched PBMCs (1.5×10^5/well), 5 μg/ml phytohemagglutinin and 10 U/ml IL-2 for two cycles, followed by stimulation with HLA-DRB404-matched PBMCs pulsed with 10 μg/ml GAD65 557I peptide and 10 U/ml IL-2. On days 10–12, clones were selected based on growth for further expansion. Resting T cells (5×10^4) were tested for antigen specificity by stimulation with irradiated HLA-DR404-matched PBMCs (1×10^5/well) with and without a specific peptide GAD65 555-567 (NFFRMVISNPAAT) in the culture (0.01–10 μg/ml). Proliferation as measured by ^{3}H-thymidine incorporation was tested after 72 h in culture. The restriction elements of the T-cell clones were confirmed by testing proliferation induced by DR0404-transfected type 1 bare-lymphocyte-syndome cell lines (BLS-1) pulsed with GAD65 peptide. Cytokine secretion by the cells was measured at 48 h after stimulation by Cytometric Beads Array assay (BD Pharmingen, BD Biosciences) according to the manufacturer's instructions. Clones were classified as Th1 or Th2 based on their cytokine production profiles (Supplementary Table 1). T-cell clones were tested for tetramer binding by staining with 10 μg/ml GAD65 or control tetramer for 1 h at 37 °C followed by fluorochrome-conjugated antibody on ice for 30 min. The T-cell clones were expanded by stimulation at 2-week intervals with either irradiated non-HLA-matched PBMCs, phytohemagglutinin (5 μg/ml) and IL-2 (10 U/ml), or GAD peptide-pulsed $DR0401^+$ PBMCs and IL-2 (10 U/ml). After 3–4 cycles of stimulation the cells were frozen and aliquots were subsequently thawed for the experiments described in this work.

Generation and characterization of stock Th1- and Th2-conditioned media solutions

Three pairs of thawed Th1 and Th2 clones were stimulated with irradiated non-HLA-matched PBMCs, phytohemagglutinin and IL-2, as described above. Cells were maintained for three weeks with periodic readministration with IL-2 and replacement of media. Whenever this was done the conditioned media was harvested and stored at 4 °C. Conditioned media was collected from the three Th1 clones in approximately equal proportions and pooled. The same was done for the Th2 cell cultures. In this manner a single stock of Th1 conditioned media and a single stock of Th2 conditioned media were generated over the course of 2 weeks. These two stocks underwent cytokine profiling as described above and the results are shown in Table 1.

Treatment of DCs with cytokines or Th1- or Th2-conditioned media

DCs generated from monocytes were collected, washed in complete media, and replated at 3×10^6 cells/well in a 6-well plate. Th1- or

Table 1 Cytokine profiles for the Th1- and Th2-conditioned media used as stock solutions for these experiments. These stock solutions were derived from pooled Th1- and Th2-clone culture supernatants

Conditioned media	IFN-γ	TNF-α	IL-10	IL-4	IL-2
Th1	1183.5	84.7	1452.6	10.6	38.9
Th2	264.4	51.2	1176.7	9571.3	0

Abbreviations: IFN, interferon; Th, T helper; TNF, tumor-necrosis factor.

Th2-conditioned media were added in 2 : 1 ratio of fresh complete media to stock conditioned media. Fresh media alone were used as a control. Alternatively, where indicated fresh media was supplemented with recombinant cytokines individually and in combination at the following concentrations: 100 IU/ml IL-2 from (Chiron, Emeryville, CA, USA); 10 ng/ml recombinant human IFN-γ (R&D Systems, Minneapolis, MN, USA); 10 ng/ml recombinant human TNF-α (BD Pharmingen, BD Biosciences), 10 ng/ml recombinant human IL-1β (BD Pharmingen, BD Biosciences). DCs were treated in this manner for 4 h prior to mRNA harvest.

Quantitiative PCR

Total RNA was harvested from T cells and DCs using the RNeasy Mini Kit from Qiagen (Valencia, CA, USA). cDNA was prepared from 350 ng total RNA reverse transcribed in a 40 μl reaction mix with random primers using the High-Capacity cDNA Archive Kit according to the manufacturer's instructions. Relative quantification of transforming growth factor-β1 gene expression was performed using Taqman Gene Expression Assay Mm03024053_m1 and eukaryotic 18S rRNA Endogenous Control part no.4333760. Briefly, 1.2 μl cDNA was amplified in 1XTaqman Fast Universal PCR Mix with 250 nM Taqman probe in a 20 μl reaction using the Fast program for 50 cycles on an ABI7900HT thermocycler. All qPCR reagents were from Applied Biosystems (Foster City, CA, USA). All samples were done in duplicate and data were analyzed using the Comparative Ct Method with software from Applied Biosystems. Estimated copy numbers were generated from a standard curve created by using a selected reference cDNA template and Taqman probe.[29]

QUANTIFICATION OF HA SYNTHESIS

H^3-glucosamine was added at a concentration of 40 μCi/ml to DC cultures. After 24 h the supernatant was removed, thereby separating each condition into soluble and cellular fractions. These fractions were then digested with pronase (100 μg/ml) in 0.5 M Tris pH 6.5 overnight at 37 °C. Following digestion, the pronase was inactivated by heating to 100 °C for 20 min. Radiolabeled macromolecules were then recovered and separated from unincorporated precursor by precipitation on nitrocellulose membranes using slot blot analysis as described previously.[30] Briefly, 200 μl of the sample was added to an equal volume of 2% cetylpyridiniumchloride, 50 mM NaCl buffer and the solution blotted onto 0.45 μm nitrocellulose membrane (Schleicher and Schuell, Keene, NH, USA). The membrane was washed for six times in 2% cetylpyridiniumchloride, 50 mM NaCl buffer and once in deionized water before air drying at room temperature overnight. Incorporation of ^{3}H-glucosamine into HA was measured by digesting an equivalent radiolabeled aliquot with *Streptomyces* hyaluronidase (2 U/ml) for 24 h at 37 °C before slot blotting. HA was measured as the amount of hyaluronidase sensitive material precipitated to the nitrocellulose membrane. To determine the amount of chondriotin sulfate and dermatan sulfate present in the sample, an equal aliquot of sample was adjusted to pH 8.0 before digesting with Chondroitin ABC lyase (0.03 U/ml; North Star BioProducts, East Falmouth, MA, USA). All scintillation counting was done on Beckman LS 6500 (Beckman Instruments, Fullerton, CA, USA).

T cell–DC binding experiments

These were modeled on previous work by Do *et al.*,[14] with modifications. DCs induced from monocytes were stained using SNARF-1 (Invitrogen). After this 1×10^5 DCs per condition were cultured on a coverslip in a 6-well plate (Corning, Corning, NY, USA) overnight. Th1- or Th2-conditioned media was added in 2 : 1 ratio of fresh complete media to conditioned media. Fresh media alone was used as a control. Alternatively, fresh media was supplemented with 100 IU/ml IL-2 and 10 ng/ml IFN-γ. DCs were maintained under these culture conditions overnight. The plates were gently washed twice to remove any conditioned media.

Primary T cells were activated for 4 days with anti-CD3/28 beads (Invitrogen) at a ratio of 1 bead to 10 cells without exogenous IL-2. Activated T cells were then labeled with 50 μM, carboxyfluorescein succinimidyl ester (CFSE; Invitrogen). $CD4^+$ T cells which were labeled by 1×10^5 CFSE were added to the plates. After incubation for 2 h, the plates were washed in PBS; the coverslips were removed and mounted on slides for analysis.

Analysis of binding was performed as follows. For each condition, at least 10 non-overlapping fields were photographed using a digital camera (Diagnostic Instruments, Sterling Height, MI, USA) attached to a Leica DM-IRB microscope (Leica Microsystems, Wetzlar, Germany). Spot Software 4.5 (Diagnostic Instruments) was used for analysis. For each field photographs were taken using the excitation laser at 488 and 568 in order to capture binding of both CFSE-labeled T cells as well as SNARF-1-labeled DCs. For each field the two images were then merged using software in order to provide an assessment of clustering involving both T cells and DCs. Using this image, for each field the number of DCs was counted as well as the number of clusters. A cluster was defined as $\geqslant 2$ T cells bound to one or more DCs.

Binding experiments were also performed using CFSE-labeled Th1- or Th2-cell clones activated in an identical manner to the primary $CD4^+$ T cells described above. The cytokine production profiles for these clones are shown in Supplementary Table 1. These T-cell clones were pre-incubated for 1 h with BD GolgiStop (BD Pharmingen, BD Biosciences). BD GolgiStop was added to prevent any further cytokine contribution from T cells to the binding assay. The T-cell clones were then washed twice and incorporated into the same binding assay protocol as above.

IMMUNOCYTOCHEMISTRY

For visualization of HA, cells were fixed in an acid alcohol formalin buffer as described by Lin *et al.*[31], thereby allowing maximum retention of the HA and associated proteins. The coverslips were blocked at room temperature with 1% bovine serum albumin/5% normal donkey serum in PBS for at least 1 h. Subsequently, they were incubated with bPG (the N- terminal HA binding region of aggrecan which has been biotinylated) as previously described.[32] Following three washes, cells wereincubated with Alexa Fluor 488 streptavidin (2 μg/ml), Alexa Fluor 647 anti-HLA-DR (L243; Biolegend, San Diego, CA, USA) (8 μg/ml) and DAPI (1 μg/ml) for 1 h. Following three washes in PBS, coverslips were mounted in Gel/Mount (Biomeda, Foster City, CA, USA), and photographed using the apparatus described above.

Statistical analysis

Statistical comparisons were made using a Student's *t*-test. Standard error is shown unless otherwise noted. Values of $P<0.05$ were considered significant.

RESULTS

Biosynthesis of HA by DCs

We first sought to quantify and characterize HA production by monocyte-derived human DCs. This was accomplished using a method by which the incorporation of radiolabeled glucosamine into HA is assessed.[33] Because glucosamine is converted into HA as well as other molecules, the proportion of HA was calculated from parallel aliquots digested with and without *Streptomyces* hyaluronidase, an enzyme specifically degrading HA;[34] chondroitinase is used as a control in these studies to confirm the specificity of the assay for HA. Using this method we found that monocyte-derived human DCs but not primary T cells produced HA (Figure 1a). The majority of this HA production was cell associated as HA was observed in the cellular fraction but not the media fraction from DC cultures (Figure 1b).

Of the three HAS genes, HAS3 was most highly expressed by monocyte-derived human DCs with minimal expression of HAS1 and no detectable expression of HAS2. Activated T cells produced negligible quantities of cell-associated or soluble HA (Figure 1a). Of note, this was also the case for unactivated T cells as well as the T-cell clones used in later experiments (data not shown). We therefore subsequently focused only on HA production by DCs.

DC production of HA was substantially abrogated upon treatment with 4-MU used at 50 μg/ml (Figure 1b). This dose of 4-MU was demonstrated to be non-toxic to DCs as ascertained by staining with 7-AAD and Annexin V (Supplementary Figure 2). This corroborates reports with other cell types that 4-MU at comparable concentrations is not directly cytotoxic.[35–37] Hyaluronidase treatment had the paradoxical effect of increasing DC production of HA (data not shown) as has been shown in other systems.[38,39]

DCs produce HA in response to Th1-conditioned media and to IL-2 and IFN-γ

We were interested in what factors might govern HA production by DCs and hypothesized that soluble factors produced by T cells might play a role, given the importance of DC–T cell cross-talk in antigen presentation. Conditioned media from Th1-clone cultures but not Th2-clone cultures had the capacity to upregulate HA production by DCs (Figure 2a). This was not the case for chondroitin sulfate, demonstrating that this effect is specific to HA.

The role of cytokines in regulating HA production by other cell types is well documented. Therefore, we suspected that a cytokine or several cytokines might be responsible for the effects seen with Th1-cultured media. To this end, we evaluated the effects of various Th1 cytokines alone or in combination on DC HA production (Figure 2b). We found that TNF-α and IL-2 alone promoted HA production while IL-1β and IFN-γ did not. However, the combination of IL-2 plus IFN-γ produced more HA than IL-2 alone while the combination of IL-2 and TNF-α performed the best. As reported above for DCs which did not receive further cytokine or cultured media treatment, the entirety of this HA production was cell associated with no detectable HA in the media fraction (data not shown). The finding of a role for IFN-γ and TNF-α in HA production is consistent with previous reports using fibroblast cell lines.[20–23] We opted to focus our further work on the contribution of IL-2 and IFN-γ to DC production of HA because these cytokines are well characterized as being produced primarily by T cells. Therefore, any IL-2 and IFN-γ in the mixed DC–T cell cultures could be expected to be of T-cell origin. TNF-α, conversely, can also be produced by DCs themselves.[40]

Interestingly, these data suggest that DCs have a previously unreported capacity to respond to IL-2. DCs do not express the high-affinity IL-2 receptor CD25 (data not shown), but we did find that DCs do express the low-affinity receptor CD122 (Supplementary Figure 1). However, neither antibodies directed at CD122 nor at IL-2 itself negated the enhanced production of HA observed upon treatment with Th1-conditioned media (data not shown). This suggests that IL-2 is not a strict requirement for enhanced DC production of HA under this condition.

The accumulation of cell-surface HA of DCs is likely to reflect the balance of production as well as degradation of HA. We therefore evaluated the effects of Th1-conditioned media and controls on the genes responsible for HA synthesis and degradation. Interestingly, Th1-conditioned media, and IL-2 and IFN-γ supplementation did not engender any increase in HAS3 mRNA (Figure 3a). Neither was there any increase in HAS1 nor HAS2 mRNA as these both remained at negligible levels under all conditions tested (data not shown). However, we did note a significant decrease in the expression of mRNA for the hyaluronidase HYAL1 with either Th1-conditioned

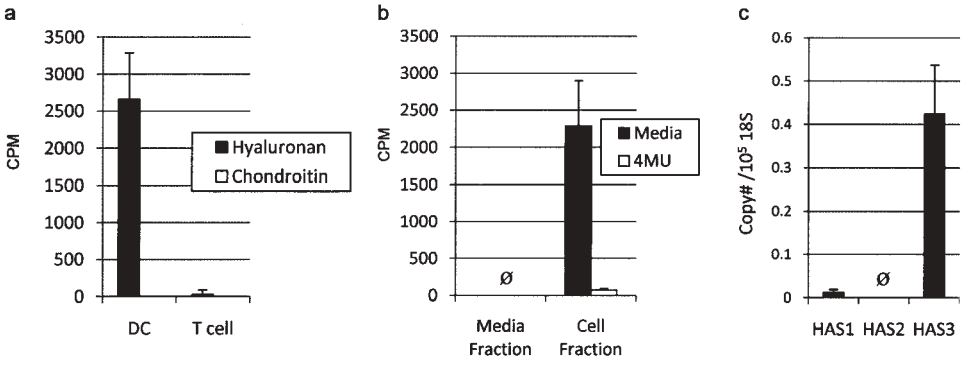

Figure 1 DCs produce cell-associated HA. (**a**) Radiolabeled glucosamine incorporation into HA by DCs and T cells. Since glucosamine is converted into HA as well as other molecules, the proportion of HA was calculated from parallel aliquots digested with and without *Streptomyces* hyaluronidase. Chondroitin ABC lyase is used as a control in these studies to confirm the specificity of the assay for HA. (**b**) Radiolabeled glucosamine incorporation into HA for the media and cell fractions of DC cultures. DCs were cultured with and without 4-MU treatment at the time of glucosamine addition. Error bars are for replicates in triplicate. Data are representative of four experiments. (**c**) mRNA expression for the three hyaluronan synthases normalized to 18S mRNA. Results include data from four independent experiments each using DCs from different individuals. CPM, counts per min; DC, dendritic cell; HA, hyaluronan; HAS, hyaluronan synthases; 4-MU, 4-methylumbelliferone.

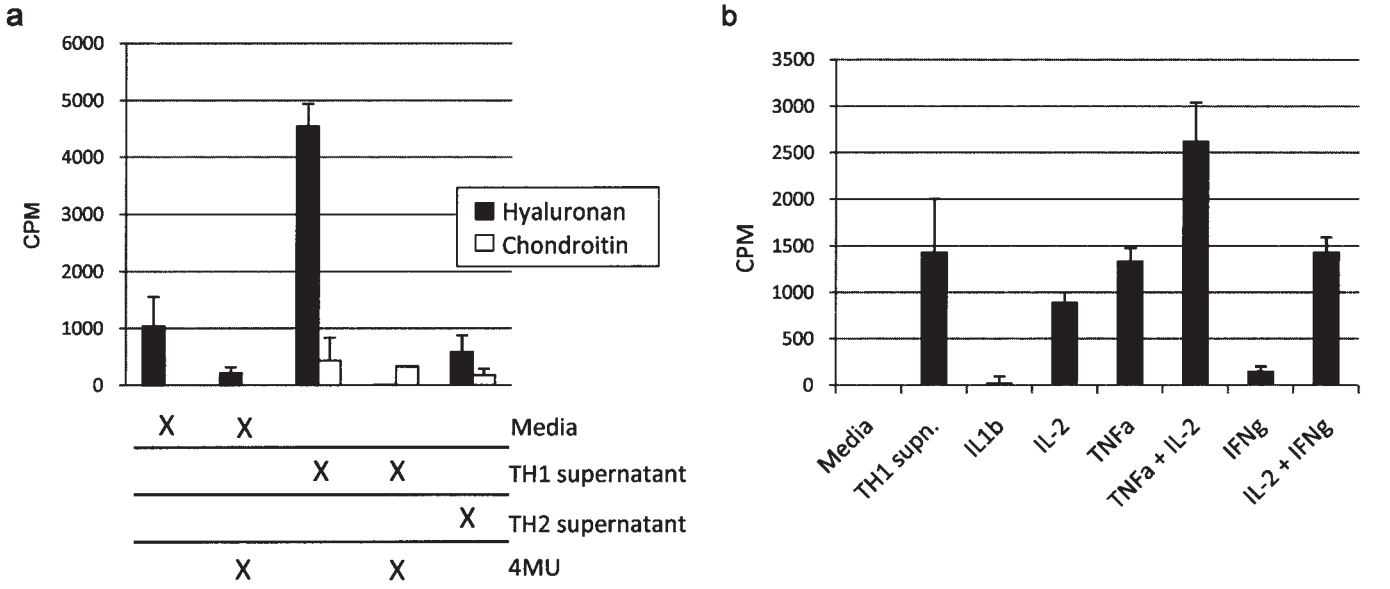

Figure 2 DCs produce cell-associated HA in response to Th1-conditioned media and to specific Th1 cytokines. (**a**) Radiolabeled glucosamine incorporation into HA or chondroitin sulfate upon coculture in the setting of Th1- or Th2-cell culture supernatants. CPM shown are for the amount of radiolabel lost upon treatment of the radiolabeled cell lysate with either *Streptomyces* hyaluronidase or chondroitin ABC lyase. (**b**) Radiolabeled glucosamine incorporation into HA upon coculture in the setting of Th1-cell culture supernatants or specific cytokines as shown. CPM shown are for the amount of radiolabel lost upon treatment of the radiolabeled cell lysate with *Streptomyces* hyaluronidase. Error bars are for replicates in triplicate; data are representative of four experiments. CPM, counts per min; DC, dendritic cell; HA, hyaluronan; IFN, interferon; Th, T helper; TNF, tumor-necrosis factor; 4-MU, 4-methylumbelliferone.

media, or IL-2 and IFN-γ supplementation (Figure 3b). This suggests that Th1-conditioned media, and IL-2 and IFN-γ may affect the HA content of DCs primarily by impacting the rate of degradation rather than production. Similar complex effects on HA production and degradation were reported for IFN-γ and TNF-α in lung fibroblasts.[41]

Conditioned media from Th1 cytokines, and IL-2 and IFN-γ supplementation promote DC spreading

Induced DCs had the typical morphological appearance of immature DCs: they were predominantly non-adherent and had few DC processes (Figure 4a). Upon treatment with Th1-conditioned media, these cells became more adherent, formed long dendrites and tended to cluster (Figure 4b). These are features associated with DC maturation and heightened capacity to present antigen.[42,43]. These morphologic changes could be abrogated by treatment with 4-MU (Figure 4c). In contrast, DCs incubated with Th2-conditioned media were only slightly altered in appearance (Figure 4d). The same changes observed with Th1-conditioned media could be seen upon treatment with IL-2 and IFN-γ (Figure 4e). As previously reported, these treatments impacted expression of CD80 and CD86 in tandem with their effects on dendritic processes.[44–46] (Data not shown).

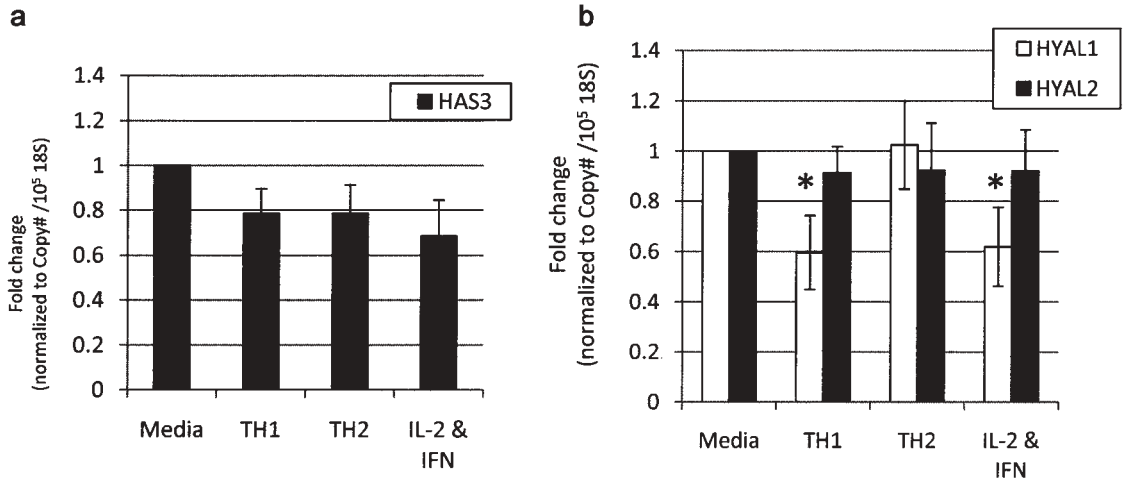

Figure 3 DCs downregulate HYAL1 in response to IL-2 and IFN-γ. (**a**) mRNA expression of HAS3 4 h following addition of Th1- and Th2-cell culture supernatants or supplementation with IL-2 and IFN-γ. (**b**) mRNA expression of the hyaluronidase genes HYAL1 and HYAL2 under the same conditions. Results include data from four independent experiments each using DCs from different individuals. * connotes conditions where there was a significant ($P \leqslant 0.05$) difference between that sample and the media-only condition. DC, dendritic cell; HAS, hyaluronan synthases; HYAL, hyaluronidase; IFN, interferon; Th, T helper.

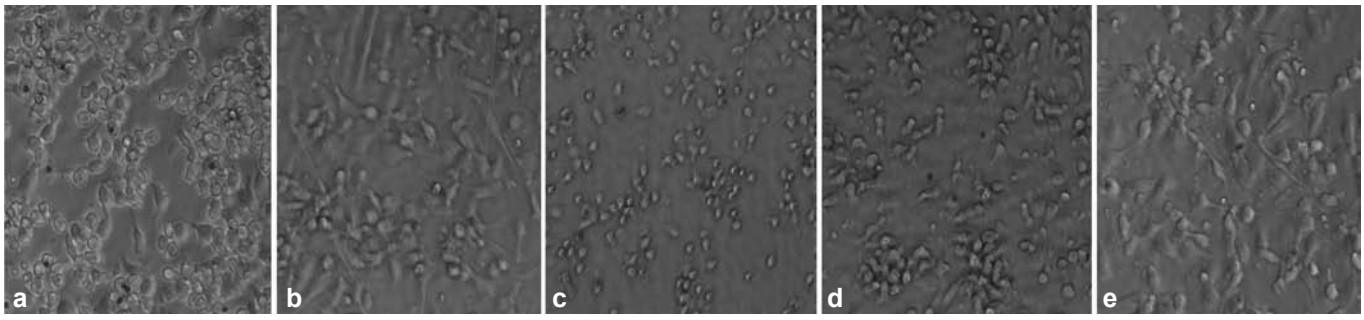

Figure 4 Conditioned media from Th1 cells promote DC spreading in an HA-dependent manner. DCs treated with (**a**) control media, (**b**) Th1-conditioned media, (**c**) Th1-conditioned media with the addition of 4-MU, (**d**) Th2-conditioned media, or (**e**) control media supplemented with IL-2 and IFN-γ. Images are shown at ×10 magnification. Data are representative of three separate experiments. DC, dendritic cell; HA, hyaluronan; IFN, interferon; Th, T helper; 4-MU, 4-methylumbelliferone.

Treatment of DCs with Th1-conditioned media as well as IFN-γ and IL-2 supplementation promote T-cell binding in an HA-dependent manner

We sought to ascertain whether HA production by DCs contributed to T-cell binding. To this end, we evaluated cluster formation between SNARF-labeled DCs and CSFE-labeled T cells. DCs pre-treated with Th1-cultured media demonstrated a significantly greater propensity to bind to primary T cells than controls (Figure 5a–e). This enhanced binding could be abrogated by inclusion of 4-MU during the pre-treatment phase (Figures 5c and e). A similar response to that seen with Th1-cultured media pre-treatment was seen upon pre-treatment of DCs with media supplemented with IFN-γ and IL-2 (Figure 5e). The addition of exogenous HA to the DC–T cell cultures did not significantly improve cluster formation (Figure 5e). These data

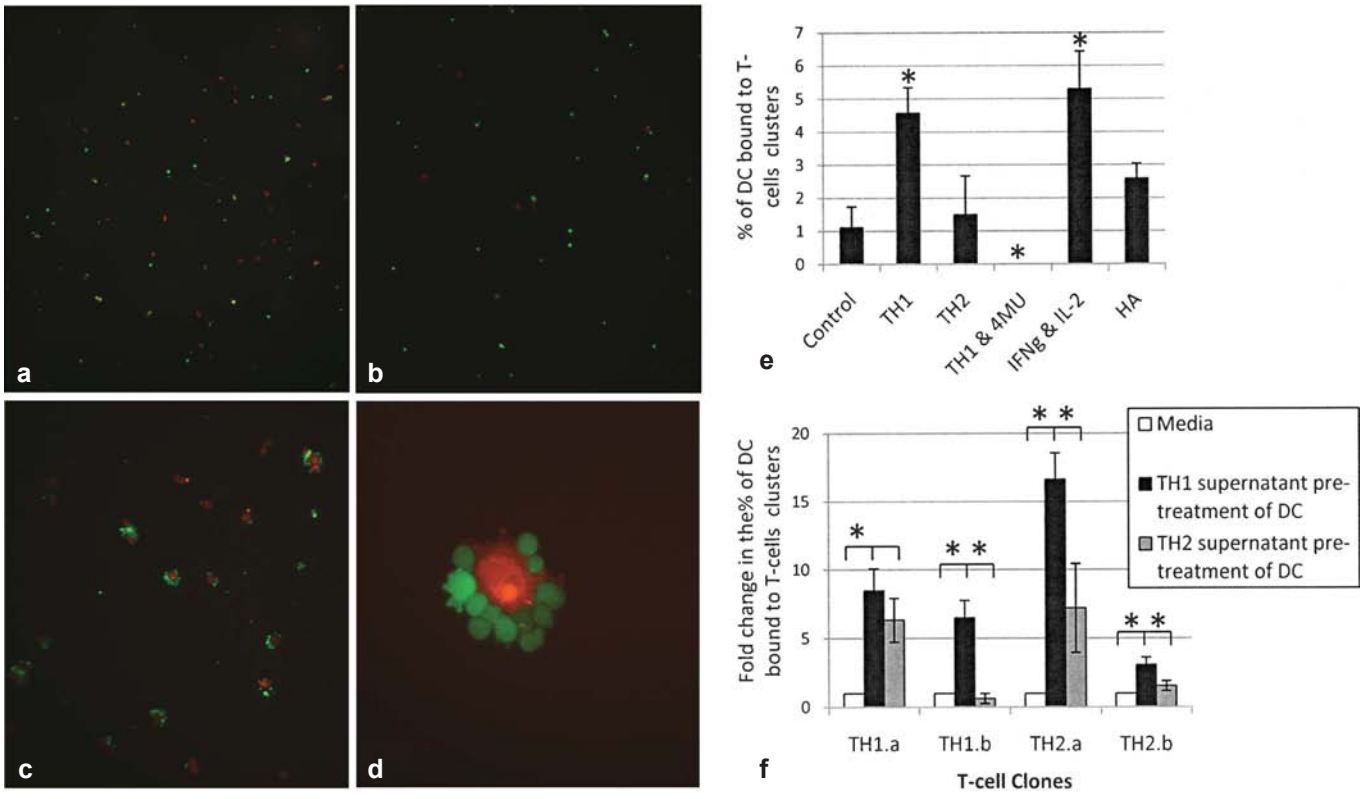

Figure 5 Treatment of DCs with Th1 cytokines promotes T-cell binding. Binding of SNARF-labeled DCs with CSFE-labeled T cells was ascertained by evaluating DC–T cell clusters. A cluster was defined as ⩾2 T cells bound to one or more DCs. The DCs were pre-treated overnight with a stock of Th1-cell culture supernatants or controls and then washed prior to the addition of the T cells. Representative images are shown for DCs pre-treated with (**a**) media alone, (**b**) Th1-cell culture supernatants and (**c**) Th1-cell culture supernatants together with 4-MU. Random fields (10–15) were evaluated per condition. The number of conjugates was normalized to the number of DCs for each field. A close-up of DC–T cell clusters present upon Th1 supernatant treatment is shown (**d**). Brightness and contrast were identical for each color in single and merged images. (**e**) The percentage of DCs pre-treated with Th1-cell culture supernatants or controls bound to activated primary T cells in a cluster. Data are representative of three separate experiments made using DCs and autologous T cells from different individuals. (**f**) Fold change in the percentage of DCs bound to T-cell clones (two Th1 and two Th2) taken from a pair of individuals (termed a and b). For each clone comparison the left bracket is for the test of significance for the Th1 supernatant condition versus media alone while the right bracket is for the Th1 supernatants comparison versus Th2 supernatants. * indicates a *P* value of <0.05. DC, dendritic cell; HA, hyaluronan; IFN, interferon; Th, T helper; 4-MU, 4-methylumbelliferone.

support the conclusion that Th1 soluble factors act on DCs in a paracrine manner to promote HA-dependent DC–T cell binding.

These experiments were repeated using Th1 and Th2 clones in order to better determine whether the effects on DC–T cell binding described here were restricted by T-cell subtype. The T-cell clones used were the same clones from which the conditioned media were derived and activated in an identical manner to the aforementioned primary T cells. These T cells were CFSE labeled and pre-treated with GolgiStop to prevent any further cytokine production by these cells. We found that in all cases T cells exhibited significantly increased binding to DCs pre-treated with Th1-conditioned media (Figure 5f). For three of the four clones analyzed, the clone bound significantly better to DCs pre-treated with Th1 cytokines, irrespective of whether the clone was a Th1 or a Th2 clone. The fourth clone, a Th1 clone, likewise demonstrated increased binding to Th1-conditioned media-treated DCs over those treated by Th2-conditioned media, but this difference was not significant (Figure 5f). These data support the conclusion that the crucial determinant in these HA-dependent binding interactions is the nature of the cytokine milieu which DCs encounter and that subsequent binding to T cells is not subtype restricted.

IFN-γ and IL-2 promote HA accumulation on dendritic processes and at the IS

Pseudopodia are cellular extensions known to be enriched for MHC class II molecules and thought to function in antigen presentation. We observed that HA tended to be concentrated on such structures upon treatment of CD4 APCs with IFN-γ and IL-2 (Figure 6a) and that these could be removed with hyaluronidase treatment (Figure 6b) and pre-treatment with 4-MU (data not shown). These structures and the HA deposits are seen clearly in cross-sectional views (Figure 6d and e).

Upon addition of activated autologous CD4 T cells to these same CD4 APCs which had been pre-treated with IFN-γ and IL-2, we observed the colocalization of HA (green) and MHC class II (red) at sites of union between cells (nuclei stained in blue) (Figure 7). MHC class II is enriched upon APCs and is a key component of the IS. The colocalization of HA and MHC class II supports the conclusion that HA is present at the IS.

DISCUSSION

We have evaluated the hypothesis that pericellular HA can function as intercellular 'glue' directly mediating T cell–DC binding. Using primary human cells, we observed HA-dependent binding between T cells and DCs. Moreover, we describe the existence of a feedforward loop wherein T-cell cytokines influence DC production of HA in a Th1-dependent manner which in turn affects the extent of DC–T cell binding in a Th1-independent manner. These data suggest that HA plays a dynamic pivotal role in DC–T cell interactions.

Human monocyte-derived DCs produce substantial cell surface-associated HA, which is associated with HAS3 expression. These results are consistent with previously published data for mouse DC

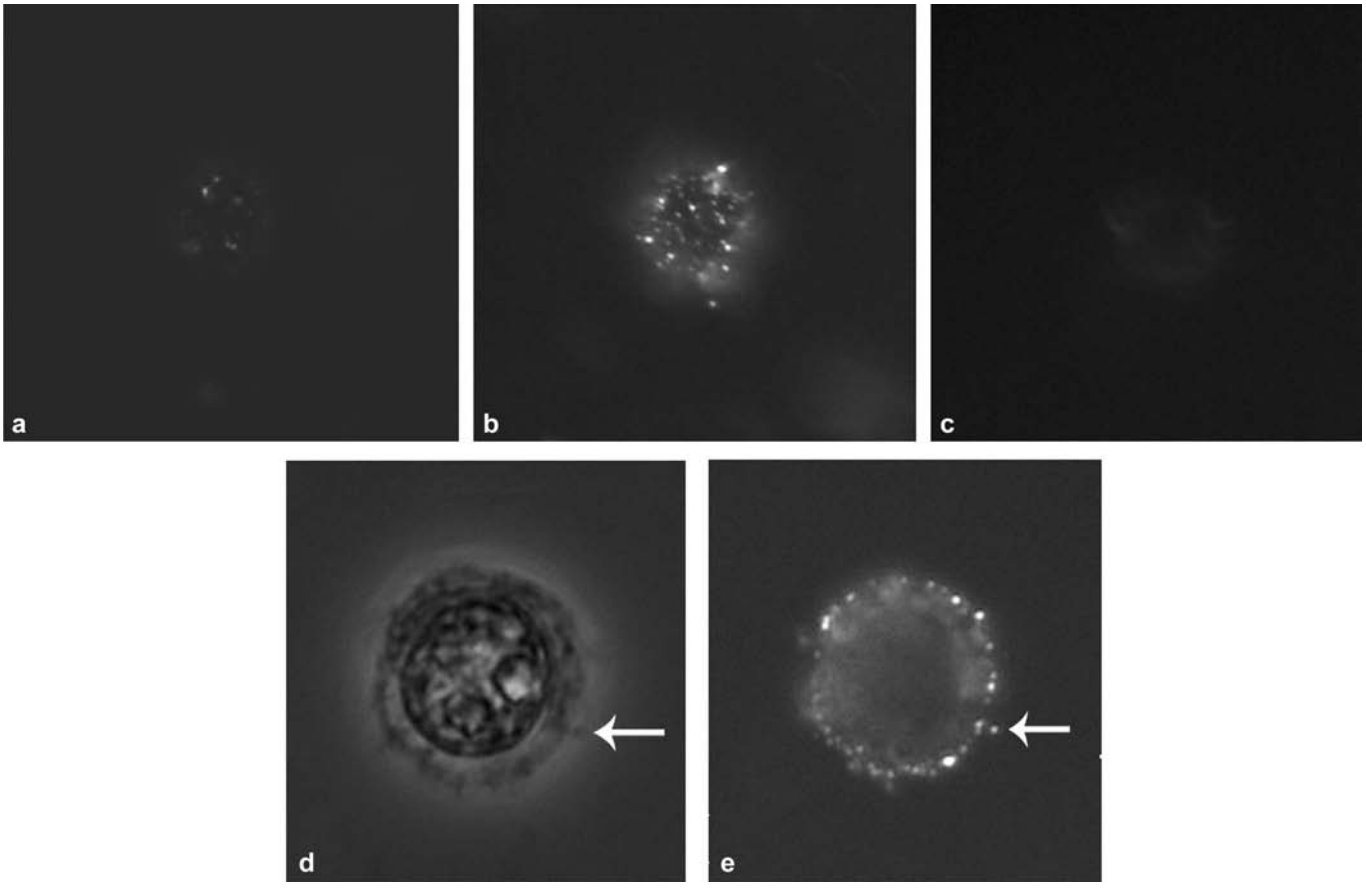

Figure 6 IFN-γ and IL-2cytokines promote HA accumulation on dendrites. (**a–d**) bPG staining of CD4 cells cultured overnight in the presence of media alone (**a**) or with the addition of IL-2 and IFN-γ (**b**). (**c**) bPG binding of IL-2/IFN-γ conditioned cells subsequently treated with HA'ase prior to staining with HABP. (**d–e**) A single cell from an IL-2 and IFN-γ conditioned culture; images are shown for both bPG staining (**d**) and phase contrast (**e**). The white arrow in both D and E points to the same pseudopodia in both views. bPG, bovine proteoglycan; DC, dendritic cell; HA, hyaluronan; HABP, hyaluronic acid binding protein; HA'ase, hyaluronidase; IFN, interferon.

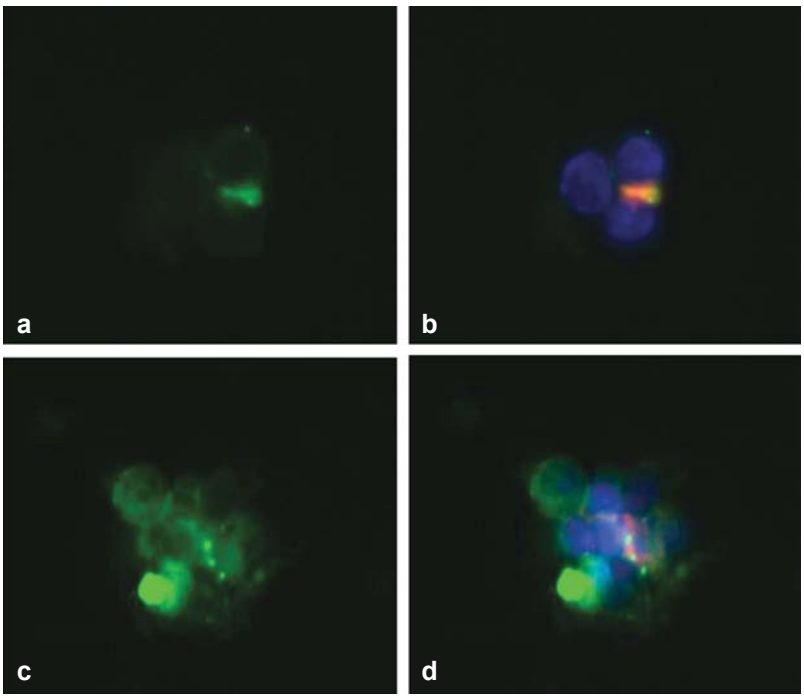

Figure 7 IFN-γ and IL-2cytokines promote focal clusters of HA accumulation at the immunological synapse. PBMCs were activated with soluble anti-CD3 and anti-CD28 Ab in the setting of exogenous IFN-γ and IL-2. Images are shown for two clusters of cells for bPG (green) alone (**a** and **c**) and for costaining for MHC class II (red) and DAPI (blue) (**b** and **d**). Treatment with 4-MU abrogated clustering as well as diminished the amount of visible hyaluronan (not shown). Brightness and contrast were identical for each color in single and merged images. This experiment was performed twice with similar results. Ab, antibodies; DAPI, 4,6-diamidino-2-phenylindole; DC, dendritic cell; HA, hyaluronan; IFN, interferon; MHC, major histocompatibility complex; PBMC, peripheral blood mononuclear cell; 4-MU, 4-methylumbelliferone.

lines and mouse bone marrow-derived DCs.[13] In contrast, we observed negligible production of HA by either freshly isolated or activated T cells. While mouse T cells are reported to produce physiologically relevant quantities of HA,[35] these data suggest that the bulk of HA present in human DC–T cell interactions is of DC origin.

Pericellular HA facilitates DC–T cell binding. 4-MU pre-treatment abrogated this binding while treatments were shown to increase HA-promoted binding. Interestingly, we find that the addition of exogenous HA to the DC–T cell cocultures did not significantly improve binding, suggesting that exogenous soluble HA was not equivalent to cell-associated HA. This binding could be mediated by interactions between HA on the surface of DCs and membrane-bound CD44 on the surface of T cells, as suggested by work with $CD44^{-/-}$ mice where CD44 expression was required on T cells but not DCs for optimal antigen presentation.[47] However, the mechanisms by which HA promotes DC–T cell binding are unlikely to be exclusively CD44 mediated. Indeed one group reported that CD44 expression on T cells is not necessary for antigen presentation by DC.[14] A variable role for charge-based interactions or the binding of other receptors to HA-associated proteoglycans could explain these conflicting data. Such alternative mechanisms could also account for data showing that the addition of an HA-binding peptide, Pep-1, did not significantly impair DC–T cell conjugate formation, whereas this treatment inhibited most other HA receptor-mediated interactions.[13] Indirect effects of HA on DC maturation and expression of adhesion molecules are also likely to contribute to binding.

Production of HA by DCs was promoted by conditioned media from Th1 clones but not Th2 clones. Similar effects were seen upon treatment with the Th1 cytokines, TNF-α and IFN-γ, in combination with IL-2. IFN-γ and TNF-α are both well known to promote antigen presentation by DCs; their effects on HA are consistent with this role. These findings square well with reports of these same cytokines alone and in concert promoting HA production by other cell types.[20–23]

These data suggest that Th1 cells may directly influence HA production by APCs by virtue of their cytokine production profiles. In the context of our aforementioned binding data, this represents a novel feedforward mechanism whereby T cells influence their own binding to DCs in an HA-dependent manner. While similar feedforward mechanisms exist elsewhere in immunology, none, to our knowledge, involve the extra-cellular matrix. Moreover, these data raise the intriguing possibility that HA production is an integral part of the Th1 program. A putative role for HA in Th1 responses is supported by reports that the viral mimetic Poly(IC)[32] and infection with the Epstein–Barr virus[48] both promote HA production.

We were interested to find that IL-2 promotes HA production by DCs because these cells do not express the high-affinity receptor for IL-2, CD25. DCs presumably respond to IL-2 through the low-affinity IL-2 receptor, CD122. We demonstrate here that monocyte-derived DCs express this receptor. CD122 expression has also been reported for bone marrow-derived DCs.[46]

We observed focal deposits of HA at sites where T cells and APCs are thought to interface. Specifically, HA deposits colocalized with MHC class II at the IS. This may help explain published data on the role of HA in antigen presentation.[11] HA deposits were also present atop cellular protrusions known to play a role in antigen presentation. Furthermore, 4-MU treatment abrogated formation of dendrites on DCs; this is consistent with reports that HA may play a role in maintaining similar structures on other cell types.[5,49,50]

IS-associated HA could contribute to antigen presentation *via* several mechanisms, potentially acting in concert. HA has osmotic properties and could promote gradients of molecules that signal at the IS.[51] HA could act as a costimulatory molecule through paracrine and/or autocrine interactions with its primary extracellular HA receptor, CD44. This molecule has been shown to complex with the T-cell antigen receptor[52] and to colocalize with lipid rafts at the IS.[47] Indeed, mice deficient for CD44 demonstrated decreased phosphotyrosine and protein kinase C-enrichment at the synapse and impaired antigen presentation.[14,47] An intriguing possibility is that HA might also directly promote the formation and stability of the IS by acting as 'intercellular glue' joining cells in apposition and impacting their engagement and activation. It is certainly the case that cells must have mechanisms for interdigitating the pericellular matrix on their surfaces, otherwise it is hard to imagine that they could achieve the close contact necessary for MHC–T-cell antigen receptor complex formation.[53–55] It seems likely that pericellular matrix interactions represent a heretofore unappreciated and potentially important level at which the IS is regulated.

ACKNOWLEDGEMENTS

This work was supported by grants from the NIH (DK46635, HL18645 and DK53004) and the JDRF (The Center for Translational Research at BRI). PLB is supported by NIH K-08 grant DK080178-01 and an NIH LRP grant. The authors would like to thank Nathan Standifer and Michael Kinsella for their helpful comments and Tuan Nguyen for tissue processing.

Note: Supplementary information is available on the Cellular & Molecular Immunology website (http://www.nature.com/cmi/).

1 Evanko SP, Tammi MI, Tammi RH, Wight TN. Hyaluronan-dependent pericellular matrix. *Adv Drug Deliv Rev* 2007; **59**: 1351–1365.
2 Haslam SM, Julien S, Burchell JM, Monk CR, Ceroni A, Garden OA *et al*. Characterizing the glycome of the mammalian immune system. *Immunol Cell Biol* 2008; **86**: 564–573.
3 Ito S. Structure and function of the glycocalyx. *Fed Proc* 1969; **28**: 12–25.
4 Ito S. Form and function of the glycocalyx on free cell surfaces. *Philos Trans R Soc Lond B Biol Sci* 1974; **268**: 55–66.
5 Rilla K, Tiihonen R, Kultti A, Tammi M, Tammi R. Pericellular hyaluronan coat visualized in live cells with a fluorescent probe is scaffolded by plasma membrane protrusions. *J Histochem Cytochem* 2008; **56**: 901–910.
6 Li Y, Heldin P. Hyaluronan production increases the malignant properties of mesothelioma cells. *Br J Cancer* 2001; **85**: 600–607.
7 Kultti A, Pasonen-Seppanen S, Jauhiainen M, Rilla KJ, Karna R, Pyoria E *et al*. 4-methylumbelliferone inhibits hyaluronan synthesis by depletion of cellular UDP-glucuronic acid and downregulation of hyaluronan synthase 2 and 3. *Exp Cell Res* 2009; **315**: 1914–1923.
8 Kakizaki I, Kojima K, Takagaki K, Endo M, Kannagi R, Ito M *et al*. A novel mechanism for the inhibition of hyaluronan biosynthesis by 4-methylumbelliferone. *J Biol Chem* 2004; **279**: 33281–33289.
9 Knudson W, Aguiar DJ, Hua Q, Knudson CB. CD44-anchored hyaluronan-rich pericellular matrices: an ultrastructural and biochemical analysis. *Exp Cell Res* 1996; **228**: 216–228.
10 de la Motte CA, Hascall VC, Calabro A, Yen-Lieberman B, Strong SA. Mononuclear leukocytes preferentially bind *via* CD44 to hyaluronan on human intestinal mucosal smooth muscle cells after virus infection or treatment with poly(I.C). *J Biol Chem* 1999; **274**: 30747–30755.
11 Evanko SP, Angello JC, Wight TN. Formation of hyaluronan- and versican-rich pericellular matrix is required for proliferation and migration of vascular smooth muscle cells. *Arterioscler Thromb Vasc Biol* 1999; **19**: 1004–1013.
12 Girish KS, Kemparaju K. The magic glue hyaluronan and its eraser hyaluronidase: a biological overview. *Life Sci* 2007; **80**: 1921–1943.
13 Mummert ME, Mummert D, Edelbaum D, Hui F, Matsue H, Takashima A. Synthesis and surface expression of hyaluronan by dendritic cells and its potential role in antigen presentation. *J Immunol* 2002; **169**: 4322–4331.
14 Do Y, Nagarkatti PS, Nagarkatti M. Role of CD44 and hyaluronic acid (HA) in activation of alloreactive and antigen-specific T cells by bone marrow-derived dendritic cells. *J Immunother* 2004; **27**: 1–12.
15 Termeer C, Benedix F, Sleeman J, Fieber C, Voith U, Ahrens T *et al*. Oligosaccharides of hyaluronan activate dendritic cells *via* Toll-like receptor 4. *J Exp Med* 2002; **195**: 99–111.
16 Bollyky PL, Falk BA, Long SA, Preisinger A, Braun KR, Wu RP *et al*. CD44 costimulation promotes FoxP3+ regulatory T cell persistence and function *via* production of IL-2, IL-10, and TGF-beta. *J Immunol* 2009; **183**: 2232–2241.
17 Huet S, Groux H, Caillou B, Valentin H, Prieur AM, Bernard A. CD44 contributes to T cell activation. *J Immunol* 1989; **143**: 798–801.
18 Jiang D, Liang J, Noble PW. Hyaluronan in tissue injury and repair. *Annu Rev Cell Dev Biol* 2007; **23**: 435–461.
19 Noble PW. Hyaluronan and its catabolic products in tissue injury and repair. *Matrix Biol* 2002; **21**: 25–29.
20 Wilkinson TS, Potter-Perigo S, Tsoi C, Altman LC, Wight TN. Pro- and anti-inflammatory factors cooperate to control hyaluronan synthesis in lung fibroblasts. *Am J Respir Cell Mol Biol* 2004; **31**: 92–99.
21 Tanimoto K, Ohno S, Fujimoto K, Honda K, Ijuin C, Tanaka N *et al*. Proinflammatory cytokines regulate the gene expression of hyaluronic acid synthetase in cultured rabbit synovial membrane cells. *Connect Tissue Res* 2001; **42**: 187–195.
22 Campo GM, Avenoso A, Campo S, Angela D, Ferlazzo AM, Calatroni A. TNF-alpha, IFN-gamma, and IL-1beta modulate hyaluronan synthase expression in human skin fibroblasts: synergistic effect by concomitat treatment with FeSO4 plus ascorbate. *Mol Cell Biochem* 2006; **292**: 169–178.
23 Campo GM, Avenoso A, Campo S, D'Ascola A, Traina P, Calatroni A. Effect of cytokines on hyaluronan synthase activity and response to oxidative stress by fibroblasts. *Br J Biomed Sci* 2009; **66**: 28–36.
24 Chenevier-Gobeaux C, Morin-Robinet S, Lemarechal H, Poiraudeau S, Ekindjian JC, Borderie D. Effects of pro- and anti-inflammatory cytokines and nitric oxide donors on hyaluronic acid synthesis by synovial cells from patients with rheumatoid arthritis. *Clin Sci (Lond)* 2004; **107**: 291–296.
25 Girard N, Maingonnat C, Bertrand P, Vasse M, Delpech B. Hyaluronectin secretion by monocytes: downregulation by IL-4 and IL-13, upregulation by IL-10. *Cytokine* 1999; **11**: 579–584.
26 Wang L, Teng W, Shan Z. Effect of IFN-gamma, IL-4 on proliferation and synthesis of hyaluronic acid and collagen in cultured human retroorbital fibroblasts *in vitro*. *Chin Med J (Engl)* 2000; **113**: 907–910.
27 Han R, Smith TJ. T helper type 1 and type 2 cytokines exert divergent influence on the induction of prostaglandin E2 and hyaluronan synthesis by interleukin-1beta in orbital fibroblasts: implications for the pathogenesis of thyroid-associated ophthalmopathy. *Endocrinology* 2006; **147**: 13–19.
28 Reijonen H, Novak EJ, Kochik S, Heninger A, Liu AW, Kwok WW *et al*. Detection of GAD65-specific T-cells by major histocompatibility complex class II tetramers in type 1 diabetic patients and at-risk subjects. *Diabetes* 2002; **51**: 1375–1382.
29 Shih SC, Smith LE. Quantitative multi-gene transcriptional profiling using real-time PCR with a master template. *Exp Mol Pathol* 2005; **79**: 14–22.
30 Agren UM, Tammi R, Tammi M. A dot-blot assay of metabolically radiolabeled hyaluronan. *Anal Biochem* 1994; **217**: 311–315.
31 Lin W, Shuster S, Maibach HI, Stern R. Patterns of hyaluronan staining are modified by fixation techniques. *J Histochem Cytochem* 1997; **45**: 1157–1163.
32 Potter-Perigo S, Johnson PY, Evanko SP, Chan CK, Braun KR, Wilkinson TS *et al*. Poly I:C stimulates versican accumulation in the extracellular matrix promoting monocyte adhesion. *Am J Respir Cell Mol Biol* 2009; in press.
33 Mapleson JL, Buchwald M. Effect of cycloheximide and dexamethasone phosphate on hyaluronic acid synthesis and secretion in cultured human skin fibroblasts. *J Cell Physiol* 1981; **109**: 215–222.
34 Agren UM, Tammi R, Tammi M. A dot-blot assay of metabolically radiolabeled hyaluronan. *Anal Biochem* 1994; **217**: 311–315.
35 Mahaffey CL, Mummert ME. Hyaluronan synthesis is required for IL-2-mediated T cell proliferation. *J Immunol* 2007; **179**: 8191–8199.
36 Nakamura T, Takagaki K, Shibata S, Tanaka K, Higuchi T, Endo M. Hyaluronic-acid-deficient extracellular matrix induced by addition of 4-methylumbelliferone to the medium of cultured human skin fibroblasts. *Biochem Biophys Res Commun* 1995; **208**: 470–475.
37 Tanaka K, Taniguchi R, Higuchi T, Ozaki T, Mizunuma H, Takagaki K. 4-methylumbelliferone inhibits hyaluronate synthesis in human uterine cervical fibroblasts. *J Obstet Gynaecol Res* 2007; **33**: 772–776.
38 Chajara A, Raoudi M, Delpech B, Leroy M, Basuyau JP, Levesque H. Circulating hyaluronan and hyaluronidase are increased in diabetic rats. *Diabetologia* 2000; **43**: 387–388.
39 Chajara A, Raoudi M, Delpech B, Leroy M, Basuyau JP, Levesque H. Increased hyaluronan and hyaluronidase production and hyaluronan degradation in injured aorta of insulin-resistant rats. *Arterioscler Thromb Vasc Biol* 2000; **20**: 1480–1487.
40 Blanco P, Palucka AK, Pascual V, Banchereau J. Dendritic cells and cytokines in human inflammatory and autoimmune diseases. *Cytokine Growth Factor Rev* 2008; **19**: 41–52.
41 Sampson PM, Rochester CL, Freundlich B, Elias JA. Cytokine regulation of human lung fibroblast hyaluronan (hyaluronic acid) production. Evidence for cytokine-regulated hyaluronan (hyaluronic acid) degradation and human lung fibroblast-derived hyaluronidase. *J Clin Invest* 1992; **90**: 1492–503.
42 Pulimood AB, Ramakrishna BS, Rita AB, Srinivasan P, Mohan V, Gupta S *et al*. Early activation of mucosal dendritic cells and macrophages in acute Campylobacter colitis and cholera: an *in vivo* study. *J Gastroenterol Hepatol* 2008; **23**: 752–758.

43 Newton PJ, Weller IV, Katz DR, Chain BM. Autologous apoptotic T cells interact with dendritic cells, but do not affect their surface phenotype or their ability to induce recall immune responses. *Clin Exp Immunol* 2003; **133**: 50–58.
44 Ito T, Amakawa R, Inaba M, Ikehara S, Inaba K, Fukuhara S. Differential regulation of human blood dendritic cell subsets by IFNs. *J Immunol* 2001; **166**: 2961–2969.
45 Koski GK, Lyakh LA, Rice NR. Rapid lipopolysaccharide-induced differentiation of CD14(+) monocytes into CD83(+) dendritic cells is modulated under serum-free conditions by exogenously added IFN-gamma and endogenously produced IL-10. *Eur J Immunol* 2001; **31**: 3773–3781.
46 Bykovskaja SN, Buffo MJ, Bunker M, Zhang H, Majors A, Herbert M *et al*. Interleukin-2-induces development of denditric cells from cord blood CD34+ cells. *J Leukoc Biol* 1998; **63**: 620–630.
47 Hegde VL, Singh NP, Nagarkatti PS, Nagarkatti M. CD44 mobilization in allogeneic dendritic cell-T cell immunological synapse plays a key role in T cell activation. *J Leukoc Biol* 2008; **84**: 134–142.
48 Stuhlmeier KM. Hyaluronan production in synoviocytes as a consequence of viral infections: HAS1 activation by Epstein-Barr virus and synthetic double- and single-stranded viral RNA analogs. *J Biol Chem* 2008; **283**: 16781–16789.
49 Rilla K, Siiskonen H, Spicer AP, Hyttinen JM, Tammi MI, Tammi RH. Plasma membrane residence of hyaluronan synthase is coupled to its enzymatic activity. *J Biol Chem* 2005; **280**: 31890–31897.
50 Knudson CB, Nofal GA, Pamintuan L, Aguiar DJ. The chondrocyte pericellular matrix: a model for hyaluronan-mediated cell-matrix interactions. *Biochem Soc Trans* 1999; **27**: 142–147.
51 Knepper MA, Saidel GM, Hascall VC, Dwyer T. Concentration of solutes in the renal inner medulla: interstitial hyaluronan as a mechano-osmotic transducer. *Am J Physiol Renal Physiol* 2003; **284**: F433–F446.
52 Yashiro-Ohtani Y, Zhou XY, Toyo-oka K, Tai XG, Park CS, Hamaoka T *et al*. Non-CD28 costimulatory molecules present in T cell rafts induce T cell costimulation by enhancing the association of TCR with rafts. *J Immunol* 2000; **164**: 1251–1259.
53 Grakoui A, Bromley SK, Sumen C, Davis MM, Shaw AS, Allen PM *et al*. The immunological synapse: a molecular machine controlling T cell activation. *Science* 1999; **285**: 221–227.
54 Dustin ML. T-cell activation through immunological synapses and kinapses. *Immunol Rev* 2008; **221**: 77–89.
55 Bromley SK, Burack WR, Johnson KG, Somersalo K, Sims TN, Sumen C *et al*. The immunological synapse. *Annu Rev Immunol* 2001; **19**: 375–396.

ECM components guide IL-10 producing regulatory T-cell (TR1) induction from effector memory T-cell precursors

Paul L. Bollyky[a,b,1], Rebecca P. Wu[a], Ben A. Falk[a], James D. Lord[a], S. Alice Long[a], Anton Preisinger[a], Brandon Teng[a], Gregory E. Holt[c], Nathan E. Standifer[d], Kathleen R. Braun[a], Cindy Fang Xie[a], Peter L. Samuels[a], Robert B. Vernon[a], John A. Gebe[a], Thomas N. Wight[a], and Gerald T. Nepom[a]

[a]Benaroya Research Institute at Virginia Mason, Seattle, WA 98101; [b]Division of Allergy and Infectious Diseases, University of Washington Medical Center, Seattle, WA 98195; [c]Division of Pulmonary, Critical Care and Sleep Medicine, University of Miami, Miami, FL 33136; and [d]Clinical Immunology, Amgen, Seattle, WA 98119-3105

Edited by Ron Germain, National Institute of Allergy and Infectious Diseases, and accepted by the Editorial Board March 31, 2011 (received for review November 18, 2010)

We describe a role for ECM as a biosensor for inflammatory microenvironments that plays a critical role in peripheral immune tolerance. We show that hyaluronan (HA) promotes induction of Foxp3- IL-10–producing regulatory T cells (TR1) from conventional T-cell precursors in both murine and human systems. This is, to our knowledge, the first description of an ECM component inducing regulatory T cells. Intact HA, characteristic of healing tissues, promotes induction of TR1 capable of abrogating disease in an IL-10–dependent mouse colitis model whereas fragmentary HA, typical of inflamed tissues, does not, indicating a decisive role for tissue integrity in this system. The TR1 precursor cells in this system are $CD4^+CD62L^-FoxP3^-$, suggesting that effector memory cells assume a regulatory phenotype when they encounter their cognate antigen in the context of intact HA. Matrix integrity cues might thereby play a central role in maintaining peripheral tolerance. This TR1 induction is mediated by CD44 cross-linking and signaling through p38 and ERK1/2. This induction is suppressed, also in a CD44-dependent manner, by osteopontin, a component of chronically inflamed ECM, indicating that CD44 signaling serves as a nexus for fate decisions regarding TR1 induction. Finally, we demonstrate that TR1 induction signals can be recapitulated using synthetic matrices. These results reveal important roles for the matrix microenvironment in immune regulation and suggest unique strategies for immunomodulation.

The tissue microenvironment undergoes major changes during inflammation and its resolution. We have studied the role of the ECM as a communications bridge to the adaptive immune system, informing infiltrating lymphocytes regarding the tissue status and guiding subsequent responses. In particular we have examined the interplay between the TR1 regulatory T cell subset and hyaluronan (HA), a component of ECM.

TR1 cells are $CD4^+FOXP3^-$ regulatory cells that play a crucial role in resolving inflammation and maintaining peripheral immune tolerance (1). TR1 mediate contact-independent immune tolerance through the secretion of substantial amounts of IL-10 (2). Although diverse experimental conditions have been used in TR1 induction (1, 3–8), the specific progenitor population and governing factors in vivo are unclear (1).

HA is a long, highly charged disaccharide with prominent roles in structural biology, wound healing, and immunology. The size of HA in a wound environment is known to correlate with the stage of injury and its resolution (9). Low molecular weight HA (LMW-HA; <15 saccharides; <3 kDa) predominate during acute and persistent inflammation and have been demonstrated to be proinflammatory and proangiogenic. Conversely, intact high molecular weight HA (HMW-HA) predominates in noninflamed or healing tissues and is thought to be inert or anti-inflammatory (9) We previously identified a role for HMW-HA in promoting the persistence and function of established $FoxP3^+$ natural T regulatory cells (nTregs) (10–12). nTregs are another regulatory T cell subset that are thought to primarily arise in the thymus (13). HA was recently reported to promote IL-10 production in intestinal biopsies upon oral administration (14). However, to our knowledge, ECM components have not been implicated in the induction of regulatory T cells and there are no described roles for HA or CD44, the primary HA receptor, in TR1 biology.

Given that TR1 cells are induced in peripheral tissues, presumably in response to local environmental cues, we hypothesized that HMW-HA may promote TR1 induction. Here we evaluate this hypothesis and the role of CD44 signaling as a nexus for fate decisions regarding TR1 induction. Finally, we use synthetic matrices to recapitulate matrix integrity cues and promote TR1 induction.

Results

Intact HA Promotes TR1 Induction from Effector Memory T-Cell Precursors. To ascertain the contribution of ECM components to TR1 induction, we devised an in vitro activation assay using immobilized plate-bound ECM components (Fig. S1*A*). To exclude $FOXP3^+$ nTregs, we used GFP/FOXP3 knock-in mice and depleted the $CD4^+$ T cells isolated from these animals of GFP/$FOXP3^+$ cells. HMW-HA had a capacity to promote IL-10 whereas other ECM molecules did not (Fig. 1*A*). HMW-HA. but not LMW-HA generated from the same HMW-HA, promoted production of IL-10 protein (Fig. 1*B*) and mRNA (Fig. S1*B*), implicating a decisive role for HA integrity in this system. Significant enhancement of other TH1, TH2, or TH17 cytokines tested was not observed (Fig. 1*C*). IFN-γ and TNF-α were increased but not significantly ($P = 0.079$ and $P = 0.504$, respectively). Blocking antibodies directed against IFN-γ or TNF-α did not diminish HA-mediated IL-10 production (Fig. S1*C*). TGF-β was not significantly increased (Fig. S1*D*). By using tissues from GFP/IL-10 knock-in mice, we found that, whereas a fraction of induced GFP/$IL\text{-}10^+$ cells produced IFN- γ^+, induced TR1 cells were otherwise negative for TNF-α, IL-2, IL-4, and IL-17 production (Fig. S1*E*). The effect of HMW-HA was dependent on TCR ligation (Fig. 1*D*). Cells induced to express IL-10 by HMW-HA costimulation retained this property even after being washed and restimulated with PMA/ionomycin (Fig. S1*F*).

Author contributions: P.L.B., J.A.G., and G.T.N. designed research; P.L.B., R.P.W., B.A.F., A.P., B.T., K.R.B., and C.F.X. performed research; P.L.S., R.B.V., and T.N.W. contributed new reagents/analytic tools; P.L.B., J.D.L., S.A.L., G.E.H., N.E.S., and J.A.G. analyzed data; and P.L.B. and G.T.N. wrote the paper.

The authors declare no conflict of interest.

This article is a PNAS Direct Submission. R.G. is a guest editor invited by the Editorial Board.

[1]To whom correspondence should be addressed. E-mail: pbollyky@benaroyaresearch.org.

This article contains supporting information online at www.pnas.org/lookup/suppl/doi:10.1073/pnas.1017360108/-/DCSupplemental.

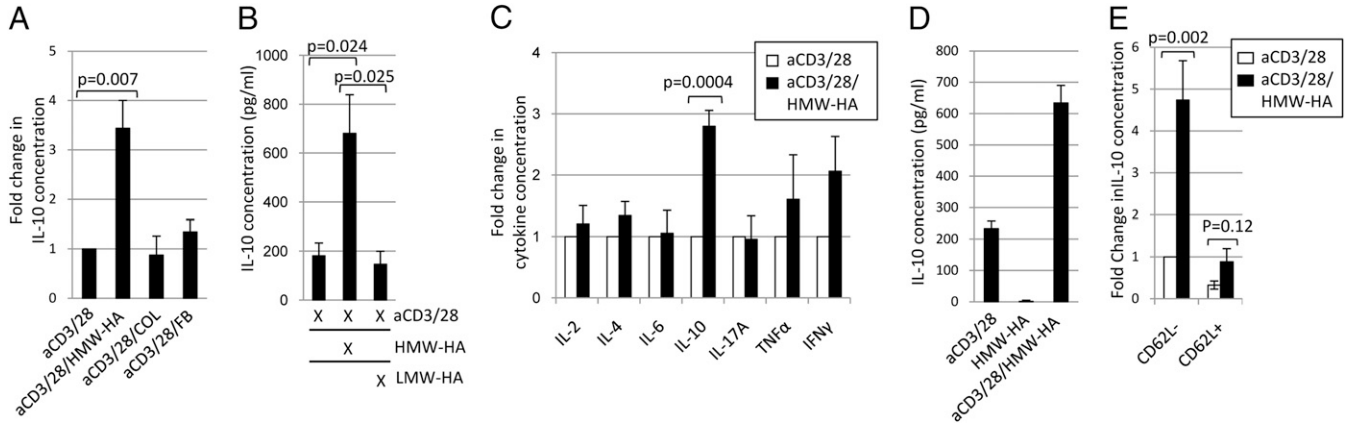

Fig. 1. HMW-HA costimulation induces a TR1-like phenotype in CD4$^+$GFP/FoxP3$^-$CD62L$^-$ effector memory T cells. (*A*) IL-10 production upon activation with aCD3/28 alone or in conjunction with the ECM components HMW-HA, COL, and fibrinogen (FB). (*B*) Effects of HMW-HA or LMW-HA treatment on IL-10 production. (*C*) Fold change in TH1, TH2, and TH17 cytokines levels upon HMW-HA costimulation ($n \geq 5$ independent experiments each for *A*–*C*). (*D*) IL-10 production upon activation with aCD3/28, HMW-HA alone, or the two reagents in combination. Each condition was performed in triplicate; the image is representative of three experiments. (*E*) Fold change in IL-10 concentration in cell culture supernatants taken from mouse CD4$^+$GFP/FoxP3$^-$ T cells sorted on the basis of CD62L expression and activated with or without HMW-HA ($n = 6$). For *A*, *C*, and *E*, data were normalized to the aCD3/28 condition, with this value equaling 1 for each experiment.

HMW-HA disproportionately promoted IL-10 production in the effector memory CD62L$^-$ fraction of CD4$^+$ T cells (Fig. 1*E*). CD62L$^-$ T cells are known to express CD44 at high levels (15), a phenotypic characteristic likely to be important in interactions with HMW-HA. In contrast, the CD62L$^+$ T cell fraction after activation produced similar amounts of IL-10 with or without HMW-HA, at levels comparable to anti-CD3 (aCD3)/28/HMW-HA treatment of freshly isolated CD62L$^-$ cells (Fig. S1*G*).

HA-Induced TR1 Cells Are Functional. The RAG.1$^{-/-}$ mouse colitis model is a well established system for evaluating IL-10–dependent regulatory T-cell effects. The infusion of CD4$^+$CD45RB^{hi} naive effector T cells typically causes colitis in these animals whereas the coinfusion of regulatory T cells abrogates colitis in an IL-10–dependent manner (9, 17). We used this model system to evaluate the regulatory capacity of TR1 cells induced with HMW-HA. Mice that received CD4$^+$FoxP3-depleted T cells activated with aCD3/28/HMW-HA exhibited significantly improved survival relative to animals that received the same cells activated with aCD3/28 alone. Freshly isolated CD4$^+$GFP/FOXP3$^+$ nTreg cells completely abrogated disease whereas infusion of PBS solution alone in conjunction with the CD4$^+$CD45RB^{hi} naive effector T cells led to the demise of 90% of the animals in that experimental group (Fig. 2*A*). These effects on survival occurred in conjunction with diminished colitis (Fig. 2*B*). Representative colonic sections clearly indicate

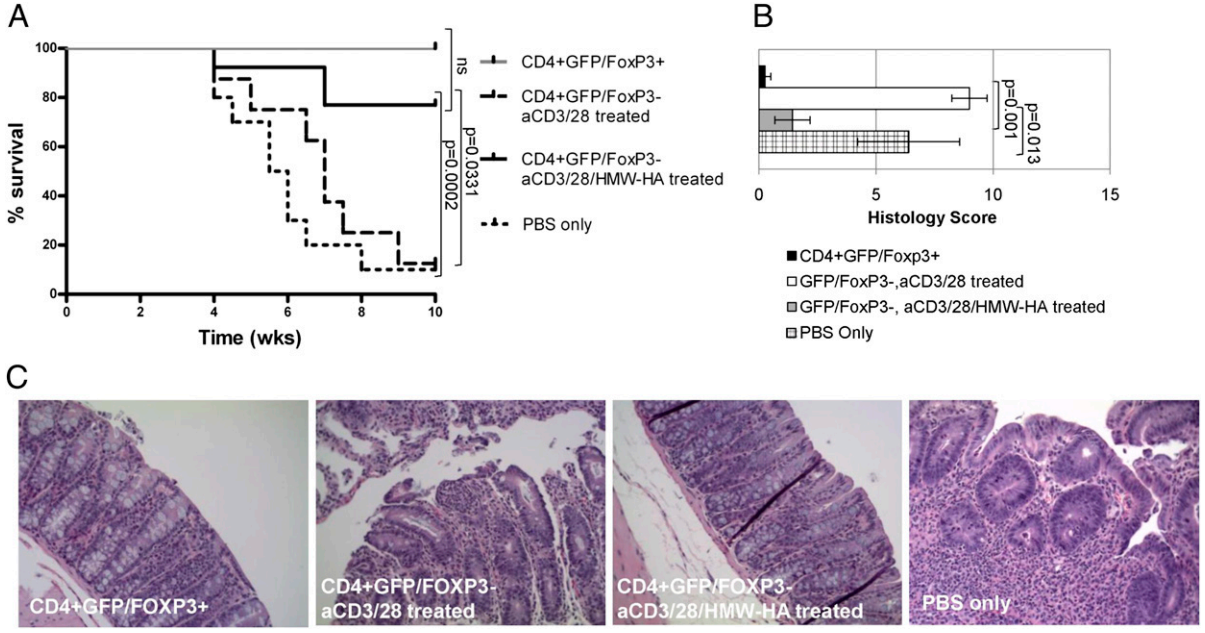

Fig. 2. Generated TR1 can suppress the development of colitis. (*A*) Impact of putative TR1 and controls on survival in an IL-10–dependent mouse colitis model (average $n = 12$ mice per group). (*B*) Histology scores for the colitis seen in the mice in *A*. (*C*) Representative histology of colon sections taken from the mice in *A* demonstrates goblet cell depletion, inflammatory infiltrate, epithelial shedding, and crypt microabscesses only in mice receiving aCD3/28-treated T cells or PBS solution.

the presence of healthy tissue with substantial numbers of goblet cells in animals treated with $CD4^+GFP/FOXP3^+$ nTregs or $CD4^+GFP/FOXP3^-$ cells treated with aCD3/28/HMW-HA. However, in mice that received $CD4^+GFP/FOXP3^-$ cells treated with aCD3/28 alone or PBS solution, pathologic features consistent with colitis are seen (Fig. 2*C*).

HA Induction of TR1 Cells Is CD44-Dependent. CD44 is the primary cell-surface receptor for HA (17). We found that $CD44^{-/-}$ mice exhibited significant impairment of IL-10 up-regulation in response to HMW-HA (Fig. 3*A*). This indicates that CD44 is necessary for HMW-HA–mediated induction of IL-10. Consistent with this, costimulation of WT $CD4^+GFP/FOXP^-$ T cells with plate-bound aCD44 robustly induced IL-10 production at the level of protein (Fig. 3*B*) and mRNA (Fig. S2*A*). However, soluble aCD44 did not up-regulate IL-10 production, revealing a requirement for CD44 cross-linking (Fig. 3*B*). The increase in IL-10 upon CD44 cross-linking was still observed following normalization to proliferation (Fig. 3*C*), dispelling the possibility that the IL-10 increase was an artifact of enhanced proliferation. Antibodies directed at ICOS-1, a costimulatory molecule with roles in T-cell activation (18), were included as a control. Unlike the cytokine profile observed upon HMW-HA treatment, CD44 cross-linking also significantly increased TNF-α and IFN-γ (Fig. S2*B*). Neither WT nor $CD44^{-/-}$ mice had detectable $CD4^+IL\text{-}10^+$ splenocytes directly ex vivo (Fig. S2*C*).

TR1 cells induced with CD44 cross-linking were functional, as demonstrated in vitro (Fig. 3*D*). However, this suppressive function was lost when T cells from $IL\text{-}10^{-/-}$ mice were used as a source of TR1 cells. Of note, CD44 costimulation of mouse $CD4^+GFP/FoxP3^-$ cells did not induce FoxP3 expression (Table S1).

Although CD44 facilitates signaling through numerous pathways, IL-10 production is reported to be primarily the product of signaling through MAP kinases, particularly those involving p38 and ERK1/2 (19). Intracellular staining for IL-10 after CD44 costimulation identified enhanced IL-10 production that was lost upon addition of specific small-molecule inhibitors of ERK1/2 and p38 signaling but not upon inhibition of MEK1 (Fig. 3*E* and *F*). This indicates that CD44 cross-linking promotes IL-10 production via a MAP kinase-dependent pathway. Consistent with this, we found that treatment with aCD44 together with a cross-linking antibody led to enhanced phosphorylation of both p38 and ERK1/2, which peaked 10 min after activation (Fig. S3 *A* and *B*). If either the cross-linking Ab or the aCD44 Ab was left out, enhanced phosphorylation of p38 and ERK1/2 was not seen. Exogenous IL-2 had a negligible impact on p38 and ERK/1/2 phosphorylation (Fig. S3 *C* and *D*). The experiments in Fig. S3 *A*–*D* were performed using human $CD4^+CD25^-$ T cells; similar results were seen with mouse cells (Fig. S3 *E* and *F*). As with HMW-HA, CD44 cross-linking disproportionately promoted IL-10 production in the $CD62L^-$, effector memory population (Fig. 3*G*).

Intact HA Promotes Induction of Human TR1. Costimulation of human $CD4^+CD25^-$ T cells with either HMW-HA or anti-CD44 antibodies significantly increased IL-10 production (Fig. S4*A*) and generated functional TR1 cells (Fig. S4*B*) but did not promote induction of Foxp3 (Fig. S4*C*). We therefore conclude that HMW-HA and CD44 also promote TR1 induction from human conventional T cells.

Exogenous IL-2 Boosts HMW-HA Induced IL-10 Production. Exogenous IL-2 significantly increased IL-10 production in the presence of plate-bound HMW-HA (Fig. S5). However, the enhanced IL-10 production seen upon IL-2 addition to the aCD3/28 condition did not reach statistical significance, leading us to suspect that

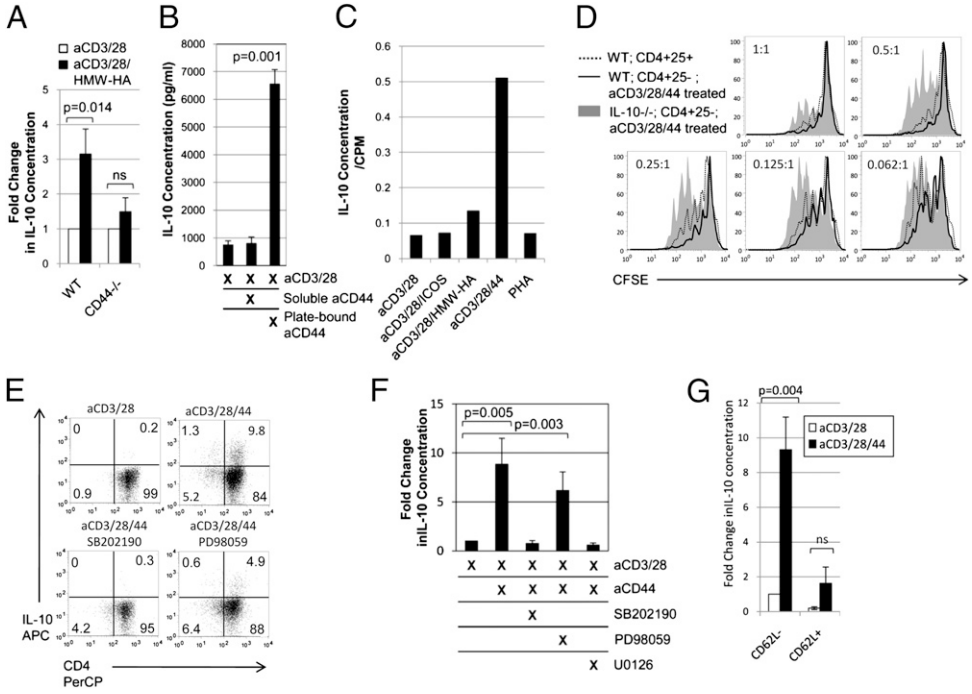

Fig. 3. CD44 cross-linking promotes MAP kinase-dependent IL-10 production. (*A*) HMW-HA–induced IL-10 production using WT or $CD44^{-/-}$ precursor T cells ($n = 7$). (*B*) IL-10 production upon costimulation with plate-bound or soluble aCD44 ($n = 5$). (*C*) Effects of CD44 cross-linking on IL-10 production, normalized to proliferation. Data are expressed as pg/mL of IL-10 produced on a per-cpm basis. (*D*) Suppression assay using TR1 cells induced with aCD44 costimulation. *C* and *D* are each representative of two experiments. Representative intracellular staining (*E*) and fold change in IL-10 production (*F*) following treatment with aCD44 and selective inhibitors of p38 (SB202190), ERK1/2 (UO126), and MEK (PD98059; $n = 5$). (*G*) Fold change in IL-10 concentration in cell culture supernatants taken from mouse $CD4^+GFP/FoxP3^-$ T cells sorted on the basis of CD62L expression and activated with or without aCD44 Ab. Data were normalized to the aCD3/28 condition of the $CD62L^-$ population, with this value equaling 1 for each experiment ($n = 4$).

the beneficial effect on IL-10 production previously reported for IL-2 (20) may not be relevant at the low levels of TCR activation used in our system.

Osteopontin Abrogates HA TR1 Induction in a CD44-Dependent Manner. In healing tissues, HA typically exists in the context of a complex ECM. We therefore asked whether other ECM components that are also CD44 ligands might impact the HA-mediated effect on TR1 induction described here. Osteopontin (OPN) is a matrix glycoprotein found in abundance in chronic inflammation and known to exacerbate autoimmunity (21, 22). Given that OPN is known to impact IL-10 production and is a CD44 ligand (23, 24), we explored the hypothesis that OPN inhibits HA-mediated TR1 induction. OPN decreased basal levels of IL-10 production seen upon aCD3/28 activation alone and negated the increase in IL-10 production seen upon HMW-HA costimulation in a dose-dependent manner (Fig. 4*A*). This was also the case for mRNA expression (Fig. S6*A*). OPN inhibited HMW-HA–mediated IL-10 production to an equivalent extent irrespective of IL-2 supplementation (Fig. S6*B*), indicating that OPN acts distal to or independent of STAT5 signaling.

OPN effects are known to be mediated by interactions with both CD44, as well as to the αVβ3 integrin receptor, to which it binds via an RGD motif (23). We observed that the decrease in basal IL-10 production upon OPN treatment was lost in CD44$^{-/-}$ mice (Fig. 4*B*), implicating CD44 in OPN effects on IL-10. However, addition of RGD peptide, but not RGE control peptide (Fig. 4*C*) or addition of an agonist antibody directed at the β3 integrin receptor subunit (Fig. 4*D*), blocked the suppression of IL-10 production by OPN. These data implicate roles for both CD44 and β3 in OPN effects on HA-mediated IL-10 production and indicate a nexus for regulatory control of the TR1 pathway by ECM components.

Synthetic ECM Hydrogel Promotes IL-10 Production. We explored the potential of biomimetics of HA-containing matrix to induce IL-10 production. Extracel is a commercially available HMW-HA and collagen (COL)-based hydrogel preparation (25), which we modified to deliver a polyclonal antigenic stimulus through the addition of streptavidin and biotinylated aCD3 before polymerization, referred to henceforth as an HA/COL gel. A schematic of this design is shown (Fig. 5*A*). CD4^{+}GFP/FOXP3^{-} T cells activated using this platform produced IL-10 in comparable quantities to that seen with plate-bound activation. Matrigel or a fibrin hydrogel did not promote IL-10 induction (Fig. 5*B*).

In tissues, IL-2 is associated with sulfated proteoglycans such as heparan sulfate (HS), possibly prolonging its half-life and function (26, 27). We therefore asked whether a synthetic matrix containing HS could be used to deliver IL-2 in conjunction with the other signals necessary for TR1 induction. Extracel-HP, a hydrogel preparation that incorporates HS in addition to collagen and HMW-HA (henceforth referred to as HA/HS/COL gel), engendered equivalent IL-10 production in the absence of exogenous IL-2. Upon IL-2 supplementation the amount of IL-10 produced was significantly increased in the setting of HA/HS/COL gel ($P = 0.037$) but not HA/COL gel ($P = 0.23$) relative to plate-bound HMW-HA (Fig. 5*C*). This is consistent with reports of enhanced functionality of cytokines in HS-bound form (28, 29). Representative staining data are shown in Fig. 5*D*. This enhancement of TR1 induction was not associated with increases in other Th1, Th2, or TH17 cytokines (Fig. 5*E*). We confirmed that HA/HS/COL gel retains IL-2 (Fig. S7).

Discussion

The local inflammatory milieu and the ECM in particular are underappreciated partners of the adaptive immune response. Herein we provide evidence of ECM modulation and control of IL-10 production, a key immunoregulatory cytokine in peripheral tissues. By using both mouse and human cells, we show that intact HA promotes induction of Foxp3^{-} IL-10–producing T cells with regulatory properties (i.e., TR1 cells) and that these function in vivo.

The TR1 cells described here differ from TR1 cells described previously in that the TR1 progenitor cells in this system are CD4^{+}CD62L^{-} effector memory cells rather than naive cells (1). This suggests that these cells have previously encountered their cognate antigens and assume a regulatory phenotype when they do so again in the context of HMW-HA. HA-induced TR1 may function in multiple stages of inflammation, as has been proposed for other TR1 (1). Our colitis data suggest that HA-induced TR1 can prevent inflammation. Conversely, a role for HA-induced TR1 in the resolution of inflammation is raised by our report that TH1 cytokines promote HA production by dendritic cells (DC) (30). Matrix integrity cues might thereby play a central role in maintaining peripheral tolerance to self antigens.

The exclusivity with which HMW-HA treatment, and particularly HMW-HA–based hydrogels, promoted IL-10 production is also noteworthy and differs from some other described TR1 cells (1). In particular, we did not observe significantly enhanced production of IFN-γ or other cytokines variably associated with TR1 cells (1). Nor did we observe induction of FoxP3, a signaling

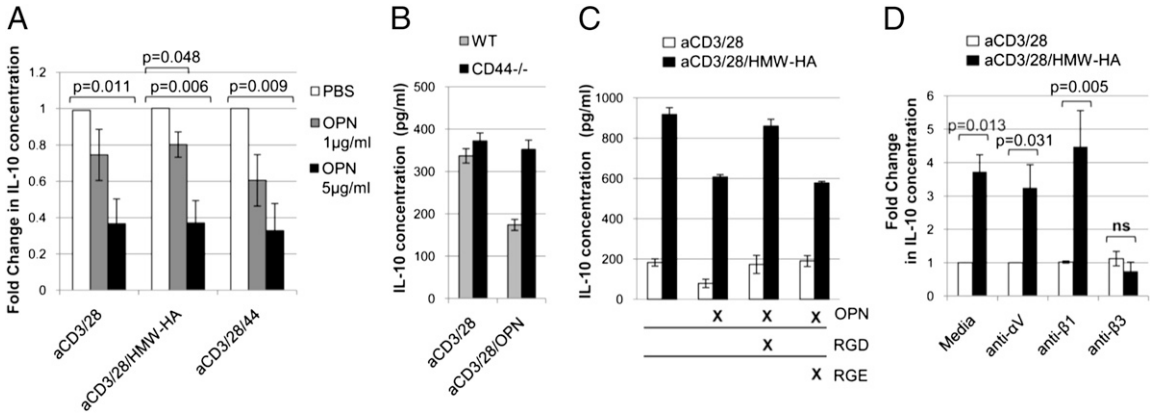

Fig. 4. OPN abrogates HMW-HA–mediated IL-10 production. (*A*) Effects of OPN concentration on IL-10 production ($n = 3$). (*B*) Effect of OPN on IL-10 production by WT and CD44$^{-/-}$ T cells. (*C*) Effect of RGD or RGE peptides on OPN-mediated suppression of IL-10 production. Data for *B* and *C* are each representative of three experiments. (*D*) Effects of integrin antibodies on HMW-HA–mediated IL-10 production ($n = 5$).

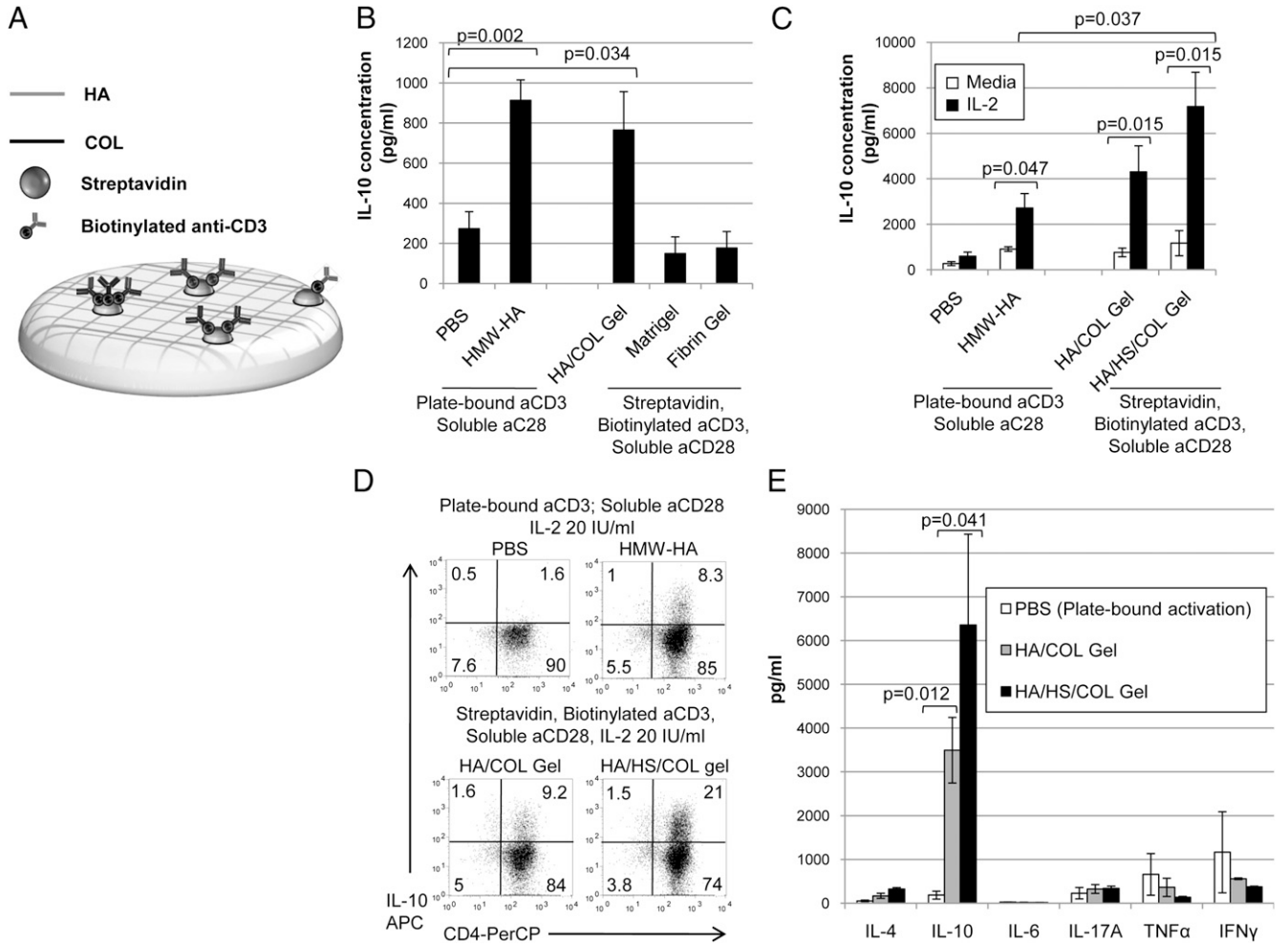

Fig. 5. A synthetic matrix promotes TR1 induction. (*A*) Schematic of a hydrogel that delivers a set of stimuli capable of inducing TR1 from conventional T-cell precursors. (*B*) IL-10 production following plate-based or hydrogel-based activation (n = 5). (*C*) The impact of supplemental IL-2 on IL-10 production in the setting of plate-based or HA/COL (Extracel) or HA/COL/HS (Extracel-HP) hydrogels (n = 5). (*D*) Representative intracellular staining for IL-10 under these same conditions. (*E*) Levels of TH1, TH2, and TH17 cytokines upon hydrogel-based activation (n = 3).

molecule associated with Tregs. As we previously reported that HMW-HA promotes Foxp3 expression by mature Tregs (10–12), this suggests differences between HMW-HA-mediated modulation of different regulatory T-cell types. Another mechanistic distinction is that intact HA promotes TGF-β production by Treg cells (11) but not TR1. Given that CD44v isoforms possess diverse ECM ligand specificities (31), it is also possible that other ECM components may differentially interact with specific regulatory subsets (30) in a highly contextual and specific manner.

We identify two levels of regulation that modulate the capability of HA to induce TR1 regulatory cells. The first is the size of HA in the system. Although HMW-HA, characteristic of healing or uninjured tissues, promotes IL-10 production, fragmentary LMW-HA, indicative of active tissue injury, does not, indicating a decisive role for HA integrity in TR1 induction. It is known that the length of HA chains dictates their ability to cross-link multiple CD44 receptors on the cell surface (32), and this cross-linking is critical to a number of CD44-mediated functions (33, 34). The requirement for CD44 cross-linking in this system provides a potential mechanistic explanation tying TR1 induction to the inflammatory milieu in vivo.

A second level of control over HMW-HA induction of TR1 cells is the influence of OPN, a matrix glycoprotein found in abundance in many settings of chronic inflammation and autoimmunity (21, 35). Our data indicate that OPN overrides HMW-HA–mediated TR1 induction in a dose-dependent manner via interactions with both CD44 and integrin receptors. These data point to a central role for CD44 in fate decisions regarding of TR1 induction. Furthermore, we demonstrate that the effect of OPN can be replicated with an antibody directed against β3 integrin. These data indicate a nexus for regulatory control of the TR1 pathway by ECM components. Given the requirement in HA-mediated TR1 induction for a TCR stimulus, DCs and other antigen-presenting cells (APCs) may serve as an important source of HA. It was recently reported that IFN-γ receptor engagement drives DC-mediated TR1 induction and inhibition of OPN production (36). We recently showed that DC production of HA was likewise promoted by IFN-γ and that HA is found at the immune synapse (30). We are currently investigating this HA/OPN/IFN-γ axis in DC-mediated TR1 induction.

Building upon our findings, we have used commercial HA-based hydrogels as platforms to provide the necessary cues for TR1 induction. These capitalize on the shared capacity of intact HA and an HA-based hydrogels to induce TR1. In this context, the hydrogel can be regarded as a synthetic biomimetic of intact ECM. The use of synthetic matrices to induce TR1 points toward novel strategies for immunomodulation.

Materials and Methods

Induction of TR1 Cells and Controls. $CD4^+GFP/FoxP3^+$ T cells (2×10^5) were activated for 96 h on plates initially coated with aCD3 (0.5 μg/mL in 50 μL) with or without CD44 antibody (1 μg/mL), washed, and then subsequently coated with 0.2 mg/mL BSA-conjugated HMW-HA or 10% BSA. After 96 h, cells and supernatants were collected for analysis. For TR1 cell induction using hydrogels, Extracel and Extracel-HP (Glycosan Biosystems) were used per the manufacturer's instructions. Biotinylated anti-CD28 Ab (1.0 μg/mL), aCD3 Ab (10 μg/mL; BD Biosciences), and streptavidin (10 μg/mL; Sigma-Aldrich) were added before cross-linking. Cells (2×10^5) were layered on gels of 25 μL volume following cross-linking. Additional information is included in *SI Materials and Methods*.

ACKNOWLEDGMENTS. We thank Drs. Zarembinski, Prestwich, and Buckner for their advice and comments. This study was supported by National Institutes of Health Grants DK046635 (to G.T.N.), HL018645 (to T.N.W.), DK080178-03 (to P.L.B.), JDRF 25-2010-648 (to T.N.W. and P.L.B.), and R-03 DK089128-01 (to P.L.B.) and by the Juvenile Diabetes Research Foundation (Center for Translational Research, Benaroya Research Institute at Virginia Mason).

1. Roncarolo MG, et al. (2006) Interleukin-10-secreting type 1 regulatory T cells in rodents and humans. *Immunol Rev* 212:28–50.
2. Vieira PL, et al. (2004) IL-10-secreting regulatory T cells do not express Foxp3 but have comparable regulatory function to naturally occurring CD4+CD25+ regulatory T cells. *J Immunol* 172:5986–5993.
3. Groux H, et al. (1997) A CD4+ T-cell subset inhibits antigen-specific T-cell responses and prevents colitis. *Nature* 389:737–742.
4. Awasthi A, et al. (2007) A dominant function for interleukin 27 in generating interleukin 10-producing anti-inflammatory T cells. *Nat Immunol* 8:1380–1389.
5. Pedersen AE, Gad M, Walter MR, Claesson MH (2004) Induction of regulatory dendritic cells by dexamethasone and 1alpha,25-dihydroxyvitamin D(3). *Immunol Lett* 91:63–69.
6. Kemper C, et al. (2003) Activation of human CD4+ cells with CD3 and CD46 induces a T-regulatory cell 1 phenotype. *Nature* 421:388–392.
7. Levings MK, et al. (2005) Differentiation of Tr1 cells by immature dendritic cells requires IL-10 but not CD25+CD4+ Tr cells. *Blood* 105:1162–1169.
8. Hawrylowicz CM, O'Garra A (2005) Potential role of interleukin-10-secreting regulatory T cells in allergy and asthma. *Nat Rev Immunol* 5:271–283.
9. Stern R, Asari AA, Sugahara KN (2006) Hyaluronan fragments: An information-rich system. *Eur J Cell Biol* 85:699–715.
10. Bollyky PL, et al. (2007) Cutting edge: High molecular weight hyaluronan promotes the suppressive effects of CD4+CD25+ regulatory T cells. *J Immunol* 179:744–747.
11. Bollyky PL, et al. (2009) CD44 costimulation promotes FoxP3+ regulatory T cell persistence and function via production of IL-2, IL-10, and TGF-beta. *J Immunol* 183: 2232–2241.
12. Bollyky PL, et al. (2009) Intact extracellular matrix and the maintenance of immune tolerance: High molecular weight hyaluronan promotes persistence of induced CD4+ CD25+ regulatory T cells. *J Leukoc Biol* 86:567–572.
13. Sakaguchi S, Setoguchi R, Yagi H, Nomura T (2006) Naturally arising Foxp3-expressing CD25+CD4+ regulatory T cells in self-tolerance and autoimmune disease. *Curr Top Microbiol Immunol* 305:51–66.
14. Asari A, Kanemitsu T, Kurihara H (2010) Oral administration of high molecular weight hyaluronan (900 kDa) controls immune system via Toll-like receptor 4 in the intestinal epithelium. *J Biol Chem* 285:24751–24758.
15. Budd RC, et al. (1987) Distinction of virgin and memory T lymphocytes. Stable acquisition of the Pgp-1 glycoprotein concomitant with antigenic stimulation. *J Immunol* 138: 3120–3129.
16. Asseman C, Mauze S, Leach MW, Coffman RL, Powrie F (1999) An essential role for interleukin 10 in the function of regulatory T cells that inhibit intestinal inflammation. *J Exp Med* 190:995–1004.
17. Laurent TC, Fraser JR (1992) Hyaluronan. *FASEB J* 6:2397–2404.
18. Dong C, et al. (2001) ICOS co-stimulatory receptor is essential for T-cell activation and function. *Nature* 409:97–101.
19. Saraiva M, O'Garra A (2010) The regulation of IL-10 production by immune cells. *Nat Rev Immunol* 10:170–181.
20. Tsuji-Takayama K, et al. (2008) The production of IL-10 by human regulatory T cells is enhanced by IL-2 through a STAT5-responsive intronic enhancer in the IL-10 locus. *J Immunol* 181:3897–3905.
21. Cantor H, Shinohara ML (2009) Regulation of T-helper-cell lineage development by osteopontin: The inside story. *Nat Rev Immunol* 9:137–141.
22. Hur EM, et al. (2007) Osteopontin-induced relapse and progression of autoimmune brain disease through enhanced survival of activated T cells. *Nat Immunol* 8:74–83.
23. Ashkar S, et al. (2000) Eta-1 (osteopontin): An early component of type-1 (cell-mediated) immunity. *Science* 287:860–864.
24. Heilmann K, et al. (2008) Osteopontin as two-sided mediator of intestinal inflammation. *J Cell Mol Med* 13:1162–1174.
25. Prestwich GD, et al. (2006) Injectable synthetic extracellular matrices for tissue engineering and repair. *Adv Exp Med Biol* 585:125–133.
26. Najjam S, Gibbs RV, Gordon MY, Rider CC (1997) Characterization of human recombinant interleukin 2 binding to heparin and heparan sulfate using an ELISA approach. *Cytokine* 9:1013–1022.
27. Wrenshall LE, Platt JL, Stevens ET, Wight TN, Miller JD (2003) Propagation and control of T cell responses by heparan sulfate-bound IL-2. *J Immunol* 170:5470–5474.
28. Schönherr E, Hausser HJ (2000) Extracellular matrix and cytokines: A functional unit. *Dev Immunol* 7:89–101.
29. Lortat-Jacob H (2009) The molecular basis and functional implications of chemokine interactions with heparan sulphate. *Curr Opin Struct Biol* 19:543–548.
30. Bollyky PL, et al. (2010) Th1 cytokines promote T-cell binding to antigen-presenting cells via enhanced hyaluronan production and accumulation at the immune synapse. *Cell Mol Immunol* 7:211–220.
31. Puré E, Cuff CA (2001) A crucial role for CD44 in inflammation. *Trends Mol Med* 7: 213–221.
32. Lesley J, Hascall VC, Tammi M, Hyman R (2000) Hyaluronan binding by cell surface CD44. *J Biol Chem* 275:26967–26975.
33. Fujii Y, Fujii K, Nakano K, Tanaka Y (2003) Crosslinking of CD44 on human osteoblastic cells upregulates ICAM-1 and VCAM-1. *FEBS Lett* 539:45–50.
34. Huet S, et al. (1989) CD44 contributes to T cell activation. *J Immunol* 143:798–801.
35. Wang KX, Denhardt DT (2008) Osteopontin: role in immune regulation and stress responses. *Cytokine Growth Factor Rev* 19:333–345.
36. Murugaiyan G, Mittal A, Weiner HL (2010) Identification of an IL-27/osteopontin axis in dendritic cells and its modulation by IFN-gamma limits IL-17-mediated autoimmune inflammation. *Proc Natl Acad Sci USA* 107:11495–11500.

Low-Dose Antigen Promotes Induction of FOXP3 in Human CD4$^+$ T Cells

S. Alice Long, Mary Rieck, Megan Tatum, Paul L. Bollyky, Rebecca P. Wu, Isabelle Muller, Jhon-Chun Ho, Heather G. Shilling, and Jane H. Buckner

Low Ag dose promotes induction and persistence of regulatory T cells (Tregs) in mice, yet few studies have addressed the role of Ag dose in the induction of adaptive CD4$^+$FOXP3$^+$ Tregs in humans. To this end, we examined the level of FOXP3 expression in human CD4$^+$CD25$^-$ T cells upon activation with autologous APCs and varying doses of peptide. Ag-specific T cells expressing FOXP3 were identified by flow cytometry using MHC class II tetramer (Tmr). We found an inverse relationship between Ag dose and the frequency of FOXP3$^+$ cells for both foreign Ag-specific and self Ag-specific T cells. Through studies of FOXP3 locus demethylation and helios expression, we determined that variation in the frequency of Tmr$^+$FOXP3$^+$ T cells was not due to expansion of natural Tregs, but instead, we found that induction, proliferation, and persistence of FOXP3$^+$ cells was similar in high- and low-dose cultures, whereas proliferation of FOXP3$^-$ T cells was favored in high Ag dose cultures. The frequency of FOXP3$^+$ cells positively correlated with suppressive function, indicative of adaptive Treg generation. The frequency of FOXP3$^+$ cells was maintained with IL-2, but not upon restimulation with Ag. Together, these data suggest that low Ag dose favors the transient generation of human Ag-specific adaptive Tregs over the proliferation of Ag-specific FOXP3$^-$ effector T cells. These adaptive Tregs could function to reduce ongoing inflammatory responses and promote low-dose tolerance in humans, especially when Ag exposure and tolerance is transient. ***The Journal of Immunology*****, 2011, 187: 3511–3520.**

FOXP3$^+$ regulatory T cells play a key role in peripheral tolerance to self Ags and control the magnitude of immune responses to foreign Ags. There are two major types of CD4$^+$FOXP3$^+$ regulatory T cells: those that are derived in the thymus (natural regulatory T cell; nTreg) and others that are generated in the periphery from CD25$^-$FOXP3$^-$ T cells (adaptive regulatory T cell; aTreg) (1, 2). nTregs and aTregs are phenotypically and functionally similar in that they express CD25^{hi}, GITR, and CTLA-4 and function in a contact-dependent manner. However, they differ in the TCR signal strength and the costimulatory and cytokine requirements for generation and expansion (3). Moreover, nTregs are thought to be a more stable cell subset (4), whereas aTregs have been described as a transient and/or less stable regulatory T cell (Treg) subset. Stable nTregs are an IL-2–dependent cell type generated through relatively high-affinity interactions with MHC and Ag in the thymus that require CD28 costimulation. In contrast, TCR signaling and costimulatory requirements for IL-2− and TGF-β−dependent peripherally derived aTregs are not as well understood. Some reports suggest that activation in the presence of suboptimal concentrations of Ag (5–11) or decreased Akt/mTOR signaling (12–14) may promote aTreg generation. Two very recent reports demonstrated that subimmunogenic activation determines aTreg generation through autonomous production of TGF-β after low TCR activation and not through exposure to exogenous TGF-β from other cells, suggesting a dominant role for TCR signal strength (15, 16). Using a murine TCR transgenic (Tg) system, Gottschalk et al. (11) demonstrated that generation of a persistent Foxp3$^+$ aTreg population resulted when low doses of an agonist peptide were used to stimulate cells. Likewise, graded activation of murine OVA-specific T cells with Ag or anti-CD3 resulted in Foxp3 expression when Ag dose and Akt activation were limited (17). Overall, these studies suggest that the quality of TCR activation, in part, instructs generation of aTreg.

Immunization or exposure to tumor Ags in human subjects results in synchronous proliferation of memory T cells that contain subpopulations of memory FOXP3$^+$ and FOXP3$^-$ T cells of similar Ag specificity (18–20). Likewise, parallel proliferation of FOXP3$^+$ and FOXP3$^-$ T cells occurs when mice are challenged with foreign Ag (21). These in vivo data suggest that both activated FOXP3$^-$ effector T cells and FOXP3$^+$ aTregs may be generated upon antigenic exposure. Thus, it is important to understand the mechanisms that control this fate decision, specifically the type of stimulation that results in the induction and persistence of FOXP3 expression. Sources of variation in TCR stimulation may include 1) level of TCR engagement that is influenced by both potency and density of the MHC–peptide–TCR interaction, 2) cytokine milieu (i.e., TGF-β and IL-6), and 3) APC maturation (22–25). In fact, using altered peptide ligands and murine TCR Tg T cells, it was found that both decreased potency and density of peptide favored Foxp3 expression upon activation (11). Understanding the factors that shift the ratio of effector and aTreg upon antigenic exposure in both mice and humans will be important for developing therapies that promote tolerance or immunity.

Low Ag dose promotes the induction and persistence of Tregs in mice. In this study, we address whether Ag dose influences the

Benaroya Research Institute at Virginia Mason, Seattle, WA 98101

Received for publication November 29, 2010. Accepted for publication July 21, 2011.

This work was supported by grants from the National Institutes of Health (DK07245 to J.H.B. and DK080178 to P.L.B.) and the Juvenile Diabetes Research Foundation (the Center for Translational Research at Benaroya Research Institute and the Center for Collaborative Cellular Therapy).

Address correspondence and reprint requests to Dr. Jane H. Buckner, Benaroya Research Institute at Virginia Mason, 1201 Ninth Avenue, Seattle, WA 98101. E-mail address: jbuckner@benaroyaresearch.org

The online version of this article contains supplemental material.

Abbreviations used in this article: aTreg, adaptive regulatory T cell; GAD, glutamic acid decarboxylase; HA, hemagglutinin; IGRP, islet-specific glucose-6-phosphate catalytic subunit-related protein; MFI, mean fluorescence intensity; nTreg, natural regulatory T cell; Tg, transgenic; Tmr, tetramer; Treg, regulatory T cell; TSDR, Treg-specific demethylated region; TT, tetanus toxin.

in vitro induction and persistence of FOXP3 in foreign Ag-specific and self Ag-specific CD4 T cell populations using HLA class II tetramers. We found that Ag dose, as opposed to TGF-β or bystander activation, had a dominant impact on the generation of functional human Ag-specific aTregs. However, the frequency of FOXP3$^+$ cells was reduced upon restimulation. This dose effect was observed with both foreign Ag-specific and self Ag-specific T cells. Together, these data suggest that low Ag dose favors the induction and proliferation of human Ag-specific FOXP3$^+$ aTregs as opposed to FOXP3$^-$ effector T cells. Determining factors that promote the generation and persistence of self Ag-specific FOXP3$^+$ aTregs while reducing FOXP3$^-$ T cell proliferation may lead to development of Ag-specific therapies that result in reduced immunogenicity and/or tolerance induction.

Materials and Methods

Human subjects and mice

PBMCs were derived from subjects participating in studies under the auspices of the Benaroya Research Institute-Juvenile Diabetes Research Foundation Center for Translational Research registry. Informed consent was obtained from all subjects according to institutional review board-approved protocols at Benaroya Research Institute (Seattle, WA). Control participants were selected based on lack of personal or family history of autoimmunity or asthma. Foxp3-GFP C57BL/6 mice were a gift from Dr. A. Rudensky. All mice were maintained in a specific pathogen-free American Association for the Accreditation of Laboratory Animal Care-accredited animal facility at the Benaroya Research Institute and handled in accordance with institutional guidelines.

Cell preparation, culture, and phenotyping

Fresh PBMCs were prepared by centrifugation over Ficoll-Hypaque gradients. CD4$^+$ T cells were purified with a CD4$^+$ no-touch T cell isolation kit (Miltenyi) followed by negative selection with Miltenyi CD25 microbeads. Autologous APCs were obtained from the positive fraction of the CD4$^+$ no-touch selection. FOXP3 expression in CD4$^+$CD25$^-$ cells was 0.1–1.2%.

CD4$^+$CD25$^-$ T cells were activated with peptide in the presence of irradiated (5000 rad) APCs at a 1:2 ratio with 6×10^6 total cells/well in a 24-well plate. In some experiments, CD4 T cell subsets were sorted based on CCR7 and CD45RA expression from negatively isolated total CD4 cells prior to culture with irradiated APCs and peptide. HLA DRB*0401 samples were activated with influenza hemagglutinin (HA) Ag (306–318), islet-specific glutamic acid decarboxylase (GAD) (555–567), glucose-6-phosphate catalytic subunit-related protein (IGRP) (247–259), Preproinsulin [76–92(88K→S)], and tetanus toxin (TT) (674–693) peptides (26–30). IL-2 (200 IU/ml; Chiron) was added at day 7. Cells were cultured for 14 d, unless stated otherwise, and stained for expression of CD4, tetramer (Tmr), FITC CD25, and Alexa 647 FOXP3 (BioLegend) as described previously (28). In some experiments, cells were costained with FITC helios (BioLegend), and in other experiments cells were costained with PE GITR or PerCP–Cy5.5 LAP from R&D Systems, PerCP–Cy5.5 PD-1 from BioLegend, or allophycocyanin CTLA-4 or FITC CD103 from BD Biosciences. HLA DRB*0401 Tmr used for staining matched the specificity of the peptide used to stimulate the culture with the exception of GAD Tmr$^+$ T cells where a Tmr loaded with 555–567I was used for detection as described previously (31). Positive Tmr staining was determined to be responses at least 0.2% and 4-fold greater than those of irrelevant control Tmr stains. FOXP3 isotype in conjunction with CD25 expression on activated T cells was used as FOXP3 staining controls as described previously (32) and shown in Supplemental Fig. 1.

Costaining for BrdU and FOXP3 was performed as described previously (14). Briefly, after overnight incubation with BrdU, cells were fixed and permeabilized using the BioLegend FOXP3 fixation buffer and then the BD Cytofix/Cytoperm and BD Cytoperm Plus buffers. Permeabilized cells were treated with DNase for 1 h at 37˚C prior to staining with FITC anti-BrdU Ab. Costaining for intracellular IL-10 was performed with BD CytoFix/Perm reagents per the manufacturer's instructions after 5-h stimulation with PMA (50 ng/ml) and ionomycin (1 μg/ml) in the presence of 1 nM GolgiStop. All phenotype data were acquired on a FACSCaliber and analyzed using FlowJo 7.6 software.

Methylation analysis

All methylation analysis was performed on cells isolated from male donors. Genomic DNA was isolated by DNeasy Blood and Tissue Kit (Qiagen) and bisulfite converted using the EpiTect Bisulfite Kit (Qiagen) according to the manufacturer's instructions. The Treg-specific demethylated region (TSDR) was amplified using bisulfite forward and reverse primers: Amp5A1 forward, 5′-TTTGGGGGTAGAGGATTTAGAG-3′; Amp5A1 reverse, 5′-CCACCTAAACCAAACCTACTACAA-3′ [modified from Baron et al. (33)]. The region of the FOXP3 promoter immediately upstream of the transcription start site was amplified using bisulfite forward and reverse primers: PROM forward, 5′-GTGAAGTGGATTGATAGAAAAGGATTA-3′; PROM reverse, 5′-CATTTAAATCTCATAATCAAAAAAAA-3′. PCR was performed in 25 μL containing 1X PCR buffer, 1 U ZymoTaq DNA polymerase (Zymo Research), bisulfite-converted genomic DNA, deoxyribonucleotide triphosphates at a final concentration of 1 mM, and forward and reverse primers at 1 mM each. PCR conditions were 95˚C for 10 min, 35–40 cycles of 95˚C for 30 s, 55˚C for 30 s, and 72˚C for 1 min, with a final extension at 72˚C for 7 min. TSDR and promoter region PCR products were Exo-SAP purified (USB Corp) and subcloned using a TOPO TA Cloning Kit (Invitrogen), and the DNA from individual bacterial colonies was sequenced with M13 forward primer using Big Dye Terminator v1.1 chemistry (Applied Biosystems).

Functional assays

For polyclonal assays, experiments were performed as described previously (34). In brief, autologous CD4$^+$CD25$^-$ responder T cells were thawed, CFSE labeled, and cultured in a round-bottom 96-well plate with or without CD25$^+$ sorted Tregs at a 1:4 ratio (Tregs/responders) Cells were stimulated with M-280 Tosylactivated Dynabeads (Invitrogen), which were preincubated with anti-CD3 (5 μg/ml) and anti-CD28 (5 μg/ml). Beads were used at a ratio of 2:1 (beads/responder cells). Analysis was performed on day 4 by flow cytometry.

For Ag-specific assays, sorted Tmr$^+$CD25^{hi} cells (2.5×10^4), thawed CD4$^+$CD25$^-$ cells (2.5×10^4) isolated from autologous PBMCs, or both were incubated with irradiated APCs (2.5×10^4), TT, and 5 μg/ml peptide Ag in a 96-well round-bottom plate as described previously (32, 35). [^{3}H]thymidine (1 μCi) was added during the final 16 h of a 6- to 7-d assay, and proliferation was measured by a scintillation counter. All culture conditions were performed in triplicate. Percent inhibition was determined based on the percentage of dividing responders in the coculture compared with that when cultured alone.

Statistics

For analysis of experiments comparing a single variable, statistical significance was analyzed using a two-sample Student *t* test unless otherwise noted. For analysis of multiple variables, a one-way ANOVA was performed or linear regression as noted in the legends to figures that accompany this article. Comparisons required a p value <0.05 for the data to be significantly different.

Results

Both level of TCR stimulation and TGF-β contribute to induction of FOXP3 expression

To dissect the relative contribution of Ag dose and cytokines on FOXP3 induction, we measured Foxp3 expression upon activation in the presence or absence of cytokines that promote Foxp3 expression in a well-defined murine system where Foxp3 and GFP are genetically linked. As shown in this study and by others (36), in the absence of costimulation, TGF-β and IL-2 are required for Foxp3 expression in mice regardless of the level of TCR activation (Fig. 1*A*). In the presence of TGF-β and IL-2, a greater percentage of murine GFP$^+$ FOXP3$^+$ aTregs were generated from GFP$^-$FOXP3$^-$ T cells when stimulated with low concentrations of anti-CD3 Ab. Thus, both cytokines and the level of TCR engagement contribute to the expression of FOXP3 in mice, and the impact of Ag dose can be observed in the presence of cytokines that promote FOXP3 expression suggesting a dominant effect of Ag dose, consistent with two very recent reports (15, 16).

In humans, addition of IL-2 and TGF-β augmented induction of polyclonal FOXP3$^+$ cells through stimulation with anti-CD3/anti-CD28–coated beads in the absence of APC (Ref. 37 and data not shown). However, in cultures containing APC and soluble anti-CD3, addition of exogenous TGF-β did not alter the frequency of aTregs (Fig. 1*B*) most likely due to TGF-β produced by or

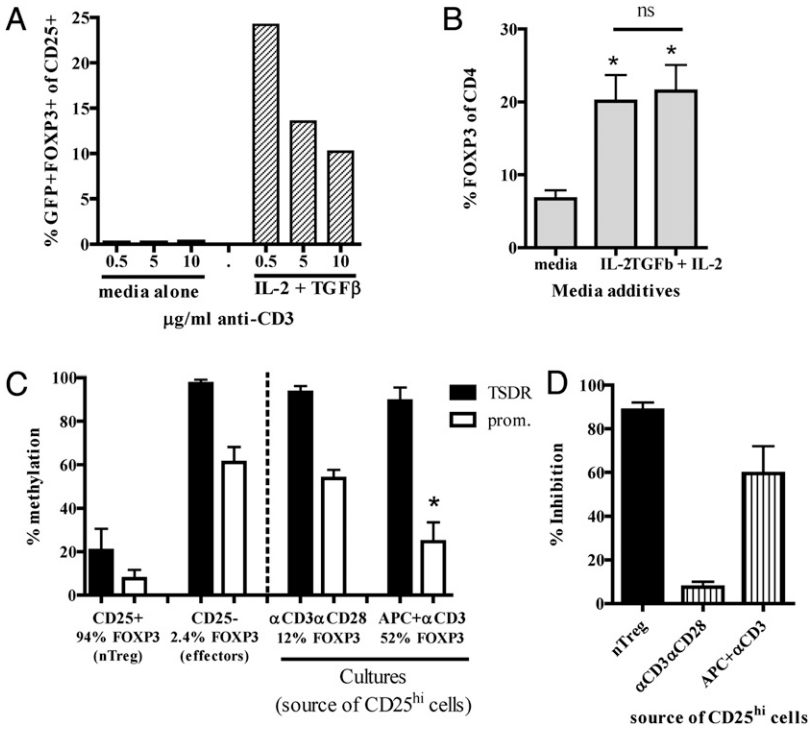

FIGURE 1. TGF-β and TCR both contribute to FOXP3 expression upon activation of CD4 T cells. *A*, GFP$^-$FOXP3$^-$ murine splenic CD4 T cells were isolated and activated with different doses of anti-CD3 in the absence or presence of IL-2 (100 IU/ml) and TGF-β (10 ng/ml). GFP$^+$FOXP3$^+$ T cells were enumerated by flow cytometry 48 h after activation. One representative experiment of three is shown. *B*, Human CD4$^+$CD25$^-$ T cells from control subjects ($n = 8$) were activated with irradiated APCs and soluble anti-CD3 (5 μg/ml) in the presence of IL-2 (100 IU/ml) and TGF-β (10 ng/ml) for 6 d. *$p < 0.05$ (significant difference from media alone as measured by a paired Student *t* test). *C*, For comparison, human CD25$^+$ (nTreg) and CD25$^-$ (effector) T cells were sorted from male donors prior to initiation of culture and assessed for methylation at the FOXP3 locus. Human male CD4$^+$CD25$^-$ T cells were activated with anti-CD3/anti-CD28 beads (1:1 bead/T cell ratio) or irradiated APCs and 5 μg/ml soluble anti-CD3 with 100 IU/ml IL-2. Nine days after activation, CD25$^+$ sorted cells were snap frozen for methylation analysis at the FOXP3 locus as described in *Materials and Methods*. FOXP3 expression in each CD25$^+$ sorted population was assessed by flow cytometry and is noted in the graph. Bars represent means ± SEM of three independent experiments. *$p < 0.05$ (significant difference in promoter methylation from anti-CD3/anti-CD28 beads as measured by a Student *t* test). *D*, CD25^{hi} sorted cells isolated from day 9 cultures of two subjects assessed for methylation in *C* were assayed for suppressive function by measuring inhibition of proliferation of CFSE-labeled CD4$^+$CD25$^-$ responder cells in the presence of CD25^{hi} sorted cells (1:4 CD25^{hi}/responder ratio).

bound to the APC (38). To determine whether the FOXP3$^+$ T cell populations induced in these cultures resemble aTregs or nTregs, we measured methylation of the FOXP3 locus and function of the sorted CD25$^+$ populations. Demethylation at the promoter and TSDR of the FOXP3 locus marks stable FOXP3$^+$ nTregs, whereas human TGF-β–induced aTregs are only demethylated at the promoter region (33, 39, 40). Culture of CD4$^+$CD25$^-$ T cells using anti-CD3/anti-CD28 beads resulted in effector cells that expressed little FOXP3 protein, whereas culture of the same cells with irradiated APCs and soluble anti-CD3 Ab increased FOXP3 expression with a concomitant decrease in promoter methylation (Fig. 1*C*). This pattern of FOXP3 protein expression and promoter demethylation are characteristic of aTregs (39). In fact, CD25$^+$ cells sorted from the APC plus soluble anti-CD3 cultures were functionally suppressive, whereas CD25$^+$ cells from bead-activated cultures were not (Fig. 1*D*). Thus, we established an in vitro culture system using APC in which we can generate functional human CD4$^+$CD25$^+$FOXP3$^+$ T cells and address the effects of Ag dose on the generation of this population.

Low Ag dose promotes an increased frequency of FOXP3$^+$ cells in human influenza-specific CD4 T cells

CD4$^+$CD25$^-$ T cells were stimulated with autologous irradiated APCs and varying doses of peptide Ag of known affinity (28, 29) as shown in Fig. 2*A*. IL-2 was added on day 7 of culture to support T cell survival and proliferation. Induction of Ag-specific FOXP3$^+$ T cells was measured by flow cytometry for Tmr, CD25, and FOXP3 expression on day 14. When analyzing the frequency of FOXP3$^+$ T cells within the HLA DRB*0401 HA Tmr$^+$ population on day 14, the highest frequency of influenza Ag-specific FOXP3$^+$ cells was observed in the low HA Ag dose (0.1 μg/ml) culture as opposed to the high HA Ag dose (10 μg/ml) culture (Fig. 2*B*). This increased frequency in FOXP3$^+$ cells at lower Ag doses was consistently observed in multiple HLA DRB*0401 subjects stimulated with HA peptide ($n = 8$) (Fig. 2*C*). Comparable results were observed in HLA DRB*0301 and DRB*0404 subjects with influenza-specific peptide stimulation (data not shown) demonstrating that the percentage of FOXP3-expressing cells 14 d after activation is enhanced with low Ag dose. These data show that Ag dose can influence the relative frequency of in vitro induction and the persistence of FOXP3$^+$ cells within the HA-specific human CD4 T cell population.

nTreg expansion does not contribute to the increased frequency of Tmr$^+$FOXP3$^+$ cells in low-dose cultures

Both nTregs and aTregs are characterized by expression of FOXP3 yet differ in their affinity, expression of helios, and demethylation (1, 2). We used independent measures to determine whether low Ag dose promoted selective expansion of nTregs that cross-react and bind HLA DRB*0401 HA Tmr with a high affinity. Using Tmr mean fluorescence intensity (MFI), a surrogate marker of TCR affinity, we found that FOXP3$^+$ and FOXP3$^-$ T cells from low Ag dose cultures express similar levels of Tmr (Fig. 3*A*) suggesting that the FOXP3$^+$ T cells are not contained within a high-affinity

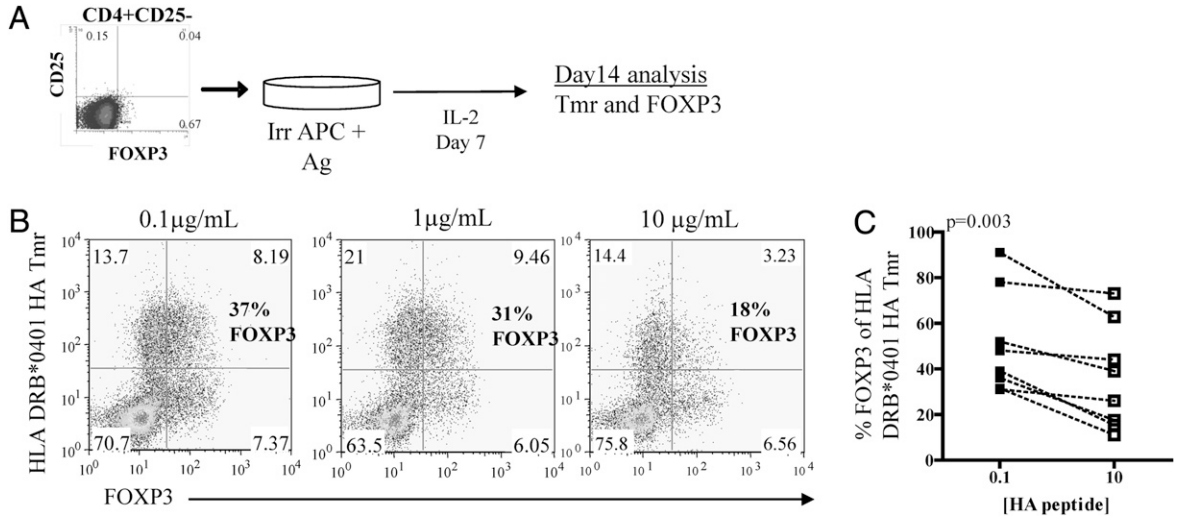

FIGURE 2. Lower doses of Ag promote an increased frequency of FOXP3$^+$ cells in influenza-specific T cell populations. *A*, CD4$^+$CD25$^-$ T cells were activated in the presence of irradiated APCs and HA peptide Ag. IL-2 (200 IU/ml) was added on day 7, and Ag-specific cells were detected using Tmr and FOXP3 staining. *B* and *C*, One representative HLA DRB*0401 sample (*B*) of eight (*C*) that were activated with different doses of HA peptide and assayed on day 14. Percent FOXP3 of Tmr is shown in bold on the dot plot and graphed in *C*. Statistical significance was determined using a paired Student *t* test.

Treg subpopulation. In addition, the frequency of bystander FOXP3$^+$ Tmr$^-$ T cells, a population likely to contain self-reactive nTregs, did not differ between cultures (Fig. 3*B*). Last, we used molecular signatures of nTregs to confirm whether low Ag dose promoted selective expansion of nTregs in our culture system. Where enough cells could be obtained, we observed >75% methylation of the TSDR in Tmr$^+$CD25^{hi} sorted populations regardless of Ag dose (n = 2, data not shown), suggesting an absence of nTregs that are demethylated at the TSDR. Recently, helios expression was shown to be selectively expressed in FOXP3$^+$ nTregs, but not in aTregs or effector CD4$^+$ T cells (41). CD4$^+$CD25$^-$ T cells were cultured as shown in Fig. 2*A*, and single-cell analysis was performed by flow cytometry for Tmr, FOXP3, and Helios expression on day 14. Consistent with data in Fig. 2, activation of CD4$^+$CD25$^-$ T cells with low-dose peptide resulted in a higher frequency of FOXP3$^+$ cells in the Tmr$^+$ population compared with that in high-dose cultures (Fig. 3*C*). The level of FOXP3 expression in the low Ag dose aTregs was less than that of nTregs in freshly isolated PBMCs but higher than that of Tmr$^+$FOXP3$^+$ cells from high-dose cultures (Supplemental Fig. 2). However, helios expression was detected in neither the low- nor high-dose cultures, whereas FOXP3^{hi}helios$^+$ cells were detected in CD4$^+$ T cells of PBMCs prior to activation and when CD25$^+$ enriched T cells were activated in a similar manner with peptide and irradiated APCs (Fig. 3*D*), as shown previously by others (41, 42). Together, these data support the hypothesis that activation with low Ag dose leads to induction of aTregs via de novo expression of FOXP3 in this in vitro culture system and not via selective outgrowth of nTregs.

Tmr$^+$FOXP3$^+$ cells arise upon activation of naive and memory cells with high and low doses of Ag, whereas high Ag dose selectively promotes FOXP3$^-$ T cell expansion

To address whether differences in the kinetics of activation explain dose-related variation in the frequency of FOXP3 expression in our culture system, we measured the frequency of FOXP3 in the Tmr$^+$ population at earlier time points in cultures where Tmr could be detected. Similar to analysis at day 14, we observed a decrease in the frequency of FOXP3$^+$ T cells within the Tmr$^+$ population (Fig. 4*A*). This is consistent with our previous observation that the frequency of FOXP3$^+$ cells in the Tmr$^+$ population for a single Ag dose was similar between day 10 and day 14 (32). We directly assessed the proliferation rate of FOXP3$^+$ cells, a population containing Tmr$^+$ cells, by measuring BrdU incorporation. Comparing the rate of proliferation of FOXP3$^+$ T cells in low and high Ag dose cultures, we found no difference in the kinetics of FOXP3$^+$ T cell proliferation (Fig. 4*B*). Thus, increased frequency of FOXP3$^+$ cells with low Ag dose was not due to delayed kinetics of FOXP3 expression upon activation.

Equivalent proliferation rates of FOXP3$^+$ cells in low and high Ag dose cultures suggest that differences in the frequency of FOXP3$^+$ cells may occur through variation in FOXP3$^-$ T cell proliferation or death. To address this hypothesis, equal numbers of sorted naive (CCR7$^+$, CD45RO$^-$), central memory (CCR7$^+$, CD45RO$^+$), and effector memory (CCR7$^-$, CD45RO$^+$) cells were stimulated with low (0.1 μg/ml) and high (10 μg/ml) doses of HA peptide. Universally, high-dose cultures resulted in a greater absolute number of Tmr$^+$ cells (Fig. 4*C*) reflecting both the relative frequency and proliferative capacity of Ag-specific cells in each sorted population. When stratified by FOXP3 expression, the absolute number of FOXP3$^+$ cells did not increase with Ag dose, consistent with equivalent rates of proliferation observed with BrdU incorporation (Fig. 4*D*). In contrast, the absolute number of FOXP3$^-$ T cells increased in high Ag dose cultures resulting in a lower frequency of Tmr$^+$FOXP3$^+$ T cells. Together, these data suggest that FOXP3$^+$ cells originate primarily from memory cells after activation with all doses of Ag tested, and a decreased frequency of HA-specific FOXP3$^+$ T cells with high Ag dose results from increased proliferation of FOXP3$^-$ T cells.

Increased frequency of influenza-specific FOXP3^{hi} T cells in low Ag dose cultures correlates with suppressive function

Transient FOXP3 expression occurs upon activation of human CD4$^+$CD25$^-$ T cells. After transient activation, a subset of T cells retains FOXP3 expression and function as Tregs (43). Previously, we demonstrated that stimulation of CD4$^+$CD25$^-$ T cells for 14 d with a single dose of Ag resulted in an Ag-specific Tmr$^+$CD25^{hi} population that stably expressed FOXP3 while not coexpressing IFN-γ. These cells functioned in an Ag-specific manner, and the potency of suppression correlated directly with the frequency of FOXP3$^+$ T cells in the sorted Tmr$^+$CD25^{hi} population (32). We tested whether FOXP3$^+$ cells induced by stimulation with either low or high Ag dose function as Tregs. We activated CD4$^+$CD25$^-$

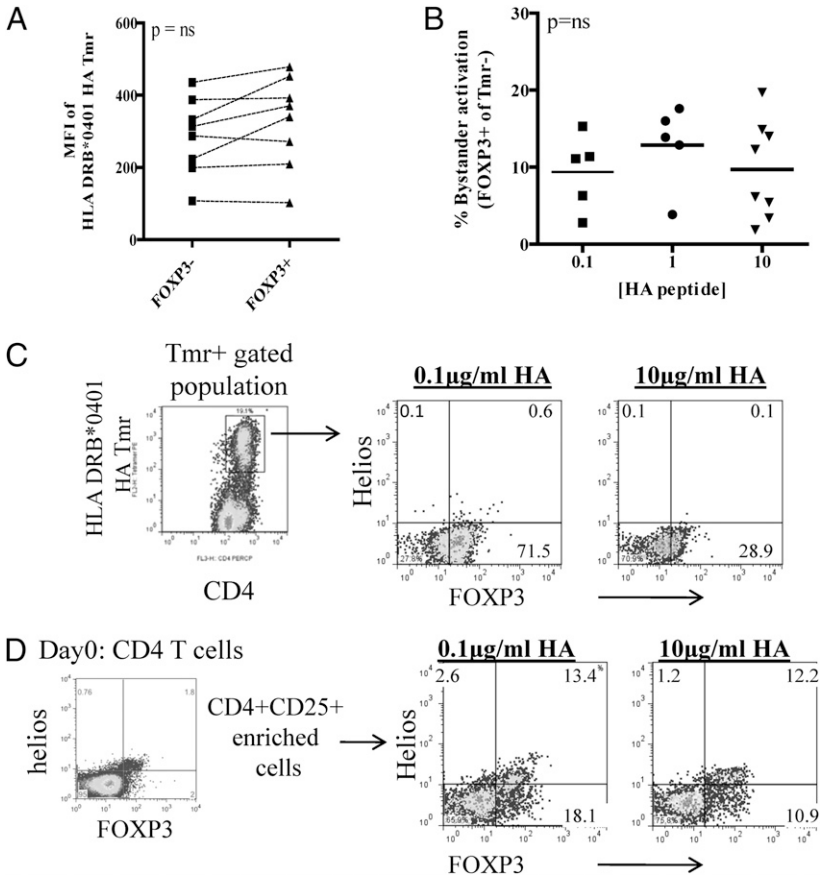

FIGURE 3. Low Ag dose does not preferentially expand human nTregs from $CD4^+CD25^-$ T cells in vitro. *A*, MFI of Tmr in the Tmr^+FOXP3^+ and Tmr^+FOXP3^- T cells was determined by flow cytometry on day 14 for $CD4^+CD25^-$ T cells activated in low-dose cultures. Statistical significance was determined using a Student paired *t* test. *B*, Bystander activation was determined for samples where responses were detected at all Ag doses tested by measuring the frequency of Tmr^-FOXP3^+ T cells of CD4 cells on day 14. Statistical significance was determined by a one-way ANOVA. *C*, $CD4^+CD25^-$ T cells were activated with high- and low-dose HA peptide as in Fig. 2. On day 14, cells were stained for Tmr, FOXP3, and helios. The frequency of $helios^+$ and $FOXP3^+$ cells of the Tmr gated population is shown for each culture. *D*, Total CD4 T cells were stained on day 0 for CD4, CD25, FOXP3, and helios. A representative helios by FOXP3 dot plot of total CD4 cells is shown. Cells enriched for $CD25^+$ cells, containing the $helios^+$ population, were cultured with low and high doses of HA peptide, and total CD4 T cells were stained on day 7 for FOXP3 and helios expression. One representative experiment of three is shown in *C* and *D*.

T cells isolated from the same subject with different doses of Ag, assessed FOXP3 and Tmr content on day 14, sorted Tmr^+CD25^{hi} T cells, and then measured inhibition of proliferation in an Ag-specific manner as done previously (32, 35). HA-specific Tmr^+CD25^+ T cells were isolated from low (0.1 μg/ml) and high (10 μg/ml) Ag dose cultures and assessed for FOXP3 content as shown in Fig. 5*A*. Sorted Tmr^+CD25^{hi} T cells were coincubated with thawed, autologous $CD4^+CD25^-$ T cells and activated with TT alone or in combination with HA, the Ag for which the $CD25^+Tmr^+$ cells were specific. In the absence of HA (TT alone cultures), addition of $CD25^+Tmr^+$ cells had no significant effect on proliferation, regardless of the dose of HA used to generated the sorted cells (Fig. 5*B*). Addition of HA-specific Tmr^+CD25^+ cells generated from both doses of Ag led to suppression of $CD4^+CD25^-$ T cell proliferation in response to TT when HA was also present (TT plus HA). As has been observed previously (32, 35), Tmr^-CD25^- T cells sorted from the same cultures failed to suppress proliferation of autologous $CD4^+CD25^-$ T cells stimulated with either TT alone or TT plus HA, whereas Tmr^-CD25^+ cells suppressed proliferation in response to both TT and TT plus HA responses (data not shown). By titrating the concentration of aTregs relative to responders, we found that sorted $CD25^{hi}$ Tmr^+ T cells generated with low Ag dose were more potent at all ratios tested (Fig. 5*C*).

Variation in function may be due to differences in the phenotype of Tmr^+FOXP3^+ cells generated with high and low doses of Ag and/or the FOXP3 content of $CD25^+Tmr^+$ cells. Comparing expression of known Treg markers in the Tmr^+FOXP3^+ population generated by stimulating $CD4^+CD25^-$ T cells from the same subject with either high or low Ag dose, we found a subtle yet significant increase in FOXP3 expression and increased CTLA-4 expression in three of the four subjects studied in the low Ag dose cultures (Fig. 5*D*). However, we found no difference in the expression levels of PD-1, CD39, or CD95 (Supplemental Fig. 3*A*). We also found no difference between Ag doses in TGF-β (as measured by LAP expression) and IL-10 secretion (Fig. 5*D*) consistent with the observation that sorted low-dose aTreg function was contact dependent and was not inhibited by blocking Abs against IL-10 and TGF-β (Supplemental Fig. 4) as was found previously with high Ag dose aTregs (32). To examine whether the composition of the $CD25^+Tmr^+$ population contributed to function, we correlated FOXP3 content with suppression. Similar to previous studies in humans with both polyclonal and Ag-specific stimulation of $CD25^+FOXP3^+$ T cells (14, 32), the frequency of $FOXP3^+$ cells in the sorted population directly correlated with the degree of inhibition of proliferation (Fig. 5*E*). To determine whether culture with high and low Ag dose also altered the composition of cells as measured by cytokine profiles of Tmr^+ cells as has been reported by others (44, 45), we measured cytokine secretion upon restimulation in the Tmr^+ cells but found no significant differences in the frequency of IFN-γ, IL-17, or IL-5 secretion, representative cytokines secreted by Th1, Th17, and Th2 cells, respectively (Supplemental Fig. 3*B*). Thus, Ag dose influences the frequency of $FOXP3^+$ cells in the CD25 T cell population and expression of FOXP3. Both of these measures correlate with suppressive function of these Ag-specific aTregs.

FOXP3 expression in human islet Ag-specific CD4 T cells is enhanced through stimulation with lower Ag dose

Variation in the induction of FOXP3 may be due to intrinsic factors but also due to T cell extrinsic factors. To test whether the generation of Ag-specific aTregs was influenced by cytokines induced through bystander activation, we performed mixed cultures with multiple different peptides known to stimulate Tmr^+ populations. We found no difference in the frequency of HA-specific $FOXP3^+$

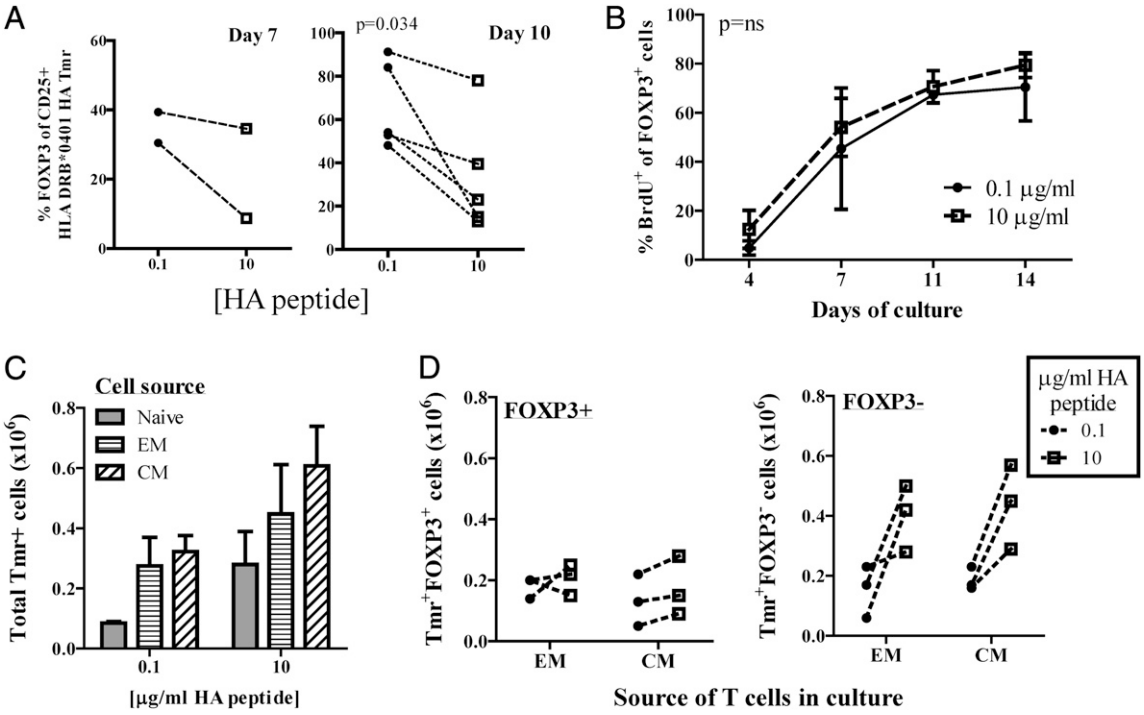

FIGURE 4. FOXP3$^+$ T cells generated in high- and low-dose cultures proliferate at equivalent rates. *A*, CD4$^+$CD25$^-$ T cells from the same subject were activated as in Fig. 2 with different doses of HA peptide and assayed for Tmr and FOXP3 content on different days after activation when Tmr was detectable. Statistical significance was determined using a paired Student *t* test. *B*, Cells were activated with low (0.1 μg/ml) and high (10 μg/ml) doses of HA peptide as in Fig. 2, and proliferation was assessed by pulsing overnight with BrdU and staining for BrdU incorporation in FOXP3$^+$ cells as described in *Materials and Methods*. Average ± SEM (n = 3 subjects) is shown. Statistical significance was determined using a paired Student *t* test at each time point. *C* and *D*, Naive (CCR7$^+$CD45RO$^-$), effector memory (EM; CCR7$^-$CD45RO$^+$), and central memory (CM; CCR7$^+$CD45RO$^+$) cells were sorted from the same individual, and equal numbers (1×10^6) of cells were placed in a 48-well plate with APC and different doses of HA peptide. The absolute number of Tmr$^+$ and FOXP3$^+$ populations was determined using total cell counts and flow cytometry for Tmr and FOXP3. Closed circles denote 0.1 μg/ml HA peptide, and open squares denote 10 μg/ml HA peptide.

cells when comparing cultures in which cells of other specificities were activated (as monitored by Tmr$^+$ cells) with cultures stimulated only with HA peptide (data not shown). To test whether intrinsic factors may influence the frequency of FOXP3$^+$ cells, we analyzed responses to well-defined self Ag-specific peptides (27, 29). Self Ag-specific T cells are generally low-affinity cells and are less frequent in peripheral blood than foreign Ag-specific cells (46, 47). Thus, induction of FOXP3 expression with low doses of self Ag may differ from that of foreign Ag-specific T cells. On average, 1.13% (range 0.14–6.6%) islet Ag-specific T cells were detected in the CD4 T cell cultures (data not shown). Two representative HLA DRB*0404 islet-specific Tmr and FOXP3 stains are shown in Fig. 6*A*. When assessing multiple subjects (n = 12) with two islet Ags, we observed a significant increase in the frequency of islet-specific FOXP3$^+$Tmr$^+$ T cells in low Ag dose (1 μg/ml) cultures compared with that in higher Ag dose (50 μg/ml) cultures (Fig. 6*B*). Together, these data suggest that lower Ag dose may promote an increased frequency of human Ag-specific FOXP3$^+$ T cells regardless of TCR specificity.

Tmr$^+$FOXP3$^+$ aTreg frequencies were maintained with IL-2, but not upon restimulation with Ag

Recently, there has been greater appreciation for the plasticity of FOXP3$^+$ populations, which is influenced, in part, by the source of the FOXP3$^+$ cells and the inflammatory milieu (48). To address the stability of Ag-specific aTreg populations, we assessed the change in FOXP3 content of sorted aTregs after restimulation with low and high doses of Ag and with anti-CD3/anti-CD28 stimulation in a functional assay. Sorted low-dose Tmr$^+$CD25$^+$ aTregs cultured with IL-2 alone maintained FOXP3 expression (Fig. 7*A*). However, FOXP3 expression was not maintained upon restimulation of the same sorted cells with irradiated autologous APCs and HA peptide, regardless of the dose of Ag used in the restimulation cultures. Polyclonal activation with anti-CD3/anti-CD28–coated beads also resulted in a loss of FOXP3$^+$ cells (data not shown). Similarly, aTregs generated with either low (0.1 μg/ml) or high (10 μg/ml) doses of HA peptide lost FOXP3 expression when placed in a functional assay with autologous responder cells (Fig. 7*B*). This suggests that higher frequencies of aTregs are not maintained upon in vitro restimulation with Ag, whereas IL-2 alone maintains aTregs.

Discussion

Both effector T cells and FOXP3$^+$ aTregs may be generated upon antigenic exposure. Thus, it is important to understand the mechanisms that promote aTreg generation as opposed to those that promote effector cell generation. We observed an inverse relationship between Ag dose and FOXP3 expression in human CD4 T cells activated with either foreign or self Ag, as has been shown recently in mice with foreign Ag (11, 15, 16). Using demethylation and helios expression, we established that low Ag dose did not preferentially expand nTregs in vitro from CD4$^+$ CD25$^-$ T cells, but instead induced generation of functional FOXP3$^+$ aTregs in which the frequency of FOXP3-expressing cells positively correlated with suppressive function. These Tmr$^+$FOXP3$^+$ cells proliferated equivalently with both low and high Ag dose. Yet, with high Ag dose stimulation, FOXP3$^-$ T cells proliferated to a greater extent resulting in a decreased frequency of FOXP3$^+$ cells. Of note, the frequency of sorted HA-specific aTregs was maintained with IL-2 alone but not upon

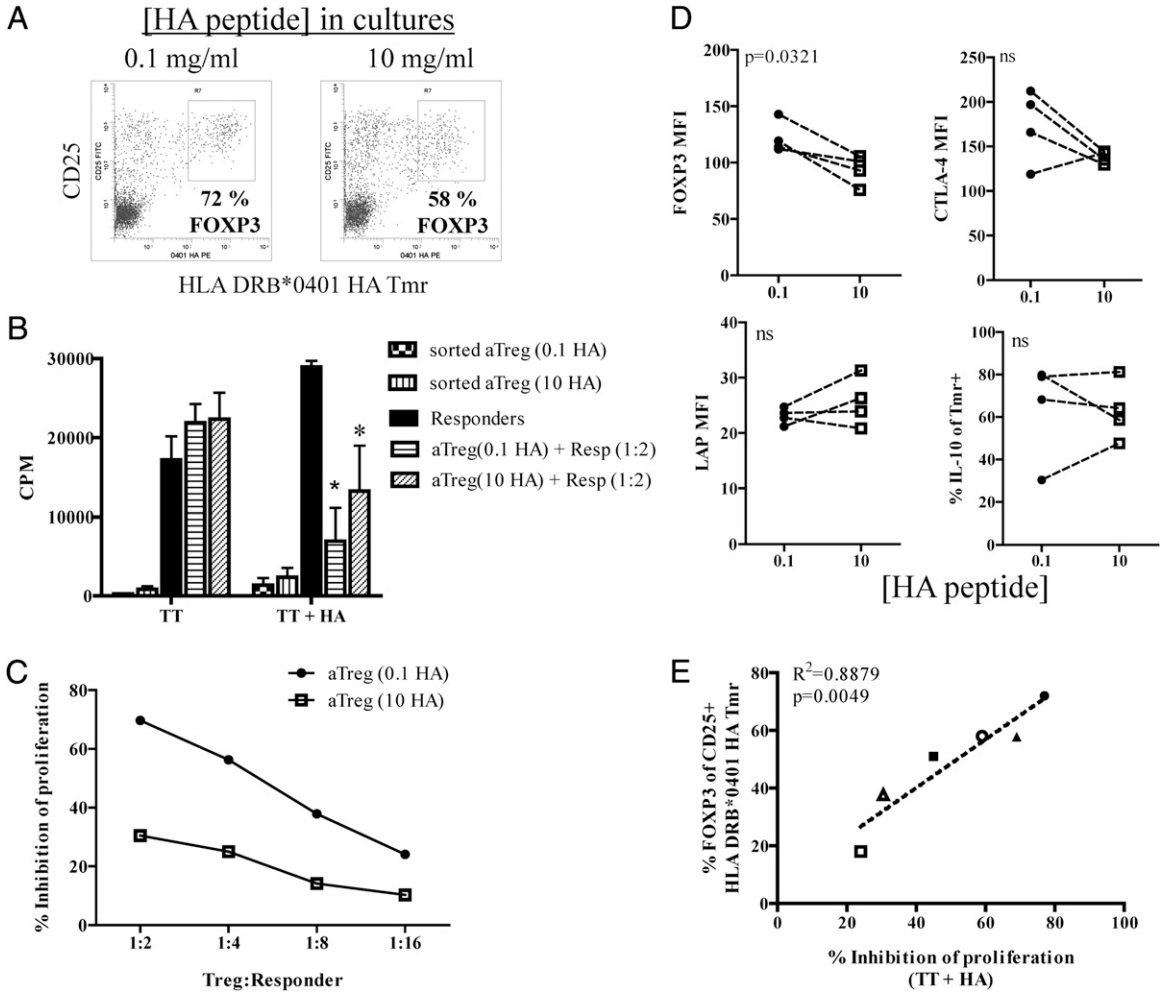

FIGURE 5. Increased frequency and expression of FOXP3 in low-dose cultures correlates with increased suppressive function. Fourteen days after activation with 0.1 μg/ml or 10 μg/ml HA peptide, $CD25^{hi}Tmr^{+}$ cells were sorted and assayed for specificity and function with 5 μg/ml HA and 1 μg/ml TT as described previously (32, 35) and in *Materials and Methods*. *A*, An aliquot of HLA DRB*0401 HA Tmr and CD25 stained cells were costained with FOXP3 to determine FOXP3 content. Percent FOXP3 of Tmr is shown in bold in representative dot plots. *B*, Function and specificity for high and low Ag dose sorted $CD25^{hi}Tmr^{+}$ cells generated from one representative sample of two is shown. Bars represent means ± SEM for triplicates within an experiment. *$p < 0.05$ (significant difference from $CD4^{+}CD25^{-}$ responder cells alone as measured by a two-sample Student *t* test). The level of suppression conferred by 0.1 μg/ml aTreg and 10 μg/ml aTreg did not differ ($p > 0.05$). *C*, Potency of function was measured by titrating aTregs from low and high Ag dose sorted $CD25^{hi}Tmr^{+}$ cells generated from the same individual. Percent inhibition of proliferation with TT plus HA peptide stimulation was compared between aTregs. One representative sample of two is shown. *D*, $Tmr^{+}FOXP3^{+}$ T cells from low and high HA peptide cultures from the same individual were costained for CTLA-4 and LAP. MFI of these markers on $Tmr^{+}FOXP3^{+}$ cells is shown for four subjects. IL-10 was detected by intracellular flow cytometry after 5-h stimulation with PMA and ionomycin as described in *Materials and Methods*. Statistical significance was determined using a paired Student *t* test. *E*, Correlation between FOXP3 expression in the sorted $CD25^{hi}Tmr^{+}$ population and function was determined by linear regression for three subjects (circles = subject 1, squares = subject 2, triangles = subject 3) for which $CD25^{hi}Tmr^{+}$ cells from both 0.1 (closed symbols) and 10 μg/ml (open symbols) cultures were generated.

restimulation with Ag. Thus, the frequency of human aTregs may be one consequence of exposure to low doses of Ag thereby promoting poor immunogenicity and transient tolerance.

The potency and duration of peptide–MHC–TCR interaction can influence the nature of the CD4 T cell response, as is well documented with high- and low-dose Ag driving Th1 and Th2 responses, respectively (reviewed in Refs. 44, 45), and low Ag dose promoting Th17 cells (49) from naive T cells. Less is known about the role of Ag dose on the induction, persistence, and stability of FOXP3 expression in human aTregs. In mice, it has been shown that TCR engagement, costimulation, and cytokines may impact the induction and persistence of FOXP3 expression, which is required for generation of aTregs (8, 11, 13, 15–17). In this study, we established a culture system in which we limit the impact of costimulation and non-T cell-derived cytokines by holding the APC population constant for all doses of Ag tested for each subject. In addition, exogenous TGF-β was not required for FOXP3 expression and thus was not added to our cultures, as was also found by Turner et al. (17) using murine BDC2.5 TCR Tg T cells activated in the presence of dendritic cells. This lack of a requirement for TGF-β may be due to sufficient amounts of biologically active TGF-β produced by or bound to the APC (38, 50). In comparison, stimulation with anti-CD3 anti-CD28 beads (Fig. 1) induced far less FOXP3 expression. Whether this is due to the quality of the stimulation through the TCR or the absence of additional signals provided by the irradiated APC is not yet known. However, increasing frequencies of $FOXP3^{+}$ cells occur in both murine (Fig. 1 and Ref. 17) and human CD4 T cells (51) early upon activation when low levels of anti-CD3 are used to activate the cells. Likewise, in our Ag-specific culture system, we found that the rate of proliferation of $FOXP3^{+}$ cells did not differ between Ag doses suggesting that aTregs are a population of cells

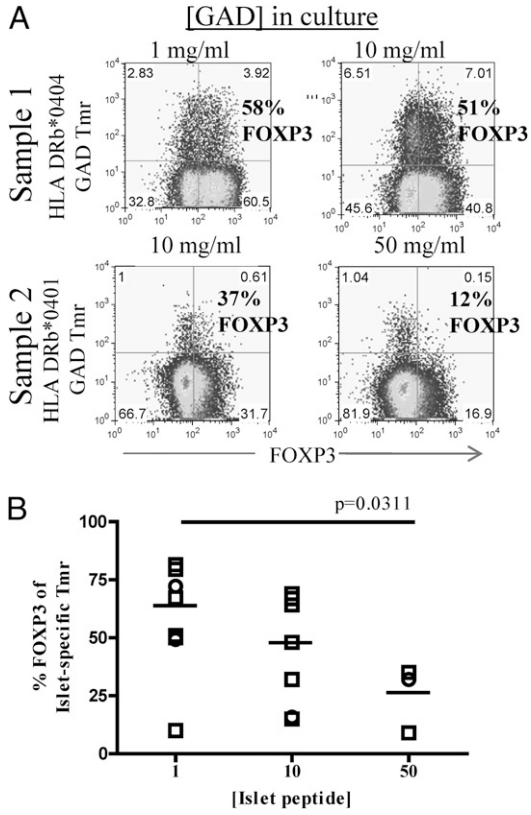

FIGURE 6. Lower doses of Ag favor an increased frequency of FOXP3$^+$ cells in islet Ag-specific T cells. CD4$^+$CD25$^-$ T cells were activated with different doses of islet Ag peptides as in Fig. 2. *A*, Tmr and FOXP3 staining is shown for one subject stimulated with different doses of GAD peptide. Frequency of FOXP3 in the Tmr$^+$ population is noted in bold in each dot plot. *B*, Frequency of islet-specific FOXP3$^+$ cells was determined by enumerating HLA DRB*0401 GAD and IGRP Tmr$^+$FOXP3$^+$ T cells as a percentage of total Tmr$^+$ T cells. Analysis of GAD-specific T cells from nine subjects is noted by open squares, and analysis of IGRP-specific T cells from three subjects is noted by open circles. Horizontal lines show the means. Statistical significance was determined using a two-sample Student *t* test.

in which FOXP3 expression is induced upon activation with high and low Ag dose and this population persists. Decreased frequency of FOXP3$^+$ cells in high Ag dose cultures occurred due to preferential activation and proliferation of FOXP3$^-$ T cells with high Ag dose. Together, these data suggest that the quality of the TCR signal may contribute to the frequency of Ag-specific aTregs.

We and others (32, 52) have demonstrated that functional self Ag-specific aTregs can be generated from CD4$^+$CD25$^-$ T cells in vitro. In this study, we further demonstrate that an increased frequency of islet-specific FOXP3$^+$ T cells was generated in vitro with low Ag dose (1 μg/ml) compared with that for high Ag dose (50 μg/ml). This suggests that generation of a greater frequency of FOXP3$^+$Tmr$^+$ cells is an inherent consequence of all human CD4 T cells activated with lower concentrations of Ag, not just high-affinity foreign Ag-specific T cells. Notably, higher concentrations of self peptide compared with foreign peptide were required to detect low-affinity self Ag-specific aTregs (1 μg/ml GAD versus 0.1 μg/ml HA) consistent with both potency and density of peptide affecting the percentage of FOXP3$^+$ cells in a population as has been shown by others in a mouse model (11). Together, these data demonstrate that exposure to limited, but detectable, foreign or self Ag may influence the frequency of FOXP3$^+$ cells in human CD4 T cells.

In humans, the plasticity of some FOXP3$^+$ populations is highlighted by the kinetics of FOXP3 expression in different cell subsets: FOXP3 expression is constitutively expressed in nTregs, is induced in aTregs, and is transiently expressed in activated T cells (2, 53). In our Ag-specific cultures, FOXP3 expression was induced and maintained with similar kinetics in low- and high-dose cultures indicative of an aTreg subset, and the frequency of FOXP3$^+$ cells remained stable upon further exposure to IL-2 (Fig. 7)—both characteristics of aTreg. However, upon restimulation through the TCR, the frequency of aTregs decreased. Although some of the loss in FOXP3 content may occur through activation-induced cell death of FOXP3$^+$ cells, in all experiments the number of cells recovered after activation far exceeded the number of FOXP3$^-$ cells in the sorted populations (data not shown) suggesting that some FOXP3$^+$ cells may have lost FOXP3 expression and represent a plastic cell population. In this experiment, FOXP3$^-$ T cells could have preferentially proliferated upon restimulation, thereby resulting in a decreased frequency of FOXP3$^+$ cells on a population level. However, the frequency of FOXP3$^+$ cells was similar after restimulation with low and high Ag doses. Whether restimulation in vitro with low-dose Ag is a potent enough stimuli to result in enhanced proliferation of FOXP3$^-$ cells observed upon primary stimulation

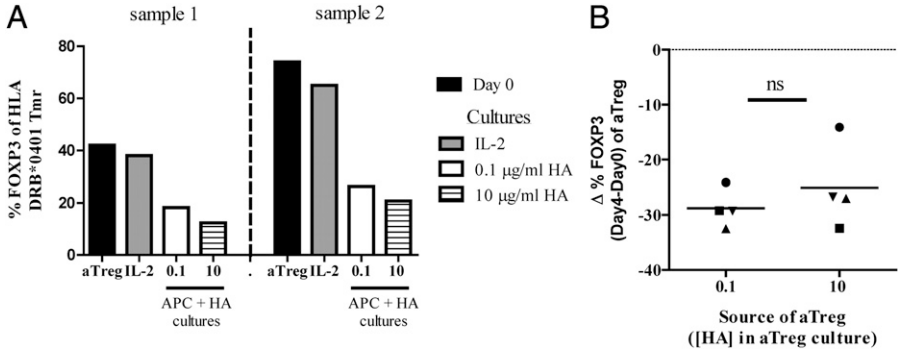

FIGURE 7. The frequency of FOXP3$^+$ cells in aTregs is not maintained upon restimulation. *A*, On day 14, CD25$^+$Tmr$^+$ T cells from low (0.1 μg/ml) Ag dose cultures were sorted and stained to assess FOXP3 content (black bars). Sorted Tmr$^+$CD25$^+$ cells were then placed in culture with IL-2 alone (gray bars) or irradiated APCs and 0.1 or 10 μg/ml HA peptide. FOXP3 content of the Tmr$^+$ population was assessed by flow cytometry 5 d after reactivation. Two control subjects with a high (>5%) frequency of Tmr staining, which allows for accurate analysis of restimulation cultures, are shown. *B*, CD25$^+$Tmr$^+$ T cells from low (0.1 μg/ml) and high (10 μg/ml) dose cultures were stained to assess FOXP3 content, sorted, and placed in a functional assay with CFSE-labeled CD4$^+$CD25$^-$ responder cells stimulated with anti-CD3/anti-CD28 beads at a 4:1 responder to Treg ratio as described in *Materials and Methods*. FOXP3 content of CFSE-negative aTregs was assessed by flow cytometry on day 4 of the functional assay. FOXP3 content prior to placement in the functional assay and on day 4 was compared and plotted as Δ (day 4 − day 0) for each culture. Different subjects are noted by different symbols (circles = subject 1, squares = subject 2, upward triangles = subject 3, downward triangles = subject 4).

exclusively in the high Ag dose culture or other mechanisms are involved is not known to date. Lastly, addition of IL-2 to these restimulation cultures or ongoing production of high levels of IL-2 in vivo may result in maintenance of these aTregs even after TCR ligation, as shown in a murine adoptive transfer model (54). We clearly demonstrated that nTregs were not expanded in our culture system. Thus, although our data do not exclude the involvement of nTregs in low-dose tolerance in vivo, they do strongly suggest that Ag dose influences the frequency of aTreg generation in vitro and that human Ag-specific aTregs could play an effective role in low-dose tolerance. This may especially be evident clinically when low-dose tolerance is transient.

Persistent expression of FOXP3 is associated with suppressive function and increased demethylation of the FOXP3 promotor region (4, 10, 32, 55, 56), whereas transient and lower expression of FOXP3 upon activation is not (53). In our cultures, we found that the frequency of $FOXP3^+$ cells in the Tmr^+ population positively correlated with suppressive function, resulting in greater suppression by $CD25^{hi}$ Tmr^+ cells sorted from low Ag dose cultures where FOXP3 content and level of expression was increased. Notably, the frequency of $FOXP3^+$ cells correlated with function for both low- and high-dose aTregs even though the level of expression of FOXP3 was higher in the low Ag dose aTregs, a phenotype typical of more potent Tregs. Moreover, even though high Ag dose aTregs expressed lower levels of FOXP3, a phenotype associated with unstable FOXP3 expression in activated effector cells, cytokine production was similar between high and low Ag dose aTregs. Together, these data suggest that the level of expression of FOXP3 in Ag-specific human aTregs does not significantly impinge upon their suppressive function. This is in contrast to the culture systems of others in which cells were activated with anti-CD3 and anti-CD28 Abs and/or assayed earlier in culture for suppressive function, and a lack of suppression was observed (51, 57, 58). Together, these data suggest that stimulation with low Ag dose in APC–peptide cultures results in an increased frequency of functional Tmr^+ aTregs in which FOXP3 expression persists and is associated with suppression.

Differentiation of $FOXP3^+$ T cells from naive T cell subsets is well established. In this study, we demonstrate that $FOXP3^+Tmr^+$ T cells can arise from naive, central memory, and effector memory CD4 T cell subsets. This may be particularly important in providing a mechanism to control the magnitude of memory responses when Ag is limited. We propose a model in which a high frequency of $FOXP3^+$ cells induced with low Ag limits perpetuation of immune responses by transiently suppressing proliferation of other cells responding to the same Ag. In contrast, activation with high Ag dose results in a greater frequency of $FOXP3^-$ cells that could overwhelm the suppressive effects of the $FOXP3^+$ cells resulting in immunogenic responses to Ag. Hence, FOXP3 expression upon activation may function to place a transient brake on low Ag dose immune responses while not limiting the magnitude of future immune responses to higher doses of the same Ag. These studies further suggest that aTregs could play a role in low-dose tolerance in vivo.

Acknowledgments

We thank Dr. John Gebe and Dr. Michael Turner for insightful discussions and critical reading of the manuscript and the investigators and staff of the Benaroya Research Institute-Juvenile Diabetes Research Foundation Center for Translational Research, the Children's Hospital and Regional Medical Center, Seattle, and the Benaroya Research Institute Diabetes Clinical Research Program for subject recruitment as well as the Benaroya Research Institute Translational Research Clinical Core for sample processing and handling.

Disclosures

The authors have no financial conflicts of interest.

References

1. Bluestone, J. A., and A. K. Abbas. 2003. Natural versus adaptive regulatory T cells. *Nat. Rev. Immunol.* 3: 253–257.
2. Curotto de Lafaille, M. A., and J. J. Lafaille. 2009. Natural and adaptive foxp3+ regulatory T cells: more of the same or a division of labor? *Immunity* 30: 626–635.
3. Horwitz, D. A., S. G. Zheng, and J. D. Gray. 2008. Natural and TGF-beta-induced Foxp3(+)CD4(+) CD25(+) regulatory T cells are not mirror images of each other. *Trends Immunol.* 29: 429–435.
4. Rubtsov, Y. P., R. E. Niec, S. Josefowicz, L. Li, J. Darce, D. Mathis, C. Benoist, and A. Y. Rudensky. 2010. Stability of the regulatory T cell lineage in vivo. *Science* 329: 1667–1671.
5. Kang, H. K., M. A. Michaels, B. R. Berner, and S. K. Datta. 2005. Very low-dose tolerance with nucleosomal peptides controls lupus and induces potent regulatory T cell subsets. *J. Immunol.* 174: 3247–3255.
6. Kretschmer, K., I. Apostolou, D. Hawiger, K. Khazaie, M. C. Nussenzweig, and H. von Boehmer. 2005. Inducing and expanding regulatory T cell populations by foreign antigen. *Nat. Immunol.* 6: 1219–1227.
7. Chen, T. C., S. P. Cobbold, P. J. Fairchild, and H. Waldmann. 2004. Generation of anergic and regulatory T cells following prolonged exposure to a harmless antigen. *J. Immunol.* 172: 5900–5907.
8. Graca, L., T. C. Chen, A. Le Moine, S. P. Cobbold, D. Howie, and H. Waldmann. 2005. Dominant tolerance: activation thresholds for peripheral generation of regulatory T cells. *Trends Immunol.* 26: 130–135.
9. Kang, J., S. J. Huddleston, J. M. Fraser, and A. Khoruts. 2008. De novo induction of antigen-specific CD4+CD25+Foxp3+ regulatory T cells in vivo following systemic antigen administration accompanied by blockade of mTOR. *J. Leukoc. Biol.* 83: 1230–1239.
10. Mahic, M., S. Yaqub, T. Bryn, K. Henjum, D. M. Eide, K. M. Torgersen, E. M. Aandahl, and K. Taskén. 2008. Differentiation of naive CD4+ T cells into CD4+CD25+FOXP3+ regulatory T cells by continuous antigen stimulation. *J. Leukoc. Biol.* 83: 1111–1117.
11. Gottschalk, R. A., E. Corse, and J. P. Allison. 2010. TCR ligand density and affinity determine peripheral induction of Foxp3 in vivo. *J. Exp. Med.* 207: 1701–1711.
12. Haxhinasto, S., D. Mathis, and C. Benoist. 2008. The AKT-mTOR axis regulates de novo differentiation of CD4+Foxp3+ cells. *J. Exp. Med.* 205: 565–574.
13. Sauer, S., L. Bruno, A. Hertweck, D. Finlay, M. Leleu, M. Spivakov, Z. A. Knight, B. S. Cobb, D. Cantrell, E. O'Connor, et al. 2008. T cell receptor signaling controls Foxp3 expression via PI3K, Akt, and mTOR. *Proc. Natl. Acad. Sci. USA* 105: 7797–7802.
14. Long, S. A., and J. H. Buckner. 2008. Combination of rapamycin and IL-2 increases de novo induction of human CD4(+)CD25(+)FOXP3(+) T cells. *J. Autoimmun.* 30: 293–302.
15. Gabryšová, L., J. R. Christensen, X. Wu, A. Kissenpfennig, B. Malissen, and A. O'Garra. 2011. Integrated T-cell receptor and costimulatory signals determine TGF-β-dependent differentiation and maintenance of Foxp3+ regulatory T cells. *Eur. J. Immunol.* 41: 1242–1248.
16. Oliveira, V. G., M. Caridade, R. S. Paiva, J. Demengeot, and L. Graca. 2011. Sub-optimal CD4+ T-cell activation triggers autonomous TGF-β-dependent conversion to Foxp3+ regulatory T cells. *Eur. J. Immunol.* 41: 1249–1255.
17. Turner, M. S., L. P. Kane, and P. A. Morel. 2009. Dominant role of antigen dose in CD4+Foxp3+ regulatory T cell induction and expansion. *J. Immunol.* 183: 4895–4903.
18. Fourcade, J., Z. Sun, P. Kudela, B. Janjic, J. M. Kirkwood, T. El-Hafnawy, and H. M. Zarour. 2010. Human tumor antigen-specific helper and regulatory T cells share common epitope specificity but exhibit distinct T cell repertoire. *J. Immunol.* 184: 6709–6718.
19. Vukmanovic-Stejic, M., Y. Zhang, J. E. Cook, J. M. Fletcher, A. McQuaid, J. E. Masters, M. H. Rustin, L. S. Taams, P. C. Beverley, D. C. Macallan, and A. N. Akbar. 2006. Human CD4+ CD25hi Foxp3+ regulatory T cells are derived by rapid turnover of memory populations in vivo. *J. Clin. Invest.* 116: 2423–2433.
20. Mittag, D., A. Scholzen, N. Varese, L. Baxter, G. Paukovics, L. C. Harrison, J. M. Rolland, and R. E. O'Hehir. 2010. The effector T cell response to ryegrass pollen is counterregulated by simultaneous induction of regulatory T cells. *J. Immunol.* 184: 4708–4716.
21. Taylor, J. J., M. Mohrs, and E. J. Pearce. 2006. Regulatory T cell responses develop in parallel to Th responses and control the magnitude and phenotype of the Th effector population. *J. Immunol.* 176: 5839–5847.
22. Roncarolo, M. G., M. K. Levings, and C. Traversari. 2001. Differentiation of T regulatory cells by immature dendritic cells. *J. Exp. Med.* 193: F5–F9.
23. Tarbell, K. V., L. Petit, X. Zuo, P. Toy, X. Luo, A. Mqadmi, H. Yang, M. Suthanthiran, S. Mojsov, and R. M. Steinman. 2007. Dendritic cell-expanded, islet-specific CD4+ CD25+ CD62L+ regulatory T cells restore normoglycemia in diabetic NOD mice. *J. Exp. Med.* 204: 191–201.
24. Zheng, S. G., J. Wang, P. Wang, J. D. Gray, and D. A. Horwitz. 2007. IL-2 is essential for TGF-beta to convert naive CD4+CD25- cells to CD25+Foxp3+ regulatory T cells and for expansion of these cells. *J. Immunol.* 178: 2018–2027.
25. Huang, H., W. Dawicki, X. Zhang, J. Town, and J. R. Gordon. 2010. Tolerogenic dendritic cells induce CD4+CD25hiFoxp3+ regulatory T cell differentiation from CD4+CD25-/loFoxp3- effector T cells. *J. Immunol.* 185: 5003–5010.

26. James, E. A., J. Bui, D. Berger, L. Huston, M. Roti, and W. W. Kwok. 2007. Tetramer-guided epitope mapping reveals broad, individualized repertoires of tetanus toxin-specific CD4+ T cells and suggests HLA-based differences in epitope recognition. *Int. Immunol.* 19: 1291–1301.
27. Masewicz, S. A., G. K. Papadopoulos, E. Swanson, L. Moriarity, A. K. Moustakas, and G. T. Nepom. 2002. Modulation of T cell response to hGAD65 peptide epitopes. *Tissue Antigens* 59: 101–112.
28. Novak, E. J., A. W. Liu, G. T. Nepom, and W. W. Kwok. 1999. MHC class II tetramers identify peptide-specific human CD4(+) T cells proliferating in response to influenza A antigen. *J. Clin. Invest.* 104: R63–R67.
29. Yang, J., E. A. James, L. Huston, N. A. Danke, A. W. Liu, and W. W. Kwok. 2006. Multiplex mapping of CD4 T cell epitopes using class II tetramers. *Clin. Immunol.* 120: 21–32.
30. Yang, J., N. A. Danke, D. Berger, S. Reichstetter, H. Reijonen, C. Greenbaum, C. Pihoker, E. A. James, and W. W. Kwok. 2006. Islet-specific glucose-6-phosphatase catalytic subunit-related protein-reactive CD4+ T cells in human subjects. *J. Immunol.* 176: 2781–2789.
31. Danke, N. A., D. M. Koelle, C. Yee, S. Beheray, and W. W. Kwok. 2004. Autoreactive T cells in healthy individuals. *J. Immunol.* 172: 5967–5972.
32. Long, S. A., M. R. Walker, M. Rieck, E. James, W. W. Kwok, S. Sanda, C. Pihoker, C. Greenbaum, G. T. Nepom, and J. H. Buckner. 2009. Functional islet-specific Treg can be generated from CD4+CD25- T cells of healthy and type 1 diabetic subjects. *Eur. J. Immunol.* 39: 612–620.
33. Baron, U., S. Floess, G. Wieczorek, K. Baumann, A. Grützkau, J. Dong, A. Thiel, T. J. Boeld, P. Hoffmann, M. Edinger, et al. 2007. DNA demethylation in the human FOXP3 locus discriminates regulatory T cells from activated FOXP3(+) conventional T cells. *Eur. J. Immunol.* 37: 2378–2389.
34. Schneider, A., M. Rieck, S. Sanda, C. Pihoker, C. Greenbaum, and J. H. Buckner. 2008. The effector T cells of diabetic subjects are resistant to regulation via CD4+ FOXP3+ regulatory T cells. *J. Immunol.* 181: 7350–7355.
35. Walker, M. R., B. D. Carson, G. T. Nepom, S. F. Ziegler, and J. H. Buckner. 2005. De novo generation of antigen-specific CD4+CD25+ regulatory T cells from human CD4+CD25- cells. *Proc. Natl. Acad. Sci. USA* 102: 4103–4108.
36. Davidson, T. S., R. J. DiPaolo, J. Andersson, and E. M. Shevach. 2007. Cutting Edge: IL-2 is essential for TGF-beta-mediated induction of Foxp3+ T regulatory cells. *J. Immunol.* 178: 4022–4026.
37. Horwitz, D. A., S. G. Zheng, J. Wang, and J. D. Gray. 2008. Critical role of IL-2 and TGF-beta in generation, function and stabilization of Foxp3+CD4+ Treg. *Eur. J. Immunol.* 38: 912–915.
38. Li, M. O., and R. A. Flavell. 2008. Contextual regulation of inflammation: a duet by transforming growth factor-beta and interleukin-10. *Immunity* 28: 468–476.
39. Janson, P. C., M. E. Winerdal, P. Marits, M. Thorn, R. Ohlsson, and O. Winqvist. 2008. FOXP3 promoter demethylation reveals the committed Treg population in humans. *PLoS ONE* 3: e1612.
40. Huehn, J., J. K. Polansky, and A. Hamann. 2009. Epigenetic control of FOXP3 expression: the key to a stable regulatory T-cell lineage? *Nat. Rev. Immunol.* 9: 83–89.
41. Thornton, A. M., P. E. Korty, D. Q. Tran, E. A. Wohlfert, P. E. Murray, Y. Belkaid, and E. M. Shevach. 2010. Expression of Helios, an Ikaros transcription factor family member, differentiates thymic-derived from peripherally induced Foxp3+ T regulatory cells. *J. Immunol.* 184: 3433–3441.
42. McClymont, S. A., A. L. Putnam, M. R. Lee, J. H. Esensten, W. Liu, M. A. Hulme, U. Hoffmüller, U. Baron, S. Olek, J. A. Bluestone, and T. M. Brusko. 2011. Plasticity of human regulatory T cells in healthy subjects and patients with type 1 diabetes. *J. Immunol.* 186: 3918–3926.
43. Buckner, J. H., and S. F. Ziegler. 2008. Functional analysis of FOXP3. *Ann. N. Y. Acad. Sci.* 1143: 151–169.
44. Constant, S. L., and K. Bottomly. 1997. Induction of Th1 and Th2 CD4+ T cell responses: the alternative approaches. *Annu. Rev. Immunol.* 15: 297–322.
45. Sundrud, M. S., and M. A. Nolan. 2010. Synergistic and combinatorial control of T cell activation and differentiation by transcription factors. *Curr. Opin. Immunol.* 22: 286–292.
46. Gebe, J. A., B. A. Falk, K. A. Rock, S. A. Kochik, A. K. Heninger, H. Reijonen, W. W. Kwok, and G. T. Nepom. 2003. Low-avidity recognition by CD4+ T cells directed to self-antigens. *Eur. J. Immunol.* 33: 1409–1417.
47. Mallone, R., S. A. Kochik, E. M. Laughlin, V. H. Gersuk, H. Reijonen, W. W. Kwok, and G. T. Nepom. 2004. Differential recognition and activation thresholds in human autoreactive GAD-specific T-cells. *Diabetes* 53: 971–977.
48. Hori, S. 2011. Regulatory T cell plasticity: beyond the controversies. *Trends Immunol.* 32: 295–300 .
49. Purvis, H. A., J. N. Stoop, J. Mann, S. Woods, A. E. Kozijn, S. Hambleton, J. H. Robinson, J. D. Isaacs, A. E. Anderson, and C. M. Hilkens. 2010. Low-strength T-cell activation promotes Th17 responses. *Blood* 116: 4829–4837.
50. Li, M. O., Y. Y. Wan, S. Sanjabi, A. K. Robertson, and R. A. Flavell. 2006. Transforming growth factor-beta regulation of immune responses. *Annu. Rev. Immunol.* 24: 99–146.
51. Noël, G., C. Brinster, G. Semana, and D. Bruniquel. 2009. Modulation of the TCR stimulation strength can render human activated CD4+ T cells suppressive. *Int. Immunol.* 21: 1025–1036.
52. Zhang, X. L., J. Peng, J. Z. Sun, J. J. Liu, C. S. Guo, Z. G. Wang, Y. Yu, Y. Shi, P. Qin, S. G. Li, et al. 2009. De novo induction of platelet-specific CD4(+)CD25(+) regulatory T cells from CD4(+)CD25(-) cells in patients with idiopathic thrombocytopenic purpura. *Blood* 113: 2568–2577.
53. Ziegler, S. F. 2007. FOXP3: not just for regulatory T cells anymore. *Eur. J. Immunol.* 37: 21–23.
54. Chen, Q., Y. C. Kim, A. Laurence, G. A. Punkosdy, and E. M. Shevach. 2011. IL-2 controls the stability of Foxp3 expression in TGF-beta-induced Foxp3+ T cells in vivo. *J. Immunol.* 186: 6329–6337.
55. Josefowicz, S. Z., C. B. Wilson, and A. Y. Rudensky. 2009. Cutting edge: TCR stimulation is sufficient for induction of Foxp3 expression in the absence of DNA methyltransferase 1. *J. Immunol.* 182: 6648–6652.
56. Zheng, Y., S. Josefowicz, A. Chaudhry, X. P. Peng, K. Forbush, and A. Y. Rudensky. 2010. Role of conserved non-coding DNA elements in the Foxp3 gene in regulatory T-cell fate. *Nature* 463: 808–812.
57. Allan, S. E., S. Q. Crome, N. K. Crellin, L. Passerini, T. S. Steiner, R. Bacchetta, M. G. Roncarolo, and M. K. Levings. 2007. Activation-induced FOXP3 in human T effector cells does not suppress proliferation or cytokine production. *Int. Immunol.* 19: 345–354.
58. Wang, J., A. Ioan-Facsinay, E. I. van der Voort, T. W. Huizinga, and R. E. Toes. 2007. Transient expression of FOXP3 in human activated nonregulatory CD4+ T cells. *Eur. J. Immunol.* 37: 129–138.

B-cell adaptor for PI3K (BCAP) negatively regulates Toll-like receptor signaling through activation of PI3K

Minjian Ni[a], Alexander W. MacFarlane IV[b], Michelle Toft[c], Clifford A. Lowell[c], Kerry S. Campbell[b], and Jessica A. Hamerman[a,1]

[a]Immunology Program, Benaroya Research Institute, Seattle, WA 98101; [b]Institute for Cancer Research, Fox Chase Cancer Center, Philadelphia, PA 19111; and [c]Department of Laboratory Medicine, University of California, San Francisco, CA 94143

Edited by Lewis L. Lanier, University of California, San Francisco, CA, and approved October 20, 2011 (received for review July 22, 2011)

Toll-like receptors (TLRs) recognize pathogens and their components, thereby initiating immune responses to infectious organisms. TLR ligation leads to the activation of NF-κB and MAPKs through well-defined pathways, but it has remained unclear how TLR signaling activates PI3K, which provides an inhibitory pathway limiting TLR responses. Here, we show that the signaling adapter B-cell adaptor for PI3K (BCAP) links TLR signaling to PI3K activation. BCAP-deficient macrophages and mice are hyperresponsive to TLR agonists and have reduced PI3K activation. The ability of BCAP to inhibit TLR responses requires its capacity to bind PI3K. BCAP is constitutively phosphorylated and associated with the p85 subunit of PI3K in macrophages. This tyrosine-phosphorylated BCAP is transiently enriched in the membrane fraction in response to LPS treatment, suggesting a model whereby TLR signaling causes the phosphorylation of the small amount of BCAP that is associated with membranes in the resting state or the translocation of phosphorylated BCAP from the cytoplasm to the membrane. This accumulation of tyrosine-phosphorylated BCAP at the membrane with its associated PI3K would then allow for the catalysis of Ptd Ins P2 to Ptd Ins P3 and downstream PI3K-dependent signals. Therefore, BCAP is an essential activator of the PI3K pathway downstream of TLR signaling, providing a brake to limit potentially pathogenic excessive TLR responses.

inflammatory response | innate immunity

Toll-like receptors (TLRs) recognize microbial components derived from a wide range of bacteria, viruses, parasites, and fungi (1). Ligand binding to TLRs causes the recruitment of the cytoplasmic adapter proteins MyD88 and/or TIR domain-containing adapter-inducing IFN-β (TRIF), resulting in a signal transduction cascade leading to the activation of the MAPK and NF-κB pathways (1). A key consequence of TLR signaling is the transcriptional regulation of proinflammatory genes, such as IL-12 p40, IL-6, and TNF. Although TLR-induced proinflammatory cytokine production is important for host defense in clearing pathogens, hyperproduction of inflammatory cytokines is associated with the pathogenesis of inflammatory and autoimmune diseases (2). Therefore, it is important to understand mechanisms that the immune system uses to control the magnitude of TLR responses.

In addition to the activation of MAPK and NF-κB pathways, TLR ligation leads to activation of the PI3K pathway (3). Although some evidence using pharmacological PI3K inhibition indicates that PI3K activation can promote TLR responses (4–6), the preponderance of studies with macrophages or dendritic cells from mice with genetically or pharmacologically altered PI3K activation indicates that PI3K activation negatively regulates TLR-induced proinflammatory cytokine production (7–12). In support of a negative role for PI3K in TLR signaling, genetic deficiency in the p85α regulatory subunit of PI3K results in increased LPS-induced IL-12 production in dendritic cells (8). Additionally, genetic deficiency in lipid phosphatases that counter the activity of PI3K, such as SRC homology 2 domain-containing inositol-5-phosphatase (SHIP) or phosphatase and tensin homolog (PTEN), results in decreased TLR responses (9, 11). Although it is clear that PI3K activity is an important negative regulator of TLR responses, the exact mechanisms by which PI3K is activated after TLR ligation are still unclear.

The PI3Ks are a family of lipid kinases that phosphorylate the 3′-hydroxyl group of phosphatidylinositol and phosphoinositides. The product of PI3K, Ptd Ins P3 (PIP3), recruits and activates a number of signaling proteins at the plasma membrane, including Akt/PKB, Bruton's tyrosine kinase, PDK, atypical PKCs, and phospholipase Cγ (13). The PI3K family is classified according to sequence homology and substrate specificity into three different types: class I, class II, and class III. Class Ia PI3Ks consist of a catalytic subunit (p110) and a regulatory subunit encoded by at least three distinct genes (p85α, p85β, and p55γ). p85α is the most abundantly expressed regulatory isoform of PI3K, and it is found constitutively associated with one of the three catalytic subunits (p110α, p110β, and p110δ) in the cytoplasm in an inactive PI3K complex (13). The p85α subunit contains two SH2 domains that bind with high affinity to phosphotyrosines within YxxM sequences found in a variety of proteins. The SH2-dependent binding to p-YxxM motifs within docking proteins causes a conformational change in p85 resulting in increased catalytic activity of the associated p110 and recruitment of PI3K to the plasma membrane, where it can access its substrate, Ptd Ins P2 (PIP2) (14). Therefore, binding of p85 to p-YxxM motifs is critical for initiating downstream signaling.

Because the binding of p85 PI3K to p-YxxM sequences is critical for activation of PI3K, we hypothesized that a YxxM-containing signaling adapter would link TLR signaling to PI3K activation. We noted that the YxxM-containing B-cell adaptor for PI3K (BCAP), encoded by the *pik3ap1* gene, is highly expressed in macrophages (15). BCAP was originally identified as a B cell-expressed adapter protein that can recruit PI3K p85 when tyrosine-phosphorylated on its four YxxM motifs after B-cell receptor (BCR) ligation and is critical for BCR-induced Akt phosphorylation (15). BCAP serves a similar role in immunoreceptor tyrosine-based activation motif (ITAM)-mediated Akt phosphorylation in natural killer (NK) cells (16). Here, we show that BCAP is a critical link between TLR ligation and PI3K activation in macrophages. Thus, in addition to its role in activating PI3K downstream of BCR cross-linking in B cells, our findings show that BCAP regulates PI3K activation from a distinct signaling pathway downstream of TLRs, resulting in a unique inhibitory role for BCAP in regulating macrophage function.

Results

Increased TLR-Induced Inflammatory Cytokine Production by BCAP-Deficient Macrophages. Because the PI3K pathway can negatively regulate IL-12 production in dendritic cells (8), we first examined IL-12 p40 production by BCAP-deficient macrophages. Bone

Author contributions: M.N., A.W.M., C.A.L., K.S.C., and J.A.H. designed research; M.N., M.T., and J.A.H. performed research; A.W.M. and K.S.C. contributed reagents; M.N. and J.A.H. analyzed data; and M.N., C.A.L., K.S.C., and J.A.H. wrote the paper.

The authors declare no conflict of interest.

This article is a PNAS Direct Submission.

[1]To whom correspondence should be addressed. E-mail: jhamerman@benaroyaresearch.org.

This article contains supporting information online at www.pnas.org/lookup/suppl/doi:10.1073/pnas.1111957108/-/DCSupplemental.

marrow (BM)-derived macrophages from WT and BCAP-deficient mice were stimulated with TLR4, TLR7, and TLR9 agonists to induce cytokine production. BCAP-deficient macrophages secreted a significantly higher amount of IL-12 p40 when stimulated with all three TLR ligands tested, indicating that BCAP negatively regulates IL-12 p40 expression in BM-derived macrophages (Fig. 1*A*). We also examined whether BCAP negatively regulates the production of other proinflammatory cytokines. Secretion of both IL-6 and TNF was higher in BCAP-deficient macrophages than in WT macrophages (Fig. 1*A*). Therefore, BCAP negatively regulates not only IL-12 p40 secretion but IL-6 and TNF secretion downstream of TLR ligation in macrophages.

TLR signaling also induces the secretion of the antiinflammatory cytokine IL-10, which can decrease inflammatory cytokine production in an autocrine and paracrine manner (17). We therefore asked whether the increased IL-12 p40, IL-6, and TNF secretion from TLR-activated BCAP-deficient macrophages was attributable to decreased IL-10 secretion. However, IL-10 secretion was not lower in LPS-treated BCAP-deficient macrophages than in WT macrophages (Fig. 1*B*). We also investigated whether BCAP negatively regulates TLR responses in vivo. BCAP-deficient mice produced significantly more IL-12 p40 in response to in vivo injection of LPS than WT mice over a 6-h time course (Fig. 1*C*). Therefore, BCAP inhibits TLR responses both in vitro and in vivo.

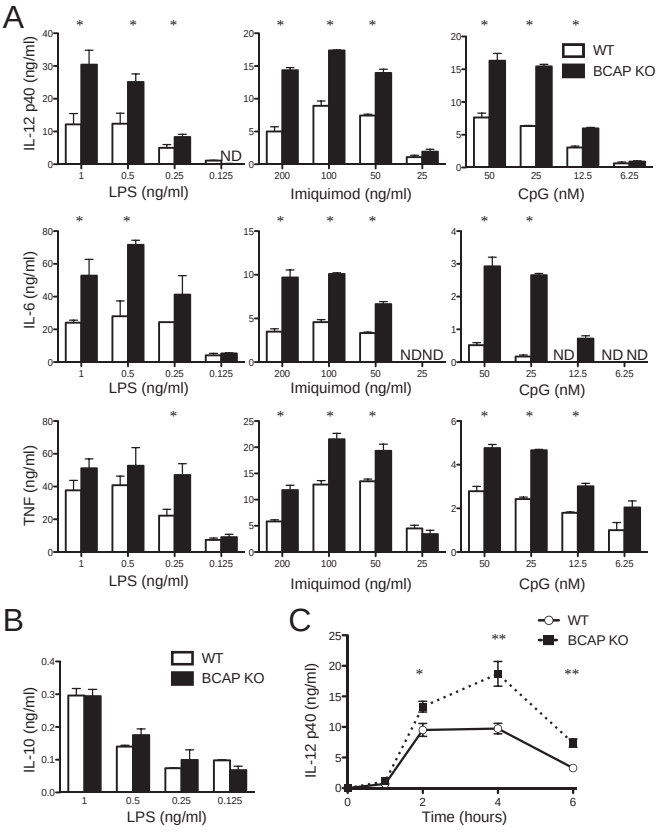

Fig. 1. BCAP negatively regulates TLR-induced inflammatory cytokine production in vitro and in vivo. (*A* and *B*) BM-derived macrophages from WT or BCAP-deficient (BCAP KO) mice were incubated with the indicated concentrations of LPS (TLR4), Imiquimod (TLR7), or CpG DNA (TLR9) for 16 h. Supernatants were collected, and the amounts of IL-12 p40, IL-6, and TNF (*A*) or IL-10 (*B*) were measured by ELISA. Data are representative of four independent experiments and are expressed as the mean ± SD of triplicate wells. $*P < 0.05$. ND, not detected. (*C*) WT or BCAP-deficient mice were injected i.p. with 1 μg/g of LPS, and plasma IL-12 p40 concentrations at 1, 2, 4, and 6 h postinjection were measured. Data are from one of three independent experiments and are expressed as the mean ± SD with $n = 4$ mice per group, with each mouse assayed in triplicate. $*P < 0.05$; $**P < 0.01$.

BCAP Deficiency Minimally Affects TLR-Induced MAPK Activation and IκBα Degradation. To investigate the molecular mechanism by which BCAP inhibits TLR-induced cytokine production, we assessed how BCAP deficiency influences MAPK and NF-κB signaling downstream of TLR ligation. The kinetics and magnitude of phosphorylation of all three MAPKs were similar in BCAP-deficient and WT macrophages after stimulation with LPS (Fig. 2*A*). In some experiments, there was a slight increase in ERK phosphorylation in BCAP-deficient macrophages in comparison to WT macrophages; however, these differences were subtle and not consistent. In WT and BCAP-deficient macrophages, IκBα, the cytoplasmic inhibitor of NF-κB, was degraded with similar kinetics and was present in similar amounts (Fig. 2*B*). These data suggested that the hyperresponsiveness to TLR stimulation in BCAP-deficient macrophages did not result from increased NF-κB or MAPK activation.

Reduced Akt Phosphorylation and PI3K Activity in BCAP-Deficient Macrophages. Because BCAP has four YxxM motifs and is associated with PI3K activation in B cells, we hypothesized that deficiency in BCAP would reduce TLR-induced Akt phosphorylation, which is dependent on PI3K activation (18). Therefore, we compared LPS-induced Akt phosphorylation in WT and BCAP-deficient macrophages. Indeed, we found that LPS-induced phosphorylation of Akt was dramatically reduced in BCAP-deficient macrophages, at both Ser473 and Thr308 residues (Fig. 3*A*), indicating a reduced capacity for PI3K to stimulate downstream Akt activation in the absence of BCAP. Interestingly, basal Akt phosphorylation at both sites was also reduced in BCAP-deficient macrophages, suggesting that BCAP functions to regulate PI3K activation in resting macrophages in addition to those activated by TLR ligation. BCAP-deficient macrophages were not defective in Akt phosphorylation in response to TNF (Fig. S1), suggesting that BCAP specifically participates in the activation of PI3K downstream of TLR signaling.

Because BCAP-deficient macrophages had reduced Akt activation in response to TLR ligation, we reasoned that the PI3K inhibitor wortmannin would have a reduced capacity to enhance TLR-induced cytokine responses by BCAP-deficient macrophages compared with WT macrophages. To test this hypothesis, we measured the increase in TLR-induced cytokine production after pretreatment of macrophages with varying doses of wortmannin. In WT macrophages, CpG DNA-stimulated IL-12 p40 and IL-6 secretion increased when cells were pretreated with wortmannin in a dose-dependent manner (Fig. 3 *B* and *C*), consistent with published data demonstrating the inhibitory impact of PI3K on TLR responses (8, 19–21). In contrast to WT macrophages, however, pretreatment of BCAP-deficient macrophages with wortmannin had little effect on IL-12 p40 or IL-6 secretion (Fig. 3 *B* and *C*), suggesting that the amount of PI3K activity suppressing TLR function is minimal in cells lacking BCAP. Together with the reduced TLR-induced Akt phosphorylation, these results demonstrate that BCAP-deficient macrophages have a defect in TLR-induced PI3K activation.

BCAP Is Constitutively Tyrosine-Phosphorylated and Associated with PI3K in Macrophages. When immunoprecipitated from resting macrophages, BCAP was found as two doublets, which correspond to the bands designated 1/2 and 3/4 by Kurosaki and colleagues (15) (Fig. 4*A*). The 1/2 and 3/4 bands of BCAP are thought to be generated by alternative splicing of the BCAP mRNA (15). Interestingly, we never observed bands 5 and 6 seen in B cells, which run at over 100 kDa. Previous studies showed that BCAP is inducibly tyrosine-phosphorylated in B cells on BCR ligation, resulting in association with the p85 subunit of PI3K (15). Surprisingly, BCAP was constitutively tyrosine-phosphorylated and associated with PI3K p85 in resting macrophages, and the magnitude of tyrosine phosphorylation did not

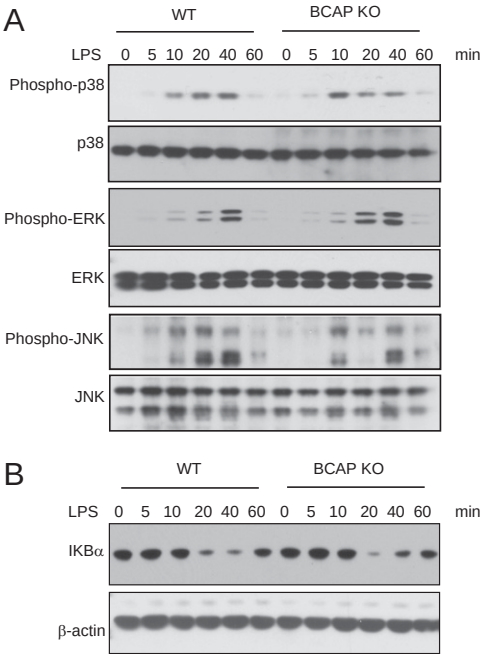

Fig. 2. BCAP deficiency has minimal effects on TLR-induced MAPK activation and IκBα degradation. BM-derived macrophages were stimulated with 1 ng/mL LPS for the indicated times, after which cells were lysed. Cytoplasmic extracts were analyzed by Western blot using antibodies specific for p38 MAPK, p42/44 ERK, and JNK or for phosphorylated versions of these proteins (*A*) or for IκBα with β-actin as a loading control (*B*). Data are representative of three independent experiments.

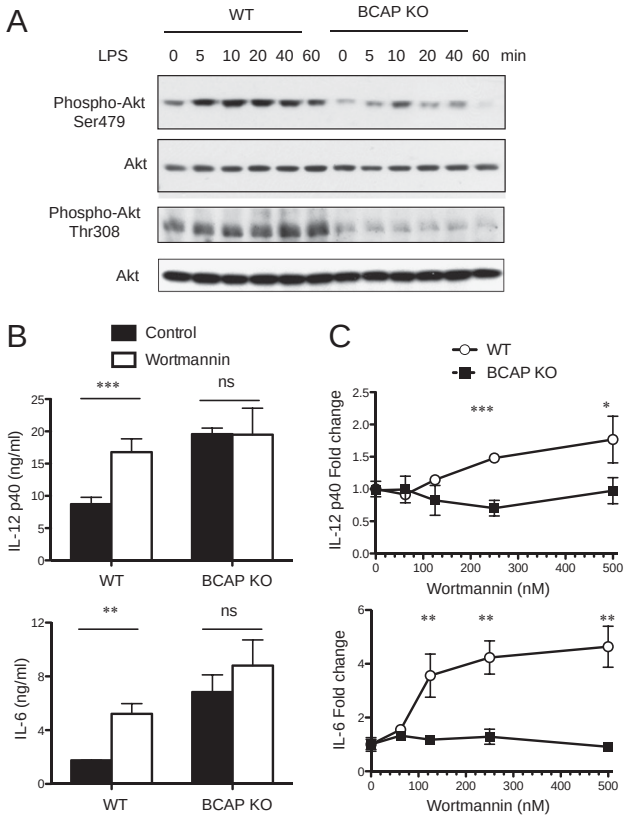

Fig. 3. PI3K activity is reduced in BCAP-deficient macrophages. (*A*) Macrophages were stimulated with 1 ng/mL LPS for the indicated time and then lysed. Cytoplasmic extracts were analyzed by Western blot using antibodies specific for phospho-Akt (Ser473 or Thr308) or Akt. (*B* and *C*) Macrophages were stimulated for 16 h with CpG DNA (25 nM) after 30 min of pretreatment with vehicle control or wortmannin. (*B*) Secretion of IL-12 p40 and IL-6 was measured by ELISA after treatment with 250 nM wortmannin. (*C*) Results are expressed as fold change compared with CpG DNA-treated, no wortmannin control, and they show the mean ± SD of triplicate wells. Data are representative of five (*A*) and three (*B* and *C*) experiments. ns, not significant; $*P < 0.05$; $**P < 0.01$; $***P < 0.001$.

increase with LPS stimulation at any time point examined, from 5 to 30 min (Fig. 4 *A* and *B*). As previously reported in B cells and NK cells, all four BCAP bands were tyrosine-phosphorylated (15, 16). Consistent with the constitutive tyrosine phosphorylation of BCAP, we also observed the association of PI3K p85 subunit in resting macrophages, and this association also did not increase with LPS stimulation (Fig. 4 *A* and *B*). These data show that BCAP is tyrosine-phosphorylated and associated with PI3K in the absence of TLR ligation, indicating that upstream signals causing BCAP tyrosine phosphorylation and PI3K recruitment are active in resting macrophages.

Neither CSF1 Receptor nor Syk Signaling Is Required for BCAP Tyrosine Phosphorylation and PI3K Association in Macrophages. Because the BM-derived macrophages used in these immunoprecipitation studies are grown in macrophage (M)-CSF, whose receptor, CSF1R, can mediate PI3K activation, we examined whether CSF1R signaling may induce BCAP phosphorylation and PI3K association. To test this hypothesis, we starved macrophages for 3 h in media without M-CSF or serum and measured BCAP tyrosine phosphorylation and PI3K association. Identical to macrophages grown continuously in M-CSF, M-CSF–starved macrophages showed constitutive BCAP tyrosine phosphorylation and PI3K association that did not change with LPS treatment (Fig. S2*A*). Therefore, we conclude that the constitutive tyrosine phosphorylation of BCAP is not mediated by CSF1R signaling.

In B cells, the Syk tyrosine kinase is required for BCAP tyrosine phosphorylation after BCR cross-linking (15). Therefore, we examined whether Syk was required for BCAP phosphorylation in macrophages. Surprisingly, the tyrosine phosphorylation of BCAP was not reduced but was dramatically increased in resting macrophages in the absence of Syk (Fig. S2*B*). This increased phosphorylation was limited to bands 3/4 and was accompanied by increased PI3K association. Thus, signaling through Syk tyrosine kinase is not required for BCAP tyrosine phosphorylation and PI3K association in macrophages.

Tyrosine-Phosphorylated BCAP Is Enriched on Membrane Fractions After LPS Treatment. YxxM-containing adapter proteins often function not only to bind and activate PI3K but to bring active PI3K to membranes where its substrate, PIP2, is found. In B cells, Okada et al. (15) found BCAP predominantly in the cytoplasm by immunofluorescence analysis and by biochemical separation of membrane and cytosolic cellular fractions followed by Western blot, with a small minority in the membrane fraction. We hypothesized that TLR signaling may cause the accumulation of tyrosine-phosphorylated BCAP at membranes where it may access PIP2. To test this hypothesis, we separated cytosolic and membrane fractions of macrophages before and after LPS treatment, as shown by the enrichment for cadherins in the membrane fraction and GAPDH in the cytosolic fraction (Fig. 4*C*, *Bottom*). We immunoprecipitated BCAP from both cytosolic and membrane fractions, and we performed Western blotting for phosphotyrosine and BCAP. As in B cells, the majority of BCAP protein was found in the cytosolic fraction, with a small but detectable amount of BCAP in the membrane fraction as seen when blotting for BCAP (Fig. 4*C*). Both the amount of tyrosine-phosphorylated BCAP and the total amount of BCAP in the membrane fraction were transiently increased 5 min after LPS treatment and returned to baseline by 10 min. Interestingly, this

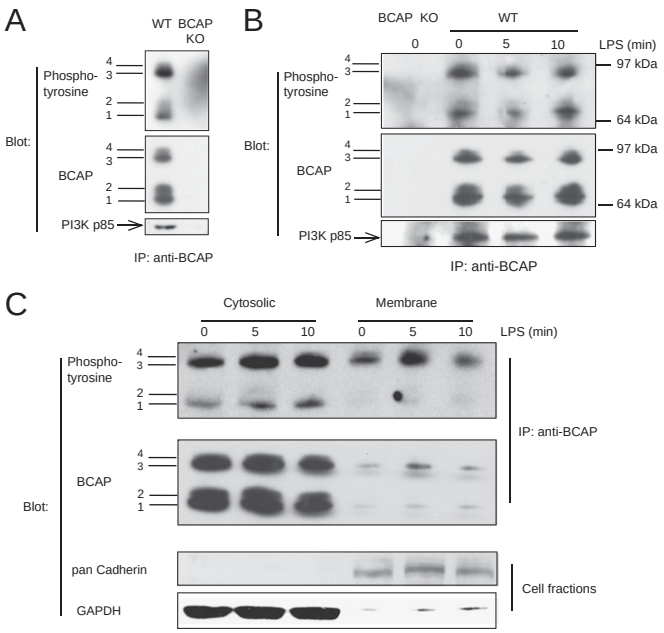

Fig. 4. BCAP is constitutively tyrosine-phosphorylated and associated with p85 PI3K in macrophages. (*A*) WT or BCAP-deficient macrophages were lysed and immunoprecipitated with anti-BCAP monoclonal antibody, separated by SDS-PAGE and immunoblotted for phosphotyrosine or BCAP. (*B*) Macrophages were treated with 1 ng/mL LPS for the indicated times and then lysed and analyzed as in *A*. (*C*) WT macrophages were treated with 1 ng/mL LPS for the indicated times, and cytosolic or membrane protein fractions were then extracted and subjected to immunoprecipitation with anti-BCAP monoclonal antibody and analyzed as in *A*. Cell fractions were also analyzed by Western blot for pan-Cadherin or GAPDH to examine the extraction efficiency. Data are representative of eight (*A*), six (*B*), and three (*C*) experiments.

increased tyrosine phosphorylation of BCAP was mainly the larger species seen in bands 3/4. This difference in tyrosine phosphorylation of BCAP isoforms in membrane and cytoplasmic fractions, along with the similarly low amount of cytosolic protein (GAPDH) in our membrane fractions, leads us to believe that the increase in tyrosine-phosphorylated and total BCAP in the membrane fractions was not attributable to contamination from cytosolic fractions. These data show that TLR signaling leads to the accumulation of the tyrosine-phosphorylated form of BCAP at membranes, presumably bringing its associated PI3K.

Reconstitution of BCAP into BCAP-Deficient Macrophages Reduces TLR Responses. To investigate whether there was a developmental deficit attributable to BCAP deficiency, we introduced BCAP and empty control constructs into WT or BCAP-deficient BM-derived macrophages through retroviral transduction. After retroviral transduction, the macrophages were activated with CpG DNA and proinflammatory cytokine production was assessed by flow cytometry, gating on the GFP-expressing retrovirally transduced cells. BCAP-deficient macrophages transduced with a control vector showed an increased percentage of cells producing IL-12 p40 and TNF compared with control virus-transduced WT macrophages, consistent with the increased cytokine secretion measured by ELISA (Fig. 5*A*). In contrast, reintroduction of BCAP into BCAP-deficient macrophages caused a reduction in the percentage of cytokine-producing cells to an amount equivalent to that of WT macrophages transduced with control vector (Fig. 5 *A* and *B*). These data suggest that there is not an early developmental defect attributable to the lack of BCAP or an effect of targeting the BCAP gene on another gene required for normal development or TLR responses. Additionally, BCAP-deficient macrophages had normal morphology and uniformly expressed F4/80, suggesting they do not have a developmental defect.

BCAP Negatively Regulates TLR-Induced Cytokine Production Through Binding to p85 Subunit of PI3K. Because tyrosine-phosphorylated BCAP recruits the PI3K p85 subunit to four YxxM motifs within BCAP to activate the PI3K pathway in B cells (15, 22), we hypothesized that the YxxM motifs of BCAP are required to inhibit TLR responses. To test this hypothesis, we transduced BCAP-deficient macrophages with a retrovirus encoding a mutant BCAP protein in which the four YxxM tyrosine residues were mutated to phenylalanines to prevent PI3K p85 binding and compared this with transduction of the WT BCAP protein or control retrovirus (23). The YxxM mutant BCAP had a greatly reduced ability to inhibit cytokine production in response to CpG DNA compared with the WT BCAP protein (Fig. 5 *C* and *D*). Interestingly, the YxxM mutant still diminished the TLR responses to a small degree compared with responses of macrophages transduced with empty vector. These data show that the ability of BCAP to inhibit TLR signaling in macrophages was mediated predominantly by PI3K recruitment and activation.

Discussion

Although TLR-mediated proinflammatory cytokine production during infection is necessary for the host to eradicate pathogens successfully, these cytokines can be detrimental if not tightly regulated. One mechanism by which TLR responses are kept in check is through activation of the PI3K pathway (3, 24). Here, we show that the signaling adapter BCAP is required for optimal signaling through the PI3K pathway in response to TLR ligation, identifying a link between TLR signaling and PI3K activation in controlling inflammatory responses. By its ability to activate PI3K, BCAP serves as a negative regulator of TLR responses both in vitro and in vivo.

BCAP functions in B and NK cells to bind and activate PI3K, leading to Akt phosphorylation (16, 25). Here, we show several pieces of evidence that the ability of BCAP to negatively regulate TLR responses depends on the PI3K pathway. We detected severely reduced LPS-induced Akt phosphorylation in BCAP-deficient macrophages compared with WT macrophages, consistent with reduced PI3K activity in the absence of BCAP. Furthermore, the effect of PI3K inhibition with wortmannin is reduced in BCAP-deficient macrophages compared with its effect in WT macrophages. This indicates that there is less TLR-induced PI3K activity in BCAP-deficient macrophages, consistent with the reduced TLR-induced Akt phosphorylation in these cells. Additionally, reconstitution of BCAP-deficient macrophages with a BCAP mutant that cannot associate with PI3K p85 because of the substitution of phenylalanines for the tyrosines in the four PI3K binding motifs found in BCAP had a significantly reduced ability to inhibit TLR responses in comparison to reconstitution with the WT protein. Therefore, we conclude that BCAP inhibits TLR responses through activation of the PI3K pathway and that BCAP is a critical link between TLR signaling and the PI3K signaling pathway in macrophages.

Unlike in B cells, where BCAP tyrosine phosphorylation and PI3K association are induced by receptor cross-linking (15, 22), BCAP was constitutively tyrosine-phosphorylated and associated with PI3K p85 in resting macrophages. In addition to TLR-induced Akt phosphorylation, basal Akt phosphorylation in the absence of activation was reduced in macrophages lacking BCAP. This suggests that BCAP-associated PI3K is also important for the basal PI3K activity in macrophages. Interestingly, the total amount of BCAP tyrosine phosphorylation and PI3K association did not change with LPS treatment, even though LPS-induced Akt phosphorylation was reduced in the absence of BCAP. The basal and LPS-induced tyrosine phosphorylation of BCAP, and its PI3K association, did not depend on signaling by M-CSF through the CSF1R, showing that cross-talk between CSF1R and BCAP does not influence BCAP function. Additionally, BCAP tyrosine phosphorylation and PI3K association did not depend on the Syk tyrosine kinase, which is required for BCR-induced BCAP activation in B cells (15). Taken together, these data suggest that the ability of BCAP to control PI3K activity in macrophages is not

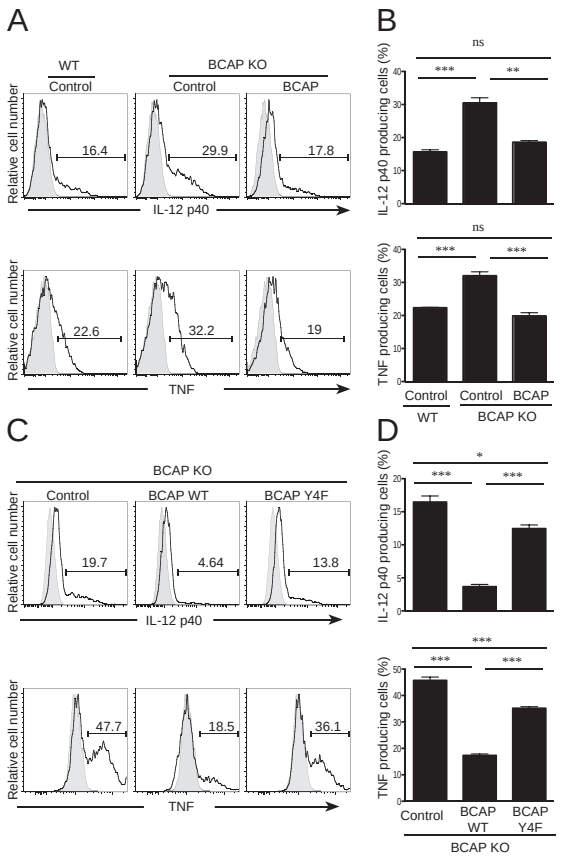

Fig. 5. BCAP negatively regulates TLR-induced cytokine production through binding to p85 subunit of PI3K. (*A* and *B*) WT or BCAP-deficient macrophages were transduced with an empty vector (control) retrovirus or retrovirus encoding WT BCAP. The macrophages were activated with CpG DNA (25 nM) in the presence of Brefeldin A for 6 h, and cytokine production was assessed by flow cytometry. Transduced cells were gated based on GFP fluorescence, and the percentage of IL-12 p40 or TNF-producing cells was determined. (*C* and *D*) BM-derived macrophages from BCAP-deficient mice were transduced with an empty vector (Control) retrovirus or retrovirus encoding WT BCAP (BCAP WT) or a BCAP tyrosine mutant (BCAP Y4F). Cytokine production was measured as in *A*. Gray histograms show staining of unstimulated cells. Data are representative of four independent experiments and are expressed as the mean ± SD of triplicate wells. ns, not significant; $*P < 0.05$; $**P < 0.01$; $***P < 0.001$.

solely through its ability to associate with the p85 regulatory subunit, distinct from how BCAP functions in B cells.

Unlike many other YxxM-containing proteins that activate PI3K, BCAP is not an integral membrane or membrane-associated protein. We found BCAP mainly in the cytosolic fraction in macrophages, as has been shown in B cells (15). In response to LPS treatment, the amount of tyrosine-phosphorylated BCAP increased transiently in the membrane fraction but not in the cytosolic fraction of macrophages. Our experiments cannot distinguish whether BCAP that is already present in the membrane fraction is inducibly tyrosine-phosphorylated after LPS treatment or whether phosphorylated BCAP is translocated from the cytoplasm to membranes in response to LPS. We propose that the function of BCAP during TLR signaling is to enrich active PI3K at membranes where it can access its substrate PIP2, thereby increasing PIP3 production and downstream signaling. This may allow for BCAP to regulate PI3K activity in two distinct steps: first, by binding p85/p110 heterodimers, thereby increasing catalytic activity, and, second, by interacting with other proteins to move to the plasma membrane or other intracellular membranes. Interestingly, we only found enrichment at the membrane of tyrosine-phosphorylated BCAP isoforms 3/4, suggesting that these isoforms may be responsible for regulating TLR responses. Identification of the signaling pathway that directs the enrichment of tyrosine-phosphorylated BCAP in the membrane fraction after TLR ligation will be the subject of future work.

The molecular mechanisms underlying PI3K negative regulation of cytokine expression are complex. One recent study suggests that PI3K regulates IL-12 production in dendritic cells through both mammalian target of rapamycin (mTOR) and glycogen synthase kinase 3b (GSK3b) pathways (12). PI3K-generated PIP3 activates Akt, which phosphorylates and causes the degradation of GSK3b. GSK3b positively regulates LPS-induced IL-12 p70 directly through transcriptional induction and indirectly through inhibition of IL-10 production. Therefore, when PI3K activity is reduced, GSK3b levels remain high, causing more IL-12 and less IL-10 to be produced. Akt also activates the mTOR pathway, which regulates IL-12 production only indirectly through induction of IL-10, again causing less IL-10 to be produced when PI3K activity is reduced. It is not likely that IL-10 is involved in BCAP-mediated suppression of IL-12 p40 secretion by macrophages because there is no decrease in TLR-induced IL-10 secretion by BCAP-deficient macrophages. We therefore favor a direct form of inhibition of IL-12 p40 secretion by BCAP-induced PI3K activity, possibly through regulation of GSK3b degradation.

Although we believe the principal role of BCAP is to activate PI3K, BCAP is not the only pathway through which PI3K gets activated in macrophages. In the absence of BCAP, we saw a small amount of basal and LPS-induced Akt phosphorylation. Therefore, other pathways exist downstream of TLRs leading to PI3K activation. TLRs have been reported to interact directly or indirectly through MyD88 with the p85 subunit to activate PI3K (5, 26), suggesting one BCAP-independent pathway leading to PI3K activation downstream of TLR ligation. Alternatively, the activation of PI3K described in these reports may depend on BCAP. Further work is required to define better whether BCAP is activated directly or indirectly by TLRs. Additionally, BCAP may have other functions during TLR signaling than activation of PI3K. BCAP is a large protein with many regions of unknown function. Our reconstitution assay with the BCAP Y→F mutant showed a small but consistent ability to inhibit TLR responses, although this was much lower than the inhibition achieved with the WT protein. This suggests that there is a function of BCAP independent of PI3K binding that can affect the magnitude of TLR responses.

Here, we show that the signaling adapter BCAP is required for optimal PI3K activation downstream of TLR ligation, identifying an elusive link between TLR signaling and PI3K activation in controlling inflammatory responses. Although BCAP serves to activate PI3K both in B cells downstream of BCR signaling and in macrophages downstream of TLR signaling, this BCAP-mediated PI3K activation has opposite effects, promoting B-cell activation and inhibiting macrophage activation, thus revealing cell type-specific roles of BCAP in regulation of cellular activation pathways. The negative regulation of TLR responses by BCAP may be beneficial to the host in limiting macrophage responses to infection and in preventing chronic inflammatory or autoimmune disorders. Therefore, BCAP provides a potential new target for designing therapeutic approaches to treat inflammation or sepsis.

Methods

Mice. We purchased C57BL/6 mice from Charles River Laboratories. BCAP-deficient mice lacking the *pik3ap1* gene (25) were back-crossed to C57BL/6 mice for nine generations. $Syk^{-/-}$ fetal liver chimeras were generated as previously described (27). All experiments and animal care procedures were performed in accordance with protocols approved by the Institutional Animal Care and Use Committees at Benaroya Research Institute; Fox Chase Cancer Center; and the University of California, San Francisco.

Macrophage Preparation. BM-derived macrophages were made as described (28).

TLR Stimulation and Cytokine Measurement. For ELISA, day 5 BM-derived macrophages were plated in a 96-well tissue plate (5×10^4 cells per well) overnight. Titrations of TLR stimuli were added for 16 h as follows: *Salmonella minnesota* R595 LPS (List Biological Laboratories), CpG DNA (ODN1826; Invivogen), and Imiquimod (Invivogen). The concentration of TNF, IL-6, IL-12 p40, and IL-10 in supernatants from triplicate wells was measured with ELISA (eBioscience). For measurement of intracellular TNF and IL-12 p40 by flow cytometry, 2×10^5 macrophages were plated in 24-well non–TC-treated plates overnight and then stimulated for 6 h with CpG DNA in the presence of Brefeldin A (10 μg/mL) for the final 2 h. Macrophages were blocked with 2.4G2 for 10 min and fixed in 4% paraformaldehyde (wt/vol), followed by permeabilization using Perm/Wash buffer (BD Bioscience). Staining for intracellular TNF and IL-12 p40 was performed using Pacific blue-labeled anti-TNF antibody and AlexFluor 647-labeled anti–IL-12 p40 (eBioscience). Cells were analyzed by flow cytometry using an LSR2 (BD Bioscience) and analyzed with FlowJo software (TreeStar).

Retroviral Transduction of Macrophages. Generation of VSVg-pseudotyped retroviruses and infection of macrophages were as described (28). Retroviral constructs were in the pMSCVIRES vector, in which the cDNA is followed by an IRES-eGFP to identify infected cells, and included control empty vector, BCAP WT, and a mutant BCAP in which the four tyrosines in the pI3K p85 binding motifs have been changed to phenylalanine (23).

Immunoprecipitation and Western Blot Analysis. Macrophages were activated with 1 ng/mL LPS or recombinant mouse TNF (Peprotech) and lysed at the indicated times in lysis buffer containing 1% Triton X-100, protease inhibitors (mammalian protease inhibitor mixture; Sigma), and sodium orthovanadate (1 mM; Sigma). For immunoprecipitation, day 6 macrophages were lysed using lysis buffer [50 mM Tris·HCl (pH 7.4), 150 mM NaCl, 1 mM EDTA, 1% Triton X-100, 0.25% sodium deoxycholate, 1 mM PMSF, 1 mM sodium orthovanadate and protease inhibitor (Sigma)]. Lysates were sequentially incubated with anti-BCAP monoclonal antibody (16) and protein A-agarose, and they were then eluted with 1× SDS sample buffer (Invitrogen). For membrane protein extraction, macrophages were removed from plates, resuspended in media, and stimulated with 1 ng/mL LPS for indicated times. Cytosolic and transmembrane proteins were extracted with a ProteoExtract Transmembrane protein extraction kit (Novagen). Cells were resuspended in Extraction Buffer 1 for cytosolic protein fraction extraction, and Extraction Buffer 2A was used subsequently to extract the membrane protein fraction. BCAP was immunoprecipitated from both fractions as described above. Lysates or immunoprecipitates were separated by Tris·bis SDS/PAGE gels (Invitrogen), transferred to PVDF (Millipore) membrane, and detected by the indicated antibodies and the Immobilon chemiluminescence system (Millipore). Antibodies for Western blotting used were specific for phosphorylated and nonphosphorylated Akt, p38 MAPK, p42/44 ERK and JNK, PI3K p85, IκBα, and pan-Cadherin (all from Cell Signaling); phosphotyrosine (4G10; Millipore); and anti-GAPDH (Trevigen).

In Vivo LPS Treatment. Mice were injected with 1 μg/g of *Escherichia coli* 055:B5 LPS (Sigma) in PBS. At the indicated times, a sample of blood was taken and plasma IL-12 p40 was determined by ELISA.

Statistical Analysis. The Student's unpaired *t* test was used in Figs. 1 and 3, and one-way ANOVA with Bonferroni's multiple comparison test was used in Fig. 4 as determined using Prism 5 software (GraphPad Software).

ACKNOWLEDGMENTS. We thank Dr. Tomohiro Kurosaki for providing retroviral BCAP plasmids and BCAP-deficient mice and members of the J.A.H. laboratory, Dr. Daniel Campbell, Dr. Steve Ziegler, and Dr. Mary Beth Humphrey for helpful discussions. This study was supported by National Institutes of Health Grant R01AI073441, National Institutes of Health American Recovery and Reinvestment Act Supplement R01AI073441S1, and Department of Defense Grant W81XWH-10-1-0149, as well as an Investigator Award from the Cancer Research Institute (to J.A.H.), National Institutes of Health Grants R01CA083859 and R01CA100226 (to K.S.C.), and Grants R01AI65495 and R01AI68150 (to C.A.L.).

1. Kawai T, Akira S (2010) The role of pattern-recognition receptors in innate immunity: Update on Toll-like receptors. *Nat Immunol* 11:373–384.
2. O'Neill LA, Bryant CE, Doyle SL (2009) Therapeutic targeting of Toll-like receptors for infectious and inflammatory diseases and cancer. *Pharmacol Rev* 61:177–197.
3. Brown J, Wang H, Hajishengallis GN, Martin M (2011) TLR-signaling networks: An integration of adaptor molecules, kinases, and cross-talk. *J Dent Res* 90:417–427.
4. Guha M, Mackman N (2002) The phosphatidylinositol 3-kinase-Akt pathway limits lipopolysaccharide activation of signaling pathways and expression of inflammatory mediators in human monocytic cells. *J Biol Chem* 277:32124–32132.
5. Rhee SH, Kim H, Moyer MP, Pothoulakis C (2006) Role of MyD88 in phosphatidylinositol 3-kinase activation by flagellin/toll-like receptor 5 engagement in colonic epithelial cells. *J Biol Chem* 281:18560–18568.
6. Re F, Strominger JL (2001) Toll-like receptor 2 (TLR2) and TLR4 differentially activate human dendritic cells. *J Biol Chem* 276:37692–37699.
7. Monick MM, et al. (2002) Phosphatidylinositol 3-kinase activity negatively regulates stability of cyclooxygenase 2 mRNA. *J Biol Chem* 277:32992–33000.
8. Fukao T, et al. (2002) PI3K-mediated negative feedback regulation of IL-12 production in DCs. *Nat Immunol* 3:875–881.
9. Kuroda S, et al. (2008) Effective clearance of intracellular Leishmania major in vivo requires Pten in macrophages. *Eur J Immunol* 38:1331–1340.
10. Martin M, et al. (2003) Role of the phosphatidylinositol 3 kinase-Akt pathway in the regulation of IL-10 and IL-12 by Porphyromonas gingivalis lipopolysaccharide. *J Immunol* 171:717–725.
11. Antignano F, Ibaraki M, Ruschmann J, Jagdeo J, Krystal G (2010) SHIP negatively regulates Flt3L-derived dendritic cell generation and positively regulates MyD88-independent TLR-induced maturation. *J Leukoc Biol* 88:925–935.
12. Ohtani M, et al. (2008) Mammalian target of rapamycin and glycogen synthase kinase 3 differentially regulate lipopolysaccharide-induced interleukin-12 production in dendritic cells. *Blood* 112:635–643.
13. Engelman JA, Luo J, Cantley LC (2006) The evolution of phosphatidylinositol 3-kinases as regulators of growth and metabolism. *Nat Rev Genet* 7:606–619.
14. Cantley LC (2002) The phosphoinositide 3-kinase pathway. *Science* 296:1655–1657.
15. Okada T, Maeda A, Iwamatsu A, Gotoh K, Kurosaki T (2000) BCAP: The tyrosine kinase substrate that connects B cell receptor to phosphoinositide 3-kinase activation. *Immunity* 13:817–827.
16. MacFarlane AW, 4th, et al. (2008) Enhanced NK-cell development and function in BCAP-deficient mice. *Blood* 112:131–140.
17. Saraiva M, O'Garra A (2010) The regulation of IL-10 production by immune cells. *Nat Rev Immunol* 10:170–181.
18. Franke TF, Kaplan DR, Cantley LC, Toker A (1997) Direct regulation of the Akt proto-oncogene product by phosphatidylinositol-3,4-bisphosphate. *Science* 275:665–668.
19. Aksoy E, et al. (2005) Inhibition of phosphoinositide 3-kinase enhances TRIF-dependent NF-kappa B activation and IFN-beta synthesis downstream of Toll-like receptor 3 and 4. *Eur J Immunol* 35:2200–2209.
20. Yang CS, et al. (2006) Intracellular network of phosphatidylinositol 3-kinase, mammalian target of the rapamycin/70 kDa ribosomal S6 kinase 1, and mitogen-activated protein kinases pathways for regulating mycobacteria-induced IL-23 expression in human macrophages. *Cell Microbiol* 8:1158–1171.
21. Hazeki K, et al. (2006) Opposite effects of wortmannin and 2-(4-morpholinyl)-8-phenyl-1(4H)-benzopyran-4-one hydrochloride on toll-like receptor-mediated nitric oxide production: Negative regulation of nuclear factor-kappaB by phosphoinositide 3-kinase. *Mol Pharmacol* 69:1717–1724.
22. Inabe K, Kurosaki T (2002) Tyrosine phosphorylation of B-cell adaptor for phosphoinositide 3-kinase is required for Akt activation in response to CD19 engagement. *Blood* 99:584–589.
23. Aiba Y, Kameyama M, Yamazaki T, Tedder TF, Kurosaki T (2008) Regulation of B-cell development by BCAP and CD19 through their binding to phosphoinositide 3-kinase. *Blood* 111:1497–1503.
24. Fukao T, Koyasu S (2003) PI3K and negative regulation of TLR signaling. *Trends Immunol* 24:358–363.
25. Yamazaki T, et al. (2002) Essential immunoregulatory role for BCAP in B cell development and function. *J Exp Med* 195:535–545.
26. Arbibe L, et al. (2000) Toll-like receptor 2-mediated NF-kappa B activation requires a Rac1-dependent pathway. *Nat Immunol* 1:533–540.
27. Mócsai A, Zhou M, Meng F, Tybulewicz VL, Lowell CA (2002) Syk is required for integrin signaling in neutrophils. *Immunity* 16:547–558.
28. Hamerman JA, Tchao NK, Lowell CA, Lanier LL (2005) Enhanced Toll-like receptor responses in the absence of signaling adaptor DAP12. *Nat Immunol* 6:579–586.

Matrix Biology 31 (2012) 90–100

Contents lists available at SciVerse ScienceDirect

Matrix Biology

journal homepage: www.elsevier.com/locate/matbio

Hyaluronan and versican in the control of human T-lymphocyte adhesion and migration

Stephen P. Evanko, Susan Potter-Perigo, Paul L. Bollyky, Gerald T. Nepom, Thomas N. Wight *

Benaroya Research Institute, Seattle, WA 98101, United States

ARTICLE INFO

Article history:
Received 11 May 2011
Received in revised form 10 October 2011
Accepted 31 October 2011

Keywords:
Hyaluronan
Versican
Lymphocyte
Migration
Myofibroblast
Inflammation

ABSTRACT

The ability of lymphocytes to migrate freely through connective tissues is vital to efficient immune function. How the extracellular matrix (ECM) may affect T-cell adhesion and migration is not well understood. We have examined the adhesion and migration of activated human T-lymphocytes on ECM made by fibroblast-like synoviocytes and lung fibroblasts. These cells were minimally interactive until treated with a viral mimetic, Poly I:C. This treatment promoted myofibroblast formation and engendered a higher-order structured ECM, rich in versican and hyaluronan, to which T-cells avidly adhered in a hyaluronidase-sensitive manner. This Poly I:C-induced matrix impeded T-cell spreading and migration on and through synoviocyte monolayers, while hyaluronidase treatment or adding versican antibody during matrix formation reversed the effect on T-cell migration. Hyaluronidase also reversed the spread myofibroblast morphology. These data suggest that the viscous hyaluronan- and versican-rich matrix binds and constrains T-lymphocytes. Using purified matrix components and solid state matrices of defined composition, we uncovered a role for versican in modulating hyaluronan-T-cell interactions. Versican prevented T-cell binding to soluble hyaluronan, as well as the amoeboid shape change on hyaluronan-coated dishes and T-cell penetration of collagen gels. Together, these data suggest that hyaluronan and versican play a role in T-cell trafficking and function in inflamed tissues.

1. Introduction

The ability of T-cells to adhere and migrate through connective tissue extracellular matrix (ECM) is vital to efficient immune responses (Korpos et al., 2009; Sorokin, 2010). T-cell migration is a multi-step process mediated by a complex assortment of integrins, matrix metalloproteases and other cell surface receptors, such as CD44, whose interactions initiate bi-directional signaling pathways (Denucci et al., 2009; Johnson and Ruffell, 2009). Among other effects, these signals result in T-cell activation and cytoskeleton rearrangements that are integral to T-cell adhesion and migration. When T-cells adhere to surfaces or tissues they usually adopt a "crawling" or "spreading" amoeboid morphology characterized by a broad lamellipodium at the leading edge and a handle-like protrusion or uropod at the rear. Cell scaffold-mediated migration strategies occur in lymph nodes, and it is likely that leukocytes move along stromal cells as part of their surveillance function in other tissues (Friedl and Weigelin, 2008). The transition from a rounded morphology to the amoeboid shape allows lymphocytes to squeeze through narrow spaces and move on collagen without reliance on matrix metalloproteases (Wolf et al., 2003). CD44 is thought to be important to crawling morphology and has been implicated in successful interstitial navigation of killer T-cells and maintenance of stable migratory polarity (Mrass et al., 2008).

The ECM components that partner with cell-surface receptors at sites of inflammation are less well understood. This is because these molecules are dynamic, complex and difficult to study in isolation. Two relatively well characterized ECM components implicated in leukocyte adhesion are hyaluronan and versican. Hyaluronan is an ECM glycosaminoglycan that serves as a ligand for CD44 and is produced in connective tissues during inflammation in a number of contexts (Day and de la Motte, 2005). Versican is a chondroitin sulfate proteoglycan that aggregates with hyaluronan, and modulates cellular adhesion (Yamagata et al., 1989; Yamagata and Kimata, 1994; Ernst et al., 1995). Hyaluronan and versican are primary constituents of the cell coat (also known as the pericellular matrix or glycocalyx) of fibroblasts, myofibroblasts, smooth muscle cells and other cell types, and participate in the regulation of cell motility, proliferation, and myofibroblast differentiation (Evanko et al., 1999; Toole, 2004; Evanko et al., 2007; Meran et al., 2007; Hattori et al., 2011). Versican is known to have a barrier/guidance function in neural crest migration and axonal growth (Landolt et al., 1995; Dutt et al., 2006). However, the influence of these ECM components on lymphocyte adhesion and migration is not well understood.

Abbreviations: ECM, extracellular matrix; Poly I:C, polyinosine-polycytidylic acid; HMWHA, high molecular weight hyaluronan; b-HABP, biotinylated hyaluronan binding protein; nTreg, natural T-reg; PBMC, peripheral blood mononuclear cell; ER, endoplasmic reticulum; HLFs, human lung fibroblasts; HFLS, human fibroblast-like synoviocytes.

* Corresponding author at: Benaroya Research Institute, 1201 9th Ave, Seattle, WA 98101-2795, United States. Fax: +1 206 342 6567.
E-mail address: twight@benaroyaresearch.org (T.N. Wight).

0945-053X/$ – see front matter © 2011 Elsevier B.V. All rights reserved.
doi:10.1016/j.matbio.2011.10.004

During chronic inflammation in both lung and synovial tissues, fibrosis and accumulation of myofibroblasts follow the accumulation of complex crosslinked hyaluronan matrices (Day and de la Motte, 2005; Kasperkovitz et al., 2005; Westergren-Thorsson et al., 2010), and this can be repeated in multiple inflammatory events. Thus, the fibroblast milieu may play a role in modulating inflammatory cell function, trafficking, and chronicity of inflammation. Inflammatory stimuli, such as viruses, viral mimics and inducers of endoplasmic reticulum (ER) stress, are known to induce production of adhesive, higher order hyaluronan- and versican-rich cable structures by smooth muscle cells and fibroblasts (de la Motte et al., 1999; Majors et al., 2003; Wang and Hascall, 2004; Selbi et al., 2006; Evanko et al., 2009; Potter-Perigo et al., 2010), and there is evidence of similar matrices in vivo (de la Motte et al., 1999). We recently reported that the viral mimic polyinosine:cytidylic acid (Poly I:C), a ligand for TLR3, promotes the deposition of versican in the hyaluronan cables in lung fibroblasts (Potter-Perigo et al., 2010). Others have found that activation of TLR3 with Poly I:C can augment myofibroblast formation via production of TGF-β (Sugiura et al., 2009). Monocyte adhesion to the hyaluronan cables of fibroblasts and other cells is hyaluronan-dependent, as shown by abolishment using hyaluronidase, which destroys the pericellular cable and coat structures. This adhesion is also partly dependent on cell surface CD44 (de la Motte et al., 1999), as well as versican that is present in the matrix (Potter-Perigo et al., 2010). Although T-lymphocytes are known to express CD44 and bind hyaluronan (Lesley et al., 1994; Bollyky et al., 2007; Ruffell and Johnson, 2008; Bollyky et al., 2009a), the role of hyaluronan-based cable structures in T-cell adhesion and function is not well understood. Because hyaluronan is known to promote migration of several cell types, we hypothesized that hyaluronan cable structures formed by fibroblasts in vitro could provide a traction mechanism, thus promoting and supporting migration of lymphocytes.

In this study, we evaluate T-lymphocyte adhesion and migratory behavior on an inflammatory ECM that is rich in hyaluronan and versican made by fibroblasts in response to Poly I:C. We show that the retention of CD4+ T-cells by human lung fibroblasts and normal human synoviocytes is promoted by Poly I:C while migration is inhibited, and these effects are reversed by treatment with hyaluronidase and anti-versican antibody. To complement these studies with native, cell-derived matrices, we have also used defined synthetic matrices to evaluate the effect of hyaluronan and versican on T-cell migration. The hypothesis that hyaluronan-dependent, versican-rich cable structures would facilitate T-cell migration is not supported.

2. Materials and methods

2.1. Reagents

Pharmaceutical grade hyaluronan with molecular weights of 1.53 MDa and 200 kDa was provided by Genzyme (Cambridge, MA, USA). *Streptomyces* hyaluronidase was obtained from Sigma-Aldrich (St Louis, MO, USA). Collagen (type I, rat tail) was from BD Biosciences (Bedford, MA). Poly I:C was from Invivogen (San Diego, CA). Biotinylated hyaluronan binding protein (b-HABP) was prepared from cartilage as described (Underhill et al. 1993). Biotinylated hyaluronan was prepared as described (Hoare et al., 1993). Monoclonal anti-versican antibodies, 2B1 and 12C5, came from North Star Bioproducts (East Falmouth, MA), and the Developmental Studies Hybridoma Bank (University of Iowa), respectively. Monoclonal antibody to human smooth muscle α actin (clone 1A4) was from Dako North America, Inc. (Carpinteria, CA).

Versican was purified from bovine aorta by a combination of 4 M guanidinium HCL extraction, ion exchange and size exclusion chromatography, as described previously (Olin et al., 2001). The versican preparation was free of contaminants as assessed by SDS-PAGE and Coomassie blue and Alcian blue staining, and was endotoxin-free (<1.0 EU/μg) as assessed using a ToxinSensor™ LAL Endotoxin Assay Kit (GenScript Corp., Piscataway, NJ). The versican preparation bound specifically to biotinylated hyaluronan on ligand blots (Supplemental Fig. 1) and to versican specific antibodies on western blots and comprised the V0 and V1 isoforms (data not shown).

A portion of the versican preparation was biotinylated, repurified on a hyaluronan affinity column, and used in an enzyme-linked sorbent assay (ELSA) to assess the ability of 12C5 antibody to inhibit biotin-versican binding to hyaluronan-coated plates and to assess direct binding of versican to T-cells. The biotinylation of versican was done essentially as described for cartilage hyaluronan binding protein (Underhill et al., 1993), with slight modification. The trypsin step was omitted and versican was biotinylated in the presence of 100 μg/ml exogenous 200 kDa hyaluronan to preserve the binding site prior to putting it on the hyaluronan affinity column.

2.2. Human blood samples

Human peripheral blood mononuclear cell (PBMC) samples were obtained from healthy volunteers with informed consent, participating in a research protocol approved by the institutional review board of the Benaroya Research Institute at Virginia Mason (BRI, Seattle, WA, USA).

2.3. Isolation of leukocyte populations

Human PBMCs were prepared by centrifugation of peripheral blood over Ficoll–Hypaque gradients. CD4+ T-cells were isolated using the Dynal CD4 Positive Isolation Kit (Invitrogen, Carlsbad, CA, USA) as per the manufacturer's instructions. Purity of the resulting cell fractions was reliably 98% CD4+ by flow cytometry; anti-CD4 Ab (RPAT4), from BD Biosciences was used for this purpose. Cells were cultured in RPMI 1640 (Invitrogen) supplemented with 10% pooled human serum, 100 μg/ml penicillin, 100 U/ml streptomycin and 1 mM Na pyruvate (Invitrogen). CD4+ T-cells were activated with anti-CD3/28 coated beads (Invitrogen) in the setting of 100 IU of recombinant IL-2 (Chiron, Emeryville, CA) for 72 h prior to their use in binding studies and other assays.

2.4. Culture and Poly I:C treatment of fibroblasts

Human lung fibroblasts (HLFs) were derived from explants of the lung, following removal of both the pleura and parenchyma, and were a generous gift from Professor Ganesh Raghu, Divison of Pulmonary and Critical Care Medicine, University of Washington, Seattle. The cells were isolated as described previously in accordance with approval from the institution's human subjects review committee (Raghu et al. 1988). HLFs were maintained in DMEM high-glucose medium supplemented with 10% FBS (HyClone; Logan, UT), 1 mM sodium pyruvate, 0.1 mM non-essential amino acids, 0.43 mg/ml GlutMAX-1, and penicillin-streptomycin (penicillin G sodium, 100 U/ml, and streptomycin sulfate, 0.10 mg/ml; Invitrogen) at 37 °C in 5% CO_2. Cells were passaged with trypsin-EDTA (0.05% trypsin and 0.53 mM tetrasodium EDTA) and were used for experiments between passages 9 and 17 after initial isolation.

Normal human fibroblast-like synoviocytes (HFLS) were purchased from Cell Applications Inc. (San Diego, CA) and grown in synoviocyte growth medium (Cell Applications). They were arrested in DMEM with 0.1% FBS and stimulated in synoviocyte growth medium with and without Poly I:C (20 μg/ml) for 20 h. HFLS were maintained in 5% CO_2 at 37 °C and passaged with trypsin-EDTA as for HLFs. Hyaluronan and versican in the cell layers were measured by ELSA using biotinylated HABP and western blotting (2B1 antibody), respectively, as described previously (Potter-Perigo et al., 2010).

For imaging and immunohistochemistry, fibroblasts or synoviocytes were seeded on glass coverslips at 3.5×10^5/well in 6-well plates in 10% FBS DMEM or synoviocyte medium. After 24 h, cells were growth arrested for 48 h in medium containing 0.1% FBS, at which point the cells were

nearly confluent. Following this period of serum deprivation, the cells tended to have very little hyaluronan on their surfaces and no cell coats by the particle exclusion assay (data not shown). Medium was then removed and cells were stimulated without or with Poly I:C (20 μg/ml) in the presence of 10% FBS to stimulate the formation of hyaluronan-based matrix cable structures (de la Motte et al. 1999) for 20 h. Alternatively, cells were sometimes seeded at 3.5×10^4/well in order to obtain sparse cultures to allow visualization of T-cells in warm up experiments. The fibroblast layers were washed with PBS and incubated with T-cells 0.5–1×10^6 at 4 °C in synoviocyte medium or RPMI containing 10% FBS. Following binding, the non-adherent T-cells were rinsed by immersion of the inverted coverslip in 200 ml of PBS using forceps (6 dips of 1 s duration).

Adhesion of calcein-labeled (Calcein AM, Invitrogen) T-cells to fibroblasts and synoviocytes was assayed in 96-well plates as described previously for monocyte adhesion (Potter-Perigo et al., 2010). Some fibroblasts were treated with *Streptomyces* hyaluronidase (0.66 U/ml) in the growth medium for 30 min at 37 °C prior to the adhesion assay.

2.5. Western analysis and ligand blotting of versican

For western and ligand blotting, versican was digested by chondroitin ABC lyase, applied to a gradient of 4–12% SDS-PAGE, and electrophoretically transferred to 0.2 μm nitrocellulose membranes (GE Healthcare, Piscataway, NJ) using a BioRad Transblot SD Semi-Dry Transfer Cell (BioRad, Hercules, CA) (Olin et al., 1999). The transferred proteins were then detected with the primary antibody to versican, 2B1 (North Star Bioproducts), and enhanced chemiluminescence (Western-Light Chemiluminescent Detection System) with CSPD proprietary luminescent substrate (Applied Biosystems, Foster City, CA). Bands were scanned and quantitated using NIH Image J. For ligand blots, to assess versican binding to biotinylated hyaluronan, 10 μg versican was electrophoresed under non-reducing and reducing conditions prior to transfer to nitrocellulose. Blot strips were incubated with biotinylated hyaluronan (prepared as described in Hoare et al., 1993). A control strip was preincubated with 500 μg/ml unlabeled hyaluronan.

2.6. Immunohistochemistry

Fibroblasts with bound T-cells on coverslips were fixed in acid-formalin-ethanol (3.7% formaldehyde-PBS, 70% ethanol, and 5% glacial acetic acid, all v/v) (Lin et al. 1997). Following rinsing in PBS, cells were stained for hyaluronan using b-HABP followed by either streptavidin-Alexa Fluor 488 or streptavidin-Texas Red in PBS containing 1% bovine serum albumin as previously described (Evanko et al., 1999). Versican was localized using monoclonal antibody 2B1 (Seikagaku Corp.; East Falmouth, MA), followed by Alexa Fluor 488-conjugated secondary antibody (Invitrogen). As controls, fibroblast cultures were predigested with hyaluronan-specific *Streptomyces* hyaluronidase (before fixation), which abolished staining with the b-HABP (data not shown, see Evanko et al., 2009), or incubated with normal mouse IgG as a control for versican staining (not shown). Smooth muscle α actin antibody (Dako) was used at 1:50 (1.4 μg/ml) on cells fixed with 10% formalin. Cells were examined using a Leica DMIRB microscope under epifluorescence optics using a 63×0.70 numerical aperture objective, and images were acquired using a Spot cooled-CCD camera and imaging program.

2.7. Time-lapse microscopy and determination of T-cell migration

CD4 + T-cells were applied to control and Poly I:C-treated synoviocyte monolayers in synoviocyte medium containing 10% FBS and 20 mM HEPES and allowed to settle for 15 min atop a microscope stage that was maintained at 37 °C. Sequential phase-contrast images were taken every 20 s for 20 min. Tracings of the migratory paths of 20 randomly selected lymphocytes from each condition were obtained with the aid of Image J. The net migration distance was used to calculate migration rate.

In some experiments, random migration through the matrix and monolayer in the Z-axis was assessed. Calcein-labeled T-cells (6×10^5 in 100 μl) were applied atop the synoviocytes and allowed to migrate for 20 min at 37 °C. Coverslips were fixed in 10% formalin for 30 min. Most of the T-cells bound and trapped by the matrix were well above the cell layer in a different focal plane which facilitated counting the number of migrated T-cells that had passed through the matrix and monolayer and were in focus at the level of the coverslip. The migrant cells were clearly discernible from the cells trapped well above. Some cultures were treated with *Streptomyces* hyaluronidase (1 U/ml in the culture medium) prior to adding the T-cells to assess the contribution of the matrix to migration through the monolayer. Thirty fields per condition were measured using the 20× objective. One-way ANOVA with Tukey's post test was performed using GraphPad Prism version 5.03 for Windows, GraphPad Software, San Diego, CA, www.graphpad.com. The data are representative of three independent experiments.

2.8. T-cell penetration of collagen gels

Collagen gels (1 mg/ml, 100 μl in DMEM) without or with added hyaluronan (100 μg/ml) or versican (5 or 20 μg/ml) or versican that was pretreated with Chondroitin ABC lyase, were cast atop flame-sterilized 22 mm coverslips. Control additives included chondroitin sulfate and Chondroitin ABC lyase (North Star Bioproducts) alone. In some experiments, chemokines CCL19 (100 ng/ml) and CCL 21 (500 ng/ml) were included in the gels to enhance T-cell migration. Care was taken to spread the 100 μl collagen solutions over the entire coverslip. After polymerization of the collagen gels for 30 min at 37 °C, activated lymphocytes (2×10^5) were applied to the upper surface of the gel in 100 μl of RPMI medium containing 10% FBS and cells were allowed to penetrate the collagen for 3 h at 37 °C. Coverslips were fixed with formalin and the number of lymphocytes that penetrated to within 50 μm of the coverslip was counted using a 20× objective with phase contrast optics and calibrated focusing. Alternatively, T-cell nuclei were stained with ToproRS (Invitrogen) and photographs were acquired at a depth of 100 μm into the gel using a Leica ICL SP5 confocal microscope, 10× objective, and the number of penetrated cells counted with the aid of Image J. A minimum of 30 fields per condition, randomly selected from the central 1 cm^2 region of the coverslip were counted. One-way ANOVA with Tukey's post test was performed as described above.

2.9. Two dimensional coatings and T-cell morphology

24-well culture dishes were coated overnight with 100 μg/ml of BSA-conjugated hyaluronan, rinsed with PBS, and then followed by PBS alone or with versican or chondroitinase-treated versican (20 μg/ml) for 1 h. Lymphocytes were applied and allowed to settle for 20–30 min. Cells were fixed and the proportions of amoeboid versus round cells were quantitated from photographs.

2.10. Soluble HA and versican binding studies

FITC-labeled hyaluronan (Sigma) and unlabled versican were incubated together for 1 h at 37 °C before addition to T-cells. In the meantime, activated human T-cells (2×10^5) were washed and resuspended in 200 μl/ml of RPMI 1640 not supplemented with serum. 4-methylumbelliferone (4-MU) from Sigma was added to the cells at 50 μg/ml also for 1 h. The FITC-labeled hyaluronan was then added (for a final concentration of 50 μg/ml) together with the indicated concentration of versican. The FITC-labeled hyaluronan and the T-cells were incubated for 1 h at 37 ° C prior to analysis. Direct binding of biotinylated versican (5 μg/ml) to T-cells pretreated with 4MU and hyaluronidase was similarly assessed. Data were acquired on a FACSCaliber (Becton

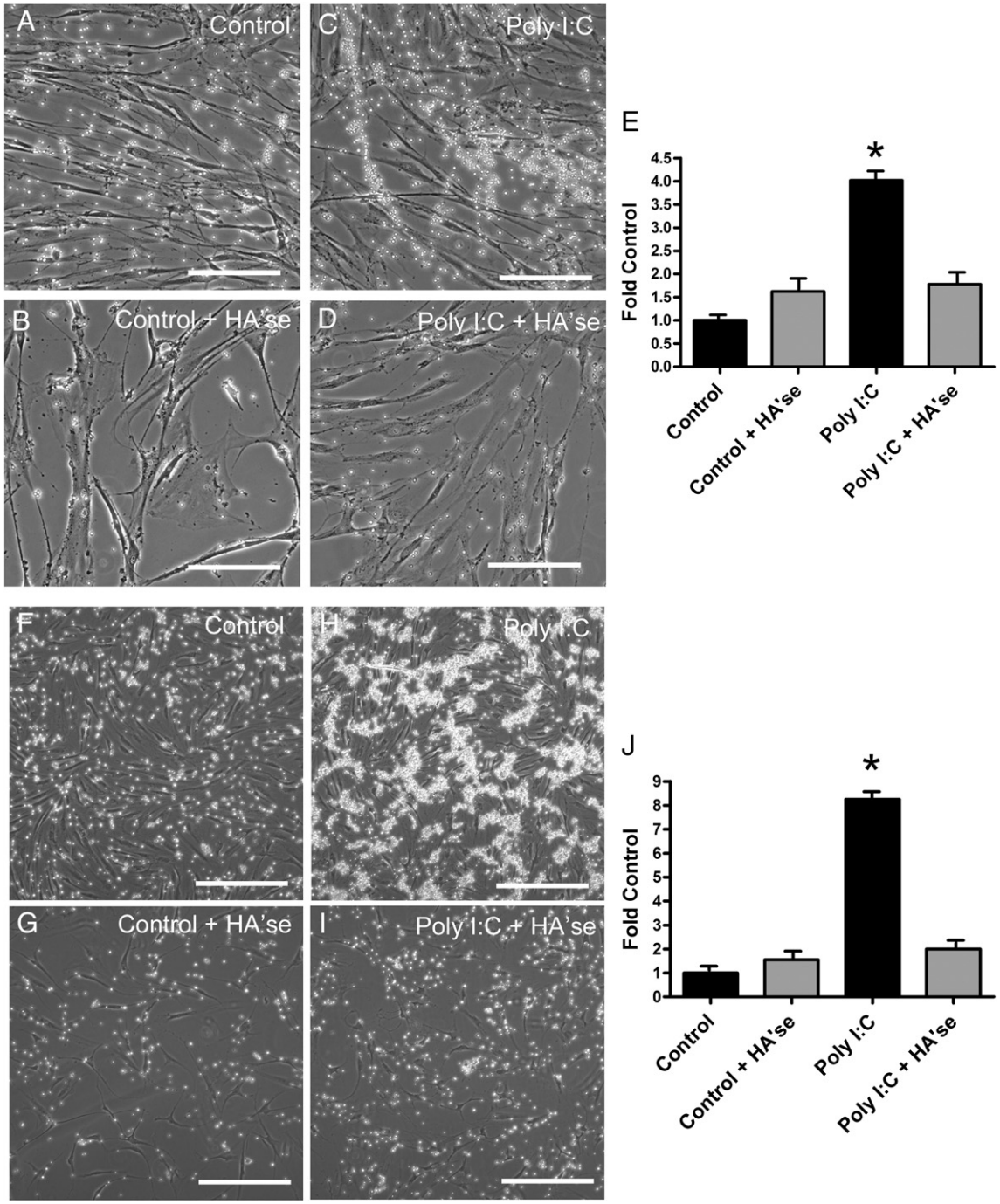

Fig. 1. Phase contrast images and quantitation of activated human CD4 + T-lymphocytes binding to control and Poly I:C-treated human lung fibroblasts (A–E, upper panels) or synoviocytes (F–J, lower panels) without or following digestion of the matrix with hyaluronidase as indicated. Bars equal 100 μm in all images. Quantitation of calcein-labeled CD4 + T-lymphocyte binding to control and Poly I:C-treated human lung fibroblasts (E) or synoviocyte like fibroblasts (J) without (black bars) or following digestion of the matrix with hyaluronidase (gray bars). *$p<0.001$ compared to control.

Dickinson). Analysis was performed using FlowJo (Tree Star, Inc.) software.

3. Results

3.1. Effect of Poly I:C on ECM production

Poly I:C had similar effects on ECM production by synoviocytes as was previously reported for lung fibroblasts (Potter-Perigo et al., 2010). In the Poly I:C-treated synoviocytes, hyaluronan was significantly increased in the cell layer by 8-fold (8.22 ± 2.34 fold, $p<0.01$), and contained a higher proportion of HMWHA as measured by gel filtration chromatography. As measured by western blotting and densitometry, versican was increased 1.77-fold compared to controls, (1.77 ± 0.22, $p<0.01$).

3.2. T-cell adhesion to fibroblast and synoviocyte matrix

Compared to untreated control fibroblasts, several-fold more activated human CD4 + T-lymphocytes bound to Poly I:C-treated HLFs or

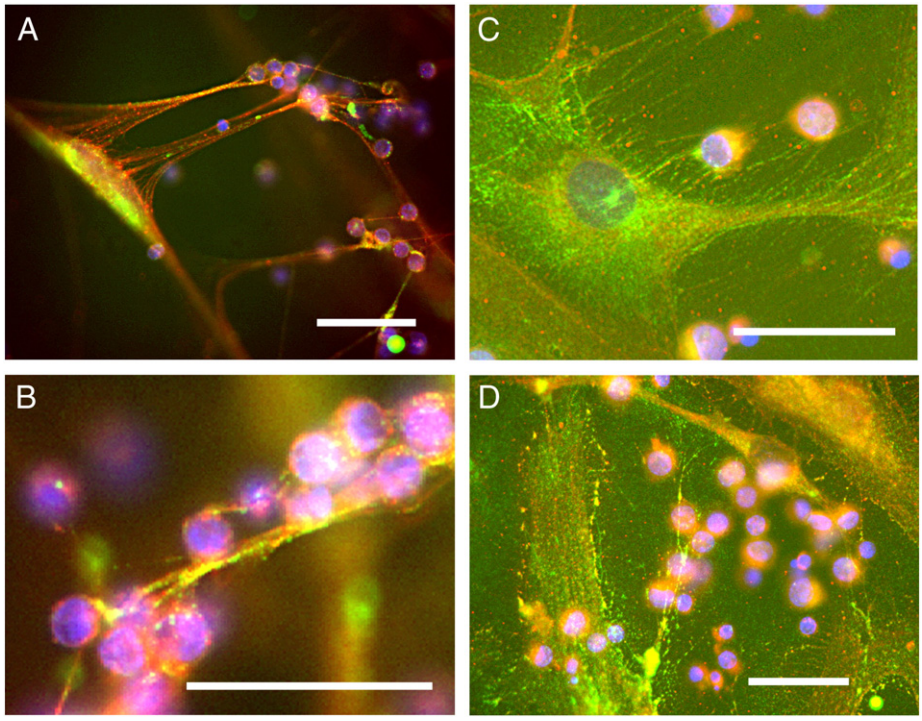

Fig. 2. T-cells bind to hyaluronan- and versican-rich matrix. Following binding of human T-cells, lung fibroblasts (A, B) and synovial fibroblasts (C, D) were fixed with acid/alcohol/formalin and stained for hyaluronan (red) using bHABP and versican (green) using monoclonal antibody (2B1). Nuclei were counterstained with DAPI. Bars equal 50 μm in all images.

fibroblast-like synoviocytes (Fig. 1). Treatment of the fibroblast monolayers with *Streptomyces* hyaluronidase abolished most of the lymphocyte adhesion to the Poly I:C-induced matrix, indicating that the adhesion was hyaluronan-dependent. Fig. 1 also shows phase contrast images of the T-cells bound to the fibroblast cell layers and the effect of hyaluronidase treatment. In lung fibroblasts, the bound T-lymphocytes were typically arrayed along cable structures (Fig. 1C), as has been reported previously for binding of monocytes to smooth muscle cells or lung fibroblasts (de la Motte et al., 1999; Potter-Perigo et al., 2010). In contrast, the T-cells adhering to the synoviocyte matrix tended to form large clumps, while the extremely long cable structures were less apparent (Fig. 1H). T-cell subsets, such as CD4 + CD25 + Treg, or TH1 and TH2 cells, were all capable of binding to the matrix of Poly I:C-treated fibroblasts in a hyaluronan-dependent manner (data not shown). Therefore, we limited the remainder of our studies to activated CD4 + T-cells.

3.3. Versican and hyaluronan localization in adhesive matrix

Versican and hyaluronan were detected in the adhesive matrix of both fibroblast types, as shown by immunohistochemistry (Fig. 2). Following Poly I:C treatment of the fibroblasts and synoviocytes, most of the T-cells were bound in the matrix some distance (roughly 50–100 μm) above the fibroblast or synoviocyte cell layer (Fig. 2A), indicating that copious amounts of matrix were produced in response to the stimulus. Consistent with the phase contrast images, the hyaluronan- and versican-enriched matrix was present in the form of long cables in the lung fibroblasts, while in the synoviocytes, the hyaluronan- and versican-rich matrix appeared as more of a dense mat or lawn and occasional broad cables, to which clumps of T-cells were bound. The synoviocyte matrix tended to have more intense versican staining than the lung fibroblasts as shown by the diffuse green signal over the entire cell layer in Fig. 2C and D. Controls for staining included digestion of the cells with *Streptomyces* hyaluronidase, which abolished staining of the matrix with the hyaluronan binding probe, and normal mouse IgG, which was also negative (data not shown).

3.4. T-cell migration and interactions with fibroblasts

Beyond adhesion, the immediate functional consequence of T-cells encountering a matrix rich in hyaluronan and versican is not clear. We hypothesized that the cable structures made by Poly I:C-treated lung fibroblasts could facilitate migratory behavior by the T-cells. However, following warm-up to physiological 37 °C, time-lapse microscopy showed no evidence for directional migration of T-cells along the hyaluronan cables. Instead, the T-cells aligned along the cables remained immobile and spherical, and eventually dispersed randomly and settled down onto the culture surface or fibroblast monolayer (Fig. 3A, B). This suggests that the cable structures made by lung fibroblasts in vitro do not support directional migration of T-cells under these conditions, and that the T-cells may, at least partially, degrade the matrix after binding. The cells tended to transition to the amoeboid shape only when they settled onto the culture surface (Fig. 3B, upper arrow). It was also evident that the pericellular matrix around the fibroblast acted as an exclusion barrier to the lymphocytes, preventing them from directly contacting the fibroblast surface in some places (Fig. 3C). This exclusion phenomenon using lymphocytes is similar to the exclusion of fixed erythrocytes in the widely used particle exclusion assay, used to identify pericellular hyaluronan coats (Evanko et al., 2007). T-cells were generally much more motile than the fibroblasts. Various kinds of direct physical interactions between the cell types were also noted. For example, T-cells crawling on the control fibroblast surfaces were sometimes deflected to change direction by microvilli on the fibroblasts. In other sequences, T-cells were physically pulled into tight clusters by the fibroblast, such as during occasional gross movements where the fibroblast retracted long cellular processes and matrix to which the T-cells had adhered (Supplemental video 1).

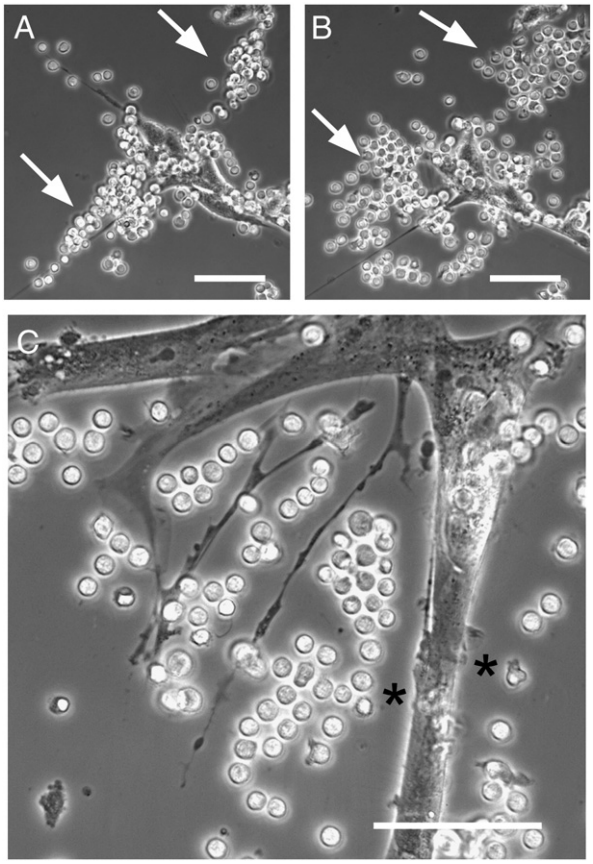

Fig. 3. T-cells bound to cable structures disperse randomly following warm up. T-cells were applied to sparse Poly I:C-treated lung fibroblasts, rinsed, and then monitored with time-lapse microscopy following warm up to physiological 37 °C. A. Immediately after washing the lymphocytes are bound along a putative hyaluronan cable (arrows) whose axis runs diagonally through the field. B. After 20 min at 37 °C, the T-cells have dispersed themselves mostly in directions perpendicular to the original axis of the cable. C. Another field showing how lymphocytes are excluded along portions of the fibroblast surface by the pericellular matrix (asterisks), much like the particle exclusion assay that employs fixed erythrocytes (Potter-Perigo et al., 2010). Bars equal 50 μm.

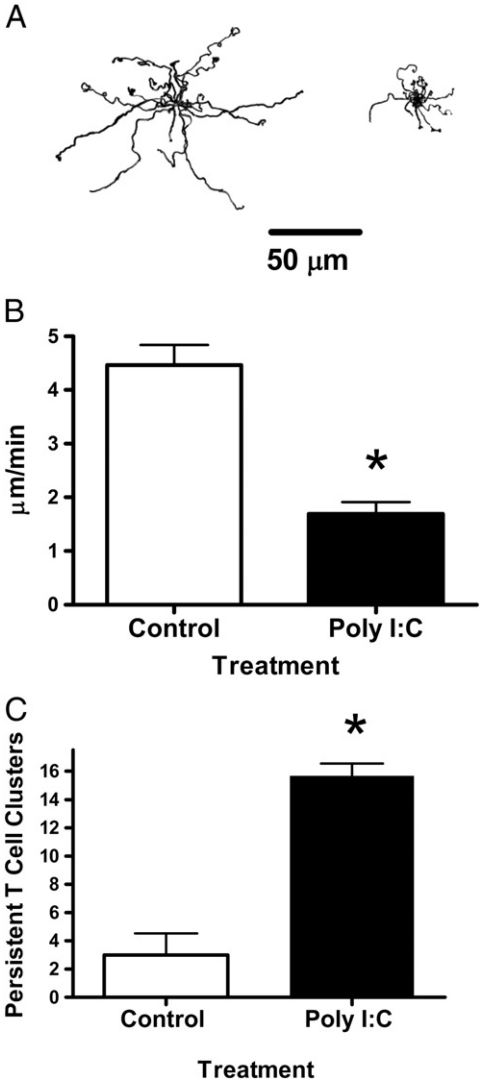

Fig. 4. T-cell migration is impeded on matrix induced by Poly I:C. A. Tracings of the migratory paths of 20 randomly selected T-cells migrating on control (left) and Poly I:C-treated (right) synoviocytes for a 20-min period. A bar indicating a distance of 50 μm is shown for reference. B. Migration rates were calculated using net distance of the migrating T-cells. C. Number of T-cell clusters that persisted for 10 min following warm up. *$p < 0.001$ compared to control.

We performed additional time-lapse studies to assess T-cell migration on monolayers of synoviocytes. (Supplemental videos 2 and 3 show T-cells on control and Poly I:C-treated synoviocytes, respectively). Given that hyaluronan tends to promote the migration of several cell types (Evanko et al., 2007), we also hypothesized that the interaction with the matrix would lead to faster migration of the T-cells. However, most of the T-cells remained clustered in the dense matrix of Poly I:C-treated synoviocytes and failed to disperse and migrate over the 20-min period after encountering the matrix. Many of the T-cells attempted to polarize by extending pseudopods in various directions, but appeared to be unable to gain traction or free themselves from the matrix. In contrast, the T-cells tended to crawl more directly on the surface of control synoviocytes, employing a cell scaffold-mediated migration strategy, and easily worked their way between and under the synoviocyte margins by amoeboid shape change. Tracings of the migratory paths of 20 representative T-cells on the ECM of control and Poly I:C -treated synoviocytes are shown in Fig. 4A. The rate of T-lymphocyte migration on the Poly I:C-induced matrix ($1.69 + 0.22$ μm/min) was significantly decreased by about 55% compared to the migration rate on control synoviocyte matrix ($4.47 + 0.37$ μm/min) (Fig. 4B). Correspondingly, the number of persistent T-cell clusters was significantly increased on the Poly I:C-induced matrix (Fig. 4C).

To assess migration along a vertical axis, the number of T-cells that passed through the synoviocyte monolayer to the level of the coverslip was measured after a 20-min warm up period. Despite the increased binding potential of the matrix, the number of T-cells that migrated through the matrix and monolayer to the coverslip was significantly decreased in the Poly I:C-treated synoviocytes and this was reversed by hyaluronidase treatment (Fig. 5A). In addition, the proportion of the total bound T-cells with the amoeboid morphology was also diminished in the Poly I:C-treated cultures (Fig. 5B). Pre-treatment of the matrix with hyaluronidase before adding the T-cells promoted the amoeboid shape in the T-cells and abolished the inhibitory effect of the Poly I:C-induced matrix on T-cell penetration to the coverslip, indicating that hyaluronan integrity or its retention of versican may be crucial to T-cell arrest and slower penetration of the fibroblast layer. Incubation of the synoviocytes with an antibody to the versican N-terminus (12C5) during the period of matrix formation also partially abolished the ability of the Poly I:C-induced matrix to impede T-cell migration to the coverslip (Fig. 5C). This antibody had no effect on the amount of hyaluronan in the cell layer (data not shown). Although T-cell adhesion to the Poly I:C-induced matrix was increased, these results suggest that, rather than facilitating migration, the matrix may prevent

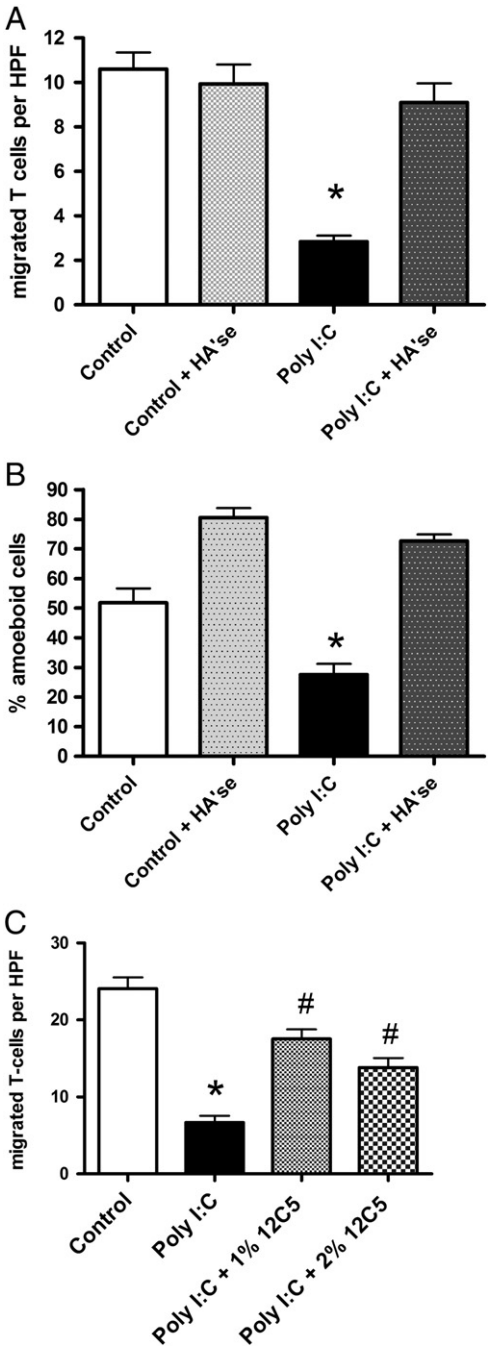

Fig. 5. Penetration of synoviocyte monolayers by T-cells is inhibited by hyaluronan- and versican-rich matrix following Poly I:C stimulation. A. The number of T-cells per high power field (HPF) that migrated to the underside of the synoviocytes without or following digestion of the formed matrix with hyaluronidase. B. The percentage of the total bound T-cells with an amoeboid morphology (same experiment as in A). C. In a separate experiment, an antibody to versican was added at two different concentrations to the fibroblasts during the period of matrix formation before addition of the T-cells. *$p<0.001$ compared to control. # $p<0.001$ compared to Poly I:C.

polarization, promote rounding and constrain T-cell migration, and that versican may be one component that is partially responsible for this effect.

3.5. Poly I:C drives myofibroblast morphology

Treatment of HFLS (Fig. 6) or lung fibroblasts (data not shown) with Poly I:C also caused a dramatic alteration in the morphology of these cells. The cells became much more spread and flattened, particularly around the nucleus (Fig. 6A). Digestion with *Streptomyces* hyaluronidase for 30 min caused a partial reversion of the synoviocytes back toward the control cell morphology. In addition, smooth muscle α actin was detected in Poly I:C-treated synoviocytes, but not in control cells (Fig. 6B). These data are consistent with previous studies showing increased stress fiber formation in lung fibroblasts (Evanko et al., 2009), and augmented myofibroblast differentiation by activation of TLR3 with Poly I:C (Sugiura et al., 2009).

3.6. Versican inhibits T-lymphocyte migration

In order to simplify assessment of the role of versican and hyaluronan in T-cell function, we also studied the interaction of T-lymphocytes with purified matrix components. In solution binding experiments, versican partially inhibited the binding of fluorescein-labeled hyaluronan to activated CD4+ T-cells, as assessed by flow cytometry (Fig. 7A, B). The inhibition of hyaluronan binding to T-cells required preincubation of the versican with the hyaluronan, suggesting that it is the interaction of versican with hyaluronan that is important for the inhibition, rather than direct competition of versican with hyaluronan for CD44 or another receptor on the T-cells. We were unable to demonstrate binding of biotinylated versican directly to 4MU-treated T-cells (Supplemental Fig. 2) nor to untreated T-cells (data not shown). Consistent with earlier studies (Bollyky et al., 2007), the CD44 blocking antibody, BU75 (Ancell Corp., Bayport, MN), only partially inhibited binding of FITC-hyaluronan to T-cells (Supplemental Fig. 2).

When T-cells were plated in dishes coated with hyaluronan alone, there was a significant increase in the proportion of cells with an amoeboid shape compared to tissue culture plastic (Fig. 8). Preincubation of the hyaluronan-coated dishes with versican or versican core protein caused a significant reduction in the proportion of T-cells with the amoeboid shape compared to hyaluronan alone. These data indicate that versican may interrupt adhesion of T-cells to plate-bound hyaluronan, promote rounding, and potentially influence the migratory ability of the T-cells.

To assess the contribution of the matrix components on T-cell migration in a three dimensional system, collagen gels were cast on coverslips without or with the inclusion of purified versican alone or in combination with hyaluronan, as well as the versican core protein and T-cell penetration into the gels over a 3-hr period was measured (Fig. 9). Hyaluronan alone significantly promoted random T-cell penetration into the collagen gels in 4 out of 7 experiments (two examples are given in Fig. 9 A, B). Versican and versican core protein significantly inhibited T-cell penetration into the collagen gels (Fig. 9B). Neither chondroitin sulfate nor the chondroitin ABC lyase enzyme used to generate the versican core protein had an effect on T-cell penetration into the collagen (Fig. 9B). Similar results were seen when versican or hyaluronan was added to the gels after the collagen had polymerized, suggesting that the diminished penetration by randomly migrating T-cells was not due to an effect of the additives on collagen polymerization or pore size (data not shown). When chemokines CCL19 and CCL21 were included in the gel to increase T-cell migration, the promotional effect of hyaluronan alone was lost, while versican alone, or added with hyaluronan, significantly reduced T-cell penetration into the collagen (Fig. 9C).

4. Discussion

The present study examines the effects of T-lymphocytes encountering matrix that is rich in hyaluronan and the hyaluronan-binding proteoglycan, versican and derived from treatment of lung fibroblasts and synoviocytes with a viral mimetic that is known to promote myofibroblast formation and hyaluronan cable formation. Others have previously shown that monocytes adhere to hyaluronan- and versican-rich cable structures induced by Poly I:C, and this adhesion is partly dependent on CD44 (de la Motte et al., 1999; Majors et al.,

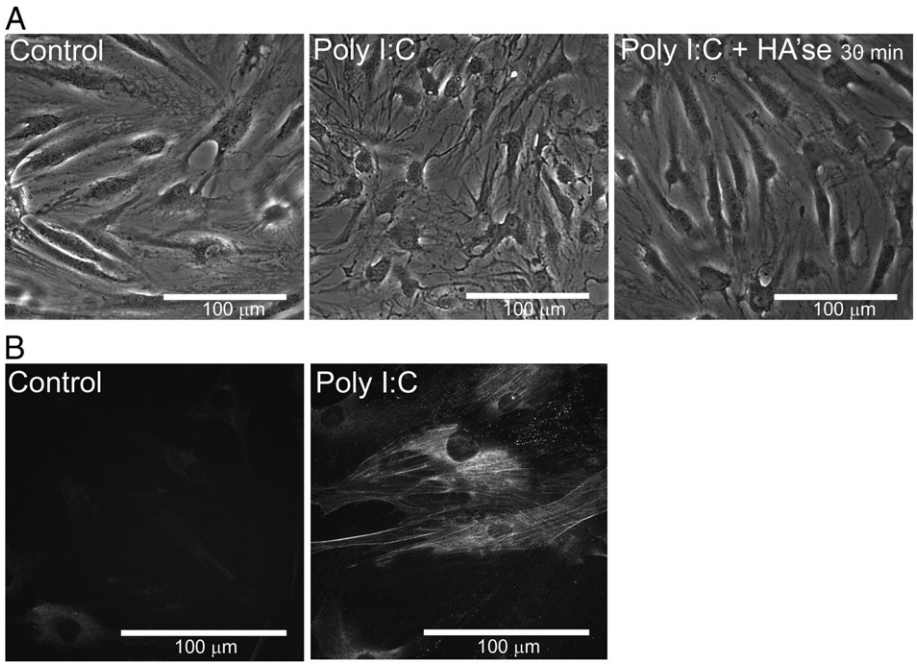

Fig. 6. Myofibroblast morphology and smooth muscle α actin expression is induced by Poly I:C. A. Phase contrast views of control (left panel) and Poly I:C-treated synoviocytes before and after digestion with *Streptomyces* hyaluronidase (middle and right panels) as indicated. B. Smooth muscle α actin staining in control and Poly I:C-treated cells. Bars in all images equal 100 μm.

2003; Wang and Hascall, 2004; Selbi et al., 2006; Evanko et al., 2009b; Potter-Perigo et al., 2010). Our results extend these observations to activated CD4+ T-lymphocytes.

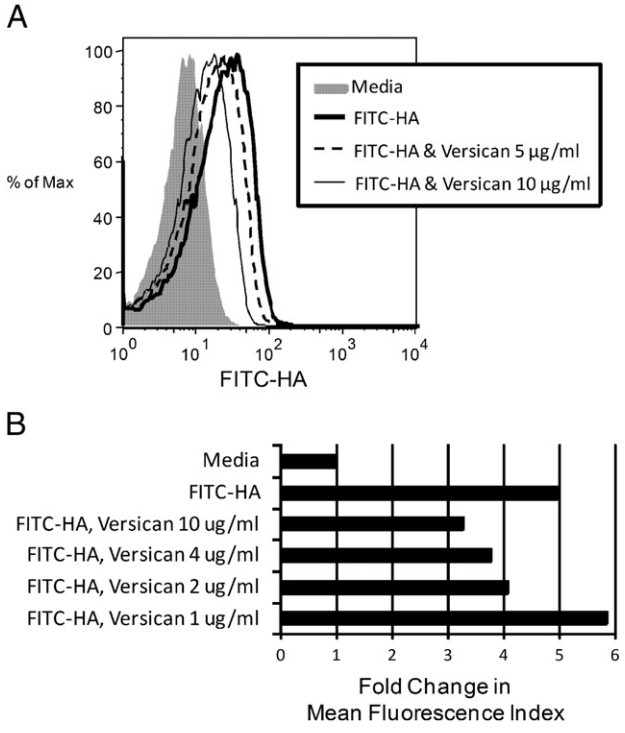

Fig. 7. Versican addition inhibits T-cell binding to FITC-labeled HMWHA. A. Histogram demonstrating FITC-HA binding to T-cells with and without preincubation of the FITC-HA with increasing amounts of versican or an equivalent volume of PBS. FITC-HA binding is shown on a logarithmic scale. Data are representative of five experiments. B. Fold change in mean fluorescence index as a measure of FITC-HA binding. CD4+ T-cells were activated with αCD3/28 coated beads and IL-2 for 4 days and washed prior to treatment with FITC-HA with or without versican at the indicated concentrations. In both A and B, FITC-HA binding was assessed by flow cytometry after cells had been washed to remove non-adherent FITC-HA.

Unexpectedly, increased binding of T-lymphocytes to the hyaluronan- and versican-rich cables made by lung fibroblasts in response to Poly I:C did not translate into directional migration along the cables.

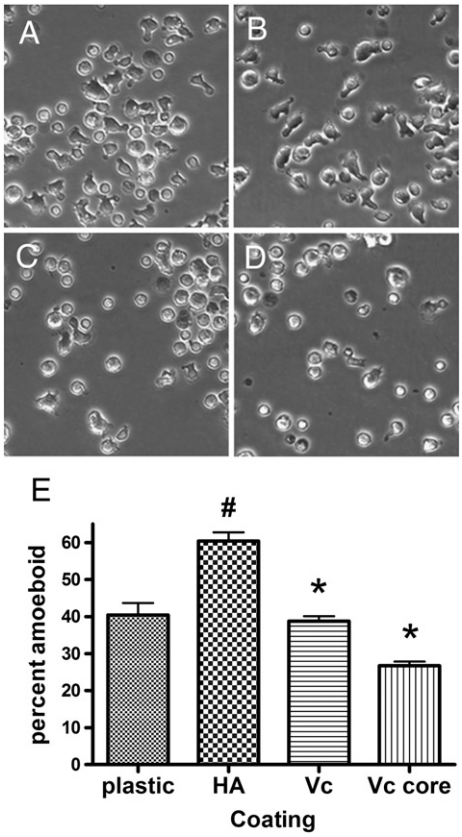

Fig. 8. Versican blocks amoeboid shape change induced by hyaluronan. A–D, phase contrast images of T-cells plated on A, tissue culture plastic; B, hyaluronan-coated surface, C, hyaluronan-coated dish followed by versican or D, versican core protein. E, Quantitation of the number of amoeboid cells. # $p<0.001$ compared to plastic. * $p<0.001$ compared to hyaluronan alone.

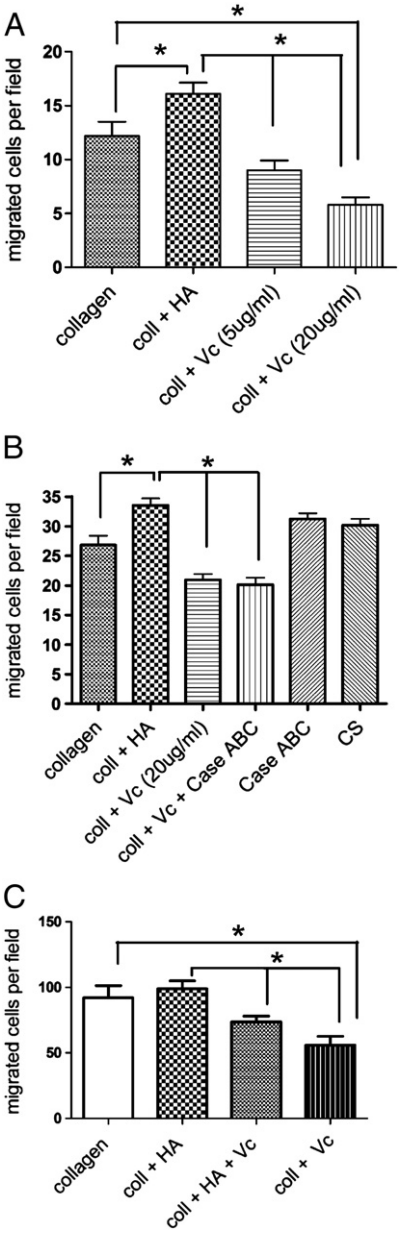

Fig. 9. Versican inhibits T-cell penetration of collagen gels. A. T-cells were applied to the top of gels containing collagen alone or with added hyaluronan (50 μg/ml) or versican at 5 and 20 μg/ml, and the number of T-cells penetrating to a depth of 100 μm after 3 h were counted. B. Another experiment was done using hyaluronan, versican, versican core protein (Vc + Case ABC), chondroitin sulfate (30 μg/ml), or chondroitin ABC lyase (10 mU). C. A third experiment was done in which the chemokines CCL19 and CCL21 were added to the gel to promote T-cell migration. * $p<0.05$.

Instead, the matrix promoted clustering, rounding and arrest of the lymphocytes and thus may interfere with polarization. The matrix also constrained T-cell migration on the surface and to the underside of the synoviocyte monolayer. T-cell penetration of the monolayer and the number of T-cells with the amoeboid shape was increased after hyaluronidase digestion of the matrix, indicating that the structural integrity of hyaluronan-based matrix was vital, and that it was not due to an effect of any residual Poly I:C in the cultures. In addition to the reversion to normal fibroblast morphology (i.e., less spread) by hyaluronidase treatment reported here, hyaluronidase digestion has been shown to induce the retraction of fine microvillous protrusions that are involved in pericellular matrix formation in fibroblasts and other cells (Kultti et al., 2006) and this may also facilitate T-cells passing through the monolayer. These data also suggest that factors which impact local production of hyaluronidases may be important in the transition from T-cell adhesion to polarized migration.

Inflammation can result in a mucinous ECM/extracellular fluid environment where high viscosity, negative charge density and other attributes of the proteoglycans may contribute to alterations in leukocyte retention and rate of migration, and this ECM tends to precede fibrosis. Hyaluronan and versican have both been shown to modulate differentiation of myofibroblasts (Hattori et al., 2011; Meran et al., 2007; Webber et al., 2009). During chronic inflammation in both lung and synovial tissues, fibrosis and accumulation of myofibroblasts tend to follow the accumulation of complex hyaluronan matrices (Day and de la Motte, 2005; Kasperkovitz et al., 2005; Westergren-Thorsson et al., 2010), and this can be repeated in multiple inflammatory events. Our data suggest that the milieu of the fibroblast or synoviocyte may modulate inflammatory cell migration and surveillance.

Previous studies have shown a selective association of myofibroblasts with high inflammation synovial tissues (Kasperkovitz et al., 2005), and fibrosis in lung tissue is common following chronic inflammation (Westergren-Thorsson et al., 2010). Our results are consistent with previous studies showing that Poly I:C augmented myofibroblast formation (Sugiura et al., 2009) as well as stress fibers and microvillous protrusions in HLF (Evanko et al., 2009). Together these results imply that this ECM of myofibroblasts induced by a viral mimetic may inhibit the migration of lymphocytes, partly through a trapping effect. In a study of lymphocyte migration in infected brain, parasite-specific CD8 + T-cells migrated on a system of inflammation-associated reticular fibers of unknown composition visualized by second harmonics (Wilson et al., 2009). The lymphocytes exhibited various other behaviors such as clustering, or rapid migration followed by constraint and rounding, but it was not clear if hyaluronan and versican, known matrix components in brain (Dours-Zimmermann et al., 2009), may have influenced migratory behavior in these studies.

Lymphocyte penetration of the synoviocyte monolayer was increased in Poly I:C-treated cultures when an antibody to an epitope in the N-terminal globular domain of versican (12C5) was added during the period of matrix formation, suggesting that versican's interaction with hyaluronan may be important for the ability of the matrix to impede T-cell migration. This antibody was previously shown to inhibit monocyte binding to the matrix of lung fibroblasts (Potter-Perigo et al., 2010). However, the 12C5 antibody was unable to block the binding of biotinylated versican to hyaluronan-coated dishes (data not shown), suggesting that it may work by other mechanisms, such as interfering with aggregate stability or versican turnover. More experiments will be required to understand how this antibody is working.

In addition, the fibroblast cell coat acted as a barrier to direct contact between T-cells and the fibroblasts, potentially impairing cell scaffold-mediated migration strategies. This, together with time-lapse video data, suggests that T-cell migration may be more efficient when direct contact is made between lymphocytes and stromal cells. The more flattened and adherent nature of myofibroblasts may also help to limit the potential of the T-cells to slip between cell margins. Overwhelming amounts of the matrix may prevent proper T-cell polarization. Further study will be required to better understand the roles of hyaluronan, versican, and the participation of myofibroblasts in the inflammatory process.

Using purified matrix components, we found that versican (V0, V1) partially prevented the binding of soluble hyaluronan to T-lymphocytes. Versican added to plate-bound hyaluronan also inhibited the amoeboid shape change induced by the hyaluronan coating alone. In a three dimensional system, we found that addition of versican or versican core protein alone, or in combination with hyaluronan, blocked T-cell migration into collagen gels. Earlier studies have found that versican can have both adhesive and antiadhesive functions (Yamagata et al., 1989; Yamagata et al., 1993; Ernst et al., 1995) and this depends in part on the geometry of

the assay system. These differences may also reflect the presence of higher order hyaluronan structures, such as cables. Others have shown that versican V0, V1 and the core protein inhibited or guided migration of neural crest cells on fibronectin by interfering with substrate adhesion (Dutt et al., 2006). Addition of aggregating proteoglycans or their G1 domains to hyaluronan can affect length and conformation of hyaluronan (Morgelin et al., 1995) and material properties, such as viscosity (Mow et al., 1984). Excess amounts of hyaluronan binding domains of the proteoglycan can destabilize hyaluronan networks (Brewton and Mayne, 1992; Morgelin et al., 1995). Thus the effects of versican on the interactions of hyaluronan with the T-cell surface may be quite complex. Previous studies have shown that versican V3 expression and CD44 silencing in melanoma cells blocked CD44-dependent hyaluronan internalization, leading to an accumulation of hyaluronan in the pericellular matrix and to changes in cell migration on hyaluronan (Hernandez et al., 2010). Our results suggest there may be a role for versican V0, V1 in modulating effects of hyaluronan on T-cell adhesion and migration.

The physiologic relevance of these findings extends beyond T-cell trafficking. Hyaluronan can play concomitant pro-tolerogenic or pro-inflammatory roles depending on its size and amount (Noble, 2002; Day and de la Motte, 2005). Several studies have looked at the influence of hyaluronan on leukocyte function. For example, we have previously reported that high molecular weight hyaluronan promotes the suppressive effects of CD4 + CD25 + regulatory T-cells in part through production of the immunosuppressive cytokine IL-10 (Bollyky et al., 2007; Bollyky et al., 2009a; Bollyky et al., 2009b). In subsequent work we have found that HMWHA also promotes IL-10 production by conventional T-cells (Bollyky et al., 2011). The data presented here indicate that the presence of versican may be one way in which the capacity of hyaluronan to affect T-cell biology is regulated.

Collectively, these results suggest that versican and hyaluronan in complex extracellular matrices synthesized by myofibroblasts may influence the rate of lymphocyte trafficking to and from inflamed tissues.

Supplementary materials related to this article can be found online at doi:10.1016/j.matbio.2011.10.004.

Acknowledgments

We would like to thank Dr. Inkyung Kang for helpful discussions, Rebecca Wu, Christina Chan, and Loreen Petty for technical assistance, and Dr. Virginia M. Green for manuscript preparation. This work was supported by National Institutes of Health grants DK046635 (to GTN); DK080178 and DK089128 (to PLB); and HL018645 and a BIRT supplement AR037296 (to TNW). This work was also supported by grants from the Juvenile Diabetes Research Foundation (nPOD 25-2010-648 (to TNW)), and The Center for Translational Research at BRI (to GTN).

References

Bollyky, P.L., Falk, B.A., Long, S.A., Preisinger, A., Braun, K.R., Wu, R.P., Evanko, S.P., Buckner, J.H., Wight, T.N., Nepom, G.T., 2009a. CD44 costimulation promotes FoxP3 + regulatory T cell persistence and function via production of IL-2, IL-10, and TGF-beta. J. Immunol. 183, 2232–2241.

Bollyky, P.L., Falk, B.A., Wu, R.P., Buckner, J.H., Wight, T.N., Nepom, G.T., 2009b. Intact extracellular matrix and the maintenance of immune tolerance: high molecular weight hyaluronan promotes persistence of induced CD4+CD25+ regulatory T cells. J. Leukoc. Biol. 86, 567–572.

Bollyky, P.L., Lord, J.D., Masewicz, S.A., Evanko, S.P., Buckner, J.H., Wight, T.N., Nepom, G.T., 2007. Cutting edge: high molecular weight hyaluronan promotes the suppressive effects of CD4+CD25+ regulatory T cells. J. Immunol. 179, 744–747.

Bollyky, P.L., Wu, R.P., Falk, B.A., Lord, J.D., Long, S.A., Preisinger, A., Teng, B., Holt, G.E., Standifer, N.E., Braun, K.R., Xie, C.F., Samuels, P.L., Vernon, R.B., Gebe, J.A., Wight, T.N., Nepom, G.T., 2011. ECM components guide IL-10 producing regulatory T-cell (TR1) induction from effector memory T-cell precursors. Proc. Natl. Acad. Sci. U. S. A. 108, 7938–7943.

Brewton, R.G., Mayne, R., 1992. Mammalian vitreous humor contains networks of hyaluronan molecules: electron microscopic analysis using the hyaluronan-binding region (G1) of aggrecan and link protein. Exp. Cell Res. 198, 237–249.

Day, A.J., de la Motte, C.A., 2005. Hyaluronan cross-linking: a protective mechanism in inflammation? Trends Immunol. 26, 637–643.

de la Motte, C.A., Hascall, V.C., Calabro, A., Yen-Lieberman, B., Strong, S.A., 1999. Mononuclear leukocytes preferentially bind via CD44 to hyaluronan on human intestinal mucosal smooth muscle cells after virus infection or treatment with poly(I.C). J. Biol. Chem. 274, 30747–30755.

Denucci, C.C., Mitchell, J.S., Shimizu, Y., 2009. Integrin function in T-cell homing to lymphoid and nonlymphoid sites: getting there and staying there. Crit. Rev. Immunol. 29, 87–109.

Dours-Zimmermann, M.T., Maurer, K., Rauch, U., Stoffel, W., Fassler, R., Zimmermann, D.R., 2009. Versican V2 assembles the extracellular matrix surrounding the nodes of ranvier in the CNS. J. Neurosci. 29, 7731–7742.

Dutt, S., Kleber, M., Matasci, M., Sommer, L., Zimmermann, D.R., 2006. Versican V0 and V1 guide migratory neural crest cells. J. Biol. Chem. 281, 12123–12131.

Ernst, H., Zanin, M.K.B., Everman, D., Hoffman, S., 1995. Receptor-mediated adhesive and anti-adhesive functions of chondroitin sulfate proteoglycan preparations from embryonic chicken brain. J. Cell Sci. 108, 3807–3816.

Evanko, S.P., Angello, J.C., Wight, T.N., 1999. Formation of hyaluronan and versican rich pericellular matrix is required for proliferation and migration of vascular smooth muscle cells. Arterioscler. Thromb. Vasc. Biol. 19, 1004–1013.

Evanko, S.P., Potter-Perigo, S., Johnson, P.Y., Wight, T.N., 2009. Organization of hyaluronan and versican in the extracellular matrix of human fibroblasts treated with the viral mimetic poly I:C. J. Histochem. Cytochem. 57, 1041–1060.

Evanko, S.P., Tammi, M.I., Tammi, R.H., Wight, T.N., 2007. Hyaluronan-dependent pericellular matrix. Adv. Drug Deliv. Rev. 59, 1351–1365.

Friedl, P., Weigelin, B., 2008. Interstitial leukocyte migration and immune function. Nat. Immunol. 9, 960–969.

Hattori, N., Carrino, D.A., Lauer, M.E., Vasanji, A., Wylie, J.D., Nelson, C.M., Apte, S.S., 2011. Pericellular versican regulates the fibroblast-myofibroblast transition. A role for ADAMTS5-mediated proteolysis. J. Biol. Chem. 286, 34298–34310.

Hernandez, D., Miquel-Serra, L., Docampo, M.J., Marco-Ramell, A., Cabrera, J., Fabra, A., Bassols, A., 2010. V3 versican isoform alters the behavior of human melanoma cells by interfering with CD44/ErbB-dependent signaling. J. Biol. Chem. 286, 1475–1485.

Hoare, K., Savani, R.C., Wang, C., Yang, B., Turley, E.A., 1993. Identification of hyaluronan binding proteins using a biotinylated hyaluronan probe. Connect. Tissue Res. 30, 117–126.

Johnson, P., Ruffell, B., 2009. CD44 and its role in inflammation and inflammatory diseases. Inflamm. Allergy Drug Targets 8, 208–220.

Kasperkovitz, P.V., Timmer, T.C., Smeets, T.J., Verbeet, N.L., Tak, P.P., van Baarsen, L.G., Baltus, B., Huizinga, T.W., Pieterman, E., Fero, M., Firestein, G.S., van der Pouw Kraan, T.C., Verweij, C.L., 2005. Fibroblast-like synoviocytes derived from patients with rheumatoid arthritis show the imprint of synovial tissue heterogeneity: evidence of a link between an increased myofibroblast-like phenotype and high-inflammation synovitis. Arthritis Rheum. 52, 430–441.

Korpos, E., Wu, C., Song, J., Hallmann, R., Sorokin, L., 2009. Role of the extracellular matrix in lymphocyte migration. Cell Tissue Res. 339, 47–57.

Kultti, A., Rilla, K., Tiihonen, R., Spicer, A.P., Tammi, R.H., Tammi, M.I., 2006. Hyaluronan synthesis induces microvillus-like cell surface protrusions. J. Biol. Chem. 281, 15821–15828.

Landolt, R.M., Vaughan, L., Winterhalter, K.H., Zimmermann, D.R., 1995. Versican is selectively expressed in embryonic tissues that act as barriers to neural crest cell migration and axon outgrowth. Development 121, 2303–2312.

Lesley, J., Howes, N., Perschl, A., Hyman, R., 1994. Hyaluronan binding function of CD44 is transiently activated on T cells during an in vivo immune response. J. Exp. Med. 180, 383–387.

Majors, A.K., Austin, R.C., de la Motte, C.A., Pyeritz, R.E., Hascall, V.C., Kessler, S.P., Sen, G., Strong, S.A., 2003. Endoplasmic reticulum stress induces hyaluronan deposition and leukocyte adhesion. J. Biol. Chem. 278, 47223–47231.

Meran, S., Thomas, D., Stephens, P., Martin, J., Bowen, T., Phillips, A., Steadman, R., 2007. Involvement of hyaluronan in regulation of fibroblast phenotype. J. Biol. Chem. 282, 25687–25697.

Morgelin, M., Paulsson, M., Heinegard, D., Aebi, U., Engel, J., 1995. Evidence of a defined spatial arrangement of hyaluronate in the central filament of cartilage proteoglycan aggregates. Biochem. J. 307, 595–601.

Mow, V.C., Mak, A.F., Lai, W.M., Rosenberg, L.C., Tang, L.H., 1984. Viscoelastic properties of proteoglycan subunits and aggregates in varying solution concentrations. J. Biomech. 17, 325–338.

Mrass, P., Kinjyo, I., Ng, L.G., Reiner, S.L., Pure, E., Weninger, W., 2008. CD44 mediates successful interstitial navigation by killer T cells and enables efficient antitumor immunity. Immunity 29, 971–985.

Noble, P.W., 2002. Hyaluronan and its catabolic products in tissue injury and repair. Matrix Biol. 21, 25–29.

Olin, K.L., Potter-Perigo, S., Barrett, P.H., Wight, T.N., Chait, A., 1999. Lipoprotein lipase enhances the binding of native and oxidized low density lipoproteins to versican and biglycan synthesized by cultured arterial smooth muscle cells. J. Biol. Chem. 274, 34629–34636.

Olin, K.L., Potter-Perigo, S., Barrett, P.H., Wight, T.N., Chait, A., 2001. Biglycan, a vascular proteoglycan, binds differently to HDL2 and HDL3: role of apoE. Arterioscler. Thromb. Vasc. Biol. 21, 129–135.

Potter-Perigo, S., Johnson, P.Y., Evanko, S.P., Chan, C.K., Braun, K.R., Wilkinson, T.S., Altman, L.C., Wight, T.N., 2010. Polyinosine-polycytidylic acid stimulates versican accumulation in the extracellular matrix promoting monocyte adhesion. Am. J. Respir. Cell Mol. Biol. 43, 109–120.

Raghu, G., Chen, Y.Y., Rusch, V., Rabinovitch, P.S., 1988. Differential proliferation of fibroblasts cultured from normal and fibrotic human lungs. Am. Rev. Respir. Dis. 138, 703–708.

Ruffell, B., Johnson, P., 2008. Hyaluronan induces cell death in activated T cells through CD44. J. Immunol. 181, 7044–7054.

Selbi, W., de la Motte, C.A., Hascall, V.C., Day, A.J., Bowen, T., Phillips, A.O., 2006. Characterization of hyaluronan cable structure and function in renal proximal tubular epithelial cells. Kidney Int. 70, 1287–1295.

Sorokin, L., 2010. The impact of the extracellular matrix on inflammation. Nat. Rev. Immunol. 10, 712–723.

Sugiura, H., Ichikawa, T., Koarai, A., Yanagisawa, S., Minakata, Y., Matsunaga, K., Hirano, T., Akamatsu, K., Ichinose, M., 2009. Activation of Toll-like receptor 3 augments myofibroblast differentiation. Am. J. Respir. Cell Mol. Biol. 40, 654–662.

Sugiyama, K., Komada, Y., Deguchi, T., Zhang, X.L., Azuma, E., Ido, M., Yamamoto, H., Sakurai, M., 1999. CD3-mediated T cell activation is inhibited by anti-CD44 monoclonal antibodies directed to the hyaluronan-binding region. Immunol. Invest. 28, 185–200.

Toole, B.P., 2004. Hyaluronan: from extracellular glue to pericellular cue. Nat. Rev. Cancer 4, 528–539.

Underhill, C.B., Nguyen, H., Shizari, M., Culty, M., 1993. CD44 positive macrophages take up hyaluronan during lung development. Dev. Biol. 155, 324–336.

Wang, A., Hascall, V.C., 2004. Hyaluronan structures synthesized by rat mesangial cells in response to hyperglycemia induce monocyte adhesion. J. Biol. Chem. 279, 10279–10285.

Webber, J., Jenkins, R.H., Meran, S., Phillips, A., Steadman, R., 2009. Modulation of TGFbeta1-dependent myofibroblast differentiation by hyaluronan. Am. J. Pathol. 175, 148–160.

Westergren-Thorsson, G., Larsen, K., Nihlberg, K., Andersson-Sjoland, A., Hallgren, O., Marko-Varga, G., Bjermer, L., 2010. Pathological airway remodelling in inflammation. Clin. Respir. J. 4 (Suppl 1), 1–8.

Wilson, E.H., Harris, T.H., Mrass, P., John, B., Tait, E.D., Wu, G.F., Pepper, M., Wherry, E.J., Dzierzinski, F., Roos, D., Haydon, P.G., Laufer, T.M., Weninger, W., Hunter, C.A., 2009. Behavior of parasite-specific effector CD8 + T cells in the brain and visualization of a kinesis-associated system of reticular fibers. Immunity 30, 300–311.

Wolf, K., Muller, R., Borgmann, S., Brocker, E.B., Friedl, P., 2003. Amoeboid shape change and contact guidance: T-lymphocyte crawling through fibrillar collagen is independent of matrix remodeling by MMPs and other proteases. Blood 102, 3262–3269.

Yamagata, M., Kimata, K., 1994. Repression of a malignant cell-substratum adhesion phenotype by inhibiting the production of the anti-adhesive proteoglycan, PG-M/versican. J. Cell Sci. 107, 2581–2590.

Yamagata, M., Saga, S., Kato, M., Bernfield, M., Kimata, K., 1993. Selective distributions of proteoglycans and their ligands in pericellular matrix of cultured fibroblasts. Implications for their roles in cell-substratum adhesion. J. Cell Sci. 106, 55–65.

Yamagata, M., Suzuki, S., Akiyama, S., Yamada, K., Kimata, K., 1989. Regulation of cell-substrate adhesion by proteoglycans immobilized on extracellular substrates. J. Biol. Chem. 264, 8012–8018.

Cell Transplantation, Vol. 21, pp. 2099–2110, 2012

0963-6897/12 $90.00 + .00
DOI: http://dx.doi.org/10.3727/096368912X636786
E-ISSN 1555-3892
www.cognizantcommunication.com

Reversal of Diabetes in Mice With a Bioengineered Islet Implant Incorporating a Type I Collagen Hydrogel and Sustained Release of Vascular Endothelial Growth Factor

Robert B. Vernon,* Anton Preisinger,* Michel D. Gooden,*
Leonard A. D'Amico,* Betty B. Yue,* Paul L. Bollyky,* Christian S. Kuhr,†
Thomas R. Hefty,† Gerald T. Nepom,* and John A. Gebe*

*Benaroya Research Institute at Virginia Mason, Seattle, WA, USA
†Virginia Mason Medical Center, Seattle, WA, USA

We have developed a bioengineered implant (BI) to evaluate strategies to promote graft survival and function in models of islet transplantation in mice. The BI, sized for implantation within a fold of intestinal mesentery, consists of a disk-shaped, polyvinyl alcohol sponge infused with a type I collagen hydrogel that contains dispersed donor islets. To promote islet vascularization, the BI incorporates a spherical alginate hydrogel for sustained release of vascular endothelial growth factor (VEGF). BIs that contained 450–500 islets from syngeneic (C57Bl/6) donors and 20 ng of VEGF reversed streptozotocin (STZ)-induced diabetes in 100% of mice (8/8), whereas BIs that contained an equivalent number of islets, but which lacked VEGF, reversed STZ-induced diabetes in only 62.5% of mice (5/8). Between these "+VEGF" and "–VEGF" groups, the time to achieve normoglycemia (8–18 days after implantation) did not differ statistically; however, transitory, postoperative hypoglycemia was markedly reduced in the +VEGF group relative to the –VEGF group. Notably, none of the mice that achieved normoglycemia in these two groups required exogenous insulin therapy once the BIs began to fully regulate levels of blood glucose. Moreover, the transplanted mice responded to glucose challenge in a near-normal manner, as compared to the responses of healthy, nondiabetic (control) mice that had not received STZ. In future studies, the BIs described here will serve as platforms to evaluate the capability of immunomodulatory compounds, delivered locally within the BI, to prevent or reverse diabetes in the setting of autoimmune (type 1) diabetes.

Key words: Diabetes; Islet; Bioengineered implant (BI); Collagen; Vascular endothelial growth factor (VEGF); Mouse

INTRODUCTION

Type 1 diabetes (T1D) is a late-stage manifestation of an autoimmune-mediated loss of insulin-secreting pancreatic -cells that results in the inability to maintain blood glucose homeostasis (28,47). Current options for the treatment of T1D are (1) daily insulin therapy (DIT), (2) transplantation of the pancreas, either without the kidney (*pancreas transplant alone – PTA*) or with the kidney (*simultaneous pancreas/kidney – SPK*) (39), or (3) transplantation of isolated islets (36). While PTA and SPK procedures can restore glucose homeostasis, they involve major surgery and require lifelong immunosuppression, with the problem of recurrent autoimmunity (18,23,41). Moreover, these procedures can result in significant complications that include acute rejection, infection with cytomegalovirus (43), and technical failure as a result of vascular thrombosis, bleeding, anastomotic leaks, or infection/pancreatitis (11,13). Consequently, these treatments are generally limited to severely diabetic patients with associated kidney disease, which leaves the majority of T1D patients with either DIT or islet transplantation to manage their disease.

DIT, which requires injection of short- or long-acting insulin formulations, has been made easier by the use of semiautomated pump devices (30). However, a significant problem of DIT is ineffective control of unrecognized hypoglycemic episodes, which are further amplified under more intensive glucose management protocols designed to reduce secondary complications (5,24,33). Presumably, this problem would not arise with a properly functioning islet graft, which would act like the native endocrine pancreas to maintain glucose homeostasis. Accordingly, there is a substantial effort to develop effective methods for islet transplantation (27). Notably, however, current

Received May 11, 2011; final acceptance December 2, 2011. Online prepub date: March 28, 2012.
Address correspondence to John A. Gebe, Ph.D., Benaroya Research Institute at Virginia Mason, 1201 Ninth Ave., Seattle, WA 98101, USA.
Tel: +1-206-287-5612; Fax: +1-206-342-6581; E-mail: jgebe@benaroyaresearch.org

islet transplant protocols for treatment of T1D have had limited success as a consequence of (1) poor survival of islets in therapeutically approved intrahepatic graft sites (1,9), (2) alloimmune rejection (34), and (3) recurrence of the underlying autoimmunity (23,40). These three critical barriers to success must be overcome for islet replacement therapy to be an effective treatment for T1D.

The present study describes a bioengineered implant (BI) that will be used as a test bed to evaluate a number of strategies to promote islet graft survival and function in the setting of T1D. The BI incorporates five features that make it useful in this role: (1) It is miniaturized for engraftment in mice—a species that includes specific strains that effectively model T1D. (2) The BI is disk-shaped for implantation in a fold made from gut mesentery that models the greater omentum of humans, which is considered a favorable site for islet engraftment due to its large size and rich, dynamic blood supply. (3) The supportive scaffold of the BI is comprised of polyvinyl alcohol (PVA) sponge, a material that is durable and easily shaped, elicits a minimal inflammatory response, and which supports neovascularization (17,32). (4) Islets within the BI are supported by a hydrogel comprised of native fibrillar type I collagen, a natural extracellular matrix (ECM) component that is biodegradable, elicits little or no immune response, and has been shown to improve -cell viability and insulin secretion in vitro (10,20,25,26). (5) To improve revascularization of the islets, the BI incorporates a spherical alginate hydrogel (an "alginate macrosphere") to provide sustained, local delivery of vascular endothelial growth factor (VEGF), a potent angiogenic cytokine.

We find that murine donor islets incorporated into BIs and transplanted into syngeneic recipients are revascularized and produce insulin. Significantly, BIs containing 450–500 donor islets reverse diabetes in streptozotocin (STZ)-treated mice. Moreover, we find that release of VEGF within the implant mitigates hypoglycemia following transplantation and improves implant performance.

MATERIALS AND METHODS

Isolation of Islets

C57Bl/6 mice 12–24 weeks of age were anesthetized by injection at 20 µl/g body weight with 2,2,2-tribromoethanol, prepared as a 2.5% solution in phosphate-buffered saline (PBS) from a 1:1 wt (g)/vol (ml) 2,2,2-tribromoethanol/*tert*-amyl alcohol stock. The descending aorta of each anesthetized mouse was transected and a 30-gauge needle was used to inject each pancreas, through the common bile duct, with 3 ml of 4°C "islet medium" comprised of RPMI 1640 containing 1.0 g $NaHCO_3$, 1 mM Na-pyruvate, 100 µg/ml penicillin, and 100 U/ml streptomycin (all from Gibco/Invitrogen), and 10% fetal bovine serum (FBS) (Atlanta Biologicals, cat. #S12450H). The islet medium was supplemented with 0.8 mg/ml of collagenase P (Roche, cat. #11-249-002-001) and filtered through a 0.22-µm filter prior to injection. Subsequently, the pancreata were excised and each placed separately in a 50-ml conical centrifuge tube on ice. When two to three pancreata were obtained, 5 ml of 37°C islet medium was added to each tube, incubated at 37°C for 13 min, then decanted, and 30 ml of 4°C islet medium was added to each tube. The tubes were shaken vigorously for 1 min to disrupt the pancreata, and the tissue suspensions were filtered through a 30-mesh metal screen to remove large debris. The filtrates were centrifuged in a Beckman GS-6 at 500 rpm for 10 min at 4°C, the supernates were discarded, and the pellets were resuspended in 5 ml of 4°C islet medium. Subsequently, 5 ml of 4°C Histopaque®-1077 (Sigma-Aldrich) was injected under the medium layer and the tubes were centrifuged for 20 min at 2,000 rpm (without applied braking). The islets were collected at the Histopaque/medium interface and washed by a 500 rpm centrifugation for 10 min through 40 ml of 4°C islet medium. The washed islets were resuspended in 4 ml of islet medium, placed in 60-mm dishes, and put in a 37°C, 5% CO_2 incubator. Once all pancreata were processed, the isolated islets were hand-picked into a new 60-mm dish, cultured overnight, and picked again the next day before being placed in BIs. Average yields were 100–150 islets per mouse.

In Vitro Assays of Glucose-Mediated Insulin Release From Islets

For standard in vitro assays, the islets were isolated, cultured overnight in islet medium, washed briefly in Hank's buffered salt solution (HBSS), and then were preincubated for 2 h at 37°C in HBSS with 5.6 mM glucose (low glucose). After the 2-h interval, samples of medium were collected for insulin measurement by enzyme-linked immunosorbent assay (ELISA) (Mercodia Insulin ELISA kit, cat. #10-1247-01). Subsequently, the islets were stimulated for 3 or 30 min with 16.6 mM glucose (high glucose) and samples of medium collected for insulin measurement by ELISA. Fold changes were calculated as insulin (high glucose)/insulin (low glucose).

For experiments evaluating the effects of VEGF on insulin secretion, purified islets were cultured overnight in islet medium, washed in HBSS, and then distributed into a 24-well tissue culture plate. Each well contained 30 islets in 1 ml of HBSS/5.6 mM glucose (low glucose) with or without 10 ng/ml of human recombinant $VEGF_{165}$ (Peprotech, cat. #100-20). Baseline (i.e., low glucose) samples of medium were collected after 2 h and then glucose was added to each well to a final concentration of 16.6 mM (high glucose). Samples of medium (50 µl) were then taken at 30 min and insulin concentrations were determined by ELISA as described above. Fold

changes were calculated as insulin (high glucose)/insulin (low glucose).

Fabrication of the PVA Scaffolds

To fabricate the PVA scaffolds for the BIs, biopsy punches (Sklar Instruments) were used to cut 6-mm-diameter disks from 2-mm-thick sheets of PVA sponge (Type CF90, 500 μm average pore size with no surfactant treatment—a generous gift from Merocel/Medtronic, Inc.). Subsequently, each disk was through-punched with a single central hole of 1.5 mm diameter and eight peripheral holes of 1 mm diameter, using correspondingly sized biopsy punches (Acuderm, Inc.). The punched disks were washed on a rocker in 50-ml centrifuge tubes filled with 40 ml of sterile distilled water (10 min per wash, repeated five times), then air-dried on Whatman filter paper, transferred to 60-mm dishes, exposed to -irradiation, and stored until needed for BI assembly.

Preparation of VEGF-Alginate Macrospheres

To prepare VEGF-alginate macrospheres, a stock solution of 4% Na alginate (Sigma-Aldrich, cat. #A0682) was prepared in deionized water and filtered at 0.45 μm, using positive pressure. A stock solution of human recombinant $VEGF_{165}$ was prepared at 100 ng/μl in sterile, deionized water with 0.1% normal mouse serum (NMS). For macrospheres containing VEGF, 32 μl of alginate stock was combined with 28 μl of sterile deionized water and 4 μl of VEGF stock and pipetted in 8 μl volumes (each containing 2% alginate and 50 ng of VEGF) onto a sheet of hydrophobic Parafilm™ "M" (Pechiney Plastic Packaging) that was cut into a narrow triangular shape. The Parafilm triangle was held vertically on a clamp positioned 5 cm above a 60-mm Petri dish filled with a solution of 100 mM $CaCl_2$. The alginate/VEGF droplets were pulled to the tip of the Parafilm triangle by gravity, where they fell one at a time into the $CaCl_2$ solution and were crosslinked by the free Ca^{2+} ions into spheres approximately 2 mm in diameter. The spheres were crosslinked for 15 min in the $CaCl_2$ solution, then washed for 2 min in 10 ml of 0.15 M NaCl/25 mM HEPES/2 mM $CaCl_2$, pH 7.0 (repeated twice), transferred to a 35-mm dish filled with serum-free Dulbecco's modified Eagle's medium (DMEM) (Gibco/Invitrogen) with 100 μg/ml penicillin and 100 U/ml streptomycin (P/S), and maintained in a tissue culture incubator until needed for BI assembly.

Preparation of Type I Collagen Solution

To prepare type I collagen solution for the BIs, 1 volume of a stock solution of rat tail native type I collagen in dilute acetic acid (Becton Dickinson) was combined with 1/9 volume of 10-strength $NaHCO_3$-saturated Medium 199 (Gibco/Invitrogen) and sufficient DMEM and NMS to yield a solution containing 2.5 mg/ml collagen and 10% NMS (42). The collagen solution was prepared just prior to assembly of the BIs and maintained on ice until needed.

Assembly of the BIs

To prepare the BIs, the dry PVA sponge scaffolds were expanded for 5 min in sterile DMEM/P/S and a single, freshly prepared alginate macrosphere was gently pressed into the 1.5-mm-diameter center hole of each scaffold. The scaffolds were then blotted on sterile Whatman filter paper, transferred to 60-mm plastic tissue culture dishes lined with UV-sterilized Parafilm M, and flooded with 60 μl of type I collagen solution containing suspended islets. The PVA sponges absorbed the collagen solution, with the majority of the islets entering the 1-mm-diameter peripheral holes. Subsequently, the dishes were covered with dish tops (lined with moist filter paper) and incubated for 30 min at 37°C/5% CO_2/100% humidity to gel the collagen. The completed BIs were transferred to a 24-well tissue culture plate filled with 500 μl/well of preequilibrated DMEM/10% NMS/P/S and maintained in a tissue culture incubator until implantation in subject mice.

Induction of Diabetes and Implantation of BIs in Mice

Three days prior to surgical implantation of BIs, C57Bl/6 mice were treated with a high dose (200 mg/kg) of STZ made as a stock solution of 7.5 mg/ml STZ in 100 mM citrate, pH 4.2 (prepared and filtered at 0.22 μm immediately prior to intraperitoneal injection). Over 90% of mice receiving STZ became diabetic within 72 h (and most became diabetic within 48 h). Blood glucose was measured everyday and insulin was given when needed (see following section), but insulin was not administered on the day of surgery. To implant BIs, mice were administered buprenorphine (0.05–0.1 mg/kg) prior to the surgery, which was performed under isoflurane. A 1-cm vertical, midline incision was made in the skin and peritoneum, a loop of the small intestine was extracted, and the BI placed on the intestinal mesentery. Subsequently, the intestinal loop was folded over the BI and returned to the peritoneal cavity. The incision was closed with absorbable sutures (for the peritoneum) and staples (for the skin). Removal of BIs was done in the same manner as implantation. All work with mice was done in an AAALAC-accredited facility and was approved by the Benaroya Research Institutional Animal Care and Use Committee.

Monitoring of Insulin and Glucose Levels and Intraperitoneal Glucose Tolerance Tests

The blood glucose levels (BGLs) and body weights of STZ-treated mice were measured once a day. BGLs were measured from a saphenous vein bleed (30-gauge needle) using a Wavesense Presto glucometer (AgaMatrix). For

insulin treatment, sustained-release Levemir® insulin (Novo Nordisk) was diluted 1:5 to 1:20 in a solution of 20 mM NaCl/5 mM Na_2HPO_4/19 mM phenol/174 mM glycerol just prior to administration and was injected subcutaneously (SC). Mice were given 0.12 U of insulin for BGLs of 250–350 mg/dl, 0.23 U for BGLs of 350–450 mg/dl, or 0.33 U for BGLs over 450 mg/dl. Mice were also given 800–1,000 µl of saline SC in the inner thigh if loss of body weight was greater than 10% from starting weight (i.e., just prior to STZ treatment). For those mice in which receipt of BIs induced normoglycemia (i.e., BGLs were <250 mg/dl), the frequency of body weight and BGL measurements was reduced.

For intraperitoneal glucose tolerance tests, mice were fasted (water, but no food) for 6 h before injection with 1 mg of glucose (in sterile PBS) per gram of body weight. BGLs in saphenous vein blood were measured at 0, 15, 30, 60, and 120 min after injection of glucose.

Histological Analyses

Implants and pancreata were fixed in neutral-buffered formalin (NBF), dehydrated, embedded in paraffin, and sectioned at 8 µm. Sections were stained with hematoxylin and eosin (H&E) for routine histological examination. For detection of von Willebrand factor (vWF), sections were subjected to epitope retrieval for 20 min at 79°C using an ethylenediaminetetraacetic acid (EDTA)-based buffer, pH 9 (Bond™ Epitope Retrieval Solution 2, Leica Microsystems, cat. #AR9640), then blocked and exposed 1 h to a 1:400 dilution of a rabbit polyclonal antibody to human vWF (Dako, cat. #A0082). Bound antibodies were visualized with a Bond™ Polymer Refine Detection Kit (Leica Microsystems, cat. #DS9800) using 3,3-diaminobenzidine as the chromogen. The vWF-labeled sections were then exposed to hematoxylin to stain cell nuclei. For detection of insulin, sections were labeled for indirect immunofluorescence with a guinea pig monoclonal antibody to human insulin (Abcam, cat. #ab7842) in conjunction with an Alexa-Fluor 488™-conjugated goat anti-guinea pig IgG secondary antibody (Molecular Probes/Invitrogen). Images were recorded with a Leica DMR brightfield/epifluorescence microscope equipped with SPOT Insight™ and RT™ digital cameras (Diagnostic Instruments).

Measurement of Release of VEGF From Alginate Macrospheres In Vitro

To measure the release of VEGF from alginate in vitro, macrospheres containing 2% alginate and 50 ng VEGF were prepared as described above. The macrospheres were placed in 96-well tissue culture plates (one sphere per well) with each of the wells filled with 200 µl of DMEM/10% FBS/P/S. The plates were placed in a tissue culture incubator maintained at 37°C/5% CO_2/100% humidity. At specific time points (1, 2, 3, 6, and 14 days of incubation), a 100-µl volume of medium was removed from each well and stored at –80°C until analysis by ELISA. Following removal of the medium at each time point, the residual medium in each well was discarded, and each well was refilled with 200 µl of fresh medium. ELISA assays were performed with a DuoSet® Human VEGF ELISA Kit (R&D Systems, cat. #DY293B).

To determine the percentage of VEGF retained in alginate macrospheres during their fabrication, freshly prepared macrospheres of 8 µl volume were each dissolved in 892 µl of PBS/100 mM EDTA, followed by addition of 100 µl of FBS to the solution. VEGF in the samples was measured by ELISA, with a solution of 50 ng/ml of VEGF in PBS/100 mM EDTA/10% FBS serving as a positive control.

Statistics

Statistical *p* values were calculated with Prism® (GraphPad Software, Inc.) using a two-tailed *t* test or, for groups, a one-way ANOVA with the Bonferroni multiple comparison test. Values of *p* for Kaplan–Meier plots were calculated using a log-rank test.

RESULTS

BI Fabrication and Islets

The body of the BI (Fig. 1A) consisted of a disk-shaped scaffold of PVA sponge infused with a type I collagen hydrogel that held the suspended islets. An alginate macrosphere was placed in the center of the construct to provide a source of VEGF. The PVA sponge was readily infiltrated by the unpolymerized collagen solution—a consequence of the large (500 µm) pore diameter of the sponge. In contrast, penetration of the sponge by suspended islets was inhibited by the relatively narrow connections between the pores (pore throats). Consequently, we punched eight peripheral holes of 1-mm diameter into the PVA sponge in order to provide open spaces for the islets to occupy (Fig. 1A, B). The diameter of the central hole in the PVA sponge was set at 1.5 mm (Fig. 1B) so that it would stretch slightly to grip the 2 mm diameter alginate macrosphere (Fig. 1C). In fully assembled BIs, the collagen hydrogel held the suspended islets firmly in place and provided additional stabilization to the macrosphere while the construct was wrapped in a fold of small-intestinal mesentery (Fig. 1D).

The viability of the islets used in the BIs was confirmed by implanting 450 freshly isolated islets under the kidney capsule of STZ-treated diabetic mice. These mice became normoglycemic within 24 h of implantation (data not shown). When similar preparations of isolated islets were incorporated into freshly made BIs (500 islets per BI), the islets increased their production of insulin in vitro following 3- or 30-min exposures to elevated (16.6 mM)

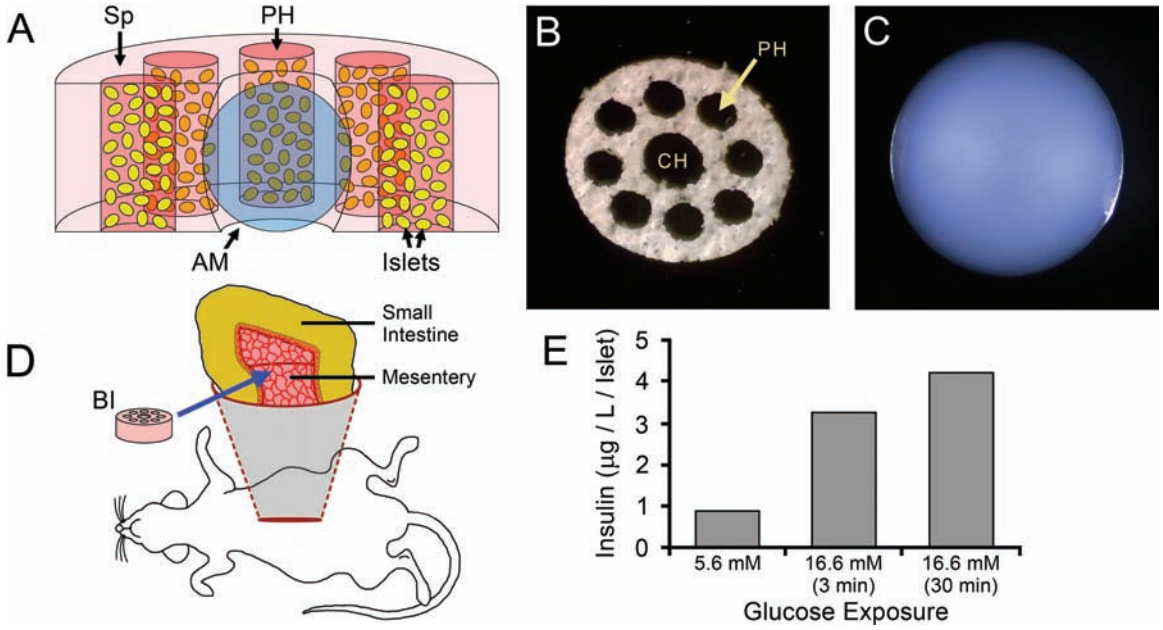

Figure 1. BI fabrication and implantation. (A) Cut-away diagram of the bioengineered islet (BI), with the components shown to scale. A disk-shaped polyvinyl alcohol (PVA) sponge (Sp) scaffold provides mechanical support. An alginate macrosphere (AM) (blue) occupies the central hole of the sponge. Eight peripheral holes (PH) in the sponge (5 appear in this cut-away) contain islets (yellow) suspended in a type 1 collagen hydrogel (reddish-pink). The collagen hydrogel also infuses the sponge (light pink). For clarity, the pores of the sponge are not depicted. (B) A PVA sponge scaffold oriented to show the central hole (CH) and peripheral holes (PH). The scaffold is 6 mm in diameter. (C) An alginate macrosphere of 2 mm diameter. (D) Diagram illustrating placement of the BI (pink disk) on the mesentery supporting a loop of small intestine. (E) Islets within freshly-made BIs (500 islets per BI) increased their production of insulin in vitro following 3- or 30-min exposures to elevated (16.6 mM) glucose, as compared to "resting" levels of insulin produced in the presence of low (5.6 mM) glucose.

glucose, as compared to "resting" levels of insulin produced in the presence of low (5.6 mM) glucose (Fig. 1E). Therefore, the materials and processes used to fabricate the BIs were not immediately harmful to the islets.

Release of VEGF From Alginate Macrospheres

Solutions of alginate are rapidly crosslinked by calcium ions to form stable hydrogels. The conditions for gelation are relatively mild, which has made alginate an attractive candidate for delivery of bioactive proteins (6,12,44), including VEGF (8,21,29). We found that a simple, gravity-driven drop generator using a nonwettable (Parafilm) surface allowed us to make spheres of smaller volume than could be made using conventional, syringe-type drop generators. The method also used reagents efficiently, as we did not have to fill a syringe body with a minimum volume of alginate/VEGF solution.

As determined by ELISA assays, freshly fabricated alginate macrospheres each retained an average of $42 \pm 2\%$ ($n = 5$) of the 50 ng of VEGF added to the alginate before calcium crosslinking (equivalent to 21 ng of VEGF per crosslinked macrosphere). This efficiency of VEGF incorporation is comparable to results obtained by others [e.g., 31% (29)] for 2% alginate hydrogels. Based on our measurement of percent incorporation of VEGF, our macrospheres released approximately 71% of their VEGF within 6 days (Fig. 2). This value is substantially higher than the 43–47% release level reported by others (29), which might be a consequence of our inclusion of

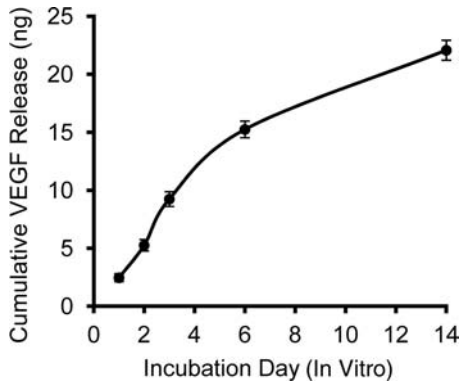

Figure 2. Cumulative release of vascular endothelial growth factor (VEGF) from 2% alginate macrospheres incubated for 14 days under physiological conditions in vitro ($n = 5$ macrospheres).

10% FBS in the culture media, in contrast to the use of serum-free media (29).

BI-Mediated Reversal of Diabetes in STZ-Treated Mice

We assessed the capacity of BIs to support islet survival and reverse acute (STZ-induced) diabetes in three groups of C57Bl/6 mice, as follows: (1) a +VEGF/+Islet group that received BIs containing 450–500 donor islets and alginate macrospheres loaded with VEGF, (2) a –VEGF/+Islet group that received BIs containing 450–500 donor islets and alginate macrospheres that lacked VEGF, and (3) a +VEGF/–Islet group that received BIs without donor islets, but with VEGF/alginate macrospheres. The BIs were surgically implanted on the intestinal mesentery under isoflurane anesthesia on day 0 in mice that were given a single high dose of STZ (200 mg/kg) 3 days earlier (day –3). The majority of recipients on the day of surgery had BGLs of at least 600 mg/dl (the maximum value on the glucometer). Basal BGLs prior to STZ-induced diabetes were 185 ± 21 mg/dl ($n = 16$). To prevent excessive diabetes-mediated weight loss, the STZ-treated mice were given daily insulin (Levemir) as needed beginning on day –2 for BGLs greater than 250 mg/dl, which lowered BGLs to near normal for at least 6 h after administration, but did not sustain normal BGLs after 24 h. This response profile allowed us to determine if a mouse was still diabetic under daily insulin therapy. All mice lost weight following STZ-induced diabetes but slowly gained weight after BIs were implanted, with the +VEGF/–Islet group exhibiting the greatest weight loss and the longest recovery time (Fig. 3A).

One hundred percent (8 of 8) of diabetic mice in the +VEGF/+Islet group became normoglycemic within 18 days postimplantation (p-i) (Fig. 3B). Normoglycemia (i.e., BGLs < 250 mg/dl) was maintained until the BIs were removed for histological analysis between 40 and 54 days p-i. In contrast, 100% (10 of 10) of diabetic mice in the +VEGF/–Islet group remained hyperglycemic until sacrifice at 21 days p-i (Fig. 3B).

When averaged collectively, the mice of the –VEGF/+Islet group also achieved normoglycemia (Fig. 3C). Compared to the +VEGF/+Islet group, the percentage of mice that became normoglycemic in the –VEGF/+Islet group was lower (62.5%, 5 of 8 mice), but there was no statistical difference between the two groups (Fig. 3D), nor was there a statistical difference between the average time required for the two groups to achieve normoglycemia after transplant (13.3 ± 3.4 days and 10.4 ± 2.1 days, respectively) (Fig. 3D). In an additional group of mice that received VEGF but only 200 islets, only 33.3% (1 of 3) of the mice became normoglycemic (Fig. 3D). As expected, we were able to reduce exogenous insulin therapy for the subset of mice within the +VEGF/+Islet and –VEGF/+Islet groups that proceeded to normoglycemia (Fig. 3E). Notably, none of the mice that achieved normoglycemia in these two groups required exogenous insulin therapy once the BIs began to fully regulate levels of blood glucose by 8–18 days p-i (e.g., Fig. 3F).

As an additional assessment of BI function, intraperitoneal glucose tolerance tests were performed at 40–50 days p-i on the subset of animals from the +VEGF/+Islet group (all eight mice) and –VEGF/+Islet group (five of eight mice) that had achieved normoglycemia (Fig. 4). Compared to healthy, nondiabetic mice that had not received STZ or BIs ($n = 10$), the BGLs of both groups of mice carrying BIs were elevated 15–30 min after glucose administration. The rise in BGL was slightly lower for the +VEGF/+Islet group than for the –VEGF/+Islet group, but the difference was not statistically significant. Within 1–2 h of challenge, the BGLs for all three groups had returned to normal levels, with no significant difference between them.

The functionality of the BIs was further confirmed upon removal, by survival surgery, of implants from four mice of the +VEGF/+Islet group at 54 days p-i. Three of these mice became hyperglycemic within 24–48 h, while the fourth mouse remained normoglycemic (data not shown). By histological assay, all four mice had little or no islet residua in their pancreata; therefore, maintenance of normoglycemia in the one mouse may have been due to migration of islets from the BI into the animal's peritoneal cavity. These islets would not have been removed when the BI was excised. In the four mice, we observed that removal of the BI caused devascularization of the adjacent intestine leading to focal necrosis; therefore, we did not perform survival surgeries on additional mice. Histological analyses of BIs explanted from the +VEGF/+Islet group at 54 days p-i (Fig. 5) revealed the presence of insulin-positive islets that were well-vascularized, as indicated by the presence of vWF-positive microvessels that contained luminal blood. The type I collagen hydrogel in which the islets were suspended prior to implantation was largely absent, although scattered remnants were observed.

By histology, there were no obvious differences at 54–77 days p-i in the level of vascularization within BIs from the +VEGF/+Islet group compared to the normoglycemic mice of the –VEGF/+Islet group (data not shown). Interestingly, however, although the +VEGF/+Islet, –VEGF/+Islet, and +VEGF/–Islet groups all exhibited similar hyperglycemic BGLs prior to surgery on day 0 (Fig. 6A, left), by 24 h p-i, seven of eight mice of the –VEGF/+Islet group were hypoglycemic (avg. 116 ± 21 mg/dl, $n = 7$), whereas only one of eight mice of the +VEGF/+Islet group was hypoglycemic (group avg. 348 ± 142 mg/dl, $n = 8$) (Fig. 6A, center). None of the mice of the +VEGF/–Islet group were hypoglycemic (group avg. 491 ± 91 mg/dl, $n = 12$). Notably, by 48 h p-i, all of

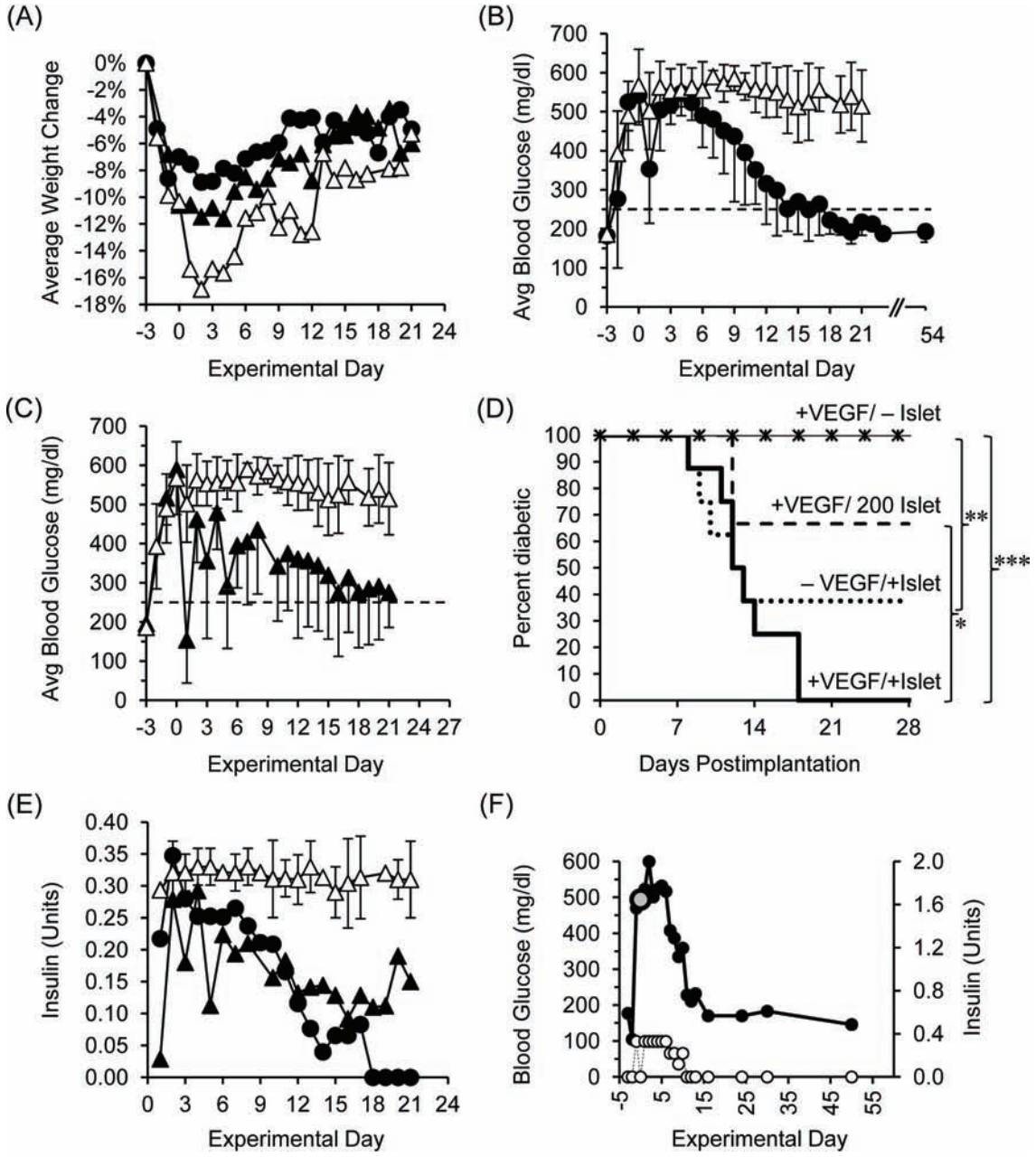

Figure 3. Responses of mice with streptozotocin (STZ)-induced diabetes to engrafted BIs. (A) Time course of weight change following engraftment of BIs, shown for the +VEGF/+Islet group (black circles), the –VEGF/+Islet group (black triangles), and the +VEGF/–Islet group (white triangles) (error bars are omitted for purposes of clarity). (B) In time course studies, the blood glucose levels (BGLs) of the +VEGF/+Islet group (black circles) fell to normal (dotted line) within 18 days p-i. Normoglycemic BGLs were maintained until the BIs were removed at 54 days p-i. In contrast, mice of the +VEGF/–Islet group (white triangles) remained hyperglycemic until sacrifice at 21 days p-i. (C) When averaged collectively, BGLs of the –VEGF/+Islet group (black triangles) fell to near-normal levels within 21 days p-i. BGLs of the +VEGF/–Islet group (white triangles) are included for comparison. (D) Kaplan–Meier plots of glucose regulation after BI implantation. BIs in +VEGF/+Islet ($n=8$) and –VEGF/+Islet ($n=8$) groups contained 450–500 islets. BIs in the +VEGF/200 Islet group ($n=3$) contained 200 islets. ***$p<0.001$, **$p<0.01$, *$p<0.05$ significant difference between the percent of animals that remained diabetic, as analyzed by a log-rank test. (E) Over time, exogenous insulin therapy could be reduced for mice of the +VEGF/+Islet group (black circles) and –VEGF/+Islet group (black triangles) that proceeded to normoglycemia. In contrast, mice of the –VEGF/–Islet group (white triangles) required a continuous, high-dose regimen of insulin. In this graph, error bars for the +VEGF/+Islet and –VEGF/+Islet groups are omitted for purposes of clarity. (F) BGLs of one mouse of the +VEGF/+Islet group, measured during the course of the experiment (black circles), are compared to the quantities of therapeutic insulin administered to the animal (white circles). The BGL measured at the time of implantation of the BI on day 0 is indicated (large gray circle). After day 10 p-i, the mouse did not require exogenous insulin.

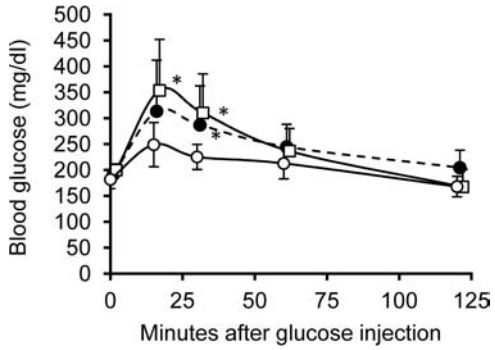

Figure 4. Response to glucose challenge of mice rendered normoglycemic by BIs. Intraperitoneal glucose tolerance tests were performed at 40–50 days p-i on the animals from the +VEGF/+Islet group (eight mice, black circles) and –VEGF/+Islet group (five mice, white squares) that had achieved normoglycemia. These results were compared to similar tests performed on healthy, nondiabetic mice that had not received STZ or BIs (control group) (white circles). By 15–30 min after challenge with glucose, both groups of mice implanted with BIs had elevated BGLs relative to controls. The rise in BGL was slightly lower for the +VEGF group than for the –VEGF group, but the difference was not statistically significant. Within 1–2 h of challenge, the difference in BGL between the three groups was nonsignificant. *$p < 0.05$ between the control group and the groups implanted with BIs.

the mice of all three groups were hyperglycemic (Fig. 6A, right). Collectively, these results indicated that inclusion of VEGF with the implanted islets substantially mitigated the transitory hypoglycemia that occurred when islets were implanted in the absence of VEGF. To further investigate this phenomenon, we cultured isolated islets for 2 h in the presence of 10 ng/ml of VEGF and a low level (5.6 mM) of glucose, followed by a 30-min stimulus with elevated (16.6 mM) glucose to elicit insulin release. We found that the exposure to VEGF significantly reduced glucose-induced insulin release, compared to cultured islets not exposed to VEGF (Fig. 6B).

DISCUSSION

To achieve successful islet transplantation for treatment of T1D, the protocol must promote islet survival in the short term. Insulin secretory function in patients who receive intraportal islet transplantation averages only ~20% of that of nondiabetic persons despite the use of islets from multiple donors (35)—a result suggesting that only a small proportion of transplanted islets successfully engraft. Reasons for this loss of islet function include (1) exposure to high concentrations of cytotoxic immunosuppressive drugs via portal blood, (2) proinflammatory cytokine release by intrahepatic endothelial cells activated by islet cell contact, (3) liver ischemia, focal necrosis, and inflammation induced by islet embolism, and (4) acute inflammatory reactions that involve platelet

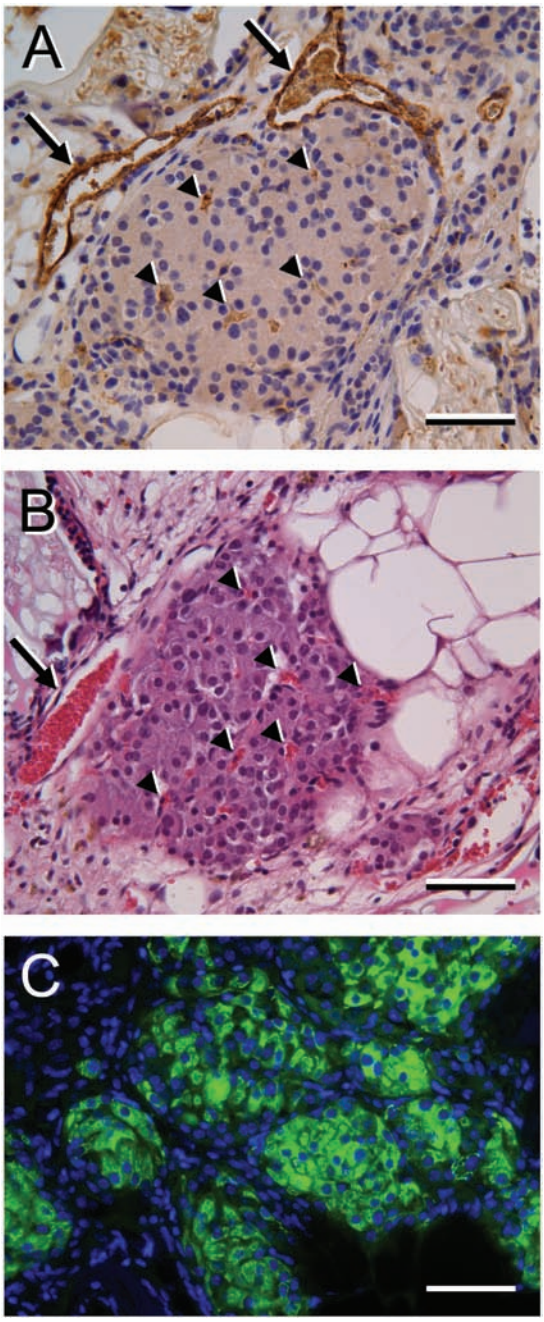

Figure 5. Histological evaluation of islets within BIs after 54 days in vivo. Mice of the +VEGF/+Islet group that had exhibited sustained normoglycemia for 54 days had their BIs excised and sectioned for histological analysis. (A) An islet labeled for von Willebrand Factor (vWF) (brown stain) exhibits profiles of large- and small-caliber microvessels (arrows and arrowheads, respectively) of the islet. Nuclei are counterstained with hematoxylin. (B) A slightly deeper section of the islet shown in (A), stained with H&E, indicates the presence of red blood cells (red stain) in the large- and small-caliber microvessels (arrow and arrowheads, respectively) of the islet. (C) Islet groups within a similar BI are strongly positive for insulin, as shown by indirect immunofluorescence (green). Cell nuclei in the section are stained with DAPI (blue). Scale bars: 100 μm (in A–C).

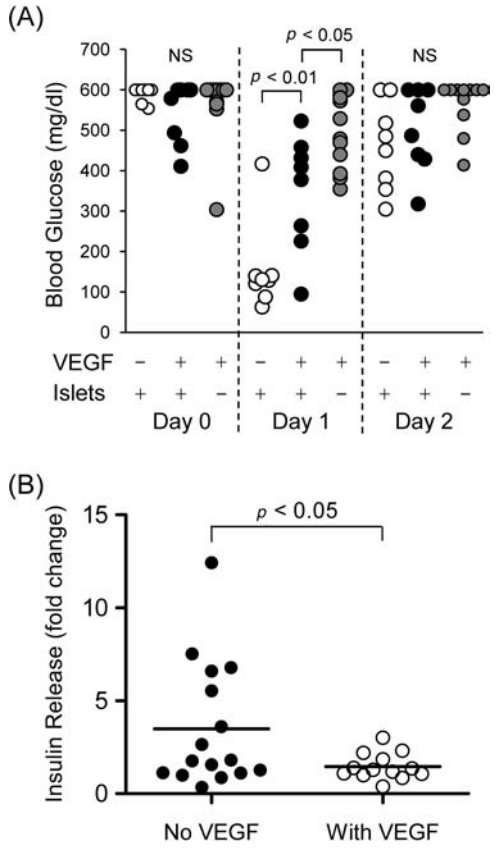

Figure 6. The presence of VEGF in BIs is associated with limitation of postoperative, transitory hypoglycemia. (A, left) Prior to surgery on day 0, all mice within the –VEGF/+Islet, +VEGF/+Islet, and +VEGF/–Islet groups (white, black, and gray circles, respectively) exhibited hyperglycemic BGLs. (A, center) By 24 h (day 1) p-i, seven of eight mice of the –VEGF/+Islet group were hypoglycemic, whereas only one of eight mice of the +VEGF/+Islet group was fully hypoglycemic. None of the mice of the +VEGF/–Islet group were hypoglycemic. (A, right) By 48 h (day 2) p-i, the hypoglycemic episodes had ended: all of the mice within the three groups were hyperglycemic. (B) Glucose-induced insulin release in vitro from isolated islets in the presence or absence of VEGF. Islets were preincubated for 2 h with a low level (5.6 mM) of glucose, with or without 10 ng/ml of VEGF, and then stimulated for 30 min with elevated (16.6 mM) glucose. Fold change represents insulin levels in media before and after glucose stimulus.

activation and binding at the islet surface, activation of coagulation and complement systems, and leukocyte infiltration of the islet mass. To address the shortcomings of the intrahepatic environment, we developed BIs for implantation in a nonhepatic site (the intestinal mesentery). We have demonstrated that these BIs can reliably reverse drug (STZ)-induced diabetes in mice.

Injection of islet suspensions under the kidney capsule (UKC) is the most frequently used model for studies of islet engraftment in mice. With the UKC model, normoglycemia can be established in STZ-treated diabetic mice within 24–48 h using 200 islets (45). In contrast to the UKC model, we observed that engraftment of islets on the mouse mesentery in BIs required a larger number of islets (200 islets were insufficient, whereas 450–500 islets were effective) and required a longer time to achieve normoglycemia (10–13 days). Similar disparities in islet number and time to functionality between UKC and mesenteric (omental) graft sites in mice have been reported by Kim et al. (16), who found that the marginal islet mass required for the omental site was twice that of the kidney site and that time to normoglycemia averaged 14 days for omental grafts, but only 3 days for UKC grafts. Notably, the omentum performed better than liver and muscle sites, which each required threefold more islets than the omentum and comparable or longer times to achieve normoglycemia (15 and 27 days for liver and muscle, respectively). The reason why engraftment of islets is less efficient in non-UKC sites relative to the UKC site is unclear but may relate to a lower availability of vasculature, particularly for muscle (16).

Despite the efficiency of UKC transplant, the limited space within the kidney capsule cannot accommodate large numbers of injected islets or complex implants that include drug delivery devices, such as the one we describe. This limitation, among others (7,31), suggests that the UKC site may be problematic for therapeutic islet transplant in human patients. In contrast, the human omentum should be able to accommodate relatively large, multicomponent BIs. Moreover, unlike the kidney, the omentum is not a critical organ and, therefore, could be excised with few negative consequences should post-transplantation complications arise.

In contrast to most other approaches in which islets are engrafted as dispersions, our BI retains the islets in a unified structure by means of a disk-shaped scaffold. The purpose of this scaffold is fourfold: (1) to keep the islets contained within a limited volume and in close proximity to the alginate delivery device in order to maximize the effects of the released cytokine; (2) to protect the relatively soft collagen hydrogel (which supports the islets directly) from physical disruption both before and after implantation; (3) to allow the BI, with all of its components, to be rapidly assembled and implanted easily without the additional complexity of a surgically produced omental/mesenteric pouch; (4) to allow the implant to be removed easily and maintained in a compact form that makes histological analysis straightforward. For the present experimental study (which has relatively short-term endpoints), nonbiodegradable PVA sponge works well as a scaffold. For therapeutic use in human patients, the PVA could be replaced by biodegradable materials that would be resorbed after the implanted islets become fully functional.

A beneficial effect of scaffolds on islet engraftment has been observed by others. Blomeier et al. (2) reported that STZ-induced diabetic mice that received intraperitoneal implants of islets infused into cylindrical polylactide/glycolide (PLG) sponge scaffolds had higher conversions and shorter times to normoglycemia, greater weight gain, and improved response to intraperitoneal glucose tolerance tests compared to control mice that received islets not retained in scaffolds. These authors demonstrated that the islets transplanted in scaffolds remained localized at the original site of implantation, whereas the nonscaffolded islets tended to be more dispersed throughout the peritoneum. Therefore, the protective environment provided by the scaffold might have contributed to better performance of the graft. These results and our own observations that scaffolds facilitate the assembly and handling of multicomponent constructs argue for the continued development of scaffolds for islet transplantation.

In our BIs, direct physical support of the islets is accomplished by a fibrillar type I collagen hydrogel. The islets are dispersed in a single volume of monomeric collagen solution, which is infused into the protective PVA scaffold and polymerized in situ into a gel-like network of fibrils. Notably, neither the PVA scaffold, with its open structure, nor the collagen gel seem to impede the rate of vascularization from the mesentery, since dispersed islets implanted into mesenteric (omental) pouches also require the same time as our BIs to engraft and function (i.e., about 2 weeks) (16).

The endocrine cells of islets in vivo are associated with a complex peri-insular and perivascular ECM, with components of the basement membrane (BM) (e.g., laminin, type IV collagen, fibronectin) predominating (38). In this context, there is evidence that addition of specific BM components to islet graft sites improves islet graft performance. Salvay et al. (37) demonstrated that islets implanted onto the epididymal fat pads of STZ-treated mice were more effective at reversing diabetes when the islets were infused into PLG sponge scaffolds preadsorbed with type IV collagen, compared with control scaffolds pretreated with serum proteins. Adsorbed fibronectin and laminin 5 were less effective than type IV collagen but were superior to the serum-treated controls. It was proposed that the adsorbed BM proteins might be improving islet function directly and/or promoting infiltration of beneficial cell types (e.g., endothelial cells) from the host, as vascularization of the ECM-treated grafts was better than vascularization of the serum-coated grafts. Collectively, these results suggest that incorporation of individual BM components (or perhaps more complex BM mixtures) into our BIs (e.g., via direct binding to or cogelation with the collagen hydrogel) might improve the overall performance of the grafts after implantation.

Reportedly, the level of vascularization of islets transplanted into the liver or kidney is lower than that of native islets in the pancreas (22), but transfection of islets to express VEGF increases vascularization following transplantation (19,46). Transfection-based approaches are therapeutically problematic; therefore, we incorporated a device (an alginate macrosphere) within the BI to achieve a local, sustained delivery of VEGF. In preliminary experiments, we produced BIs with macrospheres that incorporated high levels (160 ng) of VEGF. The VEGF in these constructs induced a very robust response from the host within 7 days of implantation in vivo, as indicated by high levels of angiogenesis, the presence of enlarged sinusoidal neovessels, and substantial vascular permeability (i.e., extravasated blood) within the BI. Although these results were a clear indication that the VEGF was biologically active, we considered this level of response to be excessive; therefore, we reduced the level of VEGF to approximately 20 ng per macrosphere for the subsequent experiments reported here. Inclusion of 20 ng of VEGF in the BI did not decrease the average time for transplanted mice to achieve normoglycemia (approximately 2 weeks), as compared to control mice with BIs that lacked VEGF. Although VEGF increased the percentage of mice that became normoglycemic compared to the controls lacking VEGF (100% vs. 62.5%), this increase was not statistically significant for our sample size ($n = 8$ mice per group). These results suggest that exogenous VEGF may not have a major effect on implant performance when therapeutically "safe" (i.e., well above the minimum) numbers of islets are used.

We were particularly interested by the finding that, with the exception of one animal, the +VEGF/+Islet group did not exhibit the hypoglycemia that occurred within 24 h p-i in the –VEGF/+Islet group. Postoperative, transitory hypoglycemia has been observed in other models of islet transplantation and may be a consequence of an acute release of insulin from stressed or dying islets. Our observations suggest that the inclusion of VEGF within BIs mitigates this acute insulin release, perhaps via direct influences on the transplanted islets, as we found that exogenous VEGF suppresses glucose-stimulated release of insulin from isolated, cultured islets. This suppressive effect of exogenous VEGF on insulin release in vitro seems to support an earlier finding that islets isolated from RIP-CRE:VEGF$^{fl/fl}$ mice, in which production of VEGF is prevented specifically in -cells, had higher levels of insulin mRNA and secreted more insulin after glucose stimulation in vitro than did islets from control mice that expressed VEGF (15). VEGF acts on endothelial cells to promote the maintenance and growth of vasculature, including the vasculature of islets, as illustrated by RIP-CRE:VEGF$^{fl/fl}$ mice, which have deficiencies in their microvessels (14).

Although prosurvival, proangiogenic responses of intraislet endothelial cells to VEGF would be expected, additional responses by these cells might include the production of paracrine factors that promote the survival and function of islet endocrine cells.

In treatments of diabetic patients that involve transplantation of islets, controlling rejection is typically accomplished by systemic immunosuppressive compounds. Dosing of these compounds is a difficult balance—levels must be low enough to permit a reasonable degree of protective immunity against pathogenic organisms, but high enough to effectively suppress allo- and autoimmune activity directed against the transplant. In the case of SPK transplants, some current immunosuppression regimens are inadequate to control autoimmunity (18,41). Moreover, no matter what the dose, systemic immunosuppression can be accompanied by a variety of undesirable side effects on tissue and organ systems that are not directly associated with the transplant. In light of the problems associated with systemic treatments, an alternative approach would be to confine the delivery of immunotherapy to the implant itself. In this way, immunomodulatory compounds could be delivered at relatively high concentrations, but within the limited volume of the implant, thereby minimizing side effects on tissues and organs outside the zone of delivery. To this end, the BI described here includes a mechanically supportive scaffold and collagen hydrogel that concentrates the islets in a small volume. Localized immunotherapy might be achieved by supplementing or replacing the collagen hydrogel with ECM components that have been shown to have immunosuppressive properties, such as hyaluronan (3,4). This ECM-based approach could be augmented by sustained release of specific, immunomodulatory cytokines [e.g., interleukin-10 (IL-10) and transforming growth factor- (TGF-)] from biocompatible storage media placed within the implant. We are currently investigating the use of alginate-based media for this purpose.

In the present study, we have developed a BI and associated protocols for its implantation that can effectively reverse STZ-induced diabetes in syngeneic mice. Our future studies will evaluate the effectiveness of the BI in the context of strains of mice that develop autoimmune diabetes. In this way, the BI will serve as a platform to evaluate the capability of a variety of immunomodulatory compounds and formulations, delivered locally, to prevent or reverse diabetes in the setting of autoimmune dysfunction.

ACKNOWLEDGMENTS: We would like to thank Dr. Rebecca Hull for her valuable help in optimizing the islet isolation procedures. This work was funded in part by Department of Defense Award W81XWH-10-1-049 (G.T.N.) and by an award from the Klorfine Foundation (R.B.V.). The authors declare no conflicts of interest.

REFERENCES

1. Alejandro, R.; Barton, F. B.; Hering, B. J.; Wease, S. 2008 Update from the Collaborative Islet Transplant Registry. Transplantation 86:1783–1788; 2008.
2. Blomeier, H.; Zhang, X.; Rives, C.; Brissova, M.; Hughes, E.; Baker, M.; Powers, A. C.; Kaufman, D. B.; Shea, L. D.; Lowe, Jr., W. L. Polymer scaffolds as synthetic microenvironments for extrahepatic islet transplantation. Transplantation 82:452–459; 2006.
3. Bollyky, P. L.; Falk, B. A.; Wu, R. P.; Buckner, J. H.; Wight, T. N.; Nepom, G. T. Intact extracellular matrix and the maintenance of immune tolerance: High molecular weight hyaluronan promotes persistence of induced $CD4^+CD25^+$ regulatory T cells. J. Leukoc. Biol. 86:567–572; 2009.
4. Bollyky, P. L.; Lord, J. D.; Masewicz, S. A.; Evanko, S. P.; Buckner, J. H.; Wight, T. N.; Nepom, G. T. Cutting edge: High molecular weight hyaluronan promotes the suppressive effects of $CD4^+CD25^+$ regulatory T cells. J. Immunol. 179:744–747; 2007.
5. DCCT Research Group Epidemiology of severe hypoglycemia in the diabetes control and complications trial. The DCCT Research Group. Am. J. Med. 90:450–459; 1991.
6. Freeman, I.; Kedem, A.; Cohen, S. The effect of sulfation of alginate hydrogels on the specific binding and controlled release of heparin-binding proteins. Biomaterials 29:3260–3268; 2008.
7. Gray, D. W.; Sutton, R.; McShane, P.; Peters, M.; Morris, P. J. Exocrine contamination impairs implantation of pancreatic islets transplanted beneath the kidney capsule. J. Surg. Res. 45:432–442; 1988.
8. Gu, F.; Amsden, B.; Neufeld, R. Sustained delivery of vascular endothelial growth factor with alginate beads. J. Control. Release 96:463–472; 2004.
9. Hirsch, D.; Odorico, J.; Radke, N.; Hanson, M.; Danobeitia, J. S.; Hullett, D.; Alejandro, R.; Ricordi, C.; Fernandez, L. A. Correction of insulin sensitivity and glucose disposal after pancreatic islet transplantation: Preliminary results. Diabetes Obes. Metab. 12:994–1003; 2010.
10. Hiscox, A. M.; Stone, A. L.; Limesand, S.; Hoying, J. B.; Williams, S. K. An islet-stabilizing implant constructed using a preformed vasculature. Tissue Eng. Part A 14:433–440; 2008.
11. Hollinger, E. F.; Powelson, J. A.; Mangus, R. S.; Kazimi, M. M.; Taber, T. E.; Goble, M. L.; Fridell, J. A. Immediate retransplantation for pancreas allograft thrombosis. Am. J. Transplant. 9:740–745; 2009.
12. Hori, Y.; Winans, A. M.; Irvine, D. J. Modular injectable matrices based on alginate solution/microsphere mixtures that gel in situ and co-deliver immunomodulatory factors. Acta Biomater. 5:969–982; 2009.
13. Humar, A.; Ramcharan, T.; Kandaswamy, R.; Gruessner, R. W.; Gruessner, A. C.; Sutherland, D. E. Technical failures after pancreas transplants: Why grafts fail and the risk factors—A multivariate analysis. Transplantation 78:1188–1192; 2004.
14. Inoue, M.; Hager, J. H.; Ferrara, N.; Gerber, H. P.; Hanahan, D. VEGF-A has a critical, nonredundant role in angiogenic switching and pancreatic beta cell carcinogenesis. Cancer Cell 1:193–202; 2002.
15. Iwashita, N.; Uchida, T.; Choi, J. B.; Azuma, K.; Ogihara, T.; Ferrara, N.; Gerber, H.; Kawamori, R.; Inoue, M.; Watada, H. Impaired insulin secretion in vivo but enhanced insulin secretion from isolated islets in pancreatic beta cell-specific vascular endothelial growth factor-A knock-out mice. Diabetologia 50:380–389; 2007.

16. Kim, H. I.; Yu, J. E.; Park, C. G.; Kim, S. J. Comparison of four pancreatic islet implantation sites. J. Korean Med. Sci. 25:203–210; 2010.
17. Koike, T.; Vernon, R. B.; Gooden, M. D.; Sadoun, E.; Reed, M. J. Inhibited angiogenesis in aging: A role for TIMP-2. J. Gerontol. A Biol. Sci. Med. Sci. 58:B798–B805; 2003.
18. Laughlin, E.; Burke, G.; Pugliese, A.; Falk, B.; Nepom, G. Recurrence of autoreactive antigen-specific $CD4^+$ T cells in autoimmune diabetes after pancreas transplantation. Clin. Immunol. 128:23–30; 2008.
19. Lee, B. W.; Lee, M.; Chae, H. Y.; Lee, S.; Kang, J. G.; Kim, C. S.; Lee, S. J.; Yoo, H. J.; Ihm, S. H. Effect of hypoxia-inducible VEGF gene expression on revascularization and graft function in mouse islet transplantation. Transpl. Int. 24:307–314; 2011.
20. Lucas-Clerc, C.; Massart, C.; Campion, J. P.; Launois, B.; Nicol, M. Long-term culture of human pancreatic islets in an extracellular matrix: Morphological and metabolic effects. Mol. Cell. Endocrinol. 94:9–20; 1993.
21. Matsusaki, M.; Sakaguchi, H.; Serizawa, T.; Akashi, M. Controlled release of vascular endothelial growth factor from alginate hydrogels nano-coated with polyelectrolyte multilayer films. J. Biomater. Sci. Polym. Ed. 18:775–783; 2007.
22. Mattsson, G.; Jansson, L.; Carlsson, P. O. Decreased vascular density in mouse pancreatic islets after transplantation. Diabetes 51:1362–1366; 2002.
23. Monti, P.; Scirpoli, M.; Maffi, P.; Ghidoli, N.; De Taddeo, F.; Bertuzzi, F.; Piemonti, L.; Falcone, M.; Secchi, A.; Bonifacio, E. Islet transplantation in patients with autoimmune diabetes induces homeostatic cytokines that expand autoreactive memory T cells. J. Clin. Invest. 118:1806–1814; 2008.
24. Muhlhauser, I.; Berger, M.; Sonnenberg, G.; Koch, J.; Jorgens, V.; Schernthaner, G.; Scholz, V.; Padagogin, D. Incidence and management of severe hypoglycemia in 434 adults with insulin-dependent diabetes mellitus. Diabetes Care 8:268–273; 1985.
25. Nagata, N.; Gu, Y.; Hori, H.; Balamurugan, A. N.; Touma, M.; Kawakami, Y.; Wang, W.; Baba, T. T.; Satake, A.; Nozawa, M.; Tabata, Y.; Inoue, K. Evaluation of insulin secretion of isolated rat islets cultured in extracellular matrix. Cell Transplant. 10:447–451; 2001.
26. Nagata, N. A.; Inoue, K.; Tabata, Y. Co-culture of extracellular matrix suppresses the cell death of rat pancreatic islets. J. Biomater. Sci. Polym. Ed. 13:579–590; 2002.
27. Narang, A. S.; Mahato, R. I. Biological and biomaterial approaches for improved islet transplantation. Pharmacol. Rev. 58:194–243; 2006.
28. Onkamo, P.; Vaananen, S.; Karvonen, M.; Tuomilehto, J. Worldwide increase in incidence of Type I diabetes—The analysis of the data on published incidence trends. Diabetologia 42:1395–1403; 1999.
29. Peters, M. C.; Isenberg, B. C.; Rowley, J. A.; Mooney, D. J. Release from alginate enhances the biological activity of vascular endothelial growth factor. J. Biomater. Sci. Polym. Ed. 9:1267–1278; 1998.
30. Pickup, J. Insulin pumps. Int. J. Clin. Pract. 170(Suppl): 16–19; 2011.
31. Rajab, A. Islet transplantation: Alternative sites. Curr. Diab. Rep. 10:332–337; 2010.
32. Reed, M. J.; Bradshaw, A. D.; Shaw, M.; Sadoun, E.; Han, N.; Ferara, N.; Funk, S.; Puolakkainen, P.; Sage, E. H. Enhanced angiogenesis characteristic of SPARC-null mice disappears with age. J. Cell. Physiol. 204:800–807; 2005.
33. Reichard, P.; Nilsson, B. Y.; Rosenqvist, U. The effect of long-term intensified insulin treatment on the development of microvascular complications of diabetes mellitus. N. Engl. J. Med. 329:304–309; 1993.
34. Roep, B. O.; Stobbe, I.; Duinkerken, G.; van Rood, J. J.; Lernmark, A.; Keymeulen, B.; Pipeleers, D.; Claas, F. H.; de Vries, R. R. Auto- and alloimmune reactivity to human islet allografts transplanted into type 1 diabetic patients. Diabetes 48:484–490; 1999.
35. Ryan, E. A.; Lakey, J. R.; Rajotte, R. V.; Korbutt, G. S.; Kin, T.; Imes, S.; Rabinovitch, A.; Elliott, J. F.; Bigam, D.; Kneteman, N. M.; Warnock, G. L.; Larsen, I.; Shapiro, A. M. Clinical outcomes and insulin secretion after islet transplantation with the Edmonton protocol. Diabetes 50:710–719; 2001.
36. Ryan, E. A.; Paty, B. W.; Senior, P. A.; Bigam, D.; Alfadhli, E.; Kneteman, N. M.; Lakey, J. R.; Shapiro, A. M. Five-year follow-up after clinical islet transplantation. Diabetes 54:2060–2069; 2005.
37. Salvay, D. M.; Rives, C. B.; Zhang, X.; Chen, F.; Kaufman, D. B.; Lowe, W. L., Jr.; Shea, L. D. Extracellular matrix protein-coated scaffolds promote the reversal of diabetes after extrahepatic islet transplantation. Transplantation 85:1456–1464; 2008.
38. Stendahl, J. C.; Kaufman, D. B.; Stupp, S. I. Extracellular matrix in pancreatic islets: Relevance to scaffold design and transplantation. Cell Transplant. 18:1–12; 2009.
39. Sutherland, D. E.; Gruessner, R. W.; Dunn, D. L.; Matas, A. J.; Humar, A.; Kandaswamy, R.; Mauer, S. M.; Kennedy, W. R.; Goetz, F. C.; Robertson, R. P.; Gruessner, A. C.; Najarian, J. S. Lessons learned from more than 1,000 pancreas transplants at a single institution. Ann. Surg. 233:463–501; 2001.
40. van Belle, T. L.; Coppieters, K. T.; von Herrath, M. G. Type 1 diabetes: Etiology, immunology, and therapeutic strategies. Physiol. Rev. 91:79–118; 2011.
41. Vendrame, F.; Pileggi, A.; Laughlin, E.; Allende, G.; Martin-Pagola, A.; Molano, R. D.; Diamantopoulos, S.; Standifer, N.; Geubtner, K.; Falk, B. A.; Ichii, H.; Takahashi, H.; Snowhite, I.; Chen, Z.; Mendez, A.; Chen, L.; Sageshima, J.; Ruiz, P.; Ciancio, G.; Ricordi, C.; Reijonen, H.; Nepom, G. T.; Burke, G. W., III; Pugliese, A. Recurrence of type 1 diabetes after simultaneous pancreas–kidney transplantation, despite immunosuppression, is associated with autoantibodies and pathogenic autoreactive CD4 T-cells. Diabetes 59:947–957; 2010.
42. Vernon, R. B.; Gooden, M. D. New technologies in vitro for analysis of cell movement on or within collagen gels. Matrix Biol. 21:661–669; 2002.
43. Vrochides, D.; Paraskevas, S.; Papanikolaou, V. Transplantation for type 1 diabetes mellitus. Whole organ or islets? Hippokratia 13:6–8; 2009.
44. Wee, S.; Gombotz, W. R. Protein release from alginate matrices. Adv. Drug Deliv. Rev. 31:267–285; 1998.
45. Yin, D.; Tao, J.; Lee, D. D.; Shen, J.; Hara, M.; Lopez, J.; Kuznetsov, A.; Philipson, L. H.; Chong, A. S. Recovery of islet beta-cell function in streptozotocin-induced diabetic mice: An indirect role for the spleen. Diabetes 55:3256–3263; 2006.
46. Zhang, N.; Richter, A.; Suriawinata, J.; Harbaran, S.; Altomonte, J.; Cong, L.; Zhang, H.; Song, K.; Meseck, M.; Bromberg, J.; Dong, H. Elevated vascular endothelial growth factor production in islets improves islet graft vascularization. Diabetes 53:963–970; 2004.
47. Ziegler, A. G.; Nepom, G. T. Prediction and pathogenesis in type 1 diabetes. Immunity 32:468–478; 2010.

European Journal of Immunology

β_2 integrins inhibit TLR responses by regulating NF-κB pathway and p38 MAPK activation

Nathan K. Yee[1,2] *and Jessica A. Hamerman*[1,2]

[1] Department of Immunology, University of Washington School of Medicine, Seattle, WA, USA
[2] Immunology Program, Benaroya Research Institute, Seattle, WA, USA

Outside-in signals from β_2 integrins require immunoreceptor tyrosine-based activation motif adapters in myeloid cells that are known to dampen TLR responses. However, the relationship between β_2 integrins and TLR regulation is unclear. Here we show that deficiency in β_2 integrins (*Itgb2*$^{-/-}$) causes hyperresponsiveness to TLR stimulation, demonstrating that β_2 integrins inhibit signals downstream of TLR ligation. *Itgb2*$^{-/-}$ macrophages and dendritic cells produced more IL-12 and IL-6 than WT cells when stimulated with TLR agonists and *Itgb2*$^{-/-}$ mice produced more inflammatory cytokines than WT mice when injected with LPS. TLR hypersensitivity was not the result of insufficient ABIN-3, A20, Hes-1, or IRAK-M expression, nor to changes in IL-10 production or sensitivity, though *Itgb2*$^{-/-}$ macrophages had reduced p38 MAPK phosphorylation after LPS treatment. Furthermore, a Cbl-b-MyD88 regulatory axis is not required for TLR inhibition in macrophages. Instead, *Itgb2*$^{-/-}$ macrophages presented with enhanced IκBα degradation, leading to changes in NF-κB recruitment to target promoters and elevated cytokine, chemokine, and anti-apoptotic gene transcription. Thus, β_2 integrins limit TLR signaling by inhibiting NF-κB pathway activation and promoting p38 MAPK activation, thereby fine-tuning TLR-induced inflammatory responses.

Keywords: Dendritic cells · Inflammation · Integrins · Macrophages · TLR

Additional supporting information may be found in the online version of this article at the publisher's web-site

Introduction

Innate immune cell activation depends on the activity of Toll-like receptors (TLRs) that bind conserved molecular features expressed on invading pathogens [1]. Upon encountering microbes, macrophages and dendritic cells (DCs) respond to TLR stimulation by inducing antimicrobial and antiviral programs that result in the rapid synthesis and secretion of inflammatory cytokines and type I interferons. In turn, this potent response must be restrained to spare host tissues from the deleterious effects of exaggerated inflammation. This is accomplished by a variety of inhibitory mechanisms, including cytoplasmic effectors that block TLR signaling directly as well as secreted negative regulators, which work together to limit the severity of the immune response [2].

Although originally considered as an archetypal cell activation pathway, signals through immunoreceptor tyrosine-based activation motifs (ITAMs) display functional heterogeneity and have been recently appreciated to cross-inhibit TLR responses [3, 4]. ITAM signaling in myeloid cells is mediated by the ITAM-containing molecules DAP12 and FcRγ, which act as signaling adapters for an extensive collection of cell surface receptors [5–7]. Following ligand binding by paired receptors, ITAM signaling via DAP12 and FcRγ in myeloid cells proximally activates Src-family kinases and Syk kinase to enable downstream signals that are

Correspondence: Dr. Jessica A. Hamerman
e-mail: jhamerman@benaroyaresearch.org

predominantly associated with cellular activation, including inducing NF-κB and MAPK pathways, and prompting the release of intracellular Ca^{2+} stores [5]. However, depending on the identity of the associated receptor and other undefined parameters, ITAM-based signaling can also induce inhibitory responses. For example, triggering of the DAP12-coupled TREM-2 receptor can dampen TLR activation in macrophages [8]. In addition, TREM-2 and/or DAP12-deficient macrophages and DCs produce more inflammatory cytokines in response to TLR stimulation [9–12], demonstrating that these adapter molecules can transduce signals attenuating TLR activation.

During an inflammatory response, leukocytes in the blood adhere to the activated vascular endothelium through the use of integrins. In particular, members of the β_2 integrin family facilitate leukocyte firm adhesion, thereby allowing for cell extravasation into the tissues [13]. In doing so, β_2 integrins not only mediate cell migration, but also influence cell functions through signals transmitted through β_2 integrin activation. This "outside-in" signaling pathway requires ITAM signals from DAP12 and FcRγ, and also involves early effectors such as the Src family kinases and Syk in neutrophils and macrophages [14,15]. Because β_2 integrins signal through ITAM adapters in myeloid cells, we hypothesized that β_2 integrin signaling may also inhibit TLR responses. There have been conflicting reports in the literature regarding the influence of β_2 integrin signaling on TLRs, with some studies demonstrating that β_2 integrins can promote TLR-induced inflammation [16–18], whereas others have reported negative roles for these integrins in TLR responses [19,20]. Therefore, the nature in which β_2 integrins interface with TLR activation and cytokine secretion is complex and unclear.

To better define the contribution of β_2 integrins to regulation of TLR signaling, we have examined inflammatory responses in the absence of all β_2 integrins. Here we demonstrate that deletion of all β_2 integrins rendered myeloid cells hypersensitive to TLR stimulation in vitro and in vivo, showing an inhibitory role for β_2 integrins in TLR responses. Furthermore, we examined potential direct and indirect mechanisms by which β_2 integrins caused this inhibition, and found that β_2 integrins have a direct effect on IκBα degradation that was pronounced in β_2 integrin-deficient cells through both early and late phases of TLR stimulation, thus implicating β_2 integrin signals in inhibiting NF-κB pathway activation to calibrate inflammatory responses.

Results

β_2 integrin-deficient macrophages hyper-respond to TLR stimulation

The four β_2 integrins, LFA-1 (lymphocyte function-associated antigen 1, $\alpha_L\beta_2$), Mac-1 (macrophage-1 antigen, $\alpha_M\beta_2$), CR4 ($\alpha_X\beta_2$), and CD11d-CD18 ($\alpha_D\beta_2$) are heterodimers that consist of distinct CD11 alpha subunits in association with the common beta chain, CD18 (β2), which is encoded by the *Itgb2* gene [21]. To examine whether β_2 integrin signaling regulates TLR responses, we compared the cytokine secretion profiles of bone marrow-derived (BM-derived) macrophages from wild-type (WT) and *Itgb2*$^{-/-}$ mice, which are deficient in CD18 and thus are unable to express any of the β_2 integrins on the cell surface (Supporting Information Fig. 1A) [22]. Despite the inability of *Itgb2*$^{-/-}$ BM-derived macrophages to express Mac-1, these cells exhibited surface F4/80 expression and upregulated MHC II in response to IFN-γ treatment (Supporting Information Fig. 1A and B), demonstrating that they were bona fide macrophages. Furthermore, β_2 integrin-deficient macrophages exhibited similar or slightly lower levels of cell surface TLR2, TLR4, and Dectin-1 protein and TLR9 mRNA (Supporting Information Fig. 1C and D).

To determine how β_2 integrin signals influence TLR activity, we stimulated *Itgb2*$^{-/-}$ BM-derived macrophages with a panel of TLR agonists, including LPS (TLR4), CpG B DNA (TLR9), and zymosan (TLR2). Zymosan is a complex yeast particle that, in addition to signaling through TLR2, also signals through Dectin-1. After 24 h of activation, *Itgb2*$^{-/-}$ BM-derived macrophages secreted significantly more IL-12 p40 than did WT control cells (Fig. 1A and Supporting Information Fig. 2A). To address whether this IL-12 p40 was participating in IL-12 p70 or IL-23 production, we assessed the induction of mRNA encoding IL-12 p35 and IL-23 p19. *Itgb2*$^{-/-}$ macrophages synthesized enhanced levels of IL-12 p35 mRNA in response to LPS when compared to WT controls, but comparable levels of IL-23 p19 mRNA (Supporting Information Fig. 2B), suggesting that β_2 integrin deletion enhances IL-12, but not IL-23, production in macrophages. Similarly, we also noted elevated IL-6 secretion in *Itgb2*$^{-/-}$ macrophages in response to TLR4, TLR9, and TLR2/Dectin-1 stimulation, though this did not reach statistical significance through multiple experiments (Fig. 1A). TNF secretion was similar in *Itgb2*$^{-/-}$ macrophages to that from WT cells (Fig. 1A and Supporting Information Fig. 2A).

We investigated the kinetics of inflammatory cytokine secretion after LPS treatment and found that the induction kinetics for IL-12 p40 and TNF release were similar between *Itgb2*$^{-/-}$ and WT macrophages (Fig. 1B and Supporting Information Fig. 2C). Yet, after 12 h of stimulation, the magnitude of IL-12 p40 secretion was greatly enhanced in *Itgb2*$^{-/-}$ macrophages as compared with levels in WT macrophages, while TNF production remained unchanged between both macrophage populations throughout the course of the experiment (Fig. 1B and Supporting Information Fig. 2C). To ascertain whether the increase in cytokine levels from *Itgb2*$^{-/-}$ macrophages was due to β_2 integrins controlling cytokine secretion, the synthesis of IL-12 p40 and TNF was assessed by intracellular cytokine staining. We observed a larger population of IL-12 p40-producing macrophages in the absence of β_2 integrins, such that at 4 h after stimulation the percentage of *Itgb2*$^{-/-}$ IL-12 p40-positive cells was approximately twice that of WT controls, whereas there was little difference in TNF production (Fig. 1C and D). Therefore, β_2 integrin ablation results in increased TLR responses from BM-derived macrophages, most strongly affecting IL-12 p40 and IL-6 production, with modest effects on TNF protein synthesis. In addition to inflammatory cytokine production, β_2 integrin signals also moderated type I IFN production downstream of TLR4 activation as *Itgb2*$^{-/-}$ macrophages expressed

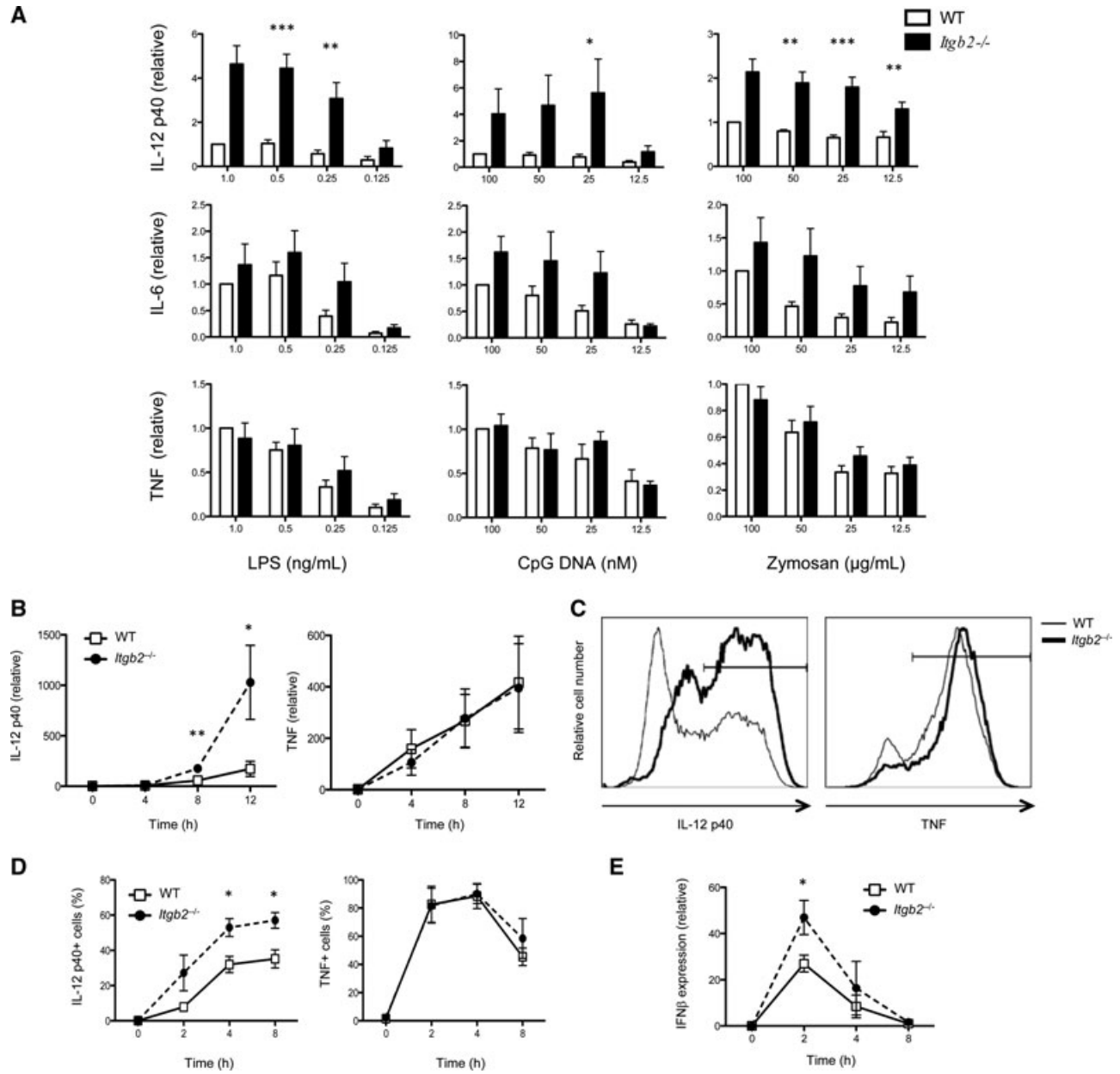

Figure 1. Deficiency in β_2 integrins renders BM-derived macrophages hypersensitive to TLR stimulation. (A) BM-derived macrophages were rested overnight and stimulated with TLR agonists for 24 h. The concentration of IL-12 p40, TNF, and IL-6 in the supernatants was measured by ELISA. The results are displayed as relative cytokine levels, with the values found for WT macrophages at the highest concentration set to 1. Data are shown as mean + SEM of five independent experiments. (B) BM-derived macrophages were stimulated with 1 ng/mL LPS for the indicated times and concentrations of cytokines in the supernatants were measured by ELISA. Relative values were derived by setting the WT time 0 value to 1. Data are shown as mean ± SEM of three independent experiments. (C and D) Macrophages were stimulated with 1 ng/mL LPS for indicated times and Brefeldin A was added for the last 2 h of stimulation. TNF and IL-12 p40 production was measured by intracellular cytokine staining and flow cytometry. (C) IL-12 p40 and TNF staining at 8 h of LPS stimulation. Gating shows cytokine-positive cells. Data shown are representative of three independent experiments performed. (D) The kinetics of IL-12 p40- and TNF-positive macrophages after LPS stimulation as assessed by the gating strategy in (C). The data are shown as mean ± SEM of three independent experiments. (E) Relative IFN-β gene expression in macrophages stimulated with 1 ng/mL LPS was analyzed by qPCR, with results normalized to GAPDH mRNA levels and the WT 8 h time point set to 1. The data shown are mean ± SEM of four independent experiments. $^{*}p < 0.05$, $^{**}p < 0.01$, and $^{***}p < 0.001$, two-tailed, unpaired student's *t*-test.

significantly more IFNβ mRNA after LPS treatment than did WT cells (Fig. 1E).

TLR responsiveness was also examined in thioglycollate-elicited peritoneal macrophages to determine whether β_2 integrins suppress TLRs in an inflammatory macrophage population. Because β_2 integrins contribute to cellular infiltration into the peritoneal cavity [23, 24] and as *Itgb2*$^{-/-}$ mice present with a profound neutrophilia [22], we were unable to

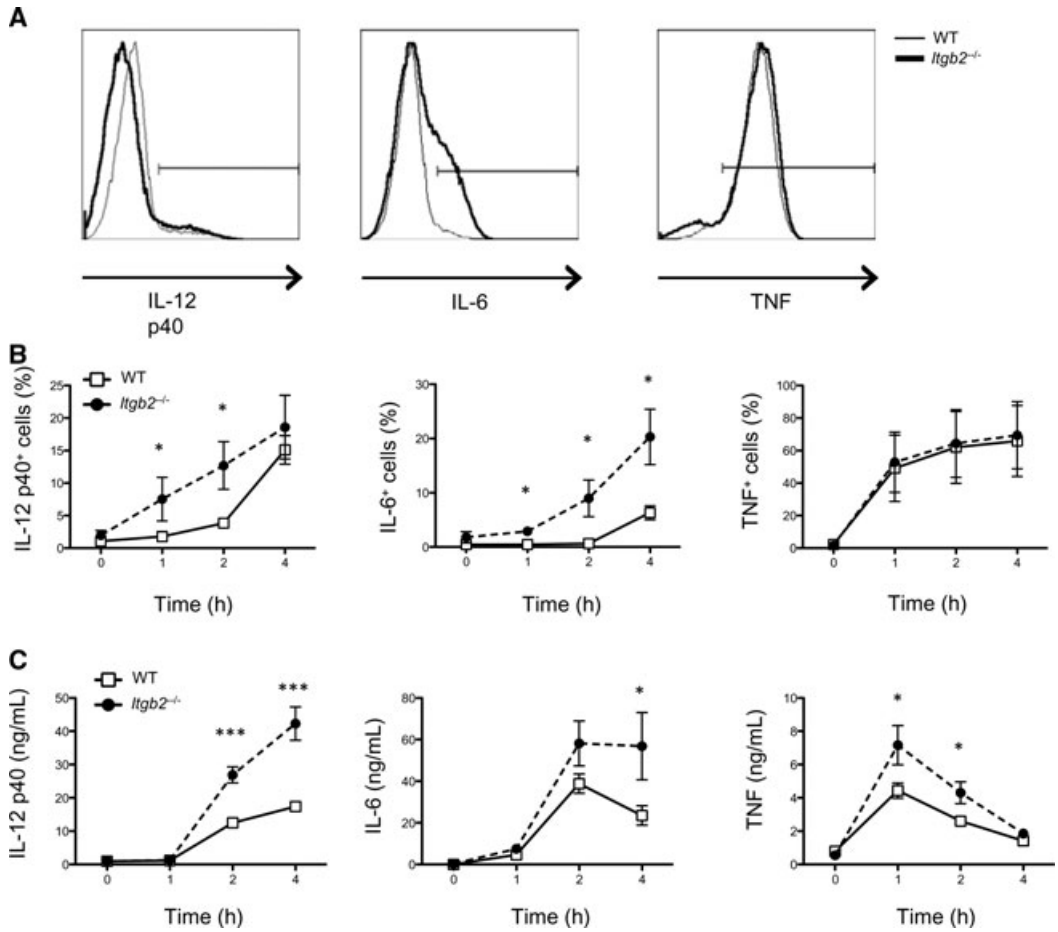

Figure 2. β_2 integrins inhibit TLR activity in inflammatory macrophages and in vivo. (A-B) D5 thioglycollate-elicited cells were enriched for F4/80$^+$ macrophages, rested overnight before treatment with 1 ng/mL LPS with Brefeldin A for the last 2 h of stimulation, and cytokine levels were determined by flow cytometry. (A) Representative histograms of IL-12 p40, IL-6, and TNF staining of F4/80$^+$ cells at 4 h after LPS treatment are shown. (B) The kinetics of cytokine-producing inflammatory macrophages based on the gating strategy found in (A). The data are displayed as mean ± SEM of four independent experiments. (C) WT ($n = 11$) and *Itgb2*$^{-/-}$ ($n = 11$) mice were injected i.p. with 1 mg/kg LPS. Blood was collected at the indicated time points and serum cytokine levels were measured by ELISA. Data are displayed as mean ± SEM of 11 mice for each genotype from three independent experiments. $^*p < 0.05$, $^{**}p < 0.01$, and $^{***}p < 0.001$, two-tailed, unpaired student's *t*-test.

obtain a pure F4/80$^+$Gr-1^{low} macrophage population, even after 4 days postinjection, unlike in WT mice (Supporting Information Fig. 3A). To minimize any effect that elevated neutrophil levels may have on macrophage responses, we purified peritoneal macrophages at day 5 post thioglycollate injection by magnetic bead enrichment (Supporting Information Fig. 3B) and recovered a population of F4/80$^+$ macrophages. Interestingly, *Itgb2*$^{-/-}$ macrophages showed a broader range of F4/80 expression than WT macrophages (Supporting Information Fig. 3B). We assessed inflammatory cytokine production in these thioglycollate-elicited macrophages by intracellular cytokine staining. F4/80^{high} *Itgb2*$^{-/-}$ peritoneal macrophages exhibited increased TLR4 responses over WT cells (Fig. 2A and B). The percentage of IL-12 p40- and IL-6-producing *Itgb2*$^{-/-}$ peritoneal macrophages was significantly elevated over WT cells following LPS stimulation, whereas TNF production remained unaffected by β_2 integrin deletion, mirroring the phenotype of BM-derived macrophages (Fig. 2B). Thus, these data demonstrate that, in addition to BM-derived macrophages, β_2 integrins also negatively regulate TLR-induced IL-12 p40 and IL-6 production in inflammatory macrophage populations.

Itgb2$^{-/-}$ mice have increased LPS-induced cytokines in vivo

To identify the contribution of β_2 integrins to inhibiting TLR responses in vivo, we injected WT and *Itgb2*$^{-/-}$ mice with LPS i.p. and measured inflammatory cytokine levels in serum up to 4 h after injection. The kinetics for TNF, IL-12 p40, and IL-6 induction were similar between WT and *Itgb2*$^{-/-}$ mice, with the peak serum concentration of each cytokine occurring at the same time in both (Fig. 2C). However, differences in the magnitude of cytokine production were observed. Serum IL-12 p40 levels were dramatically increased in *Itgb2*$^{-/-}$ mice such that by 4 h post-injection,

Itgb2$^{-/-}$ animals displayed approximately three times the concentrations observed in WT controls. *Itgb2*$^{-/-}$ mice also presented with significantly elevated serum IL-6 and TNF in response to LPS injection (Fig. 2C). While *Itgb2*$^{-/-}$ mice have changes in leukocyte populations, including increased circulating neutrophils, that make interpreting in vivo findings challenging, these data did support our in vitro findings that β_2 integrins inhibited TLR responses in two distinct macrophage populations, BM-derived macrophages and thioglycollate-elicited macrophages.

TLR inhibition by β_2 integrins does not involve changes in IL-10, ABIN-3, A20, or Hes-1 expression

TLR stimulation in macrophages results in secretion of the anti-inflammatory cytokine IL-10 that acts in an autocrine or paracrine manner to dampen TLR activation [25]. Interestingly, culture of human macrophages on fibrinogen-coated plates induces IL-10 expression, as well as the expression of proteins such as A20, Hes-1, and ABIN-3, which are known to inhibit TLR signaling [20]. Fibrinogen is a β_2 integrin ligand and plating of human macrophages onto fibrinogen-coated plates presumably induces a β_2 integrin signal, though other receptors may also be engaged [26–29]. To examine whether the TLR hypersensitivity of *Itgb2*$^{-/-}$ macrophages was due to deficiencies in these inhibitors, we analyzed their expression and function after TLR stimulation.

Itgb2$^{-/-}$ macrophages secreted similar or slightly elevated amounts of IL-10 following LPS and CpG DNA stimulation (Fig. 3A), demonstrating that *Itgb2*$^{-/-}$ macrophages were not hampered in their ability to produce IL-10. These results were mirrored in *Itgb2*$^{-/-}$ mice, which responded to i.p.-injected LPS by producing IL-10 at similar levels to WT (Fig. 3B). Furthermore, *Itgb2*$^{-/-}$ macrophages did not have defects in their response to IL-10. Treatment of macrophages with IL-10 prior to stimulation with LPS reduced cytokine production in both populations of macrophages to a similar degree (Fig. 3C and D). These data indicate that neither defects in IL-10 production nor the response to IL-10 can explain *Itgb2*$^{-/-}$ macrophage TLR hypersensitivity. Moreover, the increased TLR response of *Itgb2*$^{-/-}$ macrophages is not due to deficiencies in ABIN-3, A20, Hes-1, or IRAK-M expression, as would be hypothesized by the data presented by Wang et al. [20]. *Itgb2*$^{-/-}$ macrophages expressed significantly higher levels of ABIN-3 and Hes-1 mRNA after TLR4 stimulation and exhibited slightly higher or equivalent expression of induced IRAK-M mRNA and A20 mRNA and protein (Fig. 3E and F).

Interestingly, expression of IL-10, A20, and ABIN-3 is associated with a p38 MAPK-driven inhibitory pathway that diminishes inflammation induced by TLRs or UVB irradiation [20, 30, 31]. Despite observing equal or elevated levels of these inhibitory proteins, we noted reduced p38 phosphorylation in LPS-treated *Itgb2*$^{-/-}$ macrophages (Fig. 3G), perhaps owing to the observation that signaling through β_2 integrins themselves involves p38 MAPK pathway activation, the absence of which could lead to a deficiency in phospho-p38 levels [14]. Interestingly, phosphorylation of ERK was not different between WT and *Itgb2*$^{-/-}$ macrophages (Fig. 3G). Thus, while *Itgb2*$^{-/-}$ TLR hypersensitivity may be partially due to suppressed p38 phosphorylation, our data do not implicate IL-10, A20, or ABIN-3 in this process and suggest that other MAPK-derived suppressive mechanisms, such as p38 control of inflammatory cytokine mRNA stability [32], may be controlled by β_2 integrin signals.

CD11a, CD11b, and Cbl-b are dispensable for TLR inhibition

Itgb2$^{-/-}$ BM-derived DCs were also hypersensitive to TLR stimulation and secreted more inflammatory cytokines than WT control DCs (Supporting Information Fig. 4). Because these results generally phenocopied our observations in *Itgb2* $^{-/-}$ macrophages, we reasoned that a β_2 integrin shared between both cell types could inhibit TLR activation, such as LFA-1 (CD11a/CD18) or Mac-1 (CD11b/CD18) [21]. *Itgal*$^{-/-}$ (CD11a-deficient) and *Itgam*$^{-/-}$ (CD11b-deficient) macrophages were examined to determine if either LFA-1 or Mac-1 were required to inhibit TLR signals. Neither *Itgal*$^{-/-}$ nor *Itgam*$^{-/-}$ BM-derived macrophages demonstrated increased cytokine production over that of WT macrophages following TLR stimulation (Fig. 4A and Supporting Information Fig. 5A). Additionally, we observed a reduction in cytokine-producing *Itgam*$^{-/-}$ thioglycollate-elicited peritoneal macrophages when compared to stimulated WT cells, though this difference was not statistically significant (Fig. 4B). *Itgal*$^{-/-}$ and *Itgam*$^{-/-}$ BM-derived DCs similarly had no increases in TLR—induced inflammatory cytokine production (data not shown), revealing that neither CD11a nor CD11b acts singly to diminish TLR activation.

Signals through the β_2 integrin Mac-1 have been suggested to activate Cbl-b, an E3 ubiquitin ligase that can inhibit inflammatory responses in vivo [19]. The proposed model suggests that CD11b signaling causes Cbl-b to ubiquitinate and degrade MyD88, thereby attenuating TLR responses. However, little is known about the ability of Cbl-b to regulate TLR responses specifically in macrophages. Therefore, we evaluated how Cbl-b deficiency influenced inflammatory cytokine production in these cells. *Cblb*$^{-/-}$ BM-derived macrophages were not hypersensitive to TLR stimulation and produced equal or lower amounts of inflammatory cytokines in response to LPS, CpG DNA, and zymosan treatment (Fig. 4C and Supporting Information Fig. 5B). Furthermore, *Cblb*$^{-/-}$ thioglycollate-induced peritoneal macrophages synthesized equivalent or lower levels of inflammatory cytokines when compared with WT controls following TLR4 activation (Fig. 4D), indicating that Cbl-b is dispensable for limiting TLR activity in macrophages. The model proposed by Han et al. would also predict that β_2 integrin-deficient macrophages would have less MyD88 degradation after TLR signaling [19]. Stimulation with 10 ng/mL LPS led to similar MyD88 degradation in WT and *Itgb2*$^{-/-}$macrophages, suggesting that β_2 integrins do not inhibit TLR responses by inducing MyD88 turnover (Supporting Information Fig. 5C). We were also unable to detect changes in

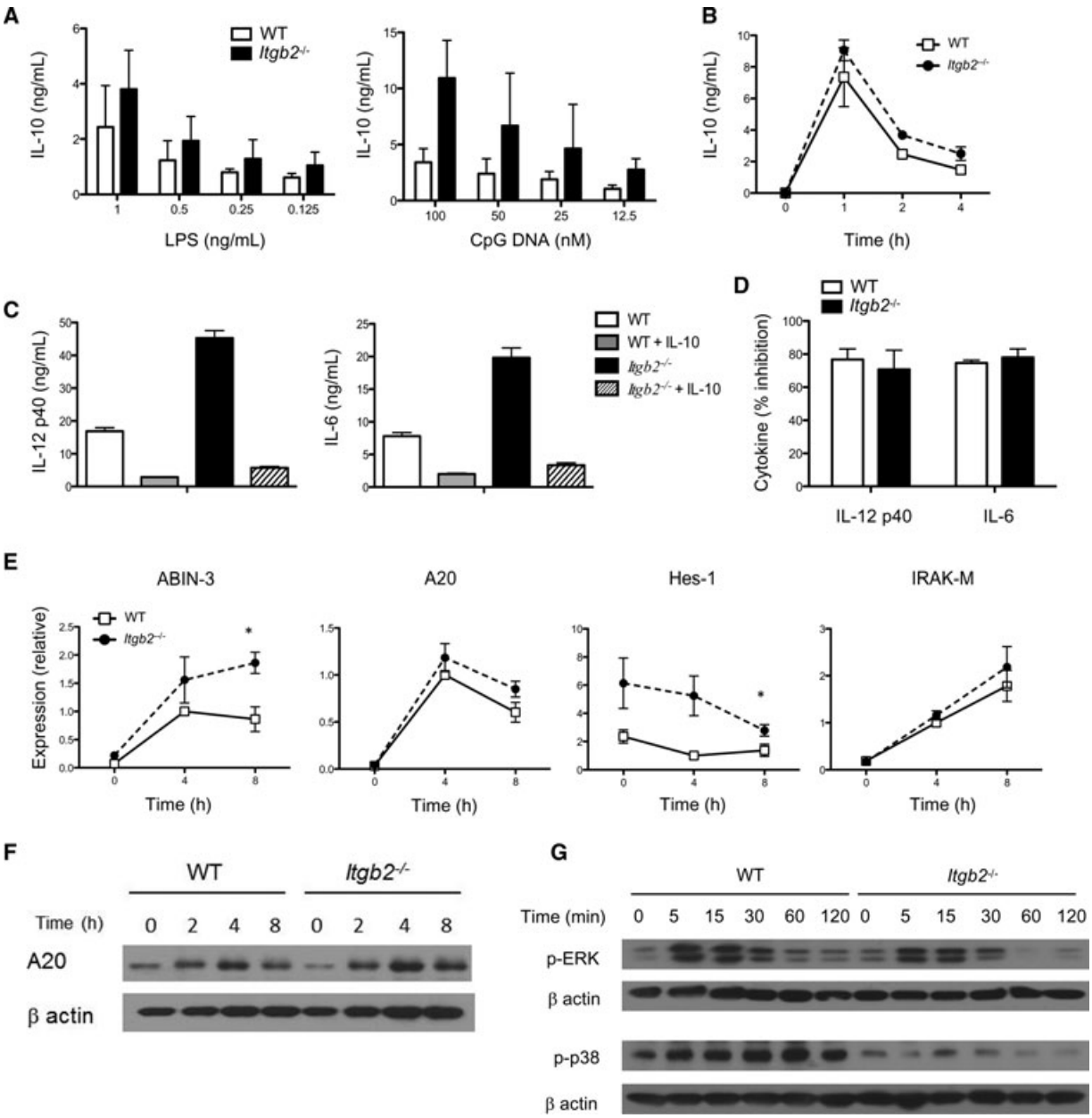

Figure 3. β_2 integrins do not inhibit TLRs by regulating IL-10, ABIN-3, A20, Hes-1, or IRAK-M expression, but do affect p38 MAPK activation. (A) BM-derived macrophages were stimulated with either LPS or CpG DNA for 24 h and IL-10 secretion was measured by ELISA. Data are shown as mean + SEM of three independent experiments. (B) WT ($n = 3$) and *Itgb2*$^{-/-}$ ($n = 3$) mice were injected i.p with 1 mg/kg LPS. Blood was collected at indicated time points and IL-10 concentration was determined by ELISA. Data are shown as mean ± SEM from one experiment and representative of three independent experiments performed. (C) Macrophages were treated with 10 ng/mL IL-10 for 30 min prior to stimulation with 1 ng/mL LPS. Cytokine production was assessed by ELISA. Data are shown as mean + SD of triplicate wells from one experiment, and are representative of three independent experiments. (D) The percent decrease in cytokine production was determined by normalizing IL-10 production generated by TLR stimulation without exogenous IL-10 treatment. Results are displayed as mean + SEM of three independent experiments. (E) Relative inhibitor expression was determined by qPCR after stimulation of macrophages with 1 ng/mL LPS for the indicated time points. Expression levels for each inhibitor were normalized to GAPDH with the WT 4 h time point set to 1, and the results are displayed as mean ± SEM of three or four independent experiments. (F and G) Western blot for (F) A20 and (G) phospho-p38 and phospho-ERK expression in 1 ng/mL LPS-stimulated macrophages, with β-actin as a loading control. The data are representative of two (F) and three (G) independent experiments performed. *$p < 0.05$, two-tailed, unpaired student's *t*-test.

MyD88 degradation in WT or *Itgb2*$^{-/-}$ macrophages treated with a lower dose of LPS (1 ng/mL), with which we observed elevated inflammatory cytokine production in β_2 integrin-deficient cells (data not shown). Interestingly, *Itgam*$^{-/-}$ and *Cblb*$^{-/-}$ macrophages also retained the ability to degrade MyD88 following LPS stimulation (Supporting Information Fig. 5C). These data reveal that a CD11b-Cbl-b inhibitory mechanism is not required for dampening TLR responses in macrophages.

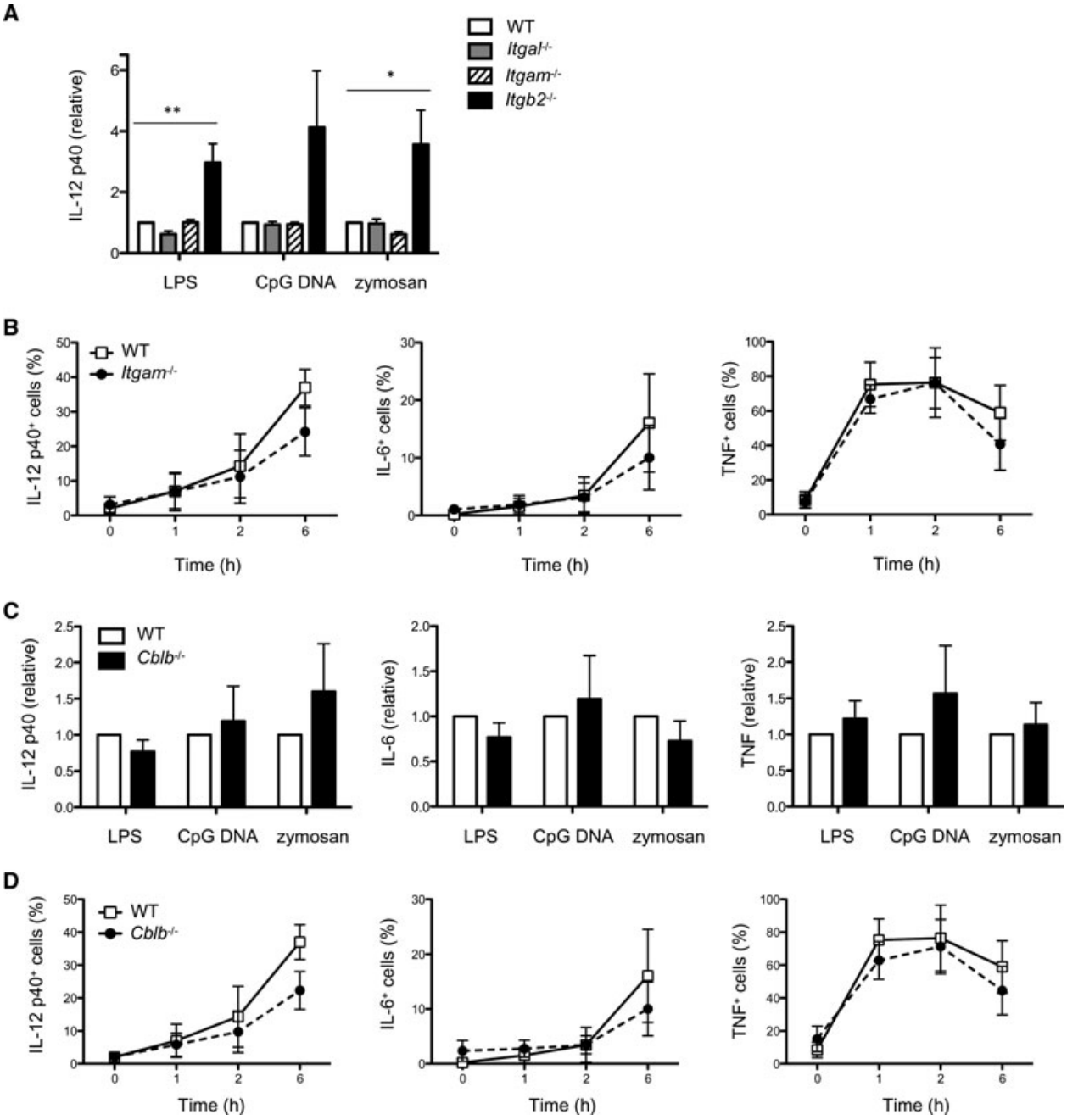

Figure 4. CD11a, CD11b, and Cbl-b are dispensable for TLR inhibition. (A) BM-derived macrophages from WT, *Itgal*$^{-/-}$ (CD11a-deficient) and *Itgam*$^{-/-}$ (CD11b-deficient), and *Itgb2*$^{-/-}$ mice were treated with 1 ng/mL LPS, 100 nM CpG DNA or 100 μg/mL zymosan particles for 24 h. IL-12 p40 concentrations in the supernatants were determined by ELISA and values are set relative to WT results for each stimulation condition. Results are shown as mean + SEM of four independent experiments. (B) F4/80$^+$ thioglycollate-elicited peritoneal macrophages were treated with 1 ng/mL LPS and IL-12 p40 production was determined by flow cytometry as in Figure 2. Data are shown as mean ± SEM of cytokine-positive cells from three independent experiments. (C) Cytokine production from BM-derived macrophages was measured by ELISA as in (A). Results are displayed as mean + SEM of three independent experiments. (D) The kinetics of cytokine-producing thioglycollate-elicited peritoneal macrophages was determined by flow cytometry as in (B). Data are shown as mean ± SEM of three independent experiments. $^*p < 0.05$, $^{**}p < 0.01$, one-way ANOVA.

β_2 integrin deficiency enhances NF-κB activation in macrophages

After eliminating several potential indirect mechanisms governing β_2 integrin-mediated TLR inhibition, we assessed whether *Itgb2*$^{-/-}$ macrophage hypersensitivity was due to differences in TLR-induced NF-κB pathway activation. To this end, we noted changes in NF-κB activation that are consistent with *Itgb2*$^{-/-}$ macrophage hypersensitivity. In canonical NF-κB signaling, NF-κB subunits are retained in the cytoplasm by binding to IκBα, which

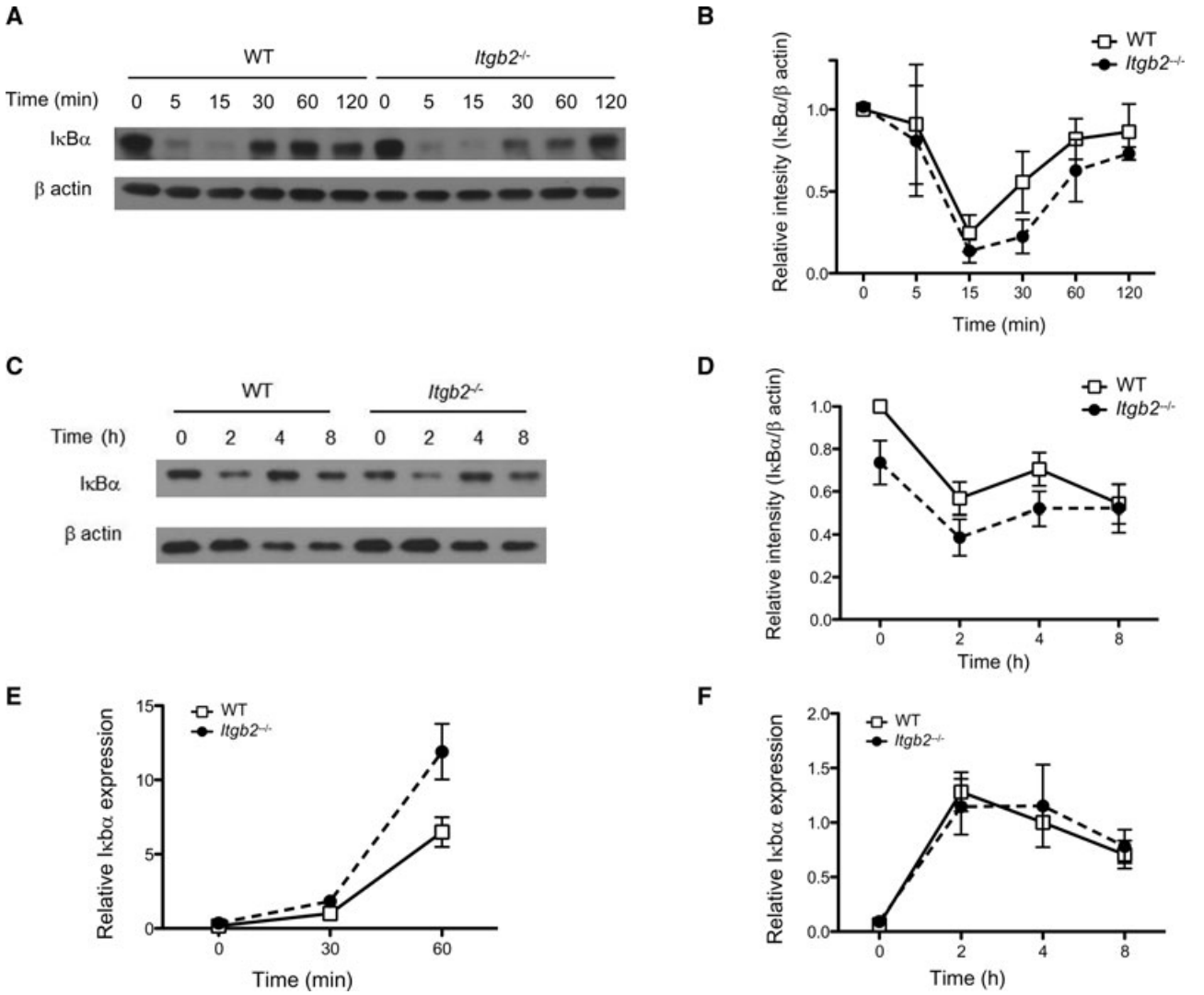

Figure 5. *Itgb2*$^{-/-}$ macrophages exhibit enhanced NF-κB pathway activation following TLR4 stimulation. (A and C) BM-derived macrophages were stimulated with 1 ng/mL LPS for the indicated times and cytoplasmic lysates were assayed for IκBα, with β-actin used as a loading control. (B and D) Densitometry analysis for IκBα levels following TLR4 stimulation. Data are shown as mean ± SEM of relative ratios of intensity (IκBα/β actin) for three independent experiments, with WT time 0 set to 1. (E and F) Relative IκBα mRNA expression following LPS stimulation, with data normalized to GAPDH expression and (E) WT time 30 min and (F) WT at time 4 h set to 1. Results are shown as mean ± SEM of two (E) and four (F) independent experiments.

in turn becomes phosphorylated and degraded after TLR stimulation to allow NF-κB proteins to enter the nucleus and enable transcription. Thus, we assessed changes in IκBα expression at early (0–120 min) and late (2–8 h) phases following TLR stimulation to gauge NF-κB pathway activation. LPS-treated WT and *Itgb2*$^{-/-}$ macrophages led to rapid NF-κB pathway activation such that the lowest amount of total IκBα occurred at 15 min after LPS treatment (Fig. 5A and B). IκBα was quickly resynthesized in WT macrophages such that near baseline levels were reached after 60 min (Fig. 5A and B). In contrast, a consistent trend toward delayed IκBα resynthesis was observed in the absence of β_2 integrins (Fig. 5A and B) suggesting an elevation in NF-κB pathway activation in *Itgb2*$^{-/-}$ macrophages. To assess phosphorylation of IκBα, we stimulated macrophages in the presence of the proteasomal inhibitor MG-132 to compensate for the rapid degradation of IκBα protein. Both WT and *Itgb2*$^{-/-}$ cells quickly phosphorylated IκBα, without an increase in phosphorylation in the *Itgb2*$^{-/-}$ cells over WT cells (Supporting Information Fig. 6A and B).

These results were coupled with similar observations at the late phase of TLR stimulation. *Itgb2*$^{-/-}$ macrophages displayed consistently lower levels of IκBα up to 4 h post-LPS treatment in comparison with WT cells, though the magnitude of this effect was modest (Fig. 5C and D). *Itgb2*$^{-/-}$ macrophages displayed similar phosphorylation of IκBα at 2 h post LPS treatment to WT macrophages, but this IκBα phosphorylation was slightly increased in *Itgb2*$^{-/-}$ macrophages over WT macrophages at 4 h post LPS treatment (Supporting Information Fig. 6C and D). Notably, increases in IκBα degradation in *Itgb2*$^{-/-}$ macrophages were not due to a defect in

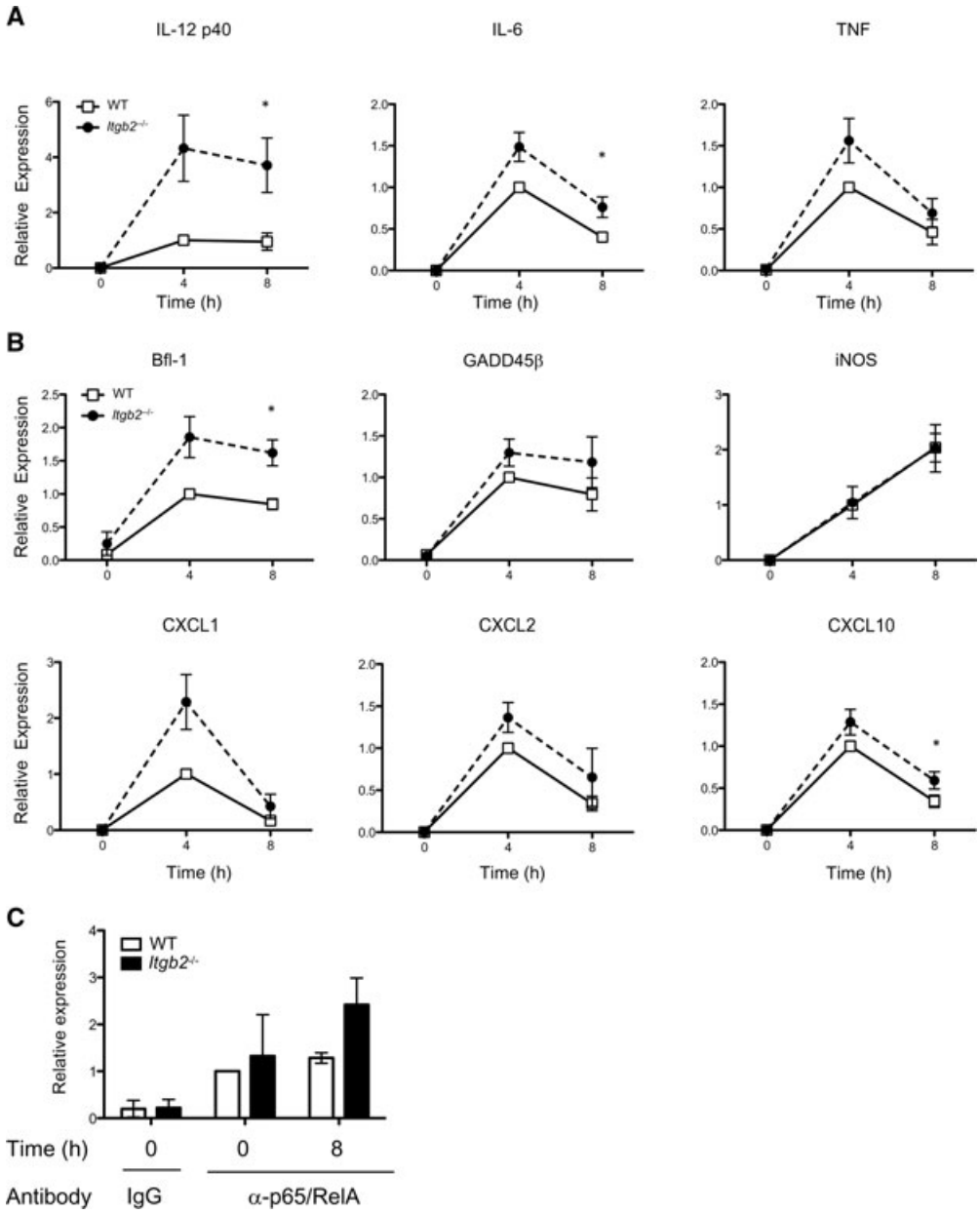

Figure 6. β_2 integrin ablation enhances NF-κB-dependent gene expression and p65/RelA recruitment to the *Il12b* promoter in *Itgb2*$^{-/-}$ macrophages. (A and B) Macrophages were stimulated with 1.0 ng/mL LPS. Expression levels of the indicated genes were determined by qPCR, with results normalized to GAPDH expression, with WT at time 4 h set to 1. The data are shown as mean ± SEM of three (A) or four (B) independent experiments. (C) ChIP analysis of LPS-stimulated macrophages for p65/RelA recruitment to the *Il12b* locus, which encodes for IL-12 p40. Results were normalized to input chromatin levels and set relative to WT at time 0. Data are shown as mean ± SD of two independent experiments. $^*p < 0.05$, two-tailed, unpaired student's *t*-test.

IκBα resynthesis in these cells. *Itgb2*$^{-/-}$ macrophages were able to transcribe IκBα mRNA at or beyond the levels observed for WT macrophages (Fig. 5E and F). Therefore, our data show that β_2 integrins can affect the magnitude of the signal leading to NF-κB activation in the cytoplasm.

We thus compared the induction of NF-κB-dependent genes induced during TLR responses in WT and *Itgb2*$^{-/-}$ macrophages. TLR hyperactivation also generated changes to the NF-κB-dependent gene transcriptional profile of *Itgb2*$^{-/-}$ macrophages. As expected, β_2 integrin-deficient macrophages produced more inflammatory cytokine transcripts than did WT control cells following TLR stimulation, with the greatest differences observed for IL-12 p40 and IL-6 mRNA (Fig. 6A). Consistent with these observations, *Itgb2*$^{-/-}$ macrophages also presented with higher levels of mRNA for many NF-κB-dependent genes [33] as compared to WT, including increases in Bfl-1, CXCL1, CXCL2, CXCL10, and GADD45β (Fig. 6B), indicating a global increase in NF-κB activity without β_2 integrin-mediated inhibition. The magnitude

of the effect of β_2 integrin deficiency varied and a curious exception to this increased gene expression profile was that of iNOS, which directs the antimicrobial nitric oxide responses, the synthesis of which was identical between *Itgb2*$^{-/-}$ and WT macrophages (Fig. 6B). Furthermore, the hyperactive NF-κB pathway activity found in *Itgb2*$^{-/-}$ macrophages was limited to TLR stimulation and was not observed after treatment of these cells with recombinant TNF, a potent NF-κB inducer (Supporting Information Fig. 6E) [34].

Activation of the NF-κB subunit p65/RelA controls the intensity of IL-12 p40 transcription [35]. Because of this, we analyzed p65/RelA activation directly by assessing its binding to the promoter of *Il12b*, which encodes IL-12 p40, by chromatin immunoprecipitation (ChIP) assay. Interestingly, p65/RelA occupancy of the *Il12b* promoter was elevated in *Itgb2*$^{-/-}$ macrophages after 8 h of TLR4 stimulation (Fig. 6C), demonstrating a direct effect of β_2 integrins on NF-κB subunit binding to the *Il12b* locus. Taken together with our gene expression data and signaling analyses, these observations clearly show that one way by which β_2 integrins suppress macrophage activation and inflammatory cytokine production is by fine-tuning NF-κB pathway activation. While β_2 integrin signals direct modest, but consistent, changes in IκBα expression after TLR stimulation, these changes are sufficient to dramatically reduce inflammatory cytokine production in myeloid cells and demonstrate a critical role for β_2 integrins in dampening TLR responses.

Discussion

A variety of cell surface receptors use ITAM-containing adapters to relay external signals and enable appropriate cellular changes, including the β_2 integrins, which signal via DAP12 and FcRγ [4, 14]. Yet while signals through DAP12 and FcR-γ have been clearly shown to block inflammation [10, 11, 36], defining the connection between the β_2 integrins themselves and inflammatory processes has proven difficult due to conflicting data showing both positive and negative regulatory roles for this family of adhesion molecules [16–20, 37]. We have clarified how β_2 integrin activation influences TLR responses by using macrophages and DCs derived from the *Itgb2*$^{-/-}$ mouse, which lack all β_2 integrin surface expression. *Itgb2*$^{-/-}$ macrophages and DCs produced more IL-12 p40 and IL-6 in response to stimulation with a variety of TLR agonists and *Itgb2*$^{-/-}$ mice generated more inflammatory cytokines after LPS injection than did WT control animals, demonstrating that β_2 integrins are essential for inhibiting TLR activity in vitro and in vivo.

While these phenotypic findings are consistent with other studies reporting a suppressive role for β_2 integrins, our use of *Itgb2*$^{-/-}$ myeloid cells provided a useful system with which to test various aspects of TLR regulation and to define the molecular requirements for β_2 integrin-mediated TLR inhibition. To this end, we have identified a novel role for β_2 integrins in calibrating NF-κB pathway activation downstream of TLR ligation. Without β_2 integrin inhibitory signals, macrophage total IκBα levels remained consistently lower throughout the course of TLR stimulation. Curiously, we did not find consistently enhanced phosphorylated IκBα levels in *Itgb2*$^{-/-}$ cells after TLR stimulation, though this may be due to complications arising from using the proteasome inhibitor MG-132 in these experiments to inhibit the rapid degradation of IκBα. However, its presence would have also inhibited normal turnover of IκBα, perhaps masking potential differences between WT and β_2 integrin-deficient cells. Nevertheless, this fine-tuning of NF-κB activation by β_2 integrins contributed to dramatic differences in the ability of macrophages to respond to TLRs and induce NF-κB-dependent gene expression. Importantly, we noted that the affected genes encompassed both "primary response" (*Tnf, Cxcl1, Cxcl2*) and "secondary response" (*Il12B, Il6*) genes that encode for inflammatory cytokines, chemokines, and anti-apoptotic functions [38]. We also observed a direct effect of β_2 integrin deletion on enhancing p65/RelA binding to the *Il12b* (IL-12 p40) promoter downstream of LPS stimulation. However, it should be noted that fine-tuning of the NF-κB pathway by β_2 integrins did not control expression of all "NF-κB-dependent" genes tested. Peculiar omissions from this list include A20 and iNOS, which were both expressed similarly between WT and *Itgb2*$^{-/-}$ macrophages, suggesting that other pathways may be influenced by β_2 integrin signals to control transcription of these genes.

One such pathway is p38 MAPK signaling. *Itgb2*$^{-/-}$ macrophages demonstrated a reduced ability to phosphorylate, and therefore activate, p38 following LPS treatment, consistent with the fact that β_2 integrin outside-in signals are known to directly activate the MAPK pathway [14]. In addition to its well-regarded proinflammatory activities [39], activation of p38 and its subordinate protein kinases MSK1 and MSK2 has been implicated in dampening inflammation through several mechanisms. For example, p38 activity limits Th1 responses to *Leishmania* by destabilizing IL-12 p40, though not TNF, mRNA stability [32]. p38 and MSK1/2-derived signals have also been shown to negatively regulate TLR responses by inhibiting inflammatory cytokine transcription directly or by promoting IL-10 synthesis through activation of CREB and Atf-1 transcription factors [30–32]. In addition to IL-10, p38-directed A20 and ABIN-3 production has previously been linked to TLR suppression by β_2 integrins [20]. However, *Itgb2*$^{-/-}$ macrophage TLR hypersensitivity could not be attributed to deficiencies in A20, ABIN-3, Hes-1 or to changes in IL-10 production or signaling, arguing against a role for these proteins in β_2 integrin-medited TLR suppression. Interestingly, *Itgb2*$^{-/-}$ macrophages presented with higher TLR-induced levels of some of these inhibitors than WT cells, likely owing to enhanced NF-κB activation. The differences between our results and those of Wang et al. [20] may be due to our use of plastic petri dishes to induce β_2 integrin signals instead of plate-bound fibrinogen, which itself is known to bind to additional receptors [26–29]. Indeed, fibrinogen's ability to dampen TLR activity in macrophages may be at least partially β_2 integrin-independent as we found that inflammatory cytokine secretion was suppressed in *Itgb2*$^{-/-}$ macrophages similar to WT cells after plating onto fibrinogen-coated plates (data not shown). Alternatively, our results may differ due to our overnight resting of macrophages after plating or other technical

differences. Despite this, β_2 integrin signaling may contribute to inhibition of TLR responses through other p38-directed processes, such as by regulating inflammatory cytokine mRNA stability [32] or by influencing NF-κB crosstalk [34,40], possibilities that remain to be tested experimentally.

Our findings are consistent with observations made in the *Itgb2*^{hypo} mouse on the PL/J background, which suffers from a chronic inflammatory skin disease similar to human psoriasis [41]. Macrophages are required for maintenance of this disease and selective disruption of NF-κB activation in macrophages improves the psoriaform lesions in *Itgb2*^{hypo} mice [41, 42]. While these results suggest a connection between β_2 integrins and NF-κB regulation, they are complicated by the ongoing disease of the animals and the presence of residual β_2 integrin signaling in all cell types. However, by using myeloid cells isolated from healthy *Itgb2*$^{-/-}$ mice on a C57BL/6 genetic background, we have avoided these issues and have clearly revealed a role for β_2 integrins in fine-tuning the NF-κB pathway, demonstrating that β_2 integrin signaling can inhibit TLR activation.

In attempting to identify the specific β_2 integrins required for TLR inhibition, we found that deletion of Mac-1 alone is insufficient to render myeloid cells hyperresponsive to TLR stimulation. This was a surprising finding given that Mac-1 activation has been proposed to regulate TLR signaling by inducing Cbl-b activity, leading to degradation of MyD88 and TRIF [19]. Cbl-b is a potent negative regulator of inflammation [43, 44] and it is known to modulate TLR4 activity in neutrophils by facilitating TLR4-MyD88 binding [45]. However, we found that Cbl-b is not required to dampen TLR activation in macrophages. *Cblb*$^{-/-}$ macrophages were not hypersensitive to TLR stimulation and Cbl-b deficiency did not change the kinetics of MyD88 degradation, as would be predicted based on the model proposed by Han et al. [19] through experiments in HEK293 cells. Thus, our data suggest that inhibiting TLR4 does not require a CD11b-Cbl-b-MyD88 regulatory axis in primary macrophages. Deleting LFA-1 was also not sufficient to cause hypersecretion of inflammatory cytokines in macrophages. We theorize that one or more integrins shared between both cell types are responsible for TLR inhibition and that compensatory integrin signaling is able to block TLR responses in *Itgal*$^{-/-}$ or *Itgam*$^{-/-}$ myeloid cells.

Our data suggest an important role for cell adhesion events in fine-tuning inflammation. β_2 integrins first encounter their ligands within the luminal side of blood vessels. By finding that β_2 integrins are required for negatively regulating TLR responses, we have highlighted the exciting prospect that cell adhesion events may limit inflammatory cytokine production in the bloodstream and thereby compartmentalize inflammatory cytokine production to the site of inflammation. Beyond this initial β_2 integrin binding, myeloid cells also encounter β_2 integrin ligands within the extracellular matrix while en route to their intended targets. Here these ligands would be modified by local inflammatory mediators [46], suggesting that distinct β_2 integrin ligands may differentially regulate TLR responses in a manner that targets inflammatory cytokine production to the infected tissue and therefore minimizes damage to the host.

Materials and methods

Mice

C57BL/6 mice were purchased from Charles River Laboratories. CD18-deficient (*Itgb2*$^{-/-}$) mice [22] were backcrossed six generations against C57BL/6 mice and were provided by Dr. Clifford Lowell (University of California, San Francisco). CD11a-deficient (*Itgal*$^{-/-}$) and CD11b-deficient (*Itgam*$^{-/-}$) animals were purchased from Jackson Laboratories [23, 47]. Cbl-b-deficient (*Cblb*$^{-/-}$) mice were backcrossed 12 generations against C57BL/6 and were provided by Dr. Phil Greenberg (University of Washington) [48]. All animals were housed in specific-pathogen-free facilities and all experiments were performed in accordance with protocols approved by the Institutional Animal Care and Use Committee at the Benaroya Research Institute.

Cell culture

BM cells were flushed from femurs and tibias, followed by erythrocyte lysis in ACK buffer (Lonza). For macrophages, BM cells were plated onto a 10 cm petri dish (Fisher Scientific) using 10 mL of BM macrophage growth medium, which consisted of DMEM supplemented with 10% FBS (Sigma), 2 mM L-glutamine (Gibco), 1 mM sodium pyruvate (Gibco), 10 mM HEPES (Lonza), penicillin/streptomycin (Gibco) and 10% CMG14–12 cell conditioned media as a source of CSF-1 [49]. BM-derived DCs were grown in DC medium, which consisted of RPMI 1640 supplemented with 10% FBS, 2 mM L-glutamine, 1 mM sodium pyruvate, 10 mM HEPES, penicillin/streptomycin and 10 ng/mL GM-CSF (Peprotech). For both macrophages and DCs, an additional 10 mL of growth medium was added after 3 days of culture. Day 6 DCs were isolated from culture by magnetic bead enrichment for MHCII$^+$ cells. Cells were treated with anti-FcγRII/III (2.4G2) followed by staining with anti-MHC II-biotin (M5/114.15.2/eBioscience), antibiotin microbeads (Miltenyi biotech) and sorting with MACS columns according to the manufacturer's instructions. The purity of CD11c$^+$ cells was >90% in WT cultures. BM-derived macrophages and DCs were used at day 6 of culture.

Peritoneal macrophage isolation

Mice were injected i.p. with 3% thioglycollate broth and peritoneal cells were isolated by lavage with Cell Dissociation Buffer (Invitrogen) 5 days after injection. Macrophages were purified by magnetic bead enrichment using anti-F4/80-biotin (BM8/eBioscience) followed by incubation with antibiotin microbeads and then sorted by MACS according to the manufacturer's instructions. F4/80$^+$ macrophages were cultured in DMEM supplemented with 10% FBS (Sigma).

TLR stimulation and ELISA

Macrophages or DCs were plated onto 96-well tissue culture-treated plates at 5×10^4 cells/well and allowed to rest for 16 h prior to stimulation. TLR agonists were added to triplicate wells at the indicated concentrations for up to 24 h. Supernatants were collected and the amount of IL-12 p40, IL-12 p70, IL-6, TNF, or IL-10 were assessed by ELISA (eBioscience). TLR agonists used were as follows: *S. Minnesota* R595 Ultra Pure LPS (List Biological Laboratories), CPG DNA (ODN1826, Invivogen), and zymosan particles (Sigma). CpG DNA and zymosan particles were incubated in 10 μg/mL polymixin B for 1 h prior to use.

Flow cytometry and intracellular cytokine staining

Macrophages were stimulated with LPS for up to 8 h in the presence of 10 μg/mL Brefeldin A for the final 2 h of stimulation. Macrophage FcRs were blocked with 2.4G2 for 10 min followed by surface staining with anti-F4/80 (BM8/eBioscience). Peritoneal cells were also surface stained with anti-Siglec F (E50–2440/BD Biosciences) and anti-Gr-1 (RB6–8C5/eBioscience). Macrophages were then fixed and permeabilized using BD Cytofix/Cytoperm Fixation/Permeabilization kit (BD Biosciences). Intracellular cytokine staining was performed using anti-IL-12 p40 (C15.6/Biolegend), anti-TNF (MP6-XT22/eBioscience), and anti-IL-6 (MP5–20F3/eBioscience). Flow cytometry analysis was conducted using an LSR2 (BD Bioscience) running FACSDiva software (BD Bioscience). All flow cytometry analyses were conducted using FlowJo software (Treestar).

LPS injection

Mice were injected with 1 μg/g LPS i.p. in PBS and blood was collected at indicated time points. Serum concentrations of IL-12 p40, IL-6, TNF, and IL-10 were determined by ELISA.

Gene expression analysis

Total RNA from LPS or TNF (Peprotech) stimulated macrophages was isolated using the RNeasy Plus kit (Qiagen) and reverse transcribed with Superscript III reverse transcriptase (Invitrogen). Real-time quantitative PCR was performed in triplicate wells using the Power SYBR Green PCR master mix (Applied Biosystems) and reactions were run on a 7900HT Real-Time PCR System (Applied Biosystems). All data were normalized to GAPDH endogenous control. Oligonucleotide primers for GAPDH and A20 were previously described [20]. Primer sequences were as follows: *Hes1*: 5′-tgccagctgatataatggaga-3′ and 5′-ccatgataggctttgatgact-3′; *TNIP3* (ABIN-3): 5′- tccttgtcttcccaggacat-3′ and 5′-ttcttcttggtggagcacact-3’; *Irak3* (IRAK-M): 5′- tcgac agatta cagtgc acaa-3′ and 5′-ggctatt cctatcaatacgct-3’; *Bcl2a1a* (Bfl-1): 5′- tttccagttttgtggca gaat-3′ and 5′-tcaaacttctttatgaagccatctt-3′; *Gadd45b*: 5′- ctgcctcctggtcacgaa-3′ and 5′- ttgcctctgctctcttcaca-3’; *Nos2* (iNOS): 5′-gggctgtcacgg agatca-3′ and 5′-ccatgatggtca cattctgc-3′; *Cxcl1*: 5′-agactccagccacactccaa-3′ and 5′-tgacagcgcagctcattg-3′; *Cxcl2*: 5′-aaaatcatccaaaagatactgaacaa-3′ and 5′- ctttggttcttccgttgagg-3′ and 5′- ctttggttcttccgttgagg-3′; *Cxcl10*: 5′- gctgccgtcattttctgc-3′ and 5′-tctcactggcccgtcatc-3′; *Il12a* (IL-12 p35) 5′- tcagaatcacaaccatcagca-3′ and 5′ cgccattatgattcagagactg-3′; *Il12b* (IL-12 p40): 5′- gattcagactccaggggaca-3′ and 5′-tggttagcttctgaggacaca-3′; *Il23a* (IL-23 p19) 5′-tccctactaggactcagccaac-3′ and 5′-agaactcaggctgggcatc-3′; *Tnf*: 5′-gtcaggttgcctctgtctca-3′ and 5′-tcagggaagagtctggaaag-3′; *Il6*: 5′- aggcataacgcactaggttt-3′ and 5′-agctggagtcacagaaggag-3′; *Ifnb*: 5′- gcactgggtggaatgagactattg-3′ and 5′- ttctgaggcatcaactgacaggtc-3′.

ChIP

ChIP was conducted as described in [35] with minor variations. Briefly, macrophages were stimulated with 1 ng/mL LPS for 8 h, washed and fixed with a 1% final concentration of formaldehyde (37% HCHO in 10–15% methanol; Fisher). Crosslinking was stopped after 10 min by addition of glycine to a final concentration of 125 mM and incubated for 10 min. Macrophages were then washed three times with ice-cold PBS and spun down, and pellets were flash frozen in a dry ice/ethanol bath and kept at –80°C until further analysis. To isolate nuclei, macrophages were first resuspended in Cell Lysis Buffer (10 mM HEPES pH 7.9, 0.5% IGEPAL-30, 1.5 mM $MgCl_2$, 10 mM KCl) and kept on ice for 25 min, vortexing every 5 min. Nuclei were then centrifuged at 4°C and resuspended in Nuclear Lysis Buffer (50 mM Tris pH 8.0, 10 mM EDTA, 1% SDS), followed by sonication in a 4°C water bath to create fragments between 200–800 bp in length. Sonicated samples were then precleared with Protein A Dynabeads (Invitrogen) for 30 min at 4°C and supernatants were collected by magnetic separation. The supernatants were then diluted 1:10 in dilution buffer (0.01% SDS, 1.1% Triton X-100, 1.2 mM EDTA, 16.7 mM Tris pH 8.1, 167 mM NaCl) and incubated with 2 μg of anti-p65/RelA (Santa Cruz) overnight at 4°C. Immunocomplexes were then collected with Protein A Dynabeads and washed with Low Salt buffer (150 mM NaCl, 0.1% SDS, 1% Triton X-100, 2 mM EDTA, 20 mM Tris-HCl pH 8.1), High Salt buffer (same as low salt but with 500 mM NaCl), LiCl buffer (0.25 M LiCl, 1% NP-40, 1% Sodium deoxycholate, 1 mM EDTA, 10 mM Tris-HCl) and two times with TE buffer. Complexes were extracted with Elution buffer (1% SDS, 0.1 M $NaHCO_3$) and protein: DNA crosslinks were reversed by treating with RNAse A and Proteinase K at 65°C. DNA was then purified (MoBio UltraClean PCR kit) and analyzed by qPCR. Normalization was accomplished by subtracting Ct values from precleared “input” chromatin. The primer sequences for the *Il12b* promoter are: 5′-ctttctgatggaaacccaaag-3′ and 5′-ggggagggaggaacttctta-3′.

Western blot

Macrophages were stimulated with indicated concentrations of LPS for various times and lysed in lysis buffer containing 1%

Triton X-100, protease inhibitors (mammalian protease inhibitor cocktail, Sigma) and 1 mM sodium orthovanadate (Sigma). For phospho-IκBα blots, macrophages were pretreated with 10 μM MG-132 (Sigma) for 30 min prior to LPS treatment. Lysates were separated by Tris-bis SDS-PAGE gels (Invitrogen) and transferred onto polyvinylidene fluoride (PVDF) membranes (Millipore). Rabbit antibodies specific for IκBα, phospho-IκBα, phospho-p42/44 ERK, phospho-p38, A20, and β actin were from Cell Signaling. Rabbit anti-MyD88 was from Biovision. An HRP-conjugated donkey antirabbit IgG was used as a secondary (GE Healthcare). Antibody binding was detected by the Immobilon chemiluminescence system (Millipore). Densitometry analysis was conducted using ImageJ software (NIH).

Statistical analysis

Student's unpaired *t*-test was used to measure statistical significance between two groups and one-way ANOVA with Dunnet's multiple comparison test was used to determine statistical significance between multiple groups against WT control. All statistical analyses were performed by Prism 5 (Graphpad Software).

Acknowledgments: We thank Dr. Clifford Lowell for providing *Itgb2*$^{-/-}$ mice and Dr. Hua Gu and Dr. Phil Greenberg for providing *Cblb*$^{-/-}$ mice. We would also like to acknowledge Dr. Amy Weinmann for advice on chromatin immunoprecipitation and thank members of our laboratory for helpful discussions and review of the manuscript.
This work was supported by NIH grants R01AI073441 and R01AI081948, an Investigator Award from the Cancer Research Institute, a pilot award from the Alliance for Lupus Research and DOD grant W81XWH-10-1-0149 (to J.A.H). N.Y. was supported in part by NIH training grant 5T32CA09537.

Conflict of interest: The authors declare no financial or commercial conflict of interest.

References

1 **Kawai, T. and Akira, S.**, The role of pattern-recognition receptors in innate immunity: update on Toll-like receptors. *Nat. Immunol.* 2010. **11:** 373–384.

2 **Liew, F. Y., Xu, D., Brint, E. K. and O'Neill, L. A. J.**, Negative regulation of toll-like receptor-mediated immune responses. *Nat. Rev. Immunol.* 2005. **5:** 446–458.

3 **Hamerman, J. A. and Lanier, L. L.**, Inhibition of immune responses by ITAM-bearing receptors. *Science's STKE*. 2006, **320**: re1.

4 **Ivashkiv, L. B.**, Cross-regulation of signaling by ITAM-associated receptors. *Nat. Immunol.* 2009. **10:** 340–347.

5 **Hamerman, J. A., Ni, M., Killebrew, J. R., Chu, C.-L. and Lowell, C. A.**, The expanding roles of ITAM adapters FcRgamma and DAP12 in myeloid cells. *Immunol. Rev.* 2009. **232:** 42–58.

6 **Lanier, L. L.**, DAP10- and DAP12-associated receptors in innate immunity. *Immunol. Rev.* 2009. **227:** 150–160.

7 **Nimmerjahn, F. and Ravetch JV**. Fcgamma receptors as regulators of immune responses. *Nat. Rev. Immunol.* 2008. **8:** 34–47.

8 **Hamerman, J. A., Jarjoura, J. R., Humphrey, M. B., Nakamura, M. C., Seaman, W. E. and Lanier, L. L.**, Cutting edge: inhibition of TLR and FcR responses in macrophages by triggering receptor expressed on myeloid cells (TREM)-2 and DAP12. *J. Immunol.* 2006. **177:** 2051–2055.

9 **Turnbull, I. R., Gilfillan, S., Cella, M., Aoshi, T., Miller, M., Piccio, L., Hernandez, M. et al.**, Cutting edge: TREM-2 attenuates macrophage activation. *J. Immunol.* 2006. **177:** 3520–3524.

10 **Chu, C.-L., Yu, Y.-L., Shen, K.-Y., Lowell, C. A., Lanier, L. L. and Hamerman, J. A.**, Increased TLR responses in dendritic cells lacking the ITAM-containing adapters DAP12 and FcRgamma. *Eur. J. Immunol.* 2008. **38:** 166–173.

11 **Hamerman, J. A., Tchao, N. K., Lowell, C. A. and Lanier, L. L.**, Enhanced Toll-like receptor responses in the absence of signaling adaptor DAP12. *Nat. Immunol.* 2005. **6:** 579–586.

12 **Ito, H. and Hamerman, J. A.**, TREM-2, triggering receptor expressed on myeloid cell-2, negatively regulates TLR responses in dendritic cells. *Eur. J. Immunol.* 2012. **42:** 176–185.

13 **Ley, K., Laudanna, C., Cybulsky, M. I. and Nourshargh, S.**, Getting to the site of inflammation: the leukocyte adhesion cascade updated. *Nat. Rev. Immunol.* 2007. **7:** 678–689.

14 **Mócsai, A., Abram, C. L., Jakus, Z., Hu, Y., Lanier, L. L. and Lowell, C. A.**, Integrin signaling in neutrophils and macrophages uses adaptors containing immunoreceptor tyrosine-based activation motifs. *Nat. Immunol.* 2006. **7:** 1326–1333.

15 **Abram, C. L. and Lowell, C. A.**, The ins and outs of leukocyte integrin signaling. *Annu. Rev. Immunol.* 2009. **27:** 339–362.

16 **Kagan, J. C. and Medzhitov, R.**, Phosphoinositide-mediated adaptor recruitment controls Toll-like receptor signaling. *Cell*. 2006. **125:** 943–955.

17 **Medvedev, A. E., Flo, T., Ingalls, R. R., Golenbock, D. T., Teti, G., Vogel, S. N. and Espevik, T.**, Involvement of CD14 and complement receptors CR3 and CR4 in nuclear factor-kappaB activation and TNF production induced by lipopolysaccharide and group B streptococcal cell walls. *J. Immunol.* 1998. **160:** 4535–4542.

18 **Perera, P. Y., Mayadas, T. N., Takeuchi, O., Akira, S., Zaks-Zilberman, M., Goyert, S. M. and Vogel, S. N.**, CD11b/CD18 acts in concert with CD14 and Toll-like receptor (TLR) 4 to elicit full lipopolysaccharide and taxol-inducible gene expression. *J. Immunol.* 2001. **166:** 574–581.

19 **Han, C., Jin, J., Xu, S., Liu, H., Li, N. and Cao, X.**, Integrin CD11b negatively regulates TLR-triggered inflammatory responses by activating Syk and promoting degradation of MyD88 and TRIF via Cbl-b. *Nat. Immunol.* 2010. **11:** 734–742.

20 **Wang, L., Gordon, R. A., Huynh, L., Su, X., Park Min, K.-H., Han, J., Arthur, J. S. et al.**, Indirect inhibition of Toll-like receptor and type I interferon responses by ITAM-coupled receptors and integrins. *Immunity*. 2010. **32:** 518–530.

21 **Luo, B.-H., Carman, C. V. and Springer, T. A.**, Structural basis of integrin regulation and signaling. *Annu. Rev. Immunol.* 2007. **25:** 619–647.

22 **Scharffetter-Kochanek, K., Lu, H., Norman, K., van Nood, N., Munoz, F., Grabbe, S., McArthur, M. et al.**, Spontaneous skin ulceration and defective T cell function in CD18 null mice. *J. Exp. Med.* 1998. **188:** 119–131.

23 **Ding, Z. M., Babensee, J. E., Simon, S. I., Lu, H., Perrard, J. L., Bullard, D. C., Dai, X. Y. et al.**, Relative contribution of LFA-1 and Mac-1 to neutrophil adhesion and migration. *J. Immunol.* 1999. **163:** 5029–5038.

24 **Mizgerd, J. P., Kubo, H., Kutkoski, G. J., Bhagwan, S. D., Scharffetter-Kochanek, K., Beaudet, A. L. and Doerschuk, C. M.**, Neutrophil emigration in the skin, lungs, and peritoneum: different requirements for CD11/CD18 revealed by CD18-deficient mice. *J. Exp. Med.* 1997. **186:** 1357–1364.

25 **Moore, K. W., de Waal Malefyt, R., Coffman, R. L. and O'Garra, A.**, Interleukin-10 and the interleukin-10 receptor. *Annu. Rev. Immunol.* 2001. **19:** 683–765.

26 **Barrera, V., Skorokhod, O. A., Baci, D., Gremo, G., Arese, P. and Schwarzer, E.**, Host fibrinogen stably bound to hemozoin rapidly activates monocytes via TLR-4 and CD11b/CD18-integrin: a new paradigm of hemozoin action. *Blood.* 2011. **117:** 5674–5682.

27 **Flick, M. J., Du, X., Witte, D. P., Jirousková, M., Soloviev, D. A., Busuttil, S. J., Plow, E. F. et al.**, Leukocyte engagement of fibrin(ogen) via the integrin receptor alphaMbeta2/Mac-1 is critical for host inflammatory response in vivo. *J. Clin. Invest.* 2004. **113:** 1596–1606.

28 **Pluskota, E. and D'Souza, S. E.**, Fibrinogen interactions with ICAM-1 (CD54) regulate endothelial cell survival. *Eur. J. Biochem.* 2000. **267:** 4693–4704.

29 **Suehiro, K., Mizuguchi, J., Nishiyama, K., Iwanaga, S., Farrell, D. H. and Ohtaki, S.**, Fibrinogen binds to integrin alpha(5)beta(1) via the carboxyl-terminal RGD site of the Aalpha-chain. *J. Biochem.* 2000. **128**: 705–710.

30 **Ananieva, O., Darragh, J., Johansen, C., Carr, J. M., McIlrath, J., Park, J. M., Wingate, A. et al.**, The kinases MSK1 and MSK2 act as negative regulators of Toll-like receptor signaling. *Nat. Immunol.* 2008. **9:** 1028–1036.

31 **Kim, C., Sano, Y., Todorova, K., Carlson, B. A., Arpa, L., Celada, A., Lawrence, T. et al.**, The kinase p38 alpha serves cell type-specific inflammatory functions in skin injury and coordinates pro- and anti-inflammatory gene expression. *Nat. Immunol.* 2008. **9:** 1019–1027.

32 **Yang, Z., Zhang, X., Darrah, P. A. and Mosser, D. M.**, The regulation of Th1 responses by the p38 MAPK. *J. Immunol.* 2010. **185:** 6205–6213.

33 **Lawrence, T., Bebien, M., Liu, G. Y., Nizet, V. and Karin, M.**, IKKalpha limits macrophage NF-kappaB activation and contributes to the resolution of inflammation. *Nature.* 2005. **434:** 1138–1143.

34 **Oeckinghaus, A., Hayden, M. S. and Ghosh, S.**, Crosstalk in NF-κB signaling pathways. *Nat. Immunol.* 2011. **12:** 695–708.

35 **Bode, K. A., Schmitz, F., Vargas, L., Heeg, K. and Dalpke, A. H.**, Kinetic of RelA activation controls magnitude of TLR-mediated IL-12p40 induction. *J Immunol.* 2009. **182:** 2176–2184.

36 **Ito, H. and Hamerman, J. A.**, TREM-2, triggering receptor expressed on myeloid cell-2, negatively regulates TLR responses in dendritic cells. *Eur. J. Immunol.* 2011. **42:** 176–185.

37 **Bai, Y., Qian, C., Qian, L., Ma, F., Hou, J., Chen, Y., Wang, Q. et al.**, Integrin CD11b negatively regulates TLR9-triggered dendritic cell cross-priming by upregulating microRNA-146a. *J. Immunol.* 2012. **188:** 5293–5302.

38 **Ramirez-Carrozzi, V. R., Braas, D., Bhatt, D. M., Cheng, C. S., Hong, C., Doty, K. R., Black, J. C. et al.**, A unifying model for the selective regulation of inducible transcription by CpG islands and nucleosome remodeling. *Cell.* 2009. **138:** 114–128.

39 **Zarubin, T. and Han, J.**, Activation and signaling of the p38 MAP kinase pathway. *Cell Res.* 2005. **15:** 11–18.

40 **Saccani, S., Pantano, S. and Natoli, G.**, p38-Dependent marking of inflammatory genes for increased NF-kappa B recruitment. *Nat. Immunol.* 2002. **3:** 69–75.

41 **Wang, H., Syrovets, T., Kess, D., Büchele, B., Hainzl, H., Lunov, O., Weiss, J. M. et al.**, Targeting NF-kappa B with a natural triterpenoid alleviates skin inflammation in a mouse model of psoriasis. *J. Immunol.* 2009. **183:** 4755–4763.

42 **Wang, H.**, Activated macrophages are essential in a murine model for T cell-mediated chronic psoriasiform skin inflammation. *J. Clin. Invest.* 2006. **116:** 2105–2114.

43 **Bachmaier, K., Krawczyk, C., Kozieradzki, I., Kong, Y. Y., Sasaki, T., Oliveira-dos-Santos, A., Mariathasan, S. et al.**, Negative regulation of lymphocyte activation and autoimmunity by the molecular adaptor Cbl-b. *Nature.* 2000. **403:** 211–216.

44 **Thien, C. B. and Langdon, W. Y.**, Cbl: many adaptations to regulate protein tyrosine kinases. *Nat. Rev. Mol. Cell. Biol.* 2001. **2:** 294–307.

45 **Bachmaier, K., Toya, S., Gao, X., Triantafillou, T., Garrean, S., Park, G. Y., Frey, R. S. et al.**, E3 ubiquitin ligase Cblb regulates the acute inflammatory response underlying lung injury. *Nat. Med.* 2007. **13:** 920–926.

46 **Adair-Kirk, T. L. and Senior, R. M.**, Fragments of extracellular matrix as mediators of inflammation. *Int. J. Biochem. Cell B.* 2008. **40:** 1101–1110.

47 **Lu, H., Smith, C. W., Perrard, J., Bullard, D., Tang, L., Shappell, S. B., Entman, M. L. et al.**, LFA-1 is sufficient in mediating neutrophil emigration in Mac-1-deficient mice. *J. Clin. Invest.* 1997. **99:** 1340–1350.

48 **Chiang, Y. J., Kole, H. K., Brown, K., Naramura, M., Fukuhara, S., Hu, R. J., Jang, I. K. et al.**, Cbl-b regulates the CD28 dependence of T-cell activation. *Nature.* 2000. **403:** 216–220.

49 **Takeshita, S., Kaji, K. and Kudo, A.**, Identification and characterization of the new osteoclast progenitor with macrophage phenotypes being able to differentiate into mature osteoclasts. *J. Bone Miner. Res.* 2000. **15:** 1477–1488.

Abbreviations: **LFA-1**: lymphocyte function-associated antigen 1 · **Mac-1**: macrophage-1 antigen

Full correspondence: Dr. Jessica A. Hamerman, Benaroya Research Institute, Immunology Program, 1201 9th Ave., Seattle, WA 98101, USA
Fax: +1-206-342-6572
e-mail: jhamerman@benaroyaresearch.org

Received: 21/3/2012
Revised: 3/12/2012
Accepted: 4/1/2013
Accepted article online: 11/1/2013

